



**STUDENT
EEICT**

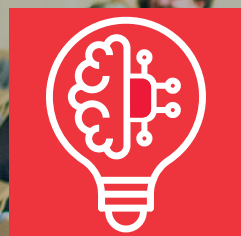
**BRNO UNIVERSITY OF TECHNOLOGY
FACULTY OF ELECTRICAL ENGINEERING AND COMMUNICATION**

PROCEEDINGS II OF THE 28TH STUDENT EEICT 2022
ELECTRICAL ENGINEERING, INFORMATION SCIENCE,
AND COMMUNICATION TECHNOLOGIES
SELECTED PAPERS

**April 26, 2022
Brno, Czech Republic**



**BRNO FACULTY OF ELECTRICAL
UNIVERSITY ENGINEERING
OF TECHNOLOGY AND COMMUNICATION**



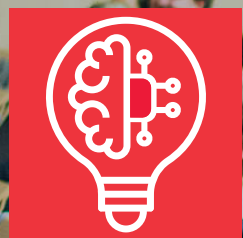
STUDENT EEICT

Title	Proceedings II of the 28 th Conference STUDENT EEICT 2022
Supervisor	Prof. Vladimír Aubrecht
Editor	Assoc. Prof. Vítězslav Novák
Publisher	Brno University of Technology, Faculty of Electrical Engineering and Communication
Year released	2022 1 st Edition

Content and language issues are the responsibility of the authors.
ISBN 978-80-214-6030-0



BRNO FACULTY OF ELECTRICAL
UNIVERSITY ENGINEERING
OF TECHNOLOGY AND COMMUNICATION



**STUDENT
EEICT**

SPONSORS

Diamond tier

Honeywell

Golden tier

Garrett
ADVANCING MOTION

onsemi

ThermoFisher
SCIENTIFIC

Valeo



BRNO FACULTY OF ELECTRICAL
UNIVERSITY ENGINEERING
OF TECHNOLOGY AND COMMUNICATION



STUDENT EEICT

SPONSORS

Silver tier



SAAB



Honored tier



ŠKODA



TECHNICAL SPONSORS & MEDIA PARTNERS



BRNO FACULTY OF ELECTRICAL
UNIVERSITY ENGINEERING
OF TECHNOLOGY AND COMMUNICATION

Contents

Foreword

M. Petrek	
Design of 6 ½ digit multimeter.....	9
J. Bures, and J. Klusacek	
Modelling of Electric Traction Vehicles with Regard to the Power Quality and Dynamics of Operation	13
V. Kaniok, T. Sýkora	
Smart home model.....	17
P. Vanek, L. Polak	
Microphone Cable Tester	21
M. Kousal, T. Frýza	
IoT Approach for Air Monitoring	27
M. Pintér, P. Raichl	
Positioning without using GNSS	31
T. Havlíková	
Piezoelectric Polyvinylidene Fluoride Nanofibers as a Scaffold used for Bone Tissue Engineering	35
P. Kopřiva, A. Otáhal	
Design of a micromanipulator for repairs of printed circuit boards	40
J. Charvot	
A Separation and Characteristics of Inner Egg Shell Membrane	45
J. Maslowski and T. Beneš	
Asset Administration Shell for PLC	49
O. Sýkora, J. Arm	
Application for Formal Testing of PLC Program	53
A. Doležal	
Control System for Management of Water Supply at a Farm	57
J. Semerád, J. Janoušek	
Fusion of Sensors for Autonomous UAV Navigation	63
A. Mošková and E. Vlachová Hutová	
Passive Optical Detection and Classification of Flying Objects	67
O. Soukenik, L. Polak, J. Kufa	
Advanced Algorithms for Compression of Videos with Ultra High Resolution	71
J. Suchacek, R. Jakubicek	
Brain Vessels Enhancement in 3D CT Data Using Eigenvalues of Hessian Matrix	75
J. Nejezchlebova, J. Schwarzerova	
Operon identifier: Identification of operon structures in the whole genome	80
P. Polakovičová, K. Sedlář	
The COG-or: the Improved Functional Annotation of Bacterial Genomes	84
W. Lazarov, Z. Martinasek	
Web Platform for Comprehensive Penetration Testing	88
D. Havránek, J. Kufa	
Weight Sensing of Beehives with IoT Connectivity	92
G. Karetka, M. Waldecker	
SDR based Shortwave Receiver	97
M. Mikulka and J. Háze	
Accumulator three phase converter	101
M. Bláha	
Implementation of procedures and evaluation of data from compliance tests of Power Generating Modules of categories A1 and A2	105
S. Macejko and J. Koudelka	
Simulations of System Wide Disturbances in the Continental Europe Synchronous Area on a Simplified Model	110
D. Ficek and M. Richter	
Pose estimation and tracking for sign language recognition	116

J. Šrámek, and O. Baštán	
Door Control Module	120
J. Novotný and T. Benešl	
Modular control system	126
M. Fiala	
Photoresist exposure via LCD panel	131
P. Brandejs, J. Skácel	
Scratch Tester	136
R. Kejzlar and J. Háze	
Automated Control of Aquarium Operation	140
M. Horník, P. Kaděra	
3D printed Double-Ridged Horn Antenna with Dielectric Lens for Free-Space Material Characterization Method	144
P. Tomíček and V. Levek	
Low noise DC amplifier with selectable gain and auto-zero functionality for use with modern integrated A/D converters	148
A. Mlčoch, P. Beneš	
Thermoanemometric flow sensor control using pulse width modulation	154
K. Pijackova, T. Gotthans, J. Gotthans	
Model Ensembling: A simple way of improving model performance for chromosome classification	158
J. Malucha	
Matlab tool for assistance in learning English words pronunciation	162
K. Heřmánková, K. Sedlář	
The Pathway Analysis of <i>Tepidimonas taiwanensis</i> LMG 22826T, Polyhydroxyalkanoate and Alkaline Protease Producer	166
M. Bubniak and P. Musil	
Quantification of a Wet Antenna Attenuation for a Measurement of Rainfall Intensity via the Metropolitan Network of Microwave Links in 10 GHz Band	172
M. Košút and A. Povalač	
CubeSat Demonstrator for Educational Purposes	176
R. Theumer and L. Langhammer	
Fractional-order integrator and its application in FLF fractional-order frequency filter	180
S. Džadíková, and Y. Safonov	
Dynamic security log processing using deep learning techniques	184
T. Cvrček, and P. Dzurenda	
Access Control System Using Multi-factor Authentication	190
P. Novák, and V. Oujezský	
Detection of Malicious Network Traffic Behavior Using JA3 Fingerprints	194
J. Mikláš and P. Procházka	
A Simple Calorimetric Measurement of SiC MOSFET Switching Loss and Comparison with Electric Measurement	198
M. Folprecht, D. Cervinka, and V. Novotna	
AC Cell Electroporation Based on Asymmetrical Waveform	204
T. Lažek, and I. Pazdera	
Comparison of two loss minimization algorithms for induction motors	210
J. Klusacek, J. Drapela	
Power Flow in Traction System and SFC Based Feeder Load Control: Sensitivity Analyses	215
P. Mičian	
Investigation of the hydrogen production by the FeCrAl nuclear fuel cladding using MELCOR 2.2	220
J. Dvořáček, J. Drápela	
A Voltage Support Schemes of Asymmetrically controlled Three-Phase Inverter-Based Generating Units	225
D. Riha	
Triboelectric Sensor – Application and Characterization	230
M. Mačák, P. Vyroubal	
Numerical Modelling of Hypersonic Flow of Spacecrafts	238
O. Mihálik and P. Fiedler	
Means of Obtaining Mamdani Fuzzy Model of Car Driver's Dynamics	243
T. Pisarenko	
Metal-organic structures as additives in polyvinylidene fluoride	248

D. Burda, A. Knápek	
Effect Of Al_2O_3 Barrier On The Field Emission Properties Of Tungsten Single-Tip Field Emitters	255
L. Zdražil, Z. Roubal	
Low-Level Measurements	259
J. Vitouš	
Correction of gradient pulse shape distortions in radial MRI.....	264
O. Mokřý, J. Vitouš	
Unfolded Low-rank + Sparse Reconstruction for MRI	271
M. Gavenčiak, V. Zvončák, and J. Mekyska	
Discovering relationship between graphomotor difficulties and isochrony in childrens online handwriting.....	276
M. Mikulec, J. Mekyska and Z. Galáž	
Parkinson's Disease Recognition based on Sleep Metrics from Actigraphy and Sleep Diaries	281
M. Ištváněk, Š. Miklánek	
Exploring the Possibilities of Automated Annotation of Classical Music with Abrupt Tempo Changes	286
T. Zemčík, K. Horák	
On Bayer demosaicing impact on image sharpness in lens quality assessment	291
P. Jedlicka, J. Hajný	
VHDL-based implementation of CRYSTALS-Kyber components on FPGA	297
P. Cívik, J. Hajný	
Secure Communication Between High-speed Network Gateways.....	303
R. Casanova-Marqués and P. Dzurenda	
Readiness of Anonymous Credentials for Real Environment Deployment.....	308
R. Juran	
Experimental Platform for Sensor Fusion Positioning Methods Evaluation	313
O. Pospíšil, P. Musil and R. Fujdiak	
Comparison of Machine Learning Models in Outdoor Temperature Sensing by Commercial Microwave Link	318
A. Kovalova and L. Hudcova	
Beam Deflection Analysis of the Turbulent Matrix Model	323



STUDENT EEICT

OPENING WORD OF THE DEAN

These Proceedings contain papers presented during the **28th annual STUDENT EEICT conference**, held at the Faculty of Electrical Engineering and Communication, Brno University of Technology, on April 26, 2022. The fruitful tradition of joining together creative students and seasoned science or research specialists and industry-based experts was not discontinued, providing again a valuable opportunity to exchange information and experience.

The EEICT involves multiple corporate partners, collaborators, and evaluators, whose intensive support is highly appreciated. Importantly, the competitive, motivating features of the conference are associated with a practical impact: In addition to encouraging students to further develop their knowledge, interests, and employability potential, the forum directly offers career opportunities through the affiliated PerFEKT JobFair, a yearly job-related workshop and exhibition complementing the actual EEICT sessions. In this context, the organizers acknowledge the long-term assistance from the Ministry of Education, Youth and Sports of the Czech Republic, which has proved essential for refining the scope and impact of the symposium.

In total, 174 peer-reviewed full papers distributed between 23 sessions were submitted, before examining boards with industry and academic specialists. The presenting authors exhibited a very high standard of knowledge and communication skills, and the best competitors received prize money and/or small gifts. These Proceedings comprise 66 award winning full papers, all selected by the conference's evaluation boards.

Our sincere thanks go to the sponsors, experts, students, and collaborators who participated in, contributed to, and made the conference a continued success.

Considering all the efforts and work invested, I hope that the **28th STUDENT EEICT (2022)** has been beneficial for all the participants.

I believe that the inspiration gathered during the event will contribute towards a further rise of open science and research, giving all the attendees a chance to freely discuss their achievements and views.

Prof. Vladimír Aubrecht

Dean of the Faculty of Electrical
Engineering and Communication



BRNO FACULTY OF ELECTRICAL
UNIVERSITY ENGINEERING
OF TECHNOLOGY AND COMMUNICATION

Design of 6 ½ digit multimeter

Martin Petrek¹

¹ Department of Electrical and Electronic Technology, Brno University of Technology, Czech Republic

E-mail: martin.petrek@vutbr.cz

Abstract—Paper summarizes individual parts of DMM (digital multimeter) and how they work. Design approach in comparison to commercial solution is in the thermal stabilization of the whole analog assembly. DMM has 8 custom designed PCBs (printed circuit board): Processor PCB, Keyboard and input backlit PCB, Analog PCB, Voltage reference PCB, Thermostat PCB, AC/DC PCB and LDO (Low dropout voltage regulator) PCB. User interface, program, thermal stabilization and mechanical construction are also described.

Keywords— 6 ½ digit multimeter, LTZ1000A, design, testing, bench multimeter, measuring device, ovenized multimeter, DMM, precise instrumentation

1. INTRODUCTION

In 2019 I decided to design and build a precise bench multimeter with thermal stabilization on budget, with parameters as in Table I: Projected parameters. After few design iterations and talks to experts I let out the budget limitation and continued designing. After a year of intermittent design, I started the process of gathering parts and finances to build the first prototype as you can see in the Figure 2: First prototype. In time of writing this paper, first prototype is built and now it is in process of programming and solving all problems which every first prototype has.

2. COMPONENTS AND PCB'S

Multimeter can be divided into block diagram showed in the Figure 1: Block diagram

User interface: Measured values are displayed on 3.5" Nextion touch screen [7]. It uses its own 48 MHz microcontroller and data are transferred to it via serial bus at speed of 115200 baud. Display is programmed in its own language. For most used actions, such as change of measuring function or START/STOP of acquisition, there is membrane keyboard with custom backlit. Banana input is also backlit for visual representation of used input terminals.

Program: Microcontroller of DMM, two-core 32bit 240 MHz ESP32 is programmed in C/C++. First core is used for programming ADC (analog to digital converter) digital filter, starting conversions and reading its result. Result is in a format of 32-bit binary number which is converted to decimal number. Slope and offset are added according to measured function and range. Acquisition frequency can be determined either by NPLC (number of power line cycles) or Sa/s (Samples per second). When NPLC is higher or equal to one, then ADC will start new conversion on every rising and falling edge of mains sinus. After desired number of NPLC the results are averaged and displayed. There is also filtering which happens inside of ADC which can't be explained due to size restrictions of this paper. Second core handle practically everything else: preparing and sending data to Nextion display as well as reading data from Nextion display, reading keyboard state, power button state, controlling input and keyboard backlit, changing ranges and controlling circuitry of Analog PCB. DMM can be also controlled through SCPI commands which are processed with second core. For now, it accepts commands via USB, but ESP32 has built in Wi-Fi and Bluetooth.

Thermal stabilization: Change in temperature can affect the parameters of all components. To fight this, DMM not only use stable resistors with very low thermal coefficient, but it also has ovenized analog PCB with reference PCB. This is done with fully analog thermostat regulator [1] with small processor cooler inside of thermally isolated 3D printed box where analog and reference board are located. This mean that maximum temperature of multimeter will by determined by oven temperature subtracted with temperature raise caused by self-heating of components. Minimum temperature, on the other hand, will be determined by isolation effectivity of box and power of heater which is about 30 W. To measure the

temperature and its stability inside of oven, there is platinum resistance thermistor and 24-bit ADC on Analog PCB.

Mechanical construction: Whole body is assembled with laser cut and CNC bent 1 mm thick stainless steel. This 4-segment body holds all PCBs and acts as most outer EMI shield. Front and back of the multimeter are finished with 3D printed PLA panels. In the middle section of the multimeter a 3D printed containment with very low infill, acting like thermal insulation for proper working of thermostat. This middle section is also isolated with stainless steel sheets for EMI shielding.

PCBs: The multimeter has total of 8 PCBs with 2 and 4 layers.

Processor PCB: 2-layer PCB. It is an important part of user interface which controls all backlit LEDs with three eight-channel serial to parallel convertors [8] and drivers. Keyboard and power button presses are monitored with parallel to serial converter. Microcontroller is socketed for easy change. Buzzer is used for sound notification.

Keyboard and input backlit PCB: 2-layer boards for custom backlit of keyboard keys and input banana plugs. Keys are backlit with red/green and white color LEDs depending on key usage. Input banana plugs are backlit with green LEDs only.

Analog PCB: 4-layer board. Board has four front ends for measuring voltage, voltage with high impedance, small currents ($I \leq 10 \text{ mA}$) and medium currents ($I \leq 1 \text{ A}$). Every front end has multiple protections in front and within it. First protections are high-energy fuses which are protecting against longer lasting overloads and are capable to safely disconnect multimeter from measured circuit. There is 440 mA fuse for small currents and all voltage measurement front ends and 3 A fuse for medium currents front end. MOV and gas discharge tube are also located in front of voltage measurement front ends. Schottky diodes, Zener diodes and TVS diodes are protecting sensitive component inside front ends. With combinations of front ends it is possible to measure: resistance in 2W or 4W mode, diode, continuity, temperature and capacitance. Signal from these front ends is switched with analog multiplexers, buffered, filtered and fed to 32-bit SAR Oversampling ADC LTC2500-32 [3] with configurable digital filter. In ADC is analog signal quantized to digital signal which is transmitted to MCU via optocoupler. Used ADC has fully differential inputs, but in effort to reduce noise, there is no circuitry to convert input signal to fully differential mode. Instead, negative input of ADC is connected to $V_{\text{REF}}/2$ and positive input of ADC is just buffered with op amp and is ranging from GND to V_{REF} . This lowers the resolution of ADC to 31-bits, which is still more than sufficient resolution for count of 1 000 000. Ranges are set with combination of analog multiplexers, relays and anti-serially connected P-Channel MOSFETs. All relays, MOSFETs and analog multiplexers are controlled through four eight-channels serial to parallel convertors. All digital signals are galvanically isolated from Processor PCB via two six-channel optocouplers.

Voltage reference PCB: 4-layer PCB with most stable, voltage reference on chip, which you can buy in quantity of one. LTZ1000A [2] is buried Zener diode with its own heater for lowering thermal coefficient to only 0.05 ppm/°C [2]. This is achieved by heating diode to stable temperature which do not change with ambient temperature. How stable the temperature will be is determined by resistors used in controlling circuitry. 0.02 ppm/°C foil resistor [6] and 8 ppm/°C resistor networks [5] are used in first prototype for setting temperature and current through Zener diode and for lowering its output voltage from circa 7.2 V to 5 V.

Thermostat PCB: 4-layer PCB. Schematic from “Thermal compensation of the optical RF delay lines for SPS damper” [1] slightly modified by me. Used and modified with author's permission. Board is designed by me to fit inside the multimeter.

AC/DC PCB: 2-layer PCB. It takes mains AC 230 V and convert it to more manageable DC voltages. Transformer is used for processor board power supply because its sinus output is used for synchronizing a frequency of ADC conversions with mains to reduce noise. All AC/DC and DC/DC convertors are medical grade. Output from this PCB is 6 V 2 A AC, 3.3 V signal for mains frequency synchronization, +9 V 1670 mA DC, $\pm 15 \text{ V}$ 200 mA DC and +5 V 6 A DC with -5 V 200 mA DC for Thermostat PCB.

LDO PCB: 4-layer PCB. It uses Ultralow Noise, Ultrahigh PSRR Linear Regulators [4] to filter a voltage from AC/DC, DC/DC convertors and transformer. Output from this PCB is +5 V 1.5 A DC for Processor PCB and +0.5 V 10 mA DC, +2.5 V 200 mA DC, +4.5 V 10 mA, +5 V 400 mA DC, +5V 1 A DC, 2x +14 V 200 mA DC, -5 V 200 mA DC, -14 V 200 mA DC for Analog board.

3. FIGURES AND TABLES

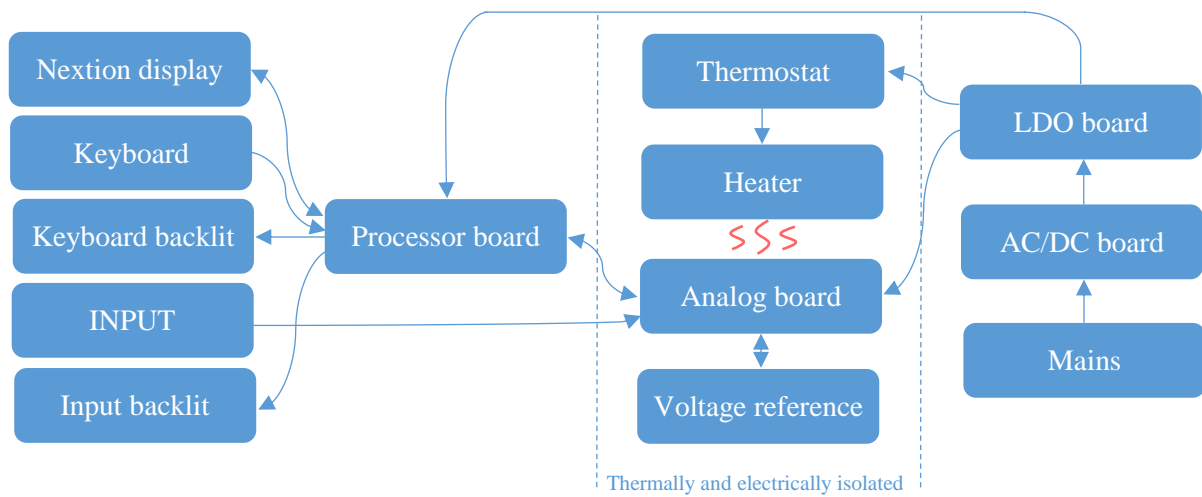


Figure 1: Block diagram

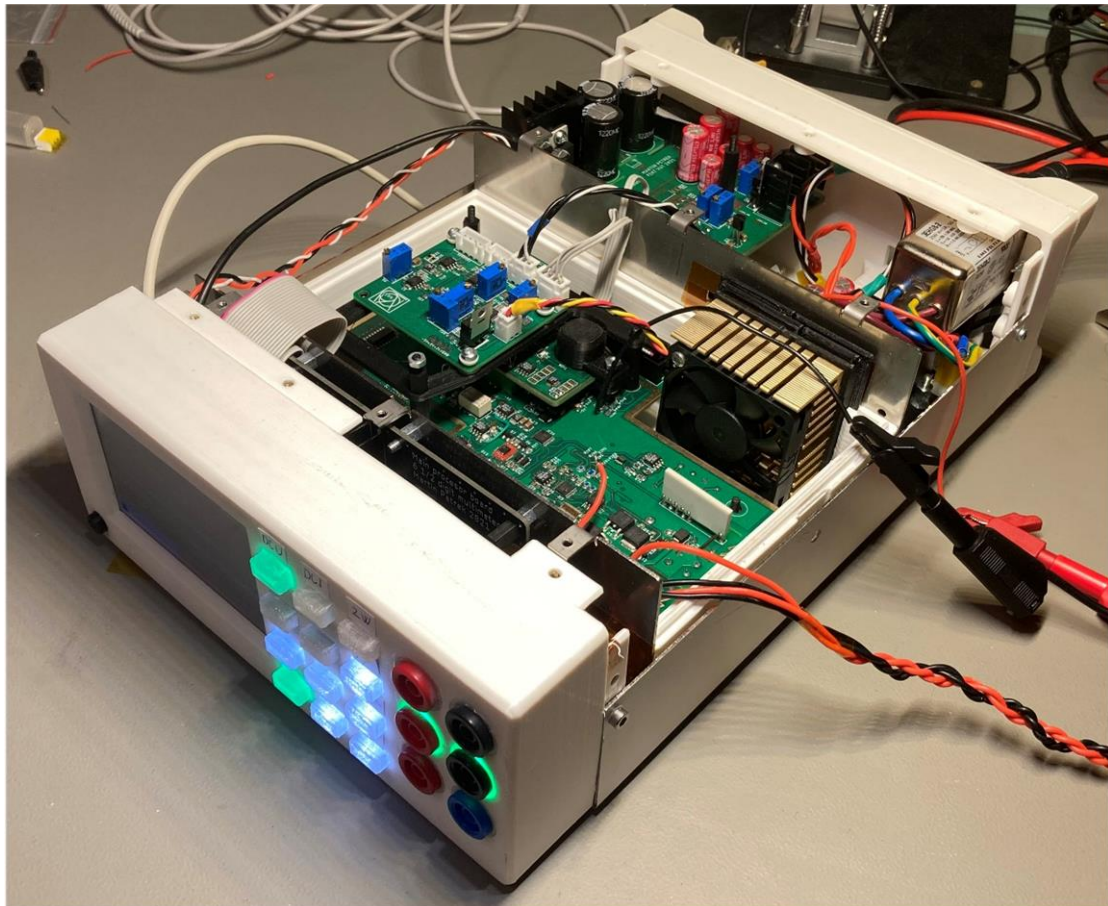


Figure 2: First prototype

Table I: Projected parameters

Count	1 000 000	
Best accuracy	10 ppm	for 10 V DC rage
Function	Range	Best resolution
DC Voltage	10 mV – 1 kV	10 nV
AC Voltage	10 mV _{p-p} – 1 kV _{p-p}	10 nV _{RMS}
DC Current	10 nA – 1 A	10 fA
AC Current	10 nA _{p-p} – 1 A _{p-p}	10 fA _{RMS}
2W Resistance	1 Ω – 100 M Ω	1 $\mu\Omega$
4W Resistance	1 Ω – 100 M Ω	1 $\mu\Omega$
Diode	2 V, selectable current: 100 pA -10 mA	1 μ V
Temperature	RTD – depends on type	100 $\mu^\circ\text{C}$
Continuity	Programable current	depends on frequency of ADC conversions

4. CONCLUSION

I'm only to see if I managed to complete all projected parameter with this first prototype. Right now, I'm in process of programming and multimeter works like it is designed. It was my most challenging and longest lasting project. My eventual goal is to make it my bachelor project, but for that I have more than a year.

ACKNOWLEDGMENT

I want to thank doc. Ing. Daniel Valúch Ph.D. for help and guidance with designing and troubleshooting of this project.

I also want to thank Ing. Ondřej Čech Ph.D. with help of finding founding's for this project and guidance.

REFERENCES

- [1] A. Lasak, "Thermal compensation of the optical RF delay lines for SPS damper," 2016, [Special e-cloud bunch spacing: ADT compatibility \(cern.ch\)](#).
- [2] Linear Technology, "LTZ1000A," 1987, [LTZ1000/LTZ1000A - Ultra Precision Reference \(analog.com\)](#).
- [3] Analog Devices, "LTC2500-32," 2018, [*LTC2500-32 - 32-Bit Oversampling ADC with Configurable Digital Filter \(analog.com\)](#)
- [4] Analog Devices, "LT3042," 2017, [LT3042 - 20V, 200mA, Ultralow Noise, Ultrahigh PSRR RF Linear Regulator \(analog.com\)](#)
- [5] Analog Devices, "LT5400," 2011, [LT5400 - Quad Matched Resistor Network \(analog.com\)](#)
- [6] Vishay Foil Resistors, "Y1629120R000Q9R," 2015, [VFCEP Series \(Z-Foil\) - Datasheet \(vishaypg.com\)](#)
- [7] Nextion, "NX4832T035," 2011, [NX4832T035 - Nextion](#)
- [8] Texas instruments , "74HC595," 2021, [SNx4HC595 8-Bit Shift Registers With 3-State Output Registers datasheet \(Rev. J\) \(ti.com\)](#)

Modelling of Electric Traction Vehicles with Regard to the Power Quality and Dynamics of Operation

J. Bures¹, and J. Klusacek¹

¹Dept. of Electrical Power Engineering, FEEC, Brno University of Technology, Czech Republic

E-mail: 220755@vut.cz, klusacekj@vut.cz

Abstract—The article deals with modelling of traction vehicles being operated in the Czech Republic in the 25 kV/50 Hz power system with respect to their consumption quality and power consumption. Models of typical locomotive categories, sorted according to their electrical equipment and typical power quality, were created in PSCAD . The models are able to simulate the locomotives dynamical operation up to the detail of power quality.

Keywords—Electric traction system, power quality, locomotive, equation of motion, PSCAD

1. INTRODUCTION

The aim of the article is to show the consumption quality of traction vehicles as a result of different topology of traction equipment of real locomotives. The main motivation is to observe the effect of traction vehicles on the traction feeder (TF) and the conversion transition from traction transformers to static converters [1]-[3]. Simple models representing the real traction vehicles enable simulation of the realistic train operation, powered from the 25 kV/50 Hz traction power system (TS) and to observe the effects that individual vehicles have on the TF. Individual parametrization of a train set in combination with external description of motion brings the possibility of evaluation both on the level of power flow and also in the detail of power consumption quality criteria: 1) current waveform harmonic distortion, 2) power factor and 3) total distortion ratio $TDR = \sqrt{I_{RMS}^2 - I_1^2} / I_1$, where I_{RMS} is RMS value of the current and I_1 is RMS value of the fundamental [4]. If there are more trains present on the line, it is possible to simulate and evaluate how they mutually affect each other during the operation with the option to choose the distance “TF-train” or “train-train”.

2. MODELLING OF A LOCOMOTIVES

Three simplified models of locomotives, called Loc 1, Loc 2 and Loc 3 where created in order to simulate the consumption character of real locomotives used in the Czech Republic. The differences are represented in Figure 1. Loc 1 uses a transformer with 32 taps, full-wave rectifier and DC traction motor as their traction equipment. The model obeys this topology while DC motors are replaced by resistors. The character of the current consumed from the catenary line (CL) is determined by the topology and by high inductance of the traction equipment of locomotives thus the current is deformed. Loc 2 represents locomotives which consists of full-wave rectifier, DC-DC step-down converter with thyristor and DC traction motors. The waveform of the consumed current is distorted similarly as for Loc 1 but the waveform is rippled with pulse-width modulation of the DC-DC converter (switching frequencies 33 1/3 Hz, 100 Hz and 300 Hz, depending on operational state). The Loc 3 traction equipment consists of transformer, active rectifier with a DC filter, three-phase DC-AC inverter and asynchronous traction motors. In the model, an active rectifier is used on the secondary windings of the transformer, where the asynchronous motor is represented by a current source that allows the power to be varied and capable of reverse the current direction. The consumed current is sinusoidal with superposed ripple caused by the pulse width modulation, attenuated by the input filter [5]. Replacing traction motors with a resistor or current source on all locomotives is a relevant solution because of the power draw and the effect of traction motors on the quality of the draw is neglected in this stage. Due to simplification of the traction equipment topology of the locomotives and of the simulation data, the waveforms of consumed current are idealized in contrast with the reality, nevertheless they show the typical signs and are sufficient for the demonstration of the difference in consumption quality of real locomotives.

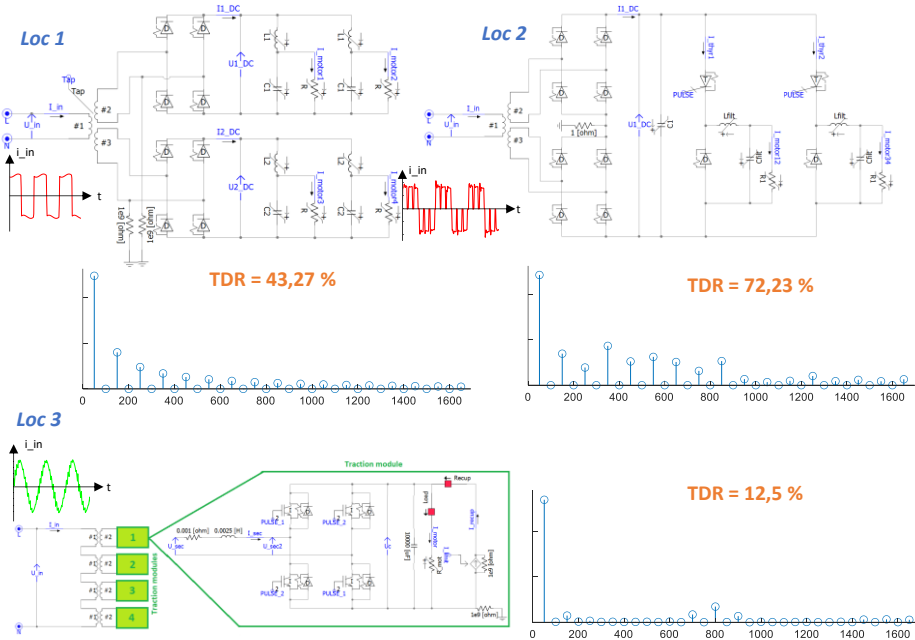


Figure 1: Simplified diagrams of Loc 1, Loc 2 and Loc 3 traction circuits with the character of the consumption current waveform.

3. DESCRIPTION OF THE MECHANICAL MOTION OF THE TRAIN

Except of the consumption quality simulation, a simulation of train motion and consumption evaluation at the level of energy flows. Train motion is described by means of the equation of motion that expresses the total mechanical torque M_{mech} on the shaft of the locomotive:

$$M_{mech} = M_A(s) + M_B(\omega) + J \cdot \frac{d\omega}{dt} = M_A(s) + k_B \cdot \omega + J \cdot a_{max}, \quad (1)$$

where $M_A(s)$ is the torque depending on the track slope, s is the track slope, $M_B(\omega)$ is torque needed to overcome the driving resistance, k_B is the coefficient representing the torque needed to overcome the driving resistance, ω is the angular speed of the axle, $J \cdot d\omega/dt$ represents the acceleration torque, where J stands for the total torque of inertia of the train and a_{max} is the maximal possible angular acceleration in the actual locomotive state. The mechanical power is calculated as:

$$P_{mech} = M_{mech} \cdot \omega = M_A(s) \cdot \omega + k_B \cdot \omega^2 + J \cdot a_{max} \cdot \omega. \quad (2)$$

Both of the equations are used for the torque characteristics of individual traction vehicles. It is divided into the area of constant power and constant torque. Demonstrative example of torque characteristics and mechanical power dependency on angular velocity of the axle of the locomotive class 242 is shown in Figure 2. Implementation of the equation of motion into individual models uses the law of energy conservation when mechanical power in the equation of motion corresponds with the electrical power of the resistive load in the locomotive models. This equivalence is provided by power regulator preserving the equivalence of calculated mechanical power of the locomotive and the active electrical power at the locomotive input for Loc 1 and Loc 2. Loc 3 holds the DC link voltage thus providing the power control.

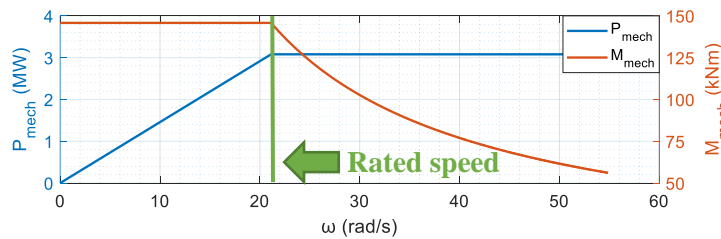


Figure 2: Torque characteristic including dependence of mechanical power on axle angular velocity of locomotive class 242.

4. SIMULATION OF THE OPERATION

The analysis of mutual influence of locomotives with different traction equipments and different nominal powers uses a model of CL with a TF 25kV/50Hz. The functionality of this model is demonstrated by models Loc 2 and Loc 3 (Figure 3).

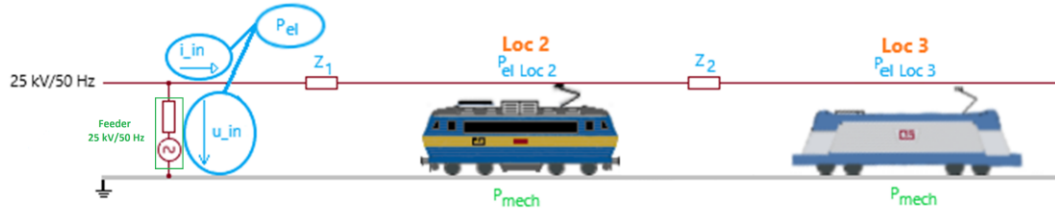


Figure 3: Model of single-track line with Loc 2 and Loc 3.

Consumed electric power of these locomotives is controlled to be equal as the mechanical power which is a result of the equation of motion (2). Figure 4 shows performance of the power regulators in Loc 2 and Loc 3 with different nominal powers; Loc 2 represents locomotive class 362, with nominal power 3060 kW and Loc 3 represents locomotive class 380 with nominal power 6400 kW. The Figure 4 shows the situation that only one locomotive is being operated on CL and it can be seen that in both cases the consumed electric power is in accordance with the calculated mechanical power after the initialization of the regulators. The power consumed from the TF is increased by the losses in the CL sections, having impedances Z_1 and Z_2 . The impedance per km value is $(0,26+j0,45) \Omega/\text{km}$ according to the [6], for single-track. The rail impedance is omitted due to the fact that its value is by order of magnitude lower, than impedance of the CL.

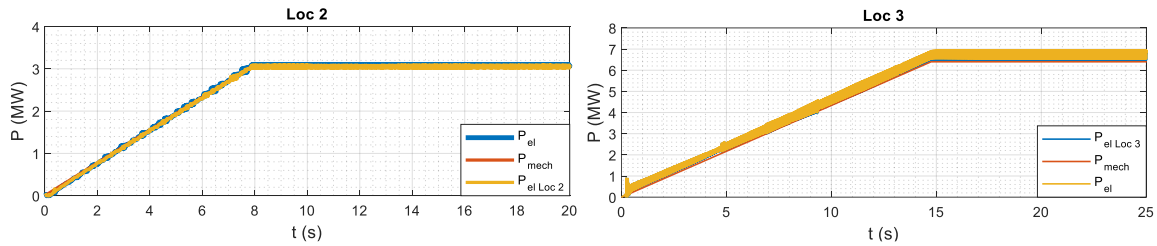


Figure 4: Mechanical power from motion equations and electrical power at the feeder during solely Loc 2 and solely Loc 3 acceleration.

In the next scenario, the simulation of Loc 2 and Loc 3 influencing each other is presented. The resulting power drawn from the electrical station is shown in Figure 5. The scenario begins with the start of Loc 3 up to power 3060 kW (see part I), which is also the nominal power of Loc 2. In the part II, the power consumed from the electrical station is increased as the Loc 2 increases the power up to nominal 3060 kW while Loc 3 still consumes 3060 kW. In the part III, the electric energy from Loc 3 is being recuperated back to the CL by 3060 kW of power and Loc 2 still consumes 3060 kW. The power supplied from Loc 3 to Loc 2 during the recuperation is decreased by the loss power in the impedance Z_2 , which is compensated by the power from the feeder. The locomotives are 1 km apart from each other at CL. In the part IV, the electrical station is loaded by the Loc 2 power only.

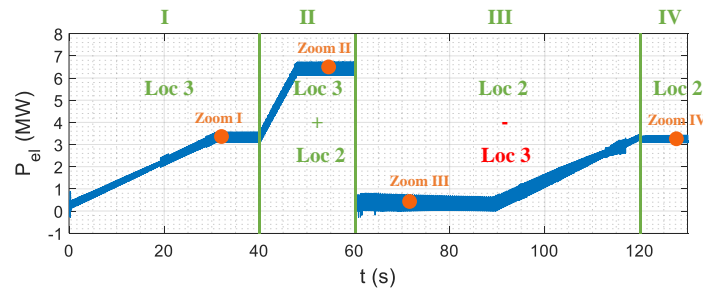


Figure 5: Flow of power drawn from the feeder during Loc 2 and Loc 3 operation.

Figure 6 shows waveforms of the feeder currents which is a sum of both locomotives currents. It is obvious that although the power supplied and the power consumed of Loc 2 and Loc 3 are in equilibrium, the energy exchange between the TS and the DS occurs. Disregarding the loss power in the catenary it is being generally classified as a non-active power.

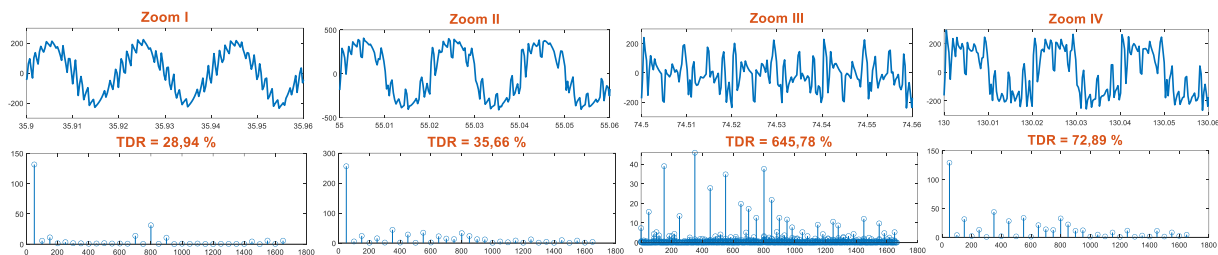


Figure 6: Current fed from the feeder during Loc 2 and Loc 3 operation.

5. CONCLUSION

According to the real topology of traction equipment, the simplified models that keep the basic principle of real traction vehicle behavior were created. Therefore, the influence of traction vehicles on 25 kV/50 Hz TS could be simulated to the detail of the power quality. The comparison of Loc 2 and Loc 3 by means of TDR has been demonstrated and the model has been tested simultaneously. The scenario of operation of two locomotives of different quality consumption points out the interaction of two locomotives by means of sum of the currents at the TF. The locomotive models can be also used for study and analysis of traction vehicles interaction with filtering-compensating devices connected to the TS or with other types of electrical stations, e.g. static converters. Models are universal so they can be parametrized by nominal parameters of various traction vehicles. Moreover, the Loc 3 can be enhanced with models of static converters of various topologies, being deployed in the modern traction vehicles.

ACKNOWLEDGMENT

This research work was carried out in the Centre for Research and Utilization of Renewable Energy. Authors gratefully acknowledge financial support from the Ministry of Education, Youth and Sports of the Czech Republic under BUT specific research programme (project No. FEKT-S-20-6449).

REFERENCES

- [1] AUBERT, S., Ph. MAIBACH, Th. SCHAAD, C. BANCEANU a Ch. ZHAO. *Static frequency converters – a flexible and cost efficient method to supply energy single phase railway grids in Australia*. ABB Switzerland Ltd.: AusRail 2015, 12.
- [2] Ufert, Martin. (2016). Static frequency converters in 50 Hz traction power substations. *eb - Elektrische Bahnen INT*. 114. 414-419.
- [3] RADIL, Lukáš, Jan KLUSÁČEK, Jiří DVOŘÁČEK a Jiří DRÁPELA. *Integrace statických frekvenčních měničů pro napájení AC trakční soustavy do distribuční soustavy z pohledu kvality elektrické energie*. ČK CIREĐ. 2021.
- [4] *Electromagnetic compatibility (EMC) - Part 2-4: Environment - Compatibility levels in industrial plants for low-frequency conducted disturbances: IEC 61000-2-4:2002*. 2002.
- [5] M. Brenna, et al. Current Distortion Evaluation in Traction 4Q Constant Switching Frequency Converters. 2009, doi:10.4236/jemaa.2009.13021
- [6] *Nastavovanie, prevádzka a údržba reléových ochrán trakčného napájacieho obvodu: Služobná rukoväť, SR 34 (E)*. (In Slovak) Praha: Nakladatelství dopravy a spojů

Smart home model

V. Kaniok, T. Sýkora

Brno University of Technology
Faculty of Electrical Engineering and Communication
Department of Control and Instrumentation
616 00 Brno, Technická 3082/12, Czech Republic

E-mail: 203244@vut.cz, 173753@vut.cz

Abstract—This article deals with the smart home and technology stack behind for properly secure and reliable system. Clarify different approaches to communication protocols and consider obstacles to these protocols. The model shows the cooperation of devices of multiple brands. The main benefit of the model is the expansion of awareness of the general public and the possibility of inclusion in students' teaching.

Keywords— smart home, MQTT, Home Assistant, ZigBee, home automation, IoT

1. INTRODUCTION

This article provides an introduction to home automation and introduces the technologies used for communication between devices. It also discusses the issue of compatibility of devices from different manufacturers on the Home Assistant platform. This platform is the most widely used open-source platform for home automation and IoT(Internet of Things). Many manufacturers officially support integration into Home Assistant and those that have not done this are often covered by the community with their support.

2. HOME AUTOMATIONS PLATFORMS

In today's market is a lot of options to choose from. Some manufacturers developing own platforms, but if you choose one of these platforms, you are vendor-locked probably for the rest of your life. And thus you are forced to buy all the equipment from one manufacturer. Another key difference between home automation platforms is where services are hosted. A lot of these systems are cloud-based, meaning that once your internet goes down you lose all the smart features. Sometimes even the actual functionality of switches and other smart devices is affected. Another downside to these cloud-based systems is the legitimate privacy concerns about these very personal data, with all of these devices providing information about your behaviour in the home, from data like when you usually come home to when you turn off the last light and head to bed. That's why our chosen system is Home Assistant, which, unlike cloud solutions, runs on a local device, so all the data doesn't need to leave your private network. Another indisputable advantage of Home Assistant is its ability to be completely customised to the user's requirements and the countless official integrations and add-ons.

2.1. Home Assistant

Home Assistant is free open-source software for creating and controlling home automation. It is a complete hub for smart home. The main application is written in python and the first version was released in 2013. According to the GitHub State of the Octoverse¹, in 2020 it became the second largest open-source project by number of contributors that is written in python. Home assistant also has apps on android, iOS and watchOS. Most commercial IoT and Home automation products have an official add-on available for this system, there are over 1700 of these official add-ons available. Home assistant's biggest focus is on security. It is a local solution therefore the data is not stored anywhere but on your device, this

¹Based on statistics published on <https://octoverse.github.com/>

is one of the biggest advantages over cloud services and other proprietary systems. It can also connect to well-known home automation ecosystems such as Google Home, Apple HomeKit, Mi Home, IKEA Smart Home. With an emphasis on security, it is possible to set which entities will be available for each of these services. UI (User interface) of home assistant is named Lovelace and an example of dashboard created in Lovelace you can see in Figure 1.

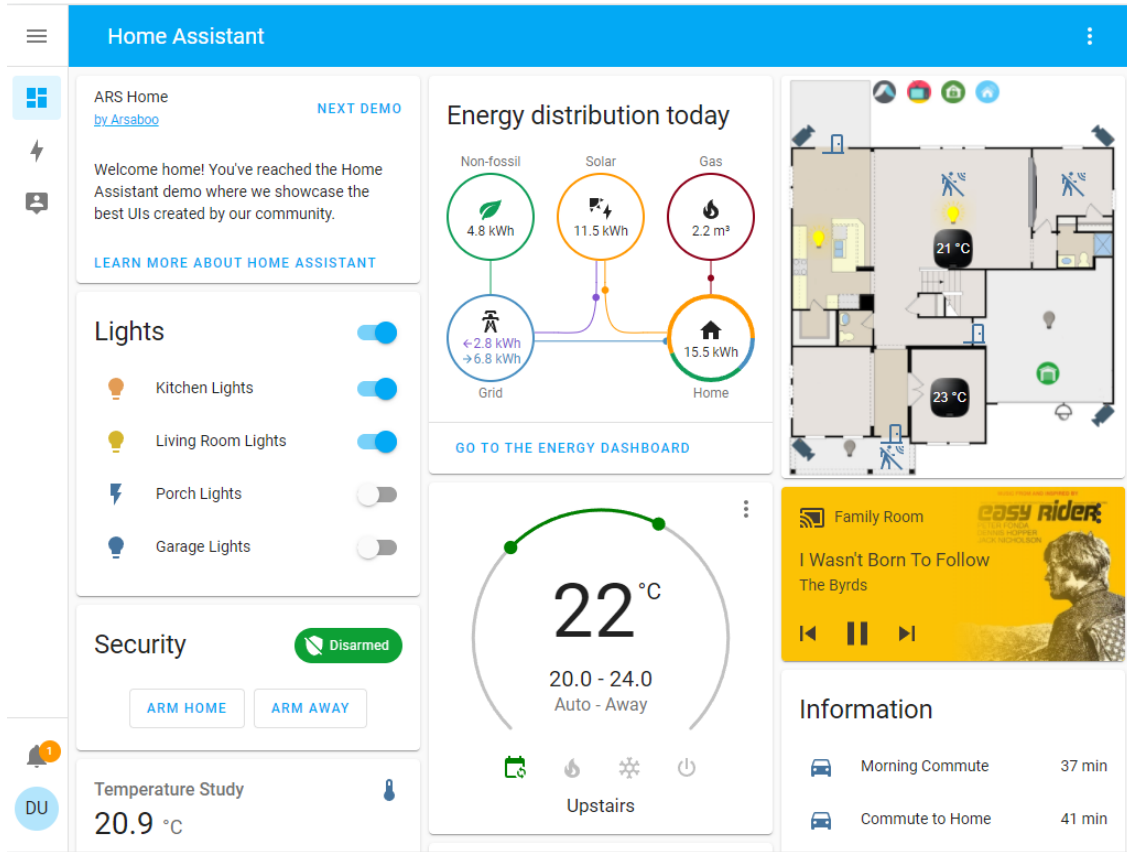


Figure 1: Home Assistant UI Lovelace[1]

3. COMMUNICATION TECHNOLOGY

This section describes the communication technology that is used on the smart home model.

3.1. MQTT

MQTT (Message Queuing Telemetry Transport) is a communication protocol originally developed by Andy Stanford-Clark and Arlen Nipper in 1999 for the transmission of oil pipeline monitoring data from the desert, so it emphasizes efficient use of the data stream, overall lightweighting and low battery requirements. The name is historically derived from the IBM MQ product line. IBM standardized this protocol with the OASIS (Organization for the Advancement of Structured Information Standards) standard, then version 3.1 also received ISO (International Organization for Standardization) standardization. MQTT is a publish/subscribe protocol that introduces the concepts of client and broker as shown in Figure 2. The broker receives all messages from each client and then forwards them according to the subscription topic to the clients. The information is organized by "topic". MQTT is based on the TCP (Transmission Control Protocol) protocol, which can be encrypted using TLS(Transport Layer Security)/SSL(Secure Sockets Layer). Both client and broker must have a TCP/IP stack. [2]

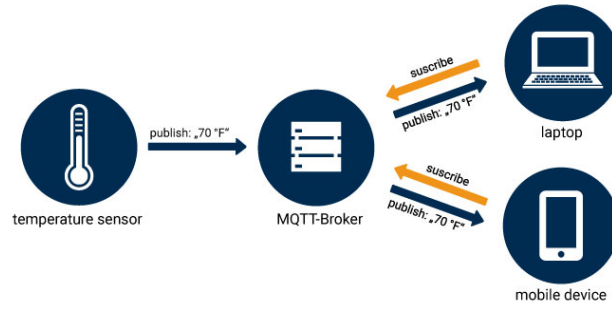


Figure 2: Schema of MQTT communication protocol [3]

The main advantages of MQTT [4]

- Lightweight protocol with the main focus on data minimization
- Topic based protocol for controlling scope of recipients
- Easy scalability up to millions of devices
- QoS (Quality of Service) specifying the importance of the messages sent
- TLS provides communications security over a computer network.

3.2. ZigBee

Zigbee is a mesh wireless protocol. It strengthens and expands the network by using a device to relay a signal to other devices. When compared to Wi-Fi, the advantage is lower energy consumption. The most recent version, ZigBee 3.0, promises improved device and version interoperability.

ZigBee2MQTT is the layer that translates ZigBee device messages to the MQTT broker and vice versa. The main advantage is then a unified communication platform. Schema of communication through Zigbee2MQTT and broker with the home assistant you can see in Figure 3.

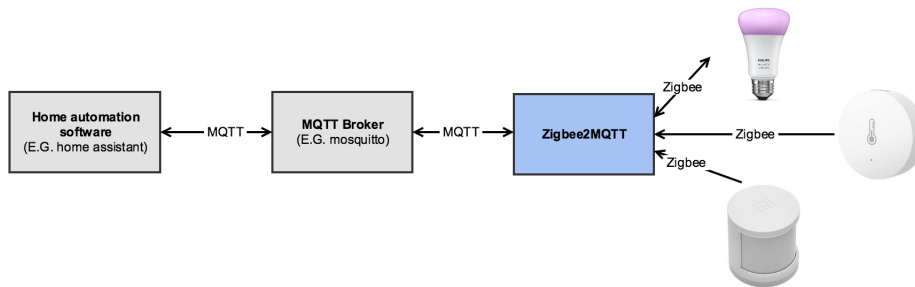


Figure 3: Schema of ZigBee2MQTT [5]

3.3. Wi-Fi

Wi-Fi is a set of wireless network protocols based on the IEEE 802.11 standard family. The 2.4 gigahertz (120 mm) UHF (Ultra High Frequency) and 5 gigahertz (60 mm) SHF (Super High Frequency) radio bands are the most often used for Wi-Fi, and both bands are split into several channels. In our case, Wi-Fi devices will use a some proprietary protocol or directly MQTT as a communication protocol.

4. SMART HOME MODEL

This section is describing the construction and used communication technologies in our model.

4.1. Communication

Our smart home model uses a combination of these communication protocols. The main gate of communication between devices and the backend is the MQTT broker. For ZigBee devices, we use translating layer of ZigBee2MQTT which translate messages between these two layers of communication. Some devices use proprietary protocol on Wi-Fi, with device manufacturer integration to communicate.

4.2. Construction

The frame structure itself is aluminium and is divided into six rooms, each representing a different segment of the house. For example, in the utility room there is a water meter, a water leak sensor and a light bulb simulating a valve to close the main water supply. In programmed automation, when a water leak is detected, the water supply is stopped and a notification is sent to the owner.

4.3. Devices used in model

The model combines Sonoff, Aqara, IKEA and our ESP32 device. Different types of switches are used such as fully wireless, wired without neutral. Furthermore, the combination of bulbs both via Wi-Fi and ZigBee. Smart sockets built directly into the installation box, smart attachments to existing sockets or switches for existing sockets. Camera system with motion detection and motion detector itself.

5. CONCLUSION

The aim of this article is to improve the overall availability of Smart home systems, with the desired result being an increased number of smart homes practising effective energy management.

The second section is sum up home automation platforms and introduces the chosen one the Home Assistant The Home Assistant platform is rapidly evolving and keeping up with the trends of the times, which is why the current emphasis is on energy management. It includes pre-made dashboards and charts for solar panels and other sustainable sources.

The third section shows a variety of communication technology and shows their advantages. The model shows the possibility of interconnecting devices from different manufacturers into one platform using MQTT with multiple end-to-end communication sources.

This model will be used as a demonstrator of a smart home and will create space for the implementation of new final theses on this topic.

ACKNOWLEDGMENT

The completion of this paper was made possible by the grant No. FEKT-S-20-6205—“Research in Automation, Cybernetics and Artificial Intelligence within Industry 4.0” financially supported by the Internal science fund of Brno University of Technology.

REFERENCES

- [1] *Home Assistant Demo* [online]. 2022 [cit. 2022-03-13]. Available from: <https://demo.home-assistant.io/>
- [2] YUAN, Michael. Getting to know MQTT. *IBM Developer* [online]. [cit. 2022-03-10]. Available from: <https://developer.ibm.com/articles/iot-mqtt-why-good-for-iot/>
- [3] MQTT_Schema. In: *OPC Router* [online]. 2020 [cit. 2022-03-13]. Available from: https://www.opc-router.de/wp-content/uploads/2020/01/MQTT_Schema_EN.jpg
- [4] 7 Advantages of MQTT protocol for IoT Devices. *Medium: esperso* [online]. 2020 [cit. 2022-02-28]. Available from: <https://medium.com/@esperso/7-benefits-of-mqtt-protocol-for-iot-e463f6a97100>
- [5] *CC2531 + ZigBee2MQTT* [online]. 2020 [cit. 2022-03-11]. Available from: https://stupidhouse.info/sites/default/files/inline-images/zigbee_cc2531_schema.png

Microphone Cable Tester

P. Vanek, L. Polak

Brno University of Technology, Faculty of Electrical Engineering and Communication,
Department of Radio Electronics, Technická 12, 616 00 Brno, Czech Republic

E-mail: xvanek39@vutbr.cz, polakl@vut.cz

Abstract—This work deals with the design and development of a time domain reflectometry method based handheld tester for microphone cables. The main aim of the work is to adopt a suitable measuring method for locating faults in microphone cables, develop electrical design and realize its practical implementation. Next, firmware for the microcontroller unit is also created. The measurement is based on a time-to-digital converter integrated circuit used in Light Detection and Ranging (LIDAR) applications. First experimental results confirmed the functionality of the proposed concept.

Keywords—Time-Domain Reflectometry, Microphone Cable, Time-to-Digital Converter

1. INTRODUCTION

During manipulation with hundreds of meters of microphone cables (e.g. a sound system of a concert hall) commonly faults could occur. To find possible faults in long cables is not an easy task. Hence, devices to localize and measure fatal faults in microphone cables are required.

In this work, a handheld device appropriate to measure and particularly localize different faults in microphone cable is introduced. As a measurement method, the impedance mismatch based time-domain reflectometry (TDR) was adopted [1]. The proposed device is developed in cooperation with company OTVP¹, which designs, manufactures and installs public address (PA) sound systems.

This short paper is organized as follows. Brief description of the TDR measurement method is presented in Section 2. The concept of the proposed microphone cable tester is described in Section 3. First outputs from the experimental verification of the realized device are discussed in Section 4. Finally, the paper is concluded in Section 5.

2. TDR METHOD

The microphone cable consists of two twisted pairs covered by metal shielding. Its structure is very close to the shielded twisted pair cables employed in Ethernet networks. The microphone cable could be understood as an impedance-matched line with characteristic impedance Z_0 . When imperfection or fault (e.g. discontinuity, short circuit) occurs in the cable, its impedance locally deviates from the value of Z_0 .

There exist several methods to localize the faults in a microphone cable. The proposed microphone cable tester adopted the TDR method. It is based on the incurred reflections from impedance discontinuities. In brief, the tester sends a measuring signal into the tested cable and measures the level of reflected power and group delay. The type of fault can be differentiated from the character of the reflected signal [2]. Examples of the reflected signals in the case of open and short circuit line are shown in **Fig. 1**. The voltage pulse response can be understood as a derivative of the line impedance depending on the distance from the connector. The time is directly proportional to the distance toward fault.

3. MICROPHONE CABLE TESTER

The measurement of the response of measuring signal requires a precision in order of nanoseconds. Every nanosecond, depending on the velocity of signal propagation, could mean approximately 10 cm of inaccuracy. Thereby, an ultra-high speed analog-to-digital converter (ADC) is required, which is not a cheap solution. There are several methods for sensing the response of a signal. In the introduced concept, a technique based on the measuring of time intervals between the transmitted measuring signal

¹ <https://www.otvp.cz/>

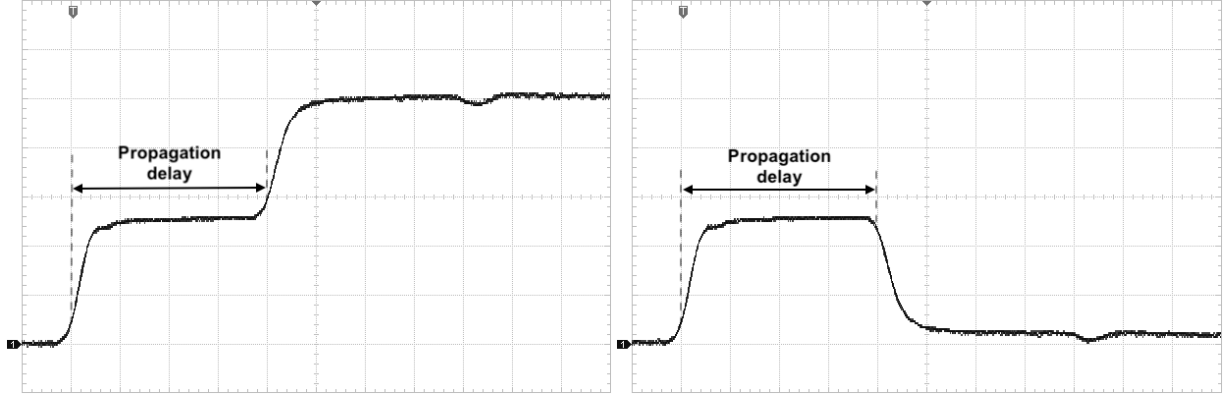


Figure 1: Reflected voltage step (1 V/div; 10 ns/div) on 1 m long line: opened (left) and shorted (right) at the end.

and reflection from mismatch is proposed. From this point of view, a time-to-digital converter (TDC) integrated circuit used in LIDAR and ultrasonic sensors applications [3] was chosen. Its IO works as fast stopwatches measuring the time-of-flight (ToF) of measuring signal. TDC is a cheap, affordable and accurate solution for the TDR application.

3.1. Topology

The topology of the developed microphone cable tester is shown in **Fig. 2**. The principle of the proposed concept can be described as follows. The microcontroller unit (MCU) is used to generate Pulse Width Modulation (PWM) signal with a frequency of 62.5 kHz, filtered by a low pass filter (LPF), that is used as a voltage reference for the comparator. Next, the MCU sends signals (separately or both at the same time) into the buffer and start pin of the TDC. The buffer is employed as an amplifier and the voltage step controlled by MCU goes directly to the measured cable only via resistor trimmer causing impedance cable matching. The typical microphone cable impedance is from 20 to 60 Ω .

Due to impedance discontinuities, reflections occur on the line. These signals with delay are the second input of the comparator. When the voltage level on the measured line is higher than the voltage reference threshold level (taken from the MCU), the comparator flips over and stops TDC. Time accumulated in TDC is directly proportional to time delay of the reflection. The typical value of the measured time delay is from units of nanoseconds to tens of microseconds. The TDC can sense the rising and falling edge of the stop trigger pin, so we are not limited only to positive polarity responses. The MCU and TDC are connected via Serial Peripheral Interface (SPI). The whole device is powered by 5 V power supply (in the future, 18650 battery cell will be used). This voltage level was chosen mainly due to the LCD power supply and as a compromise for the level of measuring signal (to guarantee acceptable signal-to-noise ratio). The TDC circuit is available only in a version of 3.3 V, so the voltage must be converted between the levels of 5 V and 3.3 V. The reference voltage for the comparator can be swept over the entire supply voltage interval.

3.2. Realization

The Atmega328P 8-bit microprocessor (Microchip) and the TDC7002 TDC (Texas Instruments), creating the core of the microphone cable tester, were used at the hardware (HW) realization of the device. They were chosen due to availability, easy of use and low cost. The main time reference is driven by a 16 MHz xtal oscillator. For experimental purposes, a single-side Printed Circuit Board (PCB) was created under home conditions. Minor power consumption is assumed for long battery life time because the device will be realized in a hand-held form. Prototype of the microphone cable tester is shown in **Fig. 3**.

3.3. User Interface (UI)

The firmware is written in programming language C++. It supports the using of user-interface (UI) created by four buttons (see **Fig. 4**). The entire UI is arranged in menus and sub-menus and the user can intuitively scroll between them by the using of arrow keys. A 20 \times 4 backlight LCD alphanumeric display is used to visualize information and outputs of the provided tests. The control of device is intuitive and robust (see **Fig. 4**). Display backlight is also switchable for lowering power consumption.

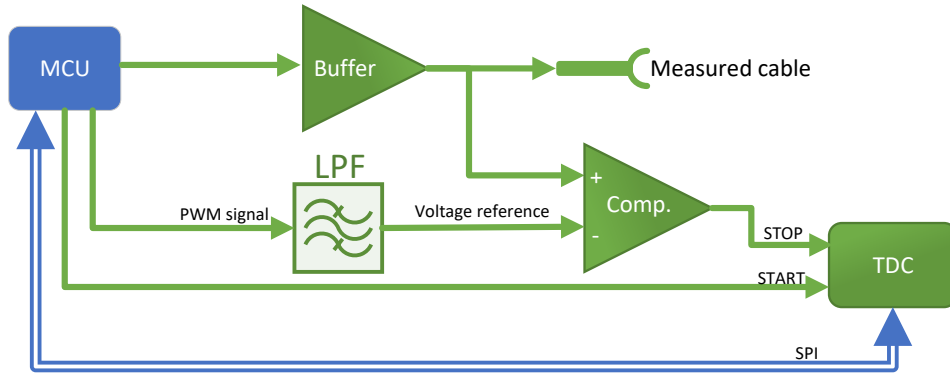


Figure 2: Topology of the proposed microphone cable tester.



Figure 3: The first prototype of the microphone cable tester.

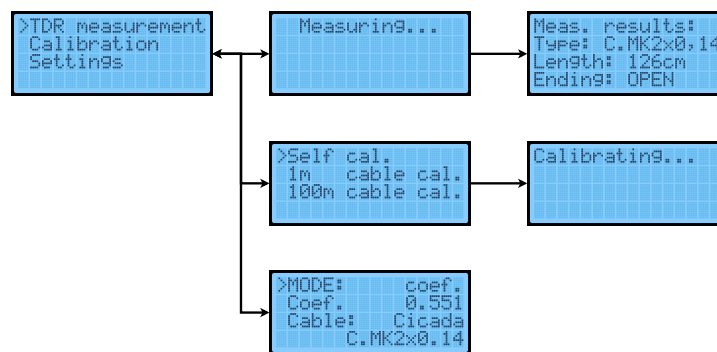


Figure 4: The hierarchy (menus and sub-menus) of UI.

4. EXPERIMENTAL VERIFICATION

The functionality of the proposed microphone cable tester has been verified in experimental measurements. To obtain results at the measurement of microphone cable in a correct form, it is important to create an appropriate measurement algorithm.

It should identify and measure variations of rising and falling edges at noisy sampled waveform. As a measuring signal, voltage step is used (instead of a pulse) which, unfortunately, results in more difficult

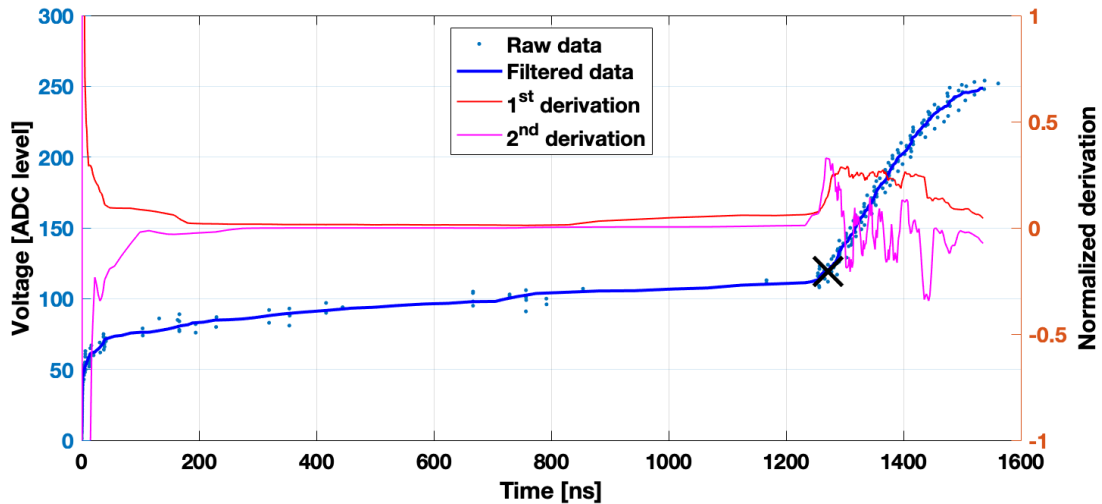


Figure 5: Visualization of the process of obtaining the rising edge (real data from 100 m long cable)

detection of points. As it was mentioned, ADC is not used because causes non-equidistant distribution of the measured points in time domain. The situation is different as in the case of equidistant samples.

The created algorithm consists of these consecutive steps: **1)** Measuring of samples for every reference value; **2)** Ordering of the the measured samples in time domain and filtering by a digital LPF; **3)** Providing numerical derivate calculation followed by filtering; **4)** Finding minimum and maximum and **5)** Calculation of time differentiation of the rising/falling edge.

For the software (SW) debugging, a script enabling calculation and visualization of data was created in program environment MATLAB. The output of the processed data is shown in **Fig. 5** (can be compared with **Fig. 1**). The filtered measured values are highlighted by a blue curve. The resulting point, which is determined by the algorithm as the beginning of reflection, is marked with a black "x". It is visible that the leading edge of the measured signal is not completely rectangular. Hence, it is very important to determine the exact place of the beginning of reflection. Numerical first and second derivatives (red and pink curves) are used for the calculation. The required time delay value defines the first leading edge and the marked point.

5. CONCLUSION

A handheld microphone cable tester, developed and created within the first part of bachelor thesis, was introduced in this short paper. Its topology as well as HW/SW parts were briefly described. Functionality of the proposed concept has been verified by experimental measurements.

Future work plans include the design of a switched-mode power supply for suitable battery supply, SW debugging and the design of professional PCB. After production of the final prototype, it is planned to test the product in real deployment of the company OTVP and its small-scale production.

ACKNOWLEDGMENT

This work was supported by the BUT internal project no. FEKT-S-20-6325. Many thanks for company OVTP, led by technical consultant Vojtěch Pecka, for the assistance in the development of tester.

REFERENCES

- [1] Q. SHI AND O. KANOUN "Detection and location of single cable fault by impedance spectroscopy", 2014 IEEE International Instrumentation and Measurement Technology Conference (I2MTC) Proceedings, 2014, pp. 595-599, doi: 10.1109/I2MTC.2014.6860813
- [2] C. P. NEMARICH, "Time domain reflectometry liquid level sensors", in IEEE Instrumentation & Measurement Magazine, vol. 4, no. 4, pp. 40-44, Dec. 2001, doi: 10.1109/5289.975464.
- [3] TEXAS INSTRUMENTS, "Time-to-Digital Converter for Time-of-Flight Applications in LIDAR, Magnetostrictive and Flow Meters", TDC7200 datasheet SNAS647D, Feb 2015 [revised Mar 2016]

PROČ ČEKAT NA BUDOUCNOST?

Vytvářej budoucnost společně s námi!
V největším R&D centru Honeywellu v Evropě
nabízíme studentské stáže, part-time či
absolventské pozice.

Registruj se pomocí QR kódu a o nových
nabídkách se dozvíš jako první!



Honeywell

PŘÍLEŽITOSTI PRO STUDENTY A ABSOLVENTY

V Honeywellu věříme, že budoucnost je taková, jakou ji společnými silami vytvoříme. Zaměřujeme se na oblasti Aerospace a Safety & Productivity Solutions.

KOHO HLEDÁME?

- Studenty a absolventy všech oborů FEKT VUT
- Zájem o dlouhodobou spolupráci a ochota dále rozvíjet znalosti z oboru
- Stáže: možnost pracovat 16–20 hodin týdně (flexibilní směny)
- Komunikativní znalost angličtiny

PŘÍKLADY POZIC

- Electrical/Electronics Engineer
- Hardware Engineer
- PLC Controls Engineer
- Systems Engineer
- Prototype/Test Technician
- Technical Support



www.honeywell.jobs.cz

careers.honeywell.com/brno

e-mail: Martina.Hanusova@Honeywell.com

IoT Approach for Air Monitoring

M. Kousal¹, T. Frýza¹

¹Department of Radio Electronics, Brno University of Technology, Czechia

E-mail: xkousa03@vutbr.cz, fryza@vut.cz

Abstract—This paper presents a development of a device that can measure air quality parameters and send them wirelessly to the remote server. There, the measured data are processed and shown to the user via user-friendly website. The aim is to create a device with the lowest possible power consumption for the possibility of battery operation. Data will be sent through available Internet of Things network, where user can select between Wi-Fi and LoRaWAN.

Keywords—IoT, ESP32, sensors, dust particles sensor, air quality, LoRaWAN, gas sensor, temperature, humidity, light intensity, UV light

1. INTRODUCTION

Nowadays, the quality of the environment and air is deteriorating and so these parameters need to be monitored. The primal parameters of air is temperature and light intensity. But there is a lot of other parameters which are important in air quality monitoring. To this category we can include humidity, air pressure, dust particles, UV light intensity and carbon dioxide concentration. These parameters are only the few that can be measured. I chose them, because there are sensors of this parameters that we can buy cheap and are widely available. This device is not only to be low power due to the battery operation but also low price for wide availability. Last but not least I must choose some communication module or transmission network for data sending.

2. SENSORS AND MEASURING

As mentioned above, I must choose a lot of sensors to measure all needed variables. The first thing I focused on was the selection of the sensor for the temperature measurement. There are many of these sensors on the market and they have very different parameters and functions. Nowadays, availability and especially price are also important for all components, so this parameter is one of the main ones considered. I chose a sensor from Sensirion called SHT40. It can measure temperature ranges -40°C to 125°C with precision 0.2°C and consumption of only $350\text{ }\mu\text{A}$. Another important feature is that the sensor can also measure humidity. Thanks to this, it is possible to save money on an additional sensor that would have to measure it. We can measure the humidity in a range of 0 to 100 % with 1.5 % accuracy. This sensor will communicate with microcontroller (MCU) through the I²C bus.

Another necessary sensor is the atmospheric pressure sensor. As before, the price and availability of this sensor must be considered. Bosch offers many affordable and relatively accurate sensors. From this company I chose a sensor with designation BMP388. This sensor allows you to measure atmospheric pressure within a range from 300 to 1250 hPa at average consumption of $3.4\text{ }\mu\text{A}$. The communication of the sensor with the MCU is again based on the I²C bus.

Another of the measured variables is the light intensity. This parameter can be measured in different ways including some photoresistor or photodiode. But I chose a sensor that is directly designed to measure this variable and provide it in digital form to MCU. The sensor is VEML7700 from Vishay Semiconductors company. Sensor can measure up to 120 000 lx that are measured using an AD (Analog to Digital) converter with 16-bit resolution. Communication with MCU is again through I²C bus and maximal current consumption is $45\text{ }\mu\text{A}$.

Second light parameter that is measured is the UV intensity value. Again, there are a lot of this sensors, but most of them are expensive or they are very poorly available. I choose ML8511 from LAPIS Semiconductors. This sensor has a photodiode and operational amplifier inside. Measured range is from 0 to 15 mW/cm^2 at 365 nm light wavelength at which is this sensor the most sensitive. This sensor does

not have any digital communication interface so the output of this sensor is raw voltage value, and I must connect it to AD converter for further processing. This sensor needs typically 300 μA for its operation.

The penultimate sensor is air quality and carbon dioxide sensor. Most manufactured and commercially available solutions are very expensive, as most sensors are designed for professional applications and go through a calibration process at factory. However, if we look at affordable sensors, there are hardly any types available. Pretty much the only affordable sensor available is SGP30 from Sensirion company. This sensor allows to measure the carbon dioxide equivalent value, which is calculated from the content of the other chemicals in the air. Range for this value is from 400 to 60000 ppm (parts per million). It also allows to get TVOC (Total Volatile Organic Compounds) which is used to get a relevant view of the measured air quality. This sensor also uses I²C communication bus and needs typical current around 48 mA at 1.8 V.

The last sensor used is the dust particle sensor. I chose the PMS5003 sensor, which is relatively cheap and mainly available in stores. This sensor can measure particulate matters (PM) with diameter 2.5 μm with range from 0 to 500 $\mu\text{g}/\text{m}^3$. This sensor needs relatively high current up to 100 mA at 5 V due to the need to blow fresh air through a fan into the measurement area. The sensor uses UART (Universal Asynchronous Receiver-Transmitter) communication to send data to the MCU.

3. MICROCONTROLLER AND COMMUNICATION MODULE

The basic element of the whole board is the control microcontroller, which ensures communication of all connected sensors, processes data and is responsible for sending them to the server. The choice of microcontroller depends mainly on the required functions, the number of GPIO (General Purpose Input Output) pins and hardware peripherals of communication buses.

There are a lot of IoT (Internet of Things) networks nowadays. One of the first networks for this type of communication was Sigfox. This network is designed for not very frequent transmission of mostly small amounts of data (maximum size for one message is 12 B). For this reason, this type of communication is inappropriate. Next bad thing is, that this network is provided only by one company, and you must pay for using it.

Next well-known IoT network is LoRaWAN. This network is operated in ISM (Industrial, Scientific and Medical) band and is free of charge. You can connect to a worldwide network TTN (The Things Network) and send data to any gateway that are in your range. The advantage of this network is that it is free of charge and the communication modules are widely available and relatively cheap.

A relatively new network is NB-IoT (Narrow Band-IoT) that is provided by emerging 5G communication networks. This network is designed exactly for these applications, such as sending data with low power consumption but still sending relatively much data. However, this network is not free of charge because it is operated by mobile operators (in Czech Republic by Vodafone).

Another usable network is WiFi. It is not planned as low power network, but you can use it at home. WiFi is available almost in every house and their adjacent gardens and around the house.

Due to all reasons mentioned above, I ended up choosing the main data transmission line through the LoRaWAN using TTN network. I must select communication module. If we look at the shop's offerings, we find that the only available and cheap module is RFM95W by Hoperf company. However, this module is mostly used by makers and is well documented and there are also software libraries available for programming. This module will use SPI (Serial Peripheral Interface) communication.

The last thing that must be selected is microcontroller. There are a lot of companies producing various types of MCUs, such as Microchip, STMicroelectronics, NXP, Espressif, Texas Instruments and other. I selected microcontroller ESP32 from Espressif company. This microcontroller is nowadays relatively cheap in compare with the others, provides a lot of hardware peripherals with deep-sleep consumption down to 5 μA , and what is its greatest advantage, it contains a built-in WiFi.

4. DATA PROCESSING AND VISUALIZATION

The measured data will be sent through the networks mentioned above, but they need to be processed and stored somewhere. Well known are servers and services like Thingspeak, Ubidots and many others. These servers allow you to create free account and use their services, but there are a lot of restrictions.

Some are restricted at number of connected devices at the same time, or do not support sending more than eight variables from one device and many more restrictions. Due to these limitations, I decided to use own solution based at free and open-source applications.

For minimal functional use I need an MQTT (Message Queueing Telemetry Transport) broker which is used to receive and send MQTT messages with all needed variables from all devices. For this application I use Eclipse Mosquitto, which is open-source implementation of the broker. Next step in data storage is database application. For this monitoring devices is very convenient using time series database instead of normal database (e.g. MySQL). The time series database gives every record made in it a unique timestamp with actual time and date. Due to this feature, you can easily get data from defined time slot or for example from last 7 days. Last needed thing in this processing chain is visualization to user. For this purpose, I used Grafana service, which is also open-source solution. This service is used to setup for getting data from database and visualization them to user in defined charts, bars or just text with e.g. minimal or maximal values. Very simple visualization of temperature from last 7 days can be found at Figure 1.



Figure 1: Simple temperature data visualization.

5. POWER SUPPLY

An important part of the whole device is the power supply. As mentioned before, this device is designed to be powered from the battery. I chose secondary cell based at LiFePO4 technology. This technology has nominal voltage value at 3.3 V and can be charged up to 3.6 V, which makes it perfect for powering devices who needs 3.3 V at its power pins. These devices almost certainly have allowed voltages up to 3.65 V. So, most sensors and microcontroller will be powered directly by this accumulator.

Next voltage value that I need is 5 V for powering the dust particle sensor. I will get this voltage from step-up converter AP1603 from Diodes Incorporated. This converter can deliver up to 200 mA. Last voltage value that I must provide to sensors will be 1.8 V that will be generated by linear regulator directly from battery. I chose NCP115 with fixed output voltage at 1.8 V from ON Semiconductor company. This regulator can provide up to 300 mA. All these regulators and power blocks can be powered off by microcontroller, when battery voltage will be too low to properly operate. This option should also help to reduce the power consumption of the entire board.

6. PCB DESIGN

The last important thing that I need to make was creating schematic and routing board. The circuit schematic was created in KiCad EDA according to the block schematic mentioned at Figure 2.

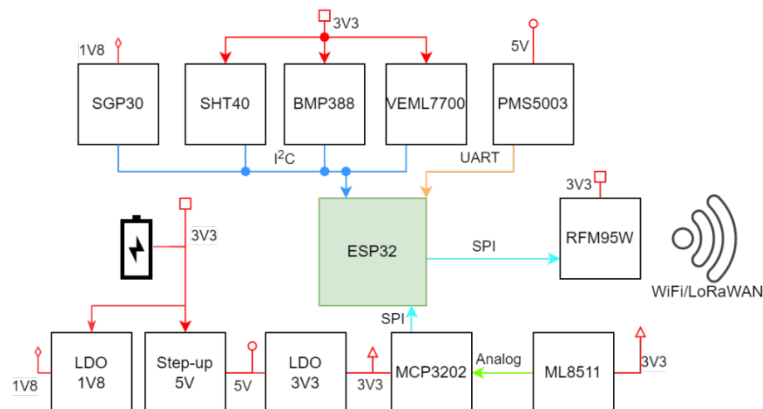


Figure 2: Block schematic diagram.

After creating schematic with all needed features and components I was able to start routing board and placing components. The PCB (Printed Circuit Board) has two layers with mainly SMD (Surface Mount Devices) components from both sides. The PCB was designed with emphasis on low power, small used area and for hand soldering all components. For this purpose, SMD components are at least in size 0603 for passive components like capacitors and resistors. Finished board from both sides is on Figure 3.

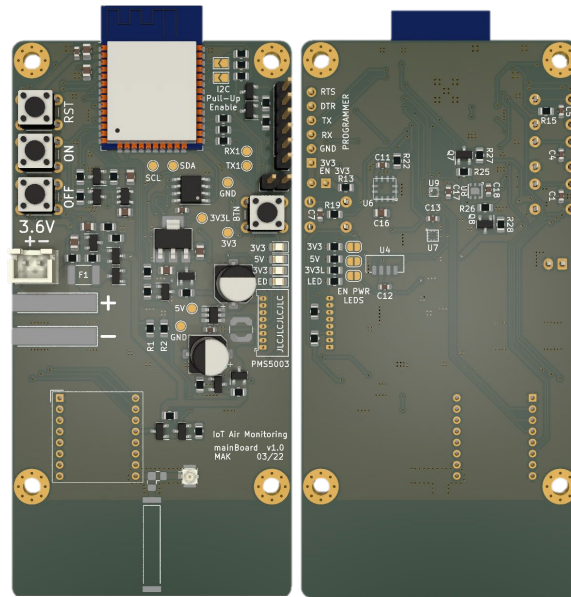


Figure 3: Finished PCB from top and bottom side.

7. CONCLUSION

As part of this work, a device with low power design and a lot of air quality sensor was created. First prototype (not shown in this paper) has idle current consumption 500 μ A and measuring and sending current between 80 to 100 mA which leads with one hour measuring period to three months working with 3200 mAh battery. This device can measure temperature, humidity, light level, UV light level, atmospheric pressure, carbon dioxide level and dust particles concentration. All sensors were driven by MCU ESP32 from Espressif and programmed using their ESP-IDF framework. The whole design was created as least costly as possible for the possibility of spreading to as many people as possible and creating an extensive monitoring network. Overall price was in January 2022 about 2000 CZK. There is no similar device of this complex format on the market nowadays.

REFERENCES

- [1] SENSIRION AG, May 2020. Datasheet SGP30: Indoor Air Quality Sensor for TVOC and CO₂eq Measurements [online]. [cit. 2022-03-11]. Available from: https://sensirion.com/media/documents/984E0DD5/61644B8B/Sensirion_Gas_Sensors_Datasheet_SGP30.pdf
- [2] VISHAY SEMICONDUCTORS. High Accuracy Ambient Light Sensor With I2C Interface [online]. 23.3.2021 [cit. 2022-03-11]. Available from: <https://www.vishay.com/docs/84286/veml7700.pdf>
- [3] PLANTOWER. Digital universal particle concentration sensor: PMS5003 series data manual [online]. 2016 [cit. 2022-03-11]. Available from: https://www.aqmd.gov/docs/default-source/aq-spec/resources-page/plantower-pms5003-manual_v2-3.pdf
- [4] ESPRESSIF SYSTEMS. ESP32 Series: Datasheet [online]. 2022 [cit. 2022-03-11]. Available from: https://www.espressif.com/sites/default/files/documentation/esp32_datasheet_en.pdf
- [5] LAPIS SEMICONDUCTOR. ML8511: UV Sensor with Voltage Output [online]. 8.3.2013 [cit. 2022-03-11]. Available from: https://cdn.sparkfun.com/datasheets/Sensors/LightImaging/ML8511_3-8-13.pdf

Positioning without using GNSS

M. Pintér¹, P. Raichl²

¹Bachelor Degree Programme (3) FEEC Brno University of Technology, Slovakia

²Researcher FEEC UTEE Brno University of Technology, Czech Republic

E-mail: xpinte06@vutbr.cz, xraich02@vut.cz

Abstract—This thesis is aimed at the development of the localization system without using GNSS. The first part describes technologies, which can be used for localization of robots in known environment. Then positioning system based on UWB technology is designed. Additionally, localization system based on DWM1000 is designed and tested.

Keywords— Positioning, UWB, Trilateration, DWM1000

1. INTRODUCTION

The aim of this work is to design a localization system which be able to locate a robot in known environment without using GNSS. The main motivation for the creation of this work is that the system could be used for military purposes or automation in the future. The most of current localization systems are dependant on receiving signals from satellites. However, these systems as most known GNSS can't be practically used for indoor-positioning. Receivers are not able to receive signals from satellites because of signals are blocked by walls and roofs.

This article looks into the available technologies for positioning. Methods for determining distance between transmitter and receiver will be also discussed. We will discuss advantages and disadvantages of each technology and methods.

2. TECHNOLOGIES FOR POSITIONING

WPS (Wi-Fi - based positioning system) is system for determination of position using Wi-fi routers or hotspots, wireless access points as source of the signal. The interesting thing about this technology is that sources of signal are basically every around us. With WPS is basically possible only use RSSI (Received signal strength, intensity) method for determining position between access points and tracked device. It's because other methods like ToA (Time of Arrival) or TDoA (Time difference of arrival) needs to have synchronized time between all sources. When you are using RSSI measured date can be influenced by an external source. Wi-Fi technology was never designed for determining position.[1]

Bluetooth is low range wireless technology, which is used for exchanging data between devices. Originally was designed as a wireless replacement of RS232. Bluetooth was also not designed for positioning. However the Apple company came up with connection with Bluetooth LE (Low energy). The result of their work was system beacon released in 2013. Each device has a unique identifier which is received by compatible device. Typical range of first versions of Bluetooth was about 10m but current Bluetooth version 5.0 declares range of 40 to 400 meters. The main disadvantage of this technology is that accuracy is dependant on the distance between source and receiver.[3]

UWB (Ultra-Wideband) technology is the successors of Bluetooth. This technology uses for transmitting information across a wide band typically around 500 MHz. So that means that UWB technology can transmit much more data during the same time in comparison with Bluetooth. Band of this technology is from 3.1 to 10.6 GHz. This technology is commonly used by researchers, in industry and other positioning areas. The aim of this technology is the achievement of high resolution, position accuracy and lower options of interference. The advantage of this system is the possibility of a combination of positioning and communication in one system. The biggest advantage of this technology is that it can be used basically with every known method for determining position between transmitter and receiver.[2]

In **table I** you can see a comparison of technologies which can be used for positioning. For each technology is described band in which works. As you can see UWB technology has the widest from all technologies. Also has the highest accuracy, range and can be used with all of the known methods for

determining position between transmitter and receiver. So we can say that UWB technology will be the best for our application.

Table I: Comparison of technologies

Technology	WPS	UWB	Bluetooth
Band	2.40-2.49 GHz 5.15-5.85 GHz	3.1-10.6 GHz	2.402-2.480 GHz
Bandwidth	22 MHz	500 MHz	1 MHz
Range	100m	290m	10m
Accuracy	10m	10cm	10m
RSSI	✓	✓	✓
AoA	✓	✓	✓
ToA	✗	✓	✓
TDoA	✗	✓	✓
ToF	✓	✓	✓

3. CHOICE OF COMPONENTS

In the **table II** we can see an overview of available UWB integrated circuits from different manufacturers. Most of it is used in commercial devices, for example NXP SR100T is integrated in newest smartphone Samsung Galaxy Note20 Ultra. Apple has also developed its own UWB integrated circuit U1, which they integrated into their devices iPhone 11, Apple Watch 6, and newer. One of the most used non-commercial and most affordable UWB integrated circuit is DW1000 from Decawave (Qorvo). They also produce DW3000 version which works in a slightly different band. So from available UWB integrated circuits DW1000 was chosen. One more reason why to chose DW1000 is that Decawave company produce module DWM1000 which integrates antenna, power management and DW1000 IC. The next thing which

Table II: Overview of available UWB integrated circuits

Manufacturer	Product name	Band	Release date
NXP	NCJ29D5	6-8.5 GHz	12.11.2019
NXP	SR100T	6-9 GHz	17.09.2019
Apple	U1	6-8.5 GHz	11.09.2019
Qorvo	DW1000	3.5-6.5 GHz	07.11.2013
Qorvo	DW3000	6-8.5 GHz	01.01.2019
CEVA	RivieraWaves UWB	3.1–10.6 GHz	24.06.2021

needed to be chosen was the right micro-controller. It is possible to use some micro-controller from the AVR family known from development kits Arduino. However, these micro-controllers have several times lower processor frequency in comparison to ESP family. Using of micro-controller from ESP family allows simple connection of the module without need to some logic level converters. The AVR micro - controller has also several times higher energy consumption. All of the ESP development boards have built-in 3.3V voltage regulator. So that allows simple power supply for micro-controller and UWB module. Most of available development kits are with ESP8266 and ESP32 processor. Very popular and affordable development board is WeMos D1 mini with the ESP8266 micro - controller. For this development board is available a lot shield modules. The small dimensions of the development board are also advantageous.

4. FIRST TEST

During the first tests the physical connection of the module with ESP board was tested. DWM1000 has also GPIO pins which can be configured for some purpose. Two of them are reserved and can be enabled as TX and RX signalization of the module. It is a useful thing during debugging and testing. At the **figure 1** you can see the first prototype connection of the module on breadboard.

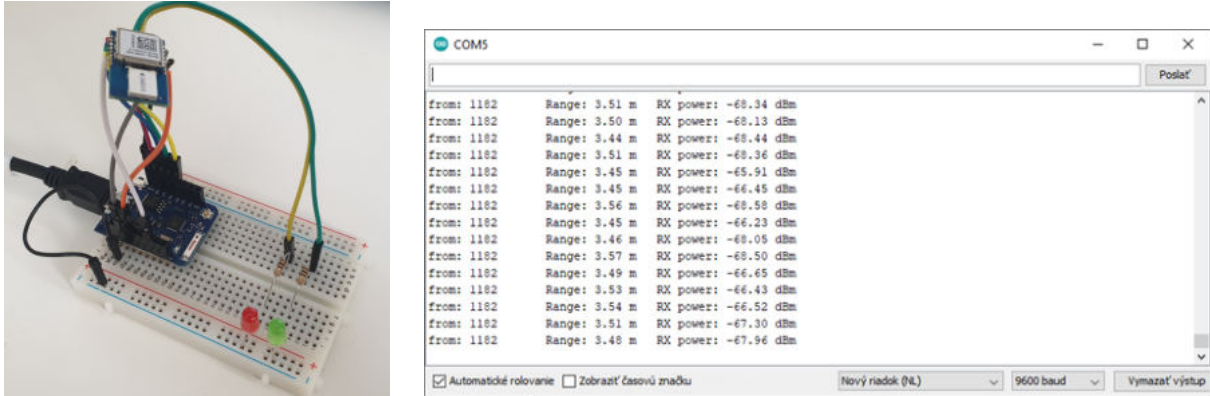


Figure 1: First tests on breadboard, sample output

5. SHIELD MODULE

After the first prototype tests the decision to make a shield module for WeMos D1 Mini development board was made. On the shield were also added leds which signalize transmission of the UWB module. Also was added an extra load which is connected to the power-supply of the UWB module. The unused pins of the UWB module were placed to the soldering pads on the bottom of the shield. UWB module is placed on the shield as the manufacturer recommends. Antenna of the UWB module needs to be placed out of the board. It is due to possible interference of the antenna. At the **figure 2** you can see PCB design and assembled shield module.

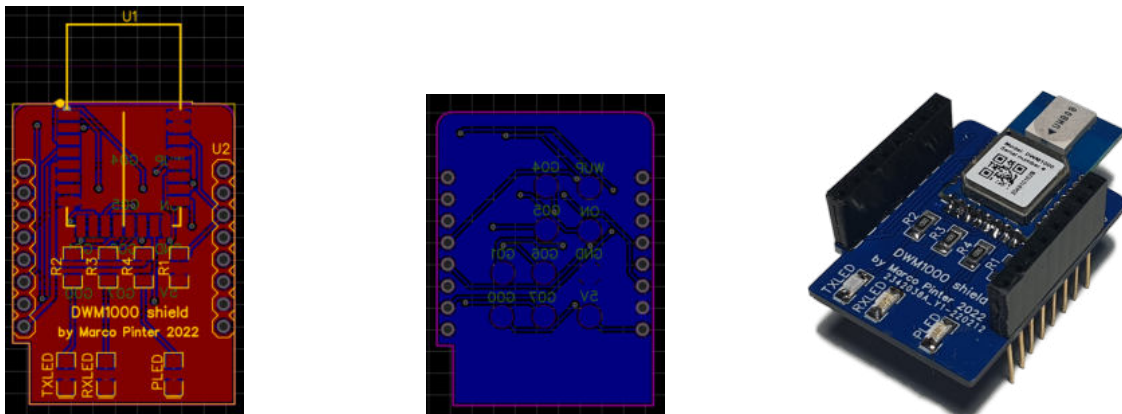


Figure 2: PCB design and completed shield module

6. ANCHORS

For determining relative position in the area with trilateration the static points needs to know the exact position of anchors. So anchors need to be a standalone source of signals with exact known positions. For the power-supply a WeMos battery shield which has built-in voltage 5V regulator for ESP board and battery charging was used. The battery cell from an old battery which I have at home was used. It's 1000mAh one cell LiPo battery. The battery case was designed then 3D printed. **Figure 3** shows assembled hardware of the anchors.



Figure 3: Battery shield, complete stack, stack with battery

7. DETERMINING RELATIVE POSITION

For relative position determination the trilateration algorithm was used. System computes relative position based on measured data itself. Tag measures distance between each anchor, then from 3 nearest will compute relative position. As was mentioned before the position of the anchors need to be known. So tag needs to know the position of the all anchors. In my solution saving configuration of anchors to flash memory of the tag was implemented. This configuration includes an address and position of the anchor. In the **figure 4** shows test data. The anchors were placed in the corners of the room.

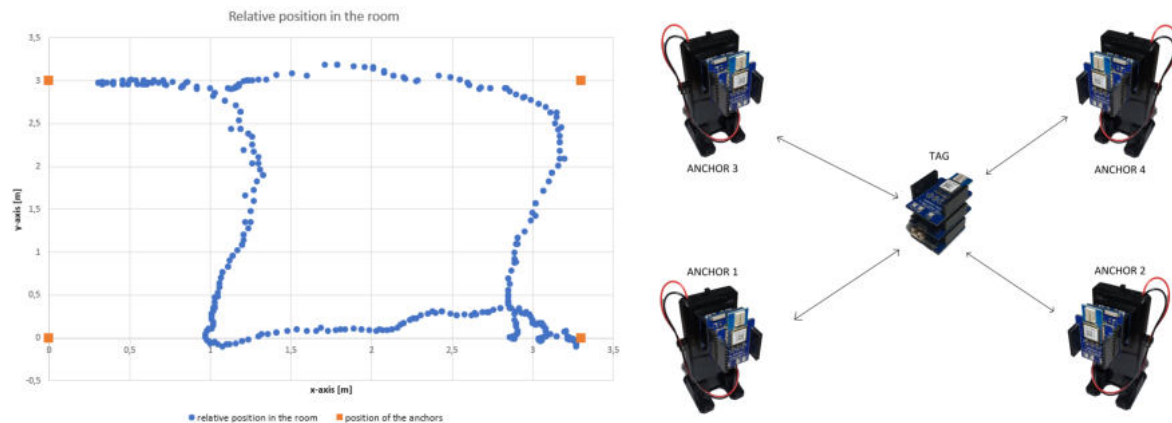


Figure 4: Sample data, placement of anchors

8. CONCLUSION

The result of the work is a working concept of the positioning system. First tests prove that this technology has potential to be used for positioning. In the process of working on this thesis the correct hardware and design of the shield module had to be chosen. After initial tests the concept still needs more testing and fine-tuning. It is also necessary to measure the accuracy of the system.

ACKNOWLEDGMENT

The research was funded from the Ministry of the Interior of the Czech Republic (MVCR) grant no. VJ02010036 (An Artificial Intelligence-Controlled Robotic System for Intelligence and Reconnaissance Operations).

REFERENCES

- [1] Henniges, R: *Current approaches of Wifi Positioning*. 2012: https://www.snet.tu-berlin.de/fileadmin/fg220/courses/WS1112/snet-project/wifi-positioning_henniges.pdf.
- [2] DWM1000: *Documentation*: <https://www.decawave.com/product/dwm1000-module/>.
- [3] Liu Liu, Bofeng Li: *Real-Time Indoor Positioning Approach Using iBeacons and Smartphone Sensors* College of Surveying and GeoInformatics, Tongji University, Shanghai 200092, China: <https://www.mdpi.com/2076-3417/10/6/2003>.

Piezoelectric Polyvinylidene Fluoride Nanofibers as a Scaffold used for Bone Tissue Engineering

Tereza Havlíková

Department of Physics, Faculty of Electrical Engineering and Communication, Brno University of Technology,
Technická 2848/8, 61600 Brno, the Czech Republic

Email: Tereza.Havlikova1@vut.cz

Abstract—The field of bone tissue engineering deals with the issue of developing compatible and non-toxic scaffolds, which provide the growing bone cells with the necessary mechanical support and suitable stimulation for proper growth and proliferation. Polyvinylidene fluoride (PVDF) nanofibers are considered to be a suitable scaffold due to their biocompatibility, fibrous structure, and characteristic piezoelectric properties, which have proven to be an important factor in cell regeneration. For this work, flexible PVDF nanofibers were successfully spun, from which the scaffolding needed for the subsequent settling of cultivated osteoblasts was created. Thereafter the structure and compatibility of this nanomaterial were assessed in relation to the study of cell adhesion to individual nanofibers.

Keywords—bone tissue engineering; polyvinylidene fluoride; piezoelectric properties; scaffolds; osteoblasts.

1. INTRODUCTION

At a time of ever-increasing incidence of musculoskeletal disorders due to obesity, sedentary work, and unhealthy or poor physical activity we are looking for the most suitable ways to replace damaged bone tissue and support its regeneration and healing. The cells needed for this therapy are grown on special scaffolds that simulate the natural extracellular matrix that cells make for their support. This scaffold also works as a network for signalization and interaction between each cell or whole tissue.

Each scaffold must meet certain requirements such as good biocompatibility and flexibility and should have hydrophilic, fibrous, porous, and piezoelectric properties. It was found that piezoelectric materials can generate and deliver an electric stimulus as a result of the application of mechanical stress without any external power source. Human bone tissue produces electric charges due to the deformation of extracellular fibrous protein - collagen, which is crucial for the right function of cellular membrane channels, therefore cell communication and growth [1]. To mimic this behavior, it was discovered that a fabrication technique called electrospinning is the most effective and low-cost method for achieving both fibrous structure and piezoelectricity in PVDF scaffolds [2].

The cells chosen for this work are osteoblasts that make up the bone tissue. Osteoblasts specialize in the synthesis of bone matrix and secretion of collagen which is needed for the bone to adjust to current load and mechanical tension. Osteoblasts are mostly found in a layer on the surface of bone structures. When new cells completely bury mature osteoblasts, they transform into osteocytes which are chiefly involved in metabolism [3].

2. MATERIALS AND METHODS

2.1 PVDF FABRICATION

The method chosen for fabricating a flexible fibrous PVDF scaffold for this experiment is called electrospinning. The basic principle of electrospinning is that an electrical potential is applied between an emitter - the spinneret and an electrically conductive collector for the produced nanofibers. The newly formed electric field stretches the electrically conductive solution which is forced to take a highly specific shape called the Taylor cone. When the electrical voltage is increased and reaches the critical value when the surface tension is no longer enough to maintain the Taylor cone, the polymer is drawn

to the surface of the spinning collector and begins to form a thin layer [4].

The electrospinning device used for this experiment was a 4SPIN (Contipro, Dolní Dobrouč, Czech Republic) with a cylindrical collector wrapped with aluminum for better separation of the formed nanomaterial from the cylinder at the end of the making process. The emitter was in a form of one needle, which the solution was passed through at a flow rate of 30 μL per minute. The voltage between the emitter and the collector was 50 kV. The used solution was a 20% solution of PVDF with a molecular weight of 275,000 g/mol in a solvent of dimethyl sulfoxide/acetone in a ratio of 7: 3, which was heated for 24 hours on a stirrer at a temperature of 80 °C and a speed of 200 rpm.

2.2 CELL SAMPLE PREPARATION

The preparation of cell samples is a standardized procedure. Modifications were chosen according to existing experiments that used cultured osteoblasts [5]. Human osteosarcoma Saos-2 cells (ATCC® HTB-85™) were maintained in complete Dulbecco's Modified Eagle's medium (DMEM) supplemented with 10% fetal bovine serum and 5% penicillin/streptomycin (50 UI \cdot mL⁻¹ and 50 μg \cdot mL⁻¹) at 37 °C in a humidified 5% CO₂ incubator. Cells were harvested by trypsinization with 0.25% trypsin-EDTA solution. Saos-2 cells were seeded at the density of $1 \times 10^3 \cdot \text{mL}^{-1}$ onto the sterile PVDF samples (1×1 cm) placed in a polystyrene microplate.

The interaction of cells with PVDF fibers was visualized by immunocytochemistry in 48 hours. Paraformaldehyde - fixed Saos-2 cells were permeabilized with a solution of 0.5 % Triton-X 100 supplemented with 2 % bovine serum albumin for 2 hours and thoroughly washed in deionized water. The actin fibers were stained with ActinGreen™ 488 (Invitrogen™) for 30 min at RT. The stained cells were imaged using a confocal microscope (CLSM) Zeiss LSM 880 with a 488 nm laser. All chemicals were purchased from Sigma Aldrich.

To observe the sample on a Lyra3 (Tescan, Brno, Czech Republic) scanning electron microscope (SEM), it was necessary to metalize the surface of the prepare. The metal coating does not only dissipate the charge, which then does not accumulate on the surface but also fixes the fibers that would be otherwise affected by the electron beam and began to twist. Thanks to this, they do not move, and it is possible to take a good picture. Gold was used to metalize the samples, which is also good for energy-dispersive X-ray spectroscopy (EDS) because gold does not disrupt the peaks on the spectrum. The EDS detector used was X-Max 50 (Oxford Instruments, Oxford, United Kingdom). An instrument called coater EM ACE600 (Leica, Wetzlar, Germany) was used for metal coating and the gold layer was 7 nm thick.

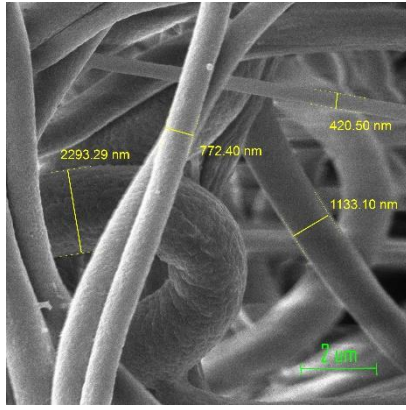
3. RESULTS

3.1 STUDYING QUALITY OF PVDF SCAFFOLD

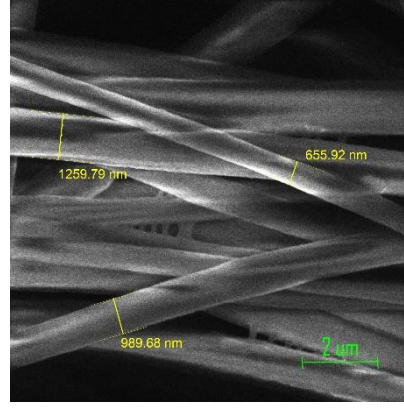
For making a good scaffold for cells to grow on is also important the overall layout of nanofibers. It is known that for some types of cells the alignment of nanofibers is essential. The right layout can be achieved during the process of electrospinning. The polymer jet has a chaotic trajectory therefore the collected fibers exhibit various orientations. The fibers can be directed during spinning by controlling the rotation speed of the collector or adjusting the electric field between electrodes [1].

Two nanofiber materials with different fiber orientations were created by this method, which were then cut down into small samples. The nanofibers were successfully spun with no greater imperfections. The occurrence of beads on the fibers was not common thanks to the right ratio of dimethyl sulfoxide and acetone. For this observation were used two types of samples. The first sample had nanofibers that were spun at a speed of 300 rpm, and the second sample had nanofibers spun at a speed of 2000 rpm. Both samples were after proper preparation and gold coating imaged by SEM under a voltage of 5 kV.

The biggest difference in samples is the very arrangement of individual fibers, which are in a non-directed sample in Figure 1a very chaotic and variously twisted and bent. On the contrary in Figure 1b can be seen fibers highly aligned and stretched in the same direction. The next important difference is the thickness of fibers which varies dramatically in the non-directed sample. The thickness difference between the widest and thinnest nanofibers in Figure 1a is 1872,79 nm. Meanwhile, Figure 1b shows directed nanofibers that were spun at a much higher speed, where the thickness of individual fibers is smaller and more consistent. The biggest thickness difference there is only 603,87 nm.



a)



b)

Figure 1: Examples of a) undirected PVDF nanofibers and b) directed PVDF nanofibers. Imaged by SEM.

3.2 OBSERVATION OF CELL ADHESION

To evaluate the degree of adhesion of individual osteoblasts to the surrounding nanofibers, a confocal microscope was chosen, in which, thanks to the green staining, it was possible to distinguish the cells from the fibers very well and observe their various attachments. The cells adhered to the fibers very nicely and could be seen using the fibers as mechanical support.

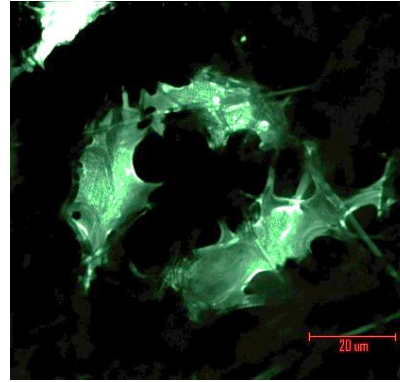
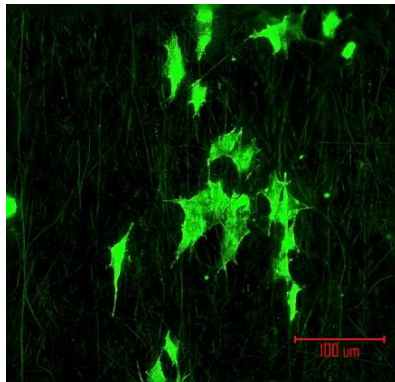
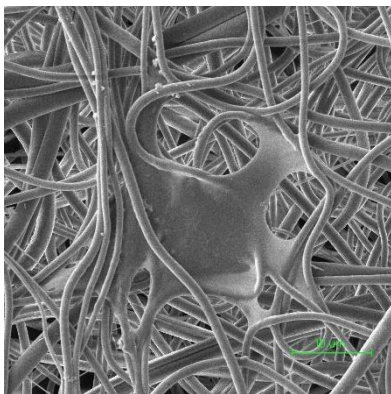
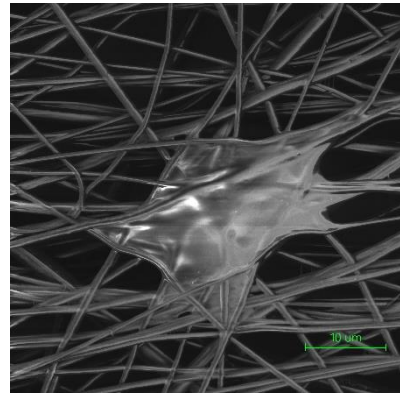


Figure 2: Stained osteoblasts on directed PVDF nanofibers imaged by CLSM.

An interesting difference in cell attachment can be seen through SEM in samples with different fiber orientations. A better result is shown on the directed nanofibers in Figure 3b, where the osteoblasts are oriented mostly parallel to the fibers, the cells are elongated, and they are in larger equally aligned groups. While on undirected nanofibers in Figure 3a the cells oriented randomly, took on more various shapes, and didn't form a greater pattern due to their random location and orientation.



a)



b)

Figure 3: Examples of a) osteoblast seated on undirected PVDF nanofibers and b) osteoblast seated on directed PVDF nanofibers. Imaged by SEM.

3.3 EDS MAP ANALYSIS

The gold-coated sample was subjected to EDS, which confirmed the elemental representation in the nanofibers and the cell itself. The main elements forming the whole sample are carbon, oxygen, and fluorine. In Figure 4b can be seen an independent representation of oxygen which is the second most represented component in the sample right after carbon and is part of both osteoblasts and PVDF nanofibers. On the other hand, in Figure 4c, it is shown that fluorine is only a part of nanofibers and does not influence or pollute the cells.

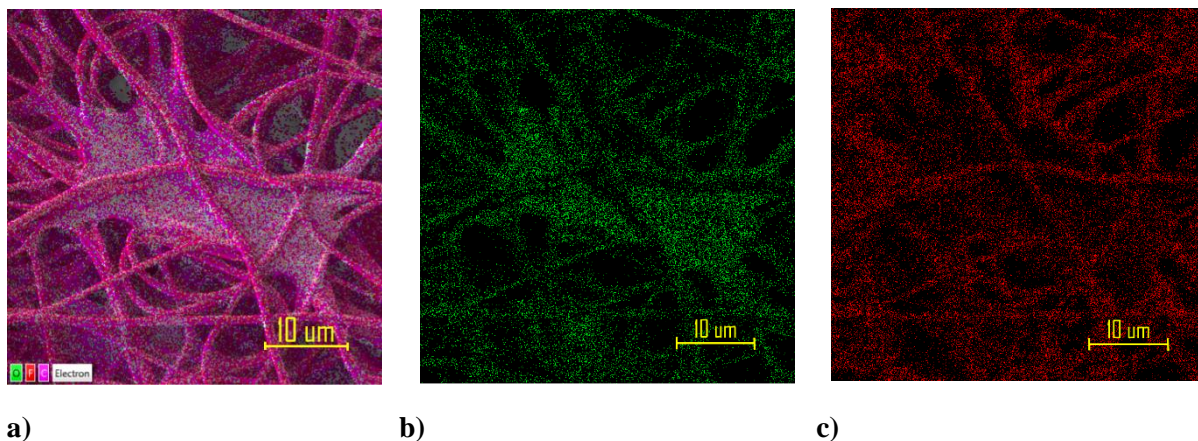


Figure 4: Results from EDS: **a)** example of colored sample according to the representation of carbon (purple), oxygen (green), and fluorine (red) in the spectrum, **b)** highlighted oxygen, and **c)** fluorine.

4. CONCLUSION

In this work a PVDF nanomaterial was created through the process of electrospinning. This material proved to be suitable for making a biocompatible scaffold for settlement of cultivated osteoblasts. Through examining the samples with SEM and CLSM, it was proven that increasing rotation speed over 2000 rpm during the process of electrospinning reduces the fiber diameter and porosity of the scaffolds. It directs the fibers to the same course, which enhances the piezoelectric properties of the material which makes the material more preferable for the right attachments of cells. The osteoblasts attached well and overall seem to exploit the potential of nanofiber support without any difficulties. The EDS map confirmed the expected elemental composition of the sample. It is a fact that PVDF is a hydrophobic material, which could be counterproductive in means of proper cell adhesion. If I were to continue this line of work, I would deal with the combination of PVDF with other materials such as polyamide 6, which is considered highly hydrophilic. I would examine the differences in cell adhesion also in combination with different cell types.

ACKNOWLEDGMENT

I would like to thank my advisor, Ing. Nikola Papež, Ph.D. for his valuable comments and guidance.

REFERENCES

- [1] Y. Li, C. Liao and S.C. Tjong, "Electrospun Polyvinylidene Fluoride-Based Fibrous Scaffolds with Piezoelectric Characteristics for Bone and Neural Tissue Engineering," *Nanomaterials* 9, no.7:952, 2019, <https://doi.org/10.3390/nano9070952>
- [2] M. Kitsara, A. Blanquer, G. Murillo, V. Humblot et al., "Permanently hydrophilic, piezoelectric PVDF nanofibrous scaffolds promoting unaided electromechanical stimulation on osteoblasts," *Nanoscale*, vol. 11, pp. 8906-8917, Royal Society of Chemistry, 2019, <http://dx.doi.org/10.1039/C8NR10384D>.
- [3] X. Wang, Z. Qiu and H. Cui, "Mineralized Collagen Bone Graft Substitutes," *Biomaterials*, UK: Woodhead Publishing, 2019, <https://doi.org/10.1016/C2017-0-03411-0>
- [4] Z. He, F. Rault, M. Lewandowski, E. Mohsenzadeh and F. Salaün, "Electrospun PVDF Nanofibers for Piezoelectric Applications: A Review of the Influence of Electrospinning

- Parameters on the β Phase and Crystallinity Enhancement," *Polymers* 13, no.2: 174, 2021, <https://doi.org/10.3390/polym13020174>
- [5] L. Hernández-Tapia, Z. Fohlerová, J. Židek, M. A. Alvarez-Perez, L. Čelko, J. Kaiser, and E. B. Montufar, "Effects of Cryopreservation on Cell Metabolic Activity and Function of Biofabricated Structures Laden with Osteoblasts," *Materials* 13, no. 8: 1966, 2020, <https://doi.org/10.3390/ma13081966>

Design of a micromanipulator for repairs of printed circuit boards

Pavel Kopřiva, Alexandr Otáhal

FEEC, Brno University of Technology, Czech Republic

E-mail: 220879@vut.cz, Alexandr.Otahal@vutbr.cz

Abstract: This work deals with design of micromanipulator based on pantographic mechanism with electronic control. The main purpose of this micromanipulator is repairing printed circuit boards, but it has been designed to be universal for any use case. The main focus is on creating device that will have the highest possible accuracy, while still being able to provide necessary force to carry out mechanical repairs of printed circuit boards. The work contains the design of the pantographic mechanism, stepper motor based electrical drive section and control circuits with power supplies.

Keywords: Micromanipulator, Pantograph, Repair of printed circuit boards, Design

1. INTRODUCTION

Printed circuit boards are the main building block of most electronical devices. Modern printed circuit boards are being made with focus on minimalization. The effort is to fit same or more complex circuits on the same, or smaller space, with utilizing the use of smaller and smaller conductive traces, vias, embedded components etc. This is increasing the complexity of printed circuit boards and also increasing the chance for failure to appear in manufacturing process, soldering process, desoldering process and during repairs. Since the printed circuit boards are so complex and the occurring failures are so small, the repairs can't be done using normal tools like tweezers etc. This process requires usage of specialized equipment designed for this purpose. The equipment in question is called micromanipulator. It is a device that allows user to manipulate with instruments in very small distances, mainly in order of micrometers.

Commercially available micromanipulators can be really expensive, so the main focus of this work is to design a special kind of micromanipulator with usage of mechanical pantographical mechanism to scale down the movement of electronical drive section, that will be significantly less expensive, while still approaching the parameters of the ones commercially available.

Pantograph is a simple mechanism that was mostly used for recreating and redrawing pictures while simultaneously changing their size. The most basic one is consisting of 4 arms that are connected in specific shape that is pictured in figure 1 [1].



Figure 1: Example of pantographic mechanism [1]

2. DESIGN

The designed micromanipulator is intended to be used for repairs of printed circuit boards, but the way it is designed in allows it to be used in any scenario. The output of this mechanism is designed as a shaft on which can be mounted anything from knives for scraping, to attachments for wirebonding. The workspace is around 25 mm x 25 mm x 25 mm, but not strictly limited to it. This is the minimal workspace with which was this device designed, the real usable workspace will be determined when the device is constructed. This device only purpose is to serve as “arm” that can move desired tool in desired space, with desired accuracy. This means that this device needs to be used alongside with some means of holding the repaired object and because of the small nature of the movements, use of some type of microscope is recommended. Because of that, this device can be used alongside with any other device, which makes it truly universal.

2.1 REQUIREMENTS

The main requirement was to create micromanipulator, that would be capable of moving tools in the order of micrometers. Second requirement was the use of pantographic mechanism to scale the movement down. Last requirement was to design electronic drive section that would allow the use of computers or joysticks for the control of the movement.

Theoretically the designed mechanism would be able to move in steps as small as 150nm, in reality this number will be much bigger because of the backlash and tolerances introduced because the mechanism will be handmade on lathe and mill. The aim will be to achieve tolerance of somewhere about 1-10µm.

Pantographic mechanism is used to scale down the movement. The design of the pantographic mechanism is inspired by design of company SINGER which is called MK1 Manipulator and it is based on patent from 1950 made by Robert Barer and A.E.Saunders-Singer [2]. This design is on figure 1. Basically, it contains two basic pantographic arms connected via ball bearings. This allows to translate and scale down movement in every axis including tilting. The design of electrical drive section was inspired by the design of Novel 5-DOF spatial parallel micromanipulator, created by Daniel Prusak, Konrad Kobus and Grzegorz Karpiel from the AGH university of Science and Technology from Krakow [3]. Their design is on figure number 2. This design was chosen because it allows full movement in all three axes, and it also allows tilting of the tip.



Figure 2: Manipulator MK1 [2]

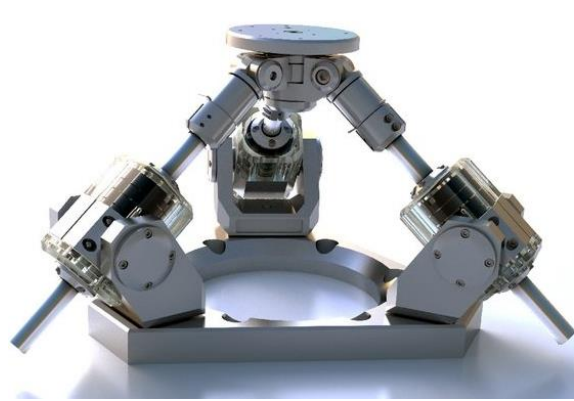


Figure 3: Novel 5-DOF micromanipulator [3]

The last requirement was to allow the use of computer or joysticks to control the micromanipulator. Because of that, the Raspberry PI ZERO control board was chosen. It is basically a small computer, so it covers the first part, and it is equipped with USB connectivity. Thanks to that it will be possible to use any kind of joystick, or other device, equipped with USB to control the micromanipulator.

2.2 MODEL

The model shown on figure 3 was created in a program called Autodesk Inventor 2022. Aluminium extrusions were chosen for the construction of the main body. Electric drive section has the same motor and axis placement as Novel 5-DOF micromanipulator. Everything else was customized in a way to be constructed from commonly available parts and or from parts that can be created on mill or lathe. Our design is made up of three identical legs. Each leg contains one stepper motor, mounted on bearings for smooth movement and trapezoidal screw for transferring rotational movement of the

motor to linear movement. The chosen stepper motor has higher strength, which is essential for any kind of mechanical repairs. The trapezoidal screws were chosen with gradient of 2 mm per rotation, for smaller sizes of steps. For now, the mechanism used for leading the nut on the screw it designed as piece of machined aluminium. If it proves to be the bottleneck in terms of accuracy and tolerance, it will be replaced with linear guides. All three legs are connected via magnetic ball bearings to one single base, which then moves just like an ordinary delta 3D printer. Thanks to the addition of ball bearings, the whole base can be tilted in any direction.

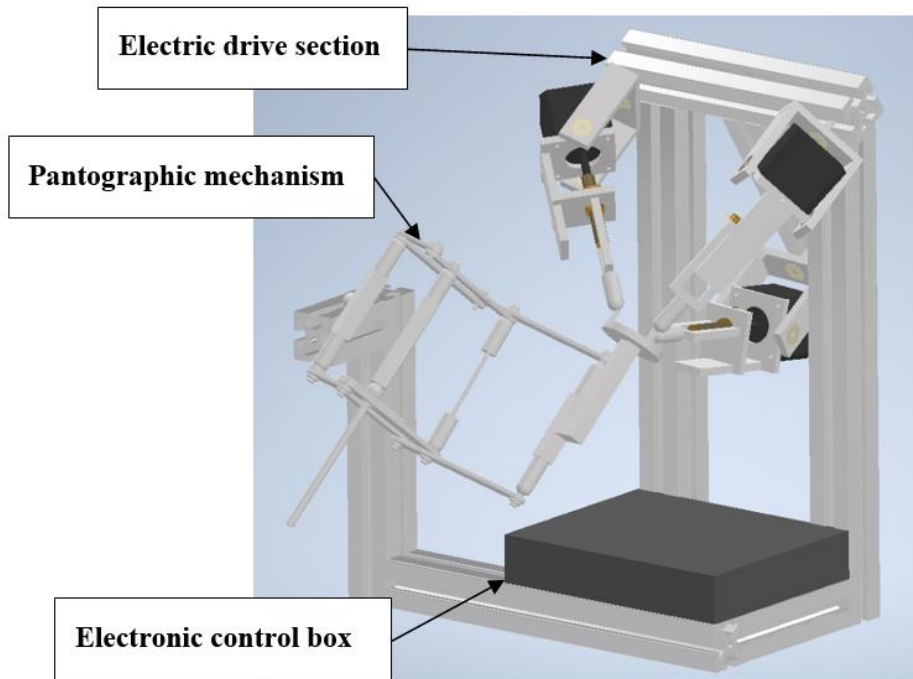


Figure 4: 3D model of designed micromanipulator

The design of pantographic mechanism is similar with Manipulator MK1 with the use of two pantographs parallel to each other and connected via ball joints. The dimensions of our design were calculated using mathematical model created in Microsoft EXCEL to find the correct lengths of arms to ensure no distortion of movement and to find out the size of movement reduction. The final movement reduction was chosen to be 4x. Similarly, to the electric drive section, the pantographic mechanism uses magnetic ball bearings.

2.3 ELECTRONICS

As was stated before, the main control board was selected to be Raspberry PI ZERO. The control program is created in Python. To power the stepper motors, specialized stepper motor drivers had to be chosen. Driver called A4988 was chosen, because it is capable to support the nominal current of our chosen stepper motors and it also allows the use of microstepping, which allows even smaller step sizes. Endstop switches were also added to the electric drive section to allow for quick calibration.

The stepper motors each require current of around 2 A at 12 V. The Raspberry PI ZERO requires around 1 A at 5 V and the stepper motor drivers require around 100 mA at either 3.3 V or 5 V. Because of the currents required to run the motors, a primary source of 12 V was chosen, which is capable of supplying 6 A. To supply the control circuits, a DC-DC step down converter was chosen for supplying 5 V.

3. CONCLUSION

This work deals with the design of pantographic micromanipulator. The final design is shown on figure 4. The design is made up of three parts. The pantographic mechanism was designed to scale down the movement of the electric drive section by the factor of four and at the same time to not distort the movement. The design of electric drive section powered by stepper motors is using ball bearings and trapezoidal screws with the gradient of 2 mm to allow for the smallest possible steps with as small play and backlash as possible. Finally, the control circuits and power supplies were chosen to accommodate the used stepper motors and to allow smooth control via any device supporting USB, mainly joysticks.

The device is currently under construction. The electric drive section is completed, alongside with the main chassis. Right now, we are waiting for ordered parts to be delivered.

The control program is also in development. The mathematical model that determines the correct movements of the motors is currently being written and tested.

REFERENCES

- [1] *Pantograph in Case by Cary of London*, National Museum of American History, Mar. 2022, [Online]. Available: https://americanhistory.si.edu/collections/search/object/nmah_904626
- [2] *MICROMANIPULATION: MK1 MANIPULATOR*, SINGER instruments, Mar. 2022, [Online]. Available: <https://www.singerinstruments.com/solution/mk1>
- [3] *Novel 5-DOF spatial parallel micromanipulator*, Research Gate, Mar. 2022, [Online]. Available: https://www.researchgate.net/figure/Novel-5-DOF-spatial-parallel-micromanipulator_fig10_269105445

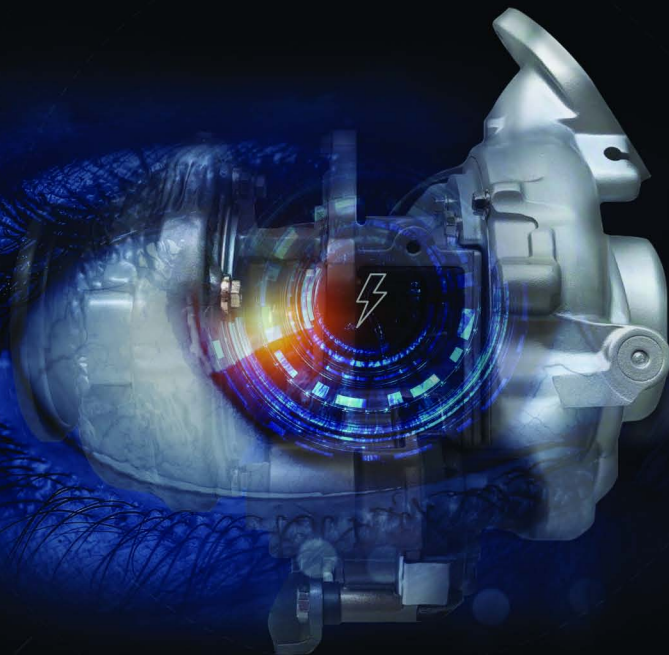
ELECTRIFICATION IS IN OUR NATURE

Start your career with us

Garrett develops exciting cutting-edge technologies that drive vehicle hybridization and electrification. From the first hydrogen fuel cell compressor for passenger cars to the industry's first electric turbo, Garrett technologies are shaping a cleaner future of mobility.



Learn more about
our hybridization
and electrification
solutions



Garrett
ADVANCING MOTION


Turbo
Technology


Electric &
Hybrid


Connected
Vehicle

A Separation and Characteristics of Inner Egg Shell Membrane

J. Charvot

Department of Physics, Faculty of Electrical Engineering and Communication, Brno University of Technology,
Technická 2848/8, 61600 Brno, the Czech Republic

E-mail: jakub.charvot@vut.cz

Abstract—The aim of this work is to characterize the inner egg shell membrane (IESM) and compare different methods of extracting it from an egg. Scanning electron microscopy (SEM) was used in a combination with energy dispersive X-Ray spectroscopy (EDX) to get an idea of membrane structure and chemical composition and impacts of the used extraction method. Significant differences were found between the measured samples, but it has not been verified whether they affect the resulting physical properties yet. The importance of this study lies mainly in the future investigation of several factors, such as piezoelectric properties, so it serves as a fundamental research.

Keywords—Egg Shell Membrane, IESM, SEM, EDX, characterization, membranes, extraction

1. INTRODUCTION

Due to a huge development in technology during last years, there is a growing need to think more and more about materials which are used to create our devices. Some materials are becoming more difficult to obtain – their extraction can be devastating for nature or expensive. Humans need to focus more on renewable and biodegradable resources. The inner egg shell membrane (IESM) is naturally piezoelectric [1] and as a result can be used to create high-tech products, for example, pressure sensors.

1.1. Inner egg shell membrane (IESM)

An egg is basically a shelter for a fetus, it contains necessary nutrients for embryonic development and provides protection to it. There are two membranes under the egg shell called inner and outer, their roles are to reinforce fragile shell and significantly increase its anti-bacterial protection [2]. This paper focuses mainly on the inner egg shell membrane due to its piezoelectric properties and greater potential for technological applications.

2. MATERIALS AND METHODS

2.1. Materials

Both hen eggs used for this observation and the cheap distilled vinegar used for membrane separation were purchased from a local supermarket, all eggs were medium size. Pure acetic acid solution (Merci, Brno, Czech Republic) served as an alternative to the vinegar. Deionized water (Merci, Brno, Czech Republic) was used to clean the extracted specimens before observation.

2.2. Membrane separation

In order to separate the membrane from the rest of the egg, various techniques have been tried. Subsequently, all samples have been compared to determine which of the methods least affected the desired properties.

At first, membrane was isolated directly from a cracked egg. It is not very hard, but it is not possible to acquire larger parts intact. The samples obtained this way were only several square centimeters in size on average.

Another way to easily separate membrane is to chemically decompose the shell. The cheap distilled vinegar was used as the first chemical solvent. It lasted about two days to fully decompose the outer shell with vinegar. In addition, for closer examination of this method two concentrations of acetic acid solution were used. In widely available kitchen vinegar concentration of acetic acid is between 4 and 18 % and further used concentrations were 30 % and 90 %.

All methods mentioned above have been tried both on boiled and unboiled eggs. After separating

the membrane, all specimens were washed in deionized water, placed on SEM stab and dried at the temperature of 60 °C for one hour. They were also coated by 7 nm of gold using the EM ACE600 (Leica, Wetzlar, Germany) coater to prepare them for SEM observation. Gold coating was preferred over carbon coating for the purpose of following EDX analysis.

2.3. Specimens measurements and observation

All specimens were observed using Lyra3 SEM (Tescan, Brno, Czech Republic). Because the membrane is a biological material, only 5 kV was used as the acceleration voltage, higher voltage could possibly damage a membrane structure. A total of 5 samples were observed from both top and bottom side. Specimens are fully described in Table I.

Different parts of the membrane from multiple specimens were also exposed to EDX analysis using X-Max 50 device (Oxford Instruments, Abingdon-on-Thames, Great Britain), acceleration voltage for the EDX was 10 kV and the measurement lasted two hours.

Table I: Specimens description.

Label	IESM separation method
S1	boiled egg in vinegar
S2	unboiled egg in vinegar
S3	directly from cracked egg (unboiled)
S4	boiled egg in 30 % acetic acid solution
S5	boiled egg in 90 % acetic acid solution

3. RESULTS

3.1. Scanning electron microscopy (SEM)

After the SEM observation of the first round of specimens, significant differences between the samples were observed, indicating that the membrane has two different looking sides. This assumption was confirmed by the observation of an additional set of specimens showing both sides of the same membrane sample. As Fig. 1 shows, the specimen S3 was torn into two pieces, which allowed us to observe both sides of the membrane simultaneously.

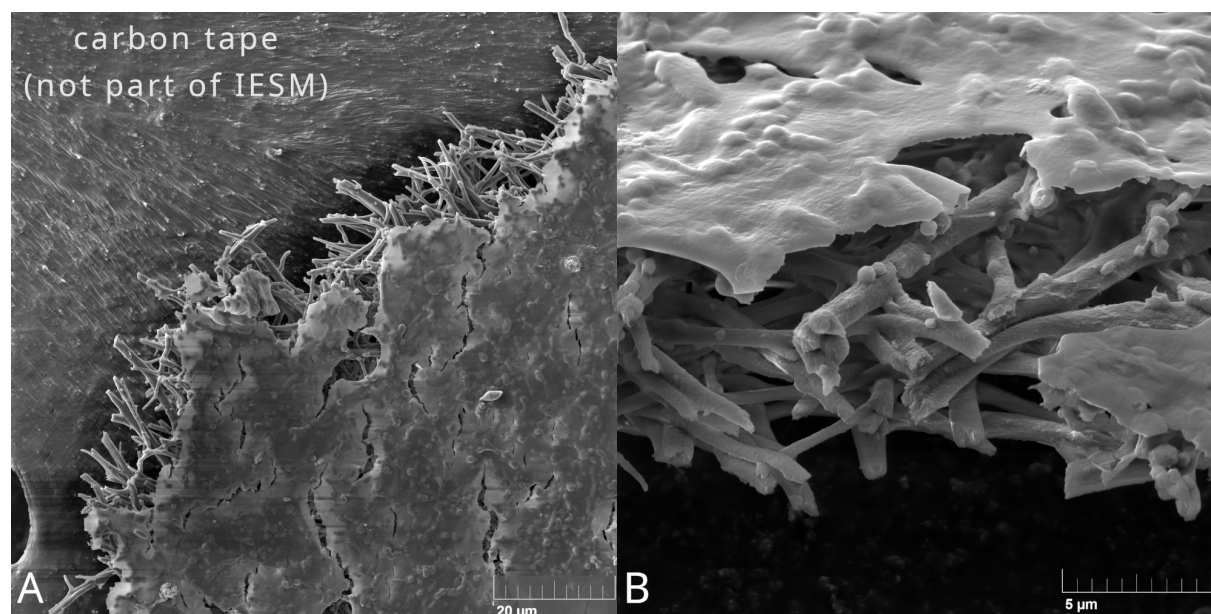


Figure 1: The torn piece (S3) clearly shows that the two sides of the membrane are different. (A) is a view from the top with carbon tape in the background, (B) is a cross-section image from 50° angle.

One side of the membrane is formed by highly porous fiber network while the other side is rather solid. As Fig. 1B shows, the more solid side is significantly thinner. From a simple calculation, the thickness of the membrane at this spot was estimated to be 8 μm . This value is not corresponding to the information provided by M. U. Khan, Q. M. Saqib and G. Hassan in their articles [3, 4] which was about 20 μm . Also, a different specimen was measured on the cleanly cut edge instead of the torn one and the observed value was about 40 μm . The thickness varies greatly and could depend on the age and size of the egg, different kinds of hens and other factors as well. To specify the values, it would be necessary to conduct further research. A detailed view of the membrane fiber side is shown on Fig. 2C and D.

All specimens were carefully observed using SEM and a few significant differences were found. On some specimens, a fiber structure was perfectly visible and fibers looked clear and compact. On the other hand, some specimens contained regularly dispersed viscous structures around 20 μm in size and a viscous cover was also on most of the fibers and between them. These differences are depicted in Fig. 2A and B. Some differences were also found on the solid side of the membrane, mainly the variation in surface roughness.

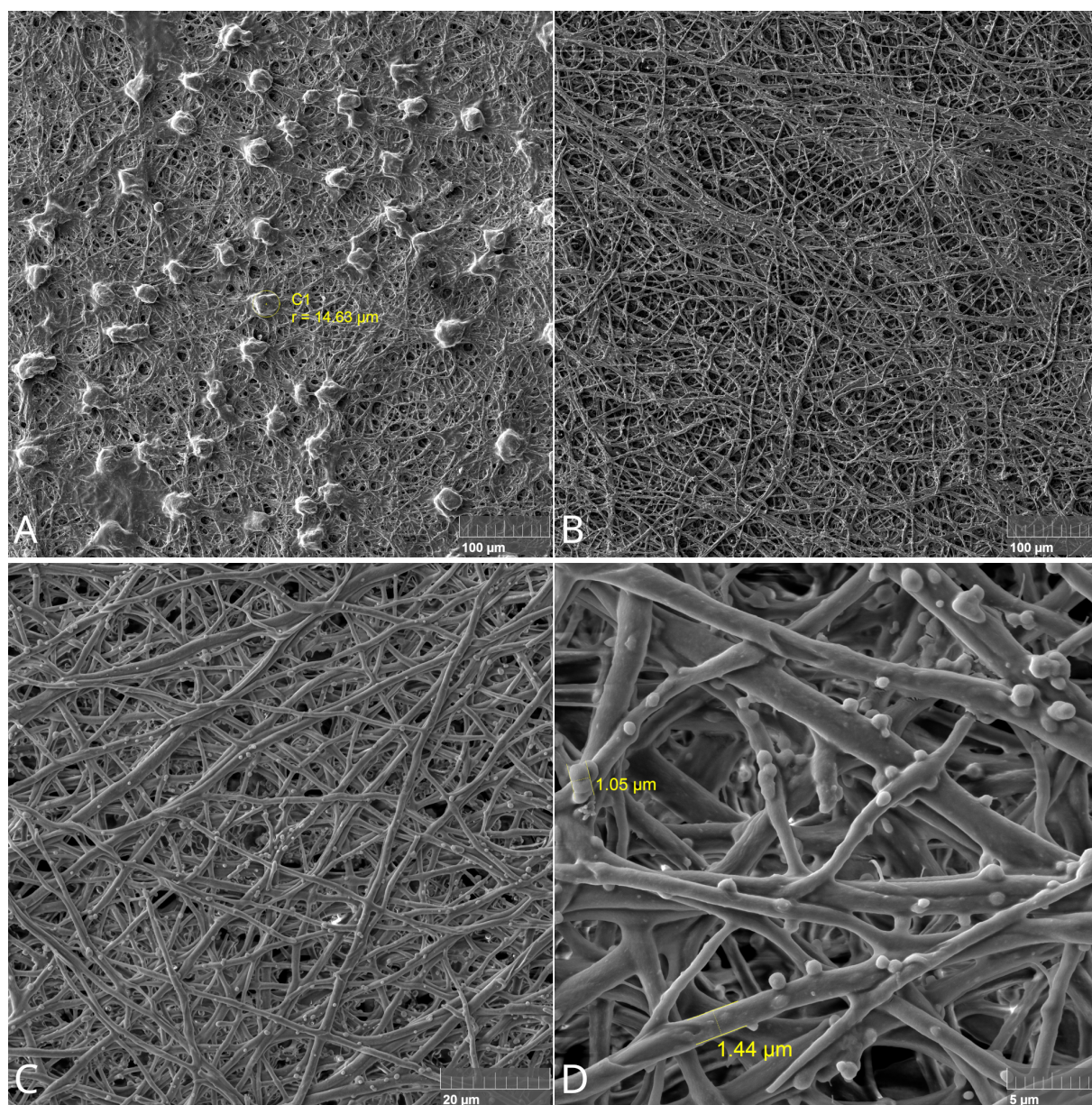


Figure 2: Difference between S2 (A) a S3 (B); More detailed images of S1 structure (C and D).

3.2. Energy dispersive X-Ray spectroscopy (EDX)

Both sides of the membrane were processed by EDX analysis to find their chemical composition. No significant differences were found and it was confirmed that the chemical composition of all investigated samples is very similar. The results also correspond with the articles mentioned above [3, 4]. On 350 eV there is probably a calcium peak hidden, interfering with the peak of carbon. Due to this it is difficult to determine the percentage distribution of the elements. The Fig. 3 contains the most interesting part of the EDX representation of the S5 specimen.

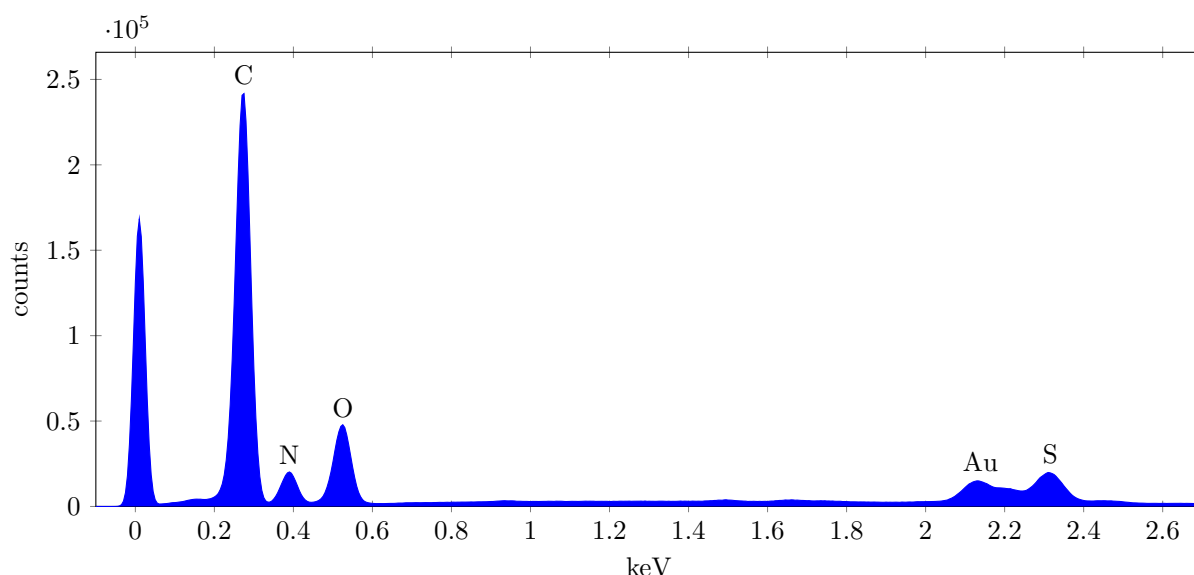


Figure 3: A part of the EDX representation of S5 (10 kV).

4. CONCLUSION

The paper describes the process of IESM characterization and several methods of extraction a membrane from an egg. Using SEM and EDX analysis, it was found that all used methods could be applied for membrane separation, but significant differences between observed specimens were found. The future study is needed to determine whether these anomalies have any impact on desired physical properties with main scope on piezoelectricity. Finding an effect of egg age to the IESM structure or properties would also be very useful.

ACKNOWLEDGMENT

I would like to thank the advisor, Ing. Nikola Papež, Ph.D. for his valuable comments and guidance during operating the technical equipment.

REFERENCES

- [1] S. K. Karan, S. Maiti, S. Paria, A. Maitra, S. K. Si, J. K. Kim, and B. B. Khatua, "A new insight towards eggshell membrane as high energy conversion efficient bio-piezoelectric energy harvester", *Materials today energy*, vol. 9, pp. 114-125, 2018, doi: [10.1016/j.mtener.2018.05.006](https://doi.org/10.1016/j.mtener.2018.05.006).
- [2] W. E. Brown, R. C. Baker, and H. B. Naylor, "The Role of the Inner Shell Membrane in Bacterial Penetration of Chicken Eggs", *Poultry science*, vol. 44, no. 5, pp. 1323-1327, 1965, doi: [10.3382/ps.0441323](https://doi.org/10.3382/ps.0441323).
- [3] Q. M. Saqib, M. U. Khan, and J. Bae, "Inner egg shell membrane based bio-compatible capacitive and piezoelectric function dominant self-powered pressure sensor array for smart electronic applications", *RSC advances*, vol. 1, no. 49, pp. 29214-29227, 2020, doi: [10.1039/D0RA02949A](https://doi.org/10.1039/D0RA02949A).
- [4] M. U. Khan, G. Hassan, and J. Bae, "Bio-compatible organic humidity sensor based on natural inner egg shell membrane with multilayer crosslinked fiber structure", *Scientific reports*, vol. 9, no. 1, pp. 5824-5824, 2019, doi: [10.1038/s41598-019-42337-0](https://doi.org/10.1038/s41598-019-42337-0).

Asset Administration Shell for PLC

J. Maslowski¹ and T. Beneš¹

¹Brno University of Technology, Department of Control and Instrumentation, Czechia

E-mail: 221003@vut.cz, tomas.benesl@vut.cz

Abstract—This work gradually summarizes key points about Asset Administration Shell (AAS) with respect to requirements for execution in practise. It also shows how AAS could be realized in Siemens PLCs using methods which are called by OPC UA client, as well as evaluates deficiencies in the proposed implementation.

Keywords—AAS, Industry 4.0, PLC, OPC UA

1. INTRODUCTION

There has been achieved great progress in the concept of Industry 4.0 over the last decade and one of its new component is Asset Administration Shell. Nowadays, PLCs are in almost every plant from the Third Industrial Revolution. This work aims to connect these newly developed concepts together with already built infrastructure in order to improve competitiveness of individual companies with little to no requirements to invest in new, expensive devices.

2. WHAT IS ASSET ADMINISTRATION SHELL?

We can imagine Asset Administration Shell (AAS) as some kind of cousin of our well-known Digital Twin, which we can hear about in almost every article (or Ad) about the topic of Industry 4.0. The AAS got much more communication possibilities, stricter rules to follow regarding its data storage and it can decide its actions based on predefined rules. The basic scheme of AAS can be seen in Figure 1.

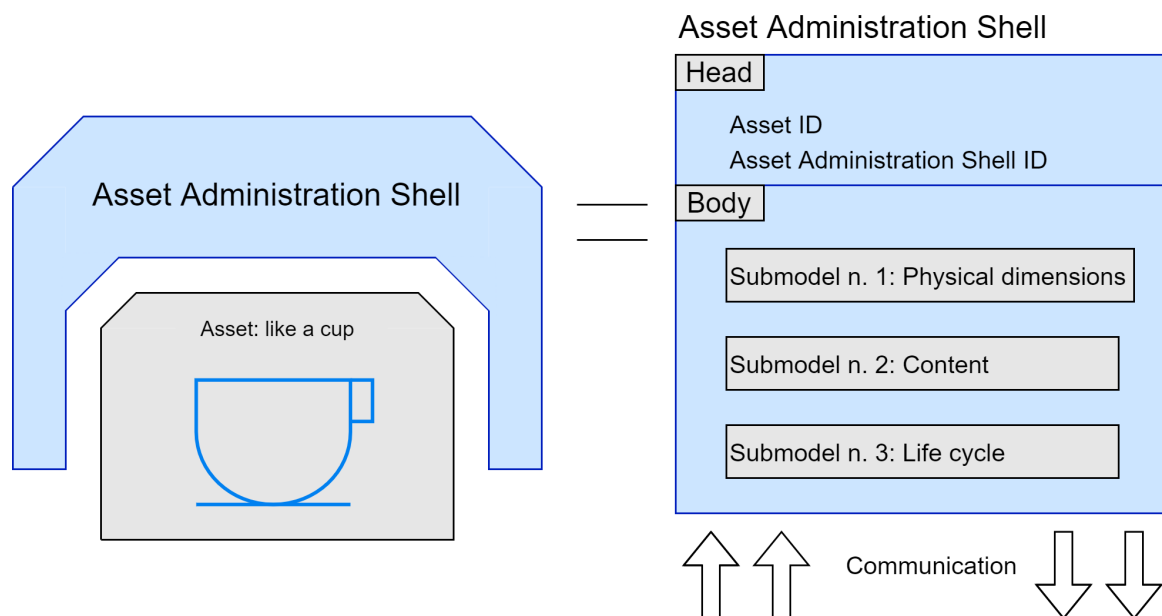


Figure 1: Asset Administration Shell.

2.1. Passive AAS

The passive AAS contains information about devices in Industry 4.0. It is composed of a head, where identification information can be found, and a body, which is divided into several submodels, each containing appropriate information about a specific device. The number of submodels varies depending

on specific requirements. It ought to react to requirements not only from production, but also from commercial or marketing areas. The AAS has to allow also other AAS and its own submodels to be referenced [1].

2.2. Active AAS

The active part of AAS allows communication with other entities that have AAS implemented too. VDI 2193-1/2 defines a unified interface for communication between devices via the I40 language. However, many of these recommendations had to be ignored because of the implementation on PLC, which has its own limitations [1] [2].

Participants in the communication are divided into 2 groups: Service Requesters and Service Providers. During communication, Service Requester (SR) asks several Service Providers for a service they require and after demand negotiations (which is done by **Support** function) choose the best suited Service Provider (SP) for their specific needs. When this happens, SP is reserved by SR and aims to get into its area of influence, where those reserved actions may be taken care of. Every entity with implemented AAS should be able to change its current status from SP into SR and vice versa [3].

3. IMPLEMENTATION

The AAS was implemented into SIMATIC S7-1200 via TIA Portal v17 on 'Barman' testbed. Current version of implementation supports multiple AAS in one PLC, which reduces hardware requirements even more in a trade of added AAS limitations. This means AAS cannot change from SP into fully capable SR as well as it adds additional identification parameters for methods.

3.1. Requirements

The method of implementation this paper suggests is not able to be utilized everywhere and neither should it be. Apart from PLCs, which we can consider proudly available, it also requires infrastructure, where individual products can move across the plant with ease, eg. a robust framework of 'smart' conveyors or manipulators. The second important requirement is diversified production itself. Application of AAS into PLC makes sense only in a plant, which changes its products frequently. Meaning utilization of AAS for static production is much lower, thus usage of the old way of centralized control is better in mentioned situation.

3.2. Data model

Each AAS has one data block (DB) in PLC with all of their data divided into standardised structures. There are 7 cyclically called functions, which have only 1 input as a string message divided by '/' character and return a string with predefined structure too. It is mandatory to send both SR and SP IDs in each message in case of the implementation with multiple AAS in one PLC, so each message consists of at least 'SR ID/SP ID'. Mentioned functions are:

Submodel Each Service Provider is divided into three main groups of services it provides. The input message for this function consists of only 2 words ('SR ID/SP ID'), asking the device which type of service provider it is. It returns 'Submodel/SR ID/SP ID/submodel_type', where submodel_type can be 'Storage', 'Manipulator' or 'Mixer'.

Support The input message contains five word message with an expected format of: 'SR ID/SP ID/operation ID/material/amount'. It returns 'Support/SR ID/SP ID/value', where value is dimensionless, in range of 0-255, where 255 stands for the best and 1 for the worst cost, 0 is reserved for not supporting at all. This gives the service requester an opportunity to choose the most suitable device. The algorithm which decides the returning value is specific for every SR, depending on plant requirements.

Reserve There are currently no queues implemented in PLC, but there are expected to be some of them in the future. The input message for this function contains only 'SR ID/SP ID' and returns 'Reserve/SR ID/SP ID/True or False', depending on whether a specific device did or did not reserve its resources for a specified Service Requester. The AAS stays in reserved state for 2 minutes after receiving and successfully acknowledging a reservation, after which function Free is called.

Free The input message of Free function has the type 'SR ID/SP ID' which cancels the reservation. After that, it returns 'Free/SR ID/SP ID'. This function is used in case of malfunction of SP or just its disconnection, which could cause deadlock in a plant.

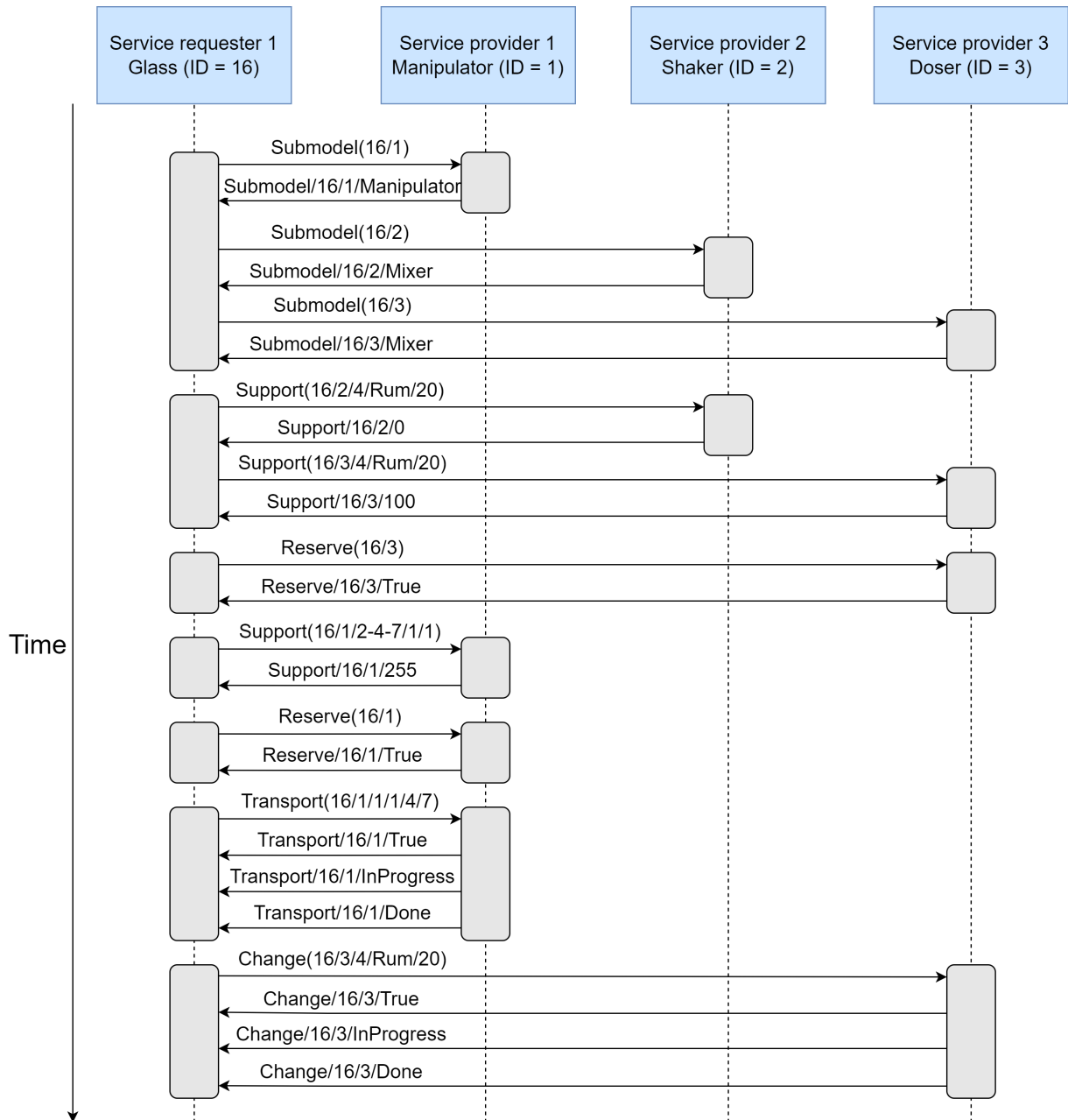


Figure 2: Example of communication.

Transport This function is available for Manipulator submodels only. Input message consists of 5 words: 'SR ID/SP ID/Asset ID/Amount/coded_starting_position/coded_final_position'. This function returns message 'Transport/SR ID/SP ID/True or False, InProgress or Stopped and Done or Failed'.

Give This function is available for Storage submodels only. Input message consists of 4 words: 'SR ID/SP ID/requested material/amount' and returns message 'Give/SR ID/SP ID/True or False, InProgress or Stopped and Done or Failed'.

Change This function is available for Mixer submodels only. The input message consists of 5 words as 'SR ID/SP ID/operation ID/material/amount' and returns message 'Change/SR ID/SP ID/True or False, InProgress or Stopped and Done or Failed'.

3.3. Communication

Communication is supported via OPC UA, where Service Requester as a client is calling predefined functions with string messages.

An example of communication can be seen in Figure 2 where the Glass as the SR is calling SP functions with an aim of carrying out its predefined recipe (saved in SR repository), which is to fill itself with 20 ml of Rum in this simple example. SR first asks what kind of submodels SPs are, then asks Mixers whether some of them can offer a service coded as '4', meaning liquid dosing. Once this service is reserved, SR is then required to get into the right position for dosing (eg. to be transported from position 4 to position 7). When SR is in position, dosing can start as the Glass requested.

3.4. Future work

Unfortunately, there are some difficulties with this implementation which should be addressed and resolved later. The first one is the queue system for reservations, which would improve continuity of production. The second major problem is the unfinished Service Requester. So far, all testing was done manually using UaExpert as a client calling PLCimp methods. Implementation program (eg. in C++), which would stand for the SR and call all required methods of Service Providers, is currently missing.

4. CONCLUSION

This work introduced the novel approach in the PLC control system by implementation of the AAS using OPC UA as a communication protocol. Decentralised control by services is a possible way to greatly improve an efficiency of specific plant types. Mentioned implementation was successfully tested manually via UaExpert and is ready for future improvement by reservation queues. It will create an environment which could be implemented in a plant if SP is implemented to represent devices.

ACKNOWLEDGMENT

The completion of this paper was made possible by the grant No. FEKT-S-20-6205 - "Research in Automation, Cybernetics and Artificial Intelligence within Industry 4.0".

REFERENCES

- [1] S. Bader, E. Barnstedt and H. Bedenbender, "Details of the Asset Administration Shell. Part 1 - The exchange of information between partners in the value chain of Industrie 4.0 (Version 3.0RC01)" [online], November 2020, [cit. 03/07/2022]. Available from https://www.plattform-i40.de/IP/Redaktion/EN/Downloads/Publikation/Details_of_the_Asset_Administration_Shell_Part1_V3.html.
- [2] A. Belyaev and C. Diedrich, "Specification "Demonstrator I4.0-Language"v3.0" [online], July 2019, [cit. 03/07/2022]. Available from https://www.researchgate.net/publication/334429449_Specification_Demonstrator_I40-Language_v30.
- [3] M. Wenger, A. Zoitl and T. Müller, "Connecting PLCs with their asset administration shell for automatic device configuration" [online], July 2018, p. 74–79, [cit. 03/07/2022]. Available from <https://ieeexplore.ieee.org/document/8472022>.

APPLICATION FOR FORMAL TESTING OF PLC PROGRAM

O. Sýkora¹, J. Arm²

¹Brno University of Technology, Department of control and instrumentation, Czech Republic

²Brno University of Technology, Department of control and instrumentation, Czech Republic

E-mail: 221017@vut.cz, arm@vut.cz

Abstract - The paper deals with developing application for testing of selected errors contained in Siemens TIA Portal V16 PLC Project. The application is being developed for the company ICE Industrial Services. The application should find bugs that programmers or PLC code generators make, but TIA Portal cannot detect them defaultly. In this moment, application is able to open or find opened TIA Portal project and load its important parts to my structure – *ProjectBlocks* structure. Application can also find some errors described in Chapter 2.

Keywords - C#, TIA Portal, TIA Portal Openness, Windows form application

1. INTRODUCTION

Code validation testing (whether desktop application development code or PLC code) is an important activity, the underestimation of which can lead to increased costs development. If the software is not tested, there is a good chance that when it continues to operate in near future mistake. At best, the problem still occurs in development phase, in the worst case for a customer who notices defects or errors and will request a repair or refund. [1]

There are 2 testing technique areas: Static software testing and dynamic software testing. If static software testing techniques is used, tester do a visual control of PLC program – visually check, if code doesn't contain any visible error. Also, can find a mistake or irregularity in the project documentation and discuss it with his colleagues. In other words, static software testing is used for error prevention. On the contrary, dynamic software testing techniques usually running the code to determine what kind and how many errors are contained in program. There are two approaches: Black box testing techniques and white box testing techniques. [2]

Black box testing means that tester may not understand at all how the tested program code works. Probably he is not allowed to even see a code. His job is to know the purpose of the program and to be able to distinguish between its correct and incorrect working. He is typing data to the application or (in PLC programming case) i.e., do an IO check – how controlled machine is working when something he pulls, activates the sensor, etc. [2]

When white box testing approach is selected, tester is code-knowledgeable person – in most cases programmer himself and he is trying diverse edge cases to error-testing a program such as statement coverage, branch coverage, condition coverage or basic path testing. [2]

There are lot of approaches and testing techniques being used in software development industry, but only four testing levels in project developing process. Unit testing is a level of SW testing, where individual units (such as station functions or function blocks) being tested. The purpose is to validate that each unit of the software performs as designed. Integration testing is a level of the SW testing process where individual units are combined and tested as a group. The purpose of this level of testing is to expose faults in the interaction between integrated units. System testing is a level of the software testing process where a complete, integrated system is tested. The purpose of this test is to evaluate the system's compliance with the specified requirements. And finally, acceptance testing is a level of the software testing process where a system is tested for acceptability. The purpose of this test is to evaluate the system's compliance with the business requirements and assess whether it is acceptable for delivery. [3]

In the field of PLC program testing, there are several approaches in use: Manual testing – basically dynamic white box testing, where programmer can watch variables behavior in the program run,

automatic testing – testing cases are generated i.e., by SCADA system. Also, formal testing techniques can be used. [4]

2. TIA PORTAL COMMON ERRORS

As the abstract says, my paper deals with developing application for testing of selected errors in PLC (ladder) code. This PLC code is written by PLC programmers in one smaller company in my city and in most cases containing lot of errors or bugs of various relevancy such as:

- Reading Temp variable before writing to it
- Not named networks
- Wrong used sensor symbolics (i.e., sensor from Station 120 used in Station 180)
- Same variable assignments on multiple coils
- For more instances of used function blocks, timers, triggers, etc. used same DB variable
- Not used variable, which is defined in the interface of the PLC block
- Too many instructions in one network
- Used bad markers
- Default name of HW components
- Not assigned partner in PN topology

Version of TIA Portal: V16

3. DIAGRAM

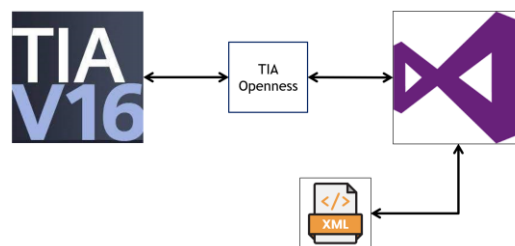


Figure 1: Simple diagram of application, communicating with TIA Portal and exporting blocks via TIA Portal Openness

4. HOW THE APPLICATION WORKS

The application for PLC code testing is being developed in Visual Studio 2019, C# programming language and as a simple windows form application. Application communicates with opened TIA Portal project via TIA Portal Openness. TIA Portal Openness is the API for WinCC and STEP7 in the TIA Portal, which enables users to create their own TIA Portal controlling application, or enabling automate their engineering tasks, or read info about HW configuration, PLC blocks, HMI devices, etc. Application can open TIA Portal or TIA Portal project or recognize and connect to opened TIA Portal project and load it into a *TiaProject* class instance in my application, which is provided by Openness and inform the user about connected project and show its name.

The main problem of Openness is that it cannot access individual networks and network parts, so the Openness is for most of the problems described in Introduction unusable. So, there must be another way to access networks and read specific information about them and this is can be realize via XML prescription of PLC blocks.

After the successfull connection is made, application will clear special folder, and then recursively export all PLC blocks from TIA Portal project to this folder, again by Openness. When this is done, application starts read info and taking it to my special structure of PLC blocks, already containing the info about all networks, parts, variable accesses, wires (ladder diagram) and FB/FC calls.

After all blocks are loaded into *ProjectBlocks* structure, application starts error finding algorithms and taking them into lists of errors. Every error, found in the structure, is recorded, and shown in the list view. Application enables user to download list view to text file. Error is identified by its name, description, project, PLC block and network in which it occurs.

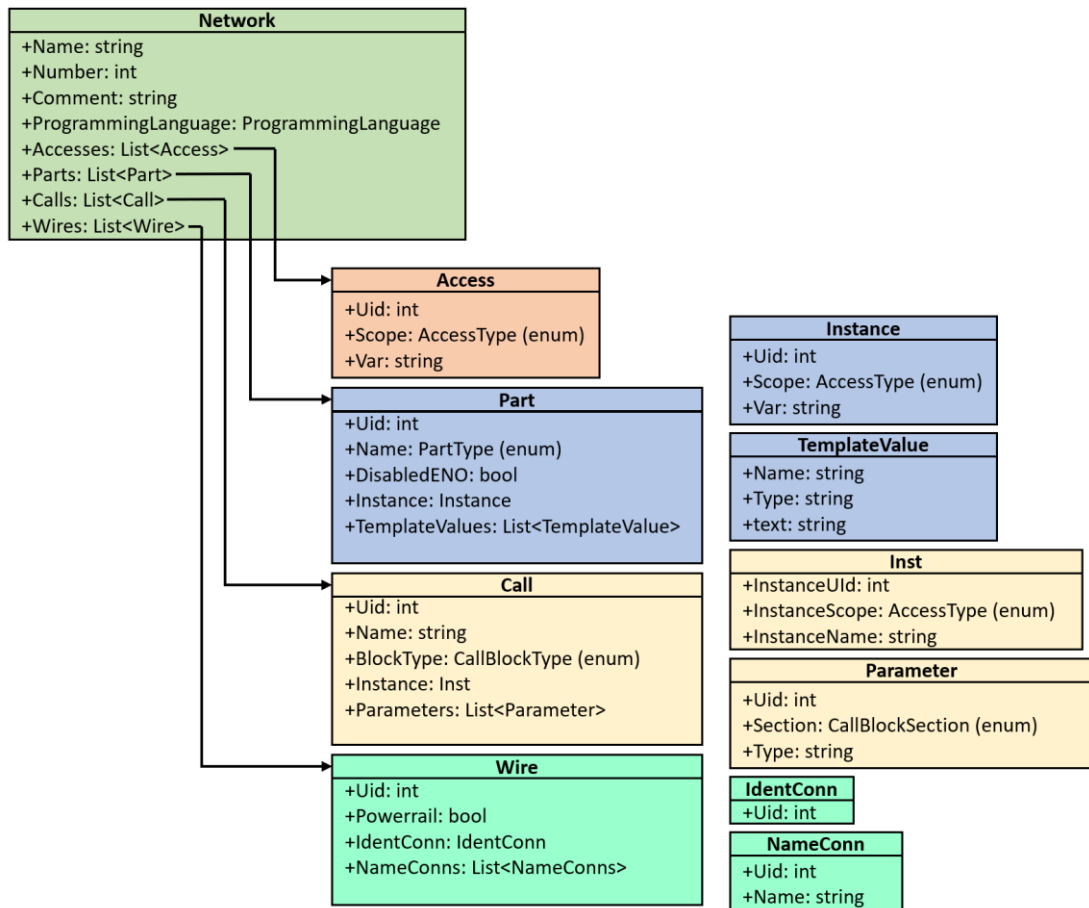


Figure 2: Network class of PLC block in *ProjectBlocks* structure

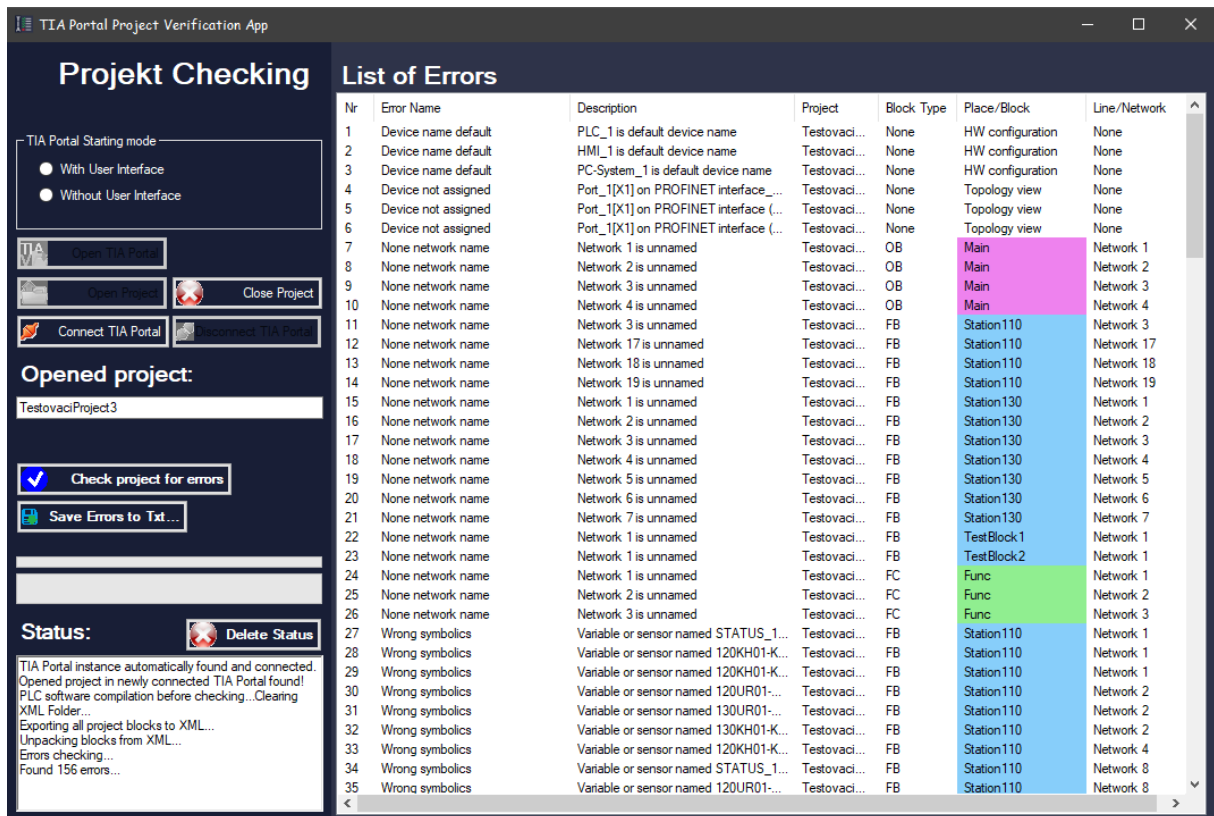


Figure 3: Application interface

If you have opened TIA Portal project, you can simply run the application. Application will automatically connect to your opened project. You can open another project in application too. The found project name is displayed. The all you need to do is click on the *Check project for errors* button and full progress of error finding will be launched. On its end, results will be displayed in the list of errors to the right on the figure 2. You can save this list to txt file.

5. CONCLUSION AND WORK PROGRESS

My work's will be purely oriented in the software field. Practically, I work only with TIA Portal, Openness, Visual Studio, XML and text editors. My work is intended for company usage.

Currently, application is almost done. All error searching algorithms are implemented and my work is focusing on improving application's reliability and stability – trying to find exception throw cases, having meeting with company consultant and make testing cases in TIA Portal.

The benefits of this work, which I consider as important, are *ProjectBlocks* structure, object-oriented application and, of course, gained experiences with TIA Portal Openness. The biggest benefit is application functionality itself – it allows programmers to detect their mistakes, which TIA Portal can't detect defaultly by compiling. This role is very important in terms of PLC code testing and finding out where the error is occurred. In company, for which I am creating this application, are also being strictly used their own datablock variables and PLC tags which allow me to implement Wrong symbolics error searching algorithm.

The main disadvantage of my application is relative long error finding time, especially if there is a huge project with lots of blocks, where each block contains over 100 networks. In this case, error finding time can reach 2-3 minutes, including blocks export to XML, blocks XML loading into *ProjectBlocks* structure and error searching itself.

Work progress

I started working on this application at the end of January 2022 and in first three weeks of work I was learning TIA Portal Openness and finding its functionalities, which can be important and crucial for my work. I found out, that Openness is unable to approach networks and interfaces of PLC blocks, but is able to export PLC blocks to XML files. And in this block XML file, networks and interface are already contained. Then I made a structure (which Networks part is shown up in fig. 2) and method, which contains algorithms of loading important parts of XML file to this structure. After that I was able to do error searching algorithms. In case of HW configuration errors, I didn't even need to use *ProjectBlocks* structure, in case of SW errors, *ProjectBlocks* structure was necessary.

ACKNOWLEDGMENT

This work was supported by Brno University of Technology and was carried out with the support of the project FEKT-S-20-6205 Research in automation, cybernetics and artificial intelligence for Industry 4.0.

REFERENCES

- [1] Sharma, L. (2021, July 7). *What is software testing and ways of software testing*. TOOLSGA. Retrieved March 11, 2022, from <https://toolsqa.com/software-testing/software-testing/>
- [2] Nidhra, S. (2012). Black Box and White Box Testing Techniques – A Literature Review. *International Journal of Embedded Systems and Applications*, 2(2), 29–50. <https://doi.org/10.5121/ijesa.2012.2204>.
- [3] *Software Testing Levels*. (2020, September 16). SOFTWARE TESTING Fundamentals. Retrieved March 11, 2022, from <https://softwaretestingfundamentals.com/software-testing-levels/>
- [4] Fernández, B., Blanco, E., & MERZKHIN, A. (2013, October). *Testing & verification of PLC code for process control*. ICALEPCS, San Francisco, USA, from https://www.researchgate.net/publication/270279486_Testing_verification_of_PLC_code_for_process_control

CONTROL SYSTEM FOR MANAGEMENT OF WATER SUPPLY AT A FARM

¹Aleš Doležal

¹Bachelor Degree Programme (3.), Brno University of Technology, Czech Republic

E-mail: xdolez89@vutbr.cz

Abstract - This paper deals with installing a new system for the supply and management of water on a farm. A PLC from Unitronics company was chosen with the appropriate modules for control and operation. The PLC program has been written in the UniLogic integrated development environment from Unistronics company using ladder language. The new system is controlled and monitored locally by the HMI panel and remotely by the website. The HMI and the website were created in the UniLogic Integrated Development Environment. The thesis also deals with selecting suitable sensors and components for system regulation.

Keywords – PLC, Control system, flowmeter, level sensor

1. INTRODUCTION

Description of the old system

The control system for water supply and management, which is currently applied on the farm, is considered outdated from an economic and safety point of view and completely inadequate to current modern standards. At the time the system was designed and commissioned, it was one of the most advanced control systems on the market. However, the gradual advent of more modern and affordable technologies has made it obsolete. Therefore, farm owners have opted for investing in a control system that will already meet the requirements of modern times e.g. remote communication, diagnostics of equipment connected to the system. Furthermore, the system should not be demanding and costly to maintain and meet the safety requirements of today.

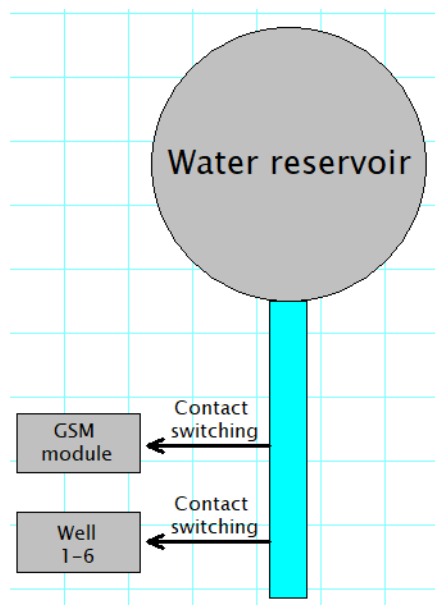


Figure 1: Block diagram of the old system

Concept of the new system

The system that will be installed in place of the existing system will work on a completely different principle of water supply to the farm. As this is not a retrofit of an existing system, the design can be implemented from scratch and does not have to follow the existing wiring. The newly installed system will meet the requirements of today's modern times, which present easier maintenance and operational requirements for the operator. The control system will be able to communicate with the operator remotely in the event of a fault, thus greatly reducing the time from fault onset to detection to fault clearance. Furthermore, the system will record operating conditions, according to which regular maintenance of the installed equipment can be planned. Last but not least, it will be possible to control and monitor the system remotely via a website.

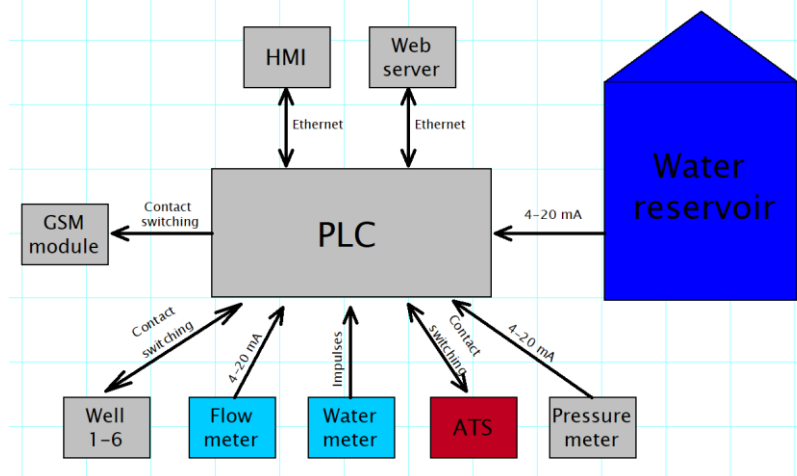


Figure 2: Block diagram of the new system

2. SOLUTION

PLC

A PLC from Unitronics was selected to control the entire water supply system. The PLC was selected based on positive experiences in previous projects. Specifically, the B10-T42 model of the Unistream series was selected, this is the most advanced PLC that Unitronics supplies. The PLC also supports a Web server option for remote communication with the PLC via the Internet. Due to the lack of digital and analog inputs, the PLC has been supplemented with expansion modules, namely the UID-1600 and WCB2 modules. The UID-1600 module is used to expand the PLC with 16 more digital inputs. The WCB2 module is used to expand the PLC by two analog inputs and 10 digital inputs.

Flowmeter

An inductive flow meter was chosen to measure the flow rate at the inlet pipe to the reservoir. The inductive flowmeter was chosen because of its low purchase price compared to other flowmeters that work on a different measuring principle (ultrasonic, turbine). Another reason why it was chosen is its design and method of flow measurement. There is no need for long stilling pipes etc.

Level gauge

A hydrostatic probe type level gauge was selected to measure the water level in the reservoir. The level gauge was selected based on the ease of installation in the reservoir and its purchase price. A two-state level sensor was selected as a backup level sensor in case of failure of the

hydrostatic probe. The hydrostatic probe measures continuously so that the actual level in the reservoir can be read.

Control system

The control system monitors the water level in the reservoir, from which the entire system is controlled. The system has created four virtual levels (level 1 - Water tank is full, level 2 - Water level in the water tank is decreasing, level 3 - Water level is low, level 4 - Water tank is empty). Based on these levels, controlled pumps are started to replenish the water in the reservoir, as well as the automatic pressure station (APS).

Levels in the water reservoir

The water is at level 1 in the reservoir. The booster pumps are off. When the water in the reservoir drops to level 2, the replenishment starts to bring the water in the reservoir to level 1. If the water intake from the water tank is greater than the inflow to the water tank and the water level drops to level 3, a text message is sent with a low-level message in the water tank. If the water level has dropped to level 4 i.e. the water tank is empty. The APS is switched off to avoid damage due to dry running and the pumps that replenish the water tank are still on.

Additional pumps

Additional pumps are located in wells around the farm. The pumps are controlled by a control circuit that communicates with the control system. In case of a request from the control system, the pumps are switched on. The pumps are equipped with several protection elements (current protection, phase failure control, and probes that monitor the water in the well). If the pumps are faulty, a fault message is sent to the control system and then a fault SMS is sent to the system operator.

APS

The APS ensures constant pressure in the farm's water supply system. The APS controls itself according to the current pressure in the line, when the pressure drops and there is enough water in the water tank the APS starts, if the APS does not start even if there is enough water in the water tank a fault SMS is sent.

Controls

The switch cabinet includes an HMI module that can be used to control and monitor the entire system. The HMI panel shows the current values of the system (outlet pressure, water level in the reservoir, faults on the equipment, etc.) To simplify operation and work on the equipment, remote access via the Internet has been established. The control and monitoring environments are identical both on the HMI panel and on the remote access via the website.

Control algorithm

Automatic switching on of the additional pump in the well.



Figure 3: Automatic switching on of the additional pump in the well

If the following conditions are met and the water in the well drops to the 2nd level, the pump switches on.

pom filtr s1 - if the filter on the supply pipe is not blocked the pump can pump

aut c1 - the switch on the switchboard door must be switched to the AUT position
aut obr1 - automatic mode must be selected on the HMI and the AUT field marked
hladina s1 - there must be sufficient water in the well
vypadek faze s1 - the pump must not be powered by 2 phases
tepelná ochrana s1 - if the pump starts to overheat the system will switch off the pump

Switch off the additional pump by the probe in the water tank

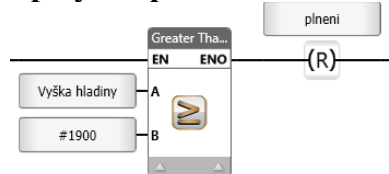


Figure 4: Switch off the additional pump by the probe in the water tank

If the level in the water tank is higher than 1900 mm the pumps in the wells will switch off.

Pump motor hours counter

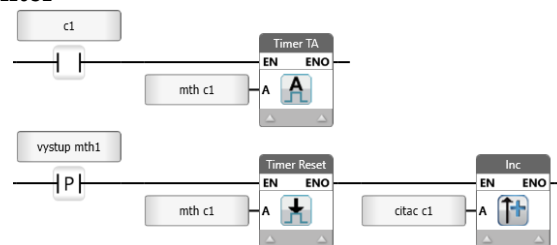


Figure 5: Pump motor hours counter

While the pump "c1" is switched on the Timer Accumulated counts for 1 hour, once the time is up the timer is reset and the counter is incremented by 1.

Probe failure in the water tank.

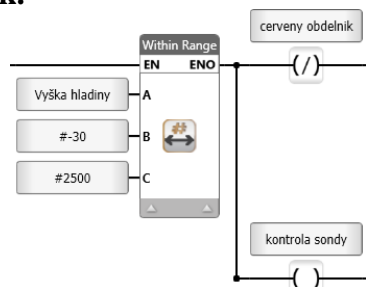


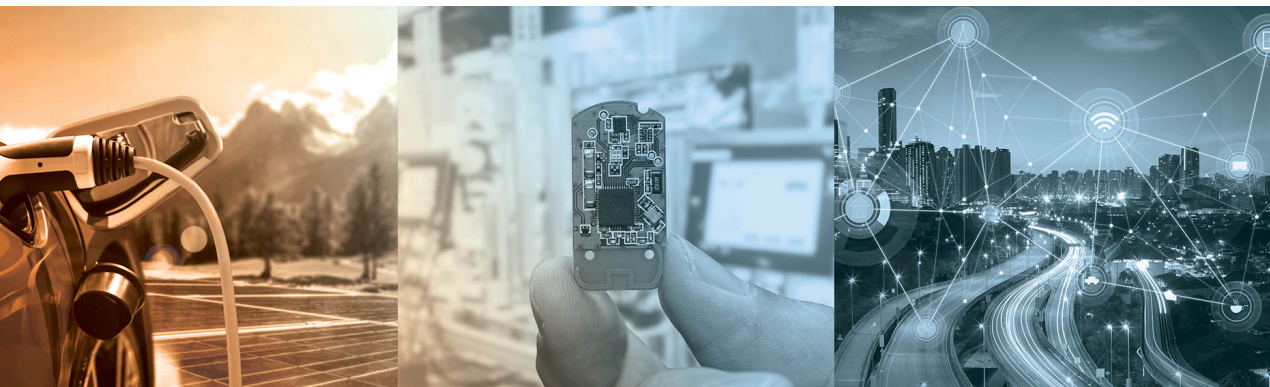
Figure 6: Probe failure in the water tank

If the probe in the water tank starts to send values out of range this condition is evaluated as a fault, the probe is disconnected and goes into semi-automatic mode. Information about the level is obtained from the float, which is located in the water tank. when a fault occurs, an SMS is sent to the system operator. The fault is displayed on the HMI as a red rectangle instead of a graphical display of the current level in the water tank.

3. CONCLUSION

The old system has been successfully upgraded to a newer and more advanced system that already meets the requirements of modern times and modern farms. Remote access has been very well received by the system operators. In the future, the new system should be complemented by sending a regular report for the past month with operational data.

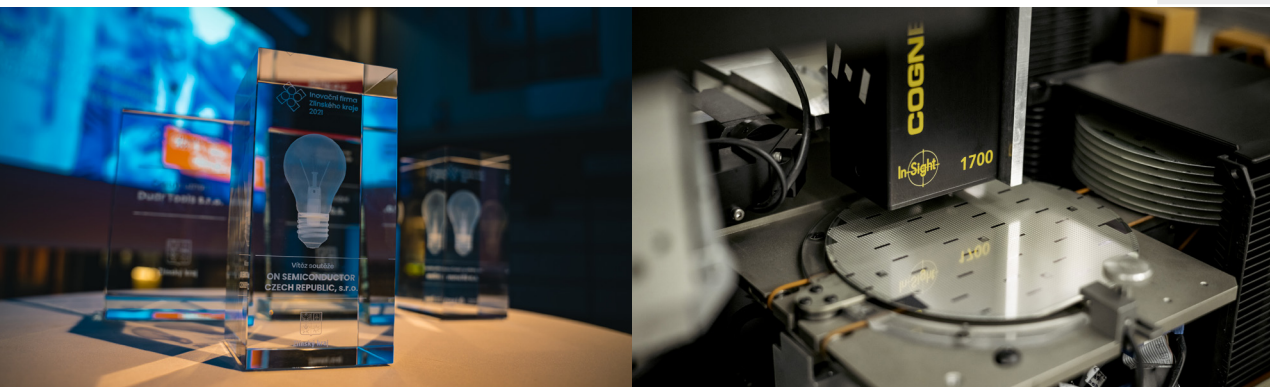
Budoucnost se děje nyní



Současná expanze výroby nám umožňuje vyrábět špičkové produkty na unikátních technologických zařízeních.

- V posledních čtyřech letech jsme investovali čtyři miliardy do posílení našich výrobních kapacit.
- Kromě výroby čipů na křemíku rozvíjíme i výrobu na karbidu křemíku. Ve výrobě čipů na karbidu křemíku se chceme stát světovou jedničkou.
- Čipy na karbidu křemíku jsou slibnou technologií. Ve srovnání s čipy na křemíku dokážou uspořit až 10% energie, která přes ně prochází.

Získali jsme prestižní ocenění Inovační firma Zlínského kraje 2021



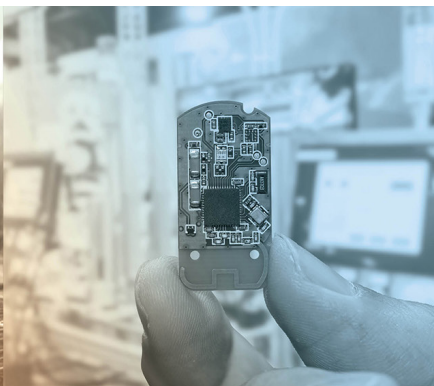
U nás si můžete plnit své sny

Nabízíme:

- Práci na technologiích a produktech, které přispívají k zelenější budoucnosti.
- Šanci být u zrodu převratných novinek v polovodičovém průmyslu.
- Cenné zkušenosti díky nejmodernějším technologiím a systémům.
- Tým odborníků na špičce technologie polovodičů.
- Nejlepší benefity v regionu.
- Zázemí stabilní mezinárodní společnosti.

onsemi™





STROJNÍ
ELEKTRO
APLIKOVANÉ VĚDY
INFORMATIKA
EKONOMIE
CHEMIE
DESIGN
JAZYKY
HUMANITNÍ
OSTATNÍ

Jsmo úspěšným světovým výrobcem polovodičů s dlouhou tradicí a více než 2000 zaměstnanci v České republice. Naše výrobky mají široké využití v různých oblastech, jako jsou spotřební a průmyslová elektronika, automobilový průmysl, telekomunikační technologie a výpočetní technika. V České republice působíme v Rožnově pod Radhoštěm a v Brně v oblastech:

- návrhu integrovaných obvodů
- výzkumu a vývoje nových technologií
- technologií výroby křemíkových desek a polovodičových čipů

NABÍZÍME

Pro studenty:

- placené stáže a brigády
- stipendia
- specifikace témat a vedení bakalářských/diplomových prací
- exkurze
- prohlídky pro veřejnost
- pro absolventy nabízíme pracovní uplatnění na zajímavých pracovních pozicích

HLEDÁME

Preferované obory:

- mikroelektronika
- radioelektronika
- výkonová elektrotechnika
- elektrotechnologie
- chemické, fyzikální a materiálové inženýrství

- anorganická a analytická chemie
- informační technologie
- průmyslové inženýrství a automatizace
- fyzika pevných látek

PRŮBĚH VÝBĚROVÉHO ŘÍZENÍ

Klademe důraz především na odborné a jazykové znalosti, které uchazeči získali během studií a předchozí praxe. Podstatným kritériem výběru je pro nás také osobnostní hledisko. Během pohovoru se setkáte se zástupcem personálního oddělení a vedoucím, který danou pracovní pozici ve svém týmu obsazuje. Společně se snažíme vytvořit přátelskou a neformální atmosféru.

„Pro mnoho lidí je práce povinnost, pro mě však práce pro onsemi znamená radost. Považuji za štěstí, že jsem se mohla stát členem skupiny neskutečně vzdělaných lidí a špičekách ve svém oboru. Ve vývoji polovodičových součástek je velká budoucnost. Jsem ráda, že jako analogový designér mám tu možnost kombinovat seberealizaci v tomto technickém odvětví a zároveň spolupráci se skvělými lidmi.“

Zuzana Kozlová
Recruiter
zuzana.kozlova@onsemi.com
+420 605 842 281

SCG Czech Design Center, s.r.o.
1. máje 2594
756 61 Rožnov pod Radhoštěm
Česká republika



Design Layout Engineer

www.ikariera.cz/cz/companies/detail/370
<https://kariera-onsemi.cz/>

PLNÝ ÚVAZEK

ČÁSTEČNÝ ÚVAZEK

BRIGÁDA

BAKALÁŘKA

DIPLOMKA

STIPENDIUM

PRAXE/STÁŽ

TRAINEE PROGRAM



PROFIL

GALERIE

VIDEO

AKTUÁLNÍ
PŘÍLEŽITOSTI
SPOLUPRÁCE

ONLINE
PRACOVNÍ
NABÍDKY

ZAMĚSTNANCI

UDÁLOSTI

ČLÁNKY

FAKTA

KONTAKTY

FUSION OF SENSORS FOR AUTONOMOUS UAV NAVIGATION

¹Jakub Semerád, ²Jiří Janoušek

¹Bachelor Degree Programme (1.), FEEC, Brno University of Technology, Czech Republic

²DCI, FEEC, Brno University of Technology, Czech Republic

E-mail: xsemer10@vutbr.cz, jiri.janousek@vut.cz

Abstract—This paper describes a UAV equipped with a control computer, flight controller, Lidar and depth camera. The UAV telemetrically communicates via the Mavlink communication protocol with a ground station where actual data can be monitored or the drone's mission can be interfered from there. This whole system produces a 2D map and a 3D color map in real time. This data can be used for obstacle avoidance, object recognition, mapping unknown environments, tracking moving objects and autonomous navigation.

Keywords—UAV, Drone, Autonomous navigation, Lidar, Depth camera, Point cloud

1. INTRODUCTION

UAVs (Unmanned Aerial Vehicles) have recently reached a stage where they can carry a lot of equipment on them and at the same time, thanks to sufficient battery capacity, they can stay in the air for a long time. Based on the specific purpose of the application, UAV can typically carry a laser or ultrasonic range finder, RGB camera, depth camera, thermal camera, spectral camera or other sensors. In many applications, a combination of multiple sensors is used for more accurate measurements. One important aspect is to detect obstacles in the flight path so that collisions can be avoided and new flight paths can be set. This approach leads to increased autonomy of the UAV, but introduces complexity in on-board computation, trajectory planning and communication with the ground station. Often UAVs are also equipped with certain actuators.

Nowadays, drones like these are already used in a large number of applications. These include infrastructure inspections, field surveys, scientific data collection, monitoring for premises security. In addition, they are useful for transporting and delivering goods, surface mining, mapping, spraying fields, monitoring the condition of natural habitats and delivering medicines.

2. SENSOR FUSION

The main element of the whole experiment will be the drone, which is robust enough to mount the necessary hardware on its structure. As shown in Figure 1, the main hardware is a Pixhawk 4 autopilot and a powerful NVIDIA Jetson Nano Developer Kit computing unit. Both units communicate with each other by serial connection. RPLIDAR A3 and Intel RealSense D455 camera module were chosen as sensor equipment. The data collected by these sensors is sent to the NVidia Jetson Nano computing unit for further processing. Using this data, the drone is able to sense its surroundings. On the Jetson Nano computing unit equipped with Ubuntu 18.04, ROS (Robotic operating system) software is installed. Packages in ROS are used to process the sensor data. Pixhawk 4 communicates with a ground station, in this case a PC. The communication can be via radio or Wi-Fi. The Mission Planner software is installed on the ground station, in which it is possible to monitor current data related to the drone flight and sensor data. All communication is handled by the MAVLINK communication protocol. UAV with sensors is shown in Figure 2.

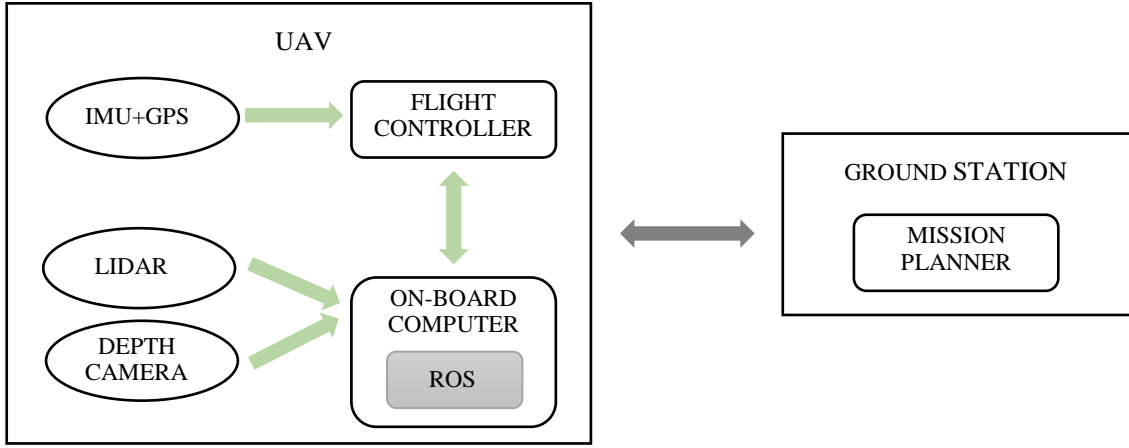


Figure 1: Block diagram of the experiment



Figure 2: UAV used in the experiment

2.1 LIDAR

Lidar (Light detection and ranging) is a system that emits laser beams, receives reflected signals from obstacles and evaluates the distance of objects. In this work a 2D RPLIDAR A3 was used. Using the Robotic Operating System (ROS), specifically the hector_slam package, it is possible to generate a real-time 2D map of the environment along with the current position and trajectory of the UAV. This whole concept is called SLAM (Simultaneous localization and mapping). This concept is suitable for mapping unknown environments both outdoors and indoors. At the same time, this data can also be used for autonomous navigation. However, for autonomous navigation, it is not appropriate to use only 2D data obtained with RPLIDAR A3, because it captures objects in only one plane. If an obstacle is in a plane slightly higher than the lidar is on the UAV and the drone is moving upwards before the lidar detects the obstacle, the UAV could crash into it. Even when mapping an unknown environment, a simple 2D map may not always be sufficient. Therefore, it is advisable to use another sensor working on a different principle [1][5].

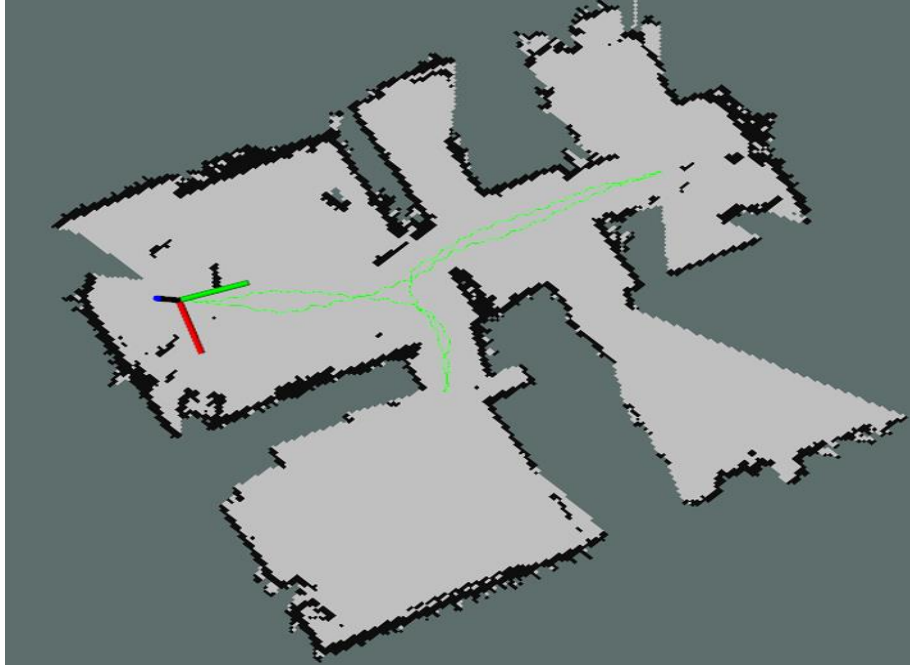


Figure 3: Data obtained from RPLIDAR A3.

2.2 DEPTH CAMERA

Depth camera works on the principle of capturing images from two lenses where the distance between them is known. Each lens records the scene separately and based on the difference in displacement of the images obtained from the two lenses, the depth of the image or distance of the objects can be calculated. This principle makes it possible to create a 3D map of the environment, shown in Figure 4. The obtained 3D data is again suitable for mapping an unknown environment and also for autonomous navigation of UAVs. In this work, the Intel RealSense D455 Depth Camera was used. This camera contains not only two lenses to obtain depth images, but also a classical RGB camera [4].

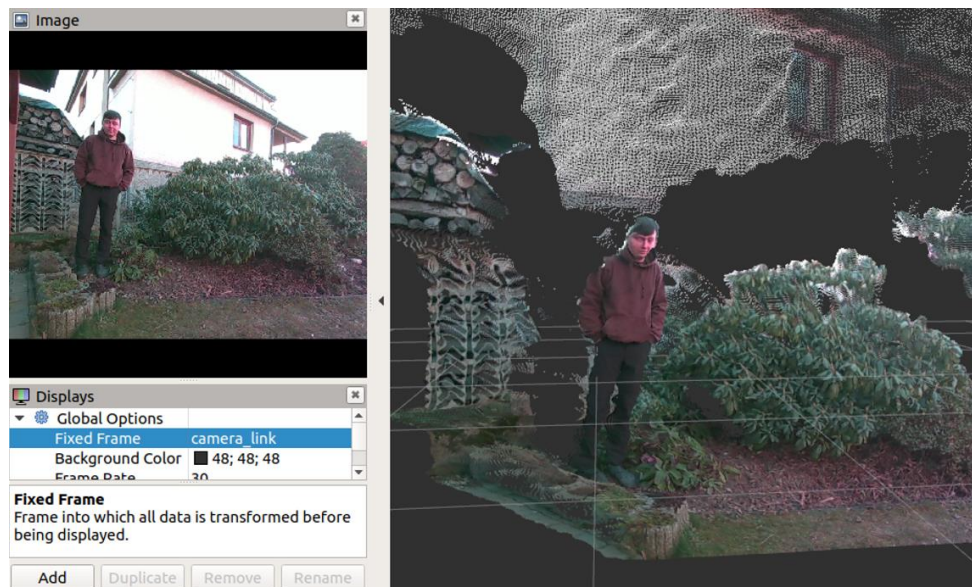


Figure 4: Data obtained from Intel RealSense D455.

3. CONCLUSION

The data obtained from the sensors is suitable for use in exploration of unknown environments, obstacle detection, autonomous navigation. Lidar obtains a 2D map of the environment along with the distances of objects from the drone in real time. Subsequent use of, for example, `hector_navigation` or `hector_localization_package` would allow real-time autonomous exploration of unknown environments while avoiding obstacles. From the Intel RealSense D455 camera, I obtain a color 3D map of the environment. Compared to Lidar data, it has a much smaller range (0.6 - 6m), where RPLIDAR A3 can sense objects up to 25m away. However, despite the shorter range, this data has a lot of uses. For example, using the `ros_object_analytics` package, it would be possible to classify objects, detect obstacles, real-time localization or tracking of a moving object [2][3][4][5].

This whole concept could be used for exploring dangerous environments, searching for lost persons, tracking moving objects, obstacle avoidance and many other applications.

ACKNOWLEDGMENT

The research was funded from the Ministry of the Interior of the Czech Republic (MVCR) grant no. VJ02010036 (An Artificial Intelligence-Controlled Robotic System for Intelligence and Reconnaissance Operations).

REFERENCES

- [1] ROS Wiki – `hector_slam`. Documentation - ROS Wiki [online]. [cit. 2021-03-12] Available from: http://wiki.ros.org/hector_slam
- [2] ROS Wiki – `tu-darmstadt-ros-pkg` Documentation - ROS Wiki [online]. [cit. 2021-03-12] Available from: https://wiki.ros.org/tu-darmstadt-ros-pkg#Quadrotor_Simulation_and_Control
- [3] GitHub - intel/ros_object_analytics. GitHub: Where the world builds software · GitHub [online]. Copyright © 2022 GitHub, Inc. [cit. cit. 2021-03-12]. Available from: https://github.com/intel/ros_object_analytics
- [4] Depth Camera D455 – Intel® RealSense™ Depth and Tracking Cameras. Intel® RealSense™ Computer Vision - Depth and Tracking cameras [online]. Copyright © Intel Corporation [cit. cit. 2021-03-12]. Available from: <https://www.intelrealsense.com/depth-camera-d455>
- [5] RPLIDAR-A3 Laser Range Scanner Parameters|SLAMTEC. 301 Moved Permanently [online]. [cit. 2021-03-12] Available from: <https://www.slamtec.com/en/Lidar/A3Spec>

PASSIVE OPTICAL DETECTION AND CLASSIFICATION OF FLYING OBJECTS

A. Mošková¹ and E. Vlachová Hutová²

¹DCI, FEEC, BRNO UNIVERSITY OF TECHNOLOGY, CZECH REPUBLIC

²DTEE, FEEC, BRNO UNIVERSITY OF TECHNOLOGY, CZECH REPUBLIC

E-mail: 221005@vut.cz, xhutov00@vut.cz

Abstract—The article presents our solution for the classification of moving flying objects in a video sequence captured by a static camera. The tool uses the extraction of scale and rotation invariant SIFT features, which allow the multi-class SVM to classify the examined object into one of the considered classes: ‘bird’, ‘plane’ or ‘negative’. The most successful of our tested models achieved accuracy of over 90% and their recall and precision for each class reached values above 90%.

Keywords— Object recognition, machine learning, SIFT, SVM, Matlab, motion detection

1. INTRODUCTION

Optical detection of flying objects in the sky in connection with their classification represents an important task in the field of computer vision and image processing. It is used in systems ensuring the scanning of airspace around airports and the prevention of collisions of aircraft with birds. Several works also deal with its use in the field of environmental research and bird monitoring [1], [2] or in systems aimed at protecting crops and vineyards from bird flocks [3].

There exist several methods of classification of flying objects and the choice depends on the application itself, the requirements, and the technical options available. A classifier, pre-trained on a suitable set of sample images, analyzing various significant features extracted from the processed images [1], [2], can be used effectively. Another possibility is the use of convolutional neural networks [1], [3].

This article focuses on the design of an algorithm for detection and classification of flying elements in the sky that could be used in some of the above applications. The aim was to create a tool with a high success rate of classification (recall and precision for each considered class ideally above 80%), which could be implemented as a relatively simple, fast, and cheap solution that does not require special hardware equipment.

2. PROPOSED METHOD

The proposed approach involves the analysis of a video sequence captured by a statically mounted camera, which aims to detect changes in consecutive frames indicating movement in the observed scene. This article presents an algorithm performing extraction of moving elements and their identification using Matlab program. The main steps of the proposed method are shown in the in the Figure 1.

2.1 TRAINING DATA ACQUISITION AND PREPROCESSING

The processed video recordings are obtained using a camera placed on a tree in a private garden near Brno-Tuřany Airport. The scene being shot is shown in the Figure 4. The selected Xiaomi YI Outdoor 1080p camera is suitable for outdoor use. It allows data transfer only via wifi, so it was necessary to create a hotspot using a Raspberry PI 3 B. A microcomputer in the Raspberry with an integrated wifi module creating a wifi network in the vicinity was connected to a module for mobile data with an inserted SIM card. The data is collected on a high-capacity SD card inside the camera, from which online downloads are available.

The retrieved data are processed by a C # program on the .NET platform, which compares binary edge representations of consecutive frames. White pixels in differential binary images correspond only to moving elements in the examined video, and they are saved along with corresponding original frames.

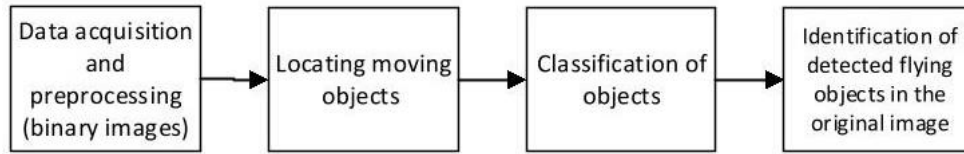


Figure 1: Flowchart of the presented approach.

2.2 MOVING OBJECTS LOCALIZATION

From the first frame of the processed video sequence a binary mask segmenting the image into the examined area of the sky (value 1) and the surroundings, which are not the subject of analysis (value 0), is created. By multiplying the mask and the differential binary image, the elements not located in the sky are filtered out. The dimensions and coordinates of the bounding boxes delimiting the remaining objects in the modified binary image, which were not eliminated by the mask, are determined by using the function searching for connected components. Cuts of the original image defined by these bounding boxes are then individually evaluated by the classifier.

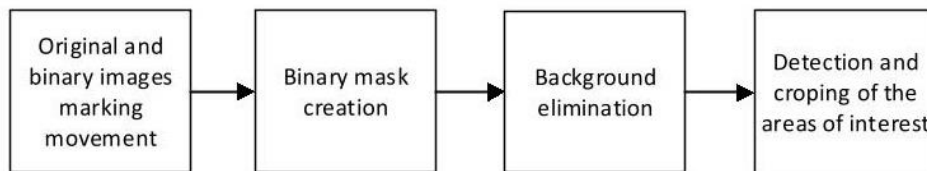


Figure 2: The approach used to detect position of moving objects in the image.

2.3 DATASET AND OBJECT CLASSIFICATION

For the purposes of classification, it was necessary to specify the classes into which the examined objects will be divided and to create a sufficiently large suitable training set of images. Using the obtained video recordings, but also photographs of flying birds and images searched on the internet, a set of 5459 images was created, consisting of 1994 representations of the class 'plane', 1144 of the class 'bird' and 2321 of the class 'negative' displaying for example moving leaves, branches, or clouds to which the motion detection algorithm is sensitive, but they do not represent objects of interest for us. The size of the images in the dataset and also the processed images varies from 2x2 pixels (branches, clouds, or very distant objects) to approximately 40x40 pixels (airplanes or birds flying close to the camera, images downloaded from the internet).

The classification of objects is realized by the analysis of significant features extracted from the examined images using the SIFT method, which is characterized by independence of scale and rotation as well as resistance to brightness or geometric transformations [4]. By classifying the features of an image into a determined number of clusters using the iterative algorithm k -means and then creating a histogram of the occurrence of clusters in the image, we obtain single descriptive vector of that image. The vector represents an optimal input for the multi-class SVM, which then ensures the classification of the object into one of the classes [5]. SVM was trained using Matlab Classification Learner App.



Figure 3: The proposed classification method.

Since some processed images are very small, the amount of extracted SIFT features may not be sufficient to ensure proper object recognition. We therefore decided to try to strengthen the classifier using color features. An RGB histogram consisting of 8 bins for each color channel was extracted from each image.

The resulting vector of length $8 \times 8 \times 8 = 512$ elements thus extended the original descriptive vector of the processed image. Figure 3 summarizes our tested classification method.

3 RESULTS AND EVALUATION

The proposed classification method was firstly validated for different values of the parameter k indicating the number of clusters grouping SIFT features and for several types of SVM kernels. Each tested classification model is evaluated according to accuracy (the rate of correct classifications among all predictions) and the parameters precision (positive predictive value PPV) and recall (true positive rate TPR) for each considered class. The results are shown in Table 1. The best-achieved are highlighted. The most successful models worked with the number of clusters $k = 100$. This parameter was used for testing descriptive vectors supplemented with color features and the results are summarized in Table 2.

We can observe that using RGB histograms as color features to support classification based on SIFT features improves statistical results and they meet our set objectives. However, it is evident that in the case of every model the ‘bird’ class is characterized by the lowest rates of both positive detection (TPR) and positive prediction (PPV), which may be due to its under-representation in the training set. In addition, the method is sensitive to adverse weather conditions (clouds, rain, or wind) in which incorrect predictions of ‘bird’ and ‘plane’ classes are more common. The extension of the set as well as its balancing could provide better results and should be the subject of further research. Figure 4 shows the results of the analysis of a video recording using our detection and classification tool working with the most successful models. The time of processing varies from 60 to 900 ms per one frame and it depends on number of located and classified moving elements in the image.

Table 1: Accuracy, Precision and Recall of tested models of classifier processing SIFT features

K	Kernel	Accuracy [%]	Plane		Bird		Negative	
			TPR[%]	PPV[%]	TPR[%]	PPV[%]	TPR[%]	PPV[%]
50	Linear	93,0	91,5	91,0	83,3	85,6	99,1	98,3
	Quadratic	93,0	93,1	93,0	88,2	88,9	98,9	98,5
	Cubic	93,0	93,2	91,6	83,7	88,2	98,8	97,8
	RBF	94,5	92,6	93,8	90,9	87,8	98,6	99,2
100	Linear	93,4	90,9	91,8	87,4	84,7	98,6	99,3
	Quadratic	95,0	93,4	93,8	90,1	89,1	98,8	98,8
	Cubic	94,8	93,4	93,0	89,0	89,3	98,9	99,0
	RBF	94,8	92,3	94,0	91,5	86,9	98,5	99,6
200	Linear	93,4	91,5	91,4	86,1	85,5	98,6	99,0
	Quadratic	94,5	92,8	93,1	88,8	88,0	98,7	98,9
	Cubic	94,5	93,0	92,8	88,5	88,0	98,7	99,1
	RBF	90,6	95,9	82,0	65,5	89,8	98,3	99,5

Table 2: Accuracy, Precision and Recall of models of classifier processing SIFT and color features

K	Kernel	Accuracy [%]	Plane		Bird		Negative	
			TPR[%]	PPV[%]	TPR[%]	PPV[%]	TPR[%]	PPV[%]
100	Linear	95,2	94,0	93,4	90,2	90,6	98,8	99,1
	Quadratic	95,9	95,2	94,3	91,4	92,3	98,8	99,1
	Cubic	96,0	95,3	94,4	91,7	92,9	98,7	98,9
	RBF	90,1	96,8	80,4	78,6	94,5	90,0	99,2



Figure 4: On the left, an example of correct aircraft detection, with display of image coordinates and class, on the right, incorrect prediction of ‘plane’ and ‘bird’ classes when detecting the movement of clouds and branches

4. CONCLUSION

The article presents an algorithm of processing video recordings of the airspace to detect and classify flying objects. The resulting classification models, using multi-class SVM fed with SIFT features and RGB color histograms extracted from previously detected moving elements of the video sequence, are characterized by high overall accuracy and also by recall and precision for all of the considered classes usually of above 90%. However, the success of the classification also depends on several more or less controllable parameters, such as camera location, image resolution or weather. The proposed algorithm could support, for example, systems aimed to scare off birds around airports or in vineyards and home gardens. The possibility of further development of the investigated method and expansion of its application lies, for example, in a combination of optical classification with analysis of audio information from the scanned scene, which is addressed in article [6] in the context of bird species differentiation.

ACKNOWLEDGEMENT

This research was funded by the Technology Agency of the Czech Republic, project number TJ04000441.

REFERENCES

- [1] R. Yoshihashi, R. Kawakami, M. Iida, and T. Naemura, “Bird detection and species classification with time-lapse images around a wind farm: Dataset construction and evaluation”, *Wind Energy*, vol. 20, no. 12, pp. 1983-1995, 2017, doi:10.1002/we.2135.
- [2] R. T'Jampens, F. Hernandez, F. Vandecasteele, and S. Verstockt, “Automatic detection, tracking and counting of birds in marine video content”, in *2016 Sixth International Conference on Image Processing Theory, Tools and Applications (IPTA)*, 2016, pp. 1-6, doi:10.1109/IPTA.2016.7821031.
- [3] P. Marcoň *et al.*, “A System Using Artificial Intelligence to Detect and Scare Bird Flocks in the Protection of Ripening Fruit,” *Sensors*, vol. 21, no. 12, p. 4244, Jun. 2021, doi: 10.3390/s21124244.
- [4] D. G. Lowe, “Object recognition from local scale-invariant features”, in *Proceedings of the Seventh IEEE International Conference on Computer Vision*, 1999, pp. 1150-1157 vol.2., doi:10.1109/ICCV.1999.790410.
- [5] G. Csurka, C. R. Dance, L. Fan, J. Willamowski, and C. Bray, “Visual categorization with bags of keypoints”, in *Workshop on Statistical Learning in Computer Vision, ECCV*, May 2004, pp. 1-22.
- [6] A. Marini, A. J. Turatti, A. S. Britto, and A. L. Koerich, “Visual and acoustic identification of bird species”, in *2015 IEEE International Conference on Acoustics, Speech and Signal Processing (ICASSP)*, 2015, pp. 2309-2313, doi:10.1109/ICASSP.2015.7178383.

Advanced Algorithms for Compression of Videos with Ultra High Resolution

O. Soukenik, L. Polak, J. Kufa

Brno University of Technology, Faculty of Electrical Engineering and Communication,
Department of Radio Electronics, Technická 12, 616 00 Brno, Czech Republic

E-mail: xsouke02@vut.cz, polakl@vut.cz, kufa@vutbr.cz

Abstract—In this paper, attention is devoted to advanced video codecs (HEVC, VVC, VP9 and AV1) and their utilization for compression of videos with Ultra High Resolution (UHD), also marked as 4K and 8K. A Python-based program employing FFmpeg multimedia framework is created to explore compression performances of such video codecs. It allows to automate encoding process and record all important information during the video compression (e.g. the required CPU time, time consumption, RAM usage). The performance of the video compression algorithms is evaluated in terms of objective quality metrics. First experimental results show that video codecs VVC and AV1 could replace HEVC and VP9 for 4K and 8K videos in the future.

Keywords— video codecs, objective metrics, FFmpeg, HEVC, VVC, VP9, AV1, Python

1. INTRODUCTION

Demand for videos in Ultra High Resolution (UHD), many times abbreviated as 4K and 8K, are gradually increasing. To broadcast video content in such a resolution with appropriate visual quality, especially in the case of Video on Demand (VoD) [1], efficient video compression algorithms (codecs) are required. The video compression tools need to be versatile and must excel with very flexible settings. The most established video codecs, High Efficiency Video Coding (HEVC) and VP9, can be utilized to compress videos with full HD resolution or 4K. However, their performances for videos with higher resolution are lower, especially at lower bitrates. Versatile Video Coding (VVC) [2] and AOMedia Video 1 (AV1) [3] are emerging compression algorithms developed for effective compression of videos in different formats. Compared to HEVC and VP9, their utilization for 4K and 8K videos can be more effective [4], [5].

In this paper, attention is devoted to compression performances of video codecs HEVC, VVC, VP9 and AV1. The visual quality of a test video compressed by these codecs is evaluated by different objective quality metrics. To automate and manage the encoding process of the video, a Python-based program employing FFmpeg¹ multimedia framework is developed and created.

This short paper is organized as follows. Video codecs used in this work are briefly introduced in Section 2. Objective metrics used to evaluate the quality of compressed videos are described in Section 3. Section 4 and Section 5 are devoted to the developed Python program to automate the process of video encoding and settings used to compression of a video, respectively. The obtained preliminary results are briefly evaluated in Section 6 while Section 7 concludes this paper.

2. ADVANCED VIDEO CODECS

The latest generation of video codecs supports computationally intensive algorithms used to improve intra frame compression by copying similar parts of a frame (intra prediction) or using a feedback with full decoding and analysis with objective metrics to improve the encoder's decision algorithm. Next, such video encoders have an additional option to make transmission more efficient for very small data stream (full prediction from surrounding blocks when the encoder assesses that the error will be small at using of an appropriate restoration filter). Significance of these improvements is visible mainly at transmission of synthetically generated contents such as game streaming, presentations and screen sharing.

In this work, we compare compression performance of video codecs HEVC, VVC, VP and AV1. HEVC and VVC have been developed within the family of H.26x video coding standards. Video codecs VP9 and AV1, compared to HEVC and VVC, are open and royalty-free, used mainly in the field of streaming (YouTube, Netflix). AV1 is developed by the Alliance for Open Media including such major companies like Apple, Facebook, Google, Microsoft, Netflix and Amazon.

¹ <https://ffmpeg.org/>

3. OBJECTIVE VIDEO QUALITY METRICS

The visual quality of a compressed video can be evaluated either by subjective or objective way. Subjective quality evaluation is based on the scores obtained from people who evaluate the video quality under laboratory conditions. The outputs of so called subjective tests have high information value (scores directly obtained from people). On the other hand, they are costly and time consuming. Objective quality metrics utilize mathematical-based algorithms to reveal the visual quality of the compressed videos. Depending on the availability of reference (uncompressed) source, these metrics can be full, reduced or non-reference (FR, RR and NR). Objective metrics are cost effective, on the other hand, but, in general, are less punctual than subjective-based studies.

In this work, the visual quality of videos is evaluated in terms of objective metrics. For this purpose, Peak Signal-to-Noise Ratio (PSNR) and Video Multimethod Assessment Fusion (VMAF) objective metrics are used. PSNR is a well-known metric used to assess initial visual quality of a video. VMAF is a combination of multiple objective quality metrics that have coefficients set using Mean Opinion Score (MOS) to make the final score closer to subjective rating.

4. TOOL FOR ENCODING OF VIDEO SEQUENCES

The process of video encoding, thanks to numerous options and settings of advanced compression algorithms, is not a straightforward task. Many times, reference implementation of these video codecs is command line based, and the definition and set of parameters can be not user friendly. Hence, within this work, a utility² for automate encoding of video sequences is created in program language Python. It allows to set and change encoding settings independently on the used video codec. In this way, a number of tasks can be easily created in a queue for processing. Because implementations of some video codecs are not scale to multiple cores of advanced processors, possibility of parallel processing to achieve higher efficiency is also considered. To process multiple video sequences, an option to batch process of them was implemented into the created utility.

The created tool employs FFmpeg library and its console utilities ffmpeg and ffprobe. FFmpeg provides an unified interface for various encoders with many options and settings. The tool was created under Linux operating system and allows to record data about CPU utilization, CPU time (from scheduler data) and memory required for encoding of a video sequence. Windows platform is supported as well.

5. EQUIPMENT AND SETTINGS

The compression performance of the used video codecs was tested on a short video sequence Chimera "Aerial" (420p 10 bit, 60fps, 1200 frames) from Netflix [6].

The compression of video has been realized on a regular desktop AMD Ryzen 5 1600AF (2. gen, Zen+) processor with a locked frequency of 3.6 GHz. It has 32 GB of 3200 MT/s and DDR4 RAM. Information about the used reference implementation of video codecs is summarized in Table I. VVenC [7] and VVdeC [8] were compiled using GCC with default settings.

Example of the used command to encode the video sequence by codec AV1 is follows:

```
ffmpeg -i <input> -c:v libaom-av1 -cpu-used 5 -b:v 0 -crf 39  
<output>.mkv.
```

The angle brackets indicate the parts of command that are variable. Argument "-c:v" is used to select the encoder (see Table I), "-cpu-used" is an encoder specific argument used for libvpx-vp9 and libaom-av1 to set the level of trade-off in quality for speed (similarly, for libx264 and libx265 it is used "-preset"). For libaom-av1 and libvpx-vp9 argument "-b:v 0" is needed for unrestricted maximal bitrate while "-crf" sets the constant Quantization Parameter (QP). Next, modes Constant Quality (CQ) and Constant Rate Factor (CRF) are used. Actual bitrate in these modes is largely dependent on that how much of temporal information is in the encoded video. Codec libvpx-vp9 was employed with "-deadline 0 -aq-mode 0", where "-deadline" is used to turn off limits for time spent on encoding of a frame and "-aq-mode" is utilized to turn off adaptive quantizer (needed for VMAF metric at high quantization levels [9]). VVenC was used with preset "fast", 12 threads and with PQPA on.

Ten values of evenly distributed QP (from 9 to 63) and CRF (from 9 to 45) were used.

²<https://github.com/ondrasouk/encoders-comparison-tool>

Table I: Used software stack

Software	Version	Source
Distribution	OpenSUSE Tumbleweed	
GCC	11.2.1	
FFmpeg	4.4.1	https://ffmpeg.org/download.html#get-sources
libvpx	1.11.0	https://www.webmproject.org/code/
libaom	3.3.0	https://aomedia.googlesource.com/aom/
libsvtav1	0.9.0	https://github.com/AOMediaCodec/SVT-AV1
libx264	0.161	https://code.videolan.org/videolan/x264
libx265	3.5	https://bitbucket.org/multicoreware/x265_git
vvenc	1.3.1	https://github.com/fraunhoferhhi/vvenc
vvdec	1.3.0	https://github.com/fraunhoferhhi/vvdec

6. RESULTS

First results (rate-distortion graphs and computational time) for video Chimera "Aerial" are shown in Fig. 1. It is visible that the best results are achieved at the using of video codecs AV1 and VVC. However, especially for AV1 and VVC, time needed for encoding (at best settings) is high, thus faster settings was chosen. The overall comparison of the used codecs using Bjontegaard-Delta (BD) method is presented in Table II. It is visible that reference libaom-av1 implementation outperforms other codecs in BD-PSNR and BD-rate, followed by VVenC and SVT-AV1.

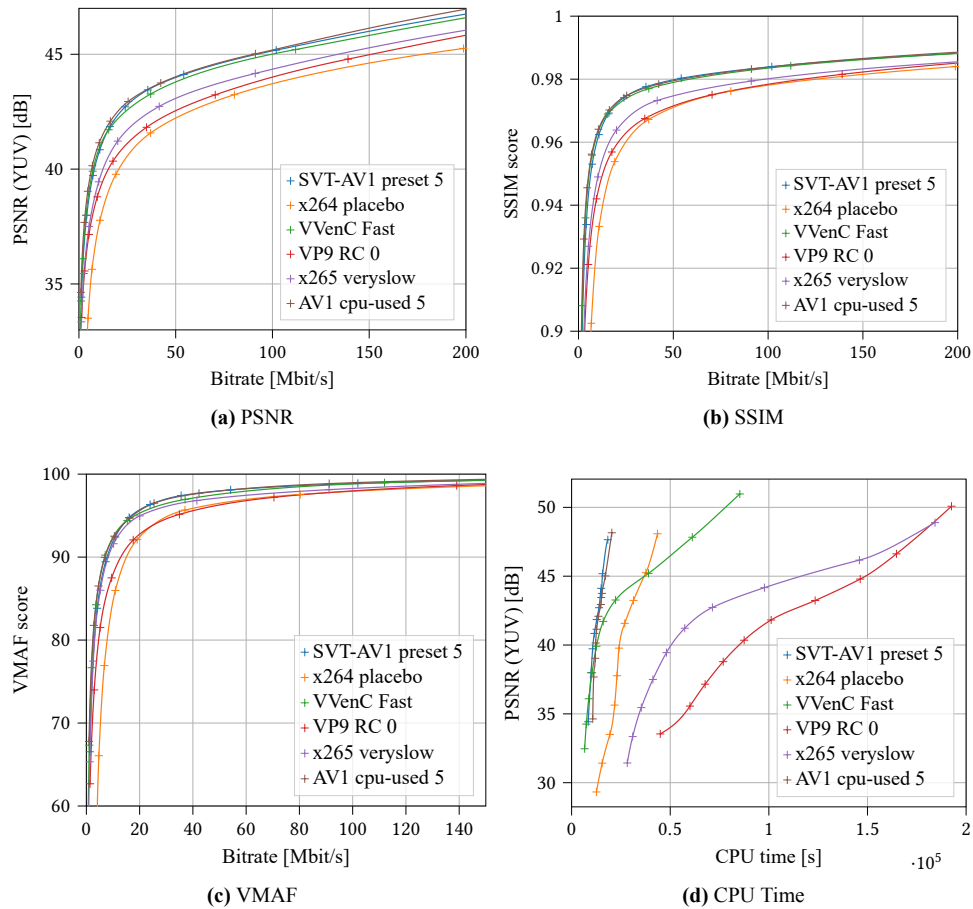
**Figure 1:** Rate-Distortion graphs and computation time for the video sequence Chimera "Aerial"

Table II: Comparison of codecs to x264 placebo

Codec and settings	BD-PSNR [dB]	BD-rate [%]
AV1 cpu-used 5	2.89	-66.00
VVenC Fast	2.46	-64.34
SVT-AV1 preset 5	2.67	-61.29
x265 veryslow	1.56	-49.17
VP9 RC 0	1.17	-32.81

7. CONCLUSION

In this short paper, attention was devoted to performance study of advanced compression algorithms HEVC, VVC, VP9 and AV1 for 4K videos. A Python-based tool employing FFmpeg multimedia framework was created to manage the whole encoding more efficiently. The visual quality of video sequences was evaluated by different objective metrics. All the results, presented in this paper, are a part of preliminary bachelor thesis.

Among others, future work plans include the extension of this study. More video sequences with different spatial and temporal information (SI and TI) will be considered. The number of the used objective quality metrics to evaluate the performance compression of video codecs will be increased. There is also planned a creation of graphical user interface for the developed tool to manage the video compression more easier.

ACKNOWLEDGMENT

This work was supported by the BUT internal project no. FEKT-S-20-6325.

REFERENCES

- [1] C. Evans, J. Issa, and S. Forrest, "The sustainable future of video entertainment, From creation to consumption," Aug. 2020, p. 35. [Online]. Available: <https://www.interdigital.com/download/5fa0694a8934bdf5f00596a>.
- [2] B. Bross, Y.-K. Wang, Y. Ye, *et al.*, "Overview of the versatile video coding (vvc) standard and its applications," *IEEE Transactions on Circuits and Systems for Video Technology*, vol. 31, no. 10, pp. 3736–3764, Oct. 2021, ISSN: 1558-2205. DOI: [10.1109/TCSVT.2021.3101953](https://doi.org/10.1109/TCSVT.2021.3101953). [Online]. Available: <https://ieeexplore.ieee.org/iel7/76/9556114/09503377.pdf>.
- [3] J. Han, B. Li, D. Mukherjee, *et al.*, "A technical overview of av1," *Proceedings of the IEEE*, vol. 109, no. 9, pp. 1435–1462, Sep. 2021, ISSN: 1558-2256. DOI: [10.1109/JPROC.2021.3058584](https://doi.org/10.1109/JPROC.2021.3058584). [Online]. Available: <https://ieeexplore.ieee.org/iel7/5/4357935/09363937.pdf>.
- [4] C. Bonnineau, W. Hamidouche, J. Fournier, N. Sidaty, J.-F. Travers, and O. Déforges, "Perceptual quality assessment of hevc and vvc standards for 8k video," *IEEE Transactions on Broadcasting*, vol. 68, no. 1, pp. 246–253, 2022. DOI: [10.1109/TBC.2022.3140710](https://doi.org/10.1109/TBC.2022.3140710).
- [5] P. Akyazi and T. Ebrahimi, "Comparison of compression efficiency between hevc/h.265, vp9 and av1 based on subjective quality assessments," in *2018 Tenth International Conference on Quality of Multimedia Experience (QoMEX)*, 2018, pp. 1–6. DOI: [10.1109/QoMEX.2018.8463294](https://doi.org/10.1109/QoMEX.2018.8463294).
- [6] NETFLIX INC. "Digital video sequence "aerial". (2015), [Online]. Available: https://media.xiph.org/video/derf/Chimera/Netflix_Aerial_4096x2160_60fps_10bit_420.zip. CC BY-NC-ND 4.0.
- [7] A. Wieckowski, J. Brandenburg, T. Hinz, *et al.*, "Vvenc: An open and optimized vvc encoder implementation," in *Proc. IEEE International Conference on Multimedia Expo Workshops (ICMEW)*, 2021, pp. 1–2. DOI: [10.1109/ICMEW53276.2021.9455944](https://doi.org/10.1109/ICMEW53276.2021.9455944).
- [8] A. Wieckowski, G. Hege, C. Bartnik, *et al.*, "Towards a live software decoder implementation for the upcoming versatile video coding (vvc) codec," in *Proc. IEEE International Conference on Image Processing (ICIP)*, 2020, pp. 3124–3128. DOI: [10.1109/ICIP40778.2020.9191199](https://doi.org/10.1109/ICIP40778.2020.9191199).
- [9] I. Katsavounidis, "Dynamic optimizer-a perceptual video encoding optimization framework," *The NETFLIX tech blog*, 2018.

Brain Vessels Enhancement in 3D CT Data Using Eigenvalues of Hessian Matrix

Jan Suchacek¹, Roman Jakubicek¹

¹Department of Biomedical Engineering, FEEC Brno University of Technology, Brno, Czech Republic

E-mail: xsuchal6@vutbr.cz, jakubicek@vut.cz

Abstract—Cerebrovascular pathologies represent very serious life-threatening diseases and therefore great importance is attached to improving the diagnostic process of these diseases. In this work, an approach for brain vessels enhancement in 3D CT angiographic data has been proposed. A 3D binary mask of the brain was constructed and used for brain tissue extraction, in which the cerebral vessels were then enhanced using advanced filters based on Hessian matrix computation and analysis of Hessian eigenvalues. A dataset of 5 anonymized patient CT scans was used to design this approach.

Keywords— Brain vessel, Hessian-based filters, vessel enhancement, CT angiography.

1. INTRODUCTION

In clinical practice, the diagnosis of brain vascular pathologies such as aneurysms or stroke is very common. Due to the nature and course of these diseases, early diagnosis and accurate determination of the cause of the pathology is essential for subsequent treatment. The most frequent diagnostic method of the cerebral vascular system is X-ray computed tomography angiography (CTA). The enhancement of cerebral vessels in angiographic volume images is of great importance for faster and more accurate diagnosis.

In this paper, an approach for the enhancement of cerebral vessels in 3D CT angiographic images is proposed. An algorithm has been proposed that leads to the construction of a 3D binary mask of the brain, which is then used to extract brain tissue from the original CT volume image. The extracted volume of brain tissue has a low contrast of vascular structures to the surrounding brain tissue and therefore this volume is very difficult for the radiologist to assess in terms of diagnosing vascular brain pathologies. It is for this reason that enhancement of the cerebral vasculature is very important to make the diagnosis more efficient. Therefore the extracted brain tissue is subjected to three Hessian-based filtering methods which output parametric images of the enhanced cerebral vessels. Such vessel enhancement significantly increases the contrast of the vessels with respect to the surrounding brain tissue, which is very important for improving the orientation of the radiologist in the 3D angiographic image under evaluation. Another possible use of the parametric image of enhanced vessels is for the segmentation of cerebral vessels. The output of the segmentation of cerebral vessels from a 3D brain volume is a binary image. In some cases, we may lose important information in the resulting image, such as about small blood vessels that can be classified as background. The segmented image is used such as in computer-aided diagnosis (CAD) systems or computer image analysis systems, but when the radiologist evaluates the images and makes a diagnosis, it is much more convenient to use a parametric image of the enhanced vessels, because in this case the radiologist himself subjectively decides about the presence and condition of the vessel. The aim of this work is cerebral vessel enhancement, not segmentation, and therefore objective evaluation of the achieved results is very difficult as there is no manually marked data available for objective comparison. Therefore, the vessels enhancement results are evaluated subjectively.

2. METHODS

2.1. Experimental data

A dataset of anonymized five patient 3D CT scans was available for the design of the cerebral vessel enhancement algorithm. The available dataset was variable, containing volumetric data scanned by different CT systems, in different hospitals, at different acquisition parameters, and two contrast phases. The available image data were stored in a standardized DICOM format that also contains a header with metadata, some of which were used in preprocessing the volume data.

2.2. Design of approach

Figure 1 shows the block diagram of the proposed approach for enhancement of cerebral blood vessels. The algorithm consists of four consecutive blocks, which will be described in more detail below.

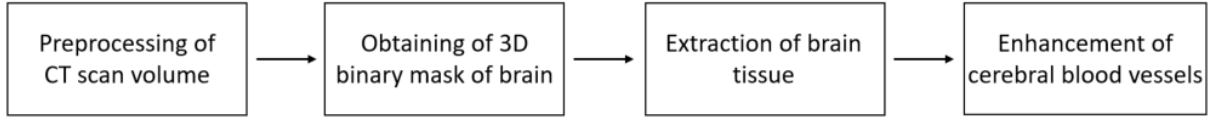


Figure 1: The block diagram of the proposed approach for enhancement of cerebral blood vessels.

2.2.1. Preprocessing of CT scan volume

Because the slices in each 3D CT scan were sorted by their numerical name, they were not sorted as they were actually scanned when the entire volume of data was uploaded. For this reason, it was necessary to first sort the slices so that their order actually matched the acquisition process. The information about the order of the slices during acquisition, which is stored in the header of each DICOM file, was used to sort the slices. Furthermore, only the region of interest, i.e. the volume containing the brain, was manually selected from the entire original CT scan volume. In the next step, this volume was transformed from the transverse plane to the sagittal plane.

2.2.2. Obtaining of 3D binary mask of brain

The multiple region growing method was used to create the binary mask of the brain. The region growing was performed in the 2D sagittal plane slice by slice. Three initial seeds were manually placed in the first slice of the brain and then in each slice, their positions were automatically recomputed according to the previous binary segment. By growing a region from the three initial seeds, three 2D brain masks were obtained in each iteration, i.e. for each slice of brain, which were then fused into one that was stored as a slice of 3D volume. Morphological volume closure (set a disk-shaped structuring element with a radius of 5 pixels) was applied to the segmented 3D brain mask, which caused smoothing of the deformed boundary and slight widening of the mask of the brain.

2.2.3. Extraction of brain tissue

The final 3D binary mask of the brain was used to extract brain tissue from the original CT scan volume. Brain extraction was performed by setting all voxels of the original CT scan lying outside the mask of the brain (represented by ones) to 0, i.e. as background. Thus, the surrounding tissues, the skull, and the patient table were removed, leaving only the volume of brain tissue with voxels represented by CT number values expressed in Hounsfield units.

2.2.4. Enhancement of cerebral blood vessels

In this study, 3 filtering techniques were used to enhance the cerebral vessels. All of the used filters were Hessian-based filters, which enhance curved structures contrasting with the background. By applying the filters to the original volume of extracted brain tissue, only the surface of the brain was enhanced without any enhanced cerebral vessels. This was due to the high contrast of the brain tissue against a null background. Therefore, it was necessary to adjust the background of the extracted brain to achieve a smooth transition between the brain tissue and the background. Therefore, the background was set to values that were calculated as the average of all CT numbers representing voxels of the extracted brain tissue. This adjusted volume was then the input image of each filter. The output of each filtering technique is a parametric three-dimensional image of the enhanced cerebral vessels. Each of the filters worked better on different types of blood vessels. Hence, the 3 parametric images were subsequently fused (summed) into one final volume in which the blood vessels are enhanced with a light color on a dark background.

2.3. Implementation of the proposed approach

The proposed approach was implemented in Matlab 2021b. The already implemented Region Growing function, which is freely downloadable on MathWorks [1], was used to create the binary mask of the brain. However, this function was originally implemented on a different segmentation task, on different image data, with different parameter settings, and with only one initial seed. Therefore, the algorithm had to be adapted to the task to be solved and the algorithm parameters were expertly optimized. The

positions of the three initial seeds were manually set in the first slice of the brain. In the following slices, the positions of the seeds were automatically recomputed according to the previous binary segment. The threshold value between the average pixel value of the growing area and the new potential seed to be added to the growing area was set to 30 HU.

Three already implemented filters were used to enhance the cerebral blood vessels. The Hessian-based Frangi Vesselness filter [2] and the Jerman Enhancement filter [3] are freely downloadable on MathWorks. The fibermetric function is directly implemented in Matlab.

2.3.1. Hessian-based Frangi Vesselness filter

Frangi filter, like most vessel filtering approaches, computes and analyses the Hessian matrix of the grayscale (angiographic) image. Hessian matrix is based on second-order derivatives of the image intensities characterizing the curvature of the image structures. Hessian-based filters aim to indicate elongated and/or rounded structures by an enhancement function based on Hessian eigenvalues. In the case of this filter, the applied enhancement function is Frangi's [4].

The imperfection of this filter using the original Frangi's enhancement function is that it suppresses rounded structures in their bends and also that the filter response reaches a peak in the centre of the structure and then gradually decreases towards the periphery. These imperfections of the original Frangi enhancement function are due to the defined way of calculating the parametric image from the eigenvalues of the Hessian matrix. Response of Frangi's enhancement function is proportional to the magnitudes of Hessian eigenvalues, which in turn are proportional to intensities of the image to be enhanced. Thus, the result of this filter is greatly influenced by the morphology of the vessels and the distribution of the contrast agent [4].

The voxel values of the parametric image obtained by Frangi filtering can be understood as the similarity of the eigenvalues of the Hessian matrix for each voxel of the original 3D image [4].

For this filter, the following parameters were set: The range of sigmas: patient 1,3,4 = [1:2], patient 2,5 = [1:4]; Step size between sigmas: patient 1-5 = 1; Frangi vesselness constant alpha: patient 1-5 = 1; Frangi vesselness constant beta: patient 1-4 = 0.5 and patient 5 = 0.1; Threshold between eigenvalues of noise and vessel structure: patient 1,2 = 45 and patient 3,4,5 = 35.

2.3.2. Jerman Enhancement filter

This filter, like the Frangi's mentioned above, is based on the calculation of the Hessian matrix of the image and Hessian eigenvalue analysis. However, it uses the Jerman enhancement function, which is an improvement of the original Frangi's enhancement function and improves its deficiencies. The method of computing the parametric image from the eigenvalues of the Hessian matrix has been modified. This led to the fact that there was no longer a decrease in the enhancement of the vessels towards their periphery. The response of the filter based on the Germans enhancement function is between 0 and 1, ideally 0 for non-vascular and 1 for vascular structures. This filter achieved a more uniform enhancement of the vascular structures than the original Frangi's enhancement filter [4].

For this filter, the following parameters were set: Sigmas: patient 1,4 = [1:2], patient 2,3,5 = 1; Spacing: patient 1-5 = [1;1;1]; Tau: patient 1-5 = 0.8.

2.3.3. Fibermetric

This method enhances elongated or tubular structures in the image using a Hessian-based multiscale Frangi vesselness filter. The underlying hypothesis is that a vessel is a bright, elongated structure within a darker background. Due to the contrast and geometric properties of the vessels, it is generally assumed that the observation of the local curvatures via the Hessian matrix analysis can allow for the determination of the position and orientation of the putative vascular structures [4].

For this filter, the following parameters were set: There were used parameter named StructureSensitivity with values for patient 1-5 = 30 except patient 2 = 50.

3. RESULTS AND DISCUSSION

On the available dataset of five patient CT scans, the following results were obtained using the approach described above. Objective evaluation of the vessels enhancement results is not possible because no manually marked data are available for objective comparison. Therefore, the obtained results are evaluated subjectively.

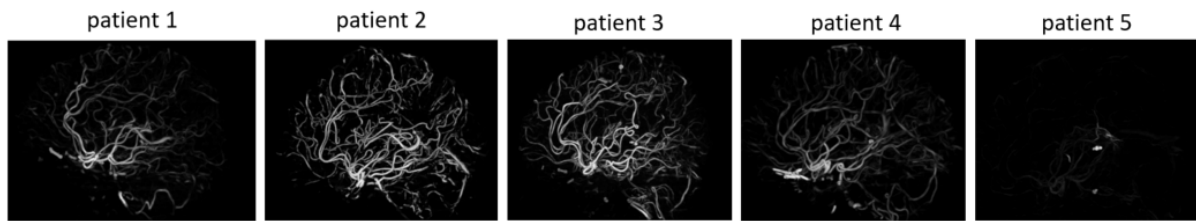


Figure 2: Resulting enhancement of cerebral vessels in the sagittal plane.

Figure 2 shows the resulting 3D images of the enhanced cerebral vessels in the sagittal plane. In the images for the first through fourth patients, the brightly enhanced cerebral vessels are clearly visible against a dark background, thus, a significant increase in the contrast of the vascular structures relative to the surrounding brain tissue was achieved. In the image of patient 5, the main cerebral vessels are enhanced, but this enhancement is relatively weak - this is due to the fact that the fifth CT scan was taken only in the second contrast phase when part of the contrast agent had already been flushed away by blood.

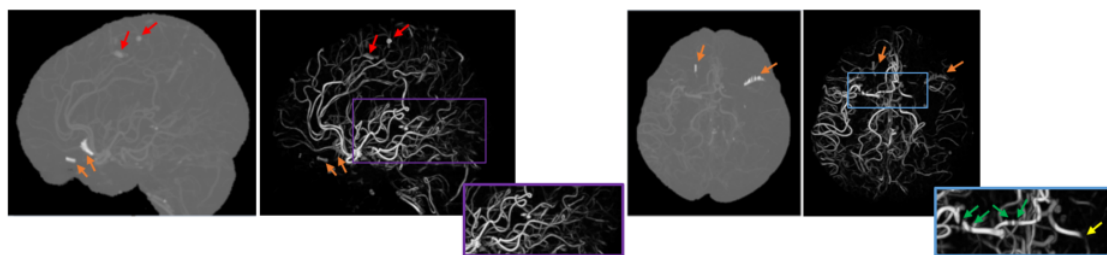


Figure 3: Extracted brain tissue and enhanced cerebral vessels for patient 3 in sagittal and transverse plane.

Figure 3 shows a comparison of the original extracted brain tissue and the enhanced cerebral vessels in the sagittal and transverse planes. Red arrows mark cerebral calcifications. Orange arrows mark the parts of the skull bone that were incorporated into the extracted brain tissue due to morphological volume closure of the 3D binary mask of the brain. In the purple frame, we can notice that all vessels are not enhanced uniformly. The thick vessels are brighter compared to the small narrow vessels, which is due to the larger amount of blood and contrast agent present in the larger vessels. Inside the blue frame, the green arrows in detail mark the interruption of the enhanced cerebral vessel, which is an imperfection of the proposed vessel enhancement approach. The yellow arrow indicates a terminated vessel, presumably due to an ischemic stroke.

4. CONCLUSION


This paper presents the proposal and implementation of an approach for the enhancement of cerebral vessels in volumetric CT data. For the task of enhancing cerebral vessels, it is first necessary to extract brain tissue from the original volumetric CT scan - for this, a segmented 3D binary mask of the brain was used. By applying three Hessian-based filters to the extracted brain tissue, a significant increase in the contrast of the vascular structures relative to the surrounding brain tissue was achieved, which is useful for a more efficient diagnostic process and therapeutic patient care.

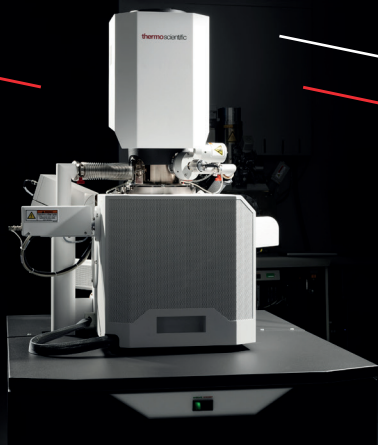
REFERENCES

- [1] D. -J. Kroon, “[Region Growing](#)”, *MATLAB Central File Exchange*. Retrieved March 13, 2022.
- [2] D. -J. Kroon, “[Hessian based Frangi Vesselness filter](#)”, *MATLAB Central File Exchange*. Retrieved March 13, 2022.
- [3] T. Jerman, “[Jerman Enhancement Filter](#)”, *Github*. Retrieved March 13, 2022.
- [4] T. Jerman, F. Pernus, B. Likar, and Z. Spiclin, “Enhancement of Vascular Structures in 3D and 2D Angiographic Images”, *IEEE Transactions on Medical Imaging*, vol. 35, no. 9, pp. 2107-2118, 2016., doi [10.1109/TMI.2016.2550102](https://doi.org/10.1109/TMI.2016.2550102).

Naše práce je věda

V našem brněnském technologickém centru vznikají špičkové elektronové mikroskopy a spektrometry, které dodáváme do celého světa. Studují se jimi viry, vznikají díky nim vakcíny, vyvíjí se lepší materiály i elektronika. Pracujeme se špičkovými technologiemi, které posouvají lidské poznání. Najdeš mezi námi odborníky na fyziku, elektroniku, software, mechanickou konstrukci nebo logistiku. Chceš toho být součástí?

 thermofisher.jobs.cz



Brno, Vlastimila Pecha 12

Operon identifier: Identification of operon structures in the whole genome

J. Nejezchlebova¹, J. Schwarzerova^{1,2}

¹Department of Biomedical Engineering Faculty of Electrical Engineering and Communication, Brno University of Technology Brno, Czech Republic

²Molecular Systems Biology (MOSYS), University of Vienna, Vienna, Austria

E-mail: xnejez10@vutbr.cz, Jana.Schwarzerova@vut.cz

Abstract — Currently, operon prediction is based on the distance of neighboring genes on the functional relationships of their products that encode proteins in a given nucleotide sequence, or on ORF distances. This study deals with the design of a new function that detects operon structures based on information from gene expression or alternatively in combination with previous information from current online available tools. The function was implemented in Python language and tested on *Clostridium beijerinckii* NRRL B-598. This bacterium has huge potential in biotechnology and research due to its fermentation product, butanol.

Keywords — Gene expression information, Transcription unit, Correlation coefficient, *Clostridium beijerinckii*

1. INTRODUCTION

Operon structures have an important role in prokaryotic gene regulation. Operons represent groups of related genes controlled by a single operator. Despite the importance of operons in bacterial gene networks, the relationship between their organization and gene expression remains poorly understood [1]. This problem has plagued us for more than 10 years and it is still not resolved. The importance of operons has implications for understanding the functional basis of genome organization and practical applications for synthetic biology [1]. A direct practical useful conceptual goal is a better understanding of overall gene regulation connected to microbial production of bio-based fuels. *Clostridium beijerinckii* NRRL B-598 is a bacterium with huge potential in microbial production of bio-based fuels because of its ability to produce butanol. This study brings forward a function that was implemented in Python language and applied on a dataset from *C. beijerinckii* NRRL B-598 with accession number, CP011966.3 (represented identifier in NCBI).

2. MATERIALS AND DATA

The dataset represents *C. beijerinckii* NRRL B-598. It includes four replicates, marked as {B, C, D, E}. Replicates B and C are presented in the study by Sedlar et al. [2]. The replicates D and E are mentioned in the study by Patakova et al. [3]. All used replicates were cultivated under standard conditions and were sequenced at six-time points {3.5, 6, 8.5, 13, 18, and 23 h} using NextSeq500.

3. METHODS

Firstly, operon structures were predicted by the online tool FGENESB (Bacterial Operon and Gene prediction) [4]. Secondly, gene expression information was extracted from RNASeq data of *C. beijerinckii* NRRL B-598. The output from NextSeq was raw data in *fastq* format. These raw data are pre-processed using the pipeline from the study by Schwarzerova et al. [5]. The final step of our study is a new Python function called Operon identifier. It was developed to predict operon structures based on gene expression information that improves operon prediction compared to other available online tools such as FGENESB [4].

3. 1 FGENESB

FGENESB: Bacterial Operon and Gene prediction is a package for automatic detection of bacterial genome annotations [4]. Unlike other online tools which predict operon structures, FGENESB differentiates operons and transcription units. Operon prediction is performed by ORF distances and frequencies of different genes adjacent to each other in known bacterial genomes. To predict operons, it was necessary to upload the *C. beijerinckii* NRRL B-598 genome in *fasta* format and select the organism closest to *C. beijerinckii* from the available options. There are three available *Clostridium*s – *C. acetobutylicum* ATCC824, *C. perfringens* str 13, and *C. tetani* E88. Genomes of these organisms were compared using BLAST [6] and *C. acetobutylicum* ATCC824, with 92% identity, was selected as the closely related organism to *C. beijerinckii* NRRL B-598.

3. 2 OPERON IDENTIFIER: IDENTIFICATION OF OPERON STRUCTURES IN THE WHOLE GENOME

The main aim of the study was to refine the operon structures based on information obtained from gene expression. Operons are groups of related genes controlled by a single operator. A high correlation of gene expression between adjacent genes indicates that the genes belong to the same operon. Pearson's correlation coefficient expresses the relationship between two variables:

$$r_{xy} = \frac{\sum(x_i - \bar{x})(y_i - \bar{y})}{\sqrt{\sum(x_i - \bar{x})^2 \sum(y_i - \bar{y})^2}} \quad (1)$$

where r_{xy} is the correlation coefficient of the linear relationship between the variables x and y. Variable x is a locus tag representing upstream genes and variable y is a locus tag representing downstream genes, and \bar{x} and \bar{y} are means of x and y variables.

In this case, correlation represents the relationship among genes which can give clues as to whether genes behave the same or not under certain conditions. When a high degree of correlation between two genes exists, there is a high probability that the genes are part of the same operon. On the other hand, when the degree of correlation is low, the genes are unlikely to be in the same operon.

Operon identifier has 77 % as the limit set of correlation. This value was calculated as the average of intra-operon correlation for all predicted operons using FGENESB.

The Operon identifier function uses Python packages NumPy[7], Pandas [8] , and Statistics[9]. The input is the aforementioned dataset, operon prediction from FGENESB, and method. The user can choose between two methods. If the user selects the first option '1', operon prediction is performed using gene expression information and operon structure prediction. If the user selects the second option '2', prediction is performed using only gene expression information. Figure 1 shows the flowchart of the second method.

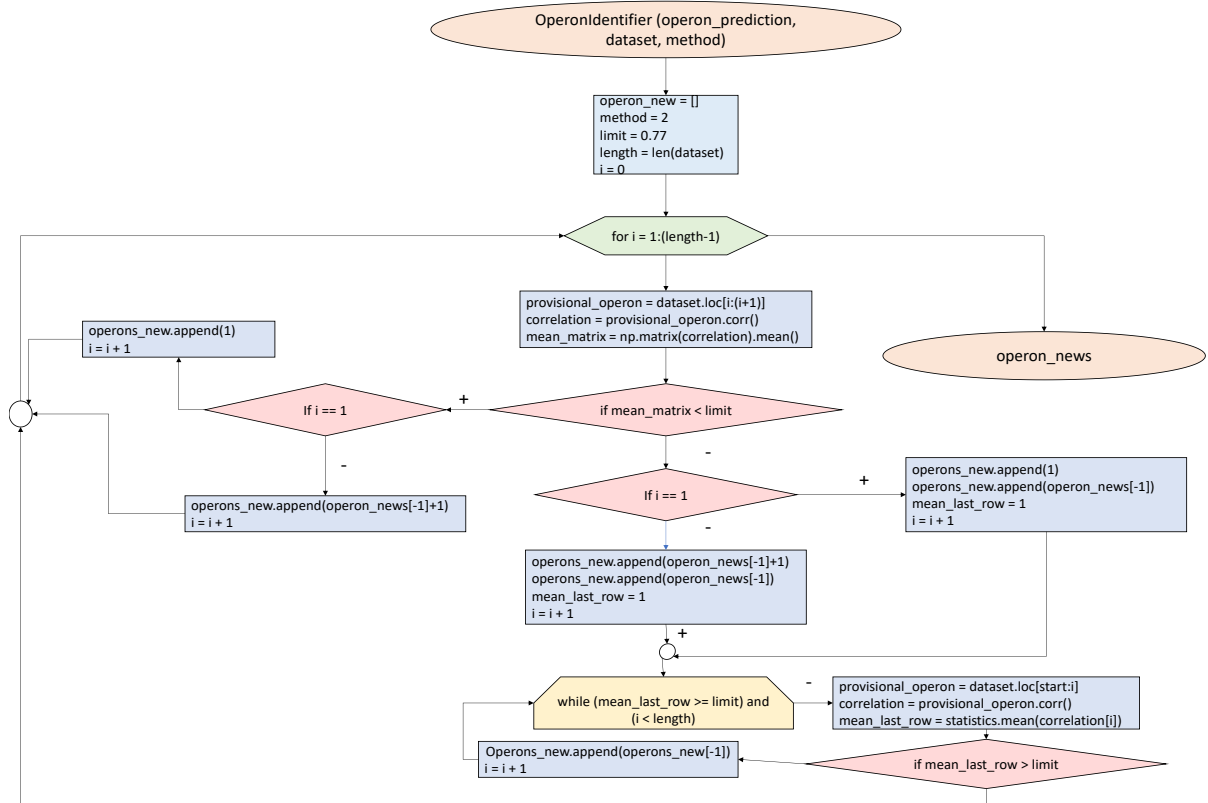


Figure 1: Flowchart of Operon identifier represents the second option rely on gene expression only

4. RESULTS AND DISCUSSION

The Operon identifier predicted 1,350 operon structures and 1,175 transcription units by the first method and 1,124 operons and 526 transcription units by the second method in *C. beijerinckii* NRRL B-598. More detailed results are shown in Table I.

Table I: Comparison of basic static quantities from operon structures of FGENESB and operon structures of Operon identifier

Parameters	FGENESB	Operon identifier	
		Method 1	Method 2
Total number of operons	1,095	1,350	1,124
Total number of transcription units	3,544	1,175	526
Maximum number of genes	31	33	32

The first method predicted more number of operon structures and transcription units than the second method. Compared to FGENESB, both methods predicted far fewer transcription units. Hence, most of the transcription units that were predicted by FGENESB were assigned to an operon structure by the Operon identifier.

Compared to the study by Schwarzerova [10], this method predicted fewer operons. Compared to the study Operon identifier distinguishes between transcription units and operons. The study doesn't consider that if only one gene is assigned to an operon, it isn't operon but it is a transcription unit. This is the reason why Operon Identifier predicted fewer operons than Operon-expresser [10]. There is also

a difference in setting the correlation limit. While Operon-expresser has the intra-operon threshold set at 75 %, the Operon identifier has a set threshold of 77 %. Also, different online tools for operon prediction were used between the two methods. Operon-expresser uses Operon-mapper [11], while Operon identifier uses the FGENESB.

5. CONCLUSION

Most operon inference tools do not use gene expression information. Nevertheless, gene expression information plays an important role in operon prediction. This paper brings an innovative tool, Operon identifier, which predicts operon structures based on gene expression information or refines operon structures already predicted by the FGENESB tool using gene expression information. The algorithm was implemented in Python and tested on *C. beijerinckii* NRRL B-598.

ACKNOWLEDGMENT

A huge thank you belongs to Iro Pierides, MSci for the professional correction of English language.

This work has been supported by grant FEKT-K-21-6878 realised within the project Quality Internal Grants of BUT (KInG BUT), Reg. No. CZ.02.2.69 /0.0/0.0/19_073/ 0016948, which is financed from the OP RDE.

REFERENCES

- [1] LIM, Han N., Yeong LEE a Razika HUSSEIN. Fundamental relationship between operon organization and gene expression
- [2] SEDLAR, Karel et. al. Transcription profiling of butanol producer *Clostridium beijerinckii* NRRL B-598 using RNA-Seq.
- [3] PATAKOVA, Petra et. al. Acidogenesis, solventogenesis, metabolic stress response and life cycle changes in *Clostridium beijerinckii* NRRL B-598 at the transcriptomic level.
- [4] FGENESB Suite of Bacterial Operon and Gene Finding Programs [online]. From: <http://www.softberry.com/berry.phtml?topic=fgenesb&group=help&subgroup=gfindb>
- [5] SCHWARZEROVÁ, Jana. Reproducible analytical pipeline for using raw RNA-Seq data from non-model organisms. ISBN: 978-80-214-5867-3
- [6] ALTSCHUL et. al. Basic local alignment search tool. *Journal of Molecular Biology*, 215(3), 403–410
- [7] HARRIS, Charles R., K. Jarrod MILLMAN, Stéfan J. VAN DER WALT, et al. Array programming with NumPy. *Nature* [online]. 2020, 585(7825), 357-362. ISSN 0028-0836. From: doi:10.1038/s41586-020-2649-2
- [8] MCKINNEY, Wes. *Data Structures for Statistical Computing in Python* [online]. In: . 2010, s. 56-61 [cit. 2022-03-23]. From doi:10.25080/Majora-92bf1922-00a
- [9] Statistics – Mathematical statistics functions [online]. From: <https://docs.python.org/3/library/statistics.html>
- [10] SCHWARZEROVÁ, Jana. OPERON-EXPRESSER: The Innovated Gene Expression-based Algorithm for Operon Structures Inference. In: *Proceedings of the 27th Conference STUDENT EEICT 2021*. Brno: Vysoké učení technické v Brně, Fakulta elektrotechniky a komunikačních technologií, 2021, s. 301-306. ISBN 978-80-214-5942-7
- [11] Blanca Taboada, Karel Estrada, Ricardo Ciria, Enrique Merino, Operon-mapper: a web server for precise operon identification in bacterial and archaeal genomes [online]. From: <https://doi.org/10.1093/bioinformatics/bty496>

The COG-or: the Improved Functional Annotation of Bacterial Genomes

P. Polakovičová¹, K. Sedlár¹

¹Department of Biomedical Engineering, Faculty of Electrical Engineering and Communication, Brno University of Technology, Czechia

E-mail: xpolak37@vut.cz, sedlar@vut.cz

Abstract—The study of bacterial organisms is given great emphasis in scientific research. By studying the bacterial genome, scientists can gain knowledge of various infectious diseases. Nowadays, it is even possible to edit genes and thus advancing the field of tailored medicine by treating many genetic diseases. Furthermore, it is becoming the norm to utilize bacteria in the industry for their ability to produce important products such as plastics, or fuels. It is therefore essential to extract the necessary information about its genes and other features. This paper focuses mainly on improving the functional annotation of bacterial genomes, classification of protein-coding sequences into clusters of orthologous groups, and visualization of the final annotated genome. For this task, the python package was developed with several functions for working with the outputs of multiple annotation tools, namely eggNOG-mapper, Operon-mapper, and Batch CD-Search. The package was tested on *Clostridium diolis* DSM 15410 and *Clostridium beijerinckii* DSM 791.

Keywords—Bacterial genome, Functional annotation, COG, eggNOG-mapper, Operon-mapper, Batch CD-Search

1. INTRODUCTION

The functional annotation of bacterial genomes reveals the role of the genetic structures encoded in the DNA sequence. A typical approach for functional annotation is applying similarity searches against several databases of protein sequences, such as Uniprot [1]. However, this approach has several disadvantages. At larger phylogenetic distances, the high similarity does not necessarily indicate the same function. In this case, identifying orthologs constitutes a fundamental task in accurate function assignment. Orthologs are genes in different species that evolved from a common ancestral gene by speciation. Several databases and tools have been developed that provide precomputed clusters of orthologous groups (COG). The most popular database of these proteins is the COG database [2] which provides manually curated groups split into 26 categories by function. Another well-known database is eggNOG [3], which includes manually curated groups from the COG database as well as automatically generated ones.

Unfortunately, a major disadvantage of COG annotation is that there is currently no suitable tool that can assign COGs to all protein-coding sequences in the genome. Also, the existing tools often differ in their assignment and their output files are confusing and hard to be visualized.

2. MATERIALS AND METHODS

To use the package COG-or, the user must firstly annotate the genome using web-based tools eggNOG-mapper [4], Operon-mapper [5], and Batch CD-Search [6], see Figure 1. The input of eggNOG-mapper and Batch CD-Search are protein-coding sequences (CDS), and the input of Operon-mapper is the genomic sequence with features coordinates in GFF3. The package then works with the decorated.gff file from eggNOG-mapper, predicted_COGs.txt, and ORFs_coordinates.txt from Operon-mapper and with hitdata.txt from Batch CD-Search.

The eggNOG-mapper is a tool for functional annotation of large sets of sequences based on fast orthology assignments using the eggNOG database. The sequence mapping is performed with DIAMOND [7] search. The Operon-mapper is a web server that is not primarily designed for COG assignments, it predicts the operons of any prokaryotic genome sequence. The homology gene

assignments are determined using `hmmsearch` [8] against models which represent COGs and ROGs (Remained Orthologous Groups). The last tool used is the Batch CD-Search, a web-based tool that can be used for scanning against COG database using RPS-BLAST (a variant of the PSI-BLAST algorithm).

The described tools offer different files in various formats, which, moreover, are not structured very well. The designed module contains functions that process outputs from individual programs. The outputs of these functions contain *sequence id*, *source*, *feature type*, *start*, *end*, *score*, *strand*, *frame*, and *attribute* for each annotated feature. The module also contains functions that make it easier to work with the Batch CD-search tool because of its inability to annotate more than 4000 sequences at once. In case the bacterium contains more CDSs, the user can split the single CDS file in half and merge them again after annotation.

The three aforementioned tools use different approaches to assign COGs to individual genes. By combining them, it is possible to achieve more reliable results and a greater percentage of coverage of the whole genome. The consensus function combines all three files and subsequently adds features such as RNA genes and pseudogenes. The output file is ready to be visualized in DNAPlotter [9], which is an interactive Java application for generating circular and linear representations of genomes.

To visualize the genome with the differentiation of each COG category, the consensus function file alone is not sufficient itself. In DNAPlotter, after loading the file, it plots the genome according to the specified features. To color the COG categories and other features, the user has to import another file in the Track Manager option. This file can be generated along with the legend also by the COG-or.

The developed package was tested on two bacteria, both published by the Department of Biomedical Engineering. *Clostridium diolis* DSM 15410 (accession number CP043998.1) was sequenced by PacBio RSII and Illumina NextSeq, and *Clostridium beijerinckii* DSM 791 (accession number CP073653.1) was sequenced with Oxford Nanopore MinION and Illumina MiSeq. All necessary input files are available in the GenBank database.

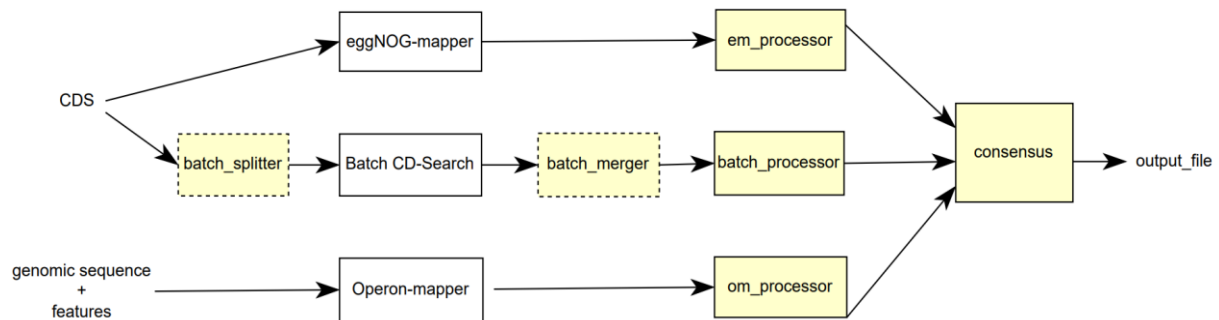


Figure 1: Schematic diagram of annotation process using the developed tool. The yellow blocks are part of the COG-or package.

3. RESULTS AND DISCUSSION

The total numbers of CDSs annotated by different tools are listed in Table I. The eggNOG-mapper was able to achieve the highest percentage of assignment of COGs for both genomes (~95%). This is not surprising as the latest version uses novel extensive reference database. On the other hand, CD-search was able to assign only 54,8% and 55,4%, respectively. The reason can be found in limited reference database used by this tool. Nevertheless, even this tool can be used to supplement eggNOG-mapper results because the COG-or package, combining various tools reached the best results, while assigning 97,02% and 97,47% CDSs in *C. beijerinckii* and *C. diolis*, respectively. Utilization of non-model organisms is advantageous to demonstrate differences between various annotation tools and improvement by the COG-or. Unfortunately, accuracy of results could not be calculated since there is no model organism with 100% COG annotation. The reason is in scarce utilization of COG system that was rediscovered in 2021 and started to be extensively used in the past few months [2].

Table I: Comparison of tools in COG assignment

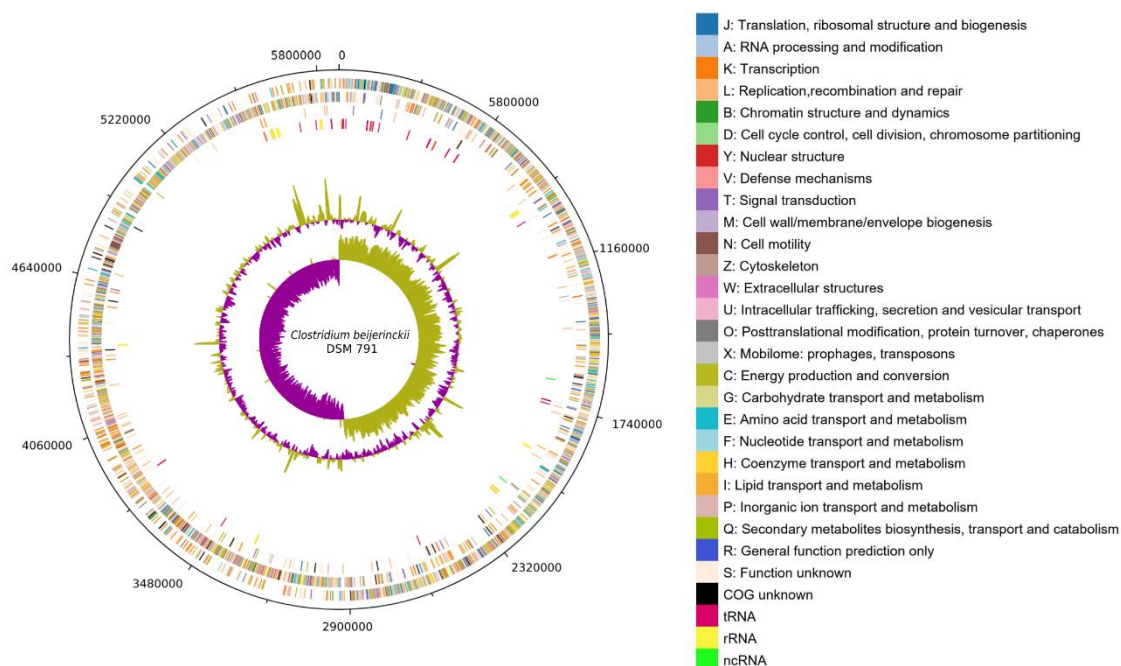
Bacterium	Number of CDS	Number of assigned COGs			
		eggNOG-mapper	Batch CD-Search	Operon-mapper	COG-or
<i>C. beijerinckii</i>	5061	4823	2771	4526	4910
<i>C. diolis</i>	5102	4884	2825	4581	4973

Furthermore, the percentages in which the COG-or package changed the COG assignment were calculated, see Table II. This means that for a given CDS the COG assigned by COG-or is different from the COG assigned by particular tool. The highest percentages can be observed for Operon-mapper (exceeding 21%). This might be caused by different primary purpose of the tool, which is operon prediction and not COG annotation. However, correct COG prediction is important for operon inference as all genes in an operon should be involved in the same biological pathway, thus belong to the same COG. The erroneous annotation by Operon-mapper could harm its ability of correct operon structure inference.

Table II: The percentage of changed assignment by the COG-or package

Bacterium	Changes in the COG assignment		
	eggNOG-mapper	Batch CD-Search	Operon-mapper
<i>C. beijerinckii</i>	2,01%	2,71%	21,98%
<i>C. diolis</i>	1,92%	2,51%	21,26%

Finally, the output of an analysis performed with the COG-or was visualized as the genome map of *Clostridium beijerinckii* DSM 791 using DNAPlotter, see Figure 2. The various colors represent the 26 COG categories as well as RNA genes. The first and the second circles show CDSs on the forward and reverse strands. The third circle represents pseudogenes and in the fourth circle, the RNA genes are plotted. The two inner circles represent GC content and GC skew.

**Figure 2:** The genome map of *Clostridium beijerinckii* DSM 791 drawn using DNAPlotter and the COG-or package.

4. CONCLUSIONS

The main topic of this paper was to develop a tool that improves the functional annotation of bacterial genomes using clusters of orthologous groups. The presented python package, the COG-or, can work efficiently with the outputs of various tools to further improve the assignment of individual CDSs to their COG group and category. The package with its several functions was tested on annotation of two bacterial genomes, *Clostridium beijerinckii* DSM 791 and *Clostridium diolis* DSM 15410. Thanks to combination of different approaches, more than 97% of protein-coding sequences were assigned a COG category for both genomes. Subsequently, the genomes were simply plotted by DNAPlotter, and individual features were visually differentiated.

In summary, we proposed the auspicious package that can definitely be utilized in modern bioinformatics. It simplifies the work with different annotation programs, improves their results and even visualize the final data. In the future, it would be desirable to run this tool via command line using the main function that incorporates the whole package. Furthermore, it could have more customize functions for genome visualization.

The COG-or is freely available online at <https://github.com/xpolak37/the-COG-or>

REFERENCES

- [1] U. Consortium, “UniProt: the universal protein knowledgebase in 2021”, Nucleic acids research, vol. 49, no. D1, pp. D480-D489, 2021.
- [2] M. Y. Galperin, Y. I. Wolf, K. S. Makarova, R. Vera Alvarez, D. Landsman, and E. V. Koonin, “COG database update: focus on microbial diversity, model organisms, and widespread pathogens”, Nucleic Acids Research, vol. 49, no. D1, pp. D274-D281, Jan. 2021.
- [3] J. Huerta-Cepas, D. Szklarczyk, D. Heller, A. Hernández-Plaza, S. K. Forslund, H. Cook, D. R. Mende, I. Letunic, T. Rattei, L. J. Jensen, C. von Mering, and P. Bork, “EggNOG 5.0: a hierarchical, functionally and phylogenetically annotated orthology resource based on 5090 organisms and 2502 viruses”, Nucleic Acids Research, vol. 47, no. D1, pp. D309-D314, Jan. 2019.
- [4] C. P. Cantalapiedra, A. Hernández-Plaza, I. Letunic, P. Bork, J. Huerta-Cepas, and K. Tamura, “EggNOG-mapper v2: Functional Annotation, Orthology Assignments, and Domain Prediction at the Metagenomic Scale”, Molecular Biology and Evolution, Oct. 2021.
- [5] B. Taboada, K. Estrada, R. Ciria, E. Merino, and J. Hancock, “Operon-mapper: a web server for precise operon identification in bacterial and archaeal genomes”, Bioinformatics, vol. 34, no. 23, pp. 4118-4120, Dec. 2018.
- [6] S. Lu, J. Wang, F. Chitsaz, M. K. Derbyshire, R. C. Geer, N. R. Gonzales, M. Gwadz, D. I. Hurwitz, G. H. Marchler, J. S. Song, N. Thanki, R. A. Yamashita, M. Yang, D. Zhang, C. Zheng, C. J. Lanczycki, and A. Marchler-Bauer, “CDD/SPARCLE: the conserved domain database in 2020”, Nucleic Acids Research, vol. 48, no. D1, pp. D265-D268, Jan. 2020.
- [7] B. Buchfink, C. Xie, and D. H. Huson, “Fast and sensitive protein alignment using DIAMOND”, Nature Methods, vol. 12, no. 1, pp. 59-60, 2015.
- [8] S. R. Eddy and W. R. Pearson, “Accelerated Profile HMM Searches”, PLoS Computational Biology, vol. 7, no. 10, Oct. 2011.
- [9] T. Carver, N. Thomson, A. Bleasby, M. Berriman, and J. Parkhill, “DNAPlotter: circular and linear interactive genome visualization”, Bioinformatics, vol. 25, no. 1, pp. 119-120, Dec. 2008.

Web Platform for Comprehensive Penetration Testing

Willi Lazarov, Zdenek Martinasek

Brno University of Technology, FEEC, Czechia

E-mail: xlazar15@vut.cz, martinasek@vut.cz

Abstract—This paper presents the design, development, and implementation of a web platform embedded in the proposed Highly Scalable Model with the main purpose of increasing the effect of penetration testing to such an extent that the time, complexity, and work required to successfully complete the entire test will be considerably lower than using currently available tools, together with greater coverage of the testing area.

Keywords—penetration testing, vulnerability assessment, web application, modularity

1. INTRODUCTION

In today's digital world, more and more organizations and users use online services. Accordingly, the number of servers hosting these services and technologies used by them is also increasing. Nowadays, servers and applications are often the targets of cyberattacks.¹ If successful, such an attack can cause damage from service disruption to theft or loss of sensitive data. In the same way, other components falling under the area of information and communication technologies are attacked, thus increasing the number of risks and the scope of the impact even further. An example of a critical impact is a cyberattack on a hospital, which can put human lives at risk [1]. The growth of threats in cyberspace has prompted the development of many penetration testing tools, which as one of the preventions against cyberattacks reveals the security risks of the tested targets. Penetration testing is a complex process and there is no complete solution on the market that would allow its full management and semi-automation through a responsive user interface together with team collaboration, individual project management, and more sophisticated visualization of the tested environment.

1.1. State of the Art

The penetration testing process may vary according to different methodologies and tested environments. For this reason, it is problematic to provide a structure for all types of tests with a single solution, because the scheme cannot be simply generalized [3]. An example is the comparison of penetration testing between network infrastructure and a web application. In the case of a computer network, the tester will work mainly with the type, subnet mask, and default gateway of the tested network. During penetration testing, the tester can discover network or endpoint devices (e.g., router, server, etc.) and different running services. On the other hand, testing a web application can expose vulnerabilities related to programming languages, frameworks, and other websites with various user inputs. Considering each possible test target, more than thousands of different test sections would need to be developed to cover the entire area. Development on this scale would likely require a large amount of time, money, and human resources. In addition, future modifications of such a solution are very problematic due to the large-scale environment. Another disadvantage is the tendency to produce a duplicate and less readable source code. Also, the process of testing and optimizing the entire solution is more demanding. All these disadvantages and shortcomings make the gradual development of such a complex tool very difficult, and therefore the problem has to be solved in a completely different way.

1.2. Contribution

The paper discusses a web-based platform as a solution to the mentioned problem with a new approach compared to available tools that are commonly used in penetration testing. The main goal was to design, develop and deploy a comprehensive environment for effective and complete penetration testing that would allow testers to collaborate with each other as well as with the developers, system administrators, managers, and other relevant persons of the tested subject. During the design and development of the platform, emphasis was placed on high modularity, scalability, and optimization of all parts of the solution. The focus was also on user experience and usability of the client part.

¹In fact, an estimated 17,6 million websites could be infected with malicious code until 2019, based on SiteLock's analysis. Compared to the previous year, this is a 59% increase with an average of 62 attacks per day [2].

2. PROPOSAL OF A HIGHLY SCALABLE MODEL

The solution to the problem mentioned in the previous chapter is the proposal of a Highly Scalable Model, which is intended for the development and subsequent efficient expansion of the platform. The actual design of the model is shown in Figure 1 and the following text explains its main parts in a general way. The model consists of three main sides – data, application, and client. The schema for using the platform is formed in the data side, where the input data is defined and the relationships between them are created. The output of this process is structured data that represents the schema of the entire platform. The structured data then determines how the dynamic data will be represented, which will enter the database only when the platform is used in the production environment and their flow is therefore completely separated from the initial phase of creating the main structure. Both of these parts are located in the database with which the application side of the proposed model communicates.

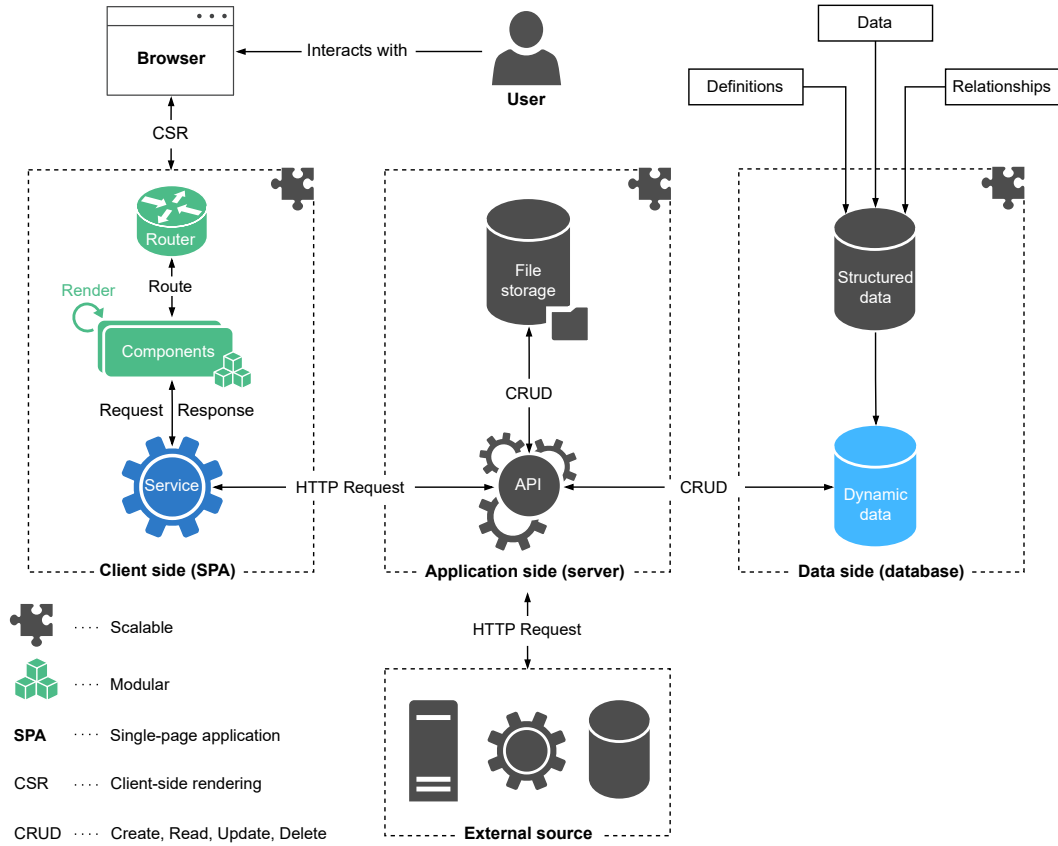


Figure 1: Highly Scalable Model

The second part of the proposed model is the application side, which consists of one or more servers that represent the model logic and communicate with the client and data side through the API (Application Programming Interface). The application server handles user authentication, authorization of all requests, and can also contain file storage. The main part of the application side is an API that returns structured data from the database for the client part based on an HTTP request or processes the corresponding dynamic data. The application server can be additionally extended with another API for communication with an external source, which can be a database, cloud storage, or another remote service. The logical part of the model can be further subdivided, following the microservices architecture, into multiple independent services with their interfaces based on different technologies [4].

The third part of the model is the client-side containing the SPA (Single-page application), with which the user interacts and sends requests to the application server. Once the user is authenticated, the application server sends the SPA, which is then loaded into the web browser. The SPA works on the principle of CSR (Client-side rendering) and therefore makes all changes on the client-side and requests only new data from the server. In the proposed model the SPA is highly modular. Based on client requests or structured data, it builds itself from its components, which then request the necessary dynamic data.

3. IMPLEMENTATION OF A WEB PLATFORM

According to the proposed model, the main goal was to implement a web platform to support penetration testing. For this purpose, a scheme for different possible test areas and targets is defined in the initial phase of the development. This process is very fast and it is possible to create a structure for different types of tests, environments, and other related parts of penetration testing in a short time. Dynamic data created or obtained during testing are then represented by nodes related to the structured data. The entire data side is managed by the relational database system MySQL. The application part is deployed on the Apache HTTP Server, which runs on Ubuntu operating system.² The main function of this part is handled by an API that communicates with SPA, server for automated penetration testing, data side, and authentication server. The entire application interface was developed using the Laravel PHP framework. On the client-side, the SPA is implemented as a modular Vue.js application programmed in TypeScript, which also ensures strict type checking of the source code. SPA handles client requests and forwards them to the application server for processing through its services.

The implemented platform communicates with other parts of the production environment. Users interact with the web platform through the web browser, into which the SPA is automatically loaded. Before the AS (Application Server) provides the SPA to the client-side, the user must authenticate himself against the UMS (User Management Server). Once the user is successfully authenticated, he is returned to the AS with the authentication token. The AS verifies the token against the UMS, and if the token is valid, the SPA is provided to the user, which is then loaded into his web browser. From now on, all further requests are sent by the SPA based on user interaction and other application events. There is only one UMS to authenticate all deployed application servers, which can be hosted on the cloud, custom servers, or client machines. The scheme of the production environment is shown in Figure 2.

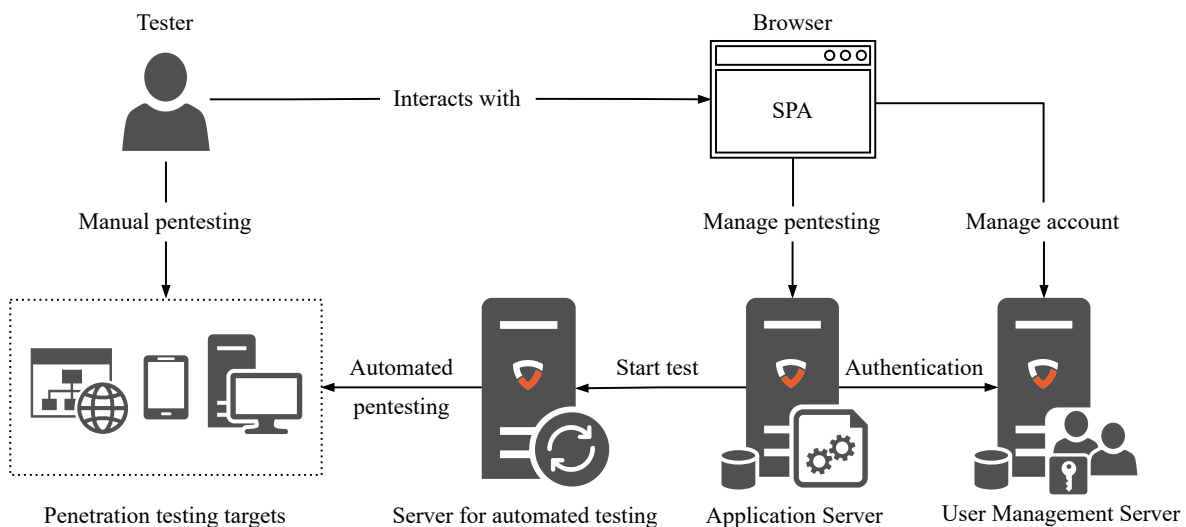


Figure 2: Web platform in production environment

An important part of the production environment is the SAT (Server for automated testing). Users either perform the penetration testing manually and upload the results to the web platform, or run automated tests against the specified target, which are executed by the SAT according to their parameters and the results are then returned to the application server for further processing. The target of a manual or automated test can be almost anything that is accessible from the Internet, and the SAT has a suitable tool for testing the specified target. The web platform, in order to support penetration testing to the maximum extent, allows testing to be managed not only by testers but by other users, such as developers, who can, for example, fix the found vulnerabilities and testers then re-verify their presence. The key final part is generating the report of the entire testing, which is very time-consuming when using a text editor. All this can be done within the web platform without the need to use additional tools.

²It is also possible to use another web server, such as Nginx running on a Linux distribution or Microsoft IIS (Internet Information Services). The only condition for full functionality is the presence of an interpreter and a database system.

Figure 3 shows the user interface that the SPA has built for the client based on the received data. On the left side of the picture is a tree of all tested nodes and their descendants. For each node, a dashboard with relevant sections (e.g. tables, tests, vulnerabilities, attachments, etc.) is built at the moment of selection. In the case of this example, SPA built a web page node with a table of tests.

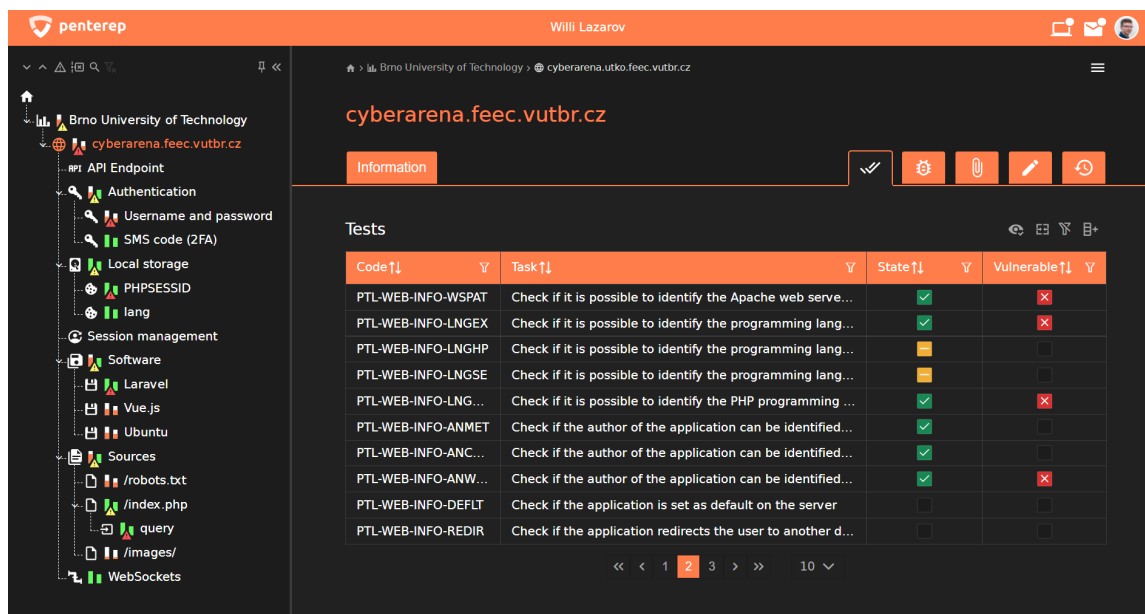


Figure 3: Single-page application user interface

4. CONCLUSION

Based on the demanding requirements on the required solution, a Highly Scalable Model was proposed, which proved to be fully suitable for the development of a web platform whose purpose is comprehensive penetration testing. From the beginning, the platform was developed with a primary focus on modularity, scalability, and optimization. Thanks to its embedding in the proposed model, it was possible to create a considerably large environment in the limited time of one year, which is gradually being extended by other parts and its possibilities of use are thus increasing over time. The main contribution of the platform is the unification of all penetration tester tasks into one place, automation of testing processes, and team collaboration between testers and other users. The result is a solution that improves the effect of penetration testing to such an extent that the time, complexity, and work required to successfully complete the entire test will be significantly lower than using the currently available tools.

ACKNOWLEDGMENT

The research described in this paper was financially supported by the Technology Agency of the Czech Republic, project No. TJ04000456.

REFERENCES

- [1] S. J. Choi, M. E. Johnson and C. U. Lehmann, "Data breach remediation efforts and their implications for hospital quality," *Health Services Research*, 54(5), 971-980, 2019, doi: [10.1111/1475-6773.13203](https://doi.org/10.1111/1475-6773.13203).
- [2] "Cybersecurity And Website Report," *SiteLock*. [Online]. Available: <https://www.sitelock.com/resources/security-report/>. [Accessed Feb. 10, 2022].
- [3] M. Denis, C. Zena and T. Hayajneh, "Penetration testing: Concepts, attack methods, and defense strategies," 2016 IEEE Long Island Systems, Applications and Technology Conference (LISAT), 2016, pp. 1–6, doi: [10.1109/LISAT.2016.7494156](https://doi.org/10.1109/LISAT.2016.7494156).
- [4] A. Sill, "The Design and Architecture of Microservices," *IEEE Cloud Computing*, 3(5), 76-80, 2016, doi: [10.1109/MCC.2016.111](https://doi.org/10.1109/MCC.2016.111).

WEIGHT SENSING OF BEEHIVES WITH IOT CONNECTIVITY

D. Havránek, J. Kufa

Brno University of Technology, FEEC, Czech Republic

E-mail: xhavra17@vutbr.cz, kufa@vut.cz

Abstract—This paper focuses on designing a device that can measure some beehive parameters, that can inform users about the conditions in a beehive. These parameters are beehive weight, internal and ambient temperature, internal and ambient humidity, and air pressure. The device allows sending the measured data wirelessly through the GSM network and interpreting the results in appropriate way. Low power consumption is desirable due to working without the reach of the distribution network.

Keywords—Beehive monitoring, sensors, IoT, GSM, ESP

1. INTRODUCTION

In the few past years, there is a significant increase of beekeepers. Especially amateur ones whose hobby has grown into a passion and whose apiary is continuously extending. The more beehives they have, the more difficult is to control all of them. The purpose of this paper is to design a device that could make their job easier by measuring and visualizing some crucial data.

The most important measured parameters are weight and temperature in a beehive. Based on these two parameters monitored through time beekeeper should be able to have an idea about what is going on in a beehive. Other measured parameters are humidity inside a beehive, ambient temperature and humidity outside of the beehive, and atmospheric pressure.

Due to continuous outdoor working, the device has to be resistant to weather conditions. That includes low temperature and high humidity. Because of the beehive location, the device has to be able to work for long periods of time powered by battery, so low power consumption is desirable. Also, the way of communicating should be able to send data for long distance and from outlying locations. Low price of the device is desirable because most of beekeepers are amateurs.

2. MEASUREMENT IN BEEKEEPING

Probably the most important parameter for beekeepers is weight. In the spring and early summer, the information about weight tells beekeeper how much honey is in a beehive, and he can better plan extracting the honey from the beehive. In the autumn and winter, the information about weight tells beekeeper how much supplies are left in the beehive. If there are not enough supplies the hive could die. To prevent this, the beekeeper has to refill their supplies. But instead of manual checking, he can use the measured information. Information about internal temperature and humidity can indicate the condition of the hive. Changes in temperature and humidity can mean that the queen bee started breeding, or it can point out the possibility of sickness of the hive. The other measured parameters are for measuring weather conditions.

3. SENSORS AND MICROCONTROLLER

To measure desirable parameters of a beehive, several sensors are used. All the sensors have been chosen concerning their accuracy, power consumption, method of communication, weather condition resistance, and price.

For measuring weight is used a single point load cell GUANG CE YZC-1B. This load cell contains several strain gauges that are connected as a Wheatstone bridge. By applying force to the load cell, it bends and the strain gauges deform. This deformation causes a change of their resistance what can be

measured as a change of voltage across the bridge. These small voltage changes are then amplified by ADC (Analog-to-Digital Converter) HX711.

Two sensors are used to measure the internal temperature of beehive. The first of them is DS18B20. Although this sensor has worse accuracy than the second one, it's cheaper and it's made in a sealed waterproof package. This makes him resistant to all conditions in a beehive, such as honey or wax. Thus, it can be used anywhere in the beehive, for example near the queen bee. DS18B20 uses for communication 1-Wire Interface. The second one is SHT40, which is used for measuring temperatures and humidity too. SHT40 uses I²C (Inter-Integrated Circuit) communication. The rest of the parameters are measured by one sensor BME280. Communication with BME280 is I²C too. Table I. shows some useful information about chosen sensors.

The microcontroller used in this device is ESP32-WROOM [1]. This microcontroller was chosen due to the sufficient number of its GPIO (General-Purpose Input/Output) pins, that can be used for communication, such as I²C, UART (Universal Asynchronous Receiver-Transmitter) or Serial communication, several ADCs, possibility of Wi-Fi (Wireless Fidelity), low power consumption, low price and relatively easy way to program it. Figure 1. shows communication between microcontroller and sensors.

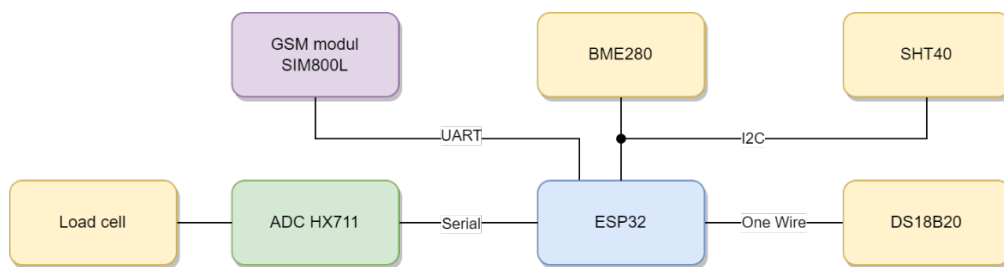


Figure 1: Communication between microcontroller and sensors

Table I: Some parameters of chosen sensors

Sensor	Measured variable	Accuracy	Range	Communication
YZC-1B	weight	0.02 %	0 to 200 kg	serial (with ADC)
DS18B20	temperature	0.5 °C	-55 to 125 °C	one wire
SHT40	temperature	0.5 °C	-40 to 125 °C	I ² C
SHT40	humidity	1.8 %	0 to 100 %RH	
BME280	temperature	1.5 %	-40 to 85 °C	I ² C
BME280	humidity	3 %	0 to 100 %RH	
BME280	air pressure	0.12 hPa	300 to 1100 hPa	

4. COMUNICATION

Beehives are usually located at outlying locations with bad signal, such as forest or meadow, that can be distant a few dozens up to a few hundred kilometers away from a beekeeper. Thus, the method of communication must have good coverage and it has to be usable for long-distance communication. The amount of data to be sent is small, so there is no need for high-speed communication. Among the considered methods of communication are LoRa (Long Range), Sigfox, NB-IoT (Narrow Band-Internet of Things), and GSM (Groupe Spécial Mobile) or GPRS (General Packet Radio Service).

The advantages of LoRa are low power consumption and this service is free. Data from the device are sent to gateway and from the gateway to the internet. The distance between a gateway and the device could be a few kilometers up to a few dozens of kilometers if there are good weather conditions. This distance is not sufficient for purpose of this device.

Sigfox is a mobile operator for IoT (Internet of Things) devices. The advantages of Sigfox are low power

consumption and good coverage in the Czech Republic. The disadvantage is a higher price. This service is charged with a pricing of about 34 CZK per month. Despite the good coverage, there are a lot of non-covered places. Especially rural locations, where is a higher probability of using this device. Thus, the coverage of Sigfox is not sufficient for the purposes of this device.

NB-IoT is narrowband network provided by mobile operators (for example Vodafone). The advantages of NB-IoT are low power consumption and good coverage in the Czech Republic. The disadvantages are pricing, which is low, but it's not for free, and unavailability for personal use. This service can be used only by companies.

The used method of communication is GPRS. Despite the higher pricing (that is comparable with Sigfox) and higher power consumption, this method seems like the best. It has the best coverage, and it can communicate to long distances. GSM and GPRS module SIM800L [2] employing UART is used for data sending. This is quad-band module supporting 850, 900, 1800 and 1900 MHz with GPRS data uplink transfer up to 85.6 kbps and operating temperature -40 up to 85 °C. This is fully sufficient for the device.

ThingSpeak is used for data visualization. ThingSpeak is a service that allows saving data on a cloud with the possibility of further processing with MATLAB. It also works with ESP32. For non-commercial purposes is ThingSpeak free with some limiting. The free version of ThingSpeak offers four channels. Every channel has eight fields for received data. The speed of sending messages is maximally fifteen messages per second. This speed is for the device fully sufficient.

5. POWER SUPPLY

Due to working without the reach of the distribution network, the device has to be powered by a battery. The battery has to be able to provide a high current because of the high power consumption by the GSM module up to 2 A at peaks. These peaks appear when communication starts and each peak lasts a few milliseconds. The Li-Ion (Lithium-Ion) 18650 battery with capacity of 3350 mAh was selected. The nominal battery voltage is 3.7 V. Photovoltaic panel and MPPT (Maximum Power Point Tracking) battery charger CN3791 was added for longer operability of the device. CN3791 is a PWM (Pulse Width Modulation) switch-mode Li-Ion battery charger controller that can be powered by photovoltaic cell with maximum power point tracking function. The circuit is designed for charging single cell Li-Ion battery in constant current and constant voltage mode. Photovoltaic panel used for battery charging is MWG-10. Peak power of this panel is 10 W with maximum power voltage 17.49 V.

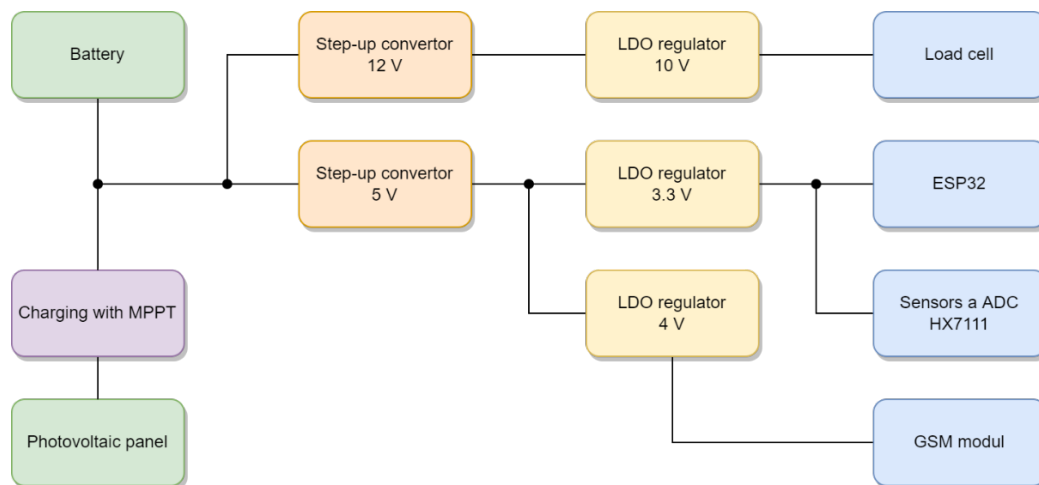


Figure 2: Power supply block diagram

The battery voltage is increased by two step-up converters to 5 V and 12 V. The 12 V is then lowered by LDO (Low Drop-Out) regulator to 10 V for supplying load cell. Output voltage from the LDO regulator is much smoother, what is desired for more accurate measurement. The 5 V are then lowered by two LDO regulators to 3.3 V and 4 V. The 4 V are used for powering up the GSM module. The 3.3 V are used for powering up microcontroller ESP32, sensors and ADC. Figure 2. shows power supply diagram.

CONCLUSION

This article contains preliminary results of student's bachelor thesis. In this project was designed device for measuring beehive parameters and weather conditions, such as weight, temperature, humidity, and air pressure. Suitable sensors, microcontroller, and the way of communication were chosen. Figure 3. shows power supply and control PCB. Figure 4. shows frame for load cell attachment. The frame is situated under a beehive and it was designed in SOLIDWORKS. The device was programmed in Arduino Framework. This device allows measuring more values than most of commercial devices and costs significantly less money. All measured data are stored in a cloud and visualized with ThingSpeak. Low power consumption, battery power supply, and photovoltaic charging allows remote working for long periods of time. Thanks to GSM and GPRS communication the designed device can work in basically any area.

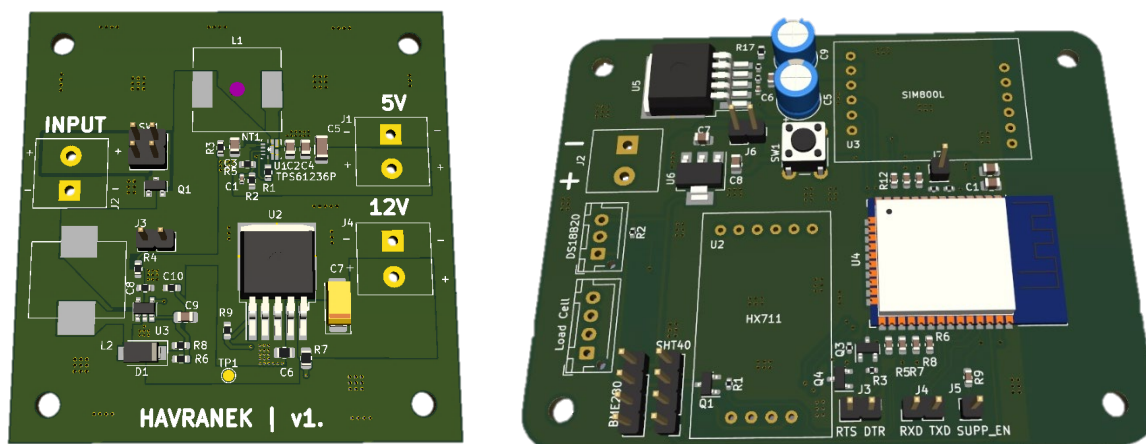


Figure 3: Power supply PCB (left) and control PCB (right)

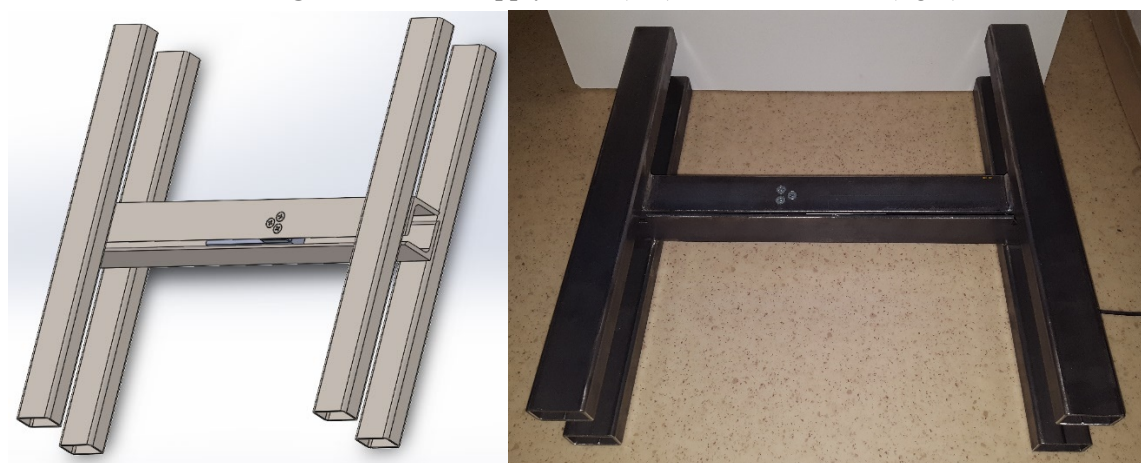


Figure 4: Frame for load cell attachment designed in SOLIDWORKS (left) and made (right)

REFERENCES

- [1] ESPRESSIF SYSTEMS. *ESP32 Series: Datasheet* [online]. 2016, 2021 [cit. 2022-03-11]. From URL: https://www.espressif.com/sites/default/files/documentation/esp32_datasheet_en.pdf.
- [2] SIMCOM. *SIM800H&SIM800L_Hardware Design_V2.02* [online]. 2015 [cit. 2022-03-11]. From URL: <https://www.gme.cy/data/attachments/dsh.775-083.1.pdf>
- [3] FARDEN, Jacob. *Handbook of modern sensors: physic, designs, and applications*. 4th ed. New York: Springer, 2010. ISBN 978-1-4419-6465-6.
- [4] PFISTER, C. *Getting started with the Internet of things*. Sebastopol, Calif.: O'Reilly Media, 2011. Make: projects. ISBN 978-1449393571.



Vyvíjíme a testujeme chytrá auta

Jdeš do toho?



valeo.jobs.cz

SMART TECHNOLOGY FOR SMARTER MOBILITY

SDR based Shortwave Receiver

G. Karetka, M. Waldecker

Brno University of Technology, Faculty of Electrical Engineering and Communication, Department of Radio Electronics, Brno, Czech Republic

E-mail: 221053@vut.cz, 192511@vut.cz

Abstract—This paper deals with proposal of shortwave radio receiver based on SDR (software defined radio). The main objective is to design and simulate shortwave radio receiver RF front-end based on Red Pitaya SDR capable of receiving DRM broadcast. The proposed design utilizes dual-conversion mixing and is able to receive signals from whole DRM spectrum range. Design includes system diagram and schematic of proposed device which was simulated at system level to determine important parameters (SNR, dynamic range, etc.).

Keywords—Shortwave receiver, Digital Radio Mondiale, Analog front-end, Software defined radio, Red Pitaya

1. INTRODUCTION

In recent years shortwave radio has been loosing on its popularity in developed countries among listeners and broadcasters. These have been shifting to higher frequencies mainly due to technical advantages of transmission (higher efficiency) and reception (higher quality of audio) with modern equipment (eg. mobile phones, small commercial radios, car radios etc.). The advantage of shortwave radio, possibility to reflect waves from ionosphere (called "sky wave" or "skip" propagation) has been made redundant due to today's satellite technology. On the other hand in developing countries shortwave broadcast using AM is still popular even today due to it's ease of reception. In recent years shortwave radio has regained popularity because of rise of digital radios, like DRM (Digital Radio Mondiale). These new broadcasting techniques use modern digital modulations with modern audio/speech compression algorithms and therefore better audio quality is achieved. Advantages of modern digital modulation include: narrower bandwidth (in comparison with AM) thus possibility to increase number of channels and reduced radiated power (in comparison with AM) therefore less is energy wasted. Scope of this paper is to systematically design and develop RF front-end for shortwave receiver primarily for receiving DRM and DRM+ on most frequencies (bands: LF, MF, HF, VHF). Minimal requirements for DRM reception must be met. Device should be designed as module "stack-able" on top of Red Pitaya (STEM^{lab} 125-14). Audio codec output should be directly accessible from FPGA, so ARM MCU is not overloaded with audio data stream.

2. ARCHITECTURE SELECTION

For sampling of the signal, Red Pitaya is used. It is Single Board computer with analog peripherals such as ADCs and DACs. Since ADC used in Red Pitaya has sampling frequency of 125 MHz, it can be used to sample bandwidth as wide as 62.5 MHz. Since this is theoretical value, in the design the calculations would assume only 80% of $f_{sampling}$ in order to create margin which equates to 50 MHz bandwidth. In order to reduce image interference that comes along with wide bandwidth of the input signal (signals ranging from LF to VHF) dual-conversion receiver architecture is implemented. It also brings possibility to use filters with high Q factor. These filters can be built out of smaller discrete components and at frequencies above few hundreds of MHz it makes sense to built them out of distributed elements. Since there are two ADC channels in Red Pitaya's ADC by using I/Q demodulator (Analog Devices ADL5387) and sampling both I and Q with different channels the bandwidth can be doubled. By doing so bandwidth can be increased up to 100 MHz which can be beneficial (sampling whole band, multiple radio stations simultaneously). Since it is not easy to build antenna with good reception ranging from tens of kHz up to hundreds of MHz two SMA connectors are present. One for 20 kHz up to 30 MHz and second for 30 MHz up to 200 MHz. Below are two tables Table I and Table II that present most important parameters

Table I: DRM receiver frequency bands [2] Table 2 (2019, p.14)

Receiver category	Frequency range	Lowest center freq.
LF	148.5 to 283.5 kHz	153 kHz
MF	526.5 to 1606.5 kHz 525 to 1715 kHz	531 kHz 530 kHz
HF 1	2.3 to 6.2 MHz	2.305 MHz
HF 2	6.2 to 27 MHz	6.205 MHz
Band I	47 to 68 MHz	47.05 MHz
Band II	76 to 108 MHz	76.05 MHz
Band III	174 to 240 MHz	174.05 MHz

Table II: S/N (dB) to achieve BER of 1×10^{-4} for DRM robustness mode D with spectrum occupancy type 3 dependent with different protection levels and code rates [1] Table A1.7 (2008, p.72)

Mod. scheme	Prot. lev.	Avg. CR	Channel 3	Channel 4	Channel 5	Channel 6
16-QAM	0	0.5	18.5	16.9	15.3	16.0
	1	0.62	21.2	19.9	18.3	19.2
64-QAM	0	0.5	24.2	22.2	20.8	22.1
	1	0.6	26.3	24.5	22.9	25.2
	2	0.71	29.2	27.6	27.2	29.3
	3	0.78	32.1	31.7	35.5	32.5

for DRM receiver being frequency ranges and signal to noise ratio that needs to be achieved in order to achieve bit error rate of values that do not corrupt streaming. In Figure 1 is presented system architecture of RF front-end of proposed device. Input consists of two SMA connectors each designated for different bands, filter with protection against transient voltage spikes, LNA followed by band select filter. After that one out of two bands can be selected by RF switch and is then passed through AGC/VGA to set constant level and upconverted to IF band. Two band pass filters are select-able each having different bandwidth. Before final I/Q demodulation signal is once again amplified in order to fully use range of ADC. Red Pitaya ADC inputs are equipped with 50 MHz low pass filters.

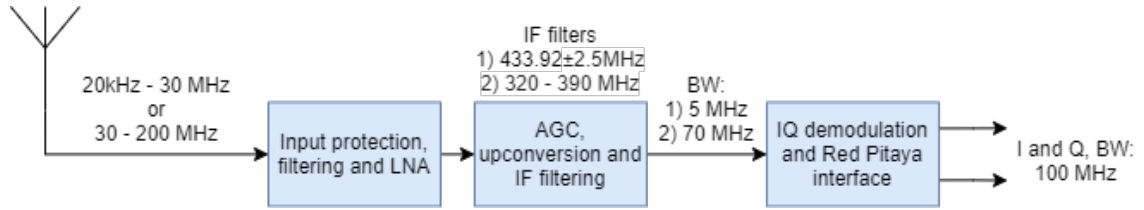


Figure 1: Overview of the RF front-end system

3. INPUT PROTECTION, FILTERING AND LNA

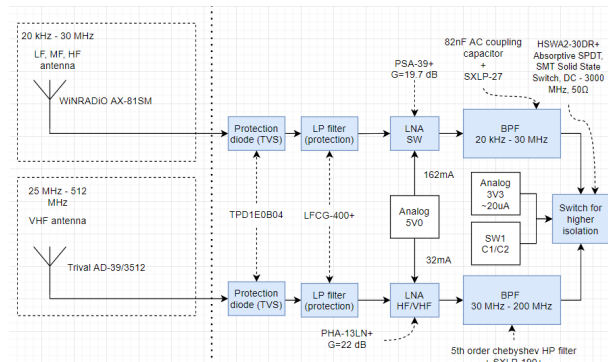


Figure 2: Overview of the RF front-end input protection, first filtering and amplification stage

In order to be able to receive both SW and HF/VHF band without the necessity for changing the antenna two SMA connectors are present. These inputs are protected with TVS suitable for RF operation in order to prevent ESD discharge. To not over-saturate LNA with out of band signals there is in each signal path low pass filter followed by LNA. Two different LNAs are selected since each presents different advantages. LNA PSA-39+ can work down to DC but requires high input current meanwhile PHA-13LN+ works from 1 MHz and consumes less current. Both amplified signals are then passed through filters to select just desired band. These filters consist of simple high-pass filter (blocking capacitor or Chebyshev filter of low order) and monolithic low pass filter. Then both signals pass through RF switch that is controlled by Red Pitaya.

4. AGC, UP CONVERSION AND IF FILTERING

As mentioned in Section 2 dual conversion architecture is selected. This architecture consist of IF module, Fig. 4, where frequency is higher than that of incoming signals. In order to set constant signal level AGC takes one of the input signals (selected by switch, described in Section 3) and normalizes its value to -5 dBm. This way difference in input LNAs gain is minimized. Selected AGC can be converted to VGA by simply replacing passive components. This possibility can be exploited if the AGC's capabilities are not sufficient. Following up converting mixer converts input signals to upper band where filtering is performed. Two filters are implemented. First filter is 5MHz SAW band-pass filter with high Q-factor and can be used to eliminate strong signals present in spectrum. Second filter is built out of discrete components and it is 70 MHz band-pass filter suitable for reception and scanning of whole band (eg. FM band). Filters have center frequency of 433 MHz and 355 MHz respectively. Input signals are up converted into this range, both generated by PLL frequency synthesizer (Analog Devices ADF4351). and Last part of the IF module consists of amplifier that boosts signal up to fully utilize dynamic range of ADC.

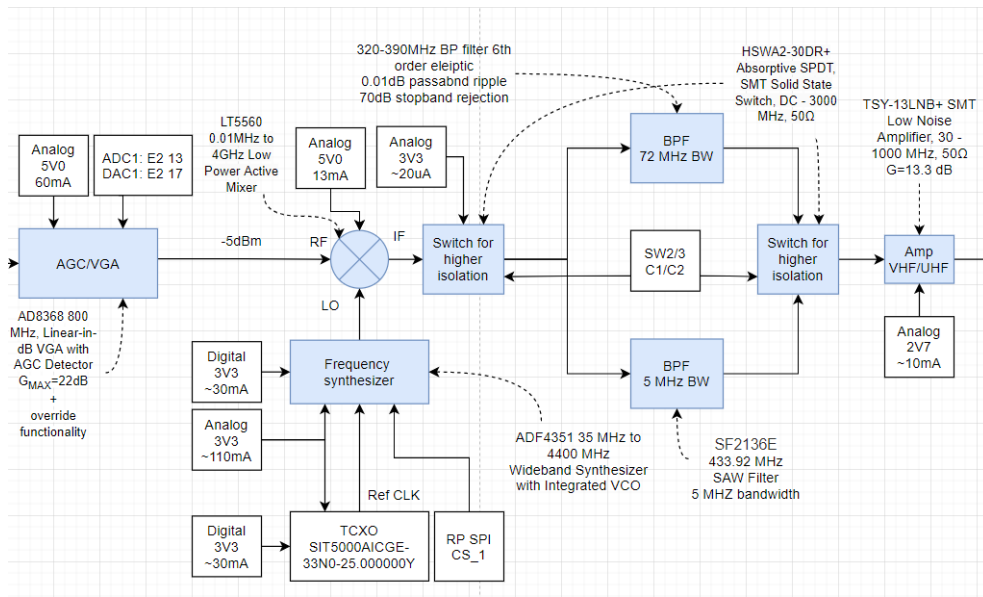


Figure 3: Overview of the RF front-end IF module

5. I/Q DEMODULATION AND RED PITAYA INTERFACE

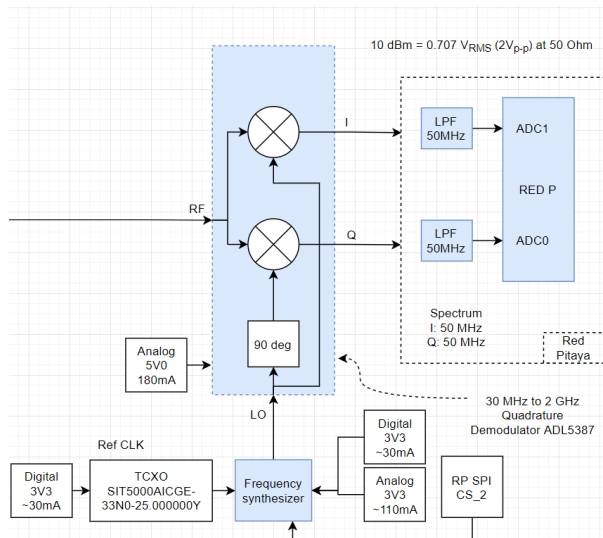


Figure 4: Overview of the RF front-end IQ module

In order to process signal digitally it need to be sampled. This is done using Red Pitaya with it's two 125 MSPS ADC channels where each channel can theoretically sample signals up to 62.5 MHz. In order to prevent aliasing there are two 50 MHz filters inside Red Pitaya. By using I/Q demodulator and by sampling I and Q by individual ADCs (in this case two channels) the bandwidth can be increased to 100 MHz. Once again this can be used to sample whole band (eg. FM band). Both I and Q signals need to be terminated by 50 Ω before entering Red Pitaya since it presents 1 M Ω input impedance. In order to be able to perform measurements without Red Pitaya I and Q signals need to be filtered on the RF front-end board.

6. SYSTEM PARAMETER SIMULATION

Two simulations of signal paths are presented with input signal of -46 dBm and respective frequency bands with full input bandwidth. Input bandwidth for SW is limited by input filter and it is 20 kHz to 30 MHz for simplicity $BW = 30$ MHz. Signal bandwidth of HF/VHF path is wider at the input ranging from 30 MHz up to 200 MHz therefore $BW = 170$ MHz. This is the worst case scenario, the whole dynamic range of ADC is used ($10 \text{ dBm}/2 V_{p-p}$ at 50Ω) at the output of AA filter). It also represents minimal sensitivity of whole device to be -96 dBm (11 dBuV) for SW path and -87 dBm (20 dBuV) for HF/VHF path. If sensitivity higher than presented is required additional amplifier or narrow band filter can be used. Last amplifier stage with TSY-13LNB+ can be bypassed thus enabling signal input of -2 dBm power. By examining whole chain it can be seen that gain can be adjusted in range of 56 dB to 22 dB this corresponds with AGC gain range (-12 dB to 22 dB). AGC is set to fixed output power of -5 dBm. In comparison with device presented in [3] the noise floor is greater due to wider bandwidth but does not allow reception above 5 MHz. IF filter implemented in presented device could reduce noise floor.

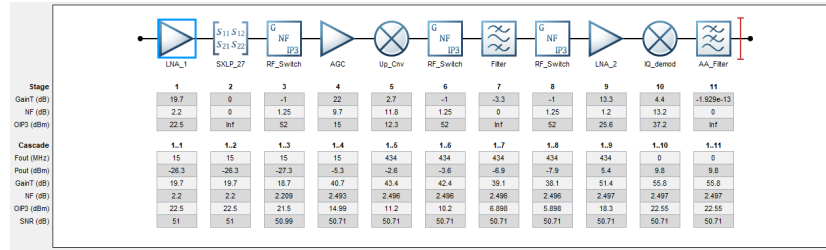


Figure 5: Example of cascade gain/noise simulation, simulated with MATLAB's RF Budget Analyzer

7. CONCLUSION

In this paper, proposed system design of DRM SDR receiver is presented. Device is then divided into three modules which are described more in depth. Whole device is simulated on system level and theoretical results are presented. Next objective is to design PCB and perform measurements of significant parameters.

Table III: Symbols and abbreviations

Abbreviation	Meaning
SDR	Software defined radio
DRM	Digital Radio Mondiale
AGC/VGA	Automatic gain control / Variable gain amplifier
LNA	Low noise amplifier
I/Q	In-phase and quadrature
TVS	Transient voltage suppressor
IF	Intermediate frequency

REFERENCES

- [1] *Technical Bases for DRM Services Coverage Planning*, DRM Consortium, Nov. 2021. [Online]. Available: <https://tech.ebu.ch/docs/tech/tech3330.pdf>
- [2] *Digital radio mondiale (drm); minimum receiver requirements for drm receivers*, DRM Consortium, Nov. 2021. [Online]. Available: https://www.drm.org/wp-content/uploads/2020/01/Minimum-Receiver-Requirements-MRR_v4.1.pdf.
- [3] WILLCOX, Donald E., Joonwan KIM, Chris LOEWEN a John WINEMAN. "Implementation of Digital Radio Mondiale receiver-part I". In: 2010 42nd Southeastern Symposium on System Theory (SSST 2010) [online]. IEEE, 2010, s. 56-59 . DOI: 10.1109/SSST.2010.5442862. Available: <http://ieeexplore.ieee.org/document/5442862/>

Accumulator three phase converter

M. Mikulka and J. Háze

Department of Microelectronics,
FEEC, Brno University of Technology, Technická 10, Czech Republic

E-mail: xmikul64@vutbr.cz, haze@vut.cz

Abstract—The paper presents description of design of a voltage converter and a 3-phase inverter with smart LCD controller. The LCD control terminal communicates via proprietary CAN interface. The final converter can supply a 3-phase output voltage with a selectable waveform, but primarily a harmonic sinusoidal (user configurable via terminal). The inverter will have an adjustable voltage (sinusoidal amplitude) in a certain range which is configured by user via control terminal also. It provides the possibility of a small correction of the output frequency and phase shift so that it can generate, for example, a two-phase 120 V grid and others.

Keywords—DC / DC converter, 3-phase inverter, DC / AC inverter, STM32, switched converters, digital control, ethernet, CAN, frequency waveform generation, powerful converter

1. INTRODUCTION

The device described in this article is used to transform electrical energy from the battery bank of a residential solar power plant to three-phase mains voltage used to drive common electrical appliances or to test them. The resulting device is utilized to generate output voltages of harmonic waveforms and waveforms composed of multiple harmonic components. The device can be operated with different output parameters such as voltage and current or frequency of output or phase delay between phases. These features make it the device very flexible in terms of ability to supply different devices and their testing.

The output voltage or current waveforms are user adjustable using the pre generated look-up tables. Furthermore, the frequency of the generated signal within a certain range is also adjustable, as well as its phase matching. The settings are easily accessible to the user via Ethernet interface or local display. Individual information about the status of the inverter is accessible to the user in the same place. The overall device consists of two parts, the inverter part and the control part used for communication with the user and the inverter itself. The control part of the device contains the user peripherals for connecting the console application and possibly logging parts or display. The inverter part contains only simple communication with the control and elements of the inverter itself. The control part could connect multiple inverters at the same time and can ensure their synchronization. It is also possible to connect other devices belonging to the same setup to the control part like MPPTs or battery health monitor, but they are not included in this work.

The converter is planned to be used primary as power backup for small house and for heating water boiler in meantime. It's designed mostly for purposes of island system converter, and it's not designed for work with mains grid connected directly into. There is a relay switching used for connecting this converter as mains instead of power grid and vice versa. Similar relay configuration is used for boiler if needed, but that isn't the case of this document.

2. CONCEPT OF THE CONVERTER

The converter board is divided into four parts. First part of the converter is input DC/DC converter^[1]. Input DC/DC converter is designed for conversion between low voltage DC input directly from battery plant and high voltage output for on-board utilization. It is designed with care for galvanic isolation, so there could be used more than one converter with the same battery as input but with completely separated outputs. This feature is planned mainly for these two cases. First case is request for multiphase outputs

which consists of 6 phases for example for some hybrid mains or for servo (or similar device) driving, where the DC offset between phases is feasible to use. Secondly most used case is in this project. One converter is used to produce mains voltage as island converter in the house cabin and the second converter is used to test other devices. Therefore, it is possible to use both sources. Also, it is completely isolated, so there does not exist any unwanted short circuit or similar problem.

Second part of the converter is AC waveform generator used to convert high on-board voltage to AC output voltages^[2]. This converter is designed as three PWM DAC / buck converters with common ground or three PWM-DACs in similar configuration. Generated waveforms have DC shift with exactly half voltage of on-board high voltage circuits. This voltage is generated with first converter as center output from two winding sections. This waveform generator is driven by main microcontroller, which allows generation of completely different waveforms for every phase. Output voltages are sensed separately, and so the currents. All current sensing is ensured by HAL current sensors supporting galvanic isolation from other devices such as microcontroller stage.

Third part of this converter is communication interface and control microcontroller, which both supports communication between user interface (PC, console etc.) and converter. Communication interfaces are galvanic isolated as well. Communication interface of converter board consists of one virtual COM port via USB and one CAN interface with synchronization lines. CAN interface communicates on custom proprietary communication described in next parts of this article. USB COM terminal contains simple UART console which is useful for fast and simple control of this board without control terminal in debug regimes or in cases of utilization as offline converter.

The last part of this converter is auxiliary power converter used to supply everything on this converter board. This power supply is designed to run from the same voltage as battery input (24 – 48V DC) and can be tied together by external wiring. In default connection case it's completely isolated so it can be powered together with other board with one power supply, but it can use separated batteries for both boards.

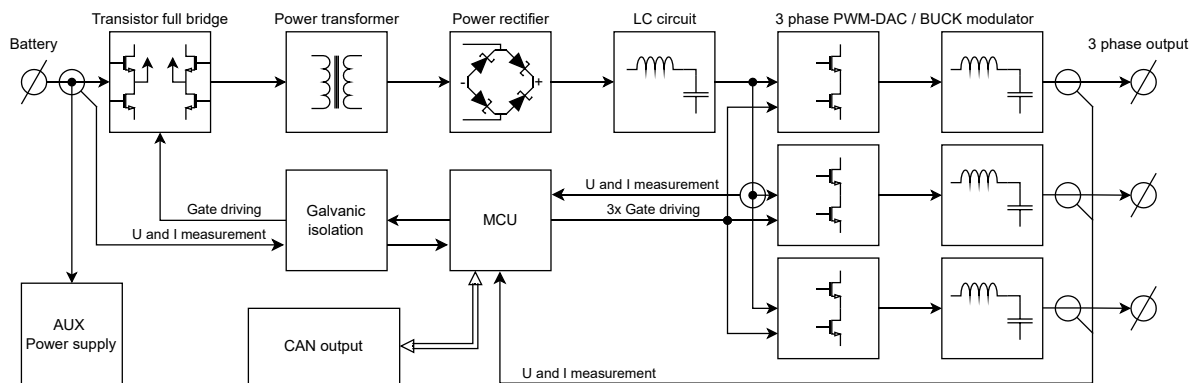


Figure 1: Partial converter block diagram

3. CONCEPT OF DISPLAY CONTROL TERMINAL

Display control terminal is considered as main control terminal now. It consists of fast microcontroller with external memory for filesystem with logged data from all devices. There is also external RAM working mainly as video buffer memory for utilized LCD which is LCD-TFT type. LCD resolution is 480x272 px and there is capacitive touch panel too. There are also SD card slot and Ethernet port for user purposes. This board is designed to be used with experienced user and it consists of three user driving parts. First part is dual DIP switch for switching between DHCP and static IP configuration of Ethernet interface. Second one is reserved at the moment, but it's planned as some kind of switch for external data application.

This board is programed for automatic data collection service from detected devices as battery health monitor, two DC/AC converters, MPPT^[3] converter for solar panels and boiler room converter. Collected data are stored in binary format in custom file types with inspiration in csv files. All data are stored in internal file system in on board NOR flash memory and can be transferred to SD card if user demands. These data can be also transferred via Ethernet interface into configured Grafana server on separated server. A selected part of these data is displayed on the LCD for fast user overview. There is lots of information and settings for every device. It isn't a good practice to place this many not connected

terms on one screen, so it has been done separately on screens for every device. In such a way, everything is nicely separated and better understandable for ordinary users as well as for inexperienced users too.

The data acquisition service works with known devices connected to the CAN interface, where they are identified, when they are started for the first time. Each device carries its own specific ID, which is partly configurable by the user, but most of it is used for system purposes. This property allows simple device identification in the system. However, it is also available as CAN bus – simple device addressing by its own address. In other words, each device sends its messages under its ID, which are received by the control unit. In this CU, the data are further processed. However, when a specific device needs to be driven by the controller, a message with the ID of that device is sent as a command message. Thus, signaling to the device, that a certain data packet is coming, which should be expected under its ID. Only broad cast packets for all devices are sent under the controller ID. Individual devices cannot send command messages (see below for the ID space partitioning) so that there can be no collision between sending data from a device and sending a command or subsequently data from the controller. The CAN interface is a standard type with an 11bit ID which is divided into three parts. The first part is the two highest bits used to identify the data packet as they carry the highest priority. These two bits make up a total of 4 possible messages which are: Error report, reserved (not currently used), command report and data report. Next 4 bits are user switchable as device designations using the BCD switch available on each device. The last remaining 5 bits are used to identify the data packet so that messages larger than 8 bytes can be easily sent without constraining the data packet. There is no protection for detecting ID collision, so only user can do this in terms of correct ID configuration. There is also only one static ID, which is ID of control terminal. This ID is user modifiable only via Ethernet interface in “additional” settings, but it’s not meant to be changed. This ID (0x00) is static type because the control terminal should have highest priority in terms of command control for every single board. This ID is also used for broad cast command packet used in danger situation on one of the devices such as battery health monitor.

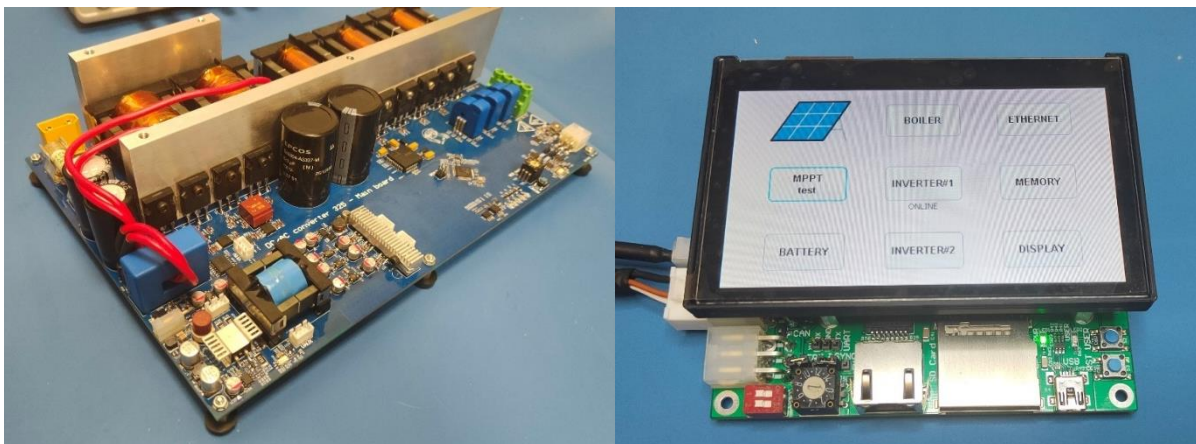


Figure 2: Converter board without passive heatsink (left) and Control terminal displaying main menu (right)

The LCD terminal also has settings page for necessary configuration such as full Ethernet configuration (IP, gateway, masks etc), LCD brightness, auto dimming settings and time setting in case of offline operation. Separated LCD page contains all operations with memories and data acquisition as data formatting or data copying to external device. There is also planned configuration for Grafana^[4] transfers, but in actual state the configuration is only on the web page.

In graphics is implemented a button, for every device with visible mark of connection state. After opening some of this device screen, the device data / setting is shown. Usually there is an actual state of the device and its necessary operation parameters shown on the screen. Also, there is a switchable time period for showcases / graphs of acquired data on this page. There isn’t any setting of waveform generation, voltage range and other parameters, because it will be so small so it will not be easily configurable. All these settings are located on a web page hosted by this device as localhost. This is a simple HTML web page with fields for filling in all the necessary data for the operation of the different parts of the device (three-phase inverter in this case). The IP address configuration of this local host is contained in the Ethernet configuration screen of the device. If DHCP settings are used, this information is displayed in the same place with the only difference being the read-only settings.

CONCLUSION

This converter is designed for 48 V lead acid accumulator input (range of about 35 V to 60 V maximum), but there are only few parts which is limiting input voltages for this ranges. PCB board is designed for a bit higher current than it runs with this specs, so it's possible to use the same board for 24 V accumulator (for example in range of 20 V to 36 V) just by replacing main transformer with different windings, fuse with bigger ratings and input capacitors may use higher capacity with lower voltage rating. There isn't any real limitation for battery type, so it can be used with LiFePo4 or other type of input power source in said voltage limits but other power sources could use different undervoltage settings. This converter is controlled by smart terminal with capability of controlling full solar system such as MPPT, inverters and battery monitor.

Actual output voltage amplitude is limited to 75 % of high voltage rail, so that is 675 V output amplitude. This amplitude is good enough for both US and European voltages (120 V and 230 V on phase) and it's also useable for full voltage swing from 85 V to 250 V for SMPS testing purposes. Output converters is also available for testing purposes of SMPS characterizations with different output waveforms such as combinations of few harmonics or some other waveform created by user. Generated waveforms are saved in on board memory, which is accessible through CAN interface allowing its changes. In consideration of total output power, there are limitations of input converter to about 2 kW. There are also some other limitations like maximum output current for every phase (about 1,2 A) and thus the final output power for AC waveform will be smaller and full 2 kW will be available only with DC voltage generation. There are also some limitations for maximum slew rate thanks to the type of the converter.

Converter itself calculates necessary parameters such as effective output voltage and current, phase shift between phases and between voltage and current, output powers and FFT for simple estimation of pseudo THD. This and some more data are transferred to the control terminal where are logged into internal memory and possibly to the Grafana server if it's available. Logged data is transferable to user SD card memory and it's downloadable through localhost webserver hosted by control terminal.

Converter has been tested for some time with boiler connected for water heating purposes, which helped with development for the algorithms for statistic calculations. In this time there wasn't observed any major issues, just overheating output inductors in case when the converter was completely sealed in construction box. In parallel with this testing, second unit was used as experimental PSU for development of SMPS battery charger. Apart from this little tests, no more specific measurements were made regarding the response time to the load or other type of load. This is mainly since the limiting factor is mainly the input energy from the panels and its outages. The switching of the load does not cause any problems for the source, which was also verified by a long-term test with a boiler and short-term tests with SMPS. In this time, there are no problems recorded, however no measurement of reaction time or recovery time took place. During part of the operation with the boiler, a personal computer hosting local Grafana server was connected to this device and there aren't any problems with outages too, even switching on the boiler thermostat didn't create a sufficient problem to cause the PC to fail.

ACKNOWLEDGMENT

The article was supported by project no. FEKT-S-20-6215, New approaches in the use of modern micro- and nanoelectronics.

REFERENCES

- [1] Pop-Calimanu, Ioana & Lica, Septimiu & Popescu, Sorin & Lascu, Dan & Lie, Ioan & Mirsu, Radu. *A New Hybrid Inductor-Based Boost DC-DC Converter Suitable for Applications in Photovoltaic Systems: Energies*. 2019.
- [2] ZHILEI, Yao, Lan XIAO a dan Yangguang YAN. *Seamless Transfer of Single-Phase Grid-Interactive Inverters between Grid-Connected and Stand-Alone Modes: IEEE Transactions on Power Electronics*. 2010.
- [3] GOMATHY, S, S SARAVANAN a S THANGAVEL. *Design and Implementation of Maximum Power Point Tracking (MPPT) Algorithm for a Standalone PV System: International Journal of Scientific & Engineering Research* 2012.

Implementation of procedures and evaluation of data from compliance tests of Power Generating Modules of categories A1 and A2

M. Bláha¹

¹Brno University of technology, Czech republic

E-mail: xblaha30@vut.cz

Abstract— The ever-increasing number of untested small Power Generating Modules (PGM) poses certain challenges and risks for Distribution System Operator (DSO) in the future, as these PGM have not been verified and therefore DSO cannot reliably predict their behavior, especially in extreme situations. However, to ensure reliable operation and power quality, it is necessary to require certain behavior of PGMs. This behavior is already almost defined, but there is lack of an accurate verification procedure and functional test workplace to enable PGM testing. This paper deals with both the principle of testing and the processing of measured data and their evaluation, together with the creation of an output measurement report. The correct data processing and representation is crucial task for a certified workplace, which would enable PGM testing.

Keywords—RES, PGM, PV, inverter, RfG, testing, data processing

1. INTRODUCTION

Renewable energy sources (RES) are currently one of the most watched topics in the field of energy. RES are expected to help meet EU targets in the areas of [1]:

- Reduction in greenhouse gas emissions by – 40 % by 2030 compared to pre-industrial times
- Reduction in primary energy imports, in particular fossil fuel imports
- Increase in power generation from the RES to 32 %

In particular reducing primary energy imports and increasing the share of RES in electricity generation, appear to be crucial at the moment, as the current situation shows that fossil fuels may become unexpectedly more expensive in adverse situations around the world. For these reasons, there is a clear need to build new RES. In particular, the development of PV systems can be expected in the Czech Republic (CZE). The owners of these houses, who were only consumers, are now becoming so-called prosumers, both consuming their generated electricity, reducing the amount that has to be produced in large power plants, but even being able to supply electricity in the event of a surplus. The term Prosumers is also associated with so-called Smart Grids. The development and use of Smart Grids in the future goes hand in hand with the possibilities of the RES, as Smart Grids are designed to change the relationship between electricity production and consumption so that consumption will be adapting to current production, especially from local sources such as the RES.

However, the increasing numbers of RES also cause significant complications. These include, in particular, increasing voltage at the point of connection, flicker, non-symmetry of voltage, etc. In order not to adversely affect the connection point, individual RES must comply with certain rules. For this reason, EU Commission Regulation 2016/631 - Requirement for Generation (RfG) [2] was created. In particular, this regulation is intended to ensure the international legal framework that further establishes minimum obligations, but in particular the scope of competence for EU Member States. Thanks to this document, individual states may require both different conditions and stricter limits compared to other Members States, in accordance with their regulations, standards and laws. In the CZE, it is mainly the document Rules of Operating Distribution Systems (RODS) – annex 4 [3], which sets out requirements for parallel connections for, for example, PGM.

2. POWER GENERATING MODULE

This concept was coined in accordance with [2]. The PGM is divided into two basic types, namely synchronous and non-synchronous. This paper deals mainly with testing of PV inverters, which are typical representative of non-synchronous PGMs. The requirements to be met by each category are divided according to their installed power. There are 4 categories in total for CZE, the first two of which also have their subcategories. These subcategories arose mainly because of the laws, standards and regulations of the CZE, which are related to the installed power resources and the voltage level to which PGM's are connected. These are law [4] and decree [5].

The paper focuses on the two lowest performance subcategories, namely A1 ($800 \text{ W} \leq P_i \leq 11 \text{ kW}$) and A2 ($11 \text{ kW} < P_i \leq 100 \text{ kW}$). The requirements that VMs must meet after connection to the grid can be divided into two groups. However, it is important to distinguish the voltage level to which the PGM supplies the generated electricity. The first group of requirements are articles that arose from [2] together with the standard [6] for low voltage level and with the standard [7] for medium voltage level. However, the analysis of individual articles together with partial details would significantly exceed the permissible scope of this work. The reason for compliance with these articles is described, for example, in [8], which deals with the verification of the LFSM-O function. Here it is possible to see that some of the inverters meet the required settings for CZE, some of them react badly and in one case even to completely the inverter from the grid, Figure 1.

The second group of requirements is defined by RODS, which states that in the CZE PGM is obliged to participate in the support of normal network operation. For the categories addressed, it is called static voltage control. PGM participates in this action mainly through generation or consumption of reactive power. Thus, PGM must be able to operate in the range of power factor from 0,9 capacitive to 0,9 inductive. This property is called Q(U) regulation. PGM, which is able to control this, positively affects the magnitude of the voltage at the connection point and its surroundings, [9]. As PGMs may not yet be required to test this feature, it often happens that the PDS requires PGMs to produce active power at a fixed power factor, such as 0,95, which can be considered to protect DSOs against PGM Q(U) misbehavior, Figure 2. P(U) control also belongs to static control. In case the Q(U) regulation is no longer sufficient to reduce or limit the further increase of the voltage above a certain limit, it is necessary to use the P(U) regulation. This is the extreme solution where the PGM module reduces its delivered active power to the network according to the voltage size. The extreme solution is mainly because the PGM and thus the owner is deprived of potential profits from the produced active power.

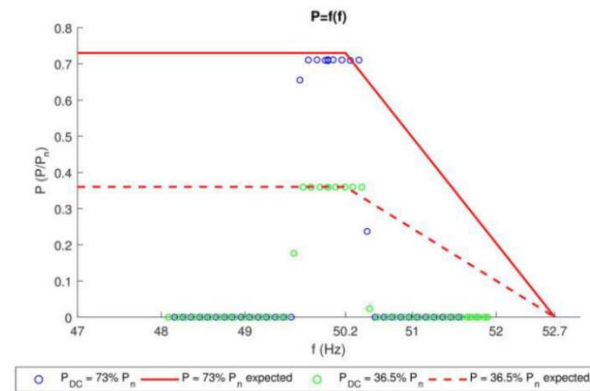


Figure 1: Incorrect power-frequency response of inverter [8]

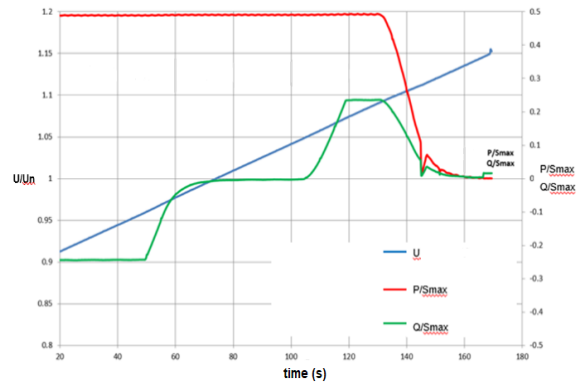


Figure 2: Example of incorrect Q(U) control of inverter [10]

In view of the above information, the introduction of the obligation to test PGM can be expected in the future.

3. TESTING OF PGM

The mentioned requirements that PGM will have to meet in the future are therefore related to behavior that will not adversely affect the quality of electricity at the place of its installation. For this reason, it is desirable to create a laboratory workplace that would address this issues. The workplace should follow the standard [11], currently only a draft, which focuses on PGM verification procedures. At present, however, there is no workplace in CZE that could handle complete testing. Therefore, it is not yet possible to verify whether PGMs meet the requirements that are currently imposed on them.

A sample of the test site is shown in Figure 3.

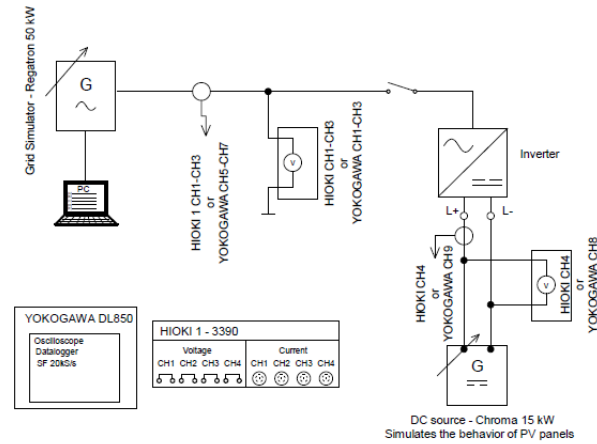


Figure 3: Simplified circuit diagram of a laboratory workplace. The power analyzer HIOKI 3390 is used for static tests and YOKAGAWA DL850 for dynamic tests.

The test sequences which verify the individual capabilities of PGM, are created via the PC in the program designed to control the grid simulator. The setting of test is based on either [3] or standards [6] and [7]. For some tests it is necessary to create up to three separate test sequences, which together with the number of partial tests, which is about 17, led to the need to create a simple test manual, which was created by the author of this paper and which is used to create test sequences. However, the creation of additional sequences can be expected, as individual DSOs or manufacturers may pay to test for their specific values. An example of a test manual is shown in Figure 4. This is a simplified set of information necessary for testing the LFSM-O testing. At present, approximately half of the test sequences in which the author participated are created using this manual. Due to the fact that the manual provides a comprehensive overview of the conditions of individual documents [3], [6], and [7], the creation of the remaining sequences is relatively simplified compared to the previous state. It is now possible to create the remaining test sequences within a maximum of several hours.

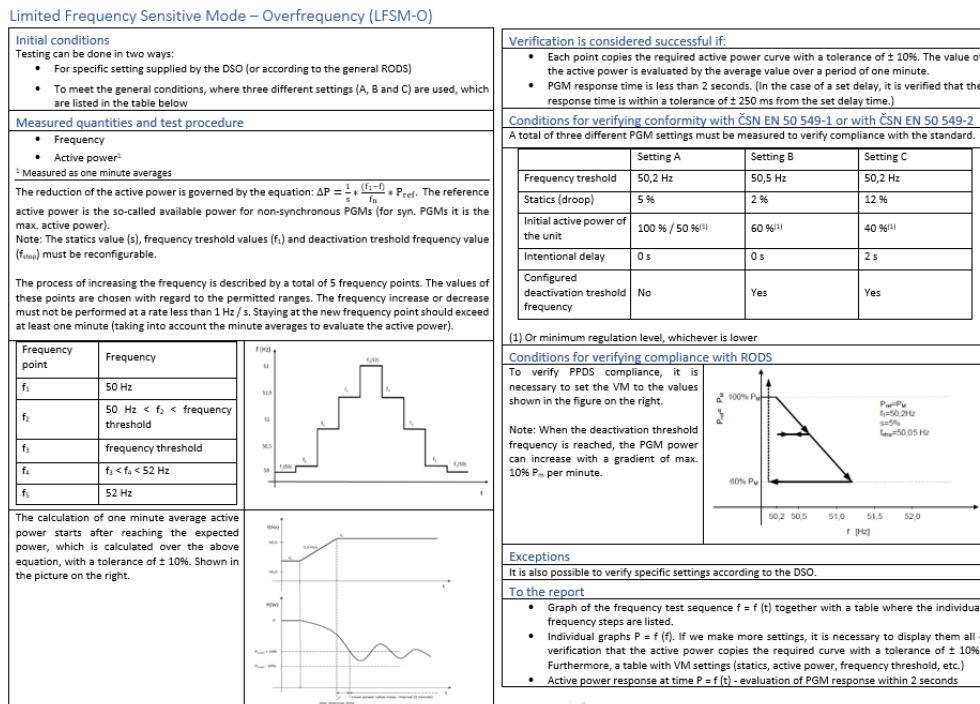


Figure 4: Sample of one of the 17 tests that are processed in the testing manual. LFSM-O manual.

The measurement process is extremely time consuming, as some tests, such as verification of the PGM frequency operating range, take several hours. However, testing of the RCT and Deyen inverters, on which several sequences were measured in recent days, revealed other adverse circumstances.

In the event that the test workplace will be used for regular testing of PGM, it is necessary to prepare an overview of the basic capabilities of the settings that will be required for each PGM. These are mainly options such as:

- Reconfiguration and deactivating protection functions
- Setting of $Q(U)$, $P(U)$ and $P(f)$ (LFSM-O) functions
- Setting the power factor to a specific value

These facts are mainly due to the fact that measurement of the above-mentioned inverters has shown that it is not possible to deactivate protection functions, which makes it impossible to perform certain types of tests. The $Q(U)$, $P(U)$ and $P(f)$ functions did not work with the Deyen inverter, despite the fact that the inverter had a user interface that allowed each function to be set. Verifying whether a given function can be set and whether its parameters have really changed is also very time consuming. In general, however, it can be said that in some cases this condition can be corrected by changing the firmware after communication with the manufacturer or other intervention. However, these solutions mean additional time that needs to be compensated financially, but it is difficult to estimate in advance how time-consuming it will be to eliminate these problems, making the whole process less efficient. For these reasons, the easiest solution seems to be to create the above-mentioned overview of basic skills, which will specify the requirements for those interested in testing. Candidates will be able to prepare the inverter so that it allows a smooth testing process, which will lead to financial savings both on the part of the applicant and time savings for the test workplace, which can be used for the next unit.

Another part of the testing process is the evaluation of the tests themselves. This involves an considerable amount of files and data, as there is also the considerable number of tests for the verification of categories A1 and A2. These data need to be evaluated to determine whether or not the inverter has passed the test. For this purpose, the computer program Matlab will be used, which allows both fast work from the data and the possibility of use for other brands of inverters. Although the creation of the script itself is more time consuming than other alternative methods, it is invaluable from the point of view of the subsequent computational speed and especially repeatability. The only condition is the use of the same measuring apparatus, because each measuring apparatus may differ not only between individual brands, but also between individual models in terms of the output of the measured data. These may be small changes, such as an different order of the measured quantities in the columns, but even this change leads to the necessary adjustments in the calculation script, which is a negative phenomenon in terms of measurement repeatability for other brands of inverters. In general, for the greatest automation of the process, it is desirable to come up with a methodology for each individual test, which would help to clearly determine the result from the processed data.

However, the most important thing is the measurement output itself. This output should be clear, unambiguous and repeatable. This protocol will thus be a kind of inverter output certificate, where, in addition to the results, important data on both the laboratory workplace and the customer will be given. However, the protocol does not have to be used only to verify the inverter's compliance with [3] or compliance with standards [6] and [7]. This is also an clear output for, for example, a inverter manufacturer who has paid for inverter measurements at the relevant laboratory for any purpose. Typically, this can be done, for example, to further improve the capabilities of its own inverter.

4. CONCLUSION

However, whether the reconfiguration process or consultation with the manufacturer is extremely time consuming, it is important to automate parts such as testing, measurement, data processing and laboratory protocol issuance as much as possible, which will increase the efficiency of the entire testing process and thus reduce the testing costs. For such automation, it was first necessary to create the test manual, which implements all the requirements of the already mentioned documents. With this manual, more than half of the test sequences have been created and are functional and tested. A new finding from the measurement, which will also help streamline the testing process, is the need to create the overview of basic skills that individual PGM applicants should meet, so as not to waste work capacity on one particular PGM when trying to reconfigure PGM settings, e.g. using new firmware after communication with the manufacturer. The scripts themselves are created with an emphasis on the simplicity and evidence of each measurement so that even in the report itself it is possible to identify at a glance whether the inverter complied or not.

ACKNOWLEDGMENT

I would like to thank the supervisor, Jan Moravek Ph.D. for methodological and other valuable advice that helped create the content of this work. I also thank Martin Vojtek Ph.D. and Michal Vrana for consultation and providing important materials.

REFERENCES

- [1] SMAGRINET – RSCH – TalTech: “Electricity and Environment [online]. [cit.2022-03-08]. Program for Engineering Researchers. <https://www.smagrinet.eu/>.
- [2] COMMISSION REGULATION (EU) 2016/631 of 14 April 2016 laying down a network code for grid connection requirements for the connection of generations to the electricity grid. In: Brussels: Official Journal of the European Union, 2016, V. 631. Also available from: <https://europa.eu/legal-content/CS/TXT/PDF/?uri=CELEX:32016R0631&from=CS>
- [3] RULES of OPERATING DISTRIBUTION SYSTEMS – annex 4 [online], 2020. Available from: https://www.cezdistribuce.cz/webpublic/file/edee/distribuce/ppds/ppds-2020_priloha-4.pdf
- [4] Law No. 458/2000 Coll. Law on Business Conditions and the Performance of State Administration in the Energy Sectors and on Amendments to Certain Laws (Energy Law). Also available from: <https://www.zakonyprolidi.cz/cs/2000-458>
- [5] Decree No. 79/2010 Coll. Decree on the dispatch control of the electricity system and on the transmission of data for the dispatch control. Also available from: <https://www.zakonyprolidi.cz/cs/2010-79>
- [6] ČSN EN 50549-1 Requirements for generating plants to be connected in parallel with distribution networks – Part 1: Connection to a LV distribution network – Generating plants up to and including Type B. 2019
- [7] ČSN EN 50549-2 Requirements for generating plants to be connected in parallel with distribution networks – Part 2: Connection to a MV distribution network – Generating plants up to and including Type B. 2019
- [8] P. Mastný, M. Vojtek, J. Morávek, M. Vrána and J. Klusáček, “Validation of PV Inverters Frequency Response Using Laboratory Test Platform,” 2020 21st International Scientific Conference on Electric Power Engineering (EPE), 2020, pp. 1-5, doi: 10.1109/EPE51172.2020.9269247.
- [9] R. Vaněk, “Regulation of U/Q local sources in MV network,” 2018. Also available from: <https://slideplayer.cz/slide/15196754/>
- [10] T. Linhart, J. Švec, S. Hes, L. Frejvald, J. Dvořák, and ČEZ Distribuce, a.s. “Testing of PV inverters in the ČEZ distribution laboratory” [online]. 2019. Available from: <https://zenodo.org/record/3555082#.YielU3rMJPZ>
- [11] EN 50549-10 Requirements for generating plants to be connected in parallel with distribution networks – Part 10: Tests demonstrating compliance of units. 2021

Simulations of System Wide Disturbances in the Continental Europe Synchronous Area on a Simplified Model

S. Macejko¹ and J. Koudelka¹

¹ Brno University of Technology, Faculty of Electrical Engineering and Communication, Dept. of Electrical Power Engineering, Brno, Czech Republic

E-mail: xmacej02@vut.cz, xkoude20@vut.cz

Abstract—The paper deals with frequency stability simulations for system wide disturbances in MODES network simulator. It describes a simplified model for Continental Europe separation from January, 8, 2021 and incident in Rogowiec substation from May, 17, 2021. It shows that the simplified model is suitable for different disturbances after minor modification. The simplified model is based on publicly available data.

Keywords—system wide disturbance, frequency stability, Continental Europe separation, dynamic simulation

1. INTRODUCTION

The Continental Europe Synchronous Area (CE) consists of 25 countries with 29 Transmission System Operators that are members of ENTSO-E. In addition, the Turkish transmission system is in synchronous parallel operation with CE, but it is not part of ENTSO-E. CE is very interconnected power system and the largest part of ENTSO-E, which leads to highly reliable operation. But even in such a resilient power system, certain aspects need to be evaluated. One of these aspects is frequency stability, which is the ability of the power system to maintain steady frequency after an imbalance between generation and load [1]. Maintaining the steady frequency is important for proper functioning of the power system components, because all devices in the power system are designed for a nominal frequency (50 Hz in this case). It is therefore necessary to assess frequency stability and dynamic simulation is one of the ways how this can be done.

After the occurrence of large active power imbalance in the interconnected power system, it is necessary to contain the emerging frequency deviation. For this purpose, Frequency Containment Process (FCP) is established. In first few seconds after the occurrence of active power imbalance, Frequency Containment Reserves (FCR) are activated on the units involved in the process. The total FCR capacity is determined from the Reference Incident, which is based on the N-2 criterion (outage of the two largest nuclear power units) with a total capacity of 3 000 MW for CE. This capacity must be fully activated for frequency deviation 200 mHz within 30 seconds. For the power deviation less than 1 500 MW, time is 15 seconds, and between 1 500 and 3 000 MW, time rise linearly to 30 seconds [2].

Incidents that exceed the Reference Incident are of interest, because it is not sure whether CE is able to withstand them. Several incidents of this type occurred in 2021. One of them was CE separation on January, 8, when busbar coupler in 400 kV Ernestinovo substation (in Croatia) was tripped by overload protection and it resulted into the separation of CE into two areas, North-West (NW), power deficient, and South-East (SE), power surplus. Power flow between these areas was approximately 5.8 GW before the incident. The disturbance is reported in [3]. Another incident occurred in 400 kV Rogowiec substation (Poland) on May, 17, when human error caused the outage of 10 units of Bełchatów Power Plant with a generating capacity of 3 322 MW. The incident is reported in [4].

These incidents also show that it is important to assess frequency stability for different cases, but to do so, a model on which such incidents can be simulated is required. Therefore, this paper focuses specifically on the simulation of these disturbances in the MODES network simulator.

2. DYNAMIC MODEL FOR DISTURBANCES

To assess the frequency stability and behaviour of CE, a simplified model, referred to as SIME (Single Machine Equivalent), is sufficient for a simple analysis. In SIME model, the behaviour of the whole

system is replaced by a single machine – a synchronous machine with a steam turbine, an automatic voltage regulator and a governor. In general, the problem of the models is the estimation of their parameters as relevant data are not always available. The major advantage of SIME is that it is clear, but its disadvantage is that it is not suitable for advanced simulation, e.g., it cannot replicate interarea oscillations. Despite its drawbacks, the SIME model is indeed suitable for simulating the general system behaviour for these cases and is therefore used in this paper.

Single-line diagrams of the grid model for the incident from January, 8 for the NW area and for the incident from May, 17, hereinafter referred to as Rogowiec, are shown in Fig. 1. Units G1 and G3 represent SIME model, G2 represents loss of generation in NW area (import from SE area and outage of units in NW area) and G4 represents outage of 10 units of Bełchatów Power Plant. Loads L1 and L3 represent the load on the power system and L2 represents the disconnected industrial loads, which occurred in France and Italy. Loads L1 and L3 are modelled as frequency dependent with an estimated load damping coefficient of 0.6 %/Hz (usually estimated between 1 and 2 %/Hz, but this estimation was modified to obtain better compliance between simulated and measured values).

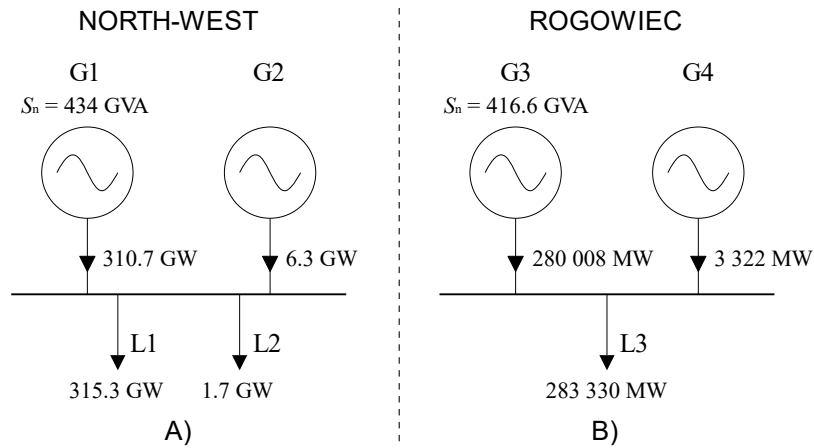


Figure 1: Single-line diagram of the grid model for the NW area (A) and Rogowiec incident (B)

Modelling approach was inspired by [5]. For the equivalent synchronous machine (G1 and G3), 6th order Park machine model was used, and for steam turbine with speed governor, TGOV1 model (described in [7]) was used with zero frictional losses factor. Table I. shows important parameters of the model for NW area and for Rogowiec. Data for NW area model were basically taken from [5] (see [6] for more details). In case of Rogowiec, basic data from [5] was modified and its dynamics are based on models of NW and SE area (see [6]), where reheater time constant T_3 of TGOV1 was determined as the parallel sum of those parameters for both areas and the ratio T_2/T_3 is the same as in the NW area. Turbine-governor droop R and inertia constant of synchronous machine is considered the same as in the NW area. The load of power system was determined from Transparency Platform [8] and rated power of the synchronous machine corresponds to approximately 70 % of the system load.

Table I: Parameters of the models

Parameter	Unit	NW	Rogowiec
Rated power	GVA	434	415.6
Max. turbine output	GW	412	394.7
Rated power factor	(-)	0.95	0.95
Active power	GW	310.7	280
Inertia constant ($2H$)	s	14.8	14.8
Turbine-governor droop (R)*	(-)	0.3	0.3
Reheater time constant (T_3) *	s	10.8	5.246
Ratio T_2/T_3 *	(-)	0.14	0.14

* MODES uses the constant K_{P2} , T_R , K_{LP} and K_{HP} , where $K_{P2}=1/R$, $T_R=T_3$, $K_{HP}=T_2/T_3$ and $K_{LP}=1-K_{HP}$

3. SIMULATIONS AND RESULTS

Incidents were simulated in MODES on the dynamic models presented above. The simulation scenario for both system disturbances is similar and simplified (compared to the real disturbances). Disturbances are applied at time 1 second, after reaching the steady-state. In case of NW area, it is the outage of 6 300 MW of generation (G2 in Fig. 1) and 1 700 MW of consumption (L2 in Fig. 1). In case of Rogowiec, it is the outage of 3 322 MW of generation (G4 in Fig. 1). The assessed variable was the frequency deviation waveform.

The simulation results are shown in Fig. 2, which shows the frequency deviation for both system disturbances, they are plotted together with measured data from the real CE power system. There are also added simulation results for NW taken from [5], which were, however, simulated on advanced grid model, not only on a SIME equivalent as presented in this paper.

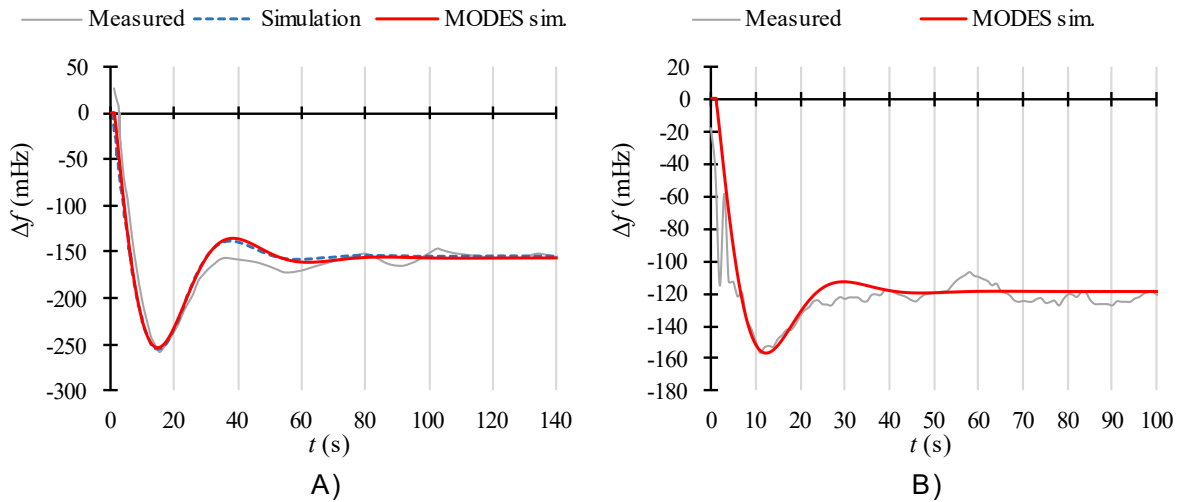


Figure 2: Frequency deviation in NW area (A) and in CE for Rogowiec substation incident (B)

Based on the results, it can be concluded that the dynamic model represents the behaviour of the power system very well. Simulation of CE separation of NW area shows the dynamic model has almost identical results as in [5], and therefore the model can be considered as validated with respect to the system behaviour as well. Further, the results show that after modification, the dynamic model can also be used to simulate other incidents, an example is the presented Rogowiec incident, where the results obtained from simulation clearly correspond to the real system behaviour. Curves obtained from simulation are smoother because, as was explained, interarea oscillations present in measured data are not replicable on the simplified model and further regulation processes latter following the disturbance were not considered in the scenario.

4. CONCLUSION

This paper describes the basic behaviour of the interconnected power system of CE after the occurrence of active power imbalance and focuses on 2 system disturbances, which were the object of simulations – CE separation from January, 8, 2021, and Bełchatów Power Plant outage due to failure in Rogowiec substation from May, 17, 2021. The Single Machine Equivalent models for both disturbances were described and simulations of these events were done on them using MODES network simulator. Simulation results show good compliance between the model and the real system behaviour, indicating that the model can be further used for other system disturbances or for assessments of fictitious scenarios. It is worth mentioning that the models were created from publicly available data compared to the other published models (e.g. [5]).

This model is currently being extended to a single-bus model, in which aggregated units are modelled based on the power source (gas units, photovoltaics and so on) and HVDC interconnections between synchronous zones. The model is being prepared for the CE separation on January, 8, 2021, and it is expected to be suitable for other disturbances that are less severe than this one, or, eventually, to be extended for more severe disturbances.

ACKNOWLEDGMENT

This research work has been carried out in the Centre for Research and Utilization of Renewable Energy (CVVOZE). Authors gratefully acknowledge financial support from the Ministry of Education, Youth and Sports of the Czech Republic under BUT specific research programme (project No. FEKT-S-20-6449).

REFERENCES

- [1] P. Kundur et al., "Definition and classification of power system stability IEEE/CIGRE joint task force on stability terms and definitions," in *IEEE Transactions on Power Systems*, vol. 19, no. 3, pp. 1387-1401, Aug. 2004, doi: 10.1109/TPWRS.2004.825981.
- [2] "Supporting Document for the Network Code on Load-Frequency Control and Reserves", June 2013. [Online]. Available: https://documents.acer.europa.eu/Official_documents/Acts_of_the_Agency/Annexes/ENTSO-E%E2%80%99s%20supporting%20document%20to%20the%20submitted%20Network%20Code%20on%20Load-Frequency%20Control%20and%20Reserves.pdf
- [3] "Continental Europe Synchronous Area Separation on 08 January 2021 – Final Report", July 2021. [Online]. Available: https://eepublicdownloads.azureedge.net/clean-documents/SOC%20documents/SOC%20Reports/entso-e_CESysSep_Final_Report_210715.pdf
- [4] "Local Grid Incident in Rogowiec (Poland) substation on 17 May 2021 – Final Report", March 2022. [Online]. Available: https://eepublicdownloads.entsoe.eu/clean-documents/news/2022/220318_Final_report_Rogowiec_incident.pdf
- [5] M. G. Ippolito, R. Musca, and G. Zizzo, "Analysis and Simulations of the Primary Frequency Control during a System Split in Continental Europe Power System," *Energies*, vol. 14, no. 5, p. 1456, Mar. 2021, doi: 10.3390/en14051456.
- [6] J. Koudelka, S. Macejko, P. Toman, T. Haba and K. Maslo, "Simplified Dynamic Model for Continental Europe Synchronous Area Separation," unpublished
- [7] IEEE Power System Dynamic Performance Committee, "Dynamic Models for Turbine-Governors in Power System Studies," IEEE PES-TR1, Jan 2013.
- [8] ENTSO-E Transparency Platform. <https://transparency.entsoe.eu/> (accessed on Feb. 25, 2022).

ABB v Brně

Lepší svět začíná s vámi

Jsme součástí globálního technologického lídra působícího v oblastech elektrotechniky, robotiky, automatizace a pohonů. Z Brna dodáváme rozváděče vysokého i nízkého napětí, modulární a digitální systémy, přístrojové transformátory a senzory. Tyto produkty míří do nejnáročnějších projektů ve více než 100 zemích světa. Najdete je mimo jiné v nejvyšší budově světa Burž Chalífa, v londýnském metru nebo v datovém centru Facebooku.



Přibližně 2000
zaměstnanců



Tržby 6,5 mld. Kč



Významné centrum
výzkumu a vývoje



Nejnáročnější
projekty ve 100
zemích světa



4 výrobní závody,
centrum digitálních
řešení, R&D a servis

Studentům a absolventům nabízíme:

- Placené brigády
- Odborné praxe
- Stáže
- Trainee program
- Vedení bakalářské nebo diplomové práce
- Hlavní pracovní poměr po ukončení studia

Kontaktujte naši náborářku:

Kristýna Podobová
kristyna.podobova@cz.abb.com
+420 739 552 428

Virtuální prohlídka



Naše jednotky

Rozváděče vysokého napětí

Výroba rozváděčů vysokého napětí se v našem závodě těší dlouhé tradici a pyšní se statusem největšího závodu svého druhu v Evropě. Co do počtu zaměstnanců, tak i plochy výroby, se jedná o největší jednotku v rámci brněnského závodu. Své produkty dodává do přibližně 100 zemí světa.

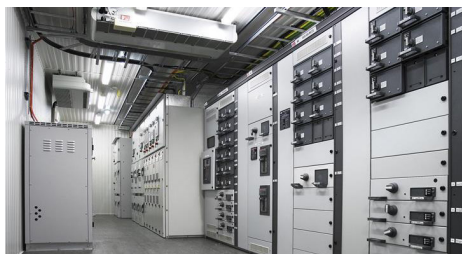


Rozváděče nízkého napětí

Rozváděče nízkého napětí fungují v režimu tzv. virtuálního závodu a sdílí svou kapacitu se závodem v polské Bielsko-Białe. Opět se jedná o jeden z největších závodů svého druhu v Evropě. Jeho produkty jsou dodávány do přibližně 50 zemí světa.

Přístrojové transformátory a senzory

Jednotka přístrojových transformátorů a senzorů je 2. největší v rámci brněnského závodu. Zároveň se jedná o největší závod svého druhu na celém světě. Vůbec první transformátor byl v závodě vyroben již v roce 1919 a jejich výroba je tak založena na více než stoletém know-how.

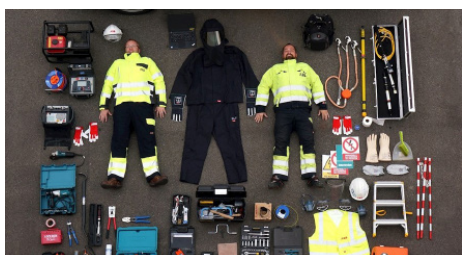
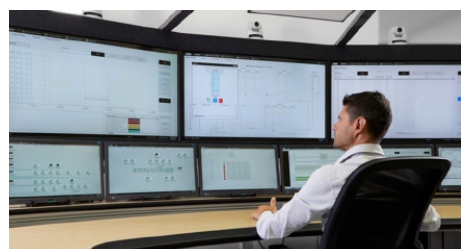


Modulární systémy

Přestože se jedná o mladou jednotku, má už za sebou několik významných milníků. Své modulární rozvodny, dodávané obvykle v kontejnerovém řešení, dodává do projektů napříč odvětvími. Nejvýznamnější z nich jsou data centra a projekty v oblasti těžby a distribuce ropy a zemního plynu.

Centrum digitálních řešení

Cílem jednotky Digital Solution Center je realizace inteligentních řešení v oblasti monitoringu, sběru a archivace dat a hlavně vzdáleného řízení distribuce energie. Zákazníkům nabízí řešení na míru, flexibilitu a vysokou přidanou hodnotu.



Servis přístrojů vysokého a nízkého napětí

Jednotka servisu spolupracuje se zákazníky v rámci oprav, údržby a vylepšování jejich zařízení po celou dobu jejich životního cyklu. U svých zákazníků v přibližně 100 zemích světa stráví technici asi 40 tisíc hodin ročně. Jednotka využívá nejmodernější nástroje včetně tréninkového centra pro zákazníky nebo rozšířené reality.

Technologické centrum

Technologické centrum se zabývá výzkumem a vývojem produktů. V rámci ABB se celosvětově jedná o velmi významnou výzkumnou jednotku. K dispozici má špičkově vybavenou laboratoř umožňující provádění nejrůznějších simulací a výrobu a testování prototypů.



Pose estimation and tracking for sign language recognition

D. Ficek¹ and M. Richter¹

¹Brno University of Technology, Czech Republic

E-mail: dominik.ficek@vut.cz, richter@vut.cz

Abstract— In this work we combine several state-of-the-art algorithms into a single pose tracking pipeline. We recognize motion, relative position and pose of human hands and face as the main information carriers as we separate the problem into three main tasks: hand and face detection, hand and face pose estimation and tracking hands and face in dynamic environment. We also propose to use measurements from pose estimation steps as a visual information indicator to solve dynamic tracking assignment problem.

Keywords— Hand and face detection, pose estimation, tracking, sign language recognition

1. INTRODUCTION

With the rise of available computational power and advances in computer vision research a universal solution to vision based sign language recognition becomes more realistic. In previous years some of the more traditional approaches were used such as using SIFT, HOG or handcrafted features [1, 2] in combination with SVM classifier. Some more recent approaches use automatic feature extraction using convolutional neural networks [3]. Some works propose to use 3D convolutional networks [4] to capture temporal features from the get go as the previously used methods relied on either Hidden Markov Models or recurrent neural networks to model temporal information. Another approach is to extract human pose [5] and use it as a feature vector for a classifier. Although the approach of pose estimation has not yielded as good results as 3D convolutional networks, we believe that this is the correct approach. One of the main arguments is that human pose as a feature is invariant to used sign language, as human hands are universal. Our vision is that an ideal sign language recognition system swaps its classification head to match interpreted language without the need to gather enough data to train the entire network in end-to-end fashion. In this work we also deviate from most of the solutions as we only estimate the pose of human hands and face. The main argument behind this decision is that the rough pose of human's arms is already represented in the relative position of hands and face.

2. DETECTION

Detecting interpreter's hands and faces is the first step of successful sign language recognition. We utilize recent advances in the field of object detection to solve this problem, namely using *YOLOv5* [6] and *EfficientDet* [7] convolutional neural network architectures.

As object detectors require substantial amount of data to generalize well, the choice of training data is crucial for success. Since the goal is to detect both human hands and faces in a single step, presence of both hand and face annotations in training data is required. These requirements are met by some human pose estimation datasets, however these datasets often don't include annotations of all humans in sample images therefore they are not suited for our needs. Apart from the mentioned datasets, to our knowledge the desired data is not publicly available. To solve this issue we train two individual detectors on hand detection dataset and face detection dataset, which we then use to cross annotate training and validation splits of used datasets with missing hand or face labels. As a hand detection dataset we use 100 DAYS OF HANDS [8], a large dataset originating from YouTube videos, containing large variety of tasks humans perform. As a face detection dataset we use WIDER FACE dataset [9], also a large scale dataset containing a wide variety of faces including difficult samples with unusual make-up, expression, occlusion or pose.

We trained several object detector models both from *YOLOv5* and *EfficientDet* families and evaluated them with mean average precision (mAP) metric on the original test splits without cross annotated labels. The evaluation results along with measured latencies are noted in Table I. From evaluation results we select *YOLOv5-S* and *YOLOv5-M* configurations as the most performant ones.

Table I: Evaluation of trained hand and face detectors

Architecture	mAP@0.3	mAP@0.5	mAP@0.7	CPU Latency ¹
<i>YOLOv5-S</i>	0.70	0.62	0.34	54.31 ms
<i>YOLOv5-M</i>	0.76	0.68	0.42	67.26 ms
<i>YOLOv5-L</i>	0.70	0.64	0.38	86.73 ms
<i>EfficientDet-D0</i>	0.58	0.49	0.25	113.24 ms
<i>EfficientDet-D1</i>	0.56	0.46	0.24	140.95 ms
<i>EfficientDet-D2</i>	0.55	0.46	0.22	154.61 ms

3. POSE ESTIMATION

In the field of pose estimation, regressing a confidence map has established itself as a go-to training method as its effectiveness has been confirmed by a number of works. Based on this knowledge we design an encoder-decoder style architecture consisting of light-weighted *EfficientNet* [10] feature extractor and three blocks of deconvolutional and normalization layers followed by a convolutional layer. This architecture, illustrated on Figure 1a, is the base of both our hand and face pose estimation models.

As the dataset used for training a face pose estimation we chose the WLFW dataset [11], a continuation of WIDER FACE dataset which contains various difficult samples, just as the original dataset, extended with 98 2D face keypoint annotations.

When selecting training data for the hand pose estimation model we have to take into account that many signs consist of difficult self occluded hand poses. This assumption severely limits the number of datasets that suite our cause as the vast majority of hand pose estimation datasets focus only on single hand pose estimation. Experiments also showed that in order to train highly performing hand pose estimation model, substantially large dataset with variety of hand poses is required. Another option taken into consideration is the possibility of training a 3D hand pose estimation model as this topic has seen an increasing focus from the research community, however the vast majority of 3D hand pose estimation datasets are either captured in predefined environment or are entirely synthetic. These constrains are a result of a difficult annotation process of depth information. As 2D hand pose estimation datasets do not suffer from these constrains we stick with 2D hand pose estimation to ensure real world generalization and overall robustness. In order to meet all set requirements we fuse several hand pose estimation datasets together, using samples from COCO WHOLE BODY dataset [12], HALPE dataset [13, 14], humanly annotated samples from [15] work by Simon et al. and synthetic RHD dataset [16] samples. The result is a database of hand pose samples marked as single hand samples or interacting hands samples, where each hand is annotated with 21 keypoints. In order to train the model, we modify the base structure to feature extractor followed by three parallel branches, first for estimating single hand pose, second for estimating interacting hand poses and the third one for binary classification consisting of convolutional layer and two dense layers. The designed hand pose estimation model is illustrated in Figure 1b.

We trained both the face and the hand pose estimation models with different feature extractor variants and evaluated keypoint regression with mean absolute error (MAE) and hand classification with area under receiver operating characteristic (ROC). Face keypoint estimation evaluation results are noted in Table II, based on these results we select architectures with *B0* and *B1* *EfficientNet* feature extractors as the most performing configurations. Results of hand pose estimation evaluation are noted in Table III. Note that measured MAE values are in pixels with respect to isolated hand or face examples scaled to 256×256 size.

Table II: Evaluation of trained face keypoint estimation models

Feature extractor	MAE	CPU Latency ¹
<i>EfficientNet-B0</i>	4.03	25.48 ms
<i>EfficientNet-B1</i>	3.87	35.40 ms
<i>EfficientNet-B2</i>	3.87	39.93 ms

¹CPU latency is measured on AMD Ryzen 5600X with 16 GB 3200 MHz memory with *Tensorflow 2.5*

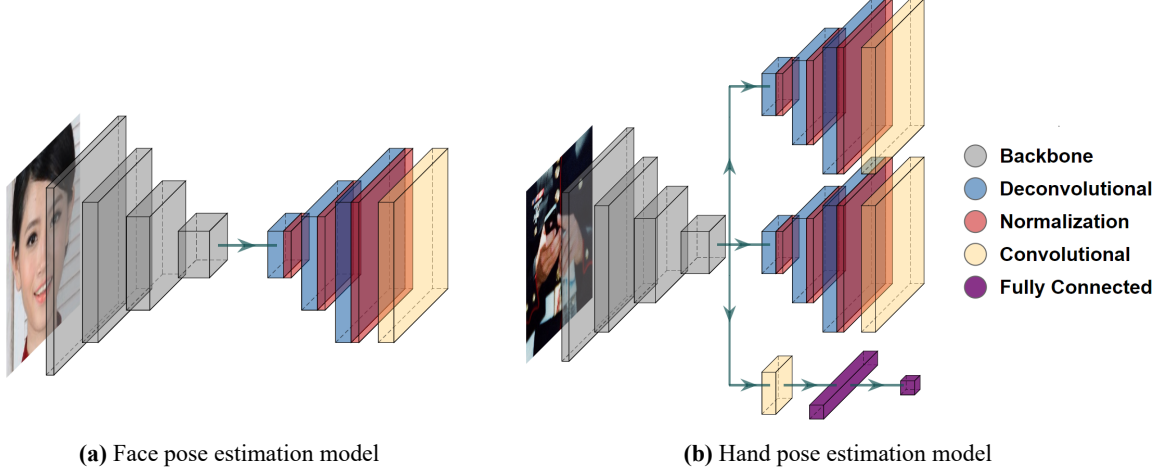


Figure 1: Designed pose estimation models

Table III: Evaluation of trained hand pose estimation models

Feature extractor	MAE _{single}	MAE _{interacting}	Area under ROC	CPU Latency ¹
<i>EfficientNet-B0</i>	13.96	16.40	0.96	32.16 ms
<i>EfficientNet-B1</i>	13.17	13.82	0.97	37.12 ms
<i>EfficientNet-B2</i>	13.25	13.79	0.97	43.44 ms
<i>EfficientNet-B3</i>	13.44	13.81	0.97	50.10 ms

4. TRACKING

The mentioned object detection and pose estimation models only operate with static image information without taking into consideration target’s movement with respect to time. As we are working in dynamic environment, it is advantageous to use the information measured in previous time steps.

We utilize the *Deep SORT* [17] algorithm introduced by Bewley et al. Authors proposed to use the Hungarian algorithm to solve the assignment problem and a linear Kalman filter to estimate state uncertainty. In their original work, authors used intersection over union (IOU) metric to construct assignment cost matrix which lead authors to limit the usage to frame-to-frame tracking, excluding target re-identification. In their follow-up work authors add visual information to the assignment cost matrix in the form of deep features and replaced IOU metric with cosine distance metric. These changes enabled the algorithm to re-identify objects that are missed for T_{lost} frames.

In our case we want to achieve frame-to-frame tracking with the ability to re-identify human hands and faces, given that we need to distinguish interpreter’s left and right hands from each other. The already mentioned approach of deep feature extraction does not seem suited for this case as deep features may bring more uncertainty to the solution and are to some degree redundant since we describe the visual information with pose estimation models. Based on these arguments, we propose to use squared keypoint distance to construct assignment cost matrix.

$$C_{ij} = \sum_{p=0}^P (x_p^i - x_p^j)^2 + (y_p^i - y_p^j)^2 \quad (1)$$

where C_{ij} is the assignment cost of i -th track with j -th detection and P is number of estimated keypoints.

5. CONCLUSION

In this work we present a complete solution for dynamic visual information processing pipeline with sign language recognition in mind as the primary use case. We trained several object detector models on a task of human hand and face detection and in similar fashion we trained several hand and face pose estimation

models. All trained models were evaluated with suited precision metrics and CPU latency measurement. We propose to use estimated hand or face keypoints as visual information descriptor for the purposes of dynamically tracking human hands and faces in video streams, which in contrast to using additional deep feature extractor does not introduce any significant additional latency to our system.

REFERENCES

- [1] Q. Yang, "Chinese sign language recognition based on video sequence appearance modeling", 2010 5th IEEE Conference on Industrial Electronics and Applications, 2010, pp. 1537-1542, [doi 10.1109/ICIEA.2010.5514688](https://doi.org/10.1109/ICIEA.2010.5514688).
- [2] S. Liwicki and M. Everingham, "Automatic recognition of fingerspelled words in British Sign Language", 2009 IEEE Computer Society Conference on Computer Vision and Pattern Recognition Workshops, 2009, pp. 50-57, [doi 10.1109/CVPRW.2009.5204291](https://doi.org/10.1109/CVPRW.2009.5204291).
- [3] P. Kishore, G. Rao, E. Kumar, M. Kumar and D. Kumar, "Selfie sign language recognition with convolutional neural networks", *International Journal of Intelligent Systems and Applications*, vol. 10, no. 10, p. 63, 2018, [doi 10.5815/ijisa.2018.10.07](https://doi.org/10.5815/ijisa.2018.10.07).
- [4] J. Huang, W. Zhou, H. Li and W. Li, "Sign Language Recognition using 3D convolutional neural networks", 2015 IEEE International Conference on Multimedia and Expo (ICME), 2015, pp. 1-6, [doi 10.1109/ICME.2015.7177428](https://doi.org/10.1109/ICME.2015.7177428).
- [5] S. Ko, J. Son, and H. Jung, "Sign language recognition with recurrent neural network using human keypoint detection", Proceedings of the 2018 conference on research in adaptive and convergent systems, 2018, pp. 326-328, [doi 10.1145/3264746.3264805](https://doi.org/10.1145/3264746.3264805).
- [6] G. Jocher et al., "ultralytics/yolov5: v3.1", 2020, [doi 10.5281/zenodo.4154370](https://doi.org/10.5281/zenodo.4154370).
- [7] M. Tan, R. Pang and Q. Le, "EfficientDet: Scalable and Efficient Object Detection", Proceedings of the IEEE/CVF conference on computer vision and pattern recognition, 2020, pp. 10781-10790, <https://arxiv.org/abs/1911.09070>.
- [8] D. Shan, J. Geng, M. Shu and F. Fouhey, "Understanding human hands in contact at internet scale", Proceedings of the IEEE/CVF conference on computer vision and pattern recognition, 2020, pp. 9869-9878, <https://arxiv.org/abs/2006.06669>.
- [9] S. Yang, P. Luo, C. Loy and X. Tang, "WIDER FACE: A Face Detection Benchmark", Proceedings of the IEEE conference on computer vision and pattern recognition, 2016, pp. 5525-5533, <https://arxiv.org/abs/1511.06523>.
- [10] M. Tan and Q. Le, "EfficientNet: Rethinking Model Scaling for Convolutional Neural Network", International conference on machine learning, PMLR, 2019, pp. 6105-6114, <https://arxiv.org/abs/1905.1194>.
- [11] W. Wu, C. Qian, S. Yang, Q. Wang, Y. Cai and Q. Zhou, "Look at Boundary: A Boundary-Aware Face Alignment Algorithm", Proceedings of the IEEE conference on computer vision and pattern recognition, 2018, pp. 2129-2138, <https://arxiv.org/abs/1805.10483v1>.
- [12] S. Jin, L. Xu, J. Xu, C. Wang, W. Liu, C. Qian, W. Ouyang and P. Luo, "Whole-Body Human Pose Estimation in the Wild", European Conference on Computer Vision. Springer, Cham, 2020, pp. 196-214, <https://arxiv.org/abs/2007.11858>.
- [13] S. Fang, S. Xie, W. Tai and C. Lu, "RMPE: Regional Multi-person Pose Estimation", Proceedings of the IEEE international conference on computer vision, 2017, pp. 2334-2343, <https://arxiv.org/abs/1612.00137>.
- [14] Y. Li, L. Xe, X. Liu, X. Huang, Y. Xu, S. Wang, H. Fang, Z. Ma, M. Chen and C. Lu, "PaStaNet: Toward Human Activity Knowledge Engine", Proceedings of the IEEE/CVF Conference on Computer Vision and Pattern Recognition, 2020, pp. 382-391, <https://arxiv.org/abs/2004.00945>.
- [15] T. Simon, H. Joo, I. Matthews and Y. Sheikh, "Hand Keypoint Detection in Single Images using Multiview Bootstrapping", Proceedings of the IEEE conference on Computer Vision and Pattern Recognition, 2017, pp. 1145-1153, <https://arxiv.org/abs/1704.07809>.
- [16] C. Zimmermann and T. Brox, "Learning to Estimate 3D Hand Pose from Single RGB Images", Proceedings of the IEEE international conference on computer vision, 2017, pp. 4903-4911, <https://arxiv.org/abs/1705.01389v3>.
- [17] N. Wojek, A. Bewley and D. Paulus, "Simple online and realtime tracking with a deep association metric", 2017 IEEE international conference on image processing (ICIP), 2017, pp. 3645-3649, [doi 10.1109/ICIP.2017.8296962](https://doi.org/10.1109/ICIP.2017.8296962).

Door Control Module

J. Šrámek¹, and O. Baštán²

¹Master's Degree Programme (2), Brno University of Technology, Czech Republic

² Supervisor, Brno University of Technology, Czech Republic

E-mail: xsrame02@vutbr.cz, ondrej.bastan@vut.cz

Abstract — This paper deals with the design and construction of a control module of a synchronous motor with permanent magnets (PMSM), developed as a reliable part of the security wall electronics for a space with a high density of people. The entire electronics (reliable, safe and information part) will be a product of the ordering company. This article deals with a brief formulation of the requirements and restrictions arising from the standards, the choice of control method and the design of schematic and hardware.

Keywords — Motor operated door, PMSM, motor, vector control, hardware design, control, embedded system

1. INTRODUCTION

Due to the risks that commonly occur in railway areas, there is a need to minimize these by creating a wall in an area with a high density of people, which will separate the hazardous area from the area in which the people move. Due to the number of people and the short period of opening the door wall, in addition to safety - which is the main matter, of course - high reliability is also necessary. Therefore, the system is divided into several parts, based on the function performed into an information, safe and reliable part.

Within this paper, a reliable (non-safe) part of the device will be designed and implemented, which main function is to control the door drive itself (PMSM with unknown parameters) with respect to meeting the standards applicable in electrical design in general, in the special environment in which the module shall operate, and in the field of motorized doors. The aim is to replace the version that was originally under consideration with an unsatisfactory interface and behavior, as it was not intended for spaces with such a passenger density.

2. MODULE REQUIREMENTS

The drive control module serves as the main peripheral of the reliable part, which is commanded by the superior system. Therefore, the goal is the most universal connection possible with the possibility of collecting data from externally connected contacts/sensors (not safely relevant) and possible control of devices with high current consumption, such as lighting and indication systems.

Due to the requirement for high availability of the device and modularity of the whole system, two RS-485 communication lines are used to connect to the master system, each one coming from the opposite direction. This ensures the possibility of removing a door module on one of the sides, without the need to put the entire system out of service and at the same time it increases reliability under normal condition.

Last but not least, the main door drive unit, which is a permanent magnet synchronous motor (PMSM), must be controlled, the parameters of which must also be measured first. The motor control consists in complying with the applicable limitations of impact forces in the event of an obstacle in the door space (resulting from the ČSN-EN 14752 standard) together with conflicting requirements for the maximum door closing time. The weight of the moving door is 75 kg and in a maximum time of 2.5 s, it must travel 2 m without exceeding the set force limits. Therefore, it is necessary to choose a suitable management method that can meet these requirements.

The whole device should be powered from two separate sources, 24V for the logical part and 48V for the power supply.

3. METHODS OF CONTROLLING PMSM

As already mentioned, the most important requirement, which also has a direct impact on the safety of the door system, is the requirement for the maximum obstacle forces that result from the relevant standard. This force also varies depending on the width of the space between the door wings - see Figure 1.

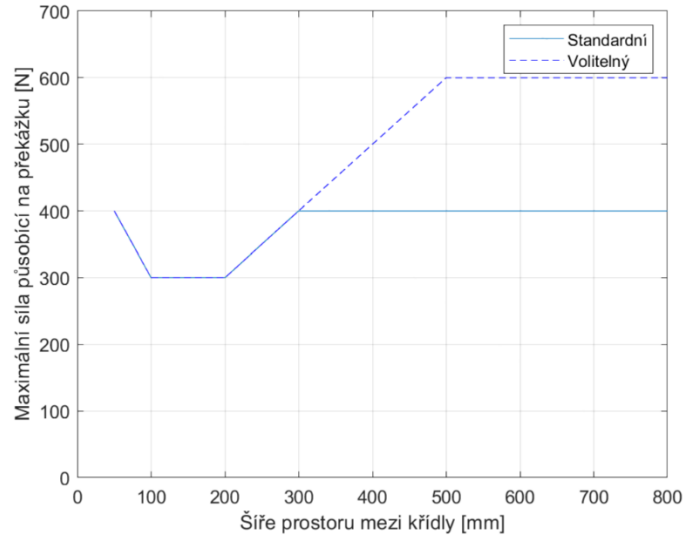


Figure 1: Max force (redrawn from norm)

For this reason, simple frequency converter-style PMSM control methods have been abandoned, as torque feedback is required. This requirement is perfectly met by the vector control - Field oriented control (FOC) - Space vector pulse width modulation (SVPWM). The basic block of the FOC algorithm is SVPWM logic, which generates control signals for switching transistors in a 3-phase bridge, to which the motor is connected. The current is sensed on two phases of the motor and passed to the Clark transform block, which converts the 3-phase stator coupled system into a rectangular system α, β also coupled to the stator. This is followed by a transformation into the rotor space via the Park transformation. The result is currents i_d and i_q . From these, the error from the set values is calculated, which is then passed to the individual PI-controllers (proportional integrative or proportional summative assuming a digital algorithm). The outputs of the controllers are individual voltages in the d and q axes. These are transformed from the rotor space to the stator coordinates α, β using the inverse Park transform. The resulting values are used as parameters of the SVPWM space vector. The whole algorithm is shown in Figure 2. [1],[2],[3]

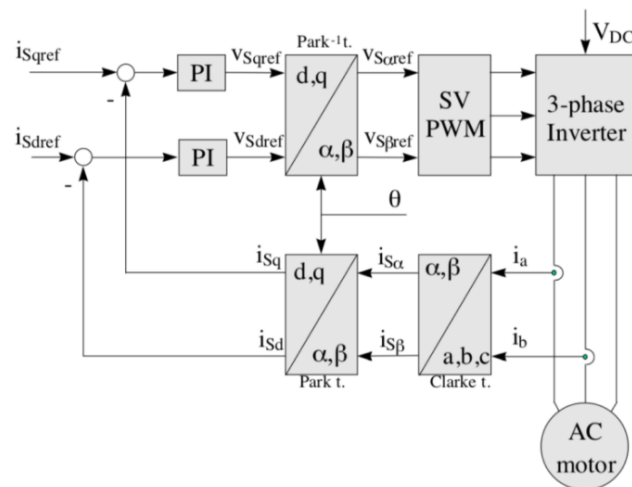


Figure 2: FOC with SVPWM [3]

As can be seen from the FOC block diagram of the PMSM control, in addition to the speed feedback, current feedback is also mandatory. It can be implemented in several ways with varying degrees of complexity and advantages. The most used methods are shown in the diagram on Figure 3. [4]

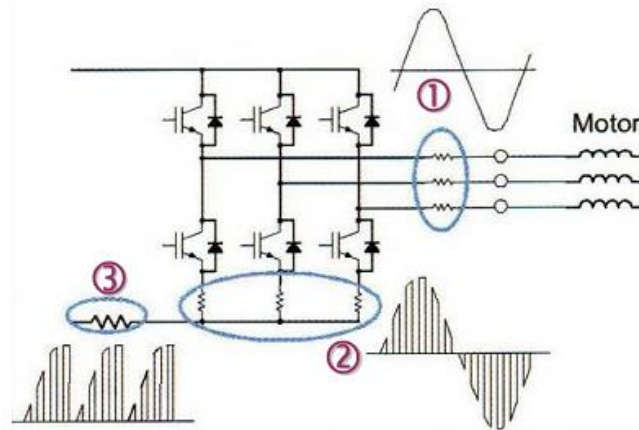


Figure 3: Current sensing principles [4]

The followings are the main methods:

1. Current measurement is realized directly on the motor phase terminals. This option is the simplest to implement in FW, but it brings negatives in the form of the need for amplifiers with a high common-mode voltage suppression factor and a high supply voltage range. Simultaneous sampling of currents is also required. [4]
2. The method of measuring in the low-side of the bridge reduces the previous disadvantages - there is no need for special amplifiers, as the matching voltage is close to zero. However, it is necessary to synchronize sampling with changes to the signal of SVPWM control algorithm. [4]
3. This method utilizes only one sensing resistor, which is common to all three phases of the bridge. It provides the biggest savings in hardware cost but is even more challenging in the signal reconstruction process in the firmware. The measured current then corresponds to the following waveforms (Figure 4). [4]

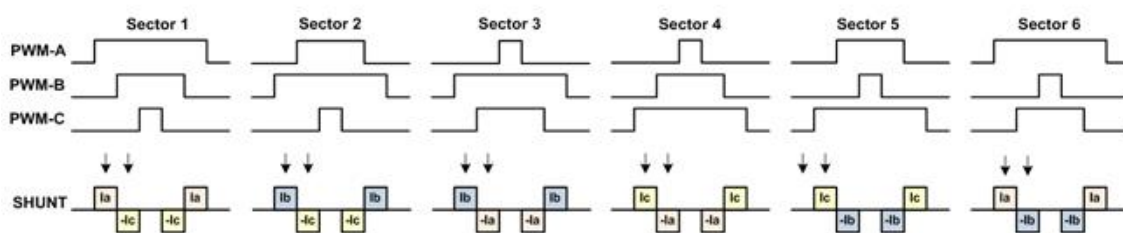


Figure 4: Current waveform [4]

It is therefore necessary to synchronize the ADC sampling with the signal changes and then calculate the currents.

After considering all the pros and cons of each method and researching the necessary components, the first discussed measurement method was chosen. However, after testing the first prototype, it was necessary to switch to method number 2 due to the loss of availability of adequate components.

4. DEVELOPMENT AND REALIZATION OF THE MODULE

Based on the requirements from the previous chapters, the module control system was designed and subsequently implemented. The microcontroller (MCU) STM32F334, from a series specializing in the

control of power converters, was chosen as the core of the system. The microcontroller is based on the ARM Cortex M3 core, running at a frequency of 72 MHz. In addition to the presence of standard peripherals corresponding to the class of this MCU, a specialized motor control timer (HRTIM) is important. [5]

The HRTIM timer provides a wide range of possible signal generation settings. It consists of a master timer and 5 secondary timers (A-E) with which it can interact using a set/reset crossbar. Each of the timers A-E then has two configurable outputs. When an error is detected, eg by a pin state change, a hardware shutdown can be performed. Other options also include connections to integrated peripherals such as ADCs, timers and comparators. Thanks to its variability and resolution, this is an ideal choice for the generating of the SVPWM signal. [5]

A user interface consisting of four control buttons and a segment display is also available for easy operation of the device during initial configuration or service intervention. If visualization or visual setting of parameters is required, a USB-C connector presenting a virtual serial line is available for communication with the configuration tool in the PC, which will be developed in the future. Due to the lack of pins on the main MCU, functions of the local user interface are performed by secondary MCU, which communicates via the SPI interface while securing the data by using a 32bit CRC.

The final solution is shown in Figure 5. Both previously mentioned RS-485 communication lines are implemented by add-on modules, which allows more flexible repair of the device in the event of a problem on the communication line. On the left side of the board, there are 5 power outputs capable of switching up to 10 A, while on the right, there are 8 inputs that are able to measure the voltage value from 0 V to approximately 65 V.

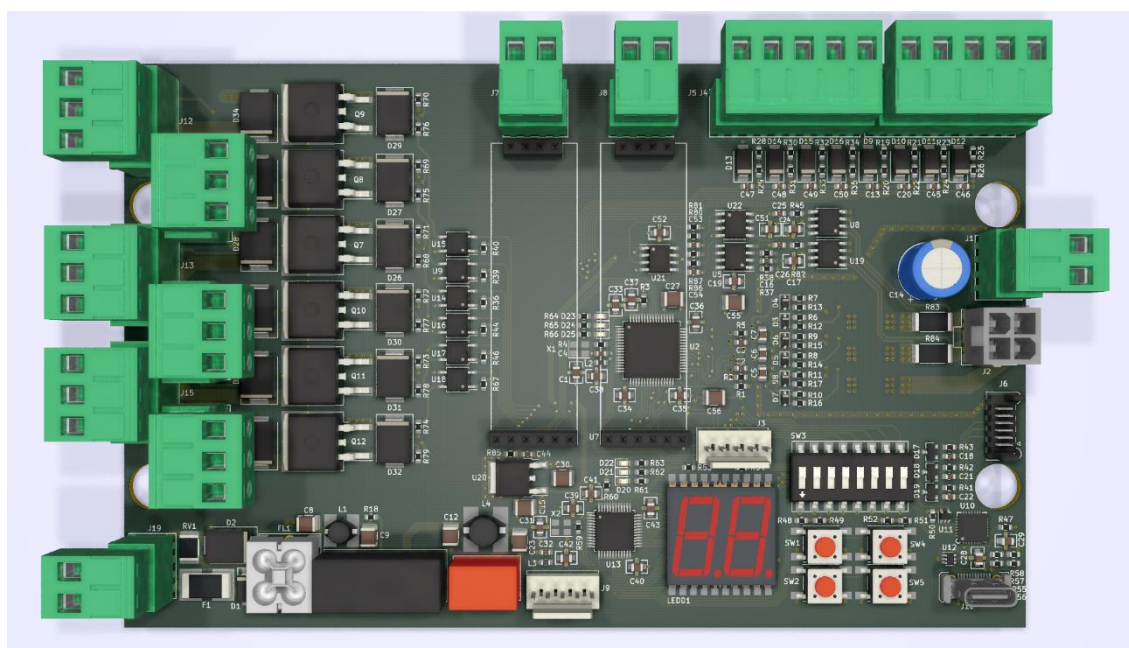


Figure 5: Render of proposed PCB

The firmware is developed in the Keil MDK-ARM program in combination with Visual Studio Code. The code itself is then written in C++ with the division of code into appropriate classes (modules) that meet the requirements of object design. The block diagram is shown in Figure 6.

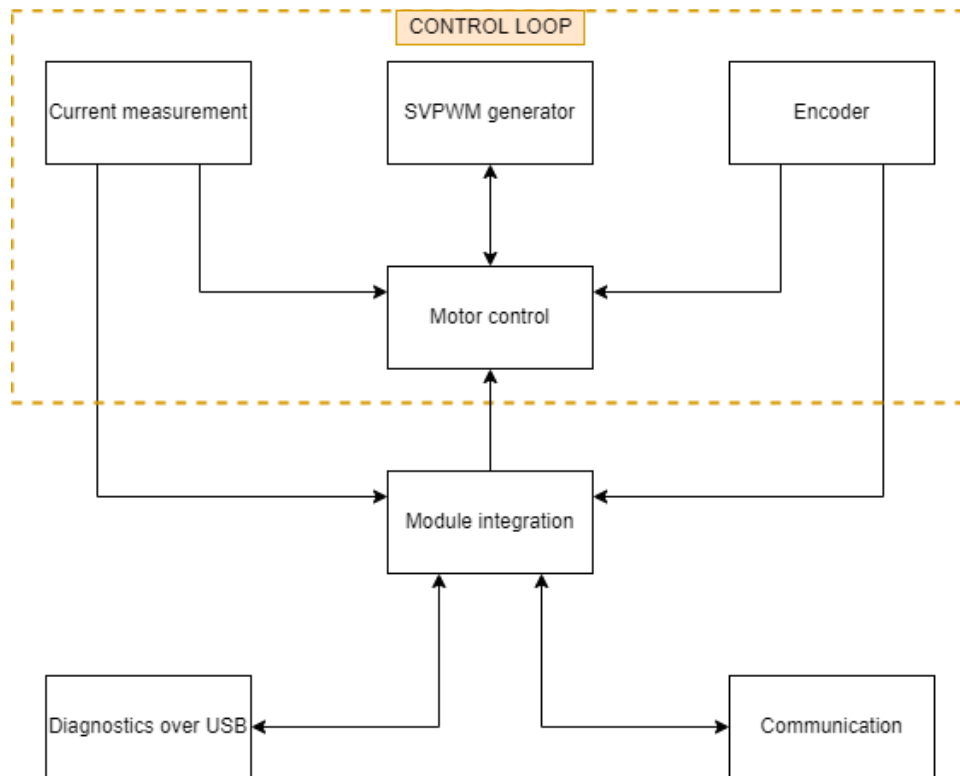


Figure 6: Firmware block diagram

The main part is the motor control module, which commands the SVPWM signal generator module based on the required parameters and feedback from the current measurement and the current rotor angle detected by the encoder. These commands are received by the main module, which integrates the control logic, received commands from the module serving the communication lines and at the same time it transmits diagnostic data or receives the configuration via the USB interface.

Completion of the firmware will be subject to further development.

5. CONCLUSION

In this article, we were introduced to the architecture of the control module for the door drive and the respective requirements. Then, the method used for the most important function block - PMSM control using space vector PWM - was selected and described in detail.

As part of the analysis of the method, research of the necessary techniques for obtaining feedback information in the control loop was performed, describing various ways of connection. After considering the pros and cons of each technique, a suitable connection was chosen.

Finally, the article deals with the selection of components and the implementation of the wiring diagram together with the subsequent realization of the PCB and a brief summary of the current state of the project. As part of further work, a controller will be designed and implemented in shown hardware.

ACKNOWLEDGMENT

This project is funded and being developed for company STARMON s.r.o.

The completion of this paper was also made possible by the grants:

No. FEKT-S-20-6205 - "Research in Automation, Cybernetics and Artificial Intelligence within Industry 4.0"

REFERENCES

- [1] MICROCHIP. Sensorless Field Oriented Control of a PMSM: AN1078 [online]. [quoted 2021-12-29] Available from: <http://ww1.microchip.com/downloads/en/AppNotes/01078B.pdf>

- [2] Space Vector PWM. Switchcraft [online]. [quoted 2021-12-29]. Available from:
<https://www.switchcraft.org/learning/2017/3/15/space-vector-pwm-intro>
- [3] Field Orientated Control of 3-Phase AC-Motors: BPRA073 [online]. Texas Instruments Europe, 1998 [quoted 2021-12-29]. Available from:
<https://www.ti.com/lit/an/bpra073/bpra073.pdf>
- [4] Precise Brushless Torque Control With Only 1 Shunt Resistor [online]. Ingenia Motion Control [quoted 2021-12-29]. Available from:
<https://www.roboticstomorrow.com/article/2012/11/precise-brushless-torque-control-with-only-1-shunt-resistor/99>
- [5] Reference manual - STM32F334xx advanced Arm®-based 32-bit MCUs: RM0364 [online]. ST Microelectronics [quoted 2021-12-29]. Available from:
https://www.st.com/resource/en/reference_manual/rm0364-stm32f334xx-advanced-armbased-32bit-mcus-stmicroelectronics.pdf

Modular control system

J. Novotný¹ and T. Beneš¹

¹Brno University of Technology, Czech Republic

E-mail: xnovotni@vut.cz, xbenes23@vut.cz

Abstract—This paper deals with the design, realization, and programming of a modular control system for general purposes. Intended uses in the application of micropower plant, where is needed low price. With an industrial control system it is easy to achieve a control result, but the costs are high. The embedded solution can be cheaper, but mass production and high knowledge of the system are required. Another difference is the size because the embedded solution can be like a black box, but PLC needs functionality more devices. The main goal was to design a modular control system and implement base program functionality for the next testing and development.

Keywords—modular control system, ARM, Cortex-M, CPU, industrial controller, Microchip, communication, RS485, CAN bus, micro hydro-power plant

1. INTRODUCTION

The project started with finding the best solution controlling for micro hydropower plant[2]. In the beginning, a simple control system was based on a compact solution without communication was created. This solution was perfect for this specific project, but when we tried to change the specification, there were problems. That is the reason why we have considered changing a simple compact solution to something more customizable.

The main idea of the work is to realize its own modular control system, which obtains all specific modules connected at one common internal communication bus. For example, the PLC doesn't implement a power analyzer inside of the control system. The own solution of control system can save the place and the cost when the mass production is introduced.

This paper deals with the design, realization, and programming of a modular control system for general purposes. The project is developed in cooperation with the company *ELZACO spol. s r.o.*

2. REQUIREMENTS FOR CONTROL SYSTEM

The control systems usually consist of a *CPU*, peripherals, and a display (optional). There is generally using digital inputs and outputs in industry. Analog inputs and outputs are less represented, but they are not unforgettable. Recently, there has been a trend to avoid analog peripherals and use communications, which saves a lot of cabling and increases accuracy. This is also linked to the decentralization of the peripherals. For micro-hydro power plants the presence of the power analyzer can be an advantage.

The modular control system has an advantage, that obtains one *CPU* module with program and communications (optional). Peripheral modules are separated and connected by an internal bus and are independent (can be replaced by a new module without uploading the user program). The display is optional and not necessary. There are two types of display solutions:

- **Separated display** from the control system, which is better for decentralization, and all cables are not routed from technology to panel with display.

- **All-in-one** solution is cheaper, but there is a requirement for cable routing from technology to the panel.

A separate display solution was chosen for easier organization in the switchboard of a possible combination.

Based on these parameters, the following modules were designed:

- **Processor unit** *normal* and *LITE*, which differ in the MCU and used peripherals.
- **DI module** obtains 22 galvanic isolated digital inputs configurable as *Sinking* or *Sourcing*.
- **DO module** obtains 20 galvanic isolated *Sourcing* digital outputs.
- **AIO module** obtains 8 galvanic isolated SW configurable analog input or outputs.
- **Power meter module** for measuring power network (usable for controlling in micro hydro power plant).
- **Display** with peripheral optimized for controlling small injection molding machine[3]:
 - **12 digital inputs, 12 digital outputs and 4 fast digital outputs** for PWM and stepper motor control.
 - **4 analog inputs and 4 thermocouples inputs.**
 - **Monochromatic graphical display, USB and RS485.**

All numbers of peripherals depend on the chosen case described in section 4.

3. COMMUNICATION PROTOCOL

The main issue is good communication between modules because the cycle of transferring all data between master and slaves modules defines the minimum cycle of the program (there is no reason to calculate with the same data). There are many *open-source* communication protocols, but they have some limitations. For the speed and the specific requirements it is better to implement own communication protocol based on available hardware. The control system consists of one master module and a few slaves modules, where data flow control by the master module is required. On the other side there are limitations by connector connecting master module with slaves modules which have only 8 (described in section 4) pins for a supply and communication. It follows from these parameters that it is best to use master-master communication, ie when each device has access to the bus and it also transmits on it. The access time is controlled by one master module, which allocates the transmission time to the other modules. Full duplex communication is not required as it meets the requirements and the treatment of full-duplex communication would be much more demanding.

The use of the *RS485* or *CAN bus* was considered. Both of this serial communication buses are based on *LVDS* (Low Voltage Differential Signal) and they use only one twisted pair for transfer signal. *RS485* was chosen, because it implements only physical layer of *ISO/OSI* model and is more flexible. *CAN bus* implement *data link* layer and not customizable, but implement more sophisticate data transferring. The own communication protocol was named as *MCSBUS* (*Modular Control System BUS*). Except for the common communication bus (*RS485*) *MCSBUS* implement definition of power supply (5 V) and signals for control modules (*Next device program*, *Device program enable*, *Return from slave* and *Return to master*) which is used for initialization modules (address assignment, detection of missing modules,...).

The data transferring model is similar to *open-source* communication protocol *MODBUS/RTU*, which is optimized for *16-bit* registers. *MCSBUS* was resigned to work with data objects and optimization for modular system. Transmitted data have this parts:

- **Address** for an addressing slave module. The address of the master module is 1, slave modules addresses are in the range of 2..255, and address 0 is reserved for *broadcast* messages from the master device (all slave devices will receive at the same time).
- **Control** obtaining information e.g. read or write message type.
- **ID** usable for addressing data objects.
- **Length** of transferred object data.
- **Data object** with required information.
- **CRC** as data integrity check calculated from all the data above.

Inner modules communication is based on *RS485*, which have some limitation. In connector of MCSBUS there are still 2 pins free and they can be used for *CAN bus*. The next generation will use *CAN bus* in these free pins for faster cyclic communication, because *CAN bus* is deterministic and usable for events (*CAN bus* using multi-master bus connection and racing in the arbitration field of the message).

For example cyclic communication processor unit with digital outputs module and digital inputs module. The communication with *RS485* needs to initiate start communication of every module, which means, that the master module sends a request and the slave module sends a response. The time of executing this cyclic communication is about 1 ms. With the *CAN bus* we can send one request message from the master module and all slave devices send a response (there is some intelligence of *CAN bus* because all devices send responses at the same time). This mechanism is used in *CANOpen* communication protocol[1].

4. DESIGN

There are various cases solutions on the market for modular solutions. The *ICS* variant from the manufacturer *Phoenix Contact* was chosen, which offers various widths, DIN rail mounting, inter-bus connectors for mounting on DIN rail, and other accessories. This system has an 8-pin internal bus connector and it offer parallel and serial connections (the connection between modules 1 and 2, 2 and 3,...). All modules are wanted to design into one size of cases (one module width) and this chosen case allows adding up to 6 connectors with 4 connections. These case connectors are designed as tool-free *Push-in*. Figure 2a is showing assembled PCBs of power meter with connectors. Figure 2b shows the modular system cases.

5. ELECTRONIC DESIGN

The main point of electronics is *MCU*, which is chosen from SAM family (Microchip) based on 32-bit ARM cortex-M *CPU*. For better cooperation (there are 6 different modules) it is better to chose similar *MCUs* (same code library). This is not possible for all modules, because some module need more performances (often declared in *MIPS*) than other. For modules, which need more performances *ATSAME70* was chosen and as less performances *MCU ATSAMC20* was chosen. The figure 1 is showing block schematic for processor unit (1a) and digital inputs (1b) modules.

6. PROGRAM

A program was written in *Microchip studio* with using of *C* programming language. *FreeRTOS* real-time OS (RTOS) was used for better using separate parts of functionality, which offers programmer use of tasks (with priority and round-robin scheduling), multiplexers (semaphores), queues, timers, and a lot of other functionalities. The main pros can be separate timing of inner functionality of control system tasks in contrast to user tasks (user functionality can be written or included as a separated file).

The best way to do programming of this control system is to develop own programming app with implementations of standards programming languages defined by standard *EN 61131-3*, but this is not easy to implement for one person developer team (better to buy PLC). Another option is to use ready-made solutions implementing *EN 61131-3*. One solution is *OpenPLC*, which runs on *Raspberry Pi*. Our own

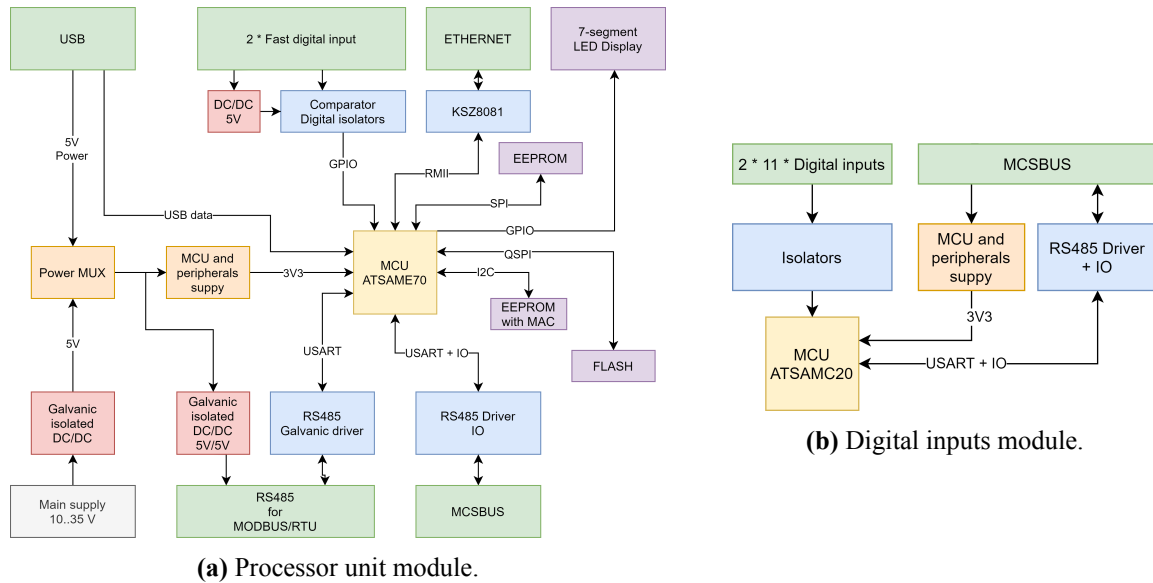


Figure 1: The block schematic of the modules modular control system.

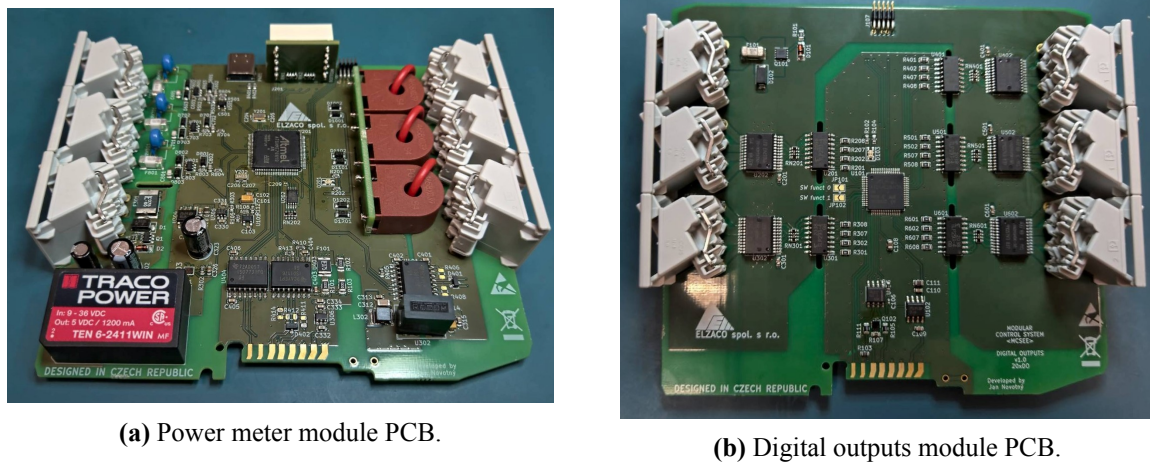


Figure 2: Assembled PCB and ICS case system.

control system is not needed to verify the functionality and the possibility of using it, and it is developed as a closed platform. However, in the future, this would only mean redesigning the processor unit, which is the biggest advantage of a modular control system.

7. CONCLUSION

I managed to design, revive and test our own modular control system for a general-purpose. The modular control system is functional and now is still being developed and functionality is being added. When somebody wants to use this control system, advance knowledge of programming in C language and *FreeRTOS* is needed, but this problem has been known from the beginning of the developing and it does not disadvantage in mass production of small hydropower plants (only one person writes and uploads the program, which is used for the lifetime of the product). In the next generations of my modular control system, shortcomings should be ironed out and additional functionality added if the control system proves to have a future.

The use of this system is not limited only as a control system, but if the control application is reprogrammed, it can be used as a remote IO over communication.

ACKNOWLEDGMENT

I would like to thank the company **ELZACO spol. s r.o.**, which offered me the background for the development and material support.

The completion of this paper was made possible by the grants:

No. FEKT-S-20-6205 - "Research in Automation, Cybernetics and Artificial Intelligence within Industry 4.0";

REFERENCES

- [1] CiA. can-cia.org [online]. *Internal documentation organization CiA* [cit. 1.2.2022] URL: <<https://www.can-cia.org/can-knowledge/>>
- [2] NOVOTNÝ, Jan. *Řídicí systém pro zařízení využívající obnovitelné zdroje energie*. Vysoké učení technické v Brně. Fakulta elektrotechniky a komunikačních technologií, 2020.
- [3] NOVOTNÝ, Jan. In: *Proceedings I of the 27st Conference STUDENT EEICT 2021: General papers* [online]. Vysoké učení technické v Brně, Fakulta elektrotechniky a komunikačních technologií, s. 213-217 [cit. 2022-03-11]. ISBN 978-80-214-5942-7.

Photoresist exposure via LCD panel

M. Fiala¹

¹Brno University of Technology, Czech Republic

E-mail: xfiala57@vut.cz

Abstract—This paper focuses on development and testing of liquid crystal display exposure device using photoresist for PCB manufacturing. The device is controlled wirelessly via dedicated application on various platforms. Most of the device was 3D printed and motif for exposure can be uploaded to the device in Gerber format, which is used all over the world as manufacturing standard format. The paper also contains CAD model, simulation, exposure results and overview of control application.

Keywords—Photoresist, liquid-crystal display, exposure, printed circuit board, ultraviolet rays, diode

1. INTRODUCTION

Nowadays, with the price of circuit boards reaching record lows, especially from Chinese manufacturers, it no longer makes much sense to try to design a home-use device that can compete with the process quality and price of professional boards. However, the big disadvantage of professional production is the delivery time for prototyping, which generally takes weeks to deliver and usually only one sample cannot be ordered. This paper aims to address this shortcoming in particular by designing a device on which it would be possible to create two-layer PCBs to verify the function of the prototype in PCB design.

The way to achieve this is to combine two processes that are divided into two steps in conventional production. The first is the creation of an exposure motif, usually realized on a thin transparent film, and then the exposure of the photoresist through this template. By using an LCD panel on which the desired motif can be displayed, the two processes can be combined into a single step, during which the motif on the display is matched to the substrate and photoresist is exposed.

2. PRINCIPE OF LIQUID CRYSTAL DISPLAY

In the state where no current flows through the electrodes and no voltage is present, the crystals are arranged in a helix that rotates the polarized light 90°. The light thus has the correct polarization for passing through the output polarization filter at the output, and the subpixel appears to be ON (See Figure 1).

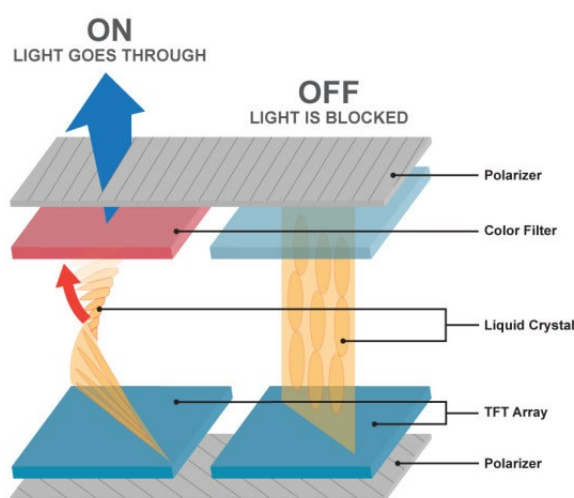


Figure 1: Subpixel structure in TFT LCD technology [1]

The moment we apply an increasing voltage to the electrodes and a current starts to pass between them, the crystals start to rotate and lose their helical shape. Passing light is rotated by an increasingly smaller angle, causing more light to be absorbed by the output polarizing filter. In a situation where the helix is completely rotated, the light is not affected by the crystals and the vast majority is absorbed into the output polarizing filter.

3. DESIGN AND SIMULATION

Body of the device was designed to be 3D printable on basic size 3D printer including the reflector piece. The device uses powerful 30 W COB led diode. The light from this diode is equally concentrated on the LCD layer with custom designed reflector. The LCD layer is driven by cheap Chinese tablet from which was the LCD panel salvaged. The Raspberry Pi Zero inside the device is responsible for power management and communication between user control app and android tablet (See Figure 2).

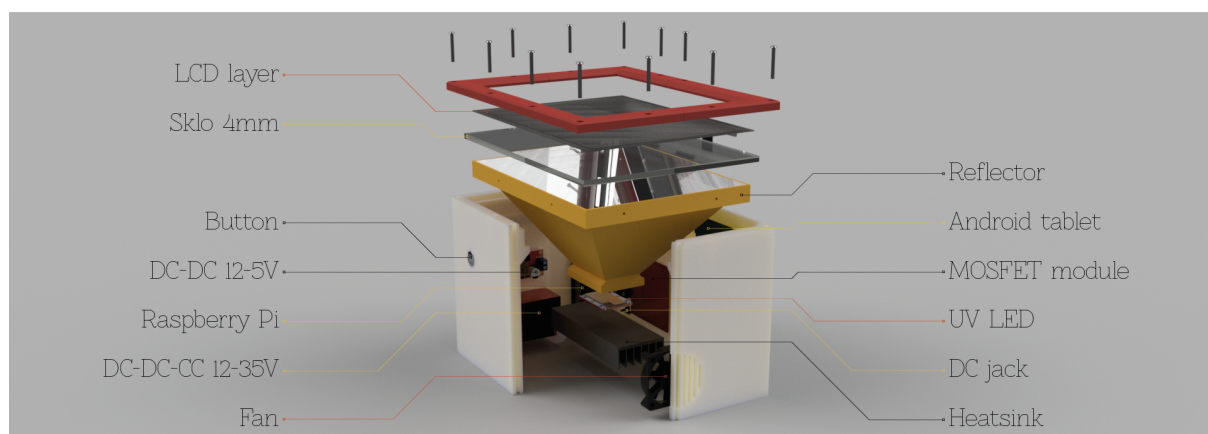


Figure 2: 3D CAD model of the device with individual components

4. REFLECTOR

By using only one point source of UV radiation, there was a need to direct the rays towards the LCD layer so that they would fall as perpendicularly as possible and their distribution would be as homogeneous as possible. Professional light simulation software LightningTrace® ZEMAX OpticStudio® was used for simulation of 3D CAD model and based on the results adequately modified.

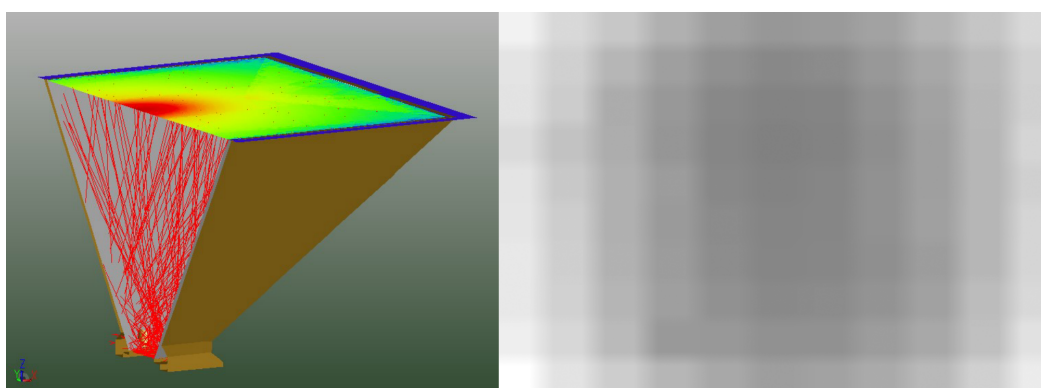


Figure 3: Light simulation of reflector with distribution of the incoming radiation in form of heat map and generated correction mask [2]

As can be seen from the simulation (See Figure 3), the distribution of incoming radiation on the LCD layer is far from homogeneous. Therefore, the values of the intensity of radiation passing through the LCD layer were measured and a correction mask was generated based on these values. This mask compensates for the so-called hot center in the middle of the display by darkening the corresponding pixels.

4.1. Power management

The main voltage source was chosen to be a network adapter with a DC Jack connector capable of supplying up to 6 A at 12 V DC to the device. This adapter was chosen based on the consumption of the individual components of the device. A voltage of 12 V is suitable because it is about half the voltage for conversion to 30 V and about twice the voltage for conversion to 5 V. The 12 V can also be used to directly power components such as fans and LED backlights.

4.2. Communication

The communication between the user application and the device is realized via Wi-Fi. The Raspberry Pi microcomputer is hosting a Wi-Fi AP to which the control application and Android tablet are connected. From the application, HTTP requests and files are sent to two HTTP servers that host the Raspberry and the android tablet to allow communication between them (See Figure 4). The optocoupler is used to turn on the Android tablet after successfully turning on the script on the Raspberry Pi.

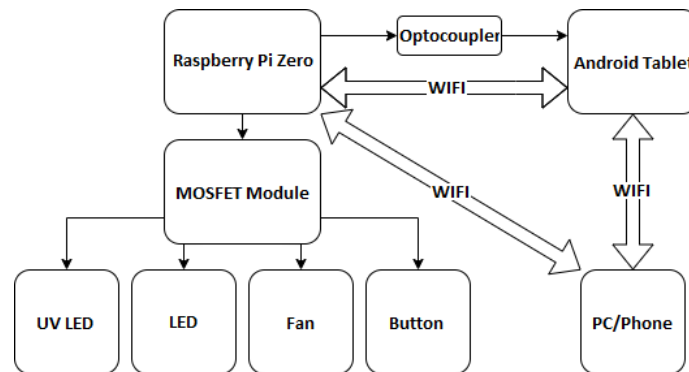


Figure 4: Connection diagram between individual components of the device

5. SOFTWARE SOLUTION

In order to control the device using this app (See Figure 5), your computer or phone needs to be connected to the device via Wi-Fi. If this condition is met, it is possible to send requests to both HTTP servers on the device. The control application contains three tabs in the bottom bar that the user can easily switch between. The first tab is used to work with the motif on the display and to send the Gerber file to the device, which will display the motif immediately. The navigation buttons are used to move the image around the display. The user can adjust the step of the movement in pixels and zoom in/out in units of per mil with the movable slider. Rotation or lock of the motif was not implemented in the prototype. The process of exposition is activated by pressing dedicated button on the device.



Figure 5: Custom Android control app

6. MEASUREMENTS AND TESTING

As you can see in the picture (See Figure 6), the smallest possible conductive path width that can be reliably reproduced is 0.254 mm. The smallest passive component that can be exposed on the device is 0603. As far as active components are concerned, the device managed to expose good quality for footprints SOP, ESOP, SOT, PLCC and DIP. An interesting finding was the resulting quality of the BGA package, which was almost perfect. Unfortunately, due to the limited thickness of the conductive paths, it could not be contacted.

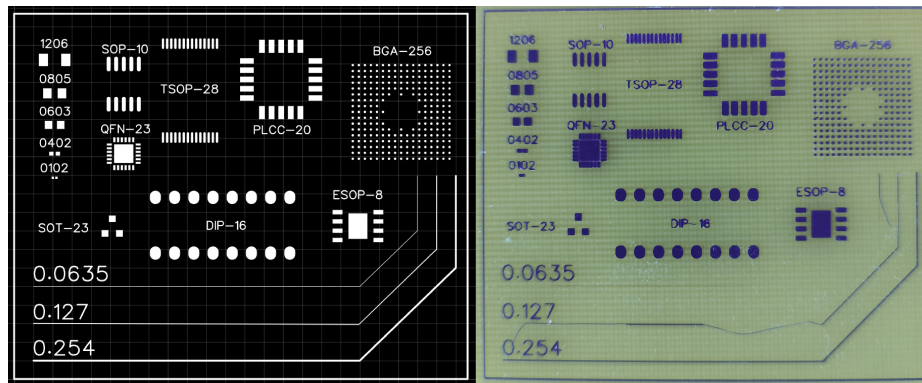


Figure 6: Exposed and developed results for some footprint types

7. CONCLUSION

The result of this work is a working prototype of a device on which it is possible to expose two-layer printed circuit boards after manual alignment of the layers. The quality of the exposed patterns was evaluated in Section 6. At the same time, a software platform has been developed for the device which is modular and can be extended in the future. The platform includes an application, through which the device can be controlled wirelessly from a PC and a mobile device, as well as an application for displaying Gerber files in high resolution on the screen.

ACKNOWLEDGMENT

I would like to thank my bachelor thesis supervisor doc. Ing. Petr Vyrubal, Ph.D. for his professional guidance, consultation, patience and helpful suggestions. I would also like to thank Markus Fußenegger for providing and modifying part of the used software.

REFERENCES

- [1] CROSS, Jason. Digital Displays Explained: LCD: Twisted Nematic (TN or TN-Film) [online]. In: . 18 Mar 2012, s. 3 [cit. 2022-02-20]. Available at: <https://www.pcworld.com/article/251988/digital-displays-explained.html>
- [2] Grayscale-Generator: Tailored Grayscale Image Generator. GitHub: Where the world builds software [online]. [cit. 2021-5-30]. Available at: <https://github.com/Garage-Science/Grayscale-Generator>

SUPER HOT CHIPS



ASICentrum

A COMPANY OF THE **SWATCH GROUP**

Naše srdce planou pro navrhování čipů!

Hledáme další nadšence, co by
rozšířili naše řady!

★ ★ ★ **JOIN US!** ★ ★ ★

ASICENTRUM PRAHA / BRNO

WE LOVE TO **DESIGN** THEM.

ČIPY KTERÉ JINDE NENAJDETE

- Navrhujeme ULTRA LOW POWER integrované obvody
- Naše čipy mají vždy něco jedinečného, co konkurence neumí
- Bluetooth, RFID NFC, RFID UHF, Sensor hubs, Optical Sensors
- Na tom všem se můžete podílet

ČESKÁ FIRMA SE ŠVÝCARSKÝM ZÁZEMÍM

- ASICentrum je středně velká firma s rodinnou atmosférou
- Jsou zde špičkoví odborníci, od kterých se můžete hodně naučit
- Švýcarské zázemí díky mateřské firmě EM Microelectronic
- Máme vlastní továrnu na výrobu integrovaných obvodů

PŘIJĎ NAVRHOVAT ČIPY

- Nabízíme brigády, diplomky a zaměstnání
- Potřebujeme návrháře, verifikátory i softwarové inženýry
- Studenty naučíme moderní techniky návrhu integrovaných obvodů
- Zaměstnanci získají obrovské zkušenosti s celým procesem vývoje čipů
- Skvělé platové ohodnocení a benefity
- Co očekáváme – zájem, chuť do práce a nezbytné základní znalosti ze školy

HLEDÁ SE KOLEGA HOMO TECHNICUS

- Digital IC Designer
- Digital IC Verification Engineer
- Embedded Software Engineer
- Digital Backend Engineer

hr@asicentrum.cz

www.hotchips.cz



em microelectronic

A COMPANY OF THE **SWATCH GROUP**

SCRATCH TESTER

P. Brandejs¹, J. Skácel²

¹ Author, Master Degree Programme at FEEC, Brno University of Technology, Czechia

² Supervisor, Doctoral Degree Programme at FEEC, Brno University of Technology, Czechia

E-mail: xbrand08@vutbr.cz, Josef.Skacel@vutbr.cz

Abstract—This paper deals with design and prototype build of a scratch tester with the focus to the ability of testing film adhesion. Scratch testing and the reasoning behind building a scratch tester is briefly discussed before focusing on the individual design aspects and decisions behind them. At the end, the concept is put through some initial testing.

Keywords—Scratch tester, Surface adhesion, Material hardness

1. INTRODUCTION

During a scratch test, a sharp stylus is moved across surface of an object, while defined amount of (normal) force is applied to its axis. This generates a scratch and a (tangential) force opposing the movement. These forces can be analyzed to find out various properties of the test subject, like hardness of the surface and adhesion of any films applied to the test subject. When analyzing the surface adhesion of a film, critical force is a necessary metric for calculations. This is the force, at which film is stripped away from the surface. For easier critical force analysis, scratch tests are often conducted with increasing normal force. For this reason, a scratch tester built for measurement of surface adhesion needs to be equipped with a force actuator able of gradual force increase. Sensors measuring both normal and tangential forces are needed. Moving in 2 axes can also be helpful, as it means the possibility of differently shaped tests or multiple tests in quick succession. [1]

Most available scratch testers are simple devices made for analysis of surface hardness and can not produce gradually increasing force, let alone any data during the test. Any devices able of doing so are a hardly justifiable expense to the labs, as they are single purpose and very expensive. The cost for devices which can measure and gradually increase the normal force starts at 300 000 CZK with the average around 2 000 000 CZK. They are usually equipped with state-of-the-art force actuators, precise force sensors and their own microscopes. This, together with relatively low production volumes, results in the very high price. However, for a lab already equipped with a microscope, its inclusion is unnecessary, and so is the precision. Even for the most challenging tests, accuracy of 5 mN or 0.5 g of force should be enough. Measuring with this precision should be easily possible with common load cells. Their output can then be used as feedback for the force actuator, greatly reducing the need for its linearity. A similar device can therefore be made at a very different price. This paper describes design and making of a device for scratch testing with gradually increasing force, able of reporting the forces induced. While this device will not be as accurate as its more expensive counterparts, the cost is expected to be under 10 000 CZK in materials. [1]

2. MECHANICAL PART

Precise force application is usually being done by displacing an elastic element. Most often, pneumatic cylinders are used, where the air acts as a spring. This solution is great, but costly and would probably drain most of the budget by itself. And since the actuator does not need to be exactly linear, a much cheaper system based on steel springs could be used. Helical compression springs were found to be the most readily available and convenient for the packaging, while providing linear enough characteristics. Two springs will be used, one to apply the force and a second one to carry the weight of the moving mass and preload the first spring. The springs were chosen to have similar enough inner diameter and appropriate stiffness, where enough force could be applied while maintaining high enough movement range. 50 N of maximum force was required with at least 20 mm of travel. The force actuator assembly

can be seen on the image bellow.

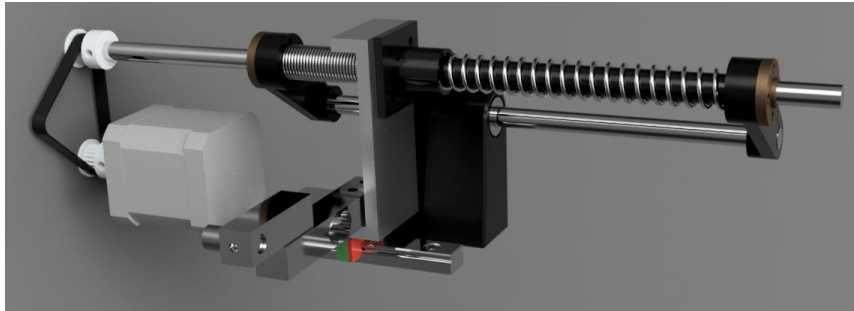


Figure 1: Force actuator

Linear motion needs to be applied to the springs to generate force. The implementation for this also needs to be cheap and simple. High movement resolution can help with reaction to the force sensor feedback. Similarly to the rest of the linear movement devices, parts regularly found in 3D printers were used. This device is similar to them in concept and the production numbers of 3D printers makes these parts cheap and readily available. A NEMA 17 stepper motor was used to drive a T8x2 leadscrew, which turns the rotational into linear motion. This combination should provide enough force to overcome the springs.

The leadscrew was then driven through the springs, compressing them between 2 nuts. This made for better packaging and also preloaded the nuts, so backlash typical for trapezoidal screws was effectively eliminated. Springs tend to twist under compression, which would lead to them dragging on the screw. To solve this problem, 3D printed tube was placed between the screw and springs for guidance. This tube was made from carbon fiber induced filament for lower friction. To allow smooth movement of the springs over the surface, it was grinded, polished, and lubricated. A linear rod was then used to guide the nuts and prevent them from rotating under the tension.

The scratching stylus is carried by an MGN12 linear rail and an aluminum part, to which it is connected via a load cell. The stylus needs to be held firmly to the horizontal forces, but any friction in the vertical direction would make precise force application difficult. The initial spring compression would be used up to overcome friction, which would introduce backlash. As this is a very critical aspect, a quality HIWIN linear rail with light preload was used. [2]

The rest of the linear movement system was made in a similar fashion. Lower quality linear rails were used to guide the axes. To drive the axes, NEMA 17 steppers and T8 trapezoidal screws with higher pitched thread were used to ensure higher movement speed. The torque from the motors was connected to the leadscrews through a closed loop belts, decoupling vibrations in the motor from the rest of the chassis. This also helps with packaging. The motor now does not need to be mounted in line with the screw, shortening overall length and width of the device. This resulted in quite small overall package and efficient use of available space.

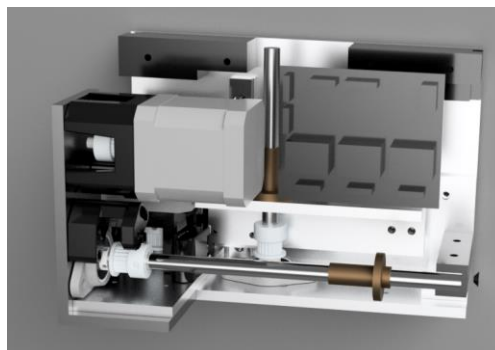


Figure 2: Packaging

The device was designed around the use of aluminum extrusions for parts, which would experience higher forces, with the rest being 3D printed from PETG for longer lifetime. 3D printing was also used in aiding the design process for aluminum parts with the concept of rapid prototyping. So far, mostly 3D printed prototype was built for testing. Plastic parts will be gradually converted to aluminum. The prototype and render of the finished device can be seen on the images below.



Figure 3: Finished device

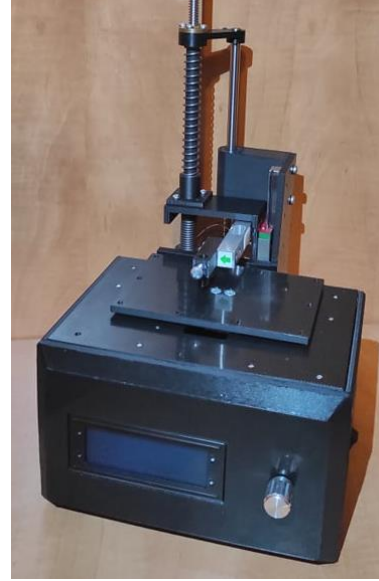


Figure 4: Current prototype

3. ELECTRONICS

The main role of the electronics is to provide control of the motors and readings from the sensors. A block diagram can be seen below.

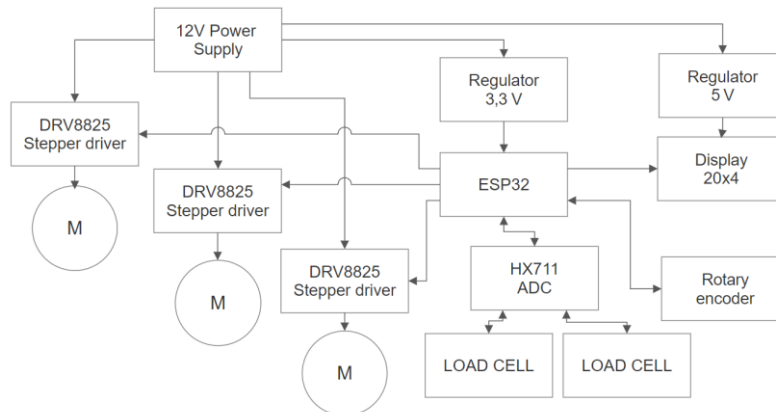


Figure 5: Device electronic block diagram

The brain of the device is ESP32 microcontroller. It is cheap, flexible, powerful enough to drive motors at high speeds and its ports are plentiful. It also enables wi-fi connectivity and a possibility of making this an IoT device. The motors will be driven via DRV8825 stepper drivers, which are again often used in 3D printers and therefore relatively cheap. With 32 microsteps, it is possible to achieve decent speeds and precisions without the motors being too loud.

For sensing the forces during scratch tests, ordinary load cells usually employed in weight scales were used. They were found to be convenient for instrument mounting and accurate enough to the point where anything better is unnecessary. The cells themselves have almost perfect rejection of perpendicular forces and outstanding linearity. A 24-bit analog to digital converter with a preamplifier was used to convert the change in resistance to voltage. This combination provides unreasonably high resolution. Most of it is lost in electrical noise and vibration, but the module was found to be accurate within ± 2 mN in initial testing. This combination is surprisingly effective for its price. [3]



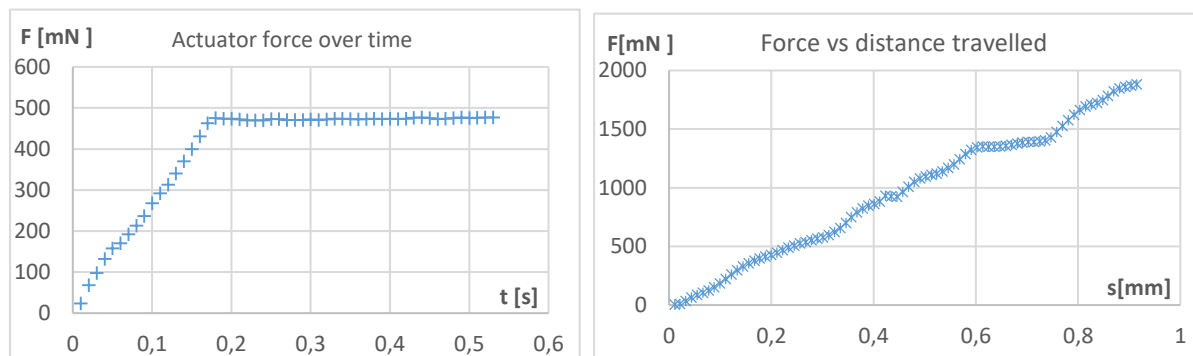
Figure 6: Load cell

For interacting with the user, a 20x4 character display and rotary encoder is used. This solution is intuitive, easy to code for and enables standalone operation with the data being stored to a micro-SD card. However, most of the communication is expected to be done through a PC, to which the device will be connected via a USB cable. Basic GCODE commands with some extensions will be used for the control. Data from the sensors with corresponding positions will be sent via the USB connection and stored in a CSV format for further analysis in MS Excel or other programs.

As for the power delivery, 12V power supply of sufficient amperage needs to be used because of the stepper motor drivers, which work best with higher voltage. Rest of the electronics work at 3,3 or 5 V with low current draw on both of these rails. For that reason, simple, low power linear regulators could be used to step the voltage down.

The software then needs to handle everything mentioned above and will be written in C++ with ESP-IDF functions. The LCD and sensors can be easily handled by already available libraries, but effective implementation of stepper driver handling was not to be found on the internet. This function will be made specifically for this device, which also enables better handling of the force actuator feedback. So far, a simple control of actuator stepper and force sensor readout was written with the data being sent via UART and received by Excel Data streamer.

This enables initial testing of individual parts, viability of the concept and optimization of the force actuator. In the first test, a displacement vs force graph was created. At higher forces, some binding could be seen, caused by deformation of the plastic parts, but at lower forces, the characteristics remained linear enough to try application of defined force. This can be seen on the second graph, where force of 450 mN was set. The target was overshoot to 480 mN, but this can be compensated for.



4. CONCLUSION

In this paper, the process of designing a scratch based on requirements laid in introduction was presented. The device fit the relatively tight budget and is pretty compact. A mostly 3D printed prototype was built to test the concept, and few initial tests were conducted to see whether it is plausible. It was found that further optimization is needed, but concept itself is fine and will be greatly improved with the introduction of aluminum parts in the near future. This build therefore has the possibility of creating a device with similar functionality to a much more expensive instruments and enable one microelectronic laboratory to possess an instrument they otherwise would not be able to justify.

REFERENCES

- [1] *Scratch Test*. [online]. 2015 [cit. 2022-01-03]. Available at: http://ksm.fsv.cvut.cz/~nemecek/teaching/dmpo/clanky/2015/Kadlicek_zav%20prace_Scratch%20test.pdf
- [2] *Linear Guideways*. [online]. [cit. 2022-01-03]. Available at: <http://motioncontrolsystems.hiwin.us/Asset/MG-Series-Catalog.pdf>
- [3] *Micro Load Cell*. [online]. 2011 [cit. 2022-01-03]. Available at: <https://www.robotshop.com/media/files/PDF/datasheet-3133.pdf>

Automated Control of Aquarium Operation

R. Kejzlar¹ and J. Háze²

¹Author, Brno University of Technology, Czech Republic

²Supervisor, Brno University of Technology, Czech Republic

E-mail: 203248@vut.cz, haze@vut.cz

Abstract— This paper deals with the complete automation of freshwater aquarium operation with an intuitive user interface in form of matrix keyboard and LCD display. The paper describes the implementation of this device with respect to important aquarium quantities and their measurement, switched output elements and control unit with program implementation. The whole system of aquarium control is also ready for control via the web interface.

Keywords— Aquaristics, Aquarium automation, AVR, ATMEGA, ESP32, pH, LCD

1. INTRODUCTION

The market analysis found that there are no complex systems for automated aquarium operation control. All commercially available control systems are taken over from other branches of the electrical engineering industry. A very common variant of aquarium control are home-made systems that combine timers, PLCs, or other systems with a hint of automated control.

Very often complex devices are intelligent IoT (Internet of Things) systems with integrated control via voice communication (eg Sonoff with Google Assistant and others) or control over the Internet. These systems are primarily intended for switching appliances in a smart home and do not have the functions of sensing important aquarium quantities or intuitive control for the aquarist. The resulting equipment depicted in this paper could take the space on the market and become popular among aquarium users.

2. BASIC CONCEPTION

To define the complete function, a block diagram (Figure 1) was created with the layout of the entire system. The block diagram contains the measured quantities, possible switching outputs and the central control unit with hardware user interface.

The heart of the entire driving system is the AVR ATMEGA 1284 microcontroller which controls all communication between sensors, outputs and the user interface. It also controls communication between the entire system and the ESP32 WIFI microcontroller using UART serial communication. Circuit ESP32 is used to create a server interface on the Internet to remotely control the entire system.

Necessary measured quantities for optimal operation of the aquarium are pH, temperature, ambient light and water level. Microcontroller ATMEGA has a precise external crystal to maintain accurate time and time operations. The user interface consists of a 4 x 4 matrix keyboard in combination with an LCD character display to create an intuitive user interface.

The entire system then automatically controls the series of outputs needed to control the aquarium comfortably. The output circuits of the system were divided into switching (lighting, heating / cooling, filter, feeding, CO2 valve, ventilation and warning in the form of an audible alarm) and control using PWM three-color RGB LED lighting.

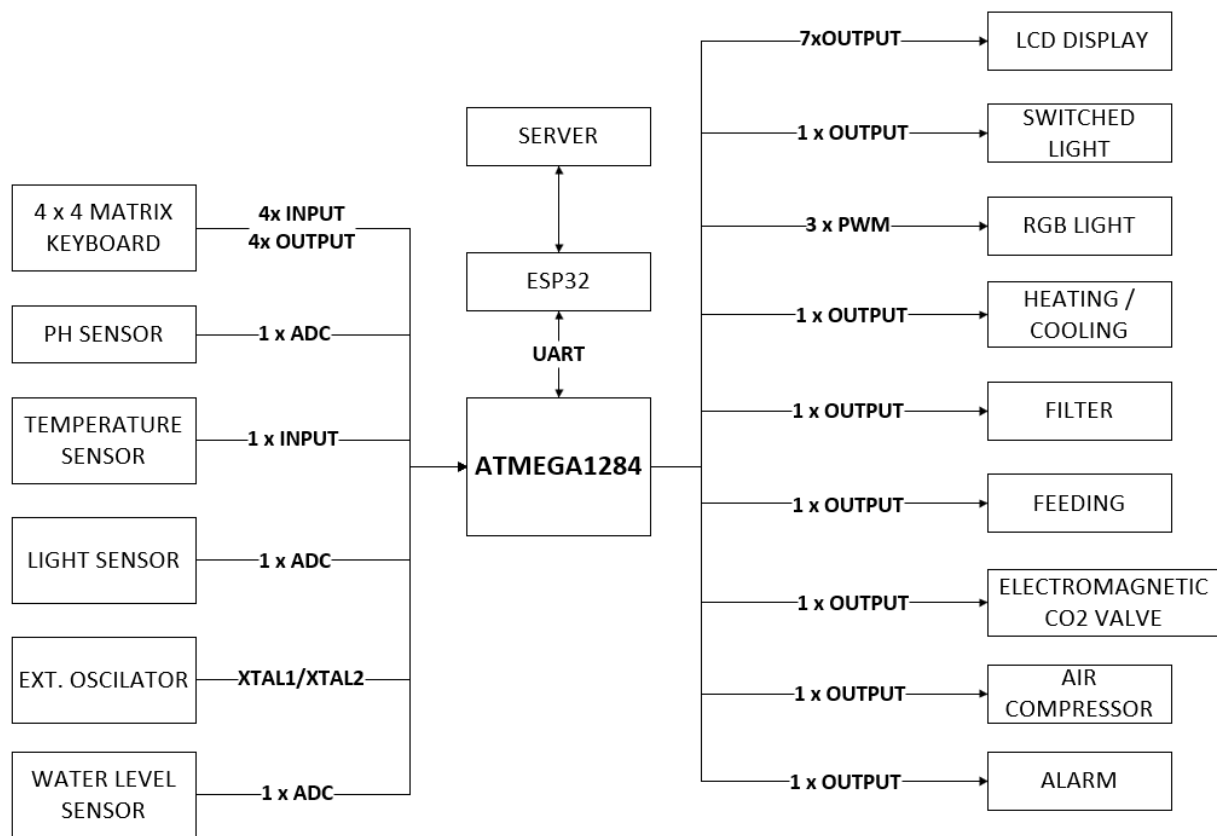


Figure 1: Block diagram of aquarium control system

3. MEASURED QUANTITIES

It is necessary to monitor important quantities for reliable control of aquarium operation. These variables include temperature, pH and the level of water that is constantly evaporating. An optional quantity is the measurement of the ambient light intensity to set the aquarium lighting and the possibility of switching individual outputs depending on the situation in aquarium ecosystem.

Temperature is basic quantity which can be measured with different methods. The typical temperature value in freshwater aquariums ranges from 10 to 30 °C.

pH is very important quantity. Acidity of water can be regulated by dosing CO₂ gas. If the concentration of CO₂ in the water is higher, acidity of water is higher. The pH is also affected by carbonate hardness.

Other measured quantities are level of water and ambient light. These quantities are only for comfort controlling of the aquarium.

4. REALIZATION

In the first part of the realization, suitable sensors for measuring quantities were selected. A semiconductor sensor DS18B20 with one-wire communication was used for temperature sensing. This sensor is very suitable for eliminating the resistance of supply wires with sufficient measurement accuracy and a good price. The E201 probe was chosen with sufficient accuracy to measure pH. The pH probe must be calibrated with a calibration solution. However, after some time, the probe must be completely replaced. To measure the intensity of illumination, a photoresistor connected to a voltage divider was selected and read by an AD converter. The Arduino shield of the resistance sensor was chosen to measure the water level. This shield must be encapsulated in a waterproof cover to prevent damage.

Subsequently, a control PCB was designed with individual functional blocks of the control unit peripherals. The board is equipped with screwless terminal blocks with intuitive connection of output devices. All switched outputs are galvanically isolated by switching relays. Voltage and current can be up to 250V / 5A at these switched outputs.

The whole system can be switched off with main switch and it is powered by a standard DC power jack with a nominal voltage of 12 V. The PCB also contains a 5 V power distribution to power sensors and microcontrollers with relays and 3.3 V for powering the ESP32 microcontroller. Voltage 12 V is used for switching RGB LED strips. Layout of PCB is shown in Figure 2.

Due to the lack of external signal control of commercially available automatic feeding systems, a second board (Figure 2) was created to control the rotating stepper motor. This board is equipped with a small microcontroller AVR ATTINY13. The microcontroller only expects an input pulse to cause the stepper motor to rotate by 360 degrees (dump the fish feed). The feeding system is equipped with one tank with mechanical adjustment of the size of the opening of the falling feed at one turn. This is how the amount of feed is set by the user. ATTINY13 sends a pulse back after completed turn and then waits for the next incoming pulse from main board.

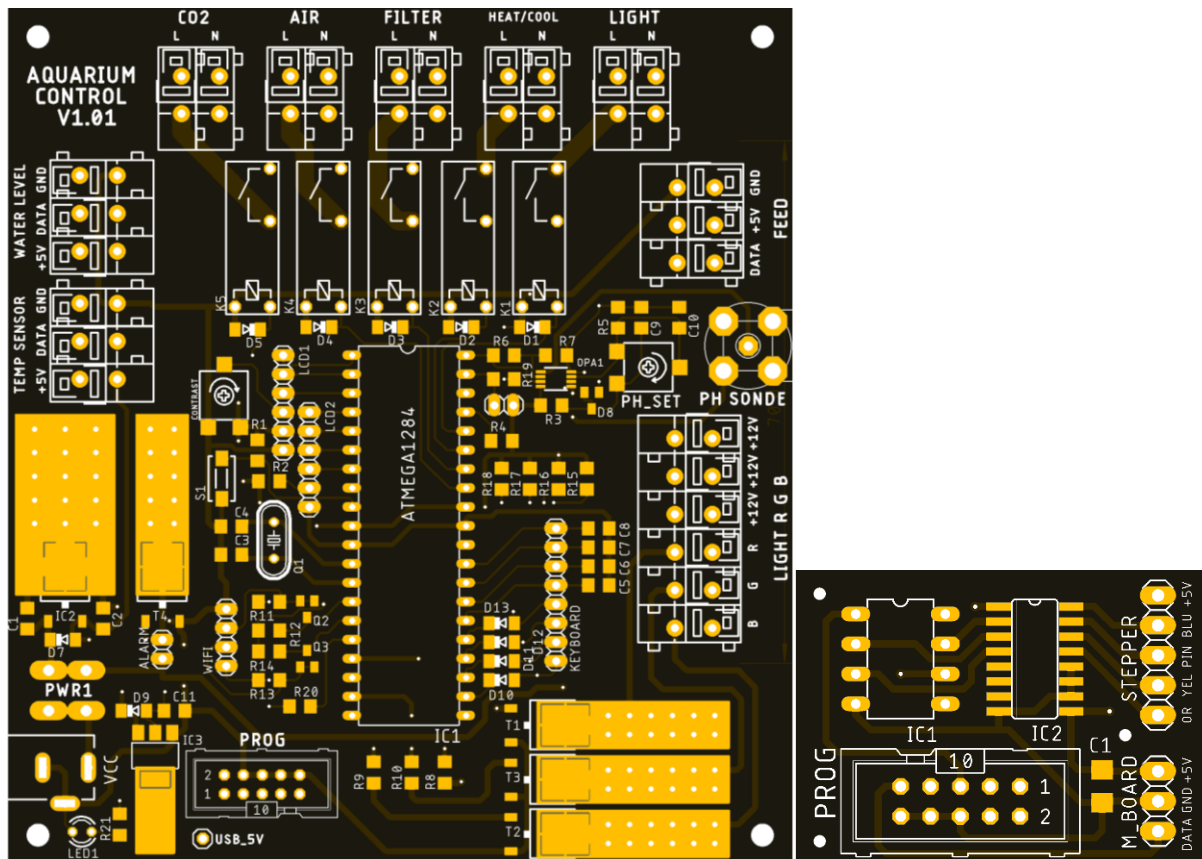


Figure 2: Main PCB of aquarium control and PCB of automatic feeding (Autodesk Eagle)

The entire device is mounted in a plastic box designed in SolidWorks and printed on a 3D printer (Figure 3). The box contains openings for cable routing of individual peripherals and four handles for mounting on a flat surface.



Figure 3: Aquarium control system in box with user interface and program menu

5. SOFTWARE

Software was written in the Microchip studio development environment in AVR GCC (C language). The software contains a complete menu controlled by a matrix keyboard. The user has the option to set all the parameters of the aquarium operation control. It is also possible to calibrate the pH probe and set key parameters of the measured quantities. The whole system therefore works as a temperature and pH regulator with adjustable notification of the measured quantities. It is also possible to time-switch the output peripherals, depending on the time, days of the week and lighting.

6. CONCLUSION

The device was completed with all important functions, a graphical interface in the form of a menu and user options to set and calibrate the necessary parameters. Depending on the time schedule, communication with the web interface using ESP32 and UART communication will be completed.

REFERENCES

- [1] *Website Invital Rostlinná akvária* [online]. 2021 [cit. 2022-03-10]. Available from: www.rostlinna-akvaria.cz
- [2] *Website Rataj Akvaristika* [online]. 2021 [cit. 2021-03-10]. Available from: www.rataj-spok.cz
- [3] *Microchip technology, ATmega164A/PA/324A/PA/644A/PA/1284/P Datasheet* [Online]. 2020[cit.2021-03-10]. Available from: www.microchip.com/downloads/en/DeviceDoc/ATmega164A_PA-324A_PA-644A_PA-1284_P_Data-Sheet-40002070B.pdf
- [4] *E-shop DRÁTEK.CZ* [Online]. 2021 [cit. 2021-03-11]. Available from: www.dratek.cz
- [5] *Portál Espressif* [Online]. 2021 [cit. 2021-12-13]. Dostupné z: www.espressif.com
- [6] *Maxim Integrated, DS18B20 datasheet* [Online]. 2021 [cit. 2021-12-14]. Available from: www.datasheets.maximintegrated.com/en/ds/DS18B20.pdf

3D PRINTED DOUBLE-RIDGED HORN ANTENNA WITH DIELECTRIC LENS FOR FREE-SPACE MATERIAL CHARACTERIZATION METHOD

M. Horník¹, P. Kaděra¹

¹Brno University of Technology, Department of Radio Electronics, Brno, Czech Republic

E-mail: xhorni15@vutbr.cz, kadera@vutbr.cz

Abstract—This article deals with the design of a 3D printed wideband horn antenna with a dielectric lens for a material characterization workplace exploiting the free-space measurement method. In this work, various ridge profiles placed in the horn antenna are studied for the optimization of the impedance matching in a wide frequency range of 2–18 GHz. The workplace consists of two horn antennas with dielectric lenses and a material sample to be characterized.

Keywords—Material characterization, double-ridged horn antenna, dielectric lens, 3D printing, metal plating, measurement, permittivity

1. INTRODUCTION

The material characterization plays an important role in microwave circuit and antenna design. Since the area of material development in additive manufacturing technologies is rapidly advancing, the need of exact materials' constitutive parameters retrieval, such as permittivity and permeability (dielectric and magnetic properties) is essential for the design process. The free-space characterization method is suitable for this purpose due to its wideband nature as the materials' parameters are dispersive. In this work, the workplace as well as the antennas are 3D printed using the fused-decomposition modelling (FDM) technology. In the FDM, an object is created by printing individual layers, mostly from a thermoplastic filament.

2. DESIGN OF THE WIDEBAND HORN ANTENNA

The requirements for antenna design are as follows: reach the minimum value of the reflection coefficient S_{11} , which is less than -10 dB in the frequency band of 2–18 GHz, and achieve a higher directivity in the E and H planes by an additional dielectric lens.

The core of the antenna is a rectangular waveguide of the width a calculated by (1), which assumes the higher TE_{30} mode ($m = 3$) and its cut-off frequency $f_m = 18.44$ GHz.

$$a = \frac{m \cdot c}{2 \cdot f_m}, \quad (1)$$

For achieving a wider frequency band, a ridge is inserted in the waveguide, which is supposed to lower the frequency of the fundamental TE_{10} mode and to suppress the higher-order TE_{20} mode. The TE_{10} mode starts to propagate from 6.15 GHz in a ridge less waveguide. The TE_{20} mode has a cut-off frequency of 10.4 GHz. With the additional ridge, the TE_{10} cut-off frequency is moved to 1.72 GHz, the TE_{20} mode is suppressed and the TE_{30} mode has a cut-off at 19.28 GHz.

The waveguide width was firstly calculated to be 24 mm and further optimized to 24.34 mm. The height b was selected to be half of the waveguide width and optimized value reaches 18.88 mm. The ridge width was calculated to be 9 mm and the ridge gap was determined by simulations as $g_r = 1.04$ mm. The simulations were performed in CST Studio Suite.

For antenna excitation, a coaxial connector with an elongated dielectric, marked RF2-156-T-00-50-G was used. The conductor must be inserted in the waveguide at the place of the highest intensity of the excited mode. Further, the purpose of the resonance chamber is to reflect an electromagnetic wave from

the enclosed wall with a phase shift of 180° and guide it back to the feeding position, where it adds to the wave leading to the antenna aperture.

The horn transforms the waveguide impedance of 50Ω to the impedance of free-space, which is 377Ω . This is realized by a gradual opening of the waveguide. The horn dimensions were calculated by the corresponding equations listed in the literature [1]. To achieve compactness of the antenna, a gain of $G = 18.4 \text{ dBi}$ was chosen for the center frequency $f = 10 \text{ GHz}$. The horn width was calculated to be $W = 122 \text{ mm}$ and optimized to 104 mm , the horn height was calculated to be $H = 82.8 \text{ mm}$ and optimized to 79 mm , and the length was calculated as $L_h = 114 \text{ mm}$. The simulation model is shown in the Fig. 1.

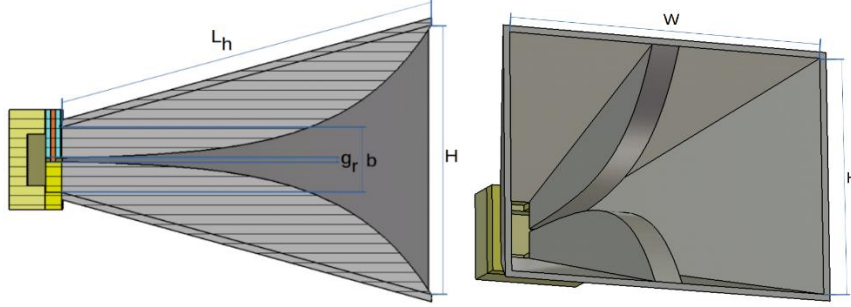


Figure 1: The simulation model of designed double-ridged horn antenna.

The ridge in the horn is an elongation of the ridge from the waveguide, however its shape can be defined by different functions which have a major impact on the final qualities of the antenna. In this work, 4 profiles were studied: quadratic, sinusoidal, exponential and Gaussian (shown in Fig. 2). Quadratic and sinusoidal profiles are similar to each other by the shape and qualities. They both have a worse reflection coefficient S_{11} near frequency of 2 GHz , but they exhibit a higher gain. Further details of this analysis can be found in [2]. The exponential profile led to the best antenna performance. It is calculated by (2), where Z_L is $g_r/2$ and Z_0 is $H/2$:

$$f(z) = \frac{g_r}{2} e^{\frac{1}{\sqrt{L_h^2 - \left(\frac{W-a}{2}\right)^2}} \ln\left(\frac{Z_L}{Z_0}\right)z} \quad (2)$$

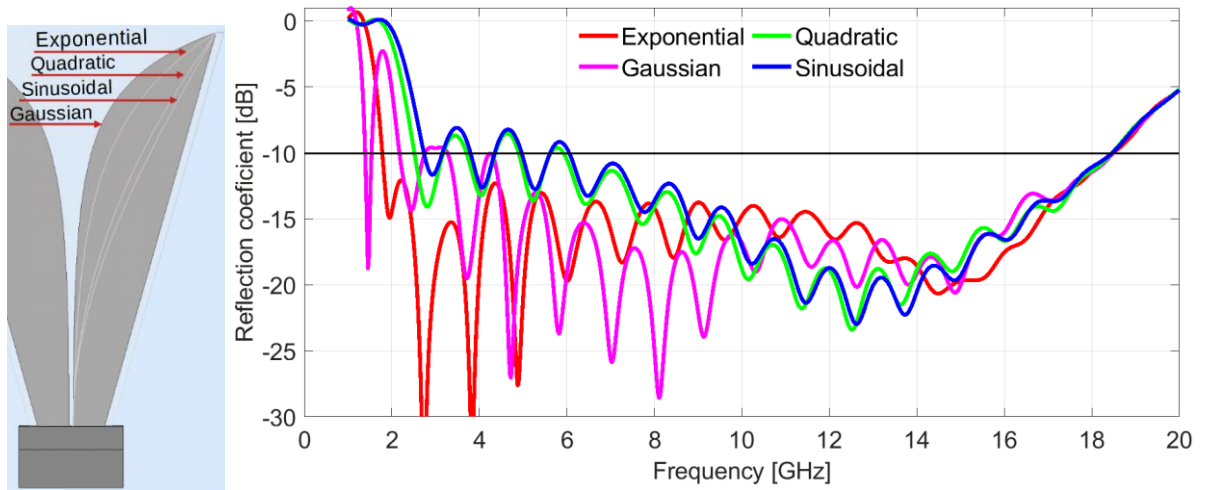


Figure 2: Ridges cutouts and corresponding reflection coefficients.

3. LENS DESIGN

For achieving a higher gain and a better focusing onto the characterized sample, two types of lenses were considered. A quasi-optical lens and a hyperbolic lens. Based on the power flow simulation, the quasi-optical lens was selected for final design because of its ability to focus the power better in the area of the sample placement. Based on this analysis, an appropriate position for the placement of the measured sample is in the distance of 115 mm from the lens aperture. In contrary, the hyperbolic lens

transforms the electromagnetic waves more into a planar wave, instead of one focal point. The lens profile is calculated by (3) [3] given that $\lambda_0 = 0.03$ mm at 10 GHz, tapering edge $TE = 20$ dB and the relative permittivity of the lens material equal to 2.6 for PLA at 10 GHz [2]. The resulting quasi-optical lens diameter and thickness are 123.2 mm and 28.6 mm, respectively. The lenses profiles and power flow simulation are shown in Fig. 3.

The quasi-optical lens is expressed in XZY Cartesian coordinate system as:

$$x^2 + y^2 = (\epsilon_r - 1)z^2 + 2f(\sqrt{\epsilon_r} - 1)z. \quad (3)$$

The hyperbolic lens equation (4) is given as follows:

$$y = -\frac{(\sqrt{\epsilon_r(R^2+f^2)}-f)+\sqrt{(\sqrt{\epsilon_r(R^2+f^2)}-f)^2-(\epsilon_r-1)(R^2-x^2)}}{(\epsilon_r-1)}, \quad (4)$$

where R is the lens radius, and f represents focal distance.

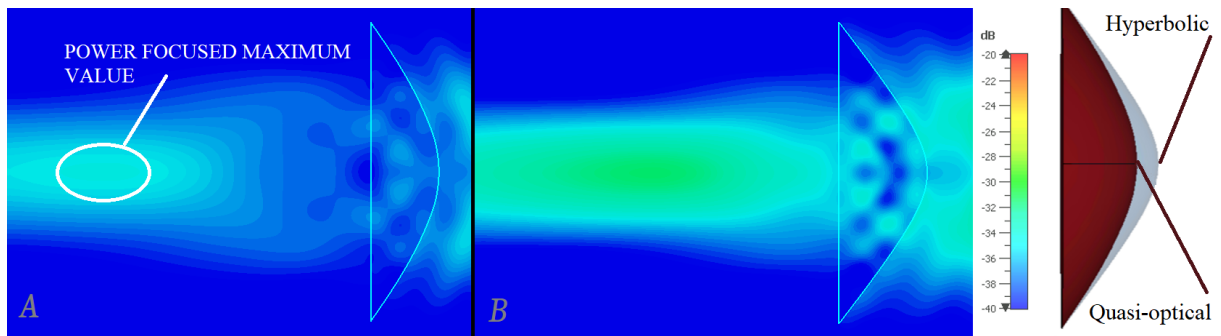


Figure 3: Lens cutout from the power flow simulation: (a) quasi-optical lens (b) hyperbolic lens.

4. LENS ANTENNA FABRICATION AND MEASUREMENT

The double-ridged horn antenna was 3D printed using X material and X FDM 3D printer, the lens was 3D printed using the PLA material and the Prusa i3 MK3S+ FDM printer. The antenna radiation patterns, and gain were measured in an anechoic chamber. The measured gain of the antenna #1 was close to the simulated values. The maximum gain achieved by antenna #1 without the lens was 15.28 dBi at 11.6 GHz and 22.8 dBi with the lens at 13.8 GHz, respectively. The addition of the lens worsens the reflection coefficient due to reflection from the lens surface by 3 dB. However, the gain was improved by 6 dB at the center frequency of 10 GHz.

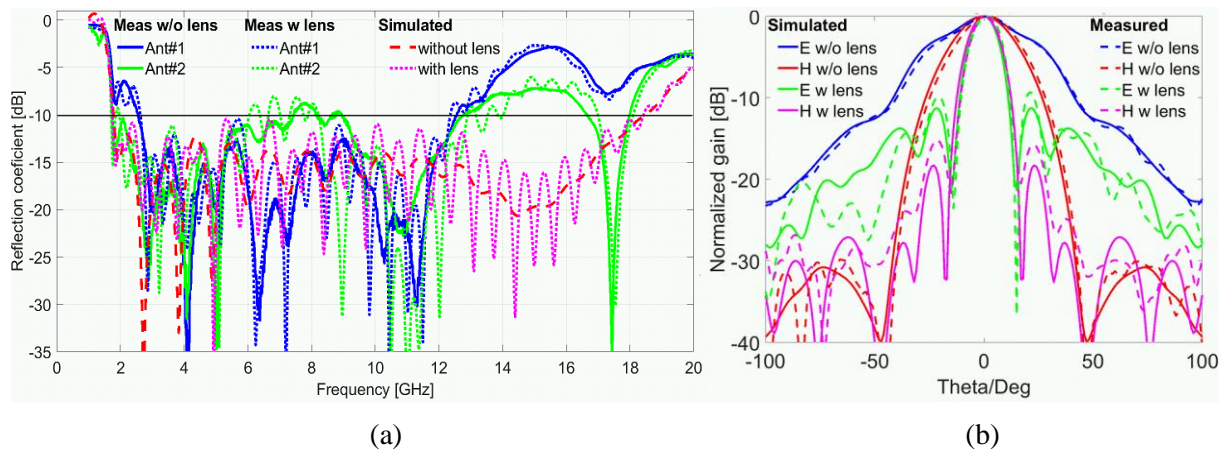


Figure 4: (a) Simulated and measured reflection coefficient of two fabricated antennas, (b) normalized simulated and measured gain with and without lens in the E and H planes at 10 GHz.

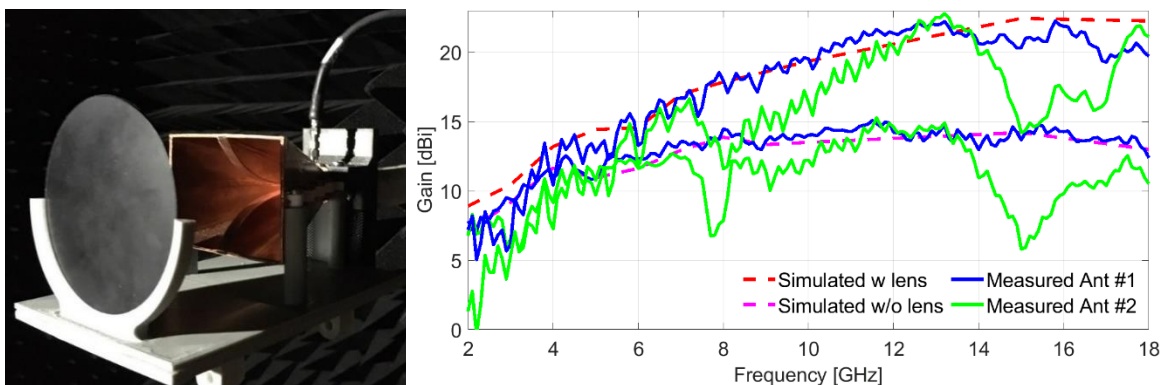


Figure 5: (a) Antenna measurement in the anechoic chamber and (b) the simulated and measured gain of the antennas with and without lens.

5. CONCLUSION

Based on a theoretical design, the double-ridged horn antenna with the quasi-optical lens was modelled and optimized. The antenna model was successfully designed in accordance with the requirements, achieving reflection coefficient close to -15 dB. The greatest impact on the change of antenna parameters have the position of the coaxial feed, the gap between ridges and the ridge profile. The manufactured antenna was plated with a copper foil, however, this method has a drawback in the insufficient copper foil bearing. A solution to this problem can be in metallization by a vacuum plating. The used FDM 3D printing method shown to be an inaccurate by means of manufacturing tolerance, e.g. the inner width of the waveguide should be 24.23 mm but after printing it was 23.8 mm, including the plated layer. The 3D printed antenna was adequately modified to comply with the requirements, especially the critical spacing between ridges, where the initial gap was 0.2 mm. By the influence of the printing imperfections and the insufficiency of the copper foil, the measured deviation of the reflection coefficient was significant between the frequency of 12 GHz and 18 GHz. Overall, the differences between the simulation and the measurement of manufactured antennas are caused mainly by the imperfection of the manufacturing process. The inaccuracies are more pronounced at higher frequencies. Subsequently, the functionality of the workplace for the verification of its function on a sample with known dielectric properties will be presented.

ACKNOWLEDGEMENT

This work was supported by the Internal Grant Agency of Brno University of Technology, project no. FEKT-S-20-6526

REFERENCES

- [1] MILLIGAN, Thomas A. *Modern Antenna Design* [online]. Hoboken, NJ, USA: John Wiley & Sons, 2005 [cit. 2021-5-25]. ISBN 9780471720614. Available at: doi:10.1002/0471720615.
- [2] HORNIK, Milan. 3D printed double-ridged antenna with dielectric lens for free space material characterization method [online]. Brno, 2021 [cit. 2021-05-27]. Available at: <https://www.vutbr.cz/en/studenti/zav-prace/detail/133584>. Bachelor's thesis. Brno University of Technology, Faculty of Electrical Engineering and Communication, Department of Radio Electronics. Thesis supervisor Ing. Petr Kadera.
- [3] HAJISAEID, E., DERICIOGLU, A. F., AKYURTLU, A. All 3-D Printed Free-Space Setup for Microwave Dielectric Characterization of Materials. In: *IEEE Transactions on Instrumentation and Measurement*, vol. 67, no. 8, 2018.

Low noise DC amplifier with selectable gain and auto-zero functionality for use with modern integrated A/D converters

P. Tomíček¹ and V. Levek²

¹Master Degree Programme (2), FEEC, Brno University of Technology

²Supervisor, FEEC, Brno University of Technology

E-mail: xtomic05@vutbr.cz, levek@vut.cz

Abstract—This paper presents the design and noise measurements of amplifier suitable for use with modern integrated A/D converters. Proposed topology is capable of both amplifying and attenuating its input signal to utilize the whole input voltage range of A/D converters. Experimental version achieved full-scale input voltage range from ± 15 V to ± 15 mV with measured input voltage noise of 0,17 ppm to 0,73 ppm of full-scale range. Suppression of offset error associated with amplifier and A/D converter systems is realized using auto-zero scheme. Resulting amplifier used in conjunction with digital filters can achieve more than 20 noise free bits on all gain settings.

Keywords—low noise, DC amplifier, selectable gain, auto-calibration, A/D converter

1. INTRODUCTION

Low noise DC amplifiers are an essential part in applications such as precision scales, thermometers and other test equipment. They amplify the input signal to utilize the full input range of A/D converter in order to increase signal to noise ratio. Due to the varying amplitude of the input signal, it is often necessary to change the gain of the amplifier and even provide attenuation. Typical solution involves first attenuating the signal using fixed voltage divider and then amplifying it by selectable gain. This increases cost, circuit complexity, worsens signal to noise ration and leads to nonstandard voltage dividers. This paper provides a different way of designing low noise amplifiers with better specifications.

2. DESIGN

There are many requirements when designing low noise DC amplifiers for instrumentation use. The obvious one is low noise. Others are low drift, minimal distortion, negligible input current and many others. In addition to these, there are can be specific requirements, such as to only use widely available voltage dividers. Experimental version of proposed amplifier is designed with following specification.

Table I: Desired parameters of designed amplifier

Parameter	Value	Unit
Min. input voltage range	± 15	V
Max. output voltage range	± 2	V
Gain settings	0,1; 1; 10; 100	-
Max. RMS input voltage noise (< 1 Hz)	30; 3; 0,3; 0,03	μ V
Supply voltage	± 17	V

Values of parameters were chosen to allow integration into complex measurement system consisting of AD7177-2 A/D converter and voltage reference module based on LM399. In this system it is critical for the amplifier to not limit the overall performance of the system. Simplified schematic of designed amplifier and the rest of the measurement system is in the figure below.

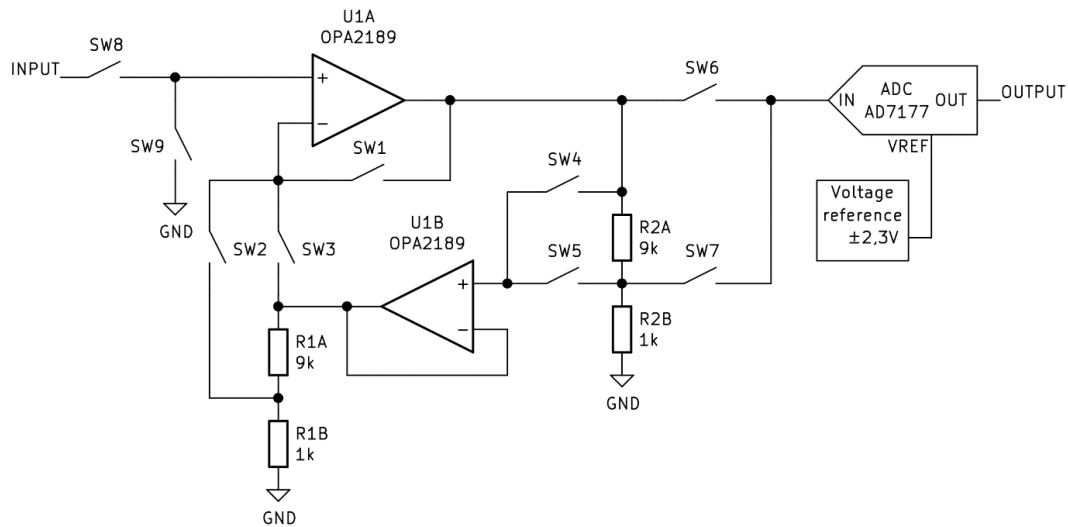


Figure I: Proposed topology of amplifier and its implementation into measurement system

Amplifier consists of two op-amps, two voltage dividers and nine solid-state switches. Both dividers are composed of two resistors with resistance of 1 k Ω and 9 k Ω . These were implemented using LT5400-8 precision resistor network integrating two of these dividers into a single package and substrate. The use of matched resistors minimizes their susceptibility to thermal effects and ensures stable divider ratio over operating conditions. Low noise is achieved due to the use of low noise zero-drift op-amps OPA2189, which have suppressed 1/f noise and input voltage noise spectrum density of 5,2 nV/Hz^{1/2}. Another advantage of these op-amps is their negligible offset dependence on temperature and small input current. All switches are implemented using MAX335 integrated circuit and have $R_{DS(ON)}$ of 100 Ω . Noise of each switch is equal to the Johnson-Nyquist noise of a resistor with resistance of $R_{DS(ON)}$, which is equal to 1,3 nV/Hz^{1/2}. It is therefore negligible compared to the noise caused by the voltage dividers and op-amps. In the table below are some possible configurations using switches SW1 to SW7.

Table II: Some of the possible configurations using switches (O – open, C – closed)

Switch	Gain						
	0,1	0,1	1	1	10	10	100
1	C	O	C	O	O	O	O
2	O	O	O	O	O	C	C
3	O	C	O	C	C	O	O
4	C	C	C	C	O	C	O
5	O	O	O	O	C	O	C
6	O	O	C	C	C	C	C
7	C	C	O	O	O	O	O

Due to the large number of possible combinations it's possible to omit some of switches. For example, switches SW1 or SW3 can be removed while not reducing the number of gain options. On the other hand, this may increase noise on some gain settings, because of a more complicated feedback path.

Offset compensation of an amplifier and the rest of the measurement system is handled by two switches SW8 and SW9. These allow shorting the input to ground and therefore measuring the offset. During digital postprocessing this offset is then subtracted from the measured input value.

One of the major disadvantages of the proposed topology is the large output voltage range of OPA2189 which is needed to achieve 0,1 gain. If the amplifier is configured incorrectly, it is possible to destroy the A/D converter by applying voltage on its inputs larger than absolute maximum allowed. This may cause destructive current flow into the input pin. One of the ways of mitigating this problem is by limiting the maximum current into the input pin through the use of series resistor. It is also possible to add fast window comparator signaling overvoltage condition. Control unit is then able to disconnect the input of A/D converter before voltage on it rises to dangerous levels.

Communication with the A/D converter and switches is carried through single SPI bus connected to the control unit. Which consists of a PIC microcontroller and supporting digital circuitry such as memories for datalogging and temperature sensors to measure ambient conditions. Communication with the user is handled through a USB bus by connecting the control unit to a PC

3. SIMULATION AND CALCULATION OF INPUT NOISE

Verification of the design was carried out in OrCAD PSpice software. Simulations were focused on the determination of input voltage noise. Amplifier was connected in all configurations shown in Table II. In cases with multiple gain configurations only the worst-case value was evaluated. Result of the simulation are in a Table III.

In the simulation it was determined that the spectral density of input voltage noise e_n is constant in frequency range from 1 mHz to over 1 kHz. This is caused by the use of zero-drift amplifiers and is expected. RMS input voltage noise u_{nRMS} is calculated by integrating the spectral density of input voltage noise e_n over the desired frequency range. For flat spectrum this calculation can be simplified by replacing the integration by multiplication such as

$$u_{nRMS} = \sqrt{\int_{f_L}^{f_H} e_n^2 df} = \sqrt{e_n^2 (f_H - f_L)}. \quad (1)$$

For frequency band from DC to 1 Hz the calculation can be further simplified to

$$u_{nRMS} = e_n. \quad (2)$$

Calculated values of RMS noise are in table below.

Table III: Simulated input voltage noise spectral density e_n and RMS noise u_{nRMS}

Gain	e_n [nV/Hz ^{1/2}]	u_{nRMS} [nV]
0,1	39	39
1	8,5	8,5
10	9,4	9,4
100	7,7	7,7

Calculated values are in the limits required by specification with great margin. That is desirable because this calculation does not include other sources of noise such as EMI, thermoelectric voltage, triboelectric effect and others.

To achieve the desired input noise the amplifiers output signal needs to be filtered by the delta-sigma A/D converter and subsequently with simple moving average (SMA) filter in the control unit. A/D converter uses sinc3 filter with output data rate of 16,7 Hz. Effective output data rate after offset compensation is then equal to 2,7 Hz. Further reduction of noise is made by averaging 16 subsequent samples in SMA filter. Frequency response of sinc3 and SMA filter and their combination is below.

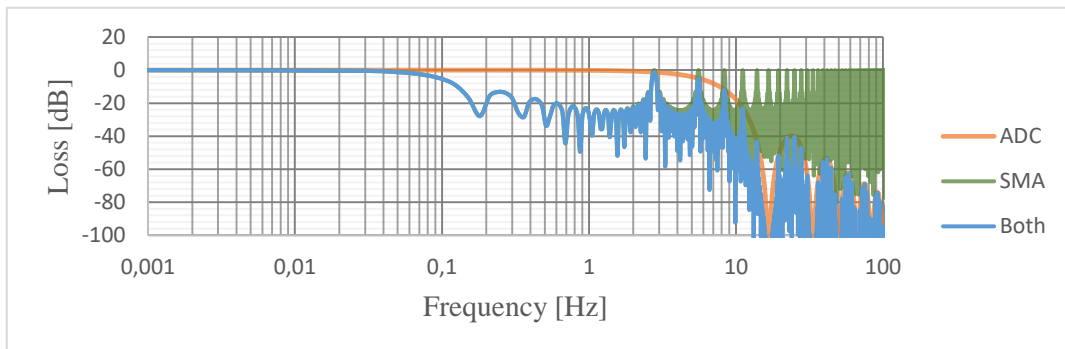


Figure II: Frequency response of sinc3 and SMA filter and their combination

Using the combination of these filters makes the effective noise bandwidth ENBW equal to 0,86 Hz. That is below the required 1 Hz bandwidth and filtering will be sufficient.

4. MEASUREMENT OF INPUT NOISE

Practical measurement of input noise was realized using the measurement system as seen in Figure I. Input terminals were shorted with a piece of wire to eliminate noise caused by the signal source and the system was placed in a metal box to suppress the effects of air currents. System was turned on and was left to stabilize for several hours. After this the measurement itself was started and left to stabilize for several minutes. When the voltage stabilized, datalogging with a frequency of 2 Hz, using the A/D converter of the system, was started for two hours. This cycle was repeated (except for turning the system on) for other gain settings. Subsequently RMS values of noise were calculated. Comparison of calculated and measured values of noise are below.

Table IV: Comparison of calculated u_{nCALC} , measured u_{nMEAS} and required u_{nREQ} input RMS noise

Gain	Input voltage range [mV]	u_{nCALC} [nV]	u_{nMEAS} [nV]	$u_{nMEASrel}$ [ppm]	u_{nREQ} [nV]
0,1	± 15000	39	5033	0,17	30000
1	± 1500	8,5	515	0,17	3000
10	± 150	9,4	52	0,17	300
100	± 15	7,7	22	0,73	30

Measured values u_{nMEAS} comply with the required values. On the other hand, there is large difference between calculated u_{nCALC} and measured values u_{nMEAS} . However, the relative value of noise $u_{nMEASrel}$ has an virtually constant value on gain settings 0,1; 1 and 10. This indicates that the excessive noise is not caused by the amplifier. Rather, it is caused by the A/D converter or voltage reference module, or both.

5. CONCLUSION

In this paper design of low noise DC amplifier with wide input voltage range and switchable gain was proposed, analyzed and measured. Proposed topology has several advantages such as possible attenuation of input signal, usage of common resistor dividers, low part count and low noise.

Designed amplifier allows switching gain between values of 0,1; 1; 10 and 100. Calculated input noise value on all gain setting is on the order of nanovolts up to tens of nanovolts. Amplifier was realized and implemented into complex measurement system consisting of A/D converter and voltage reference module. Subsequent measurements were performed on this device using the integrated A/D converter.

With input terminal shorted to ground input voltage noise of the amplifier was measured for two hours. This measurement was repeated for all gain settings. Results from this show that only with the gain set to 100 does the noise of the amplifier significantly represents itself in the input noise. On all other gain settings, the noise of the amplifier was below the level of the rest of the system.

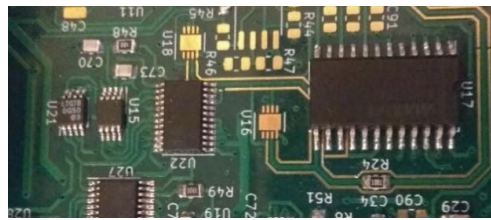


Figure III: Proposed amplifier implemented in complex system

REFERENCES

- [1] P. Horowitz and W. Hill, *The Art of Electronics*. New York: Cambridge University Press, 2021.
- [2] N. Beev, "Analog-to-digital conversion beyond 20 bits," *2018 IEEE International Instrumentation and Measurement Technology Conference (I2MTC)*, 2018, pp. 1-6, doi: 10.1109/I2MTC.2018.8409543.
- [3] *Low Level Measurements Handbook: Precision DC Current, Voltage, and Resistance Measurements*. Seventh edition. Keithley, 2014.
- [4] B. Lizon. *Fundamentals of Precision ADC Noise Analysis: Design tips and tricks to reduce noise with delta-sigma ADCs*. Texas Instruments, 2020.



SAAB AB serves the global market with world-leading products, services and solutions from military defence to civil security. With operations in over 100 countries, Saab continuously develops, adapts and improves new technology to meet customers' changing needs.



SAAB

OUR VISION

It is a human right to feel safe. Since Saab was started, we have strived to keep society and people safe. Through systems and solutions that increase security, we can make this possible.

OUR MISSION

By pushing mental and technological boundaries we make people safe. Our mission describes how we work to achieve our vision. By improving and updating technological systems and solutions, we increase security in society, for its citizens and for those whose job it is to maintain security. We also contribute insight into how threats to our security change and develop innovative new solutions that make society secure.

OUR VALUES

Trust

We are honest and reliable global citizens, and we keep our promises.

Expertise

We combine a strong history of knowledge with constant learning.

Drive

We have a passion for innovation, are open to change and committed to being fast and flexible.

www.saab.com





DYNAMICS - WHO WE ARE

- A leader in precision engagement systems
- Meeting the global market's requirements
- Worldwide customer base in over 60 countries



SAAB

Business unit Dynamics is a workplace for more than 2200 employees all around the world. We offer a market-leading product portfolio comprising of ground combat weapons, missile systems, torpedoes, unmanned underwater vehicles, training systems and signature management systems for armed forces around the world as well as unmanned underwater vehicles for the offshore industry.

TRAINING AND SIMULATION

Product portfolio covers the full range of training solutions including capabilities and products for live and virtual training.

We understand training and provide scalable state-of-the-art training solutions for military, security and emergency services all over the world.

Live training

- Instrumented training systems

Live fire training

- Range equipment

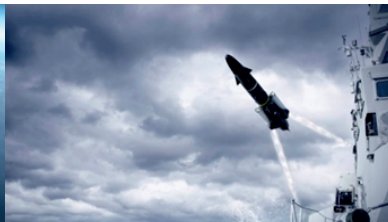
Virtual training and integration

- Ground combat simulators

Training services

- Logistical and operational support

www.saab.com



Thermoanemometric flow sensor control using pulse width modulation

A. Mlčoch¹, P. Beneš¹

¹Brno University of Technology, Czech Republic

E-mail: xmlcoc11@vut.cz, benes@vut.cz

Abstract—PWM control of the heated element in constant temperature difference mode was designed and tested for the thermal flowmeter. The reason for using this solution is to extend the operating range and reduce the power losses of the control elements. The proposed solution allows linearization and adjustment of the operating point to the desired flow range and fluid temperature without any change in the wiring or electronics. The functionality of this solution was demonstrated over a range of 80 kg/h with a repeatability of 2 %.

Keywords— PWM, thermoanemometric flowmeter, heat transfer, Joule heat, synchronised measurement, temperature regulation, PS regulator, flow measurement

1. INTRODUCTION

The heat transfer-based flow sensors are accurate and reliable class of flow sensors. A standard design is usually based on a constant power supplied to the heated resistance temperature detector. The temperature difference depends on the flow rate.[1] This solution is relatively simple to implement, but at zero flow the heated resistor overheats. The constant temperature mode of the heated thermometer can also be used (Fig. 1a).[2] At constant ambient temperature, constant temperature mode and constant temperature difference mode are equivalent. However, the constant temperature difference mode can operate over a wider range of ambient temperatures and is therefore more suitable for example for industrial applications. Its computational complexity is higher.

Electrical circuits usually use operational amplifiers (OA) to regulate power consumption.[3] The OA does not have sufficient output power. When power is controlled by a transistor in linear gain mode, significant power losses are occurring in this transistor. Pulse Width Modulation (PWM) control can be used to eliminate transistor power dissipation (Fig. 1b). When controlling the sensor using PWM, precise synchronization of the measurements with the PWM control is required. It is also necessary to take into account the transients in the analog part of the circuit. The power taken from the heated thermometer can be approximated using King's equation: [4][5]:

$$P = (A + B \cdot v^n) \cdot \Delta T, \quad (1)$$

where P stands for power losses, A is the parameter of conduction thermal losses, B is the parameter of convection thermal losses, v is mean velocity in the pipe, n is empiric coefficient dependent on sensor geometry, and ΔT is differential of the temperature between heat element and ambient.

Using this equation, the flow rate of the fluid through the pipe can be calculated. For high sensitivity it is desirable to use The Wheatstone bridge measurement circuit (Fig. 1), where R_s is the resistance thermometer and R , R_1 and R_2 are the balancing resistances of the bridge. The output value of the measurement is usually the output voltage at the OA.[3][5]

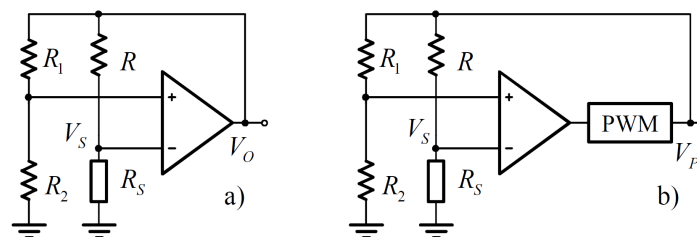


Figure 1: a) Classical configuration with OA. b) Classical configuration with OA and PWM.[3]

2. USED MEASUREMENT HARDWARE

This solution uses the difference voltage measurement. Two Wheatstone bridges are used, allowing the heater and ambient temperature to be measured separately. Using one bridge for both thermometers would make it impossible to measure the ambient temperature. Also, the differential temperature could not be measured with such accuracy because the reference thermometer could be heated. A certain disadvantage of this approach is the need to measure 4 voltage channels, two bridge differential voltages and two supply voltages. Due to PWM control, all these voltages have to be measured in very short time intervals, within about $20\ \mu\text{s}$. An Analog-Digital converter (ADC) measures the bridges differential voltage and its supply voltage. Voltage values are digitally processed by microcontroller. When using PWM, the measurement is made at a higher voltage than if the bridge was powered by a constant voltage, giving the measuring bridge a higher sensitivity. For those reasons, the operational amplifier does not have to be used.

The ambient temperature reference bridge contains a Pt1000 resistance thermometer with nominal resistance $1000\ \Omega$. The bridge operates in pulse mode with a $5\ \text{V}$ supply voltage. The pulse is only a few microseconds wide. Temperature can be measured at rates from lower to higher tens of samples per second. This leads to a sufficiently low average power consumption and therefore self-induced heat can be neglected.

The heated bridge contains a Pt50 resistance thermometer with a low nominal resistance value $50\ \Omega$. The bridge is powered by $15\ \text{V}$. The thermometer warms up to the desired temperature thanks to Joule heating. Power supply is realized by PWM. The time constant of the heated thermometer must be much longer than the PWM pulse time. The base clock frequency is $16\ \text{MHz}$ and the PWM frequency is up to $62\ \text{kHz}$ (in 8-bit configuration) or slower with more accurate multi-bit control. The power consumption is up to $2.2\ \text{W}$, depending on the momentary flow rate. The bridge is controlled by a PNP switching transistor for medium frequency band up to $100\ \text{MHz}$. The temperature difference of the heated thermometer compared to the environment can be set in software. For the highest possible sensitivity and signal-to-noise ratio, it is advisable to keep the temperature difference as high as possible. For the purpose of this article, the temperature difference $\Delta T = 50\ \text{K}$ is used.

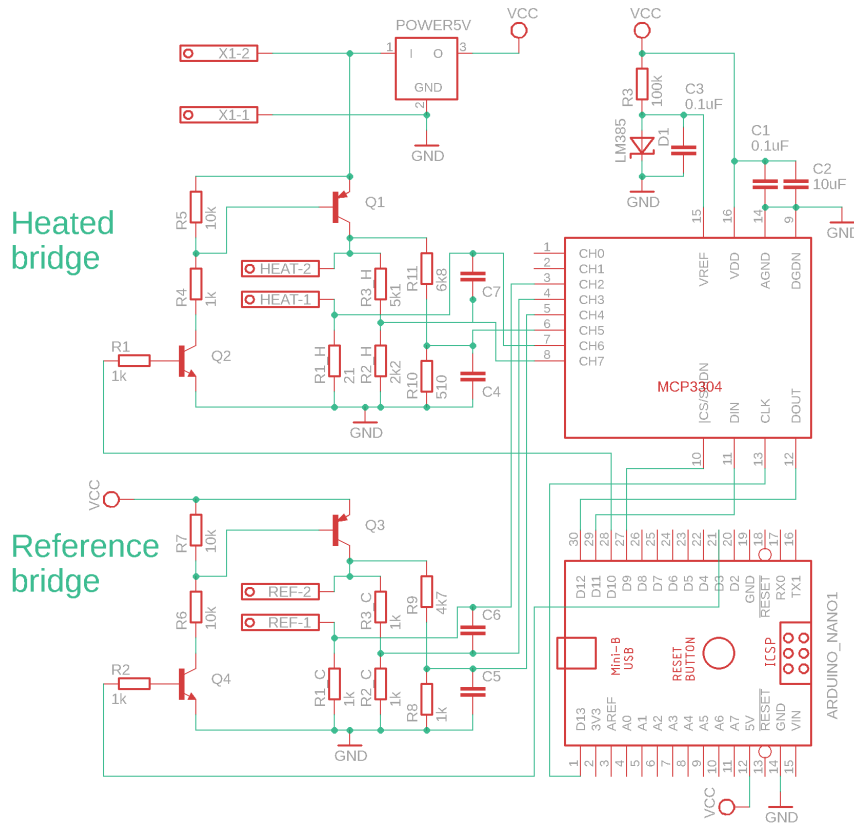


Figure 2: Electrical circuit.

3. SENSOR CONTROL

In the context of regulation, it is a first-order system. The time constant of the thermometer was measured using pulses in the bridge supply voltage. The waveforms were analyzed with an oscilloscope. A strong dependence of the time constant on the actual flow rate was found (Fig. 3). The time constant is in the range of 32 ms to 220 ms. This places certain demands on the speed of the control loop. The controller needs to be designed to be capable of responding as quickly as possible to the changing parameters of the system. Temperature overshoot is not a problem. For the sake of accurate temperature measurement, the waveform must not be oscillating. For a first-order system, a controller with two time constants is undesirable, so only a PS controller was chosen. The controller was chosen so that it could be designed for a non-oscillating waveform. The structure of the controller is[6]:

$$F(z) = K_R \cdot \left(1 + \frac{T_s}{T_i} \cdot \frac{z}{z-1} \right) \quad (2)$$

If a non-oscillating waveform is required, calculate the controller constants according to the equations:

$$K_R = \frac{\pi \cdot T(t)}{9 \cdot T_s \cdot K(t)}; \quad T_i = T(t) \quad (3)$$

where $F(z)$ is regulator frequency transmission, K_R is regulator gain, T_s is sampling period, T_i is regulator integration constant, $T(t)$ is time-varying time constant of the system (thermometer), and $K(t)$ is time-varying system gain.

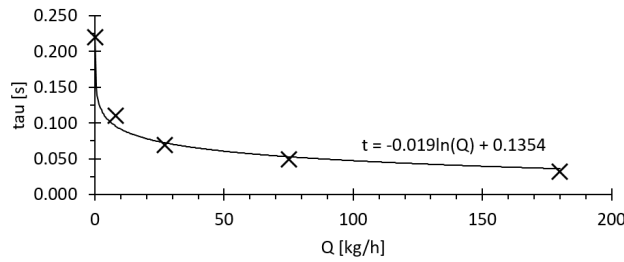


Figure 3: Dependence of the time constant on the flow rate.

4. MEASUREMENT

Both differential voltage and bridge supply voltage measurements are measured using an interrupt with a 2 MHz timer. The measurement itself takes approximately 10 μ s. By shifting the time point of the measurement interrupt in the PWM cycle, all sections of the PWM waveform can be measured in 0.5 μ s steps. The effect of the thermometer time constant on the measurement can be seen in the differential voltage of the bridge (Fig 4). This must be taken into account in the subsequent flow calculations. Measurements showed that the supply voltage is reliably constant at the time of measurement, the ripple is approximately 20 mV at 15 V, i.e. within 0.2 %.

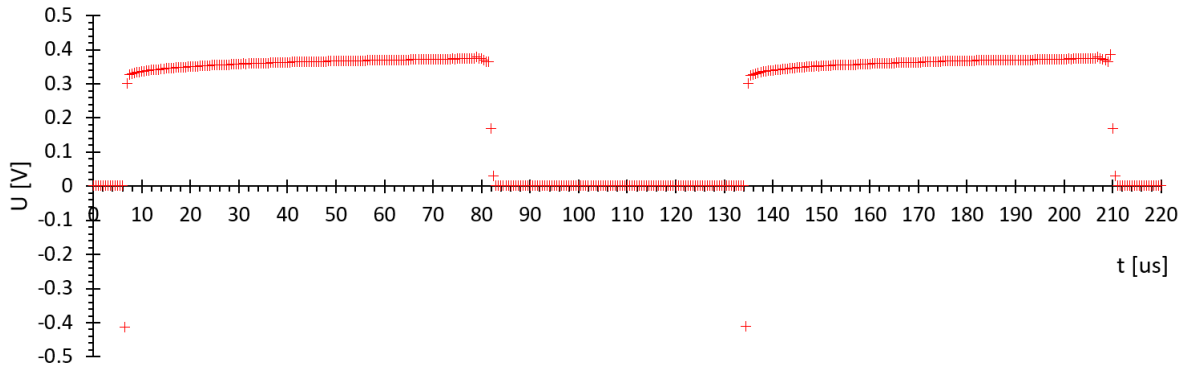


Figure 4: Bridge differential voltage, heated bridge.

An experimental flow measurement was carried out. As can be seen in Fig. 5, the mathematical model fits reasonably well for flows up to 100 kg/h. The software does not yet include automatic calibration and the parameters of the mathematical model are not precisely measurable. A correction is therefore necessary for the results.

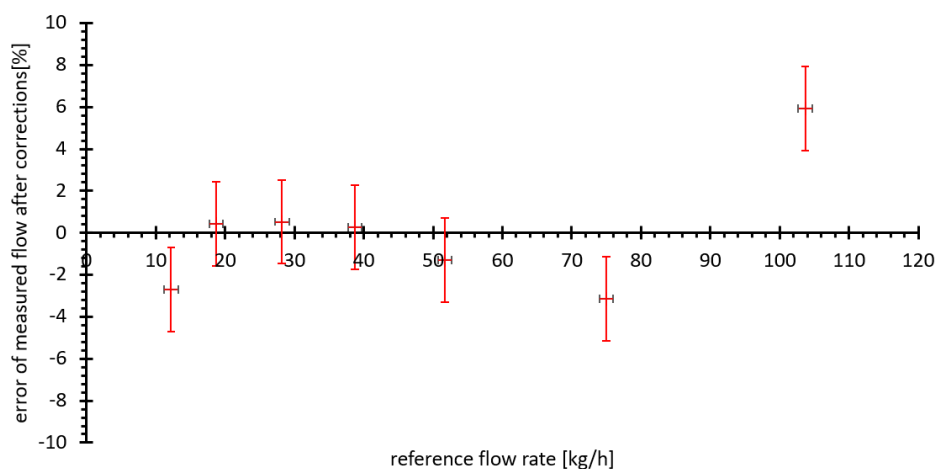


Figure 5: Measurement error after corrections.

5. CONCLUSION

It has been shown that the thermal flow meter sensor can be operated in constant temperature difference mode using PWM control. The solution has so far operated with an accuracy of $\pm 5\%$ up to a range of 80 kg/h, with an estimated repeatability of 2 %. This concept can be further developed to refine existing flow measurements. Obviously, it will be necessary to solve e.g. automatic model calibration or model refinement, as can be seen in Fig. 5.

ACKNOWLEDGMENT

I would like to thank Doc. Petr Beneš for providing me with the opportunity to continue my laboratory and research activities.

REFERENCES

- [1] Low Flow Liquid Meters [online]. Columbus (Ohio, USA): INTEC, 2005 [cit. 2022-03-13]. Available from: <https://intekflow.com/flow-measurement-instruments/low-flow-meters-liquid/>
- [2] Thermal Mass flow sensor for liquids [online]. Freemansburg (Pensylvánie, USA): Bronkhorst [cit. 2022-03-13]. Available from: <https://www.bronkhorst.com/en-us/service-support/knowledge-base/thermal-mass-flow-sensor-for-liquids/>
- [3] V. S. G. Martins, R. C. S. Freire, a S. Y. C. Catunda, „Sensitivity analysis and automatic adjustment of a controlled-temperature thermoresistive-based anemometer”, 2012 IEEE International Instrumentation and Measurement Technology Conference Proceedings, May. 2012, s. 1876–1880, doi: 10.1109/I2MTC.2012.6229378.
- [4] OLIN, PH.D, John G. ”A standard for manufacturers of thermal dispersion mass flow meters”. *Sierra Instruments, Inc.*: CEO, Founder. October 15, 2008.
- [5] S. Viana Leal, S. Y. C. Catunda, L. A. S. Ribeiro, a R. C. S. Freire, ”Automatic dynamic range adjustment of a controlled-temperature thermoresistive-based anemometer”, 2010 IEEE Instrumentation and Measurement Technology Conference Proceedings, May 2010, s. 268–272. doi: 10.1109/IMTC.2010.5488004.
- [6] PIVOŇKA, Petr. Číslíková řídicí technika [online]. 1. Brno: Skriptum VUT, 2012 [cit. 2022-03-13].

Model Ensembling: A simple way of improving model performance for chromosome classification

Kristyna Pijackova¹, Tomas Gotthans¹, Jakub Gotthans¹

¹Department of Radio Electronics, Brno University of Technology, Czech Republic

E-mail: xpijac02@vutbr.cz, gotthans@vutbr.cz, jgotthans@vutbr.cz

Abstract—This paper deals with chromosome classification via convolutional neural networks and model ensembling. Chromosome classification is a part of a procedure in karyotyping, where the chromosomes should be paired and ordered so that they are prepared for inspection of abnormalities. Model ensembling was used as a technique to improve overall classification accuracy by using all of the trained models. We achieved 94.8 % accuracy for a Q-band BioImlab dataset and 97.48 % for a G-band chromosome CIR dataset.

Keywords—chromosome classification, deep learning, model ensembling, convolutional neural networks

1. INTRODUCTION

Chromosome classification is a part of karyotyping, a method used for inspecting chromosomal structures for a detection of genetic disorders. Karyotyping can be a time-intensive process and available software still relies heavily on interaction of cytogenetics [1]. Recent papers (e.g. [2–5]) in this field are focused on applying deep neural networks to solve this task to make the process automated and more reliable. The performance of a deep learning model depends on many things - model architecture, chosen hyperparameters, available dataset, etc... For this reason, it is common to train and test the data on multiple architectures and choose the best-performing one.

Our approach in this paper is slightly different, to further improve the overall accuracy, we use predictions from all of our trained models. This technique is called model ensembling, and it allowed us to improve overall accuracy compared to the best model by ~ 1 % for a CIR dataset [4] and by ~ 2.5 % for a BioImlab dataset [6].

2. METHODOLOGY

Model ensembling is based on an assumption that each well-trained model can extract different features. It is therefore convenient to have base models with different architecture types, as it is more probable this way, that each model will capture different information from the input data. Therefore, after pooling predictions of multiple models, we get a more accurate description of the data [7]. Equation 1 shows a simple way of model ensembling for n models with assigned weights w , where $\sum w = 1$.

$$predictions = \sum_{i=1}^n model_i \cdot w_i, \quad (1)$$

As our base models, we chose four convolutional neural networks - Xception [8], MobilenetV2 [9], EfficientnetB2 [10] and ResNet18 [11]. As the architectures of the models are different, they have the potential to be successfully used for ensembling. Along with that, they also have a relatively small number of parameters and can be directly imported from Keras API [12], except for ResNet18. The classifier head for the Xception, Mobilenet, and Efficientnet was customized and is shown in Fig.1. It includes Average Global/Maximum Pooling layers, which are then concatenated to capture richer features, followed by Dense and Dropout layers. The models also contain a data augmentation layer placed after an input layer, only active during a training phase. In this layer, we included random flipping, small rotations, translation, and random contrast adjustments to compensate for the small dataset sizes.

All four models were trained with an Adam optimizer with a starting learning rate $7e^{-4}$, which was gradually lowered via callback after a stalling validation loss. The ResNet model was trained

from scratch. The Xception, Mobilenet, and Efficientnet were imported with pre-trained weights on an ImageNet dataset, which saved us between 10 to 20 epochs of training. However, the whole architecture needed to be re-trained, as fine-tuning of the classifier head resulted in poor model performance on its own.

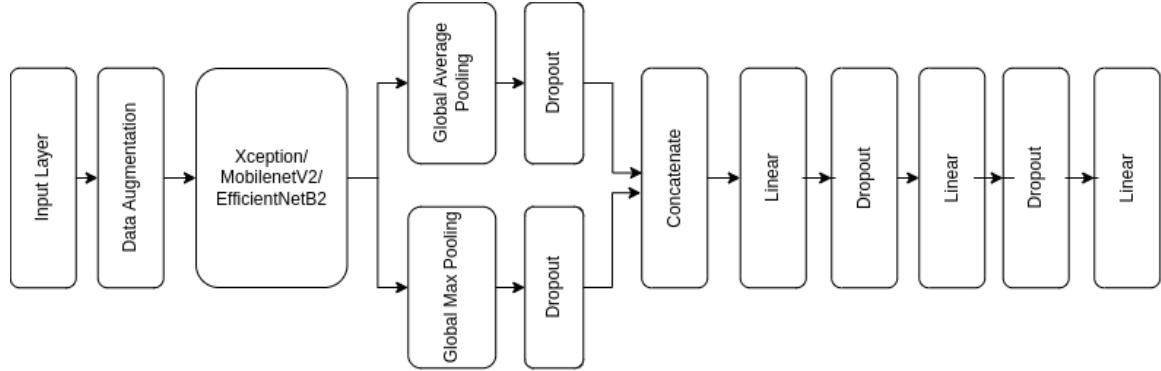


Figure 1: Classifier Structure

3. DATASETS

BioImlab

This data collection contains a total of 6683 Q-band chromosome images, acquired at a BioImlab laboratory at the University of Padova, Italy. The images were obtained by staining the chromosomes with fluorescent dye quinacrine, which concentrates in different regions of the chromosomes, which then appear bright or dark [6]. The data is available at <http://bioimlab.dei.unipd.it>.

CIR

The CIR Dataset was obtained from 65 karyograms at the Medical Genetic Centre and Maternal and Children Metabolic-Genetic Key Laboratory of Guangdong Women and Children Hospital. This dataset contains 2990 G-band chromosomes. The data is available at <https://github.com/CloudDataLab/CIR-Net>.

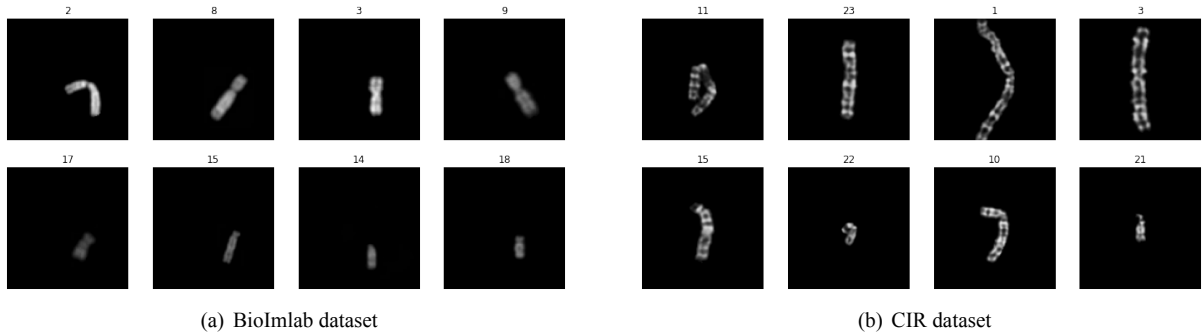


Figure 2: Sample images from datasets

If we take a look at Fig. 2, we can see, that the chromosome images are very different. The chromosomes in the BioImlab dataset vary severely in the chromosome scaling. By looking at the top middle chromosomes in Fig. 2(a), we can notice, that chromosome from class 8 is bigger than the one from class 3, as these two come from other karyotypes. However, this would not be the case, as chromosome 3 is generally longer than chromosome 8. Compared to the CIR chromosomes in Fig. 2(b), the Bioimlab data are also more blurry and the banding patterns are not as easy to spot. default

4. RESULTS

All four models were trained on each dataset with a 75:10:15 train-validation-test ratio in Google Colab environment on an available GPU. Their accuracy overview is listed in Tab. I. We can see, that Xception and Efficientnet score high accuracy for both datasets. However, by ensembling all of the four models

together, we were able to further improve the accuracy by 2.49 % for the BioImlab dataset and by 0.96 % for the CIR dataset.

The best weights combinations for BioImlab were [0.32, 0.24, 0.31, 0.13] and [0.18, 0.19, 0.43, 0.20] for the CIR dataset, with the following order of the models [Xception, Mobilenet, Efficientnet, Resnet]. As we need predictions from all four models to get a final decision, the run-time inference corresponds to a summation of the run-times of each used model. When measured on a Tesla T4 GPU, the run-time of the single models was between 2 and 4 ms per image, whereas the ensembled model took 12 ms per image.

The ensembling method also proved to work well in comparison to results available in other papers. These results were summarized in Tab. II, where our method outperformed the second-best models by 0.6 % and 1.5 % for BioImlab and CIR datasets respectively.

Model	Dataset	Accuracy	Dataset	Accuracy
Xception		91.92 %		96.56 %
MobilenetV2		83.46 %		90.14 %
EfficientnetB2	BioImlab	92.29 %	CIR	95.41 %
ResNet18		84.45 %		94.50 %
Model Ensemble		94.78 %		97.48 %

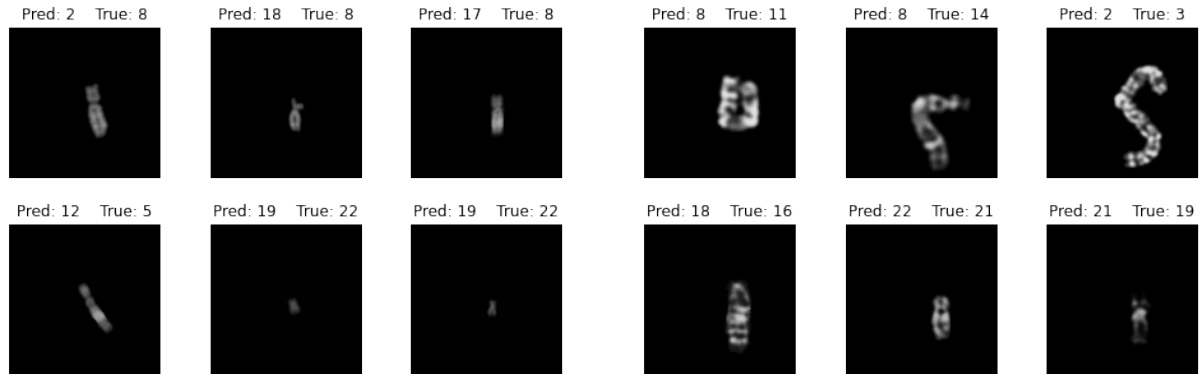
Table I: Model performance on different models

Model	Source	Dataset	Accuracy
Model Ensemble	Ours	BioImlab	94.78 %
VGG19	[2]	BioImlab	94.11 %
SENet50	[3]	BioImlab	92.58 %
Model Ensemble	Ours	CIR	97.48 %
CIR-Net	[4]	CIR	95.98 %
LseNet3733	[3]	CIR	86.11 %

Table II: Model comparison

The problem with the size differences of the same classes in the BioImlab dataset is also visible in Fig. 3(a). The top row shows us three examples of misclassified class 8, which might be hard to classify as the same class even for an inexperienced person. When it comes to misclassification in the CIR dataset shown in Fig. 3(b), it seems, that the biggest challenge is severely bent chromosomes.

For our future work, we would like to further increase the accuracy by adding a siamese neural network after the classification models. Siamese networks are usually trained to measure the similarity between two or more images. As we only have 46 chromosomes to classify when doing karyotyping for single-cell images, the pairs of chromosomes are fairly similar. Our idea behind this is to measure the similarity between more than two images classified as the same class and find a match to the non-matching image among the rest of the images which are missing their pair.



(a) BioImlab dataset - most confusion comes from inconsistent chromosome sizes of the same classes

(b) CIR dataset - misclassified images are often severely bent

Figure 3: Samples of falsely classified chromosome classes

5. CONCLUSION

This paper demonstrated model ensembling as a simple way how to utilize multiple trained models to improve overall accuracy for chromosome classification. We have trained four different convolutional

models separately on two datasets and later found the best weights for their pooling. We were able to achieve 94.78 % accuracy for a BioImlab dataset and 97.48 % accuracy for a CIR dataset. The ensembled model did not only outperformed all of the trained models by at least 2.49 %, and by 0.96 % for the BioImlab and the CIR datasets respectively but also scored the best accuracy compared to results from other papers. In our future work, we would like to further improve the accuracy with siamese neural network during karyotyping by measuring the similarity between misclassified images and matching similar pairs together.

ACKNOWLEDGMENT

This paper and the research behind it would not have been possible without the support of GK SERVIS spol. s.r.o. company.

REFERENCES

- [1] A. P. Britto and G. Ravindran, "A review of cytogenetics and its automation," *Journal of Medical Sciences*, vol. 7, no. 1, pp. 1–18, 2006.
- [2] M. S. Al-Kharraz, L. A. Elrefaei, and M. A. Fadel, "Automated system for chromosome karyotyping to recognize the most common numerical abnormalities using deep learning," *IEEE Access*, vol. 8, pp. 157727–157747, 2020.
- [3] C. Wang, M. Han, Y. Wu, Z. Wang, F. Ma, and J. Su, "CNN based Chromosome Classification Architecture for Combined Dataset," 2021 6th International Conference on Communication, Image and Signal Processing (CCISP), 2021.
- [4] C. Lin, G. Zhao, Z. Yang, A. Yin, X. Wang, L. Guo, H. Chen, Z. Ma, L. Zhao, H. Luo, T. Wang, B. Ding, X. Pang, and Q. Chen, "CIR-NET: Automatic classification of human chromosome based on inception-resnet architecture," *IEEE/ACM Transactions on Computational Biology and Bioinformatics*, pp. 1–1, 2020.
- [5] R. S. Remya, S. Hariharan, V. Vinod, D. J. Fernandez, N. M. M. Ajmal, and C. Gopakumar, "A comprehensive study on convolutional neural networks for chromosome classification," 2020 Advanced Computing and Communication Technologies for High Performance Applications (ACCTHPA), 2020.
- [6] E. Poletti, E. Grisan, and A. Ruggeri, "Automatic classification of chromosomes in Q-band images," 2008 30th Annual International Conference of the IEEE Engineering in Medicine and Biology Society, 2008.
- [7] F. Chollet, "Chapter 13 Best practices for the real world," in *Deep learning with python*, 2nd ed., Greenwich, USA: Manning Publications, 2021, pp. 412–430. ISBN 9781617296864
- [8] F. Chollet "Xception: Deep learning with depthwise separable convolutions." *Proceedings of the IEEE conference on computer vision and pattern recognition*. 2017.
- [9] M. Sandler, et al. "Mobilenetv2: Inverted residuals and linear bottlenecks." *Proceedings of the IEEE conference on computer vision and pattern recognition*. 2018.
- [10] M. Tan, Q. Le "Efficientnet: Rethinking model scaling for convolutional neural networks." *International conference on machine learning*. PMLR, 2019.
- [11] K. He, et al. "Deep residual learning for image recognition." *Proceedings of the IEEE conference on computer vision and pattern recognition*. 2016.
- [12] "Keras API" [online] <https://keras.io/api/>

Matlab Tool for Assistance in Learning English Words Pronunciation

Jan Malucha

Brno University of Technology, Czech Republic

E-mail: xmaluc00@vutbr.cz

Abstract—This paper presents a MATLAB module to assist students in learning the correct pronunciation of individual English words. The measurement of pronunciation correctness is based on evaluation of prosodic speech parameters using three methods. A brief introduction to these prosodic parameters is given, along with a description of the developed tool. Program testing was performed with a native and non-native speaker.

Keywords—speech signal, pronunciation, prosody

1. INTRODUCTION

Verbal communication is one of the key elements of social life. Anglocentrism has been unrivaled in global communication at all levels since the 1990s. The English language has taken on the role of the new lingua franca, whose knowledge determines access to information and opportunities; this trend is likely to continue. However, research by the Czech Statistical Office shows that only 42% of Czech citizens aged 18 to 69 speak English, with most of this percentage having only a basic or minimal knowledge of English [1]. Since most Czech users of English as well as other foreign languages very rarely get an opportunity to converse with a foreign speaker, it can be assumed that the ability to pronounce correctly (and thus communicate verbally) in a foreign language is even lower in the Czech Republic than the reading skills. According to [2], a very narrow space is also devoted to the teaching of pronunciation in education. However, given the growing trend of international connection and the growing importance of English, it makes great sense to focus on teaching pronunciation, which also encourages efforts to develop software tools to support and streamline this teaching. A number of such tools have been developed over the years, with attention given to them in [3] or [4], for example.

2. PROSODY

From the point of view of phonetics, the basic means of speech communication is a continuous sound stream. From the acoustic point of view, it is a vibration of the transmission medium excited by the speech system, but for the analysis of speech signal, it is understood as a chain of noise and tone acoustic components forming individual sounds - vowels. Thus, the vowel is an elementary segment of speech and the suprasegmental segment is a syllable [5]. We then understand prosody as a set of properties of speech signal segments related to the speech modification, or speech flow modulation. This modulation is realized through the so-called modulation factors - accent and rhythm of speech are given by the factor of strength or **energy**, tempo and rhythm are given by the factor of **duration**, tone and intonation are given by the factor of **pitch**. Since there are some typical attributes related to these factors in a language, it is possible to analyze the correctness of the pronunciation by determining these parameters during the speech signal. The meaning of prosody is described in [6]. Statistics of voiced speech can be seen in [7].

3. AIMS

The aim of this paper is to present our MATLAB tool developed for analysis of the input speech signal of a *student's* word along with its processing and evaluation with respect to the correctness of pronunciation. The prosodic criteria on which this analysis is based are **energy**, **duration**, and **pitch**, from which information about speech accent, melody, and length of word segments is derived. Accuracy assessment is based on a comparison with the *lecturer's* reference word. The output for practical usability is simple graphical and verbal feedback to the pronunciation, referring to the accented phonemes, word melody and segment lengths.

4. TOOL DESCRIPTION

The program is based on the method of short-time analysis. At first, the input signal is divided into short-time segments of 20 ms and the processing then takes place individually in these segments, thus achieving the stationarity of the processed speech data. The overall structure is outlined in Fig. 1. Because two signals (*student* and *lecturer*) are compared and the difference in duration of both signals is assumed due to faster or slower speech, both signals are normalized to the percentage axis. The tool itself consists of three main algorithms supported by a number of auxiliary algorithms. It was implemented in MATLAB.

The method used for **energy** analysis is STE (short time energy). This procedure determines the energy of the short-time segment by calculating the power and the sum [8]. It is built into a complex algorithm, the input of which is a speech signal and the output is both a graph of energy along the signal and a table comparing the energies of selected sections of the *student's* and *lecturer's* signal. Thanks to this, it is possible to provide information about the difference of the accent, i.e. accented syllables, between the *student's* and *lecturer's* signals. The **duration** analysis also uses STE methods, this time built into a second algorithm, which identifies voiced, unvoiced and silent sections of the signal by comparing the course of energy over time with experimentally selected thresholds. These parts can be understood as a precursor to phonemes; the algorithm then determines the positions of the voicing transitions in time, compares these transitions for the *student* and *lecturer* signal in the table and gives information about the duration of individual sections. The **tone** along the time axis, i.e. melody, is determined in the third algorithm using the time domain method. Fourier transform including modifications [9] and autocorrelation methods [10] have traditionally been used to estimate frequency in speech. The computational procedure AMDF [11] is used here, which is based on the autocorrelation function. This method is built into an algorithm, the output of which is a graph of the normalized pitch course centered around its mean value. It can clearly show the positions of raises and drops of the voice along the timeline – the up-crossing of the mean value is considered a voice raise, down-crossing indicates the opposite. These increases and decreases are then located, saved and compared in a table for both the *student* and *lecturer* signal, and a brief verbal feedback about the melody is provided to the user.

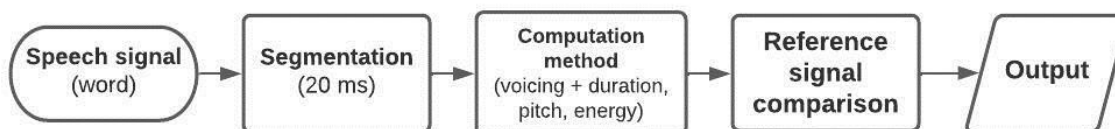


Figure 1: Program flowchart

5. PRACTICAL APPLICATIONS AND RESULTS

The practical significance of the tool lies in the support of independent pronunciation learning of English words without the presence of a teacher. The English language is relatively sensitive to correct intelligibility, and incorrect articulation or duration of the sound can often cause a complete change in the meaning of the word (e.g. the difference between the words “hid” and “heed”). Intonation, as a combination of melody and accent, is also one of the key prosodic properties of language, influencing a whole range of means of expression, such as emphasis and emotion.

Test analysis of these phenomena was performed on the English word “processing”. The recording of this expression, spoken by a native speaker (*lecturer*), is in .mp3 format and has duration of 985 ms. The *student* record is in the same format and has length of 944 ms. For this reason, both signals are fitted to the percentage x-axis. The first parameter analyzed is **duration**. The following graph in Fig. 2 shows the waveforms of the input signals and the division into voiced / unvoiced parts by a thick black line, where a high value indicates voiced parts and low value means unvoiced parts. It provides the *student* with feedback on the duration of individual sections in comparison with the *lecturer*.

Graphic information about the duration of individual parts is supplemented by verbal feedback to the student in the following way: “The first section (unvoiced) is 4% shorter; the second section (voiced) is 4% shorter, the third section (unvoiced) is 2% longer, the fourth section (voiced) is 4% longer, the fifth section (unvoiced) is 2% shorter, the sixth section (voiced) is 3% longer.”

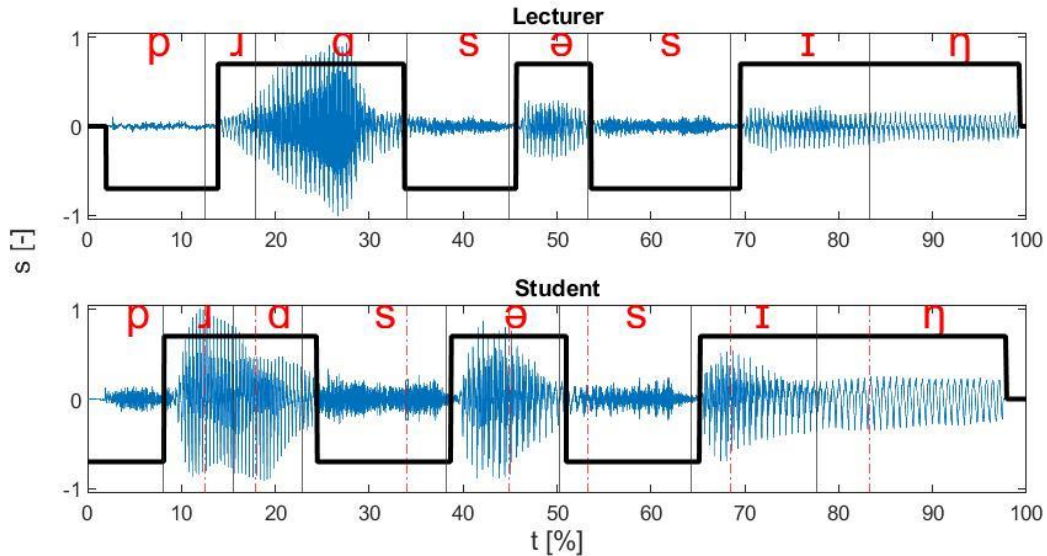


Figure 2: Duration of voiced and unvoiced segments

Energy the accent is another analyzed parameter. The graphs in Fig. 3 show the course of the normalized signal energy, centered around the mean value. This achieves a state where the volume of speech is irrelevant and only the emphasis on individual sounds or syllables is taken into account. The chart also serves as a simple feedback about the accent. Verbal feedback provides the student with information in the following way: “Phoneme /ɹ/ should be unstressed; phoneme /ɪ/ should be unstressed.”

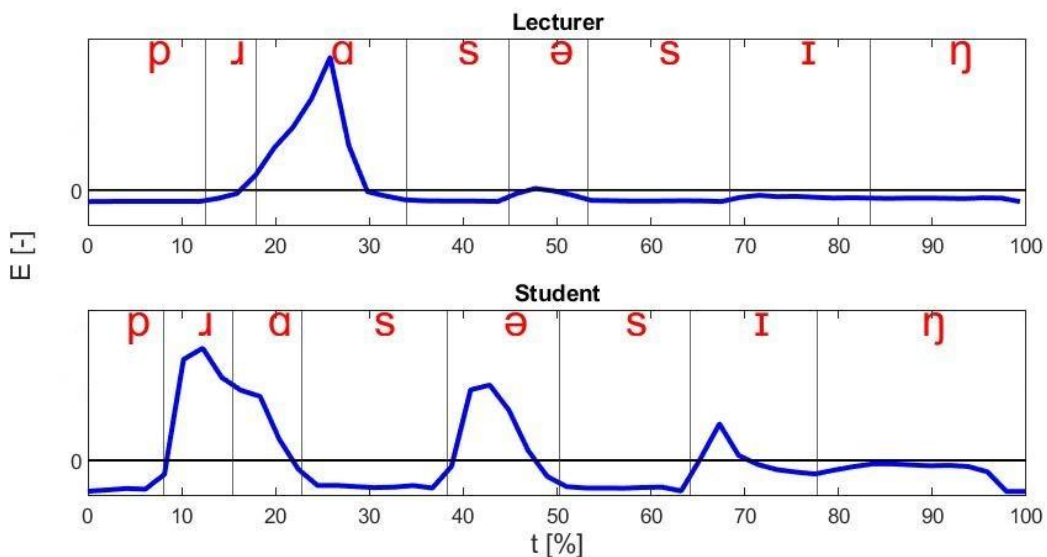
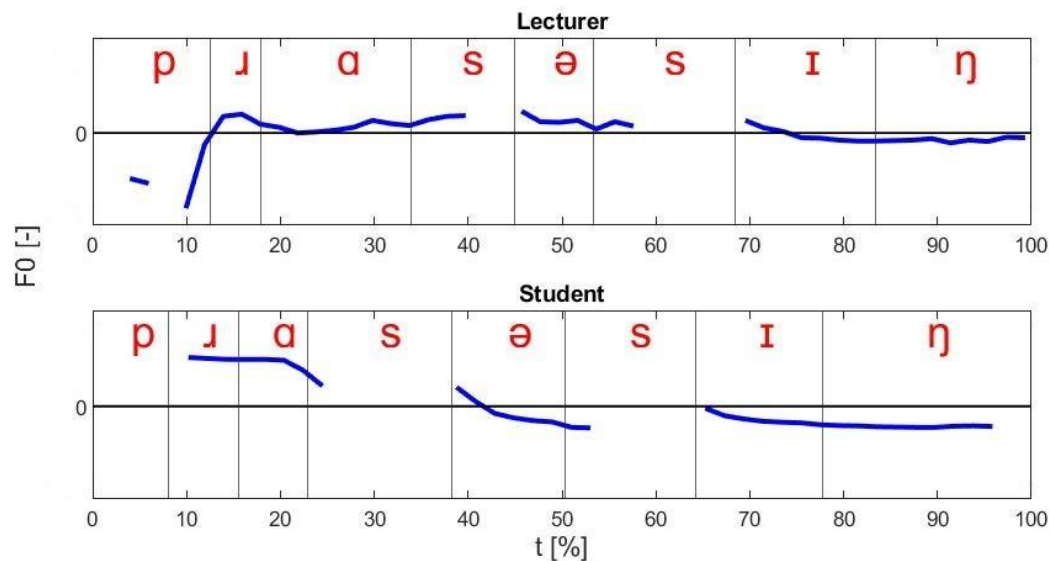


Figure 3: Energy (accent)

The third pronunciation parameter analyzed is pitch. The graphs in Fig. 4 show course of normalized tone and it gives key information about the locations of the raises or drops of the voice. It can be seen that the *lecturer's* signal shows a voice raise around 14% and a voice drop near 78%, yet the *student's* record shows only one voice drop around 44%. The verbal feedback here is: “Voice rise missing at the /ɹ/ phoneme; voice fall missing at the /ɪ/ phoneme; voice fall at the /ə/ phoneme is incorrect.”

CONCLUSION

English places great emphasis on correct pronunciation and intelligibility of speech. However, pronunciation training is often neglected in language learning. The presented program therefore has great potential for increasing the ability of correct pronunciation, both in the form of an integrated module for dictionaries and in the form of a separate teaching tool. The goal of further development will be the extension of other methods of real-time pronunciation control.



The Pathway Analysis of *Tepidimonas taiwanensis* LMG 22826^T, Polyhydroxyalkanoate and Alkaline Protease Producer

K. Heřmánková¹, K. Sedlář¹

¹ Department of Biomedical Engineering, Faculty of Electrical Engineering and Communication, Brno University of Technology, Czech Republic

E-mail: xherma30@vut.cz, sedlar@vut.cz

Abstract—The complete genome sequence of thermophilic type strain *Tepidimonas tawanensis* LMG 22826^T confirmed the earlier statement of its high biotechnological potential. Thanks to its reported ability to produce alkaline proteases and to synthesize polyhydroxyalkanoates (PHA), *T. taiwanensis* is worth our attention. Here, we present further descriptive analysis based on pathways detection which provides us better understanding of the core of such significant properties. This information can be then used in *in silico* modeling approaches. In total, 108 biological pathways were detected, *phaCAB* operon and granule-associated proteins - phasins were found and butanoate pathway comparison with other PHA producing bacteria was provided. Finally, simplified PHA synthesis pathway was introduced.

Keywords—butanoate, metabolism, bioplastics, biotechnology

1. INTRODUCTION

In recent years, the aim is to find ‘eco-friendly’ alternatives to plastics that will not be derived from petrochemicals as they are now. Promising candidates for such purposes are biodegradable, biocompatible, and renewable polymers - polyhydroxyalkanoates (PHA) that have become popular and widely studied substances. PHA are produced by a wide range of bacteria, archaea, and even plants. Most interest is dedicated to synthesis of PHA by bacteria where the production relates to a response to a limited number of essential substrates. PHA then serve as the source of energy and help bacteria to survive in less prosperous conditions [1].

To decrease the costs of PHA production, one of the approaches is a synthesis by thermophilic bacteria. These bacteria are capable of living in higher temperatures and can produce PHA in these contamination free conditions [2]. The process can be then less cost demanding.

In this paper, we provide insight into such process in the thermophilic bacterium *Tepidimonas tawanensis* LMG 22826^T.

2. MATERIALS AND METHODS

The genome of type strain *T. taiwanensis* can be obtained from the GenBank under the accession number CP083911.1. Additional two bacteria, *Shlegelella Thermodepolymerans* DSM 15344 and *Aneurinibacillus Thermoaerophilus* CCM 8960, with accession numbers CP064338.1 and CP080764.1, respectively, were used for comparison. KEGG-related tools [3] were used for the analysis such as KEGG PATHWAY for identification of pathways by searching for homologous genes. Phasin proteins were found using KEGG GENES, the comparison of bacteria pathways was formed with Reconstruct tool in KEGG Mapper, and the final pathway of PHA synthesis was created in PathVisio software [4].

3. RESULTS AND DISCUSSION

Overall, 108 pathways were labeled as present in *T. taiwanensis*. As it was expected, ‘Metabolism’ derived pathways make approximately 80% of detected pathways. Other pathways were assigned to ‘Environmental Information Processing’, ‘Cellular Processes’ or ‘Genetic Information Processing’.

group’.

3.1. PHA PRODUCTION

The ability to produce PHA by *T. tawanensis* LMG 22826^T was already experimentally proved with the cultivation of bacterium on grape pomace extract with the highest use of glucose and fructose as sources of carbon [5]. A member of the PHA family, polyhydroxybutyrate (PHB) was found to be synthesized, precisely 3-hydroxybutyrate (3HB) [5] which has potential to be used in a wide range of applications from plastics to the medical industry.

3.2. BUTANOATE METABOLISM PATHWAY

Main steps of the PHA production are included in a butanoate metabolism pathway. To compare the PHA synthesis apparatus on genome level, butanoate metabolism pathways of three PHA producing bacteria were merged into a single pathway, see Figure 1. The pathway consists of rectangles being enzymes, arrows expressing metabolic reactions, and dots standing for other molecules. White rectangles are gene products that weren’t found in bacterial genomes and the colored ones were present. Green, pink, and blue rectangles define enzymes found in *T. taiwanensis* LMG 22862^T, *S. thermodepolymerans* DSM 15344, and *A. thermoaerophilus* CCM 8960, respectively.

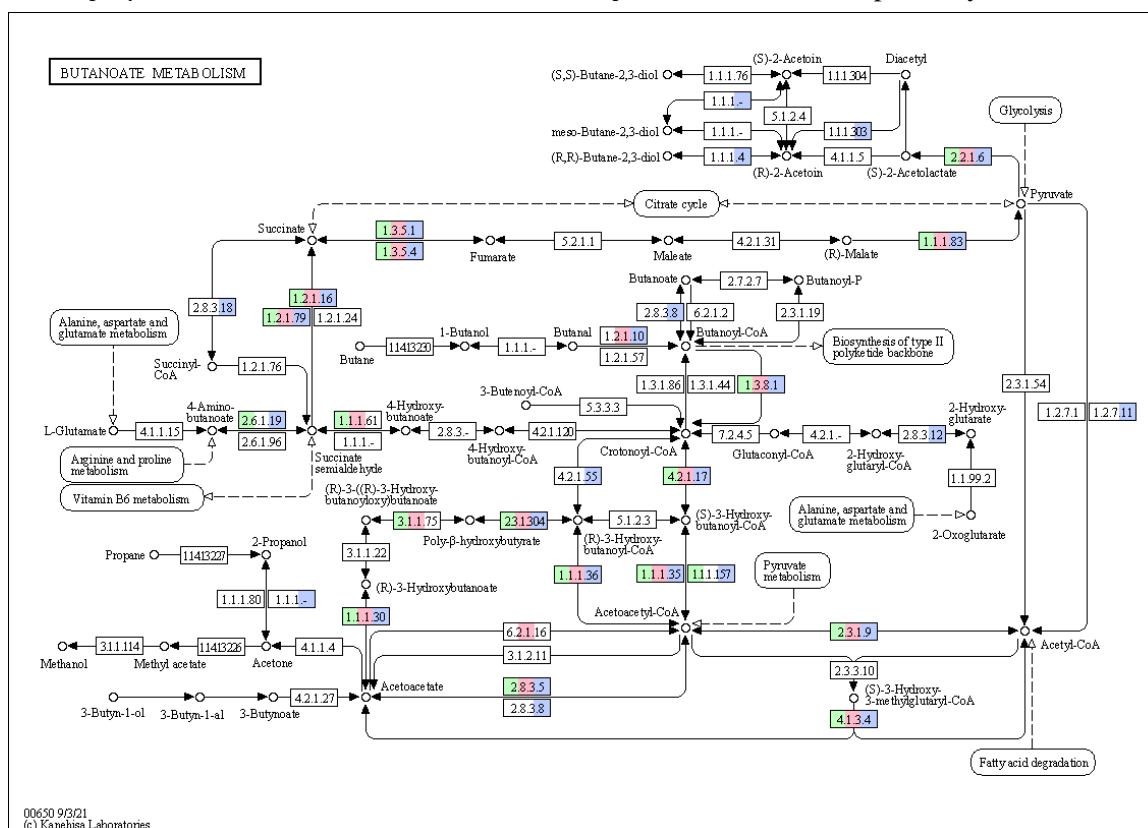
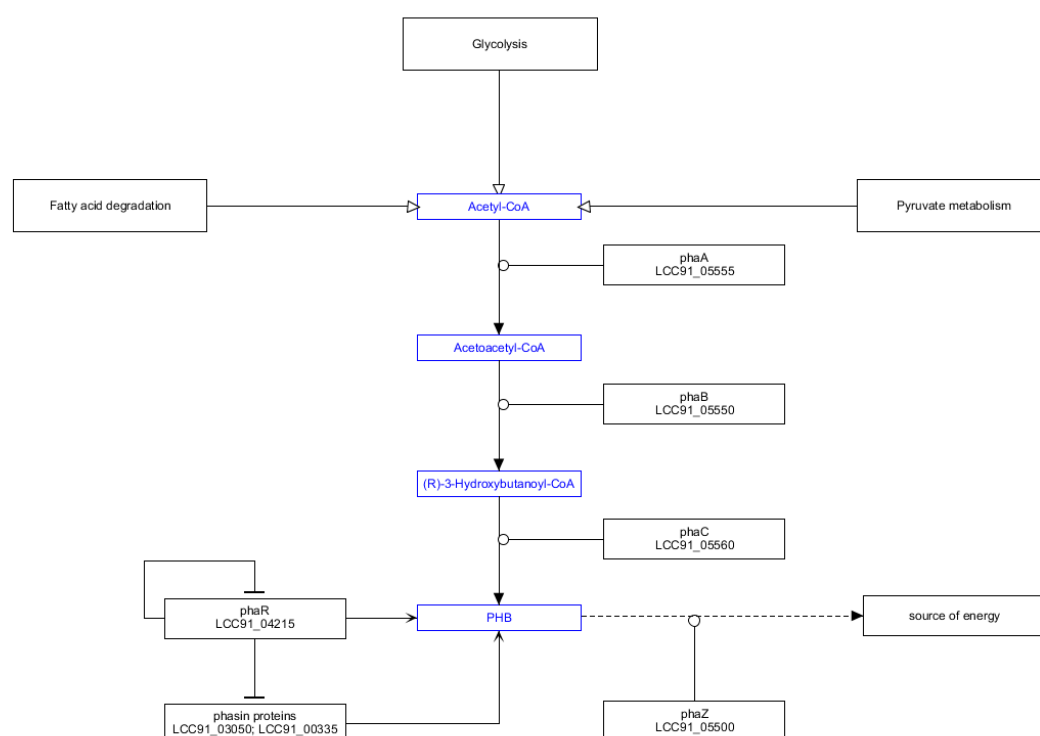


Figure 1: Butanoate metabolism pathway comparison of three PHA producing bacteria. Green, pink, and blue color define enzymes found in *T. taiwanensis* LMG 22862^T, *S. thermodepolymerans* DSM 15344, and *A. thermoaerophilus* CCM 8960, respectively.

At first sight, the difference between the third mentioned bacterium is significant in comparison to the difference between the first two bacteria. As the main variation can be considered the lack of *phaZ* (Enzyme Commission number - EC:3.1.1.75) gene encoding PHA depolymerase enzyme. This enzyme has been reported to have a significant impact on PHA maintenance in a cell [6], because it generally serves as a decomposing machinery of PHA granules in case of a starving bacterium. In fact, *A. thermoaerophilus* CCM 8960 owns gene coding PHA depolymerase as was detected recently [unpublished results]. Similarly, for the first two bacteria, it seems that the only source of *acetyl-CoA* and/or *acetoacetyl-CoA*, the main chemical compounds in PHA synthesis process, is pyruvate metabolism and fatty acid degradation, respectively. However, deeper insight revealed that there is an

alternative pathway in the glycolysis which can convert *pyruvate* to *acetyl-CoA*, but it isn't included in this pathway. This fact can be somehow limiting, and we should be still skeptical when we are using such predictive tools.

Besides already reported *phaC* gene encoding PHA synthase, *acetyl-CoA acetyltransferase* (*phaA* gene – LCC91_05555) and *acetoacetyl-CoA reductase* (*phaB* gene – LCC91_05550) was found in *T. taiwanensis* genome. These genes together form an operon marked as *phaCAB* which is responsible for the chain of reactions that leads to PHA production. Further, *T. taiwanensis* genome possesses depolymerase encoded in *phaZ* gene and *phaR* gene known as transcriptional repressor. The *phaR* gene can be also found as a subunit of PHA synthase class IV where serves as an essential part of synthesis machinery [2]. The role of *phaR* gene seems to be also important for the PHA synthesis of other classes because the lack of this gene was shown to lead to increased or even stopped production of these granules [1]. Basically, *phaR* gene autoregulates itself in the mean of repressor and it also represses the production of granule-associated proteins known as phasins [1]. With this knowledge, the genome was additionally searched for phasins. Two proteins were successfully detected as phasin family proteins (LCC91_00335, LCC91_03050).



3.3. ALKALINE PROTEASES

genome assembly [8]. The genome sequence revealed the presence of genes coding many alkaline proteases but only three of them encoded for extracellular proteases that are used in many industries, such as detergent or medical industry [9].

Only one of these three alkaline proteases was detected in a pathway. Serine protease (EC 3.4.20.107), as a product of *degP/htrA* gene (LCC91_09805), manages proteolysis of misfolded proteins in periplasm. This gene is a part of Two-component system pathway which provides a connection of an outer environment with an intracellular one. Unfortunately, connection of serine protease with the outer environment is missing. In that case, further understanding of the process responsible for producing the serine protease by *T. taiwanensis* remains hidden and additional experiments will be needed.

Apart from serine protease, the genome of *T. taiwanensis* also has the gene encoding lysyl endopeptidase (LCC91_10460, EC:3.4.21.50) and protease IV (LCC91_01535, EC:3.4.21.-). The first mentioned is produced by many bacteria and has been already selling as a commercial product and protease IV has suitable properties for usage in the detergent industry [8].

4. CONCLUSIONS

This paper aimed to provide deeper insight into mechanisms that induce such biotechnological potential of *Tepidimonas taiwanensis* LMG 22862^T. The pathway detection revealed 108 pathways, the most of them belonging to 'Metabolism' pathway group. Further, phasin proteins were found in the genome, as well as genes that completed the *phaCAB* operon and corresponding locus tags were reported. Finally, the simplified pathway of PHA synthesis by this bacterium was introduced and can also serve as the knowledge base for possible modeling purposes.

REFERENCES

- [1] M. Pötter and A. Steinbüchel, "Poly(3-hydroxybutyrate) Granule-Associated Proteins: Impacts on Poly(3-hydroxybutyrate) Synthesis and Degradation†," *Biomacromolecules*, vol. 6, no. 2, pp. 552–560, Mar. 2005, doi: 10.1021/BM049401N.
- [2] S. Obruča *et al.*, "Polyhydroxyalkanoates synthesis by halophiles and thermophiles: towards sustainable production of microbial bioplastics," *Biotechnology Advances*, p. 107906, Jan. 2022, doi: 10.1016/J.BIOTECHADV.2022.107906.
- [3] M. Kanehisa and S. Goto, "KEGG: kyoto encyclopedia of genes and genomes," *Nucleic acids research*, vol. 28, no. 1, pp. 27–30, Jan. 2000, doi: 10.1093/NAR/28.1.27.
- [4] M. Kutmon *et al.*, "PathVisio 3: An Extendable Pathway Analysis Toolbox," *PLOS Computational Biology*, vol. 11, no. 2, p. e1004085, 2015, doi: 10.1371/JOURNAL.PCBI.1004085.
- [5] X. Kourilova *et al.*, "Biotechnological Conversion of Grape Pomace to Poly(3-hydroxybutyrate) by Moderately Thermophilic Bacterium *Tepidimonas taiwanensis*," *Bioengineering 2021, Vol. 8, Page 141*, vol. 8, no. 10, p. 141, Oct. 2021, doi: 10.3390/BIOENGINEERING8100141.
- [6] S. Arias, M. Bassas-Galia, G. Molinari, and K. N. Timmis, "Tight coupling of polymerization and depolymerization of polyhydroxyalkanoates ensures efficient management of carbon resources in *Pseudomonas putida*," *Microbial Biotechnology*, vol. 6, no. 5, pp. 551–563, Sep. 2013, doi: 10.1111/1751-7915.12040.
- [7] T. L. Chen, Y. J. Chou, W. M. Chen, B. Arun, and C. C. Young, "*Tepidimonas taiwanensis* sp. nov., a novel alkaline-protease-producing bacterium isolated from a hot spring," *Extremophiles*, vol. 10, no. 1, pp. 35–40, Feb. 2006, doi: 10.1007/S00792-005-0469-9/TABLES/2.
- [8] K. Hermankova *et al.*, "Complete Genome Sequence of the Type Strain *Tepidimonas taiwanensis* LMG 22862^T, a Thermophilic Alkaline Protease and Polyhydroxyalkanoate Producer," *Genome Biology and Evolution*, vol. 13, no. 12, Dec. 2021, doi: 10.1093/GBE/EVAB280.
- [9] R. Gupta, Q. Beg, and P. Lorenz, "Bacterial alkaline proteases: molecular approaches and industrial applications," *Applied Microbiology and Biotechnology 2002 59:1*, vol. 59, no. 1, pp. 15–32, 2002, doi: 10.1007/S00253-002-0975-Y.

NXP SEMICONDUCTORS CZECH REPUBLIC



NXP Semiconductors se zabývá vývojem a výrobou mikroprocesorů a analogových součástek pro automobilový a spotřební průmysl, počítačové sítě a bezdrátové komunikace. V České republice je společnost NXP Semiconductors zastoupena vývojovými centry v Rožnově pod Radhoštěm a Brně. V moderních laboratořích pracuje mezinárodní tým čítající více než 300 odborníků z oblastí **Vision, SW Tools, Multicore, Motor Control, Security and Connectivity, Embedded Software, Operating Systems, Analog Products, Customer Support, Software Validation and Verification, Industrial Connectivity, Pricing a Marketing** a v neposlední řadě **zákaznické centrum spolu s technicko-obchodním oddělením.**

Kariéra ve firmě NXP znamená krok do budoucnosti – jak profesně, tak osobnostně. Společnost NXP je globálním hráčem v oblasti technologie a vývoje aplikací, měnících náš každodenní život. Náš tým tvoří ambiciózní profesionálové, pracujících v mezinárodním prostředí. **Hledáme nové, motivované a talentované kolegy, kteří se spolu s námi postaví výzvám budoucího vývoje v otevřeném prostředí, které firma NXP nabízí.**



NXP SEMICONDUCTORS CZECH REPUBLIC

Hledáme talentované STUDENTY



Právě nabíráme na tyto studentské pozice:

Embedded HW/SW Developer – Rožnov, Brno

SW Technical specialist – Brno

Embedded SW Developer – Rožnov

Systems Engineering Intern – Rožnov, Brno

SW R&D MICR Intern – Rožnov/Brno

ML/AI SW Intern – Rožnov/Brno

Audio Linux Framework Intern - Brno

Studentům nabízíme:

Práci na reálných projektech, technický mentoring

Výborné mzdové ohodnocení a časovou flexibilitu

Pomoc s bakalářskou, diplomovou či disertační prací

Spolupráci s kapacitami svého oboru

michaela.latiokova@nxp.com

www.nxp.com/czechrepublic

Zajímáte se o:

Vývoj Emb. Aplikací

**Strojové učení/umělá
inteligence**

Internet of Things

**Vývoj validačních /
testovacích technologií**

SW Konfigurační nástroje

**AUTOSAR a multicore
řešení**

*Embedded operační
systémy*

**Security v embedded
systémech**



Quantification of a Wet Antenna Attenuation for a Measurement of Rainfall Intensity via the Metropolitan Network of Microwave Links in 10 GHz Band

Milan Bubniak¹ and Petr Musil¹

¹Department of Telecommunications, Brno University of Technology, Czech Republic

E-mail: xbubni03@vutbr.cz, xmusal56@vutbr.cz

Abstract—Commercial microwave links can be utilized as an effective sensor network for a rainfall measurement. However, there are various obstacles that must be overcome, from which the most significant seems to be an effect of wet antenna attenuation. In this paper, the rainfall calculation has been performed in both a single-link way and an area calculation via the RAINLINK algorithm on the group of real 10 GHz metropolitan microwave links. Conclusion summarizes the resulting wet antenna attenuation values and evaluates the performed measurement.

Keywords—microwave link, commercial telecommunication network, precipitation, rainfall, wet antenna attenuation, rain intensity, rain gauge, meteorological radar, RAINLINK

1. INTRODUCTION

Measurement of rainfall by a network of commercial point-to-point microwave links seems to be a promising way to further refine existing meteorological precipitation measurement methods. Figure 1 shows a simplified diagram of the measurement principle. P_t is a transmitted electromagnetic power and P_r is a received electromagnetic power, while A_0 is a sum of a general attenuation due to a free-space path loss, wave reflection, diffraction etc., and A is an investigated attenuation due to rainfall (in fact it is a combination of a raindrops electromagnetic scattering and absorption and a wet antenna attenuation).

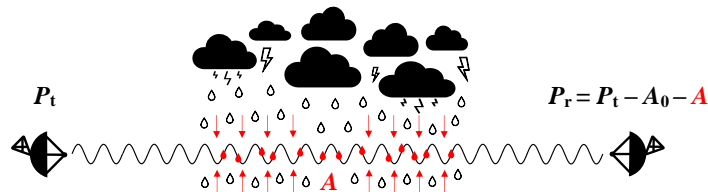


Figure 1: Simplified diagram of the measurement of a rainfall by a point-to-point microwave link

Regarding the state of the research, Dutch researchers R. Uijlenhoet, A. Overeem, and H. Leijnse are one of the first and most active contributors in this area. They have published a number of papers and conducted several practical experiments and were the first to write the RAINLINK algorithm [3] which source code is publicly available. In 2018, they published a comprehensive paper summarizing then current research in the field [1]. Other active researchers in this field are the Germans Ch. Chwala and H. Kunstmann who among other papers and experiments also published a summary paper in 2018 reviewing the whole research [2].

The most significant current challenge in the field of rainfall measurement by microwave links is the effect known as a wet antenna attenuation (WAA). [1, 2, 7] It is the attenuation caused by a thin layer of water which forms during the rains on the radome cover of the antenna. No model or method of calculating this phenomenon has been widely standardized so far due to missing need for WAA behavior specification until the beginning of experimentation with the measurement of rainfall by microwave links.

One of the researchers group which deal with the issue of WAA and precipitation attenuation in general are P. Valtr, P. Pečač, M. Fencel, V. Bareš and J. Pastorek from CTU in Prague. Among the papers they published there is the one [4] on quantifying of WAA on microwave links operating in Prague at frequencies around 38 GHz. Next paper specifies [5] on the basis of empirical measurements based on the same methods on links operating at 32 GHz a new model for determining WAA, given as a function

of rain intensity R . Other paper confirms the significant underestimation of the calculated theoretical attenuations according to the ITU-R P.838 recommendation compared to the measured values [6], even when the calculation of the distance factor r according to ITU-R P.530 recommendation is included. The difference is due to the lack of WAA compensation. The last cited paper compares the accuracy of precipitation measurements through the microwave network in Prague [7], using two methods of WAA compensation, with data validation against rain gauges and urban runoff sensors. The first method of compensation is WAA given by a constant value. The second way is to use the rain intensity function R from the research in the previous article [5]. The results show that the use of a constant WAA value leads to less accurate results with underestimating the intensity of light rains and overestimating the intensity of heavy rains. The use of the function led to relatively accurate predictions of precipitation totals validated from values of water runoff in a given river catchment area.

2. PRINCIPLE

The most common method of calculating rainfall from microwave signal attenuation is via the expression of rain intensity R from the power-law equation for calculating rainfall attenuation A according to ITU-R P.838 [8]. This equation is an empirical approximation of the derived equations based on the complex scattering function of raindrops and spectrum of raindrops. Then the following applies to the intensity R :

$$R = \sqrt[\alpha]{\frac{A}{k \cdot d}} \quad (1)$$

where R denotes rain intensity in mm/h, A means attenuation due to rainfall in dB, d is a link path length in m, and α with k are empirical dimensionless coefficients gathered from table depending on frequency. However, the ITU-R P.838 was originally designed only for use in methods for a prediction of rain attenuation and it does not take WAA into account in any form.

The general procedure for measuring rainfall by microwave links is much more complex and consists of the following sequence of steps: 1. acquisition of input data, 2. identification of rain events, 3. determination of the reference value, 4. calculation of rain intensity, 5. data interpolation, 6. output generation [1].

3. SINGLE LINK MEASURES

First, a manual single calculations of rainfall was performed for four commercial microwave links in Prague operating in 10 GHz free frequency band. The aim was to measure the level of attenuation by the WAA on these particular links. All of the links used antennas with a diameter of 0.6 m on both sides of the link and three of them operated with vertical and one with horizontal polarization. The average values of the received signal power for an intervals of 5 minutes are used for the calculation, from which the average value of rain intensity R for these intervals is calculated according to equation 1. The 5-minute intensities thus obtained are then integrated into hourly rainfall totals in a floating time window of 5 minutes. Apart from the net value of the rainfall total, the value affected by the application of the distance factor r described in ITU-R P.530 is also calculated. These rainfall totals are validated by totals from the MERGE2 precipitation estimation system operated by Czech Hydrometeorological Institute (CHMI) at both endpoints A and B of the given microwave link. The choice of the WAA value was made empirically so that the calculated rainfall total with factor r correlates as much as possible with at least one of the endpoint (A and B) rainfall courses from the MERGE2 application. A simple WAA model was chosen for this measurement, based on percentage calibration of each link.

Table I: Single measurements of rainfall totals validated against totals from the MERGE2 – WAA calibration event

Link	Total · r (mm)	Total (mm)	MERGE A (mm)	MERGE B (mm)	R^2 with A (-)	R^2 with B (-)	WAA (%)	WAA (dB)	d (km)
1	10.4	13.1	9.8	9.4	0.92	0.94	65	1.28	3.28
2	10.5	13.2	10.0	9.3	0.91	0.93	63	1.30	3.41
3	10.9	13.0	11.5	9.8	0.87	0.93	60	1.47	6.14
4	15.3	17.7	12.6	9.4	0.87	0.92	60	1.80	6.85

As can be seen in Table I, size of the fraction indicating, what percentage is attributable to WAA (and rain attenuation), was determined for each link on selected calibration rain event. The table also shows the WAA absolutes. The percentages are between 60 and 65 %, while the absolute values are ranging between 1.28 and 1.80 dB. In the next Table II, the percentages obtained from Table I have been made immutable and they have been verified on another rain event. It can be seemed while WAA absolutes are different, ranging between 1.23 and 1.63 dB, the microwave rainfall totals still show a good correlation with CHMI measurements.

Table II: Single measurements of rainfall totals validated against totals from the MERGE2 – WAA validation event

Link	Total · r (mm)	Total (mm)	MERGE A (mm)	MERGE B (mm)	R ² with A (-)	R ² with B (-)	WAA (%)	WAA (dB)	d (km)
1	21.8	27.1	21.6	18.6	0.91	0.95	65	1.35	3.28
2	21.4	26.6	21.8	19.1	0.93	0.94	63	1.23	3.41
3	25.1	28.2	22.2	21.1	0.93	0.95	60	1.63	6.14
4	18.5	21.8	20.2	12.8	0.93	0.88	60	1.33	6.85

4. AREA RAINFALL MEASUREMENT

For an area measurement the *RAINLINK: Retrieval algorithm for rainfall mapping from microwave links in a cellular communication network* [3] was used. It is a set of functions and scripts written in R language publicly available on [GitHub](#). Since original RAINLINK with its configuration values is meant to be used with microwave links from cellular networks with paths covering large areas, several adjustments of parameters were done mainly to the interpolation method of ordinary kriging which is used in the calculation. For the purposes of this paper a custom interpolation grid was created, measuring 35×35 km and completely covering the territory of Prague and the surrounding areas with a spatial resolution of 100 m. Therefore the generated interpolation grid for Prague contains a total of 122 500 interpolation polygons and covers an area of 1 225 km². Of the available set of 127 links located in the Prague metropolitan area, only 39 were left in the final phase for calculation in the RAINLINK. This significant decrease was caused by filtering links whose received signal data was not usable for the RAINLINK input, in almost all cases due to significant short-term fluctuations in received signal power with strong correlation to unit temperature. Locations of the four precipitation gauges operated by CHMI, labeled as A, B, C, and D, against which results were validated, are shown in the left part of Figure 2. Locations of the microwave links included in the calculation are displayed too but slightly randomly shifted due to the protection of the provider's sensitive data, thus they are not at the exact coordinates.

The RAINLINK allows WAA compensation by only a constant value applied to all links included in the calculation. Therefore this value was empirically set to 1.55 dB which approximately corresponds to the values in the Tables I and II. Furthermore, variogram of the kriging interpolation was adjusted to suppress the highest local extremes.

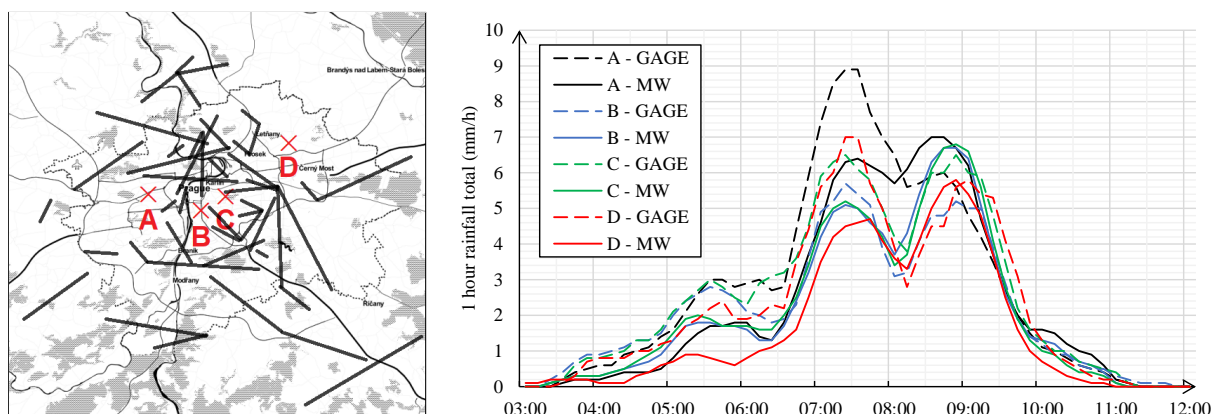


Figure 2: Left: Locations of the link paths and gauges; Right: Rainfall courses of the calculated data and gauges

One of the calculated rain events in Prague took place on 1th of August 03:00 – 1th of August 2021 12:00 UTC. It was a medium convection rain with a double top. The time courses of the calculated interpolated values from RAINLINK were read on the positions of the A, B, C, D gauges. These and the gauges courses are shown in the comparison in the right part of the Figure 2. Good matches of the microwave courses with CHMI gauges can be observed with R^2 value ranging between 0.93 and 0.97 for the all four gauges locations. Also, the gauges A and D, where the highest differences between microwave data and gauges can be seen, are located in the areas where the link network is rather sparse, so in these locations microwave data depends more on the performed interpolation and they have higher estimation character.

5. CONCLUSION

When compensating WAA during the manual calculation, slightly different WAA values were obtained for each link, ranging from 1.23 dB to 1.80 dB. For measurement in this paper, simple method of WAA quantification model based on setting a percentage of the total attenuation individually for each link was created. Therefore, this model is bounded to rain intensity R . Despite the simplicity of the method, a comparison with another rain event showed that satisfactory results could be obtained. Overall, correlation coefficients ranging between 0.87 and 0.95 were achieved.

During the area rainfall measurement using the RAINLINK algorithm, a high agreement with the rain gauges was achieved on the rain gauges located in the areas densely covered by links (gauges B and C).

It can be assumed that due to varying values across the links the WAA can be also linked to the physical state of a particular link, e.g. aging of the radom antenna cover etc. These results leads to a proposal of a WAA compensation method based on an individual WAA calibration for each link by a rain event with a known course of precipitation (e.g. from CHMI data). Currently there are no other studies on WAA on the microwave links operating in 10 GHz frequency band against which a comparison could be made.

ACKNOWLEDGMENT

This project was supported by company CBL Communication by light s.r.o. which provided access to the recorded parameters of its Prague commercial microwave links for the purposes of this work.

REFERENCES

- [1] R. Uijlenhoet, A. Overeem, and H. Leijnse, “Opportunistic remote sensing of rainfall using microwave links from cellular communication networks”, *WIREs Water*, vol. 5, no. 4, 2018, doi: [10.1002/wat2.1289](https://doi.org/10.1002/wat2.1289).
- [2] C. Chwala and H. Kunstmann, “Commercial microwave link networks for rainfall observation: Assessment of the current status and future challenges”, *WIREs Water*, vol. 6, no. 2, 2019, doi: [10.1002/wat2.1337](https://doi.org/10.1002/wat2.1337).
- [3] A. Overeem, H. Leijnse, and R. Uijlenhoet, “Retrieval algorithm for rainfall mapping from microwave links in a cellular communication network”, *Atmospheric Measurement Techniques*, vol. 9, no. 5, pp. 2425-2444, 2016, doi: [10.5194/amt-9-2425-2016](https://doi.org/10.5194/amt-9-2425-2016).
- [4] M. Fencl, P. Valtr, M. Kvicera, and V. Bares, “Quantifying Wet Antenna Attenuation in 38-GHz Commercial Microwave Links of Cellular Backhaul”, *IEEE Geoscience and Remote Sensing Letters*, vol. 16, no. 4, pp. 514-518, 2019, doi: [10.1109/LGRS.2018.2876696](https://doi.org/10.1109/LGRS.2018.2876696).
- [5] P. Valtr, M. Fencl, and V. Bares, “Excess Attenuation Caused by Antenna Wetting of Terrestrial Microwave Links at 32 GHz”, *IEEE Antennas and Wireless Propagation Letters*, vol. 18, no. 8, pp. 1636-1640, 2019, doi: [10.1109/LAWP.2019.2925455](https://doi.org/10.1109/LAWP.2019.2925455).
- [6] P. Valtr and P. Pechač, “On Distance Factor in Rain Attenuation Predictions”, in *2019 13th European Conference on Antennas and Propagation (EuCAP)*, 2019.
- [7] J. Pastorek, M. Fencl, J. Rieckermann, and V. Bareš, “The importance of adequate correction for the wet antenna effect when predicting urban rainfall-runoff using microwave link data”, *AGU Fall Meeting 2020*, 2020, doi: [10.13140/RG.2.2.33571.48168](https://doi.org/10.13140/RG.2.2.33571.48168).
- [8] ITU-R P.838-3: Specific attenuation model for rain for use in prediction methods. Geneva: International Telecommunication Union, 2005.

CubeSat Demonstrator for Educational Purposes

M. Košút and A. Povalač

Department of Radio Electronics

FEEC, Brno University of TEchnology, Technická 12, Brno, Czech Republic

E-mail: 203263@vut.cz, povalac@vutbr.cz

Abstract—This paper describes the design of a CubeSat with a 1U (10x10x10 cm) size, which will be used in laboratory tasks. It includes six photovoltaic cells, mounted on the top of its mechanical construction. Cells will produce electricity to power all systems and to charge the onboard NiMH batteries to make the CubeSat independent of other sources of energy. The proposed design of an onboard computer combined with a communication system and an electrical power supply system is based on off-the-shelf components. Students will make other subsystems, which will communicate with the built-in onboard computer which will handle incoming data. Modularity, possible future expandability, and easy repair in case of any failure were the key optimization parameters of the design.

Keywords—CubeSat, onboard computer, communication system, electrical power supply

1. INTRODUCTION

The goal of this paper is to describe the design of a 1U sized CubeSat suitable for demonstration purposes in the laboratory. To make CubeSat expendable and easily repairable in the future, the design must meet requirements such as using component packages that are big enough to replace them or making the systems modular and based on off-the-shelf components easily available on the market. On top of the designed subsystems, students will create their custom block, which will be connected to the system bus pin header. This concept is great for education, because students can earn experience from many areas, such as electrical and PCB design, firmware debugging or project management, in the case of working in a group. The onboard computer will save the data from all subsystems interconnected with an RS485 differential communication bus to the onboard EEPROM memory and transmit them via ISM 433 MHz band communication system to the ground station, connected to a PC for later analysis.

2. CUBESAT SYSTEMS

In general, CubeSat consists of several subsystems that are necessary to be fully functional as a unit. The main subsystems used in CubeSats are [1] [2]:

- Onboard computer (OBC) – control of all CubeSat operations and saving measured data through digital communication interfaces such as RS485, CAN, SPI, I2C, etc.
- Communication system (COM) – communication with a ground station; frequency and communication speed are determined by the requirements of the CubeSat mission.
- Electrical power supply (EPS) – the main function is to generate, store and distribute different voltages across the main system bus; used mainly photovoltaic cells are used for power generation due to size constraints, Lithium or Nickel Metal Hydride batteries are used for energy storage.
- Attitude determination and control system (ADCS) – position determination and control of the CubeSat; composed of sensors used to determine location and position change relatively to Earth or stars, position change is completed through magnetorquers which are interacting with Earth's magnetic field or heavy rotating wheels each one in one axis.
- Payload – the main purpose of the CubeSat mission; typically some experiment, science research, earth monitoring, testing new systems developed for large space missions etc.

3. EPS DESIGN

The block diagram of EPS design is shown in Figure 1. Energy from six photovoltaic cells is stored in three Nickel Metal Hydride (Eneloop) batteries connected in series. Batteries are protected against a short circuit with 1.5 A recoverable fuses. Charging and discharging currents are measured with hall-effect current sensor MCA1101-05-3, which has a linear convert characteristic.

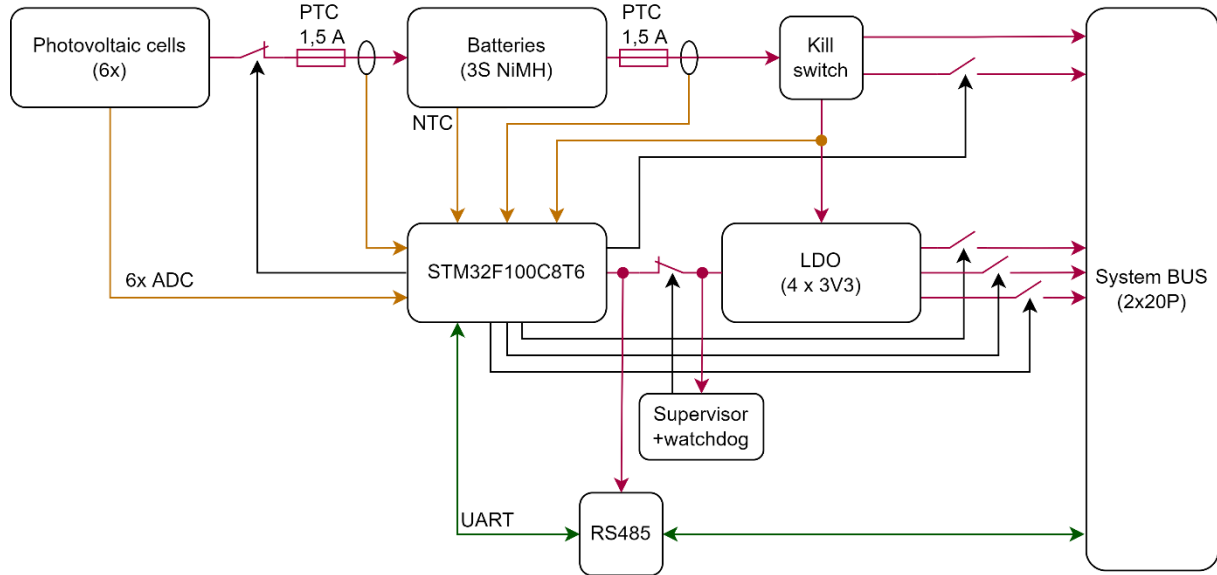


Figure 1: Block diagram of EPS

The main power rail is disconnected through a Kill switch, in case CubeSat is in a deployer, not deployed into a free space yet. It is a simple switch that disconnects all systems from the power using a P-channel MOSFET. Unregulated battery voltage is divided into four 3.3 V power rails regulated with low dropout regulators. Each power rail is proposed for one CubeSat subsystem. The power rail that powers the EPS is connected to a supervisor IC with a watchdog, in case of MCU failure it will be restarted. The main EPS microcontroller is STM32F100C8T6, which monitors all photovoltaic cell voltages, battery voltage, charging and discharging currents and temperature of the battery through 10 channels of the built-in ADC. In case of excess current drain from the battery, the MCU can disconnect any power rail connected to the system bus connector. The system bus is a simple 2x20 pin stack-through header.

The MCU will send all measured values and current states of the EPS to the OBC through the RS485 bus. **Figure 2** shows a 3D model of the designed two-layer PCB.

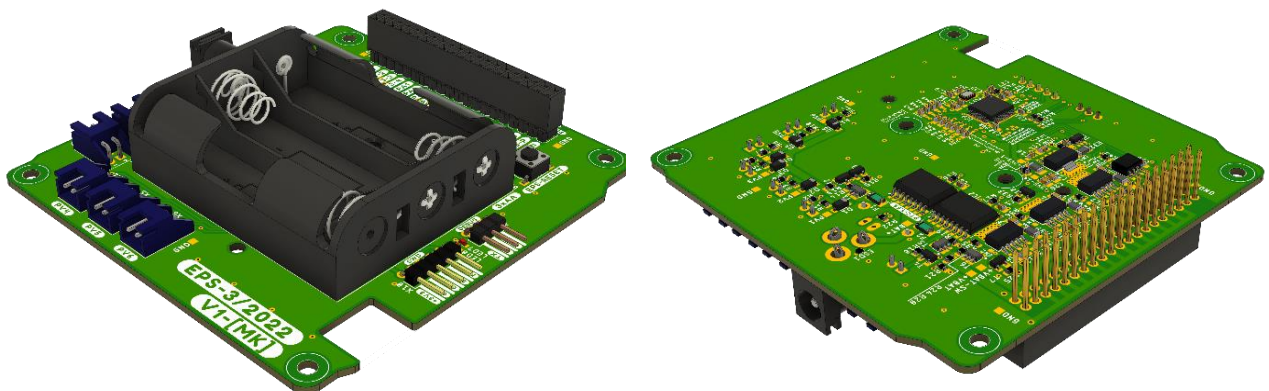


Figure 2: 3D model of the EPS

4. OBC+COM DESIGN

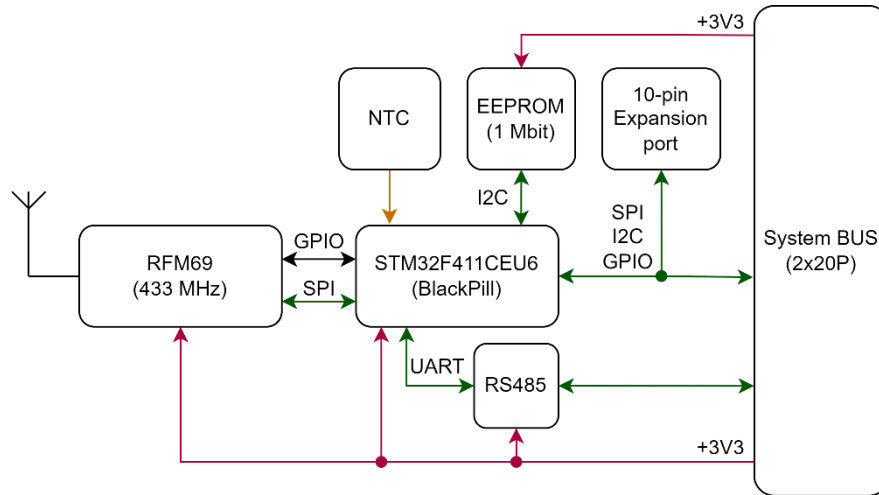


Figure 3: Block diagram of the OBC+COM

The communication system is on the PCB together with the onboard computer. The design is shown in **Figure 3**. The main microcontroller is STM32F411CEU6 soldered on the BlackPill development board, to maintain possible future scalability and reparability. RFM69HW wireless transceiver module is used for communication with a ground station. This transceiver uses the 433 MHz band, FSK modulation with maximum output power up to +20 dBm (100 mW) and communication speed up to 300 kbit/s. It has integrated packet transmission including CRC-16 checksum and AES-128 encryption [3]. The MCU is connected to RFM69 with an SPI bus. The MCU receives data from other subsystems through the RS485 bus, processes them, and saves it into a 1 Mbit EEPROM memory via I2C protocol. After receiving a special command, the MCU will read all saved data and send it wirelessly to the ground station. An NTC thermistor is used for temperature measurement. It is connected to an ADC channel of the MCU. All unused pins and communication interfaces of the BlackPill development board are connected to the system bus, as well as to the expansion port next to the MCU for possible future use. **Figure 4** shows a 3D model of the designed two-layer PCB.

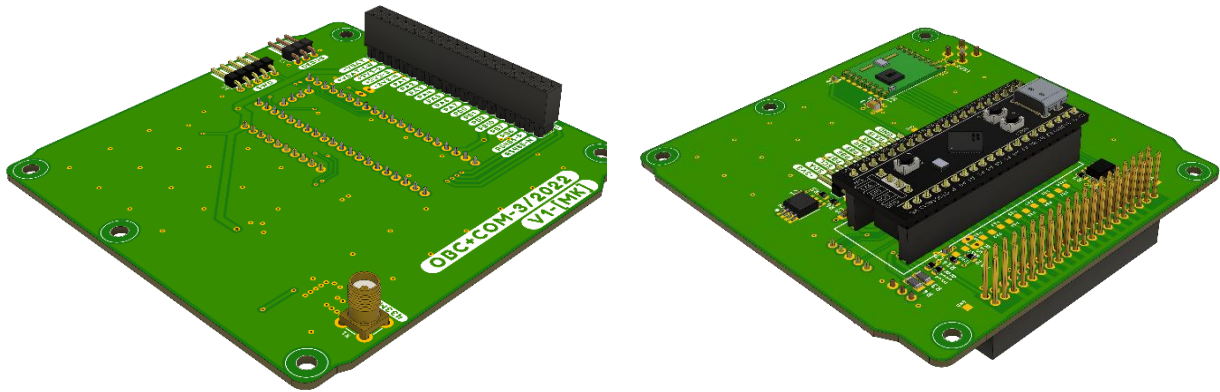


Figure 4: 3D model of OBC+COM

5. MECHANICAL CONSTRUCTION

CubeSats have a defined dimensions, to reduce the overall price of the system because standardized parts and deployers are used. They are usually made from aluminum. For demonstration purposes the goal was to design a 1U size which has defined dimensions to 10x10x10 cm. The mechanical construction is printed on a 3D printer to reduce the overall price and maintain reparability. As a base, a model from the Thingiverse portal was used [4]. Photovoltaic cells will be mounted on all six sides, to produce energy from a light source (halogen/LED light). **Figure 5** shows the final assembly of the demonstration CubeSat with built-in batteries and a basic monopole antenna mounted on the SMA connector, easily replaceable with other types such as dipole on angled SMA outside of the CubeSat. Six photovoltaic cells will be mounted outside of the frame (not shown in the picture).

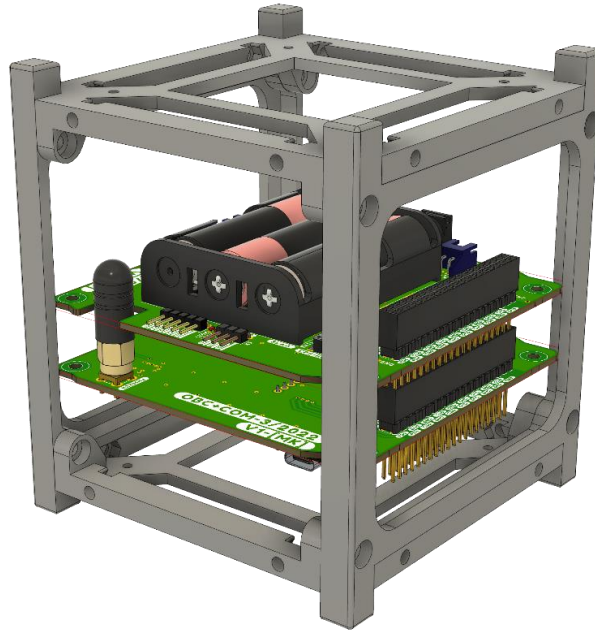


Figure 5: Final assembly of the demonstration CubeSat

6. GROUND STATION DESIGN

The design of the ground station is based on the RFM69HW wireless transceiver module with an SPI bus. A 2-layer PCB with Arduino shield dimensions and pin headers is connected to the Nucleo-F030R8 development board. The wireless module has the SMA connector for an antenna. This stack is then connected to a PC to transfer received data or wirelessly transmit commands to the CubeSat.

7. CONCLUSION

This paper deals with the design of the CubeSat. The result is finalized schematic design and printed circuit boards of both the onboard computer combined with the communication system and the electrical power supply system, ready to be manufactured. The electrical power supply system has its own monitoring microcontroller to sense important voltages, currents, and temperature of batteries. In case of any failure, the microcontroller can switch off any power rail based on the excess current drain.

Designed CubeSats OBC+COM and EPS subsystems are the base for students. They will design their custom subsystem PCBs connected to the system bus. The onboard computer will handle incoming data, save, or transmit them wirelessly to the ground station. The design of separate subsystems on additional PCBs with firmware debugging makes this concept a great educational outcome for students.

ACKNOWLEDGMENT

This work was supported by the Internal Grant Agency of Brno University of Technology, project no. FEKT-S-20-6526.

REFERENCES

- [1] STAKEM, Patrick. Cubesat engineering. 2017. ISBN 978-1520754017.
- [2] CAPPELLETTI, Chantal, Simone BATTISTINI a Benjamin K. MALPHRUS. CubeSat Handbook: From Mission Design to Operations. Elsevier Science, 2020. ISBN 978-0-12-817884-3.
- [3] HopeRF: RFM69HW RF Transceiver (Datasheet) [online]. [cit. 2021-12-25]. Available at: <https://www.hoperf.com/data/upload/portal/20190306/RFM69HW-V1.3%20Datasheet.pdf>
- [4] MakerBot Thingiverse: Universal 1U Cubesat [online]. 2020 [cit. 2021-12-20]. Available at: <https://www.thingiverse.com/thing:4096437>

Fractional-order integrator and its application in FLF fractional-order frequency filter

R. Theumer¹ and L. Langhammer²

¹Author, Brno University of Technology, Department of Radioelectronics, Czech republic

²Supervisor, Brno University of Technology, Department of Radioelectronics, Czech republic

E-mail: 203359@vut.cz, langhammer@vut.cz

Abstract—The main aim of this paper is to introduce the proposal of fractional integrator by approximation of the integer-order follow-the-leader-feedback topology (FLF). Current differencing transconductance amplifier (CDTA) is used in the integrator due to the higher versatility of this building block. The proposed integrator is also implemented to the frequency filter, creating a fractional-order frequency filter in FLF topology. The main advantage of this circuit is its electronic controllability. The resulting circuits (integrator and filter) are simulated in OrCAD using a transistor models in TSMC 0.18 μm technology.

Keywords—fractional integrator, fractional filter, active elements, CDTA, FLF topology

1. INTRODUCTION

Electronic circuits with fractional transfer are becoming more and more significant in last years in the field of analogue electronics and signal processing, Frequency-shift keying modulation technique using fractional-order structures [1][2], for example. Current research is, among others, focused on design of basic analogue building blocks with fractional transfer, such as integrators and differentiators. The main requirement is versatility of designed circuit structures. Electronic controllability of the circuit parameters significantly contributes to the required versatility. For that reason, nonconventional active elements with ability of controlling their parameters (transconductance, voltage or current gain, etc.) are often used or basic active elements are modified to provide the additional possibility of control.

In the first part of this paper, CDTA (element allowing to control the transfer of current differencing unit (CDU) and transconductance of the second OTA (operational transconductance amplifier) stage) and adjustable current amplifier (ACA) are used for design of the fractional order integrator. Thanks to the electronic parameter control, the frequency and order of the structure can be easily tuned. In the next part of this paper, the proposed integrator is implemented into the frequency filter.

2. CDTA ACTIVE ELEMENT

Two-stage CDTA consist of the CDU stage and transconductance amplifier stage. This element is meant for using in current-mode circuit, because it has two current input p and n and one or more current outputs. The CDU is implemented by the OTA instead of the pair of current conveyors. Because the OTA has voltage input, I/U converter in the simplest variant of the parallel grounded resistors must be connected before the CDU unit. For the unit gain of the CDU unit applies $R = g_{m_CDU}^{-1} [\Omega]$, where g_{m_CDU} is the transconductance of the OTA realized CDU unit.

In Figure 1 general schematic of the CDTA element is depicted. For marked currents and voltages applies $U_p = U_n = 0$, $I_z = I_p - I_n$ and $I_x = g_{m_amp} U_x$. The inner structure of the CDTA is depicted in the Figure 2. The TSMC 0.18 μm transistor-level model of the OTA does not allow to achieve higher values of transconductance so input parallel resistors R must be quite high. Thus input resistance of the CDTA is too high, specifically 670 Ω (ideal value of current input resistance is zero). The higher input resistance can be reduced by a suitable implementation of the OTA in the CDU unit. For example, commercially available LT1228 allows to achieve transconductance up to 10 mS. The bandwidth in which this model of the CDTA can be used is 37 MHz.

Possible advantage of this realization CDU, respectively CDTA, is possibility to modify this active element into the fully-differential form (necessary to use multi output OTAs) [3]. Another potential advantage lies in the possibility of replacement the resistors R by controllable resistance (for example

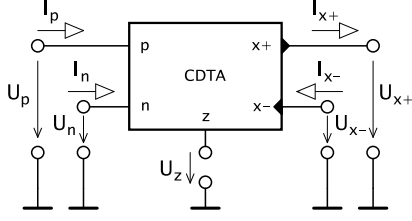


Figure 1: General schematic of the CDTA element

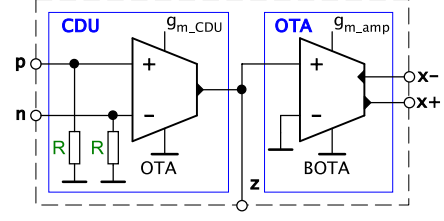


Figure 2: CDTA inner structure ($R = 670 \Omega$)

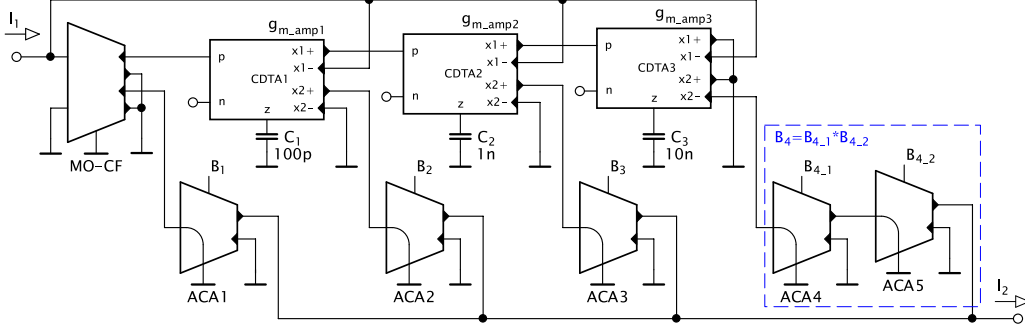


Figure 3: Schematic of the fractional integrator realized by approximation of the integer-order FLF topology

OTA realized as a controllable resistor). This modification would make it possible to control the transfer of the CDU unit. In this particular implementation, the pair of the parallel passive resistors is sufficient (saving active elements).

3. FLF FRACTIONAL-ORDER INTEGRATOR/DIFFERENTIATOR

There is currently no available commercial element with fractional transfer. The fractional order of the element is marked by α . The ideal lossless integrator with fractional transfer has slope of the modul $S = -20\alpha$ dB/decade and constant phase $\varphi = (-90\alpha)^\circ$. The realization of fractional-order integrator or differentiator lies in approximation of fractional-order behavior which is valid for a limited bandwidth. In this case, where fractional behavior is achieved by approximation of the integer-order FLF structure, validity bandwidth of the approximation is depending on integer order n of the FLF cascade.

A CFE approximation (continuous fraction expansion) was used to design fractional integrator. Because the used FLF structure is 3rd-order, the following relationships for 3rd-order approx. have been used

$$\begin{aligned} a_0 &= \alpha^3 + 6\alpha^2 + 11\alpha + 6 & a_1 &= -3\alpha^3 - 6\alpha^2 + 27\alpha + 54 \\ a_2 &= 3\alpha^3 - 6\alpha^2 - 27\alpha + 54 & a_3 &= -\alpha^3 + 6\alpha^2 - 11\alpha + 6 \end{aligned}$$

where α means fractional order and for integrator realization yields $\alpha \in (-1; 0)$ [4]. The coefficients a_0 to a_3 have been substituted into the 3rd-order approximation of the Laplace operator s^α

$$s^\alpha \approx \frac{\left(\frac{a_0}{a_3}\right)s^3 + \left(\frac{a_1}{a_3}\right)s^2 + \left(\frac{a_2}{a_3}\right)s + 1}{s^3 + \left(\frac{a_2}{a_3}\right)s^2 + \left(\frac{a_1}{a_3}\right)s + \left(\frac{a_0}{a_3}\right)} = \frac{a_0s^3 + a_1s^2 + a_2s + a_3}{a_3s^3 + a_2s^2 + a_1s + a_0} \quad (1)$$

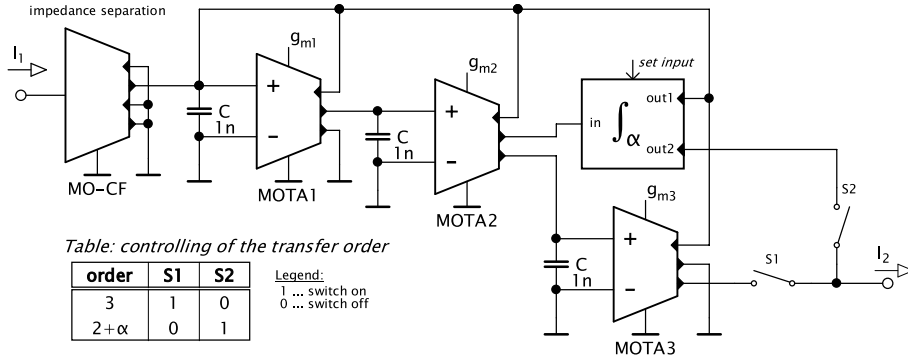
and then the values g_m , B were calculated by the comparison of eq. (1) with transfer function of the FLF structure depicted in Figure 3 expressed as

$$K_{I_FLF}(s) = \frac{s^3 C_1 C_2 C_3 B_1 + s^2 C_2 C_3 g_{m1} B_2 + s C_3 g_{m1} g_{m2} B_3 + g_{m1} g_{m2} g_{m3} B_4}{s^3 C_1 C_2 C_3 + s^2 C_2 C_3 g_{m1} + s C_3 g_{m1} g_{m2} + g_{m1} g_{m2} g_{m3}} \quad (2)$$

which was found by symbolic analysis in Snap software. The designed integrator has center frequency $\omega_0 = 1 \text{ rad s}^{-1}$. It is necessary to multiply each transconductance by $\tau^{-1} = \omega_0 = 2\pi f_0$ to increase center frequency. Resulting values of g_m , B for different fractional order and $f_0 = 100 \text{ kHz}$ are listed in the Table I. Values of the capacitors have been selected $C_1 = 100 \text{ pF}$, $C_2 = 1 \text{ nF}$ and $C_3 = 10 \text{ nF}$. Unfortunately, the values of the current gain are too high for fractional order $\alpha = 0.7$ and higher. There

Table I: Values of $g_{m,i}$ and B_i for realization of fractional-order integrator, $f_0 = 100$ kHz

α	0.1	0.2	0.3	0.4	0.5	0.6	0.7	0.8	0.9
g_{m_amp1} [μ S]	497	440	391	350	314	283	255	230	208
g_{m_amp2} [μ S]	568	514	464	419	377	338	303	269	238
g_{m_amp3} [μ S]	608	524	444	370	300	233	170	110	54
B_1 [—]	0.69	0.48	0.33	0.22	0.14	0.10	0.05	0.03	0.01
B_2 [—]	0.90	0.82	0.74	0.67	0.60	0.54	0.48	0.43	0.38
B_3 [—]	1.11	1.22	1.35	1.50	1.67	1.86	2.08	2.33	2.63
B_4 [—]	1.44	2.01	3.07	4.59	7.00	10.00	20.00	33.33	100.00

**Figure 4:** Schematic of the fractional-order controllable filter

is no commercially available amplifier, which would provide such a high gain. The pair of the amplifiers ACA4 and ACA5 allows us to realized at least orders 0.5 and 0.6 (gain $B_4 = B_{ACA4} \cdot B_{ACA5}$).

4. FRACTIONAL-ORDER FREQUENCY FILTER

This section shows the application of the proposed fractional-order integrator in frequency filter. The filter design from [5] was used. It is a 3rd-order Butterworth filter in FLF topology too, which consists of three OTA-C integrators. The last OTA-C integrator in the cascade was replaced by the proposed fractional-order integrator. This adjustment created a frequency filter with electronically tunable order in range $\alpha = 2 \div 2.6$. The OTA-C integrators are created using multiple output OTA so there are available many outputs of both polarities. This allows both integrators to be connected (fractional order and 1st-order OTA-C) behind the second OTA-C section.

Characteristics equation of the filtering structure from Figure 4

$$CE_{FLF} = s^3 + s^2 \frac{g_{m1}}{C_1} + s \frac{g_{m1}g_{m2}}{C_1C_2} + \frac{g_{m1}g_{m2}g_{m3}}{C_1C_2C_3} = s^3b_3 + s^2b_2 + sb_1 + b_0 \quad (3)$$

was found by symbolic analysis in Snap software. Parameters of filter tolerance tolerance field (for the design of higher order filters) are: characteristics frequency $f_0 = 100$ kHz, maximal band-pass ripple $K_{max} = -3$ dB, band-stop frequency $f_{att} = 1$ MHz, band-stop attenuation $K_{min} = -59$ dB and Butterworth approximation. Values of the g_m for 3rd-order filter are $g_{m1} = 314 \mu$ S, $g_{m2} = 628 \mu$ S and $g_{m3} = 1.26$ mS if all of the capacitors are $C = 1$ nF.

5. SIMULATIONS

Designed circuits (integrator and filter) were simulated in OrCAD Pspice. Transistor-level models of multiple output transconductance amplifier (MOTA), multiple output current follower (MO-CF) and adjustable current amplifier (ACA) in CMOS TSMC 0.18 μ m technology were used [6].

Frequency characteristics (module and phase) of the proposed fractional-order integrator are in Figure 5a and 5b. Module characteristics of the fractional-order filter are in Figure 5c. Possibility of frequency tuning is shown on graph in Figure 5d. Dashed lines represent ideal simulation with the level 1 models of active elements and solid lines represent simulations with the transistor-level models.

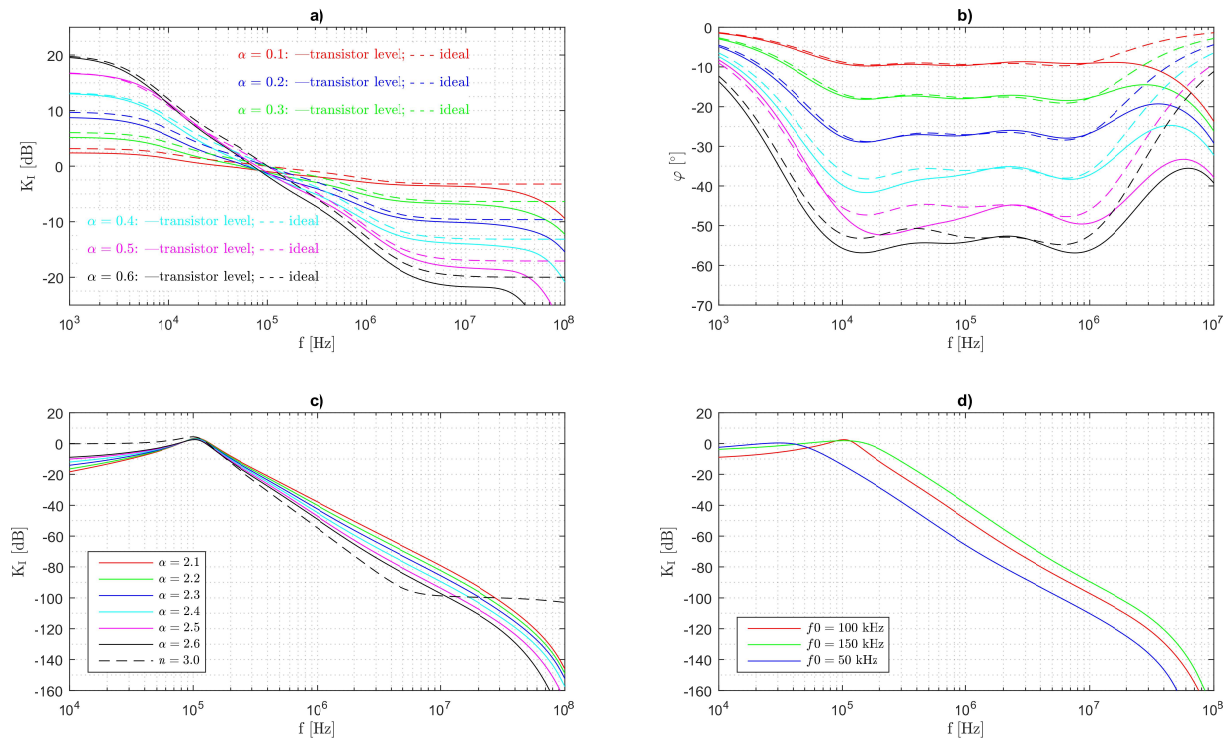


Figure 5: Frequency characteristics of the proposed fractional-order integrator and frequency filter

6. CONCLUSION

Disadvantages of this proposed circuits are 1) impossibility to achieve orders higher than $\alpha = 0.6$ and 2) large number of active elements. The first mentioned disadvantage can be eliminated if ACA were implemented by an element capable of achieving high gains. Significant advantage is electronic controllability. It is possible to tune characteristics frequency of the filter and fractional order by a proportional change of all transconductances, current gains respectively. From the attached graphs it is obvious, that bandwidth of validity of the approximation is about 2.5 decades (approx 4 kHz ÷ 2 MHz).

REFERENCES

- [1] Dvořák, J., Kubánek, D., Koton, J., Jeřábek J., Smékal, D. [online]. *Adjustable Multiphase Sinusoidal Oscillator with Fractional-Order Elements*. Proceedings of the 10th IEEE International Congress on Ultra Modern Telecommunications and Control Systems, pp. 1-6, 2019. DOI: <https://doi.org/10.1109/ICUMT48472.2019.8970842>.
- [2] Sung-Jin Kim, Won-Yong Choi, Kang-In Heo, Gyu Moon. [online]. *A Frequency-Shift Keying Modulation Technique Using a Fractal Ring-Oscillator*. International Journal of Multimedia and Ubiquitous Engineering, Vol. 10, No. 11, pp. 397-406, 2015. DOI: <https://dx.doi.org/10.14257/ijmue.2015.10.11.38>.
- [3] Biolek, D., Vávra, J. [online]. *Precise implementation of CDTA*. Brno: Department of Electrical Engineering, Faculty of Military Technology, University of Defence. Theoretical and applied electrical engineering, Vol. 15, No. 5, 2017. DOI: [10.15598/aece.v15i5.2515](https://doi.org/10.15598/aece.v15i5.2515)
- [4] Tsirimokou, G., Kartci, A., Koton, J., Herencsar, N., Psychalinos, C. [online] *Comparative study of Discrete Component Realizations of Fractional-Order Capacitor and Inductor Active Emulators*. Journal of Circuits, Systems and Computers, 27(11), 2018. DOI: <http://dx.doi.org/10.1142/S0218126618501700>
- [5] Theumer, R. *Synthesis of electronically reconfigurable 3rd-order FLF-OS filter in single ended and fully differential design*. Proceedings II of the 26th Conference STUDENT EEICT 2020. Brno University of Technology, FEEC, 2020. ISBN 978-80-214-5067-7.
- [6] Langhammer, L., Dvořák, J., Jeřábek, J., Koton, J., Šotner, R. [online] *Fractional-order low-pass filter with electronic tunability of its order and pole frequency*. Journal of Electrical Engineering, Vol. 69, No. 1, pp. 3-13, 2018. DOI: <https://doi.org/10.1515/jee-2018-0001>

Dynamic security log processing using deep learning techniques

S. Džadíková, and Y. Safonov

Brno University of Technology, Czech Republic

E-mail: Slavomira.Dzadikova@vut.cz, Yehor.Safonov@vutbr.cz

Abstract—Recently, the number of discovered cyber attacks increases rapidly. Tools for stealing personal data, destroying systems, or controlling infrastructure become continuously sophisticated to achieve malicious aims. Companies are trying to reduce the number of risks on their assets by using various security monitoring devices and tools. SIEM solutions are used for security monitoring, allowing different logs to be correlated. They offer visibility for security teams and allow early response to attacks. The main problem of SIEM software is the implementation of log parsing, which directly influences correlation rules efficiency. Usually, the biggest limitation is parsing dynamic log structures from different event sources. The main contribution of this paper is to apply advanced deep neural networks which use attention mechanisms for efficient log content parsing and its understanding. The proposed question answering model for feature extraction from raw logs should achieve automatic log procession. Obtained results show indisputable advantages of deep attention techniques compared to the common approaches.

Keywords—Correlation, deep learning, log processing, meta key extraction, natural language processing, SIEM, question answering

1. INTRODUCTION

A cyber attack is an attack targeting computer systems via cyberspace to disable, destroy, steal information, or control computing infrastructure. More than 300,000 thousand samples of malicious code are created daily – keyloggers, trojans, viruses, adware [1]. Their main aim is to steal personal data. In 2020, during the global coronavirus pandemic ransomware attacks grew by more than 150 % [2]. A small sample proves that consistent monitoring of the environment and data analysis are the most important components for each organisation [1]. Security systems like EDR (*Endpoint Detection and Response*) and SIEM (*Security Information and Event Management*) provide visibility in infrastructure, detection of cyber attacks, and raise alerts for security teams. The growing number of cyber attacks is leading to the development and improvement of defence techniques that will be able to react dynamically to cyber security threats.

Security systems use raw logs for their analysis and correlation, which must be parsed before any correlation is established. In SIEM systems, log parsing is handled by special connectors, which are different for each vendor because of different log formats. The parsing process is extremely difficult for the implementation where human interaction is needed. The natural language processing (NLP) model using a question answering technique may provide autonomous log parsing for different log types. [3, 4]

The manual log parsing method, called *regex*, is based on regular expression matching. The procedure has several disadvantages. The first one is the hardness of writing regex expressions because they must not be overly or too loosely constrained. The second complex problem is managing regex expressions for different applications, data sources, and their versions. The next disadvantage reflects complicated parser modifications. It means that the slight difference in the input rule may break the whole expression matching process. Finally, using hundreds of regexes over every single log is computationally expensive.

Another approach is the template-generation method, log parsing is proceeded via template matching, template-based algorithms like Drain or Spell generate a set of templates or regular expressions used for log parsing. Templates are using wildcards to represent the variable's position in the log. Template-based algorithms do not become better with more data, they are not truly learning algorithms and there is no way to tune these algorithms, however, they may be used for solving log clustering problems. Log parsing algorithm based on machine learning technique benefits with easier training and managing and also such algorithms are more robust to changes in input logs. [4]

2. PROPOSAL OF AI-BASED LOG PROCESSING

SIEM is one of the most important security systems for computer infrastructures. It collects different types of events from various devices located on the network, such as firewall, IDS/IPS (*Intrusion Detection System/Intrusion Prevention System*), antivirus programs from end-stations, authentication systems, and applications. Collected events are aggregated, normalised, and converted to the SIEM understandable format. After events modifications, SIEM correlates different events for the identification of malicious activities in real-time. The system generates alerts when the correlation rule is fulfilled. The biggest benefit of SIEM systems is the correlation between different log sources, so a wide spectrum of patterns and behaviours can be detected. Correlation rules are usually programmed by humans, or they are generated by the system when there is observed some pattern of behaviour in a period of time, or there is detected anomalous behaviour compared to normal events in the environment. [3]

SIEM system developed during the research is using a deep learning technique for automatic log parsing. This procedure should address log parsing struggles with specific vendor technical language. Conventional SIEM systems contain a specific connector for each vendor that is responsible for log parsing and normalisation. Implementation of such a system is a time-consuming activity that requires a highly experienced expert. One of the discussed approaches of parsing is using deep learning models, for example, natural language processing models [4]. NLP is a scientific area at the crossroads of artificial intelligence, linguistics, and cognitive psychology, which seeks to achieve the quality of human speech processing using techniques for the analysis and representation of natural text [5].

We consider log records to be mostly unstructured data, as formats may vary between devices or services, with large amounts of semantic information, which often cannot be captured by statistical analysis. Logs are an expression of events using natural language. The natural text means any text, the only condition is the language for people communication. Therefore, logs are an ideal candidate for NLP. The model applies the question answering method, which performs the task of mining the answer to a question posed by a person in a pre-structured database or documents in natural language [6, 7].

Parsed information generate tags representing behavioural patterns. Finally, alerts will be generated based on the patterns and suspicious behaviour according to signatures or anomalies. Pattern search can be performed by LSTM (*Long short-term memory*) model. The process is shown in the Figure 1.



Figure 1: Work process of developed SIEM.

2.1. Dataset preparation

The goal in creating the dataset was to create a set that resembled the Stanford Question Answering Dataset (SQuAD) in its elements or fields. The SQuAD focuses on reading comprehension, contains questions asked on published articles on Wikipedia, where the answers to the questions are passages from the submitted article or some range of sentences, or it is also possible that the question is unanswerable.

In order to create the dataset, free available system log records in their original raw format, which are intended for scientific purposes were searched. In the initial phase, event logs were selected from the Linux platform and the Apache web server.

Raw log data were parsed by GROK parser in Elastic Stack environment, then logs were transformed from CSV file to JSON format and finally into SQuAD format. The SQuAD dataset contains fields such as index, text paragraph, question, unique identification number, initial answer position, and text of the answer. Whole dataset creation, an example of JSON format and final division into training, validation, and testing set in ratio 6:2:2 is visualised in the Figure 2.

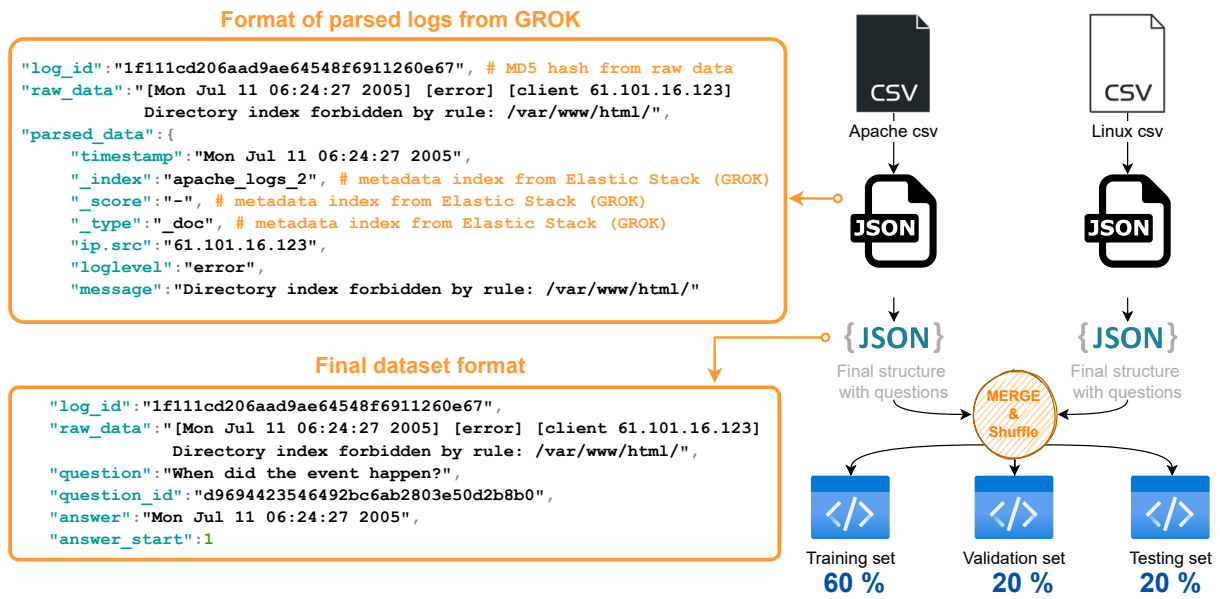


Figure 2: Dataset preparation process and an example of JSON formats.

2.2. Data preprocessing

Data must be in an understandable format for the model's training phase, so it is necessary to tokenize the data. Tokenization is a process that changes text, strings to a token list, and also adds attention to it.

2.3. Fine-tuning of the question answering model

Nowadays, developers typically use pre-trained models to implement NLP tasks, which are deep-learning models trained on a large dataset to perform specific NLP tasks. Models are reusable and can be fine-tuned for a specific application. Pre-trained models are mostly free accessible for developers in libraries PyTorch and Tensorflow. The most efficient models are using transformers architecture and one of them is BERT (Bidirectional Encoder Representations from Transformers). BERT is developed by Google and it is able to perform eleven NLP tasks, including question answering that has been tested on the Stanford Question Answering Dataset. The model is pre-trained on Wikipedia articles and its accuracy on SQuAD is 93.2 % while outperforming human performance by 2 %. [8, 9]

For the research it was decided to choose DistilBERT pre-trained model from Huggingface repository, it is a transformer and smaller, faster, cheaper, and lighter version of BERT, which was trained by distillation. It has 40 % fewer parameters, is 60 % faster, and retains almost 95 % of the performance of the original BERT. [10, 11]. The example of log parsing is shown in the Figure 3.

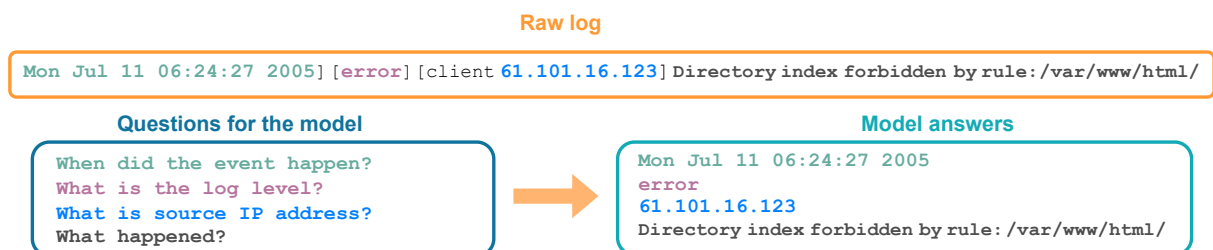


Figure 3: Log parsing using the question answering model.

3. RESULTS AND DISCUSSION

The current state of development is up to step 3 in the figure 1, which includes the parsing part of the mechanism. During this phase, an experimental environment was prepared where Elastic Stack was deployed. The Elastic Stack used GROK processor for log parsing and dataset creation, in the next step scripts were developed that ensure conversion from CSV format to JSON format, the final format

contains raw log, identification of log, question and expected answer. Finally, the development of the question answering model that would be responsible for automatic log parsing.

Therefore, necessary to prepare a more accurate dataset and parsing, this would be achieved by own advanced experimental environment – the environment consists of Windows endpoints, Linux endpoints, domain controller, mail server, web server, firewall, the mentioned infrastructure will generate raw logs for Elastic Stack for dataset creation. Models for solving the question answering task based on several pre-trained models will be created and the results will be compared. The output of the model will be treated as tags that indicate patterns of behaviour. Using a Python script or later LSTM network, it will be possible to mark suspicious patterns of behaviour and generate notifications. The results can be sent to the Kibana interface, where other graph-based analysis and anomaly search methods can be used.

The result of the whole work will be a self-employed module that will be able to work with the original log records (from the systems on which the network will be learned) without any need for division, log parsing, and will be able to mark suspicious patterns of behaviour.

4. CONCLUSION

The article presents a SIEM system design that is able to automatically parse logs and subsequently detect suspicious behaviour and anomalies. Automatic log parsing using a deep learning model based on natural language processing saves time creating rules and templates necessary for classic manual or template-based methods.

Acknowledgement

The research described in this paper was financed by the Ministry of Interior under grant VI20192022149.

REFERENCES

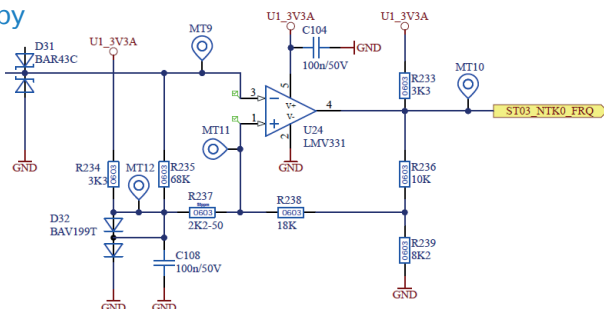
- [1] BULAO, Jacquelyn. How Many Cyber Attacks Happen Per Day in 2021? *TechJury* [online]. TechJury.net, ©2021, December 7, 2021 [cit. 2021-12-11]. <<https://techjury.net/blog/how-many-cyber-attacks-per-day/#gref>>
- [2] FIRCH, Jason. 10 Cyber Security Trends You Can't Ignore In 2021. *Purplesec* [online]. PurpleSec [cit. 2021-12-11]. <<https://purplesec.us/cyber-security-trends-2021/#CyberWarfare>>
- [3] BHATT, Sandeep, Pratyusa K. MANADHATA a Loai ZOMLOT. *The Operational Role of Security Information and Event Management Systems*. 2014, **12**(5), 35-41. ISSN 1540-7993. doi:10.1109/MSP.2014.103
- [4] SETIANTO, Febrian, Erion TSANI, Fatima SADIQ, Georgios DOMALIS, Dimitris TSAKALIDIS a Panos KOSTAKOS. GPT-2C: A GPT-2 parser for Cowrie honeypot logs. *CoRR* [online]. 2021 [cit. 2022-03-11]. Dostupné z: <<https://doi.org/10.48550/arXiv.2109.06595>>
- [5] LIDDY, Elizabeth D. Natural Language Processing. *Encyclopedia of Library and Information Science*. 2nd. NY. Marcel Decker, 2001. <<https://surface.syr.edu/cgi/viewcontent.cgi?referer=&httpsredir=1&article=1019&context=cnlp>>
- [6] ELWORTHY, David. Question Answering using a large NLP System. *NIST Special Publication 500-249: The Ninth Text REtrieval Conference (TREC 9)* [online]. NIST, 01-Aug 2000, 298 – 303 [cit. 2021-12-12]. <<https://files.eric.ed.gov/fulltext/ED477468.pdf#page=298>>
- [7] A literature review on question answering techniques, paradigms and systems. *Journal of King Saud University - Computer and Information Sciences* [online]. 2020, (10), 635-646 [cit. 2021-11-20]. ISSN 1319-1578. <<https://doi.org/10.1016/j.jksuci.2018.08.005>>
- [8] YAO, Mariya. 10 Leading Language Models For NLP In 2021. *TOPBOTS* [online]. Copyright © 2021, May 11, 2021 [cit. 2021-11-20]. Dostupné z: <<https://www.topbots.com/leading-nlp-language-models-2020/#language-models-2020-8>>
- [9] KUMAR, Ajitesh. NLP Pre-trained Models Explained with Examples. *Data Analytics* [online]. Data Analytics, © 2021, September 21, 2021 [cit. 2021-11-20]. <<https://vitalflux.com/nlp-pre-trained-models-explained-with-examples/>>
- [10] DistilBERT. *Hugging Face* [online]. © Hugging Face [cit. 2021-12-11]. <https://huggingface.co/docs/transformers/model_doc/distilbert>
- [11] *Hugging Face* [online]. © Hugging Face [cit. 2021-12-11]. <<https://huggingface.co>>

- 
- System Engineer Aerospace
 - Model Based Design Engineer (Matlab, dSPACE)
 - Test Engineer
 - Embedded HW Engineer
 - Embedded SW Engineer
- 



Na čem budeš pracovat

- Vývoj řídicích systémů (ECU, FADEC) pro letecké motory
- Vývoj řídicích systémů pro palivové a hydraulická aktuátory
- Vývoj výkonové elektroniky (AC/DC, DC/DC měniče)
- Verifikace řídicích systémů v provozu
- Certifikace v souladu s leteckou legislativou
- Zavedení do sériové výroby



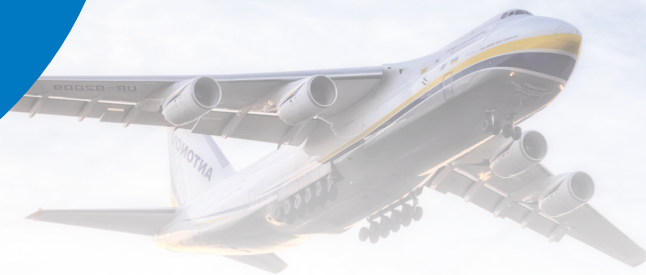
Kontakt:



kariera@unis.cz



www.unis-daac.cz/cs/kariera



UNIS, a. s.

Hlavní činností společnosti **UNIS, a.s.** je realizace projektů v investiční výstavbě zaměřené do oborů zpracování ropy a zemního plynu, petrochemie, chemie a energetiky v dodavatelské formě tzv. „na klíč“. K ostatním aktivitám společnosti **UNIS** patří – Zákaznický i vlastní vývoj a výroba SW i HW v oblastech leteckého, mikroprocesorového a automobilového průmyslu. „Výrobní informační systém MES“ (Manufacturing Execution System), vyvíjený a distribuovaný pod značkou **PHARIS®**, je nasazován pro komplexní řízení výroby v diskrétních výrobcích. Zkušební laboratoře **VTP UNIS** nabízí zkoušky elektromagnetické kompatibility **EMC**, zkoušky mechanické a klimatické odolnosti.

Nabízíme

- Zajímavou a dlouhodobou práci na vývojovém projektu
- **Kontinuální profesní a mzdový růst**
- Pružnou pracovní dobu a systém odměňování
- **1 týden dovolené navíc**
- Stravování v místě pracoviště

Místo výkonu práce:
Brno

Hledáme

- Analytické a komunikační schopnosti
- **Schopnost formulovat technické požadavky na zařízení**
- Základní inženýrské znalosti z oboru elektro a programování
- **Dobrou znalost oborové technické angličtiny**
- Aktivní a inovativní přístup

Typ nabídky:
HPP, brigáda, stáž, trainee program, diplomová práce, ostatní

Kontakt:

✉ kariera@unis.cz



www.unis-daac.cz/cs/kariera

Access Control System Using Multi-factor Authentication

T. Cvrček¹, and P. Dzurenda¹

¹Department of Telecommunications, Brno University of Technology, Brno, Czech Republic

E-mail: tadeas.cvrcek@vutbr.cz, dzurenda@vut.cz

Abstract—A secure user authentication process is a key prerequisite for ensuring the security of the entire electronic system. On the other hand, current systems usually deploy many constrained devices with limited computational power, memory space and cryptographic support. This makes it hard to deploy secure cryptographic mechanisms in this environment. In this article, we present our multifactor authentication system using a reader with a secure module represented with MultOS smart card and an Android smart phone acting as a user authentication device. The system supports NFC (Near Field Communication) communication interface for intermediating communication between smart phone and reader, supports additional authentication factors (e.g. PIN code or fingerprint) and is easily implementable even on very constrained devices such as smart cards.

Keywords—MultOS, Android, Authentication, Secure Access Module, Multi-Factor, Access Control, Cryptography, Security, Smart Card, Authenticated Key Agreement

1. INTRODUCTION

Nowadays, the environment of Internet of Things (IoT) is growing significantly and the Industry 4.0 one is becoming more relevant. However, both environments require to be secure, to connect sensors and gadgets to common network. Losing data or compromising the network would mean possibility of losing assets, or even threat subjects themselves. On the other hand, authentication in the IoT environment is limited by constrained devices. These devices have limited performance due to their size and power consumption requirements. However, it is still necessary to provide authentication methods even in such environment.

One of the best ways to authenticate an entity is to use Multi-Factor Authentication (MFA), which is becoming important across the services we use especially nowadays. According to the directive 2015/2366, the European Union (EU) requires users to use MFA for money transactions with nominal value of 50 Euros and above [1]. MFA defines three factor types: knowledge (e.g., Personal Identification Number (PIN) and password), possession (e.g., smart card, smart phone and wearables), and inherent (e.g., behavioral and physical biometrics). According to the EU law, at least two of these types must be used.

In this paper, we developed and implemented a multi-factor access control system based on Authentication and Key Agreement (AKA) protocol published in [2]. Our implementation deploys a hardware reader with a slot for Secure Access Module (SAM) and internal clock, and the Android smart phone acting as a user authentication token. The proposed solution is secure, efficient, and easy to run on IoT devices with different computational power.

2. MULTI-FACTOR ACCESS CONTROL SYSTEM

The implemented system deploys Google Android based smart phone with Near Field Communication (NFC) support, SAM module in a form of smart card, and access terminal (i.e., single board computer or microchip embedded in the door card reader). The terminal provides communication interface between the SAM and smart phone. This terminal is connected to an electric door lock, that in case of successful authentication allows the user to open the door and access protected area. For development purposes, the Raspberry Pi 3 Model B+ has been used as the terminal. The communication protocol between the terminal and SAM/smart phone has request-response communication model and uses Application Protocol Data Units (APDU). The protocol is used for communication between a smart card and a smart phone, because both have required software support and they can not communicate directly.

The system uses SAM module. This module is integrated in the terminal and provides hardware acceleration of cryptographic primitives and secure memory management. As SAM module, one can use many available smart card platforms. In our case, we use MultOS smart card. The authentication protocol is based on AKA protocol [2] and allows us to perform two factor authentication, namely: 1) possession (i.e., smart phone) and knowledge (i.e., PIN code) or 2) possession (i.e., smart phone) and biometric (i.e., fingerprint). The general architecture of our access control system and the principle how the multi-factor authentication process works with smart phone is depicted in Figure 1.



Figure 1: Multi-factor authentication system using smart phone and embedded SAM module.

We refer to [2] for more details of AKA principles. We implemented applications for both Android phone and SAM module. The Algorithm 1 shows the cryptographic core of the access terminal (i.e., MultOS smart card) whereas Algorithm 2 shows the cryptographic core of the user device (i.e., Android phone).

Algorithm 1 AKA-SERVER-SIGNVERIFY(Y, sk_S, pk_C)

```

1:  $r_S \leftarrow_R \mathbb{Z}_q^*$ 
2:  $t_S \leftarrow g^{r_S}$ 
3:  $e_S \leftarrow \mathcal{H}(Y, t_S)$ 
4:  $s_S \leftarrow r_S - e_S \cdot sk_S \bmod q$ 
5: Send:  $Y, \sigma = (e_S, s_S)$ 
    $\triangleleft \triangleright$  AKA-CLIENT-PROOFVERIFY
6: Receive:  $\pi = (e_C, s_C)$ 
7:  $t' \leftarrow g^{s_C} \cdot pk_C^{e_C}$ 
8:  $\kappa \leftarrow t'^{r_S}$ 
9:  $\tau_S \leftarrow e_C \stackrel{?}{=} \mathcal{H}(Y, t', \kappa)$ 
10: return  $\tau_S = 0/1, \kappa$ 

```

Algorithm 2 AKA-CLIENT-PROOFVERIFY(Y, σ, pk_S, sk_C)

```

1:  $t'_S \leftarrow g^{s_S} \cdot pk_S^{e_S}$ 
2:  $\tau_C \leftarrow e_S \stackrel{?}{=} \mathcal{H}(Y, t'_S)$ 
3: if  $\tau_C = 0$  then exit
4:  $r_C \leftarrow_R \mathbb{Z}_q^*$ 
5:  $t \leftarrow g^{r_C}$ 
6:  $\kappa \leftarrow t'^{r_C}$ 
7:  $e_C \leftarrow \mathcal{H}(Y, t, \kappa)$ 
8:  $sp_{IN} \leftarrow \mathcal{H}(PIN)$ 
9:  $s_C \leftarrow r_C - e_C \cdot (sk_C + sp_{IN}) \bmod q$ 
10: return  $\tau_C = 0/1, \pi = (e_C, s_C), \kappa$ 

```

Both algorithms need to perform modular and elliptic-curve operations, hash functions to authenticate communicating entities and establish common secret for future encryption of communication channel. In our implementation, we used secp256k1 elliptic curve, SHA-1 hash and 3DES-ECB cipher algorithms. In user application, one have to provide valid PIN code to be successfully authenticated. During authentication process a symmetric key is established. The key is used to encrypt user token sent from smart phone. The token contains time information, that can be used by terminal to clarify if the user has enough permissions and has been successfully authenticated by using another factor.

Testing terminal application for Raspberry Pi uses psc-lite external library, that makes it possible to create communication channel between any devices communicating via APDU messages. Since the Android Development Kit (ADK) tool does not provide any public elliptic-curve function calls, we used micro-ecc library to compute elliptic-curve operations. To do so, we implemented the core functions on smart phone in C++ using Android Native Development Kit (NDK). NDK allows us to archive much better performance results during cryptographic core execution comparing with Java libraries.

3. IMPLEMENTATIONS ASPECTS

Smart cards differ in processor performances, memory capacities and cryptographic support. The AKA protocol needs to use a secure hash function, a cipher algorithm, and perform operations over

elliptic-curve such as scalar point multiplication and point additions, as shown in Algorithm 1 and 2. However, different smart cards have different cryptographic support, and therefore, we have to select the most satisfying one, see [3] for more details. For example, JavaCard platform can offer smart card development environment based on Java programming language. These cards support wide range of secure cryptographic algorithms, however, they miss the support of modular arithmetic operations. BasicCard platform is based on Basic programming language. This platform offers a variety of algorithms, but is very limited in performance. MultOS platform can be programmed using C or Assembly language. All functions are provided by integrated framework. These cards show the best performance results and are considered very secure. In fact, they are used also in bank systems. Smart cards platform based on .NET framework called .NET Cards do not provide needed features, such as elliptic-curve operations. A detailed overview of cryptographic support across different smart card platforms is presented in Table I.

Table I: Smart card cryptographic support.

	JavaCard	BasicCard	MultOS	.NET Card
3DES	Yes	Yes	Yes	Yes
AES	Yes	Yes	Yes	Yes
DSA	Yes	No	No	No
SHA-1	Yes	Yes	Yes	Yes
SHA-2	Yes	Yes	Yes	Yes
SHA-3	Yes	No	No	No
MOD ¹	No	Yes	Yes	No
ECOP ²	No	Yes	Yes	No

Note: ¹Modular arithmetics, ²Elliptic-curve operations

In order to make our system more flexible, we optimized the APDU communication model. In particular, we use APDU encapsulation technique, which allows generating and inserting APDU command messages for the receiver to the APDU response message of the sender. Thanks to these techniques, the terminal does not need to know the communication protocol, it just simply forwards APDU messages between these two devices. The terminal starts with SELECT command message sent to the SAM module (i.e, smart card). This message is only for selecting the applet we want to use. Then the terminal waits for the smart phone to be attached. After that, SELECT command is transmitted to the smart phone, which responds with a data payload containing the APDU message and status code. The message in the data payload is then directly sent to the SAM by the terminal and the status code is removed. The SAM can also put a message to the data payload and send it back according to the status code. This communication method works indefinitely unless a specified status code is detected by the terminal. The status code represents the result of the authentication process.

4. EXPERIMENTAL RESULTS

The implemented experimental Android application contains of user interface, as one can see on the left side in Figure 2. A user can register to the application, reset any existing registration and turn on the authentication mode. The user registration requests the PIN code from the user. Then, the PIN code is required from the user to turn on the authentication mode. The mode is running for 30 s. If the user decides to clear all data, it is possible to trigger the reset process through the reset button. As an alternative to the PIN code, the user can use a fingerprint as a second authentication factor. This does not impact the cryptographic core of the authentication protocol. The difference is that the user is not required to insert the PIN code during the authentication phase. Note that the PIN code is stored in the application and is protected with the fingerprint of the user.

The development environment uses Raspberry Pi as common interface. The service for APDU transactions has its own output. If the application runs in debug mode, the log is printed to the terminal. The log of successful authentication of the user is depicted on the right side of Figure 2. The SAM module in the terminal determines the authentication result. If the authentication is successful, the SAM returns status code 0x9001, otherwise it returns 0x9002. The authentication result message carries

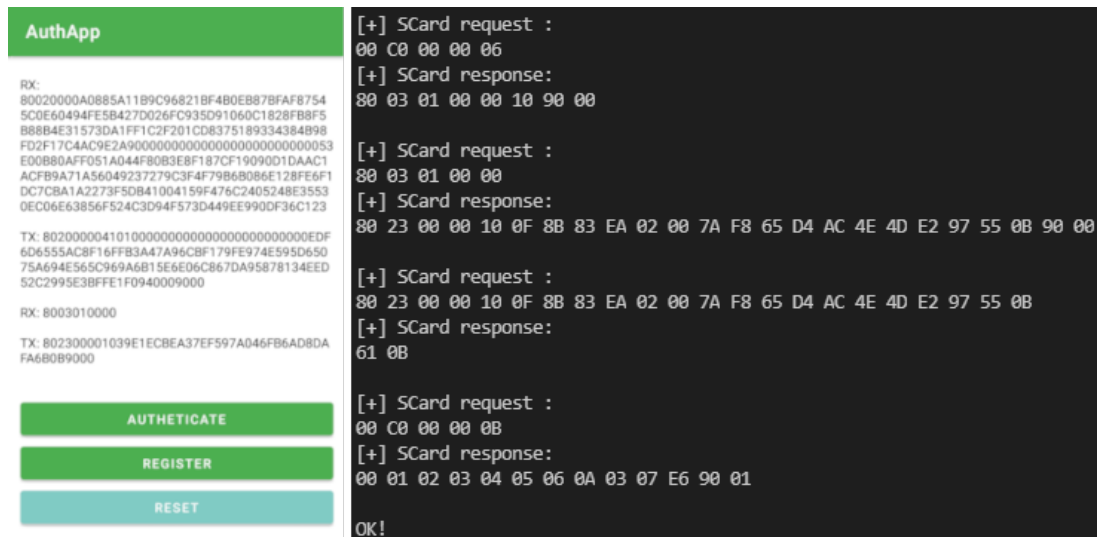


Figure 2: Smart phone application screen (left side) and log of successful authentication (right side).

an information with timestamp. The timestamp comes from smart phone and is encrypted using the symmetric key from AKA protocol. It serves to decide if the system can allow the user to enter a protected area in specific time period. Our benchmarks show how time consuming the implemented protocol is. The used smart card for verification part of the protocol is ML4-G17 model with MultOS version 4.2.1 and for user side we consider Huawei Nova 3 smart phone. The smart phone runs Kirin 970 processor clocked at 2.4 GHz with four ARM Cortex A73 cores and four ARM Cortex A53 cores. The protocol requires almost 2.6 s on SAM module and only 0.2 s on smart phone.

5. CONCLUSION

In this paper, we present our access control system using multi-factor authentication protocol, hardware terminal with embedded SAM module and clock, and Android smart phone application for users to prove their identities. The implementation is secure, not too computationally demanding and ready to run on IoT devices. In order to make the system more dynamic, flexible and extend usability of APDU communication model across various devices, we extended it with encapsulation method that makes possible to forward APDU messages between SAM and user's device without intervention from terminal. In the future, we are about to extend the system with addition peripheral devices, that user would be able to use as another authentication factor. Such device could be for example a smartwatch.

ACKNOWLEDGMENT

This research has been supported by the grant VJ01010084 of the Ministry of the Interior of the Czech Republic, "Digital evidence in criminal proceedings" in programme Impakt 1 (2022-2025).

REFERENCES

- [1] European Parliament, Council of the European Union, "Directive (EU) 2015/2366 of the European Parliament and of the Council of 25 November 2015 on payment services in the internal market, amending Directives 2002/65/EC, 2009/110/EC and 2013/36/EU and Regulation (EU) No 1093/2010, and repealing Directive 2007/64/EC", 2015, <https://eur-lex.europa.eu/legal-content/EN/ALL/?uri=celex:32015L2366>.
- [2] P. Dzrenda, S. Ricci, R. C. Marqués, J. Hajný, P. Číka, "Secret sharing-based authenticated key agreement protocol", The 16th International Conference on Availability, Reliability and Security, 2021, doi:10.1145/3465481.3470057.
- [3] L. Malina, P. Dzrenda, J. Hajný, Z. Martinásek, "Assessment of Cryptography Support and Security on Programmable Smart Cards", The 41st International Conference on Telecommunications and Signal Processing (TSP), 2018, <https://ieeexplore.ieee.org/document/8441334>.

Detection of Malicious Network Traffic Behavior Using JA3 Fingerprints

Pavel Novák¹, and Václav Oujezský²

^{1,2}Faculty of Informatics – Masaryk University, Czech Republic

E-mail: 468940@mail.muni.cz, oujezsky@fi.muni.cz

Abstract—This paper presents a novel approach for classifying spoof network traffic based on JA3 fingerprint clustering. In particular, it concerns the detection of so-called zero-day malware. The proposed method does not work with known JA3 hashes. However, it compares the JA3 fingerprint of captured traffic with JA3 fingerprints of traffic with predefined criteria, such as the use of current cipher suites or protocol, for classification.

Keywords—clustering, detection, JA3, JA3s, malware

1. INTRODUCTION

The amount of encrypted network traffic has increased dramatically in recent years. It is valuable to protect users' data against eavesdropping or modification. Nevertheless, encryption also opened new opportunities for malware developers because it makes hiding malicious communication more effortless. This problem has become much more critical because the portion of CC (Command and Control) server encrypted communication generated by the malware was around 45 % last year, and the number is increasing every year. Encrypted traffic is much more harder to analyze because of privacy issues and performance demands. This inevitably leads to massive research in this area and the development of techniques to classify encrypted traffic.

While encrypted traffic is beneficial for legitimate users and protects user data, it also makes it easier to hide traffic generated by malware. There can be several types of such malware traffic. It can be network activity caused by worms, phishing campaigns, or communication with command and control servers. Encrypting such traffic effectively eliminates detections based on known signatures, such as detecting specific text strings or patterns in the communication. An encrypted traffic inspection is usually tricky because of privacy concerns and the difficulty of the decryption process. A possible solution is behavioral methods. These analyze the behavior of the communicating parties and look for anomalies. The second group of methods is based on traffic fingerprinting or monitoring the basic parameters of communication that occur in unencrypted form. One particular method is the JA3 fingerprint [1]. JA3 collects parameters that occur in unencrypted form while establishing a secure connection. However, JA3-based detections are based on direct matches. Thus, malware is not detected in the case of an unknown fingerprint. For example, there is currently a collection of JA3 fingerprints that have been obtained by analyzing more than 25,000,000 PCAPs generated by malware samples [2]. As the source states, these samples have not been tested against “good” traffic, i.e., they do not ensure malware detection.

The novel method described in this paper attempts to address this problem. The core of this work is to verify the ability to detect unsolicited encrypted traffic based on the similarity of JA3 fingerprints and to analyze what differences exist during the establishment of a secure channel of benign and malignant parties. Therefore, the method proposed in this paper uses the selected clustering methods to analyze and cluster JA3 fingerprints. Results of these methods will be analyzed and compared. This research aims to experimentally verify whether this detection method is applicable and which algorithm is best suited for this task. Accuracy, performance, and usability on a large volume of data will be assessed.

2. JA3 METHOD AND JA3 OUTPUT FORMAT

JA3, the version of the JA3 for the server fingerprinting JA3s, and the active version of JA3 – JARM are three fingerprinting methods developed by John Althouse and his team in 2017 [1, 3]. The JA3 fingerprint is created from data obtained from the ClientHello Message when establishing a secured connection. The specific values extracted from this message are the TLS (Transport Layer Security) version, accepted ciphers, list of extensions, elliptic curves, and elliptic curve format. Values from the specified fields are represented as strings and then hashed using the MD5 (Message-Digest) hash function. The MD5 hash is also the resulting JA3 fingerprint.

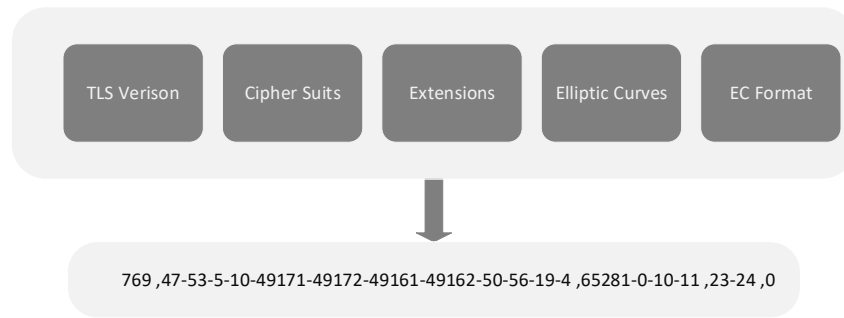


Figure 1: JA3 Creation Scheme.

The output of JA3 is a text string of variable length. It contains five sections separated by a hyphen. A comma separates the individual values. Due to the variable length, the MD5 hash of JA3 is usually used as the resulting fingerprint in practice. Figure 1 shows the schema of the JA3 fingerprinting process.

Due to the nature of the JA3 fingerprint as a text string, clustering methods and metrics suitable for this type of output were considered in the design of the method. A more specific description is given in Section 3.

3. APPLICABLE CLUSTERING ALGORITHMS

Clustering is the task of dividing input data into similar groups. The division is done so that the points assigned to the same group are “more similar” in some sense. Clustering can be divided into two basic groups. The first group of methods is called hard clustering methods. These methods assign each sample to one cluster, i.e., for each cluster and each sample, the given sample belongs to the cluster or not. The opposite approach is called soft clustering methods. These methods can assign one sample to multiple clusters with some probability [4]. An overview of clustering algorithms that could be used is below.

K-means method, e.g., Lloyd algorithm iteratively divides the set of samples into k disjoint clusters. Each cluster has a centroid μ_j , which is a mean of all samples within the cluster. In the first iteration, the centroids are usually randomly selected. In each iteration, clusters are created by assigning a sample to the closest centroid. The centroid position is then adjusted, so it is the mean of the entire cluster. This process is repeated until the centroid position is not changing significantly. This algorithm is not optimal because a result can be only the local optimum [5].

OPTICS (Ordering Points to Identify the Clustering Structure) is a density-based clustering algorithm. It is a generalization of another well-known clustering algorithm – DBSCAN (Density-based Spatial Clustering of Applications with Noise). This algorithm arranges the samples in order in such a way that the two closest samples are always immediately after each other. The resulting clusters are determined by splitting the sequence at points where the relative distance exceeds a given threshold. This approach has the advantage over the similar DBSCAN algorithm of identifying clusters with different densities [6, 7].

Brown clustering is usually applied when working with text and analyzing context. The method is based on the assumption that words of similar meaning occur in the text in a similar context. This means that the distribution of words that immediately precede or follow are similar for similar words. This method is agglomerative. In the beginning, each word is in its cluster, and gradually, the clusters merge [8].

In order to measure the distance between samples, three discrete metrics – the Levenshtein, Damerau - Levenshtein, and Hamming metrics, will be considered in the context of clustering. These metrics will be used in the normalized form as the length of the strings in the different parts of the JA3 fingerprints are different and could potentially bias the results [9].

4. EARLY RESULTS

The initial part of the research aimed to verify two hypotheses about malware secure communication. The first hypothesis was that encrypted malware communication is similar across families. The second hypothesis was that the JA3 fingerprint parameters of malware-generated traffic differ from the JA3 fingerprints of benign traffic. Initial validation was performed using two test datasets. Both datasets contained the same set of randomly selected JA3 fingerprints of benign traffic. These samples were obtained from the JA3 database [10]. The remaining JA3 fingerprints were obtained by using analysis

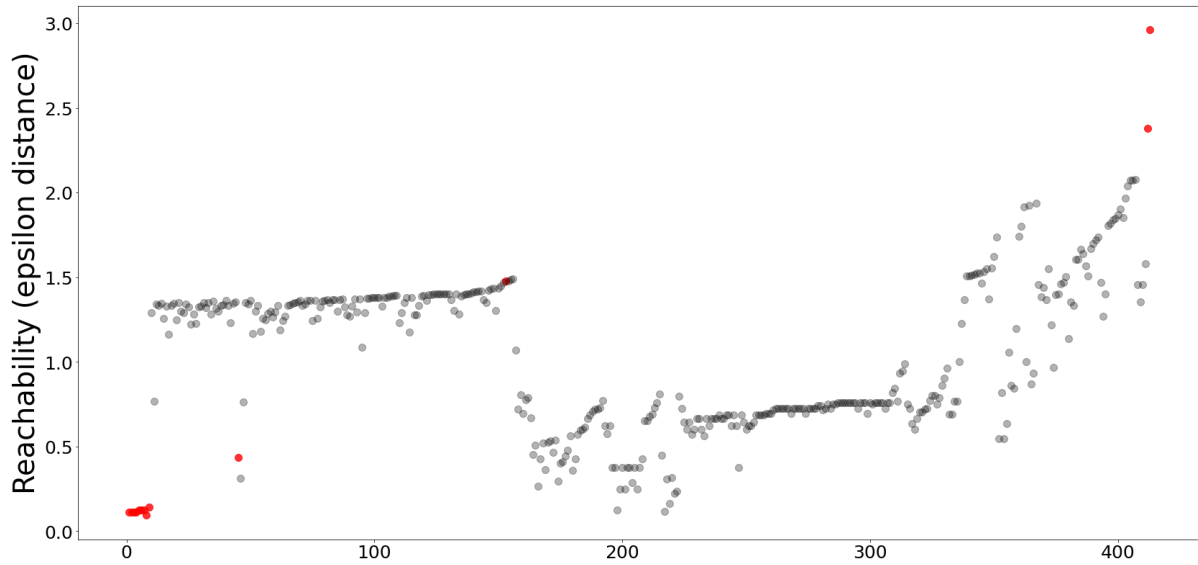


Figure 2: OPTICS – Reachability Graph of Malware and Clean Samples.

of pcap files from the malware database [11]. The first test dataset contained communication samples of different versions of Qakbot, Emotet, Dridex, and Cobalt Strike malware. The clustering algorithm used in this phase was OPTICS along with the Damerau-Levenshtein normalized metric applied on individual parts of JA3 separately and summed together. The OPTICS algorithm was chosen because it does not require any prior knowledge about clusters in the dataset, and it is easy to extract clustering information from the ordering. Figure 2 shows the reachability plot as a result of applying the OPTICS algorithm to the first dataset. Red points indicate malware samples, and grey points correspond to malignant communication.

This algorithm sorts samples so that the two closest samples are next to each other. The x-axis corresponds to the ordering of points, and the y-axis corresponds to the distance of the nearest sample. In other words, the malware samples form the densest group in the whole dataset. It confirms the first hypothesis, namely that malware communication within a family is very similar. The second observation is that the malware samples form a separate cluster, which is quite distant from neighboring clusters. It confirms the second hypothesis. Several malware samples were outside this cluster, but they were also quite different from the benign traffic. Thus, they can be considered as outliers.

The second dataset contained samples of RAT malware, specifically the NetWire and the Revenge RAT [11]. The results were similar to the first case. Malware samples formed a separate group with similar JA3 fingerprints, which were quite different from the benign traffic. From this perspective, the results look pretty promising in terms of possible applications in detection. Since the malware samples perform similarities in terms of their JA3 hashes, we would be able to use the K nearest neighbors classification algorithm to recognize unknown malicious traffic.

5. DISCUSSION

This method could significantly help detect zero-day malware and identify its traffic on the network in the future. Moreover, this method does not require any disclosure of the privacy of the communicating parties. Detection is based on freely observable attributes and does not disclose users' privacy. This method is also relatively easy to implement. JA3 fingerprints can be collected by most network probes currently in use. Moreover, their collection and computation are neither computationally nor memory intensive. Moreover, JA3 fingerprints are currently implemented in several intrusion detection systems, like Suricata.

This method, of course, has its drawbacks as well. The most important one is its relative ease of deception. If the malware mimics the TLS handshake of a legitimate program, the communication will not be correctly detected by this method. Another possible disadvantage is the incorrect result of the used clustering algorithms. In particular, the K-means algorithm is very susceptible to influence by outliers. It can then lead to suboptimal clustering and incorrect results.

Several possible extensions and modifications of the proposed method can be suggested for future improvements by considering the mentioned disadvantages. One possibility is combining this method with other zero-day malware detection methods. Specifically, these include algorithms that look for anomalies in network behavior. The second option is to use another fingerprinting method that contains more information than JA3. One example of such could be the Mercury method [12]. In addition to the attributes present in JA3, Mercury also uses all the TLS handshake extensions. One of them is a Server Name Identifier, which provides the server name with which the client communicates. Using such information could help to detect malicious traffic more precisely. However, Mercury is not as widely used as JA3 nowadays.

6. CONCLUSION

This paper presented the proposal of a novel method for classifying encrypted traffic based on the similarity of JA3 fingerprints. This work aims to verify if there are differences in the TLS channel establishment process between malware and benign traffic that could be used for traffic classification. The research involves comparing several selected clustering algorithms. This paper presents the first results of experiments performed with the OPTICS clustering algorithm. The first results have shown differences in JA3 fingerprints compared to benign traffic, which could be used to classify the encrypted traffic.

REFERENCES

- [1] J. Althouse, "Tls fingerprinting with ja3 and ja3s," 2019. [Online]. Available: <https://engineering.salesforce.com/tls-fingerprinting-with-ja3-and-ja3s-247362855967>
- [2] "Sslbl | malicious ja3 fingerprints," Switzerland, [2022]. [Online]. Available: <https://sslbl.abuse.ch/ja3-fingerprints/>
- [3] J. Althouse, "Easily identify malicious servers on the internet with jarm," 5 2021. [Online]. Available: <https://engineering.salesforce.com/easily-identify-malicious-servers-on-the-internet-with-jarm-e095edac525a>
- [4] "Clustering: Types of clustering: Clustering applications," Oct 2020. [Online]. Available: <https://www.analyticsvidhya.com/blog/2016/11/an-introduction-to-clustering-and-different-methods-of-clustering/#:~:text=Clustering%20is%20the%20task%20of,and%20assign%20them%20into%20clusters>
- [5] J. A. Hartigan, M. A. Wong *et al.*, "A k-means clustering algorithm," *Applied statistics*, 1979. [Online]. Available: <https://www.stat.cmu.edu/~rnugent/PCMI2016/papers/HartiganKMeans.pdf>
- [6] M. Ankerst, M. M. Breunig, H.-P. Kriegel, and J. Sander, "Optics: Ordering points to identify the clustering structure," in *Proceedings of the 1999 ACM SIGMOD International Conference on Management of Data*. Association for Computing Machinery, 1999. [Online]. Available: <https://doi.org/10.1145/304182.304187>
- [7] E. Schubert, J. Sander, M. Ester, H. P. Kriegel, and X. Xu, "DbSCAN revisited, revisited: Why and how you should (still) use dbSCAN," *Association for Computing Machinery*, 2017. [Online]. Available: <https://doi.org/10.1145/3068335>
- [8] P. Brown, V. Dellapietra, P. Souza, J. Lai, and R. Mercer, "Class-based n-gram models of natural language," *Computational Linguistics*, 1992.
- [9] F. J. Damerau, "A technique for computer detection and correction of spelling errors," *Commun. ACM*, 1964. [Online]. Available: <https://doi.org/10.1145/363958.363994>
- [10] Ja3er, ja3er.com. [Online]. Available: <https://ja3er.com/>
- [11] Malware traffic database, malware-traffic-analysis.net. [Online]. Available: <https://www.malware-traffic-analysis.net/>
- [12] B. E. David McGrew and B. Anderson. (2020) Mercury: Fast tls, tcp, and ip fingerprinting. [Online]. Available: <https://github.com/cisco/mercury>

A Simple Calorimetric Measurement of SiC MOSFET Switching Loss and Comparison with Electric Measurement

J. Mikláš¹ and P. Procházka²

¹Brno University of Technology, Czech Republic

²Brno University of Technology, Czech Republic

E-mail: jan.miklas@vut.cz, prochazkap@vut.cz

Abstract—This paper proposes a simple and accessible method for dynamic calorimetric measurement of ultra-fast power semiconductor devices switching loss. It utilizes a temperature rise monitoring of a copper cube thermally coupled with a semiconductor chip. No special chambers or heat exchangers are used and no additional wiring compared to standard electric pulsed test. This provides an opportunity to perform a direct comparison with traditional electric power loss measurement, including all of the parasitic influences and further investigation of power loss with intentional varying of particular elements impact, which absent in available literature. The paper establishes the test method and setup as well as a basic comparison of calorimetric and electric measurement.

Keywords— Power Semiconductor SiC MOSFET Switching Loss, Parasitic Waveform Distortion, Calorimetric Power Loss Measurement, Electrical Measurement, Double Pulse Test, Measurement Methods Comparison

1. INTRODUCTION

1.1. Switching Loss

An accurate determination of switching loss in power switching semiconductor devices plays a crucial role in optimum power converter design. Operating temperature of semiconductors should not be much below the maximum junction temperature rating aiming towards to increasing a system power density and/or efficiency allowed by increasing the switching frequency, which is in turn allowed by recent device technology improvements. An obvious downside of the increased device switching speed is increased *ringing* during switching and a rapid decrease of switching loss measurement accuracy when measured by oscilloscope. The main reasons are parasitic interference of measured signals, additional parasitic influence introduced by test probes [1] and parasitic elements within test system or even within the semiconductor itself [2] influencing the actual power loss.

For this reason, an increasing effort for calorimetric measurements has being reported recently, i.e. the thermal method of semiconductor power loss measurement in the similar fashion as in case of magnetic materials loss measurement [3], that is likewise frequency-dependent and relevant electric quantities cannot be directly accessed.

1.2. Calorimetric Measurement

The term “calorimetric measurement” of power loss refers to many types of apparatus employing the fact, that a loss energy is always in form of heat. The purpose of calorimeter - i.e. thermally isolated system capable of some kind of thermal measurement - is either to conserve the produced heat at defined time period and measure the temperature change after transient thermal event; or to ensure all of the produced heat is transferred by coolant whose flow rate, input and output temperature are known in steady thermal state.

Static calorimetric measurement use many kinds of calorimeter construction. They differ in type of coolant, heat exchanger, number and insulation of chamber etc. Typically water or air is used as coolant. Air allows by far the simplest construction, however its parameters are much more dependent on operating conditions than that of water, and a flow rate measurement is more difficult. A brief overview of different technologies and relevant references are provided in [4]. Authors later describe a construction of *double jacked calorimeter* with two chambers, one inside another, where the outer chamber air temperature is

actively controlled to match the inner chamber temperature. The heat transfer through the inner chamber walls is completely eliminated. A detailed description of principally similar calorimeter as carried out in [5].

Dynamic calorimetric measurement incorporates a temperature rise monitoring during transient thermal event. The method is attractive. The measurement precision of this kind of methods is reported to be comparable with static measurements [6], [7].

2. ELECTRIC MEASUREMENT

Prior to calorimetric calibration measurements, a bunch of electric measurements was performed as a quantitative reference. A four-lead device was used, i.e. with so called Kelvin-contact source incorporated, sometimes called as sense contact, referring to four-terminal sensing, as this source terminal does not carry the load current. The main function of separated “sensing” source is, however, the proper gate driving. It protects the driving signal carried between gate and source terminal from parasitic distortion by inductive voltage drop across the main source terminal during switching the current with high di/dt . Voltage drop decreases the driving voltage during turning-on, which in turn slows down the action, as can be seen on current rise double-slope on Fig. 2.

It is generally believed that “Kelvin source” provides also a more credible drain-source switching voltage measurement signal for the same reason.

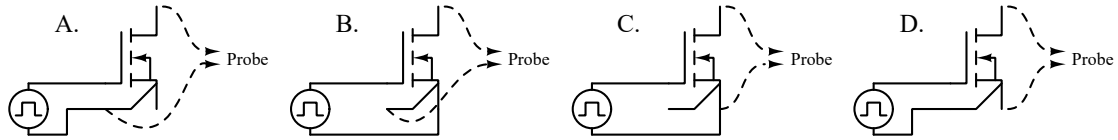


Figure 1: Wiring diagrams for different combinations of gate drive and probe connections.

The sensing and gate driving connections are intentionally wired both the wrong and proper way to test the parasitic elements effects. This results in 4 combinations representing 4 test scenarios as listed on Fig. 1. Scenarios A, B correspond to proper drain-source voltage sensing while A, D correspond to proper gate driving. Test case C, i.e. wrong driving and wrong sensing, pertains to classic three-lead device without Kelvin contact.

Probe connection (A vs. D) should affect the electric measurement results while gate drive signal connection (A vs. B) must affect both electric and calorimetric measurements as it affects the actual loss.

2.1. Test setup

All of the transient electric measurements were performed on low-inductive DC link as described in [8].

A recent SiC MOSFET “12M1H060” was selected as a device under test (DUT) for calibration measurements; with SiC diode “IDH16G120” as a freewheeling diode.

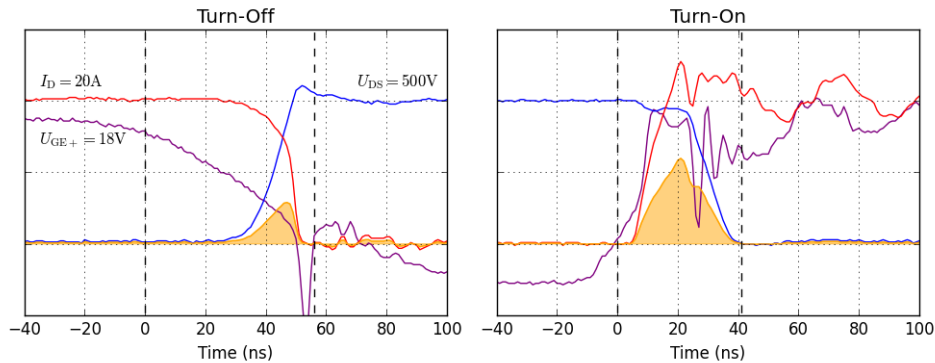


Figure 2: Switching waveforms for test scenario “C”, corresponding to three-lead device without “Kelvin source”.

Switching waveforms for test case “C” are depicted on Fig. 2. The turn-on transient is slowed down as described before, so that the ringing during turn-on event is not as awful as for scenarios “A” and “D”.

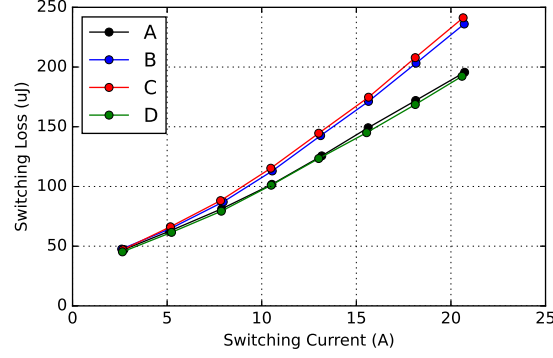


Figure 3: Electrically measured switching loss at $U_{DC} = 500$ V.

Total switching loss ($E_{off} + E_{on}$) as a function of switched load current is showed on Fig. 3 for all of the test scenarios. Interestingly, the influence of measurement probe connection seems to be negligible. This is provably caused by simultaneous increase of E_{on} and decrease of E_{off} , however this phenomenon is out of scope this paper. Test case A results in lower switching loss than test case B, as expected. The difference increases with increasing current due to increased di/dt .

3. CALORIMETRIC MEASUREMENT

3.1. Method

A dynamic temperature rise monitoring of a solid body thermally-coupled with semiconductor chip (e.g. the device package baseplate) during a linearized initial phase of heating process has been established as simple and fast yet accurate method.

The temperature rise ΔT of solid body with thermal capacity C_θ heated by constant power P with respect to time can be described as linearly rising function by simple calorimetric calculations as follows:

$$\Delta T(t) = \frac{P}{C_\theta} t \quad (1)$$

Therefore, knowing the thermal capacity and ensuring the linear temperature rise, the unknown power loss dissipated within the body can be readily expressed as:

$$P = \frac{C_\theta \Delta T}{\Delta t} \quad (2)$$

where ΔT stands for measured temperature rise and Δt for the heating time.

In addition to perfect thermal coupling - achieved by soldering - a high thermal capacity, low body thermal resistivity and high body-to-ambient thermal resistivity is required for a proper solid body, which is intended to be heated. That means, a large body volume and small surface area. This ensures the high thermal time constant and uniform temperature distribution. For example, a typical discrete parts package such as TO-247 does not comply the first requirement, while a ribbed heat-sink violates the last one. After some empirical investigation, a copper cube of at least 20 – 30 times higher volume compared to TO-247 baseplate was selected as an optimum body.

3.2. Test setup

Unlike the electric pulse test, the test current cannot be limited by a single pulse width as the thermal time constant exceeds the electrical transient by several orders of magnitude.

For this reason, a two-switches half-bridge topology is usually incorporated, which allows current regulation by alternating switching of two switches. However, we utilized a different approach. The current is limited by a power resistor in series with inductor (parasitic inductance of load resistor may, but don't have to be sufficient), as depicted on Fig. 4.

An adequate load inductance is desirable in addition to power resistor to filter the load current during switched-current mode and provide a constant turn-on and turn-off current level. Thereafter, the test current is adjustable via duty cycle D according to:

$$I_{\text{mean}} = \frac{U_{\text{DC}}}{R_{\text{load}}} D \quad (3)$$

where V_{DC} stands for DC-link voltage, R_{load} the load resistance. Transistor on-state voltage drop is neglected assuming $U_{\text{DC}} > 300 \text{ V}$.

The main downside of this approach is a significant power consumption, i.e. it implements a power supply with high output power capability and a load resistor capable of high power dissipation. On the other hand, the benefits are non-negligible. First of all, it allows keeping the one-switch topology and a complete test setup used for electrical measurement. Practically zero additional stray inductance or other parasitic elements is introduced as no additional wiring is used. Identity of test setup is essential in effort of credible comparison of test method results.

The temperature of copper cube is monitored by PT100 type thermistor and data logging is performed by digital multimeter controlled by computer. The temperature distribution uniformity within the copper cube was experimentally checked not to exceed 1 % when heated 20 °C above the room temperature.

3.3. Separation of Conduction Loss

Separation of conduction and switching loss becomes another necessary step during calorimetric loss analysis. In method proposed by us, this is possible by an accurate steady state measurement of on-state voltage and current. Current is limited by DC-link voltage and load resistor value. DC-link voltage can be varied to tune the current value to desired level.

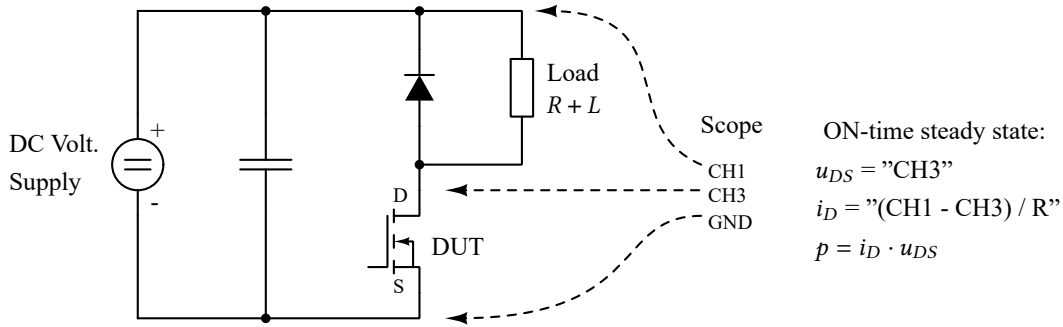


Figure 4: Schematic diagram of electric setup used for calorimetric measurement.

The total conduction power loss during switched operation can be easily computed from measured on-state conduction loss P_{con} and known duty cycle D as follows:

$$P_{\text{con,D}} = P_{\text{con}} \cdot D \quad (4)$$

4. CALIBRATION

For whole measurement, the heated copper cube thermal capacity C_θ value is an essential piece of information. It can be expressed by at least 2 approaches.

The first approach rise from a basic calorimetric heat calculation for known thermal power as follows:

$$P \Delta t = C_\theta \Delta T \quad (5)$$

where Δt stands for heating time and ΔT the temperature rise.

Record of a temperature rise measurement at constant power $P = 0.531 \text{ W}$ dissipated in DUT in form of conduction loss is depicted on Fig. 5. The following values were recorded from initial 20 seconds: $\Delta t = 20 \text{ s}$, $\Delta T = 0.25 \text{ K}$. From (5): $C_\theta = 0.531 \frac{20}{0.25} = 42.48 \frac{\text{J}}{\text{K}}$. The identical slope of temperature rise was measured also at time intervals of 10 s and 40 s, proving the validity of initial rise linearization.

Second approach is based on monitoring the whole transient event until the steady state, when all input power is transferred to the ambient. The temperature gradient between uniformly heated copper body and ambient determines the equivalent body-to-ambient thermal resistance $R_{\text{theta}} = \frac{\Delta T}{P}$. Then: $C_\theta = \frac{\tau}{R_\theta}$, with

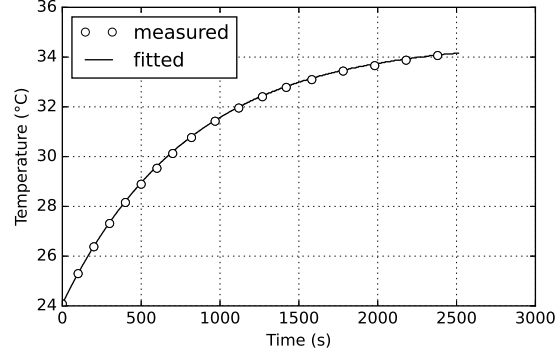


Figure 5: Transient temperature rise at constant power $P = 0.531$ W. The fitted exponential curve with time constant 807 s and steady state temperature 34.63 °C.

τ recognized from the transient temperature rise record. According to the exponential curve fitted on the measured values by least-squares method as depicted on Fig. 5, the steady state temperature is 34.63 °C and a time constant $\tau = 807$ s. That implies $R_{\theta} = \frac{34.63-24}{0.531} = 19.84 \frac{\text{K}}{\text{W}}$ and $C_{\theta} = \frac{807}{19.84} = 40,6 \frac{\text{J}}{\text{K}}$.

5. OBTAINING RESULTS AND COMPARISON WITH ELECTRICAL MEASUREMENT

A brief explanation of measurement data processing will be presented here.

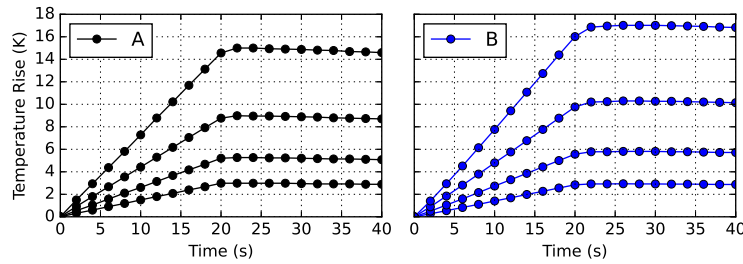


Figure 6: Temperature rise of DUT during a constant current switching. Two charts belong to different gate driving scenarios and each of the lines belongs to different current levels.

Sample records of heating measurement with respect to time are presented on Fig. 6. The two charts correspond to different gate driving scenarios as defined on Fig. 1 at different current levels. Higher temperature of course belongs to higher current. Also, higher loss is expected at scenario “B” due to turn-on switching event being slowed down by parasitic voltage drop on source node.

The current level has been set by duty cycle D . Due to varying D , the slope of the temperature rise is affected by different conduction loss in addition to different switching loss. Therefore, the conduction loss must be separated according to section 3.3 after calculation of total power loss (2).

The test results as a function of current are showed on Fig. 7 as well as comparison with electrical measurement results.

The comparison of the methods prove the assumption that electrical measurement of power transistor switching loss may return excessively optimistic results. This effect is caused primarily by inductive under-shoot during turn-off and capacitive under-shoot during turn-on and by test signals parasitic distortion. Mainly the inductive voltage drop is dependent on di/dt , which increases with increasing current level, so that the difference between the test methods results is growing rapidly at high currents. It should be emphasized that maximum current level presented on this paper is relatively low when compared to typical application, so the electrical test method error may be significant.

6. CONCLUSION

The calorimetric test established on this paper provides reachable and relatively fast alternative method of device switching loss measurement. In section 5 it is shown that a traditional and widely utilized

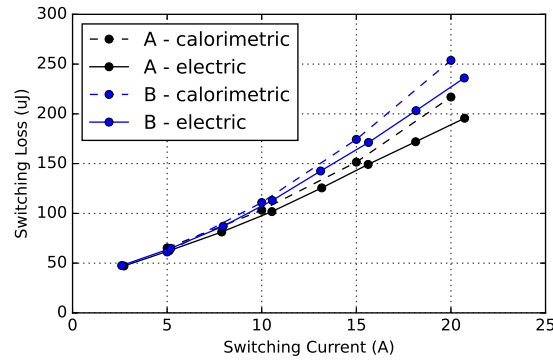


Figure 7: Comparison of test results of electric and calorimetric results for different gate drive cases at $U_{DC} = 500$ V.

electrical test may result in excessively optimistic results, especially at high current and ultra-fast wide bandgap devices spread on the market nowadays.

As high current operation is usually critical for optimum device design for given application, the overblown optimistic results given result in critical undersizing of switching device and subsequent system failure.

This risk is known in available literature and among professionals, so the presented method aims to provide an absent way of effect quantification and contribute to finer, more exact and reliable device optimization.

ACKNOWLEDGMENT

This research work has been carried out in the Centre for Research and Utilization of Renewable Energy (CVVOZE). Authors gratefully acknowledge financial support from the Ministry of Education, Youth and Sports under institutional support and BUT specific research programme (project No. FEKT-S-20-6379).

REFERENCES

- [1] K. Ammous et al., "Error in estimation of power switching losses based on electrical measurements," 2000 IEEE 31st Annual Power Electronics Specialists Conference. Conference Proceedings (Cat. No.00CH37018), 2000, pp. 286-291 vol.1, doi: 10.1109/PESC.2000.878859.
- [2] M. Gaucci et al., "On the Origin of the C_{oss} -Losses in Soft-Switching GaN-on-Si Power HEMTs," in IEEE Journal of Emerging and Selected Topics in Power Electronics, vol. 7, no. 2, 2019
- [3] P. Papamanolis, T. Guillod, F. Krismer and J. W. Kolar, "Transient Calorimetric Measurement of Ferrite Core Losses up to 50 MHz," in IEEE Transactions on Power Electronics, vol. 36, 2021
- [4] D. Christen, U. Badstuebner, J. Biela and J. W. Kolar, "Calorimetric Power Loss Measurement for Highly Efficient Converters," The 2010 International Power Electronics Conference - ECCE ASIA -, 2010, pp. 1438-1445, doi: 10.1109/IPEC.2010.5544503.
- [5] S. D. J. Weier, M. A. Shafi and R. A. McMahon, "Precision Calorimetry for the Accurate Measurement of Losses in Power Electronic Devices," 2008 IEEE Industry Applications Society Annual Meeting, 2008, pp. 1-7, doi: 10.1109/08IAS.2008.361.
- [6] D. Neumayr, M. Gaucci, D. Bortis and J. W. Kolar, "New calorimetric power transistor soft-switching loss measurement based on accurate temperature rise monitoring," 2017 29th International Symposium on Power Semiconductor Devices and IC's (ISPSD), 2017, pp. 447-450
- [7] J. Weimer and I. Kallfass, "Soft-Switching Losses in GaN and SiC Power Transistors Based on New Calorimetric Measurements," 2019 31st International Symposium on Power Semiconductor Devices and ICs (ISPSD), 2019, pp. 455-458, doi: 10.1109/ISPSD.2019.8757650.
- [8] Prochazka, P., Miklas, J., Pazdera, I., Patocka, M., Knobloch, J., Cipin, R.: "Measurement of Power Transistors Dynamic Parameters". In: Mechatronics 2017, p.571-577, ISBN 978-3-319-65959-6

AC Cell Electroporation Based on Asymmetrical Waveform

M. Folprecht¹, D. Cervinka¹, and V. Novotna¹

¹Brno University of Technology, Czech Republic

E-mail: Martin.Folprecht@vut.cz, cervinka@vut.cz, novotnav@vut.cz

Abstract—This paper discusses an application of different waveforms during a cell electroporation process. Latest scientific papers emphasize advantages of asymmetrical waveform applied to tissue. Higher effect of the electroporation process is reached and muscle contractions are less significant. Most high-voltage generators are based on a controlled discharge of storage capacitors. We present a different solution of the generator, where a power part contains a pulse transformer.

Keywords—Asymmetrical waveform, capacitor discharge, cell electroporation, DC-AC inverter, high frequency, MOSFET transistor, pulse transformer.

1. INTRODUCTION

Cell electroporation is a relatively new, less invasive method of a tissue ablation, which is based on the application of short high-voltage pulses. It can be used for treatment of some diseases, e.g., cancer, cardiac arrhythmia, etc. Older DC electroporation requires unipolar voltage pulses, while modern and more advantageous AC electroporation uses bursts of bipolar pulses. Lower risk of arrhythmia, lower muscle contractions and non-existent electrolysis are the main advantages of this method [1]. Latest studies refer about the use of asymmetrical waveform during this process, that can bring higher effect compared to more common symmetrical waveform. High-voltage generators developed at FEEC BUT contain pulse transformer in their power part. The aim of this paper is to show, that asymmetrical voltage can be produced by generator with step-up pulse transformer.

2. COMMONLY APPLIED WAVEFORMS

Different waveforms can be used for the electroporation process. Some examples are shown in Fig. 1. Exponential pulses (A) characterized by voltage peak V_m and time constant τ are suitable for inserting of DNA molecules into the cell. The voltage peak in units of kV provides a permeabilization of a cell wall and a low-voltage tail transfers appropriate molecules [2]. These pulses can be up to units of ms long. Square and rectangular pulses are mainly used in clinical practice, because it is easy to control an amount of delivered energy and to reproduce a setup of the equipment [3]. These waveforms are suitable for DC and AC electroporation. In the case of AC electroporation, pulses in individual burst can have different duty cycle. For example BUT AC generator [4] produces bipolar pulses with permanent duty cycle 0.5 (B). In publication [5], authors applied pulses with lower duty cycle (C). Higher electroporation effect can be reached, when asymmetrical pulses are used.

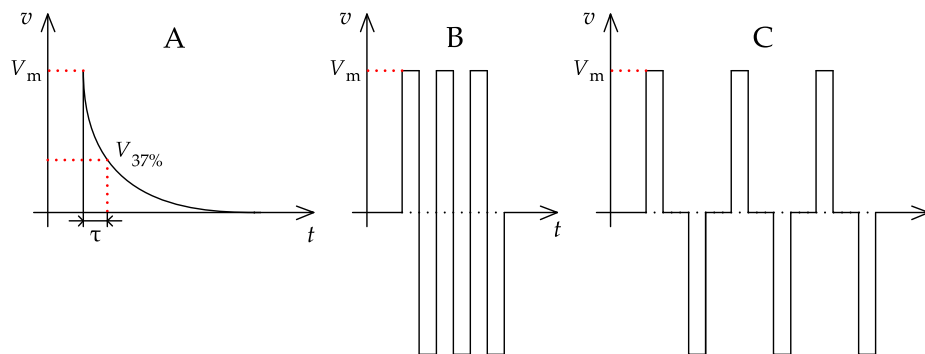


Figure 1: Examples of commonly used waveforms.

3. ADVANTAGES OF ASYMMETRICAL PULSES

Positive voltage pulse causes an electric intensity with the same orientation as the unipolar pulse during DC electroporation. According to study [6], creation of nanopores in the cell wall depends strongly non-linearly on a membrane voltage. For this reason, it is very convenient to apply higher electric intensity for a shorter time than lower intensity for a longer time. And moreover, a positive value of electric intensity should be higher than a value of intensity in the opposite direction. As the result, positive pulse should be higher and shorter than the negative to reach higher electroporation effect. Area of positive and negative current pulses caused by asymmetrical voltage must be equal to achieve a zero DC component. DC component is undesired due to electrolysis, which leads to creation of gaseous bubbles, that can endanger a patient. Authors of mentioned study observed, that asymmetrical pulses had higher electroporation effect than symmetrical pulses with the same energy transferred during one period at the same frequency. Authors also claimed, that asymmetrical pulses transferred more energy than symmetrical pulses with the same charge. An example of symmetrical and asymmetrical waveform is drawn in Fig. 2 [6].

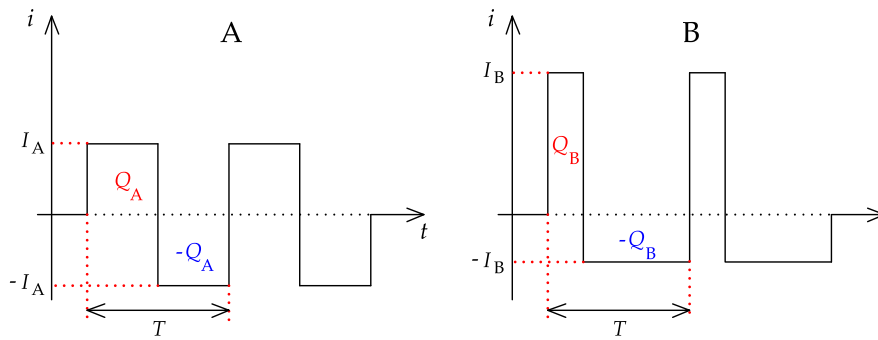


Figure 2: Symmetrical and asymmetrical waveform [6].

All labeled charges are the same. Symmetrical pulses (A) have the same lengths $\frac{1}{2}T$ and amplitudes $I_A = -I_A$. Positive asymmetrical pulse has the length of $\frac{1}{4}T$ and amplitude $I_B = 2I_A$. Negative pulse must then have the length of $\frac{3}{4}T$ and amplitude $-I_B = \frac{2}{3}I_A$ so that the negative charge $-Q_B$ is the same as the positive charge Q_B . If symmetrical pulses (A) transfer energy W during one period T , then asymmetrical pulses (B) transfer energy $\frac{4}{3}W$ during the same time. In order to be able to compare electroporation effect of both waveforms, it is necessary that the same energy or the same charge is transferred during one period T . Authors used symmetrical and asymmetrical waveform with frequency of 167 kHz. Symmetrical pulses had amplitudes ± 600 V, while asymmetrical pulses had positive amplitude $+544$ V and negative amplitude -221 V. In both cases, 10 bursts with a length of 2 ms were applied and a space between bursts was 400 ms. A total energy 10×20 J was delivered, but asymmetrical pulses transferred during single period T only 92 % of charge of symmetrical pulses. As the result, lesions caused by asymmetrical waveform were deeper than lesions caused by symmetrical pulses [6].

4. USE OF TRANSISTORS IN HV GENERATORS

Transistors are very suitable for high-voltage sources of square and rectangular pulses. These generators have low weight and dimensions. They can be constructed from common parts, so they are relatively cheap and it is possible to develop the generator with a wider range of parameters than is commercially available. The use of power transistors is limited by their maximum drain to source voltage, drain current and especially by their switching times. For this reason, power transistors are not suitable for ns and ps pulses generating. But this claim may not be valid in the near future, because the parameters of power transistors are improving rapidly [2].

There are two main groups of electroporation generators: devices with HV storage capacitors and generators with step-up pulse transformer. The first group is more common, typical example is a commercial NanoKnife device proposed for DC electroporation. Power part of these generators is simple, because voltage pulses are created by the main transistor switch, which connects storage capacitors with application electrodes for a certain time. Rise and fall times of pulses are affected practically only by switching time of the transistor switch. Some generators contain additional transistor,

that grounds the output terminal and cuts off the fall time [7]. But there is a certain risk of pulse with uncontrolled length, when the main transistor switch is short-circuited. For this reason, the generator must be equipped with some safety switch, that disconnects the patient in the case of the main switch malfunction. Safety requirements also lead to increase of demands on control circuits [2]. Storage capacitors are charged from rectified AC mains through voltage regulator, namely isolated DC-DC converter, where the pulse transformer provides a galvanic isolation of the patient. Typical block diagram of HV generator with storage capacitors can be seen in Fig. 3. Marx generators, where spark gaps are replaced by power transistors, can be also included in this group. This topology produces unipolar pulses suitable for DC electroporation. For AC method, a pair of generators is necessary [8].

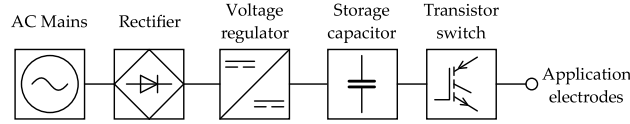


Figure 3: Typical block diagram of generator with storage capacitors.

DC-DC converter or DC-AC inverter with step-up pulse transformer is another solution of generators for electroporation. The transformer provides the galvanic isolation of the patient from AC mains and its turns ratio determines maximum output voltage. Storage capacitors are placed into a DC bus at the power part. Low-voltage electrolytic capacitors also consume less space than high-voltage film capacitors in generators without step-up transformer, if we consider the same amount of stored energy. Mentioned risk of uncontrolled discharge of capacitors is completely eliminated here, because when the power transistor fails, DC bus is short-circuited. This is the main feature of all generators developed at FEEC BUT. The main disadvantage of this solution is a leakage inductance of the transformer, which makes rise and fall times of pulses longer compared to devices with storage capacitors. Parasitic capacitance of windings is another problem. But excellent security for the patient can be seen as the main advantage in terms of future certification. Typical block diagram of generator with step-up pulse transformer is shown in Fig. 4. Secondary HV rectifier in dashed block is used only in generators for DC electroporation [9].

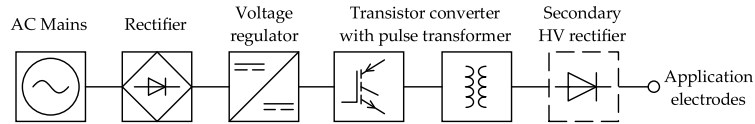


Figure 4: Typical block diagram of generator with pulse transformer.

5. GENERATOR OF ASYMMETRICAL WAVEFORM WITH PULSE TRANSFORMER

Pulse transformer is a common part of DC-DC switch mode supplies or DC-AC inverters. At these devices, symmetrical pulses are usually transformed. But transformer is also able to transform asymmetrical waveform, when certain conditions are met. Flux linkage Ψ (magnetic flux in core Φ) is a time integral from primary voltage v_1 (1) [10].

$$\Psi(t) = N_1 \Phi(t) = \int v_1(t) dt \quad (1)$$

N_1 is a number of primary turns. Primary voltage pulses v_1 are rectangular. Then flux linkage Ψ , magnetic flux Φ and also magnetizing current I_μ have triangular shape. To avoid a saturation of the transformer core, the value of integral from positive pulse $+V_1$ must be equal to the value of integral from negative pulse $-V_2$. If we consider, that the pulse period T consists of positive pulse t_1 and negative pulse t_2 , then areas of both pulses must be equal (2) [10].

$$V_1 t_1 = -V_2 t_2 \quad (2)$$

If this condition is met, primary voltage v_1 does not contain a DC component, which would cause the saturation of the core. Power part of the generator requires two independent DC buses with different voltages V_1 and V_2 (see Fig. 5). Each DC bus is created from electrolytic capacitors, which are charged from rectified AC mains through voltage regulator. Primary voltage v_1 is positive, when both transistors T_1 and T_4 are switched on and negative, when transistors T_2 and T_3 in opposite diagonal are switched on. Secondary voltage v_2 has the same shape as primary voltage v_1 , but its amplitudes are different with turns ratio $\frac{N_2}{N_1}$. Primary current i_1 is a sum of secondary current i_2 transformed to primary side and magnetizing current i_μ . Capacitor C_1 eliminates the DC magnetization of the transformer, when the DC component of primary voltage v_1 occurs. Snubber R_2, C_2 is connected to the secondary winding [10].

Load is represented by resistor R , but real tissue has a resistive-capacitive character. Charging of capacitive component of the load causes undesired current peaks and reaction of an overcurrent protection. For this reason, variable inductors L_3 and L_4 are connected between secondary winding and output terminals. These inductors suppress capacitive current peaks and also limit capacitive current, which flows from the mains through the parasitic capacitance of the transformer and body of the patient to the ground. Because the load resistance is changed during the electroporation process and depends on many factors, such as area of electrodes, tissue conductivity, etc, inductors are variable. They can also be totally short-circuited [4].

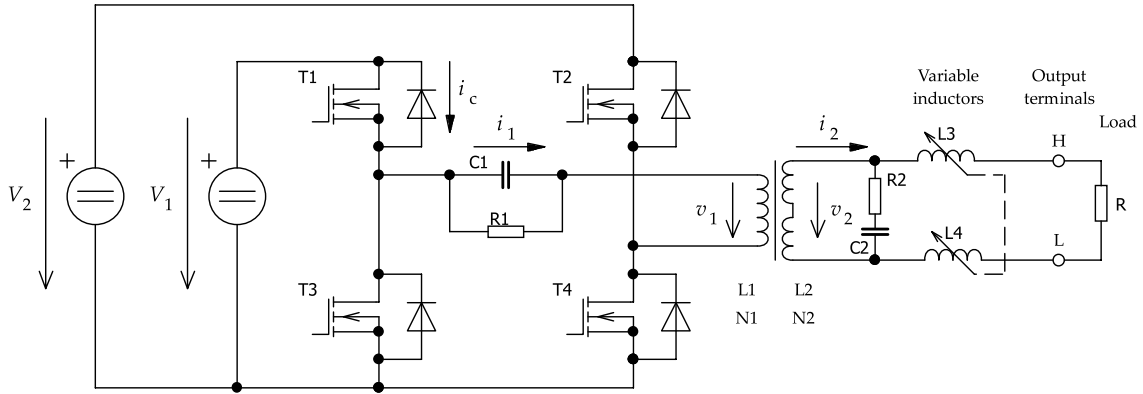


Figure 5: Circuit diagram of DC-AC inverter.

Both voltage regulators in DC buses must be controlled by control unit with microprocessor. In terms of dynamics, it is faster to change times t_1 and t_2 than amplitudes V_1 and V_2 . For this reason, the user sets pulse frequency f (pulse period T), positive amplitude V_1 and length of the positive pulse t_1 . Then the processor unit calculates remaining values V_2 and t_2 . Both voltages V_1 and V_2 are permanently measured and the processor must be able to modify the time t_2 immediately, when some voltage deviation occurs. Only then the zero DC component of primary voltage v_1 is achieved. Primary current i_1 is sensed to protect power transistors T_1 – T_4 . When it exceeds its maximum value, power part is disabled. It is obvious, that demands on the processor unit are high. The user can also set the length of the burst, the number of bursts and the space between them. All significant values will be displayed on touch screen. New generator will be designed as a compact portable device, which will be able to be used in various research institutes.

6. CONCLUSION

This paper is focused on possible solution of HV electroporation generator, which is able to produce asymmetrical waveform. Application of asymmetrical voltage pulses is the latest trend at research of AC electroporation. Asymmetrical pulses have higher effect than symmetrical pulses with the same energy. Most of HV generators are based on controlled discharge of storage capacitors into the tissue. This solution is simple, but there is a certain risk of uncontrolled discharge of the capacitor, when the transistor switch is short-circuited. We present different generator, where pulse transformer is used and where mentioned risk is eliminated. Pulse transformer can transform asymmetrical voltage pulses, when the integral from positive voltage is the same as the integral from the negative voltage. This requirement places the great demands on the control circuits, but excellent safety for the patient outweighs this disadvantage and facilitates any future certification.

ACKNOWLEDGMENT

This research work has been carried out in the Centre for Research and Utilization of Renewable Energy (CVVOZE). Authors gratefully acknowledge financial support from the Ministry of Education, Youth and Sports under institutional support and BUT specific research programme (project No. FEKT-S-20-6379).

This work was supported by the Ministry of Health of the Czech Republic, grant no. NU21-08-00561, NT11128-4/2010, and 15-32484a, and programme for conceptual development of research organization (FNBr, 65269705), and by the Ministry of Education, Youth and Sports - specific research project of Masaryk University MUNI/A/1342/2020.

REFERENCES

- [1] J. Li, X.B. Zhang, J.J. Wang, et al, “Comparison between high-frequency irreversible electroporation and irreversible electroporation ablation of small swine liver: follow-up of DCE-MRI and pathological observations”, *Chinese Medical Journal*, vol. 134, no.17, pp. 2081-2090, 2021, ISSN 0366-6999, [doi:10.1097/CM9.0000000000001663](https://doi.org/10.1097/CM9.0000000000001663).
- [2] M. Rebersek, D. Miklavcic, C. Bertacchini and M. Sack, “Cell Membrane Electroporation-Part 3: The Equipment”, *IEEE Electrical Insulation Magazine*, vol. 30, no. 3, pp. 8-18, 2014, [doi:10.1109/MEI.2014.6804737](https://doi.org/10.1109/MEI.2014.6804737).
- [3] M. Rebersek and D. Miklavcic, “Advantages and Disadvantages of Different Concepts of Electroporation Pulse Generation”, *Automatika*, Taylor and Francis, vol. 52, no. 1, pp. 12-19, 2017, ISSN 0005-1144, [doi:10.1080/00051144.2011.11828399](https://doi.org/10.1080/00051144.2011.11828399).
- [4] M. Folprecht, D. Cervinka and P. Prochazka, “Compact High-Voltage AC Generator with Pulse Transformer for High-Frequency Irreversible Electroporation (H-FIRE)”, *Electronics*, vol. 10, no. 23, 2021, ISSN 2079-9292, [doi:10.3390/electronics10232898](https://doi.org/10.3390/electronics10232898).
- [5] V. M. Ringel-Scaia, N. Beitel-White, M. F. Lorenzo, et al, “High-frequency irreversible electroporation is an effective tumor ablation strategy that induces immunologic cell death and promotes systemic anti-tumor immunity”, *EBioMedicine*, vol. 44, pp. 112-125, 2019, ISSN 23523964, [doi:10.1016/j.ebiom.2019.05.036](https://doi.org/10.1016/j.ebiom.2019.05.036).
- [6] R. van Es, M. K. Konings, B. C. Du Pré, et al, “High-frequency irreversible electroporation for cardiac ablation using an asymmetrical waveform”, *BioMedical Engineering OnLine*, vol. 18, no. 1, 2019, ISSN 1475-925X, [doi:10.1186/s12938-019-0693-7](https://doi.org/10.1186/s12938-019-0693-7).
- [7] V. Stankevic, P. Simonis, N. Zurauskiene, A. Stirke, A. Dervinis, V. Bleizgys, S. Kersulis and S. Balevicius, “Compact Square-Wave Pulse Electroporator with Controlled Electroporation Efficiency and Cell Viability”, *Symmetry*, vol. 12, no.3, 2020, ISSN 2073-8994, [doi:10.3390/sym12030412](https://doi.org/10.3390/sym12030412).
- [8] L.M. REDONDO, M. Zahyka and A. Kandratsyev, “Solid-State Generation of High-Frequency Burst of Bipolar Pulses for Medical Applications”, *IEEE Transactions on Plasma Science*, vol. 47, no.8, 2019, pp. 4091-4095, ISSN 0093-3813, [doi:10.1109/TPS.2019.2923570](https://doi.org/10.1109/TPS.2019.2923570).
- [9] D. Cervinka, and V. Novotna, “High-Voltage Pulse Source for Cell Electroporation”, *Mechatronics 2017: Advances in Intelligent Systems and Computing*, Springer International Publishing, 2018, pp. 80-86, ISBN 978-3-319-65959-6, [doi:10.1007/978-3-319-65959-6](https://doi.org/10.1007/978-3-319-65959-6).
- [10] M. H. Rashid, *Power Electronics Handbook*, 4, UK: Butterworth-Heinemann, 2018, ISBN 978-0-12-811407-0.

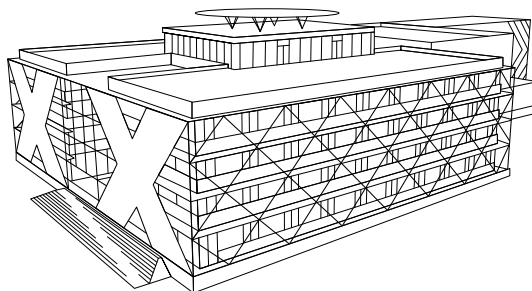


DĚLÁME CHYTRÉ TECHNOLOGIE
A ŘÍDÍME DOPRAVU.
TADY I VE SVĚTĚ.

www.cross-traffic.com

KDO JSME?

Jsme to my, kdo z obyčejných měst dělá chytrá města. Staráme se o to, aby se dobře parkovalo, průjezd městem byl rychlejší a bez kolon, aby silnice a dálnice nebyly přetížené a aby bylo možné efektivně řídit dopravu. Je nás na to více než 160, máme vlastní tým IT vývojářů a spoustu dalších lidí, kteří se starají o hladký průběh našich projektů. Pracujeme v 55 zemích světa, ale sídlo máme ve Zlíně. Můžeš si vybrat technologie, které tě zajímají, a pracovat na projektech na té nejvyšší úrovni, které lze v našem oboru dosáhnout.



KOHO HLEDÁME?

Technicky zdatné, jazykově vybavené zaměstnance zapálené pro elektrotechniku s chutí pracovat a rozvíjet se.

- PROGRAMÁTOŘY (SW & HW)
- SALES ENGINEERY
- ELEKTROINŽENÝRY
- ELEKTROTECHNIKY



VÁŽENÍ
ZA JÍZDU



ŘÍZENÍ
DOPRAVY



PARKOVACÍ
SYSTÉMY



SILNIČNÍ
METEOROLOGIE



DETEKCE
PŘESTUPKŮ



DETEKCE
DOPRAVY



5 TÝDNŮ
DOVOLENÉ



13. PLAT



PRUŽNÁ
PRACOVNÍ DOBA



NOTEBOOK, MOBIL
A MOBILNÍ TARIF



PŘÍSPĚVEK
NA STRAVOVÁNÍ



KURZY
A VZDĚLÁVÁNÍ



PŘÍSPĚVEK NA
SPORTOVNÍ AKTIVITY



DOSTANEŠ SE
DO CELÉHO SVĚTA



ZAÚJALI JSME TĚ?

Pošli životopis na kariera@cross.cz.
Potkáme se a pokud nám to bude spolu
klapat, rádi tě vezmeme mezi sebe.

Comparison of two loss minimization algorithms for induction motors

T. Lažek¹, and I. Pazdera¹

¹Brno University of Technology, Czech Republic

E-mail: Tomas.Lazek@vut.cz, pazderai@vut.cz

Abstract—This paper discusses two loss minimization algorithms for induction motor drives. Firstly, equivalent models in the form of Gamma and inverse Gamma are shown, from which the loss models were obtained. Then, the procedure for determining the two algorithms is presented. The results show that it is easier to determine the loss minimization algorithm for rotor flux. In terms of accuracy, both algorithms are similarly accurate.

Keywords—calculation comparison, induction motor drives, loss minimization algorithm, power losses

1. INTRODUCTION

The largest consumers of electricity are electric induction motor drives. These motors are simple in design, robust, reliable, and have high efficiency, but this can drop if the speed and torque are varied over a wide range.

The efficiency of an induction motor can be increased by reducing losses through the appropriate linkage flux. One of the commonly used strategies is model-based method determining the optimal linkage flux. [1].

The aim of this paper is to present the procedure of determining the algorithm of optimal linkage flux from the motor parameters for stator and rotor field-oriented control. The calculations are different for both types of control and this paper shows a description of the differences and an evaluation of the results.

2. INDUCTION MACHINE MODEL IN STEADY STATE

For determining the optimal linkage flux algorithm, it is useful to add a resistor represent the iron resistance to the model. This resistor is placed parallel to the magnetizing inductance on the stator side. Detailed development of the model can be found in [2].

The models most commonly used are in the form of a gamma network (Γ -network) and an inverse gamma network (Γ -network). In general, the Γ -network is used for stator field-oriented control and the Γ -network for rotor field-oriented control.

The steady-state model in the form Γ -network shown in Fig. 1 is defined in the rotating (d,q) stator flux frame, hence $\Psi_{sd} = \Psi_s$ and $\Psi_{sq} = 0$.

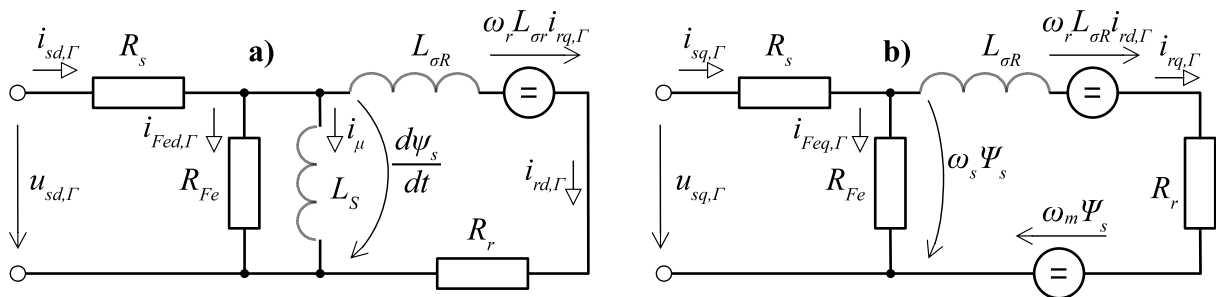


Figure 1: Steady-state induction machine equivalent circuit (Γ -network) in: a) d-axis and b) q-axis

In steady state, the coils can be considered as a short circuit. Then, for the stator voltage in q-axis

$$u_{sq,\Gamma} = R_s i_{sq,\Gamma} + \omega_s \Psi_s = \omega_r L_{\sigma s} i_{rd,\Gamma} + R_r i_{rq,\Gamma} + \omega_m \Psi_s, \quad (1)$$

where ω_r is the rotor frequency, which is defined as the difference of synchronous frequency ω_s and mechanical speed ω_m . $\omega_s \Psi_s$ represents the voltage on the rotor side. Since resistance R_{Fe} is many times greater than rotor resistance R_r , currents $i_{Fed,\Gamma}$ and $i_{Feq,\Gamma}$ can be considered zero. It is advantageous to express the current in the q-axis as a function of torque and stator linkage flux. For stator currents on the d- and q-axes, we can write

$$i_{sd,\Gamma} = i_{Fed,\Gamma} + i_{\mu,\Gamma} + i_{rd,\Gamma} = \frac{\Psi_s}{L_s} + \frac{\omega_r L_{\sigma R} i_{rq,\Gamma}}{R_r}, \quad (2)$$

$$i_{sq,\Gamma} = i_{Feq,\Gamma} + i_{rq,\Gamma} = \frac{2M}{3p\Psi_s}, \quad (3)$$

where p is the number of pole-pairs. Furthermore, the Fig. 1 shows that the voltage across the resistor R_{Fe} is $\omega_s \Psi_s$.

Fig. 2 shows the steady-state model in the form T-network which is defined in the rotating (d,q) rotor flux frame. Then $\Psi_{rd} = \Psi_r$ and $\Psi_{rq} = 0$.

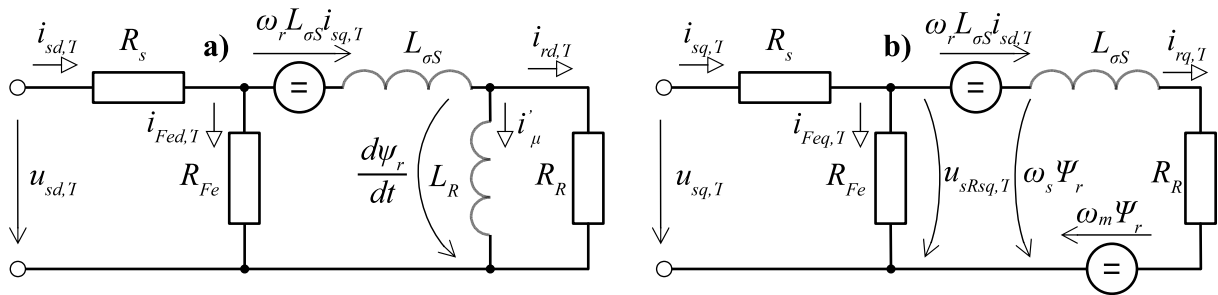


Figure 2: Steady-state induction machine equivalent circuit (T-network) in: a) d-axis and b) q-axis

Similarly to the previous model, the coils in steady-state can be considered as a short circuit. The rotor current in the d-axis can be considered as zero, due to the zero voltage on the L_R inductance. The induced voltage from the q-axis lies across the resistor R_{Fe} . This voltage is very small due to the small leakage inductance $L_{\sigma S}$. Then for the current in d-axis

$$i_{sd,\Gamma} = i_{Fed,\Gamma} + i_{rd,\Gamma} = \frac{\Psi_r}{R_R}. \quad (4)$$

Since the resistance of R_{Fe} is many times greater than the resistance of R_R , the current through R_{Fe} can be neglected. Then the current in the q-axis can be described as follows

$$i_{sq,\Gamma} = i_{Feq,\Gamma} + i_{rq,\Gamma} = \frac{2M}{3p\Psi_r}. \quad (5)$$

3. LOSS MODEL

In the rotating flux frame (d, q), electrical losses can be determined very easily. First, iron losses can be calculated by dividing the voltage $u_{R,Fe}^2$ by the resistance R_{Fe} . However, the iron resistance must not be constant because the iron losses consist of eddy current losses and hysteresis losses. According to [2], these two values can be combined to create a simple linear dependence of the total iron losses on frequency. Then the iron losses can be calculated

$$P_{Fe} = \frac{3}{2} \frac{u_{R,Fe}^2}{R_{Fe}} = \frac{3}{2} \frac{u_{R,Fe}^2}{R_{Fe0}(\omega_s/\omega_0)} = \frac{3}{2} \frac{u_{R,Fe}^2 \omega_0}{R_{Fe0} \omega_s}, \quad (6)$$

where ω_0 is the frequency at which the resistance R_{Fe0} is determined.

Stator currents flow through the stator winding in both axes. Then for joule losses in the stator winding

$$P_{js} = \frac{3}{2} R_s (i_{sd}^2 + i_{sq}^2). \quad (7)$$

The same situation occurs when determining the joule losses in the rotor. Currents flow through the rotor winding in both axes then

$$P_{jr} = \frac{3}{2} R_r (i_{rd}^2 + i_{rq}^2). \quad (8)$$

To determine the analytical expression of the optimum linkage flux, it is useful to express all quantities as functions of torque, linkage flux, and speed. Therefore, the synchronous frequency can be described by neglecting the rotor frequency as $\omega_s = p\omega_m$.

The expression of the iron losses in the Γ -network is given by equation (6). As mentioned above, the voltage across the resistor R_{Fe} is determined by $\omega_s \Psi_s$. Then for iron losses is true

$$P_{Fe,\Gamma} = \frac{3}{2} \frac{\omega_m p \omega_0 \Psi_s^2}{R_{Fe0}}. \quad (9)$$

In the case of Joule losses, it is easy to determine both currents in the q-axis using the equation (3). More complicated is the expression of currents in the d-axis. ω_r appears in equation (2), which can be expressed from equation (1). In [3] is shown that ω_r can be calculated as follows

$$\omega_{r,\Gamma} = \frac{2 R_r M}{3 p \Psi_s^2}. \quad (10)$$

Substituting equation (10) into (2) gives an expression for the Joule losses in the rotor

$$P_{jr,\Gamma} = \frac{3}{2} \left(\frac{R_r M^2}{p^2 \Psi_s^2} \right) + \frac{8}{27} \left(\frac{R_r M^4 L_{\sigma R}^2}{p^4 \Psi_s^6} \right). \quad (11)$$

Equation (2) is substituted into the equation for the stator current (2). Then for the Joule losses in the stator

$$P_{js,\Gamma} = \frac{3}{2} \left(\frac{R_s \Psi_s^2}{L_s^2} \right) + \frac{4}{3} \left(\frac{R_s M^2 L_{\sigma R}}{p^2 \Psi_s^2 L_m} \right) + \frac{8}{27} \left(\frac{R_s \cdot M^4 \cdot L_{\sigma R}^2}{p^4 \Psi_s^6} \right) + \frac{3}{2} \left(\frac{R_s M^2}{p^2 \Psi_s^2} \right). \quad (12)$$

The term in equations (11) and (12) that contains Ψ^{-6} has very little effect on the accuracy of the loss calculation, as demonstrated in [3]. So, this term can be neglected.

For the T-network, iron losses can be expressed similarly according to equation (6), with the voltage on R_{Fe} defined as $\Psi_r \omega_s + L_{\sigma S} i_{sd} \Gamma \omega_s$ (from Fig. 2). Then the iron losses can be written

$$P_{Fe,T} = \frac{3}{2} \frac{\omega_m p \omega_0 \Psi_r^2 (1 + L_{\sigma S} / L_R)^2}{R_{Fe0}}. \quad (13)$$

Since the rotor current in the d-axis is zero and the rotor current in the q-axis is determined by equation (5), determining the rotor Joule losses is easy:

$$P_{jr,T} = \frac{3}{2} R_r \frac{4M^2}{9p^2 \Psi_r^2}. \quad (14)$$

Since the stator current in the d-axis is equal to the magnetizing current, then for Joule losses in the stator

$$P_{js,T} = \frac{3}{2} \frac{R_s \Psi_r^2}{L_R^2} + \frac{4M^2}{9p^2 \Psi_r^2}. \quad (15)$$

4. LOSS MINIMIZATION ALGORITHM

Finding the optimal steady-state linkage flux can be done by solving the following equation

$$\frac{\partial}{\partial \Psi} \{P_{Fe} + P_{js} + P_{jr}\} = 0. \quad (16)$$

Analytical expression for the optimal stator flux for Γ -network

$$\Psi_{s,opt} = \sqrt{M} \sqrt{\frac{2L_s}{3p}} \sqrt{\frac{R_s(2k_l + 1) + R_r}{\omega_m L_s^2 F + R_s}}, \quad (17)$$

where $k_l = L_{\sigma R}/L_s$ and $F = \omega_0 p / R_{Fe0}$. Finally, the analytical expression for the optimal rotor flux for T-network

$$\Psi_{r,opt} = \sqrt{M} \sqrt{\frac{2L_R}{3p}} \sqrt{\frac{R_{Fe} L_R^2 (R_s + R_R)}{\omega_m \omega_0 p L_R^2 (1 + L_{\sigma S}/L_R)^2 + R_{Fe} R_s}}. \quad (18)$$

5. RESULTS

The algorithm was verified on a real induction machine, whose parameters can be found in [4]. The dependence of the total losses on the stator flux, respectively, rotor flux for three different torques and two mechanical speed (3000 min^{-1} and 1500 min^{-1}) can be seen in Fig. 3 respectively Fig. 4. Furthermore, the points of optimum flux calculated according to the equation (17) respectively (18) for the corresponding torque and speed are marked with a cross in the graph.

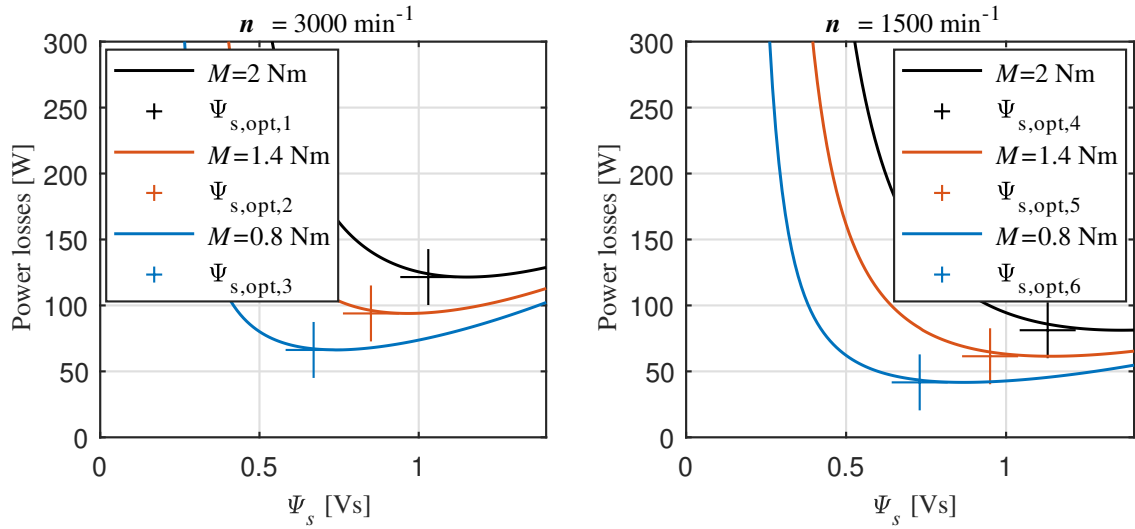


Figure 3: Dependence of total power losses on stator flux Ψ_s at different torques and speeds

Table I shows the calculated values of the optimum linkage flux according equation (17) respectively (18) and the values of the ideal linkage flux at which the motor has the lowest losses, deviation and percentage deviation for a given torque, and speed.

Table I: Comparison of ideal linkage flux Ψ_{id} and calculated optimal linkage flux Ψ_{opt}

n [min^{-1}]	M [Nm]	Γ -network				T-network			
		$\Psi_{s,id}$ [Vs]	$\Psi_{s,opt}$ [Vs]	δ [Vs]	δ [%]	$\Psi_{r,id}$ [Vs]	$\Psi_{r,opt}$ [Vs]	δ [Vs]	δ [%]
3000	0.8	0.74	0.67	0.07	9.46	0.68	0.62	0.06	8.82
	1.4	0.98	0.85	0.13	13.27	0.88	0.79	0.09	10.23
	2.0	1.15	1.03	0.12	10.43	1.05	0.93	0.12	11.43
1500	0.8	0.87	0.73	0.14	16.09	0.79	0.69	0.10	12.66
	1.4	1.14	0.95	0.19	16.67	1.05	0.89	0.16	15.24
	2.0	1.36	1.13	0.23	16.91	1.25	1.03	0.22	17.60

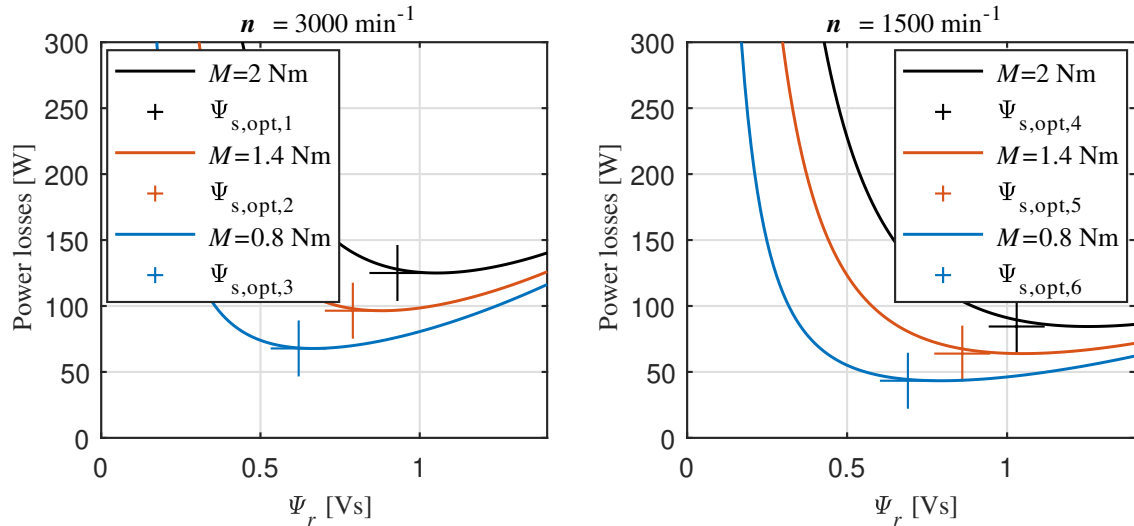


Figure 4: Dependence of total power losses on rotor flux Ψ_r at different torques and speeds

Furthermore, the Table I shows that the deviation of the calculated optimal linkage flux differs from the ideal value by tens of percent. However, the graphs show that the total loss curve is very flat in the region of the minimum. Therefore, the resulting power loss when applying the calculated optimum linkage flux will not be as large compared to the power loss at the ideal flux value.

6. CONCLUSION

The aim of this paper was to present a comparison of the computation loss minimization algorithm for the equivalent circuit in form Γ -network and T-network of the induction motor. The minimization algorithms are derived from both equivalent circuits. The derivation of the algorithm for rotor flux orientation is simpler. The algorithm for stator flux orientation leads to a complex expression for the losses. In general, the rotor flux oriented algorithm performs better. However, both algorithms can be considered as accurate because, as shown in the Fig. 3 and Fig. 4, the flux-dependent loss curve is very flat. Hence, the deviations in the algorithm will not cause a large loss increase.

ACKNOWLEDGMENT

This research work has been carried out in the Centre for Research and Utilization of Renewable Energy (CVVOZE). Authors gratefully acknowledge financial support from the Ministry of Education, Youth and Sports under institutional support and BUT specific research programme (project No. FEKT-S-20-6379).

REFERENCES

- [1] M. N. Uddin and S. W. Nam, "New Online Loss-Minimization-Based Control of an Induction Motor Drive," in *IEEE Transactions on Power Electronics*, vol. 23, no. 2, pp. 926-933, March 2008, doi: 10.1109/TPEL.2007.915029.
- [2] N. P. Quang and J. A. Dittich, *Vector Control of Three-Phase AC Machines System Development in the Practice*. Berlin, Germany: Springer-Verlag, 2008.
- [3] LAŽEK, Tomáš. Induction motor control with respect to maximum efficiency [online]. Brno, 2021 [cit. 2022-03-11]. Available from: <https://www.vutbr.cz/studenti/zav-prace/detail/135590>. Doctoral Thesis Topic. Vysoké učení technické v Brně, Fakulta elektrotechniky a komunikačních technologií, Department of Power Electrical and Electronic Engineering. Supervisor Ivo Pazdera.
- [4] M. Toman, R. Cipin, P. Vorel and M. Mach, "Algorithm for IM Optimal Flux Determination Respecting Nonlinearities and Thermal Influences," 2018 IEEE International Conference on Environment and Electrical Engineering and 2018 IEEE Industrial and Commercial Power Systems Europe (EEEIC / I&CPS Europe), Palermo, 2018, pp. 1-5, doi: 10.1109/EEEIC.2018.8493953.

Power Flow in Traction System and SFC Based Feeder Load Control: Sensitivity Analyses

J. Klusacek¹, J. Drapela¹

¹Dept. of Electrical Power Engineering, FEEC, Brno University of Technology, Czech Republic

E-mail: klusacekj@vut.cz, drapela@vut.cz

Abstract— The paper presents an analysis of active and reactive power control in AC 25 kV 50 Hz railway traction system consisting of both static frequency converter feeder and conventional single-phase transformer feeder. Limits of power sharing between the traction system feeders by means of the converter output voltage is analyzed and, additionally, control strategies aiming to increase the availability of the static frequency converters for services in distribution system is proposed.

Keywords—railway, static frequency converter, power flow control, unbalance

1. INTRODUCTION

In the Czech Republic, the AC railway traction systems (RTS) 25 kV 50 Hz are connected to the distribution system (DS), typically employing single-phase 110 kV(±8x2%)/27 kV transformers (TR) and the RTS is divided into single-side fed phase-insulated sections, typically 20 to 30 km long [1],[2]. Consequently, the single-phase transformer-based RTS exhibits following deficiencies: 1) on the RTS side - voltage drops reducing the traction vehicles power and split sections with neutral fields; and 2) on DS side - voltage unbalance in DS increasing in severity during recuperative braking. In recent years, however, the four-quadrant static frequency converters (SFC) are being employed in DS to RTS interfacing; primarily in order to improve the power quality at DS terminals and to increase the control capabilities in RTS [3]-[5]. Secondly, a potential for SFCs to be employed in DS voltage control is recognized. Therefore, the paper is focused on analysis of capabilities and limits of SFC based RTS feeder in controlled sharing of the moving train power consumption in cooperation with conventional TR based feeder, under realistic conditions. The problem is introduced using simplified analytic model and the practical range of voltage amplitude and angle is obtained by means of steady-state sensitivity analysis conducted in PSCAD simulating developed simplified model with realistic parametrization.

2. FUNDAMENTALS OF POWER TRANSMISSION CONTROL

In general, a train powered in Figure 1 from LOC node can be electrically considered as a general constant power load (P_{LOC} , Q_{LOC}) fed from two single-phase AC feeders with variable amplitude and angle. Whereas the TR feeder in node T,MV represents via transformer connected DS, while a SFC feeding unit is constituted by a voltage source in node SFC. It is assumed in this stage, that the voltage phasor $V_{T,HV}$ has fixed amplitude and angle. On the other hand, the voltage phasor V_{SFC} has variable both amplitude $|V_{SFC}|$ and angle δ_{SFC} . It is also depicted, that the voltage amplitude is being kept in specific range at all nodes, while the voltage angle can be varied in relatively wide range. The active and reactive power fed from node SFC to node LOC (P_{SFC} , Q_{SFC}) is related to V_{LOC} , V_{SFC} and impedance between nodes SFC and LOC (Z_{SFC}) according to (1) and (2), which has been derived in [1] for three-phase transmission. Catenary shunt parameters are omitted.

$$P_{SFC} = \frac{|V_{SFC}| \cdot |V_{LOC}|}{|Z_{SFC}|} \cdot \cos(\rho_{SFC} + \delta_{LOC} - \delta_{SFC}) - \frac{|V_{LOC}|^2}{|Z_{SFC}|} \cdot \cos(\rho_{SFC}) \quad (1)$$

$$Q_{SFC} = \frac{|V_{SFC}| \cdot |V_{LOC}|}{|Z_{SFC}|} \cdot \sin(\rho_{SFC} + \delta_{LOC} - \delta_{SFC}) - \frac{|V_{LOC}|^2}{|Z_{SFC}|} \cdot \sin(\rho_{SFC}) \quad (2)$$

It should be noted, that the equations cannot be simplified as in case of high voltage (HV) transmission

line parameters (i.e. $R \ll X$, $Z \approx X \angle (\pi/2)$, $\sin(\delta_{SFC} - \delta_{LOC}) \approx (\delta_{SFC} - \delta_{LOC})$, $\cos(\delta_{SFC} - \delta_{LOC}) \approx 1$) as presented in [1], because the 25 kV traction system ratio $R/X \approx 1$ does not allow the same simplification. Furthermore, (1) and (2) presumes the V_{LOC} to be constant, omitting the voltage drop on Z_T . Due to the complexity of the problem, the sensitivity of the power distribution over the feeders on variable phasor V_{SFC} , hence the system operation area, is analyzed using a sensitivity analysis in next sections.

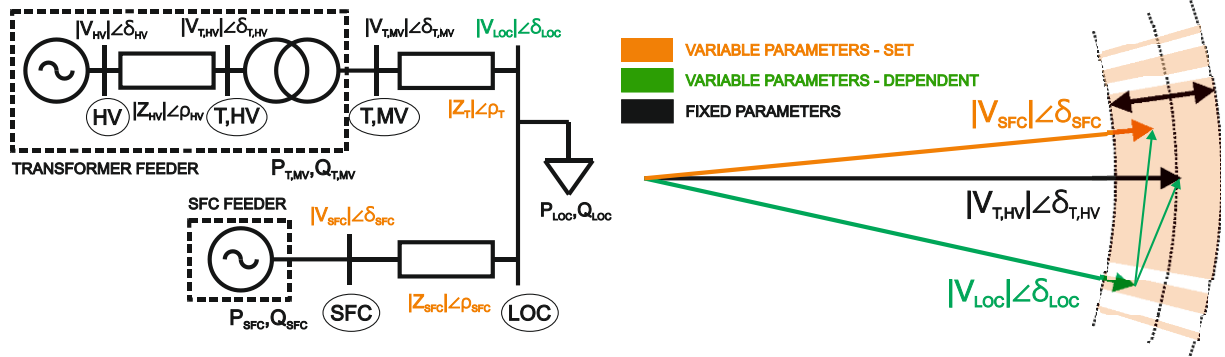


Figure 1: Single-pole model of the two-side fed railway load (left) and phasor diagram (right).

3. SENSITIVITY ANALYSIS MODEL

The analyzed power supply system scheme is depicted in Figure 2A. The DS is demonstrated as 110 kV high voltage (HV) ideal feeder and two radial branches with the same impedance Z_{HV} representing together a feeder of rather low short circuit power system. The RTS consists of two feeders (SFC and TR, respectively) feeding the RTS load. The train operates with constant power (P_{LOC} , Q_{LOC}) supplied via catenary with line impedances Z_{SFC} (from SFC to load) and Z_T (from TR to load), respectively. The impedances Z_{SFC} and Z_T varies inversely in proportion to each other to simulate the train position while their sum is kept constant representing the section of maximal length $l_{tot} = 30$ km [2] with impedance per kilometer z_k (see the Table 1).

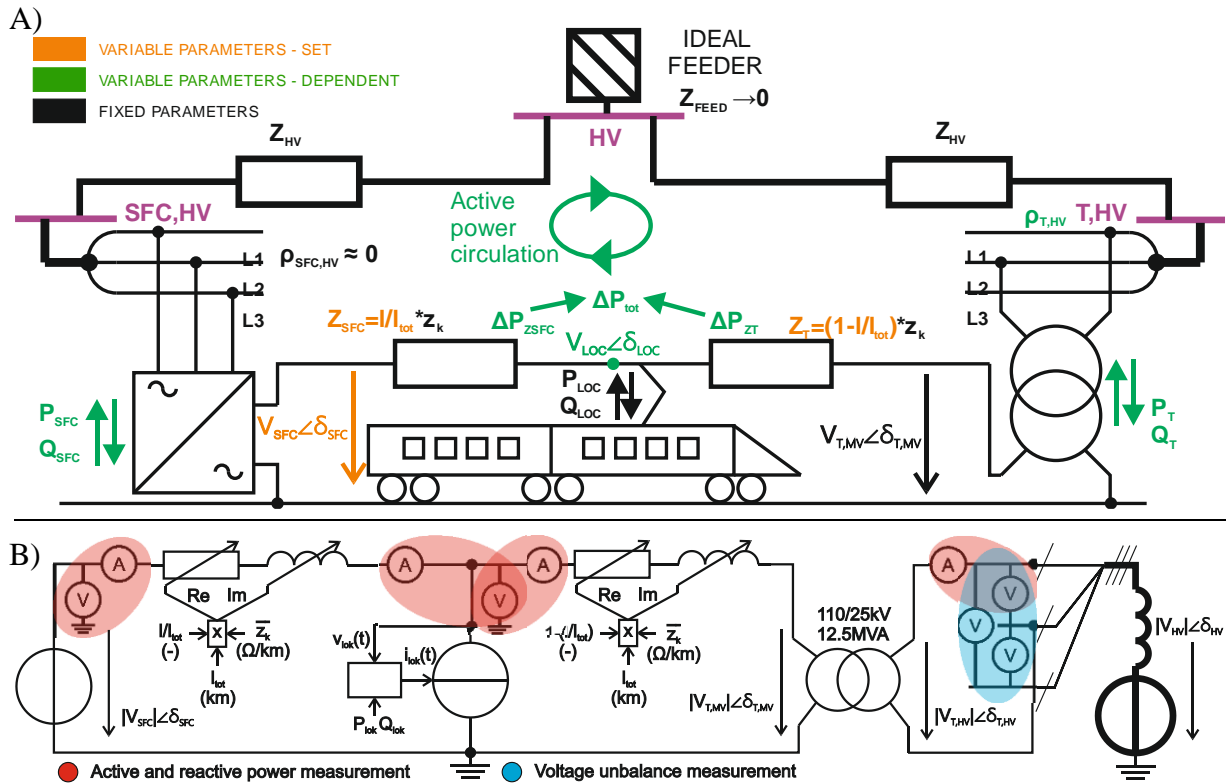


Figure 2: Power supply scheme of single-track railway (A), simplified model in PSCAD (B).

According to the fact that the sensitivity analysis is evaluated in steady-states, the equivalent model developed in PSCAD has been simplified as seen in Figure 2B. Assuming balanced voltage of HV feeder and power balance at SFC three-phase terminal, the HV line from HV feeder to SFC is omitted and the SFC is modelled as a single-phase voltage source in RTS with variable/controllable voltage phasor V_{SFC} . On the other hand, the HV line from HV feeder to transformer is not omitted due to power unbalance at the TR terminals hence the HV system is modelled as a voltage source with fixed voltage angle $\delta_{T,HV} = 0$ in the node T,HV, being the reference angle. The model of the train consists of a current source controlled to provide requested constant active and reactive power. The observed parameters are active and reactive power fed by SFC and by DS via the TR (P_{SFC} , Q_{SFC} and P_T , Q_T respectively), set voltage V_{SFC} , voltage amplitude at the train pantograph $|V_{LOC}|$, total losses in the catenary system ΔP_{tot} voltage unbalance in the node T,HV ($\rho_{T,HV} = |V_{T,HV}^-|/|V_{T,HV}^+|$ where $V_{T,HV}^+$ and $V_{T,HV}^-$ are positive and negative sequences of $V_{T,HV}$) and set relative train position l/l_{tot} . Additionally, the active power circulation (APC) in loop with distribution system is detected if following inequality is met:

$$|P_{SFC}| + |P_T| > |P_{LOC}| + \Delta P_{tot}. \quad (3)$$

Table 1: Sensitivity analysis model parameters.

Parameter	Symbol	Value
HV line impedance (for $S_{k3f} = 1150$ MVA)	Z_{HV}	$(0+j10.52) \Omega$
Length of the railway section	l_{tot}	30 km [2]
SFC voltage amplitude ¹ (range and step)	V_{SFC}	(19, 19.5,..., 27, 27.5) kV [7]
SFC voltage angle (range and step)	δ_{SFC}	(-16, -15,...15, 16) deg
Catenary impedance per kilometer	z_k	$(0.26+j0.45) \Omega/\text{km}$ [2]
Angle of the voltage phasor in T,HV node	$\delta_{T,HV}$	0 deg
Feeder voltage phasor amplitude (L-L)	V_{FEED}	110 kV
Traction transformer specifications	-----	110/25 kV, 12.5 MVA, u_k : 12.5 %
Active and reactive power of the train	P_{LOC} , Q_{LOC}	6.4 MW, 2.1 MVar
Relative train position (range and step)	l/l_{tot}	(0.1,0.2...0.8, 0.9)

¹ Allowed voltage range for 25 kV traction systems acc. to [7].

4. SIMULATION RESULTS

The results of the sensitivity analysis obtained from simulation are presented in Figure 3 to Figure 5 where the V_{SFC} amplitude and angle are at horizontal axes. The active power fed by SFC and TR (P_{SFC} and P_T , respectively) is depicted as a surface of green and blue set of colors in the Figure 3A, where the increasing brightness indicates the train movement in three positions from the SFC feeder toward the TR feeder ($l/l_{tot} = \{0.1;0.5;0.9\}$). It can be seen that in each position (e.g. $l/l_{tot} = 0.1$) the train active power might be shared between the feeders as desired by means of V_{SFC} . Nevertheless, the area marked with red points is limiting for the V_{SFC} in context of potential APC while it is varying with train position. The red planes represent a power band from 0 to P_{LOC} which roughly borders the feeder powers range without APC (borders are not precisely the same due to the power loss in the catenary system). It can be therefore deducted, that train power sharing strategies, while preventing the APC, requires the knowledge of the power in the system hence the synchronized real-time measurement of the power at all feeders would be necessary. However, the synchronized measurement at TR feeder could be omitted in a case of strategies aiming to $P_{SFC}=0$ (or $Q_{SFC}=0$), i.e. zero active (or reactive) SFC power control strategy. Nevertheless, the strategy strongly reduces the SFC in the role of RTS feeder in favor of DS. Black lines in Figure 3A indicates, that the intersection of the P_T and P_{SFC} , representing the equal distribution of power between the feeders ($P_T = P_{SFC}$), are drifting with train position. Moreover, the reactive power equal distribution lines ($Q_T = Q_{SFC}$) in Figure 3B has perpendicular direction to the active power lines $P_T = P_{SFC}$ from Figure 3A.

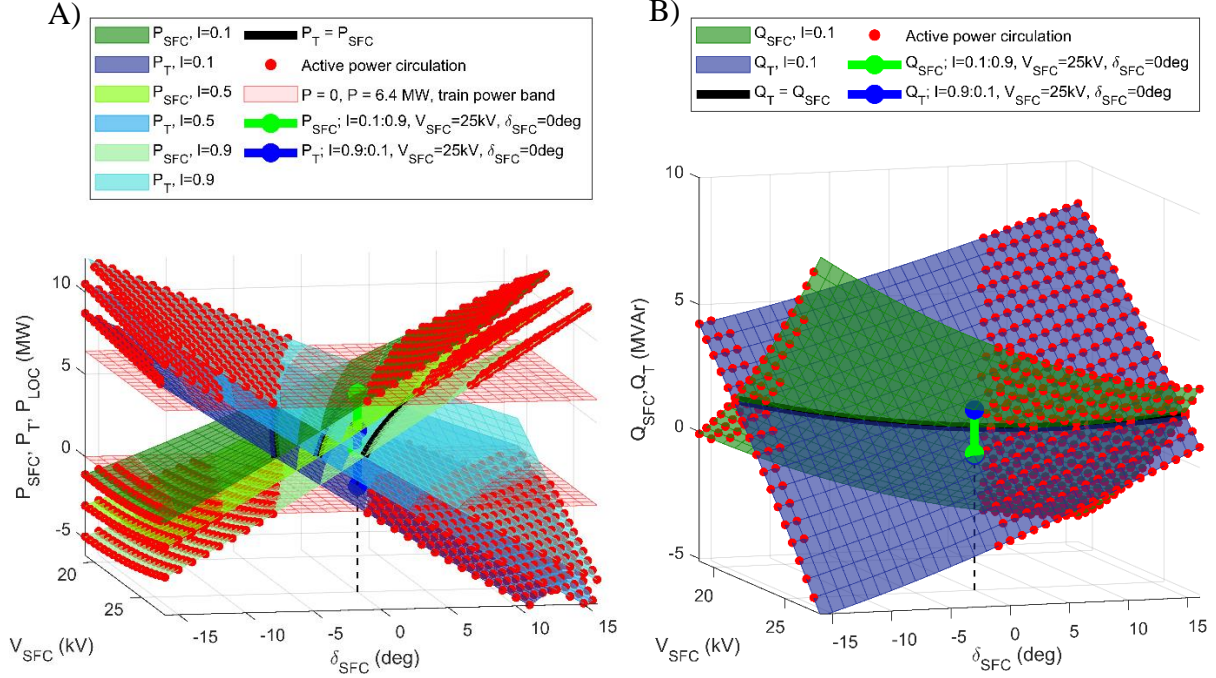


Figure 3: SFC and TR active power (A) and reactive power (B) as a function of V_{SFC} .

The drift of the V_{SFC} settings with train movement is evident even more in Figure 4A where the train position is on vertical axis and P_{LOC} , Q_{LOC} are constant. The lines interpolate the V_{SFC} set points in train positions while two control strategies are proposed: ① $P_T = P_{SFC}$; $Q_T = Q_{SFC}$; i.e. equal power distribution control strategy and ② $P_{SFC} = 0$; $Q_T = 0$; i.e. the SFC is available to DS while still providing the reactive power in RTS thus the TR feeder power factor is close to unity. The Figure 4B-C are the top view projections and the operational area of V_{SFC} with variable train position is highlighted for the strategies.

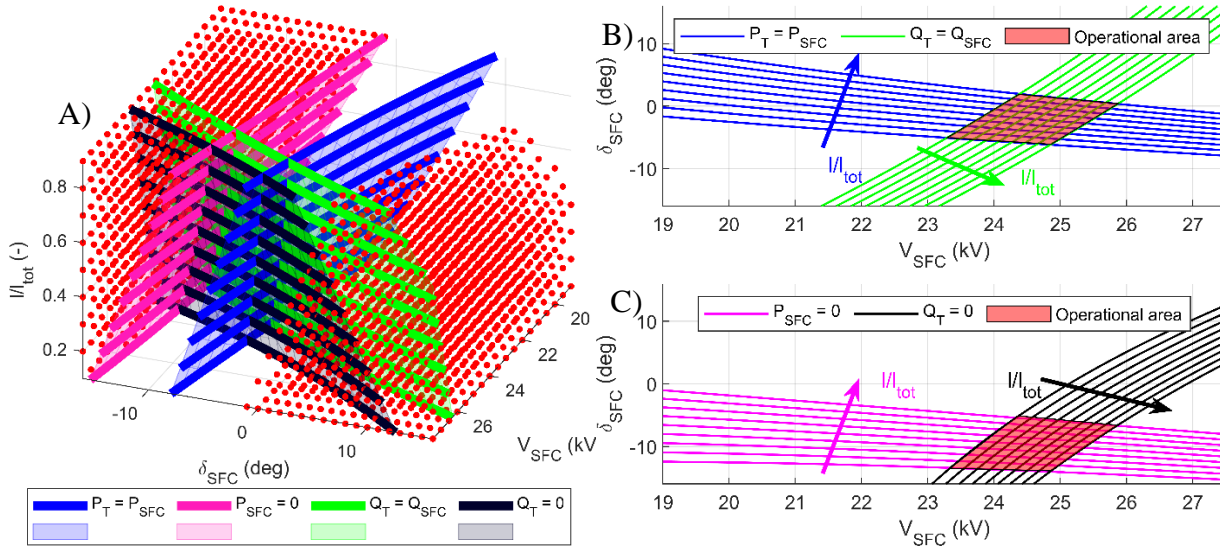


Figure 4: V_{SFC} among train positions for proposed control strategies (A), top view of the operational area for control strategies ① and ②, (B) and (C) respectively.

The loss power in catenary system and voltage unbalance at the TR feeder HV side is shown in Figure 5A and B, respectively. It can be seen that the power losses will be the lowest when $|V_{SFC}| = 25$ kV and $\delta_{SFC} = 0$ deg considering one of train positions (e.g. $I/I_{tot} = 0.5$), i.e. close to voltage vector V_T , and it decreases with increasing $|V_{SFC}|$. Similarly, it can be seen in Figure 5B that the voltage unbalance decreases with increasing $|V_{SFC}|$ and the unbalance minimum drifts to higher δ_{SFC} as the train approaches the TR feeder. It might be deduced that the ② is less favorable in terms of both voltage unbalance and loss power as the V_{SFC} angle has generally lower values than in case of ①.

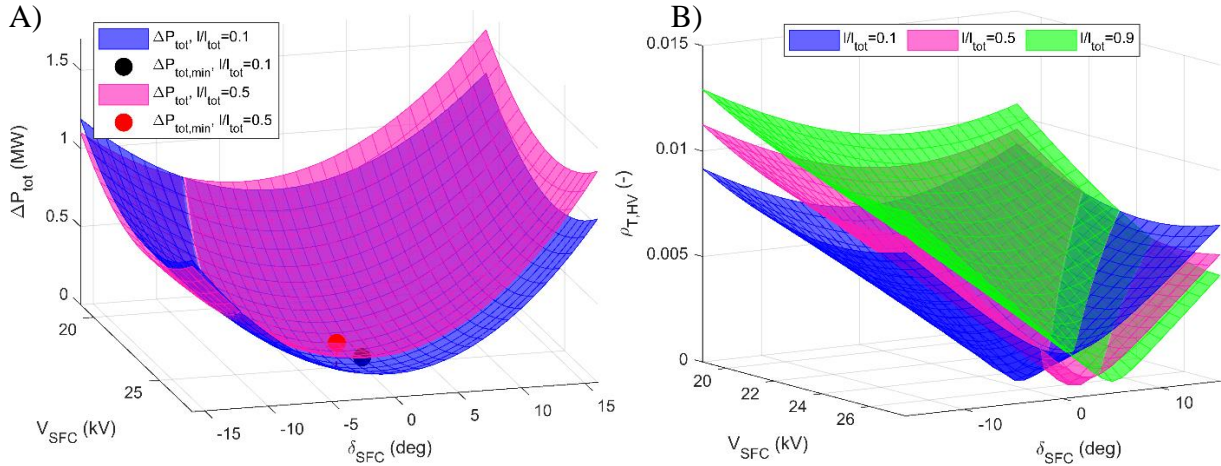


Figure 5: Loss power (A) and voltage unbalance (B) as a function of SFC voltage phasor angle and amplitude.

5. CONCLUSION

The operational range of the V_{SFC} at SFC single-phase terminal for two proposed power sharing control strategies between railway traction feeders has been highlighted. It has been presented graphically, how the operational area varies under the strategies in realistic RTS. It has been also shown how the active power circulation constraint affects the operational area, how the loss power in the RTS catenary and voltage unbalance at the single-phase TR feeder terminal develop under variable V_{SFC} and train movement. It has been also proved, that the concept of controlled load power sharing among feeders may decrease the primary duty of the SFC feeder and thus increase the probability of SFC deployment in DS voltage control, as a secondary use. Additionally, the necessity for synchronized power measurement at feeders in application stage has been highlighted. Nevertheless, droop functions approximating the system behavior in the most probable operational states might be developed in future studies in order to reduce the emphasis on the synchronized measurement.

ACKNOWLEDGMENT

This research work was carried out in the Centre for Research and Utilization of Renewable Energy. Authors gratefully acknowledge financial support from the Ministry of Education, Youth and Sports of the Czech Republic under BUT specific research programme (project No. FEKT-S-20-6449).

REFERENCES

- [1] V. Blahnik et al. "Application of Power Electronic Converter for Actual Topologies AC Traction Substation," 2020 International Conference on Applied Electronics, 2020.
- [2] "SR 34 (E) Sluzobna rukovat: Nastavovanie, prevadzka a udrzba releovych ochran trakneho napajacieho obvodu" (in Slovak).
- [3] Ch. Zhao et al. Static Frequency Converters – A Flexible and Cost Efficient Method to Supply Single Phase Railway Grids in Australia. Melbourne, AusRAIL, 2015.
- [4] M. Ufert, "Static frequency converters for use in 50 Hz railway traction power supply substations", pp. 203-212, 15th International Conference in Railway Engineering Design and Operation, 2016.
- [5] X. He et al., "Advanced Cophase Traction Power Supply System Based on Three-Phase to Single-Phase Converter," in IEEE Transactions on Power Electronics, vol. 29, no. 10, Oct. 2014.
- [6] P. Schavemaker, L. Sluis. *Electrical Power System Essentials*. Second Edition. Chennai, India: John Wiley, 2017. ISBN 9781118803462.
- [7] EN 50388 ed.2. Railway Applications – Power supply and rolling stock –Technical criteria for the coordination between power supply (substation) and rolling stock to achieve interoperability.

Investigation of the hydrogen production by the FeCrAl nuclear fuel cladding using MELCOR 2.2

P. Mičian

Brno University of Technology, Faculty of Electrical Engineering and Communication, Dept. of Electrical Power Engineering, Czech Republic

E-mail: Peter.Mician@vut.cz

Abstract—This paper deals with hydrogen production in nuclear power reactors by cladding of the fuel. The description of accident tolerant fuel, especially FeCrAl cladding material and its oxidation is presented. Model is based on Phebus facility, that was build for better understanding of phenomena occurring during severe accidents in light water reactors. Conventional used zirconium cladding was replaced by FeCrAl alloy and simulated by MELCOR code. This software is plant risk assessment tool for simulating light water reactors and its accidents. Results shows significantly decrease of hydrogen production.

Keywords—accident tolerant fuel, MELCOR, FeCrAl, hydrogen production

1. INTRODUCTION

After disaster in Fukushima there has been an increase in development of accident tolerant fuel (ATF), which should be more tolerant to extreme conditions. To enhance safety of current fleet of light water reactors, number of international working groups are intensive focusing on ATF. The main goals are to retain radionuclides within the fuel and to improve material for cladding, to significantly slowing down the exothermic oxidation of Zr-based material in steam environment.

Two ways of development ATF are: firstly, improvement of the material of fuel pallet and secondly, improvement of cladding material. Cladding material can be improved by coating on the commercially used cladding based on zirconium or replaced the whole cladding by another suitable material. The emphasis is on material which have significantly higher oxidation resistance. A typical example is the iron-chromium-aluminium (FeCrAl) alloys, which possesses desired properties.

2. FECRAL

The iron-chromium-aluminium alloys are typically used within a range of industrial applications, especially where high temperature oxidation resistance is needed [1]. Over past half of century FeCrAl was considering as cladding material for fuel elements in the nuclear power plants. But from early days of nuclear power reactors, Zr-based alloys were chosen for light water reactors fuel cladding, because of their low neutron absorption, good thermal conductivity, high melting point and adequate corrosion resistance. After 2011 Fukushima accident interest in nuclear power applications of FeCrAl alloys has extremely risen. The objective of the studies is to delay severe core degradation by reducing heat generated by exothermic reaction of Zr-based cladding with steam. Also to reduce hydrogen production, because of the ignition risks.

FeCrAl alloys has excellent resistance against oxidation up to 1560 °C, which is close to its melting point [2]. FeCrAl has two different mechanisms of oxidation. If the water temperature is around 300 °C, that corresponds to normal conditions in light water reactors, the alumina layer on the surface of cladding will dissolve and protective chromium oxide will form in this place. After that, if accident conditions will appear, the chromium oxide layer will evaporate and an alumina layer will form to protect the tube. It leads to a conclusion that chromium is protecting the cladding during normal operation conditions and aluminium is protecting the alloy at temperatures higher than 1100 °C. The visualisation of these processes can be seen in Fig. 1 [3].

One of the drawbacks of FeCrAl alloys are higher parasitic neutron absorption. For the similar neutron absorption has to be cladding made from FeCrAl half thickness compare to conventionally used Zr-based cladding. There are also challenges about brittle after neutron irradiation and problems with releasing tritium to the coolant, too [4].

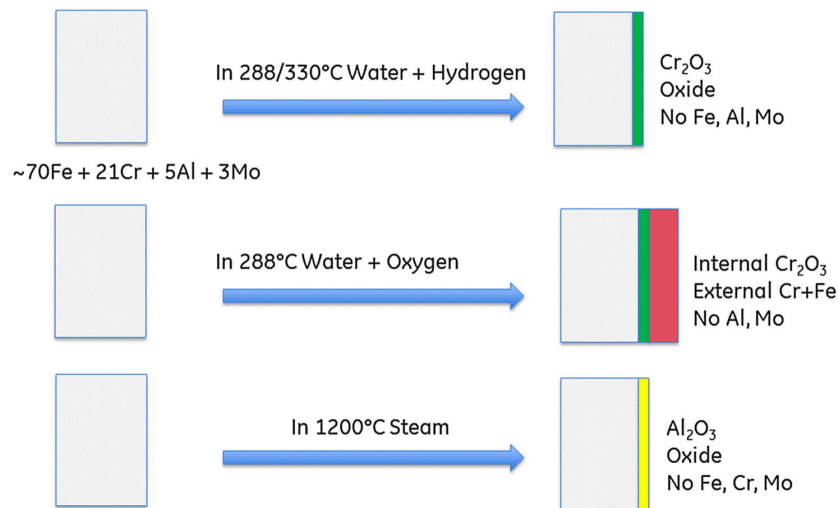


Figure 1: Schematic representation of the oxide processes on FeCrAl alloys under normal and accident conditions in light water reactors [3].

3. METHODOLOGY

If cooling of the nuclear reactor core is absent for a longer period of time, decay heat and exothermic chemical reactions heats up the fuel, that can eventually resulting in melting. The impact of various cladding materials from a thermodynamic point of view have been conducted [5]. One of the severe accidents analysis tools is MELCOR code, developed by Sandia National Laboratories for U.S. Nuclear Regulatory Commission. It is a second generation plant risk assessment tool. MELCOR code is fully integrated, engineering level computer code focused on progression of severe accident phenomena in light water reactors. These include thermal-hydraulic response of the reactor system, cavity and the containment, loss of coolant phenomena like fuel heat up, cladding oxidation, degradation and melting of the fuel, hydrogen production, fission products release and transport etc [6, 7].

In this work as a reference experiment was used model of experimental facility Phebus. This facility was operated in France between 1988 and 2010. Main purpose was study phenomena occurring during light water reactor severe accidents. The core is a scaled down version of 900 MWe pressurized water reactor by ratio of 1/5000. Test train contains coolant inlet, test bundle, experimental circuit and containment vessel.

This work is focused on test bundle, which contains 20 fuel rods with 12.6 mm pitch and 1 meter height. In Fig. 2, there can be seen the radial cross section of the fuel bundle with its description and in the right side of the picture, there is post-test radiography of the bundle but in axial direction [8]. During experiment, bundle power was increasing to 36.5 kW and the steam mass flow rate was varying from 0.5 to 2.2 g/s, to simulate the accident conditions. The core is divided into 2 radial rings and 14 axial levels. The inner ring has the radius of 21.33 mm and contains the first row of fuel rods and control rod made from silver-indium-cadmium. The outer ring has the radius of 36.5 mm and contains the outer fuel rods. The main events of the experiment happened in degradation phase, that lasted 20 000 seconds. The calculation was initiated 5000 seconds before start of the transient, to obtain steady state.

In the MELCOR code input, which was created for simulating FPT1 test at Phebus, the material for the cladding of the fuel was changed to FeCrAl. The FeCrAl alloy was define as a user specified core material and for application in the generic oxidation model as well. Changes were done in the material package and core package of the code, namely material definition, populating core components with the user defined material and the oxidation parameters of the material. For the fuel cladding and its oxide wide range of properties have to be input into MELCOR code, for example heat capacity, thermal conductivity, emissivity, melting point and others. These material properties was input for FeCrAl with ratio 74% / 21% / 5% and are in [6], too. The changes in fuel geometry, like thickness of cladding or pitch, were not considered. In the further investigation, there should be keep in mind other technical specifications of FeCrAl, for example neutron absorption, melting point and mechanical strength.

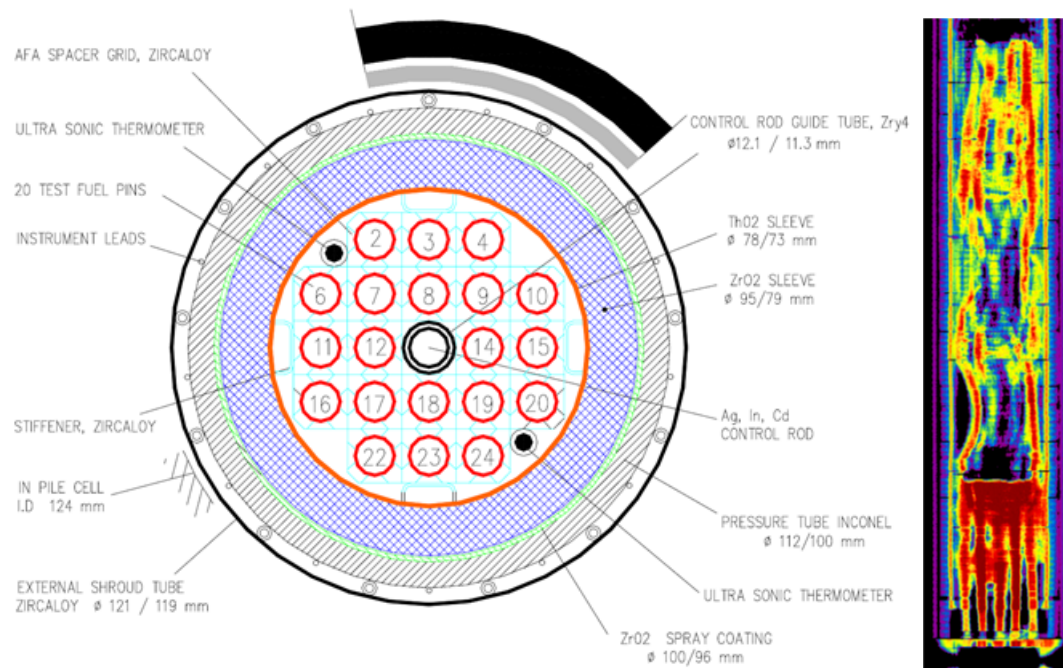


Figure 2: Radial cross section and post-test axial radiography of Phebus fuel bundle [8].

4. RESULTS AND DISCUSSION

The simulation was done on the personal computer with Microsoft Windows operating system. When the computing server with Linux operating system was used, results were slightly different. This is the challenge for future focus on these differences.

The main results can be seen in Fig. 3 with the hydrogen production, where in the left side is comparison between cladding composed by Zirconium and FeCrAl. The blue line and blue crosses correspond to Zirconium cladding. The line is results of simulation and crosses are data from measurements at Phebus facility during FPT1 experiment. The difference in hydrogen production is significant. For conventional zirconium cladding in FPT1 test, the mass of produced hydrogen was 96 g, by simulation it is slightly over-predicted around 13 grams. To compare, produced hydrogen when FeCrAl is used for cladding is 21 grams, what is remarkable decrease. The hydrogen produced by FeCrAl is very low, because in figure there is summary of the hydrogen produced by spacer grids, stiffeners and support plate as well. The red line in figure is prediction, when FeCrAl cladding is not melting and survive at its position till the end of the experiment. This condition was redefined in input to investigate the whole time span.

In the right side of figure, there is detailed view just on FeCrAl cladding till time of melting almost whole

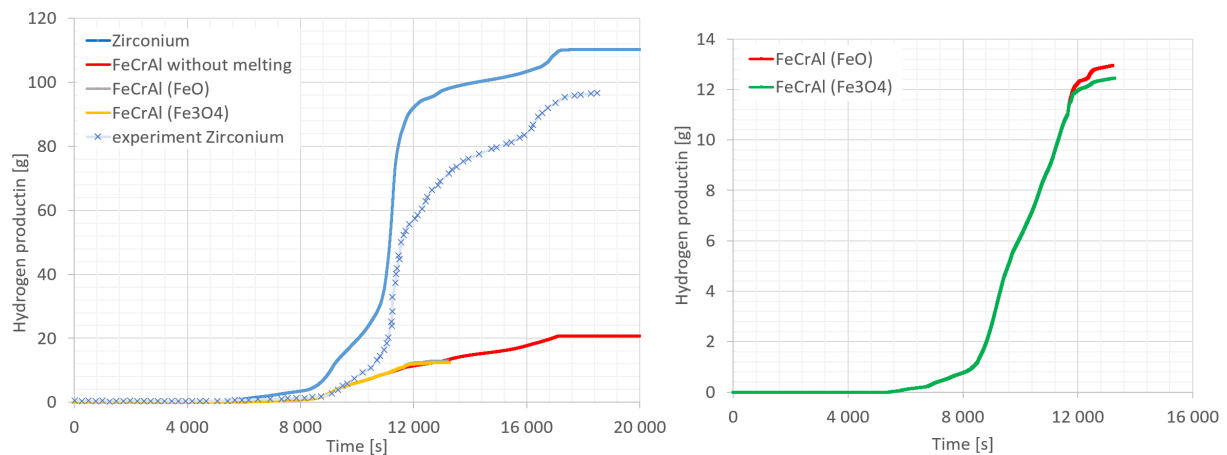
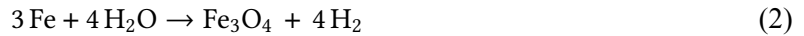


Figure 3: Comparison of hydrogen production.

cladding material. The total hydrogen production till 13 200 seconds is 13 respectively 12.5 grams in comparison with 98 grams produced by zirconium in simulation and 71 grams in experiment. In this graph the focus is on the different approach to oxidation reactions. The red line with label FeCrAl (FeO) corresponds to prefer oxidation reaction



and the production of hydrogen is gentle greater if the reaction



is used. The green line with label FeCrAl (Fe₃O₄) is conducted with preference of oxidation reaction 2. The difference in amount of hydrogen is very small and just in the last hundreds of seconds. This can be caused by different sensitivity to higher temperatures and also different collapsing of cladding material during oxidation.

The visualisation of the simulated fuel bundle is in Fig. 4. The visualisation was done by Symbolic Nuclear Analysis Package (SNAP) software, which can be used as for the creating input for MELCOR, computing it and for making more readable outputs as well [9]. In the left side of figure, there is the mass distribution of UO₂ fuel pellets, FeCrAl as cladding and the mass of oxidized FeCrAl before test and in the right side there are the same columns with mass distribution after the test. In the distribution of UO₂ and FeCrAl can be seen that in the central ring of the bundle occurred melting and collapsing of whole fuel rods with its content. In comparison with the post-test radiography in Fig. 2, the good match can be considered. In the columns that corresponds to FeCrAl oxide can be seen where the oxidation occurs the most. It is within the nodes in the center of the bundle with highest temperatures and in the molten bulk, too.

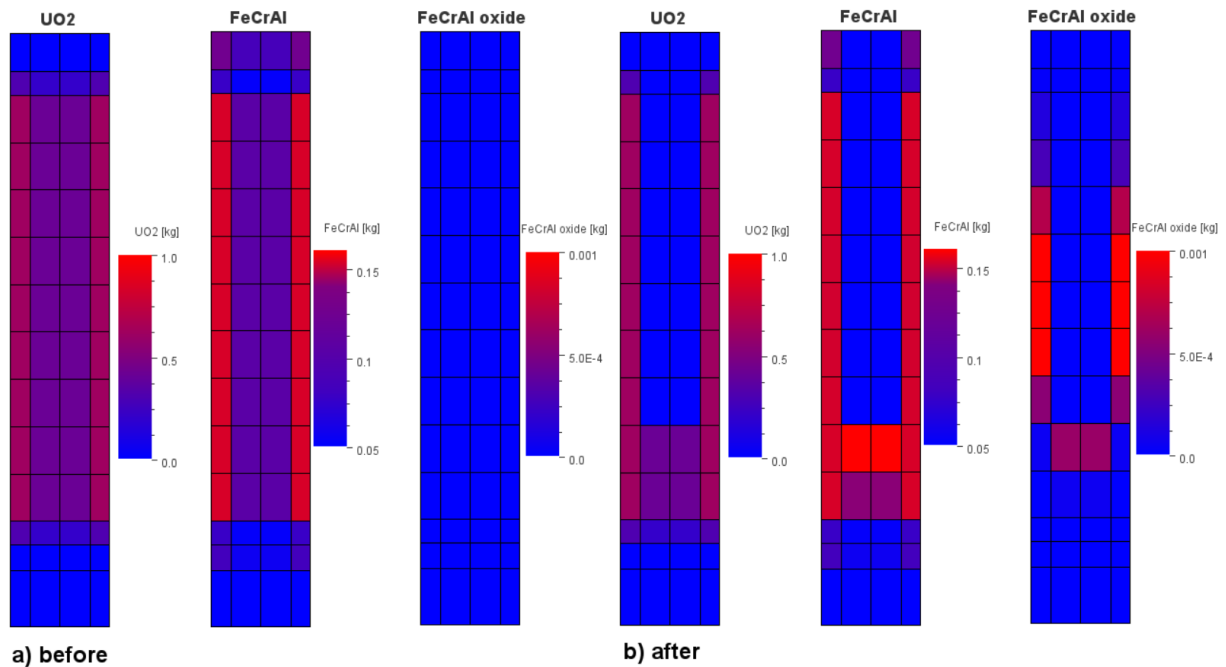


Figure 4: Mass distribution of UO₂, FeCrAl and FeCrAl oxide a) before test and b) after test.

5. CONCLUSION

To summarize, FeCrAl alloys as ATF cladding material produce less hydrogen as the conventional cladding based on zirconium. The reduction is around 80% compare to the simulation and the experiment. Also, there are small differences if alternative oxidation reactions are preferred by MELCOR. The melting of the fuel rods occurs, and mass distribution is similar to the post-test radiography of the fuel bundle, too.

In the simulation there are still components made from zirconium. To decrease hydrogen production more, these components should be replaced as well. In order to optimize FeCrAl as an alternative cladding material, engineering design improvements could be made. There are challenges as neutron absorption, mechanical strength and melting point.

ACKNOWLEDGMENT

This research work has been carried out in the Centre for Research and Utilization of Renewable Energy (CVVOZE). Author gratefully acknowledge financial support from the Technology Agency of the Czech Republic (project No. TM02000039). I would like to also acknowledge my supervisor, Karel Katovský, for his mentoring and help.

REFERENCES

- [1] K. G. Field, M. A. Snead, Y. Yamamoto, and K. A. Terrani, *Handbook on the Material Properties of FeCrAl Alloys for Nuclear Power Production Applications (FY18 Version: Revision 1)*. Oak Ridge: Oak Ridge National Lab.(ORNL), 2018.
- [2] J. W. McMurray, R. Hu, S. V. Ushakov, D. Shin, B. A. Pint, K. A. Terrani and A. Navrotsky, “Solid-liquid phase equilibria of Fe-Cr-Al alloys and spinels”, *Journal of Nuclear Materials*, vol. 492, p. 128-133, 2017, doi [10.1016/j.jnucmat.2017.05.016](https://doi.org/10.1016/j.jnucmat.2017.05.016).
- [3] R. B. Rebak, “Versatile oxide films protect FeCrAl alloys under normal operation and accident conditions in light water power reactors”, *JOM*, vol. 70, no. 2, p. 176-185, 2018, doi [10.1007/s11837-017-2705-z](https://doi.org/10.1007/s11837-017-2705-z).
- [4] A. Strasser, J. Santucci, K. Lindquist, W. Yario, G. Stern, L. Goldstein and L. Joseph, *Evaluation of stainless steel cladding for use in current design LWRs. Final report.*. New York: Stoller (SM) Corp., 1982.
- [5] M. T. Farmer, L. Leibowitz, K. A. Terrani, and K. R. Robb, “Scoping assessments of ATF impact on late-stage accident progression including molten core–concrete interaction”, *Journal of Nuclear Materials*, vol. 448, no. 1-3, p. 534-540, 2014, doi [10.1016/j.jnucmat.2013.12.022](https://doi.org/10.1016/j.jnucmat.2013.12.022).
- [6] L.L. Humphries, B.A. Beeny, F. Gelbard, D.L. Louie, J. Phillips, R.C. Schmidt and N.E. Bixler, *MELCOR Computer Code Manuals, Primer and Users’ Guide*. Albuquerque: Sandia National Laboratories, 2021.
- [7] L.L. Humphries, B.A. Beeny, F. Gelbard, T. Haskin, D.L. Louie, J. Phillips, R.C. Schmidt and N.E. Bixler, *MELCOR Computer Code Manuals, Reference Manual*. Albuquerque: Sandia National Laboratories, 2021.
- [8] B. Clément, T. Haste, *Comparison Report on International Standard Problem ISP-46 (PHEBUS FPTI)*. France: NT SEMAR, 2004.
- [9] *Symbolic Nuclear Analysis Package (SNAP): User’s Manual, Version 3.1.9*. Bloomsburg: Applied Programming Technology, Inc., 2021.

A Voltage Support Schemes of Asymmetrically controlled Three-Phase Inverter-Based Generating Units

J. Dvořáček¹, J. Drápela¹

¹Dept. of Electrical Power Engineering, FEEC, Brno University of Technology, Czech Republic

E-mail: dvoracekj@vut.cz, drapela@vut.cz

Abstract—Paper provides insight into possibility of asymmetrical three-phase inverter high-level control as additional grid support in low voltage networks. The asymmetrical control may assist with lowering asymmetry in areas with large single-phase load/generation penetration. Proposed and implemented control schemes are tested with laboratory equipment utilizing artificial network. Results are evaluated based on their effect on voltage asymmetry reduction and neutral conductor current magnitude.

Keywords— three-phase inverter-interfaced generating unit, photovoltaic source, battery energy storage system, voltage asymmetry, grid support functions, asymmetrical control

1. INTRODUCTION

Ongoing transition from a centralized electric power generating facilities to more decentralized energy resources (DER) leads to an increased number of a power generating units (PGU) installed into low-voltage (LV) network; increasingly supplemented by battery energy storage systems (BESS) [1]. It turns out that PGUs and BESSs in the LV distribution system (DS) have a significant local influence on the voltage magnitude and affect (even in combination with asymmetrical loads) its asymmetry [2]. However, it may not be only the deterioration of voltage quality indices in DS [3]. The DERs may also contribute intentionally to their improvement. Particularly, three-phase inverter-interfaced DERs with ability of asymmetrical current injection are of potential to compensate voltage asymmetry, typically linked to LV DS. Therefore, asymmetrical current injection higher-level control may assist voltage symmetrization in LV DS with large single-phase demand or generation assets. The paper aims to several proposed asymmetrical current/power distribution control schemes and their experimental verification. In order to assess the control strategies performance, the algorithms are implemented with use of an instrumentation platform controlling a three-phase hybrid inverter.

2. INTEGRATION OF LV INVERTERS-BASED GENERATING UNITS

There are multiple options for inverter-interfaced DER topology and its integration into LV DS. Relevant examples are documented in figure 1. Despite equipment at the inverter DC side terminals (photovoltaic (PV) strings or BESS), the inverter's topology is important in view of the study. In general, single-phase or three-phase inverters may be used, whereas 3-phase asymmetrical controlled injection to the DS is achievable by three-phase unit or three single-phase units only.

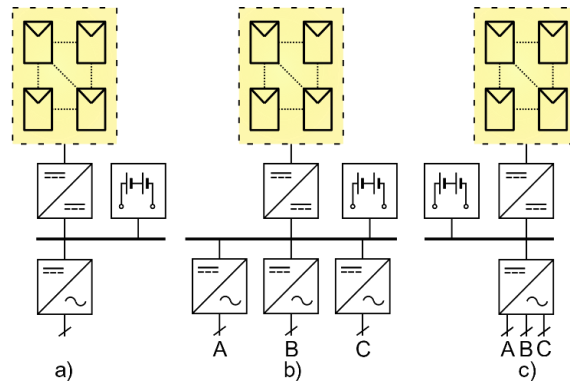


Figure 1: Basic topologies of inverter-interfaced generating units' connection to three-phase LV network; a) single-phase inverter, b) three single-phase inverters, c) single three-phase inverter

Current or power disposable (assumed as constant) at DC link (DC/AC converters are typically operated as current source) is to be provided into AC three-phase system via following control schemes:

- Symmetrical – current is distributed symmetrically into all phases regardless of system voltage asymmetry; as this is a standard control of symmetrical 3-phase inverters.
- Asymmetrical - phase currents are controlled by chosen strategy while sum of distributed currents remains constant. Obviously, this is not available for single-phase connection (figure 1a), while it is to be natural in the case of three single-phase inverters in figure 1b). Finally, asymmetrical control of the 3-phase inverter (figure 1c) is available for specialized 3-phase PV inverters or BESS converters only.

As stated in (1) for fundamental frequency, voltage drop across a AC supply system impedance is affected by active and reactive current. Since (1) applies for L-N voltages as well as L-L, asymmetrical distribution of current will affect voltage asymmetry, and inversely, can contribute intentionally to its symmetrization.

$$\Delta U \cong R \cdot I_a \pm X \cdot I_r, \quad (1)$$

where ΔU denotes voltage drop magnitude, R resistance and X reactance at supply/delivery point, I_a means active and I_r reactive current, respectively, and all at fundamental system frequency.

A. Considered Asymmetrical Power Control Approaches

It is desirable to restrict total active power limiting to minimum due to the unwanted active power generation disturbances. Important condition to asymmetrical power control is therefore to pass through all available power from DC interlink (P_D or I_D) when possible and up to the inverter AC rated current I_R . Current oriented (CO) and power oriented (PO) strategies presented in table 1 are considered for AC side phase distribution. The naming is chosen with respect to their calculation and their desirable effect is to balance voltage by means of phase-by-phase (*ph*) active current/power distribution. Schemes are chosen for power generation, where the phase current/power is calculated directly proportional according to chosen scheme to supply more power to phase with lower voltage. For consumption (a case of BESS), phase current/power would have to be distributed with inverse proportions to achieve lower demand on phase with lower voltage.

Table 1: Considered control strategies

Current oriented		Power oriented	
Notation	Voltage exponent, n (-)	Notation	Voltage exponent, n (-)
A) $I(ph) \equiv$	0	D) $P(ph)/U(ph) \equiv$	-1
B) $I(ph) \times U(ph) \equiv$	1	E) $P(ph) \equiv$	0
C) $I(ph) \times U^2(ph) \equiv$	2	F) $P(ph) \times U(ph) \equiv$	1

Respective phase current for CO strategies is calculated acc. to (2). With PO strategies, respective phase active power is calculated acc. to (3). Calculation differences are expressed with voltage exponent as presented in table 1. Strategies on same row should be (acc. to their respective calculation) equivalent.

$$I_A \cdot U_A^n = I_B \cdot U_B^n = I_C \cdot U_C^n \wedge I_A + I_B + I_C = \sum_{ph=A,B,C} I_{D,ph} \leftarrow I_{\Sigma D} \wedge \{I_A, I_B, I_C\} \leq I_R, \quad (2)$$

where I_A, I_B, I_C are currents flowing through respective phases and U_A, U_B, U_C are measured L-N voltages. The I_D and I_R denotes disposable and rated current, respectively. The n is an exponent listen in table 1.

$$P_A \cdot U_A^n = P_B \cdot U_B^n = P_C \cdot U_C^n \wedge P_A + P_B + P_C = \sum_{ph=A,B,C} P_{D,ph} \leftarrow P_{\Sigma D} \wedge \{I_A, I_B, I_C\} \leq I_R, \quad (3)$$

where P_A, P_B, P_C denote power inputs into respective. The P_D means disposable power.

3. EXPERIMENTAL VERIFICATION

Experimental verification was conducted using setup depicted in figure 2. Due to unavailability of commercial product with direct reference value (power, voltage, frequency etc.) input, custom system

was composed using three single-phase digitally controlled hybrid converters Studer XTM-4000-48 and a virtual instrumentation based external current/power control loop [4]. The outer current/power setup loop consists of National instruments (NI) cDAQ measuring platform and a PQ control SW developed in LabVIEW and providing requested AC side current/power setting for the converters via RS232 communication. The converters terminal voltages and currents are measured using NI 9225 module and NI 9239 module in combination with Chauvin Arnoux C173 current transducers, respectively. The PQ control SW implements active current or power redistribution algorithms as defined in section 2.

Test setup consists of grid-connected 4-quadrant artificial AC grid simulator providing controllable 4-wire LV network [5]. The converters (Studer XTM-4000-48) are connected to each phase through identical impedance. Converters are provided by common DC link powered by two Li-Ion battery packs connected in parallel supported by a DC power supply. Used XTM converters accept only current magnitude and phase input from control loop. This is an important attribute of used setup as power in PO strategies is inputted as current considering actual voltage level. Moreover, current setup with resolution of 0.2 A is accepted by the XTM converters only. Measurement for the performance evaluation purpose at AC terminals of the PGU is performed by a power analyzer and data logger HIOKI PW3390. The table 2 presents impedances used in test setup according to figure 2. Impedances Z_L and Z_N were chosen according to reference impedance [6] and expected loading of the network.

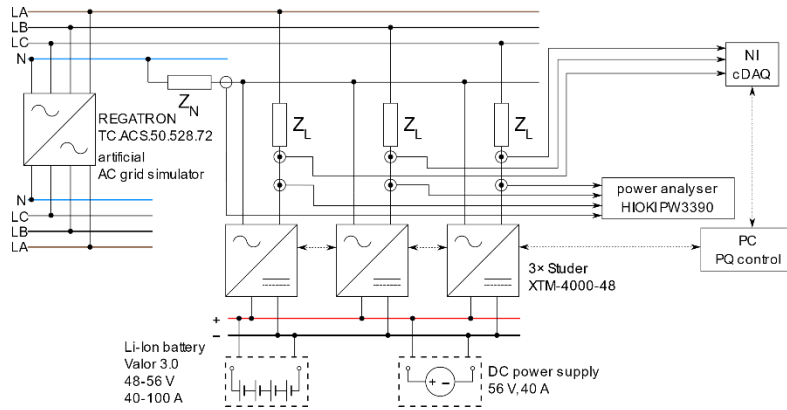


Figure 2: Test setup diagram

Table 2: Test system impedances

Test setup		Referenced in [6]	
Label	Value (Ω)	Label	Value (Ω)
Z_L	$(0.28 + j0.18)$	$Z_{L,ref}$	$(0.24 + j0.15)$
Z_N	$(0.20 + j0.11)$	$Z_{N,ref}$	$(0.16 + j0.10)$

Table 3: Considered nominal values

Grid simulator		Each inverter	
Parameter	Value	Parameter	Value
U_n (L-N)	220 V	$P_{D,ph}$	1500 W
f_n	50 Hz		

B. Testing Scenario

The grid simulator was set up to output voltage profile as show in figure 3 with nonstandard nominal value according to table 3. Lower voltage was chosen to prevent automatic power curtailment of inverter due to positive error of its internal voltage measurement. Nominal by-phase power according to table 3 was chosen due to maximal power safely provided by used DC sources.

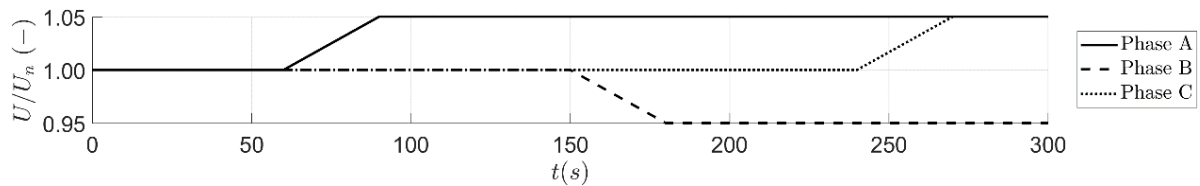


Figure 3: Test voltage profile

4. EVALUATION OF THE ASYMMETRICAL POWER CONTROL APPROACHES

Suitability of control strategy is evaluated using coefficient of voltage asymmetry calculated at fundamental frequency with (4) [7] and by means of fundamental frequency current at neutral conductor. All visualized data were also smoothed using moving average function to eliminate ripple.

$$k_{u2} = \frac{U_{2k}}{U_{1k}}, \quad (4)$$

where k_{u2} denotes coefficient of voltage asymmetry, U_{1k} means positive sequence voltage at fundamental frequency, and U_{2k} is negative sequence voltage at fundamental frequency.

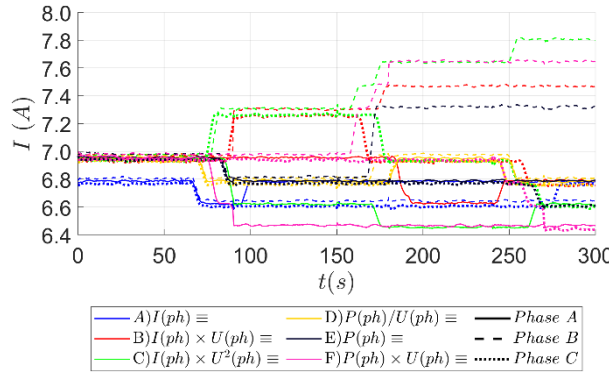


Figure 4: Inverter AC current (fund. freq.)

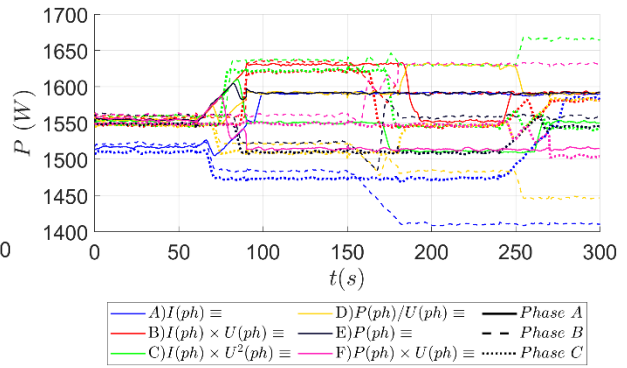


Figure 5: Inverter active power output

Results are affected by stepped current input. It is not set exactly but in steps by 0.2 A only as seen in figure 4. Therefore, power output is also stepped as referenced in figure 5. This limitation is particularly evident with strategies A) and D) as phase currents are not kept constant and with B) and E) as the active power output differs between phases.

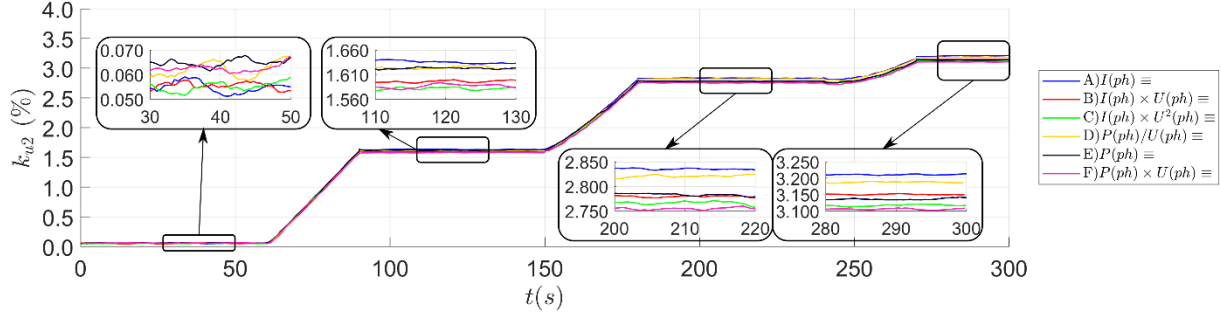


Figure 6: Coefficient of voltage asymmetry (fund. freq.)

Even though strategies A) and D); B) and E); C) and F) were assumed to have similar effect, actual values presented in figure 4 and figure 5 indicate differences between respective CO and PO. This may be caused by aforementioned limitation. Similarly, for strategies A) and D), respective phase currents deviate much less throughout test setup than with using other strategies.

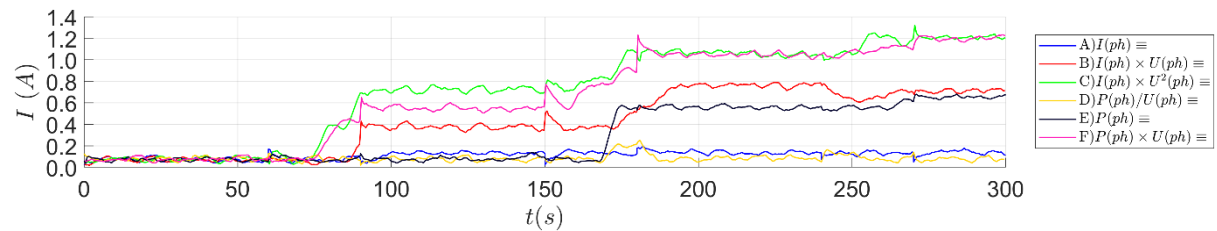


Figure 7: Neutral conductor current (fund. freq.)

Finally, using B) and E), active power output is less deviated (than with other strategies) across phases as seen in figure 5. Using C) and F), current in phases with lower voltage is set higher. A difference of

CO and PO is likely caused by difference in referencing voltage magnitude. PO respects actual voltage level, while CO is referenced to nominal/rated voltage in the tested control loop. Effect on reducing asymmetry is not significant in this power level as seen in figure 6. However, the response is present and consistent throughout testing. Lowest asymmetry was achieved utilizing C)/ F) – utilizing phase voltage in effect for current/power control additionally to other PO and CO focused on constant current/power. Also, the B)/ E) (const. P) mitigate asymmetry better than A)/F) (const. I).

Downside of asymmetrical control strategy is its impact on current flowing through neutral conductor, as shown in figure 4. Strategies able to remedy asymmetry more throughout test at POC show significantly higher current through neutral conductor than other strategies. Difference between PO and CO is again due to measurement and reference differences.

5. CONCLUSION

The paper has been aimed on several higher-level control strategies for asymmetrical current/power control of grid connected three-phase DC/AC converters. The asymmetrical injection based on line-neutral voltage magnitude is intentionally employed in favor of the supply voltage symmetrization, therefore, providing the supply network goal-directed support. Performance of the strategies in generating mode were assessed using laboratory testing equipment. However, similar control may be addressed for a BESS charging mode. Benefit from the asymmetrical control strategies to voltage symmetrization contribution, in comparison to symmetrical injection, was proven. The strategies were proposed rather less invasive, therefore, the effect of controlled asymmetrical by-phase distribution of the single PGU was relatively small. If coexistence of contribution from multiple units across a LV DS will occur the stronger effect may be expected. On other hand, asymmetrical injection exhibits neutral conductor current whose magnitude rises with level of the set injection asymmetry obviously. The resulting neutral wire current may cause additional losses, which might be undesirable. More thorough testing is required to establish solid ground for selecting proper asymmetrical control strategy if shown sufficient grid supporting potential.

ACKNOWLEDGMENT

This research work has been carried out in the Centre for Research and Utilization of Renewable Energy (CVVOZE). Authors gratefully acknowledge financial support from the Ministry of Education, Youth and Sports of the Czech Republic under BUT specific research program (project No. FEKT-S-20-6449).

REFERENCES

- [1] Michael I. Henderson, Damir Novosel, and Mariesa L. Crow, “Electric Power Grid Modernization Trends, Challenges, and Opportunities,” IEEE, 2017
- [2] M. Vrana *et al.*, “Battery Storage and Charging Systems Power Control Supporting Voltage in Charging Mode,” *2020 19th International Conference on Harmonics and Quality of Power (ICHQP)*, 2020, pp. 1-6, doi: 10.1109/ICHQP46026.2020.9177889.
- [3] *Voltage characteristics of electricity supplied by public distribution networks*, EN 50160:2010, 2010.
- [4] J. Drapela, J., et al., “Power Generating Modules Field Testing Concepts for Verification of Compliance with Operational Requirements,” *2020 21st International Scientific Conference on Electric Power Engineering (EPE)*, 2020, pp. 1-6, doi: 10.1109/EPE51172.2020.9269230.
- [5] “Grid Simulators & Systems.” Regatron. <https://www.regatron.com/product/products-by-application/grid-simulators#general-overview> (accessed 2022-03-13).
- [6] *Electromagnetic compatibility (EMC) – Part 3-3: Limits – Limitation of voltage changes, voltage fluctuations and flicker in public low-voltage supply systems, for equipment with rated current ≤ 16 A per phase and not subject to conditional connection*, EN 61000-3-3, 2013.
- [7] *Electromagnetic compatibility (EMC) – Part 4-27: Testing and measurement techniques – Unbalance, immunity test*, EN 61000-4-27, 2000.

TRIBOELECTRIC SENSOR APPLICATION AND CHARACTERIZATION

D. Riha¹

¹ Department of Physics, Faculty of Electrical Engineering and Communication, Brno University of Technology, Technická 10, 616 00 Brno, Czech Republic

E-mail: xrihad01@vutbr.cz

Abstract— This work describes advantages and possibilities of use triboelectric sensors. Sensor is possible to use for estimation applied force and movement (displacement). It opens door to wide spectrum of use, finally the sensor could be used for fitness applications especially for estimations of any applied force.

Keywords—BUT, FEEC, EEICT, PVDF, Sensor, Impact, Energy harvesting, TENG, Electrospinning.

1. INTRODUCTION

Triboelectric systems are very popular for energy harvesting purposes. It opens door for investigation of sensing possibilities in wide industrial branch and also for all sensing of natural process where any movement as acceleration are possible to measure. Triboelectric phenomenon could be used also for sensing of position. There are many applications: self-powered human motion sensors [1], self-powered automobile sensors [2]. Example of position sensing is possible to see from a work by authors Chen et al [3]. Energy harvesting describe flexible Nano generators [4], internet of things [5], environmental monitoring systems [6]. There are also many other applications in biomedicine as non-invasive biomedical monitoring systems [7].

Triboelectricity

Triboelectric nanogenerator (TENG) was first published in 2012 as an effective means to harvest wasted kinetic energy [8]. Since then, a lot of researchers have been trying applied this new approach in many applications. The working principle of TENG is based on triboelectric effect where separation of static charges between two contacting surfaces occurs [9–11]. TENG converts mechanical motion into electricity [12–15]. The triboelectric effect is caused by the transfer of electrons [11,16], ions [10] or charged materials [9], or a combination of these factors [17]. Very important parameter is a triboelectric surface charge density σ of TENG. Has been demonstrated that the magnitude of the σ is quadratically related to the output power density of the TENG [18,19]. Improving σ can be done by means of material choice, structural optimization, artificial ion injection and so on [20–25]. Nevertheless, a TENG operating on air is limited by the air avalanche breakdown, as can be deduced from Panchen's law [26].

Active material

Polyvinylidene fluoride (PVDF) are the highly used negative material by many researchers for high-performance TENG [27–32] and self-powered sensors [29,33].

Electrospinning is considered as a simple, versatile, cost-effective and promising approach to fabricate continuous flexible nanofibers with many unique properties and features such as huge surface area, high surface roughness and flexibility [34,35]. This fact led us to fabricate a simple triboelectric sensor based on a PVDF fibrous structure.

Polyvinylidene fluoride material was made by electrospinning method. This procedure is very common for manufacturing of very fine non-woven fabric [36–39]. Product of used machine is PVDF non-woven fabric placed on aluminium foil. Our experiment was focused on fabrication of a simple triboelectric sensor based on this fibrous material. We have fabricated three concepts of triboelectric sensors where we have evaluated sensitivity of these sensors. Our goal was analysing which concept will be more suitable for continuous monitoring of movement and which system is more suitable for energy

harvesting.

2. MATERIALS AND METHODS

Manufacturing of PVDF

We used PVDF with molar weight 275,000 g/mol (Sigma Aldrich, St. Louis, MO, USA). As solvents we used dimethyl sulfoxide p.a. (DMSO, Sigma Aldrich, St. Louis, MO, USA) and acetone (Ac, Sigma Aldrich, St. Louis, MO, USA). Solutions were electrostatically spined by machine 4spin (Contipro a.s., Dolni Dobrouc, Czech Republic).

Fibres are possible to rectifier to one direction, or it is possible to place them random as non-woven fabric. We are able to change thickness of final product simply by change of manufacturing time. Spined material is used without removing it from substrate for all sensing elements. We prepared material with thickness from 20 to 100 μm (pressed state). Fibres have diameter from 600 to 1200 nm, and thickness could be partially controlled by electric field between needle and substrate and also partially also by chemical compounds of input solution.

The morphology of the electrospun fibers was investigated by scanning electron microscopy (SEM, Verios 460 L, FEI Czech Republic s.r.o., Brno, The Czech Republic).

Concept of the sensor

Sensing part of this sensor was based on flexible electrodes. This concept was chosen to achieve better sensing properties as linearity and repeatability. Finally, permanent contact of electrode with active material was made in contact pressure mode. There were made stack which could cover also low frequency slow motion displacements due to higher surface of active material and electrodes. Construction details are possible to see from Figure 2 and Figure 3. Figure 1 show bended electrodes where active material is placed from both sides.



Figure 1: Encapsulated stack – triboelectric stack system.

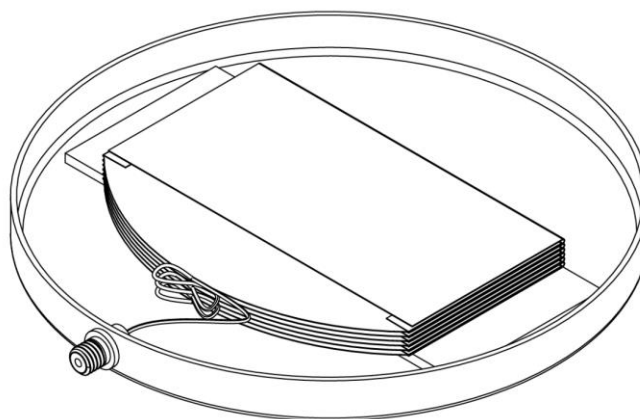


Figure 2: Encapsulated stack – internal system.

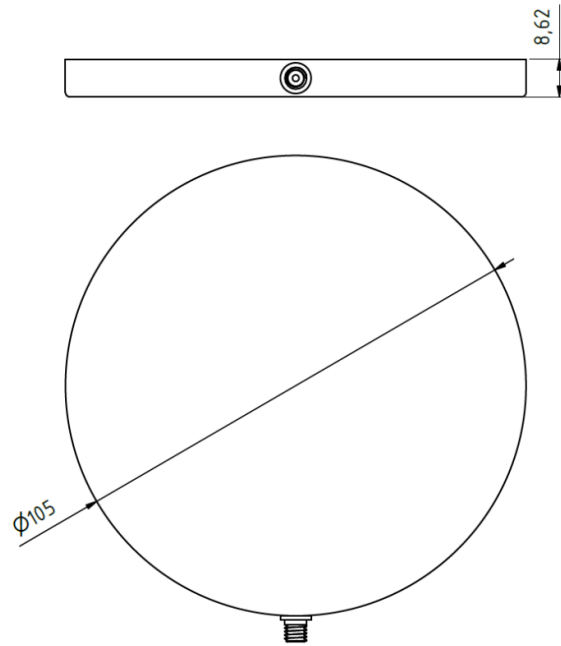


Figure 3: Encapsulated stack – external dimension.

Testing configuration

Sensor was mechanically connected to configurable holder made for testing triboelectric samples, see Figure 4. The charge output of the sensor was evaluated by electrometer 6517b (Keithley, USA) and experimental charge amplifier. The exciting part consisting of the impact rod was controlled by vibration test system TV 50018 (Tira, Germany). The displacement of exciting impact rod was measured via interferometer ILD 1402-10 (Micro Epsilon, Germany). Applied force was measured by force sensor PCB Piezotronics type ICP model 208C01. Output voltages generated by electrometer 6517b and experimental charge amplifier were measured by oscilloscope DSOX2024A (Keysight, USA). The same oscilloscope was used for evaluation of displacement of the exciter measured by interferometer. Oscilloscope was used due to fast setting of each channel and possibility to read all signals during continual tests. Higher resolution wasn't necessary also due to low resolution of output signal from sensor of displacement and sufficient signal to noise ratio as is possible to see in chapter Results and discussion (Figure 6).

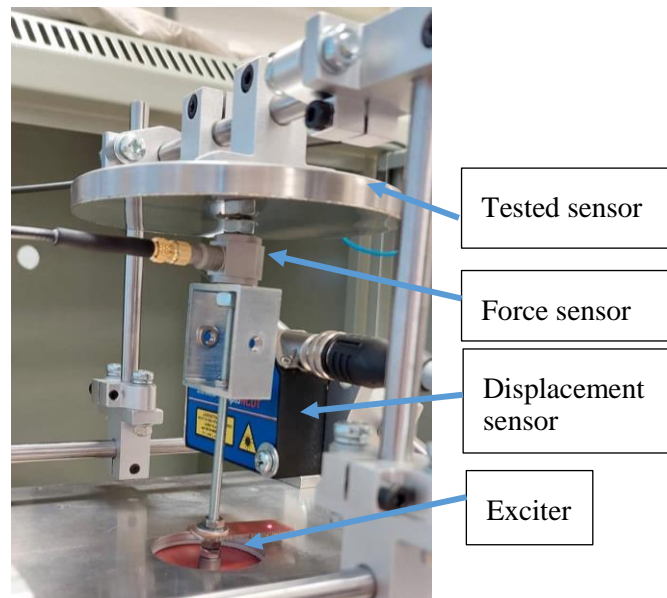


Figure 4: mechanical configuration of tests

RESULTS AND DISCUSSION

We made and used non-woven example, see Figure 5 for SEM image as a basic active material.

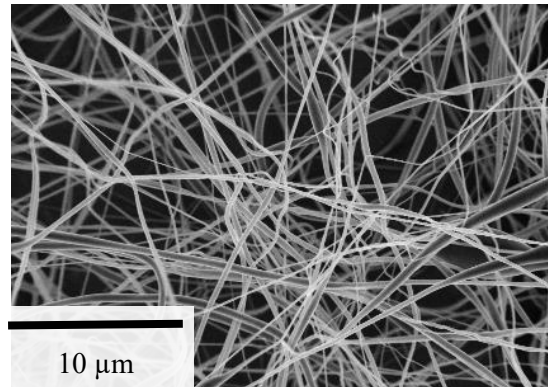


Figure 5: non-woven fabric, SEM image, captured by CEITEC NANO

Typical use

The sensor is possible to use for very small displacement measurement, applied force measurement and for other physical movement (change of air and liquid pressure, acoustical signals). Typical response of output signal is possible to see in Figure 6. Output signal is affected by stiffness of membrane, it brings phase shift due to input force and lower fidelity of carried information.

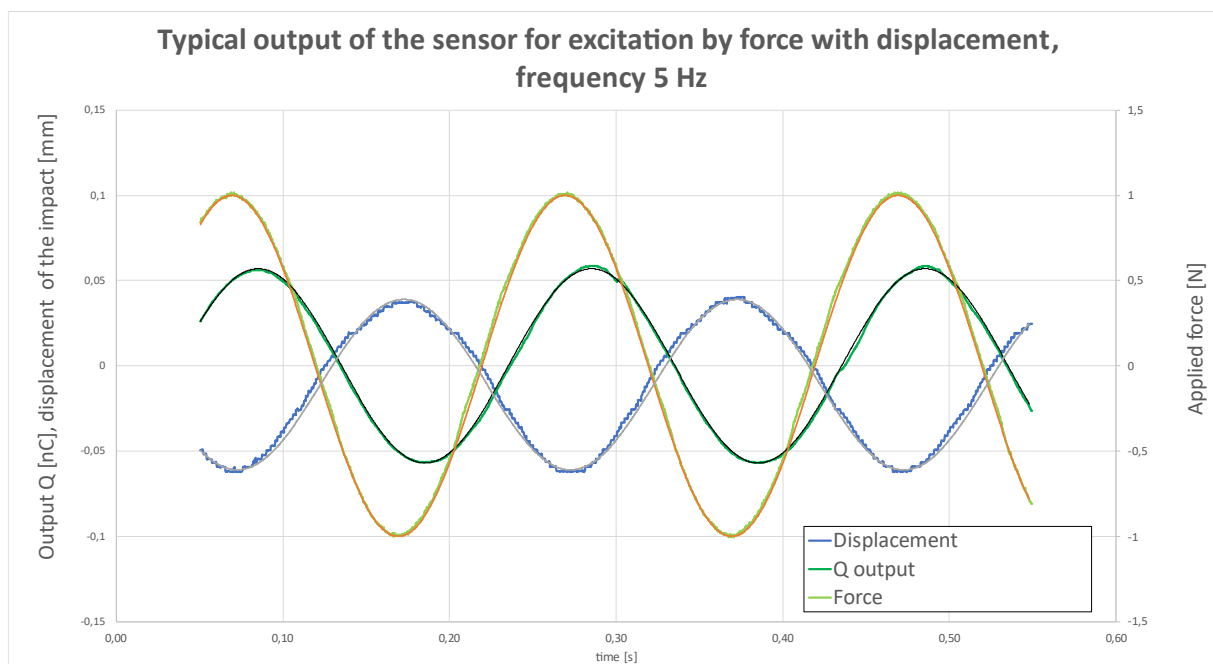


Figure 6: Output signal, applied force and measured displacement

Frequency response

Sensor is possible to use for signals with very low frequency up to frequency 10 Hz for force measurement and up to frequency 100 Hz for displace measurement. Results are possible to see in Figure 7. Force measurement was measured with experimental charge amplifier with higher charge sensitivity, than results for displacement sensitivity, there was necessary to use maximal displacement 0.1 mm peak-peak.

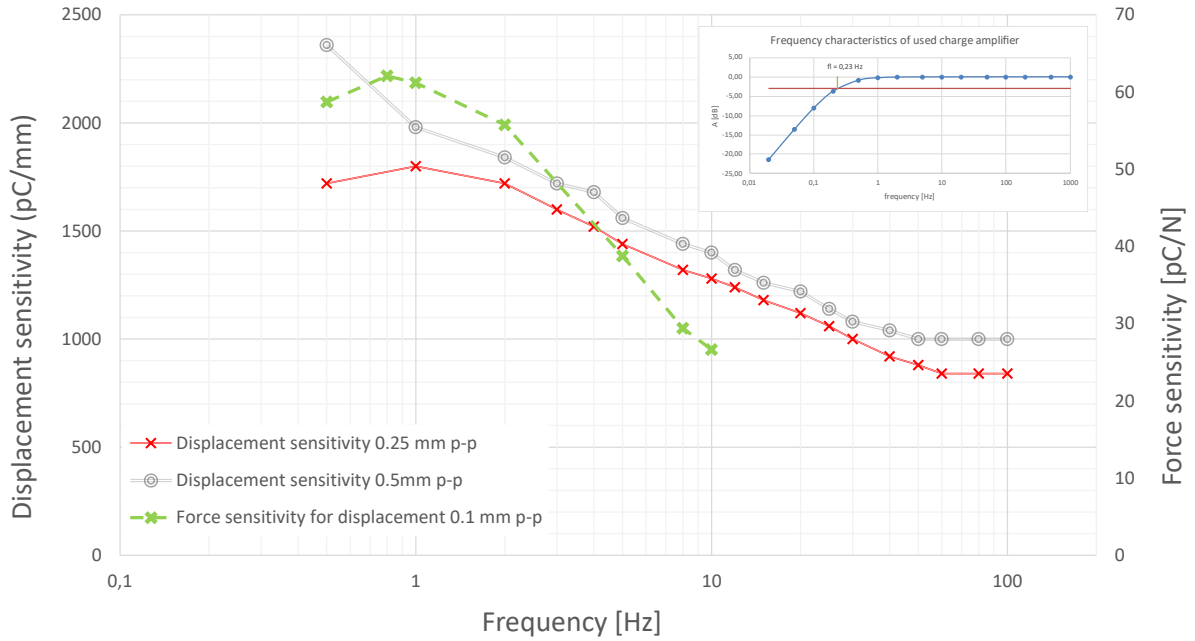


Figure 7: Frequency response for applied force and measured displacement

Stability of sensitivity in time

The sensor was built in January 2021 and output signal didn't show any changes due to time aging to these days. Aging effect can be seen at piezo electric accelerometers.

Example of fitness/industrial use

The sensor could sense changes of displacement and also changes of applied force. Sensor could be possible to use for estimation applied force, which is needed for lifting mass, there are examples in Figure 8.

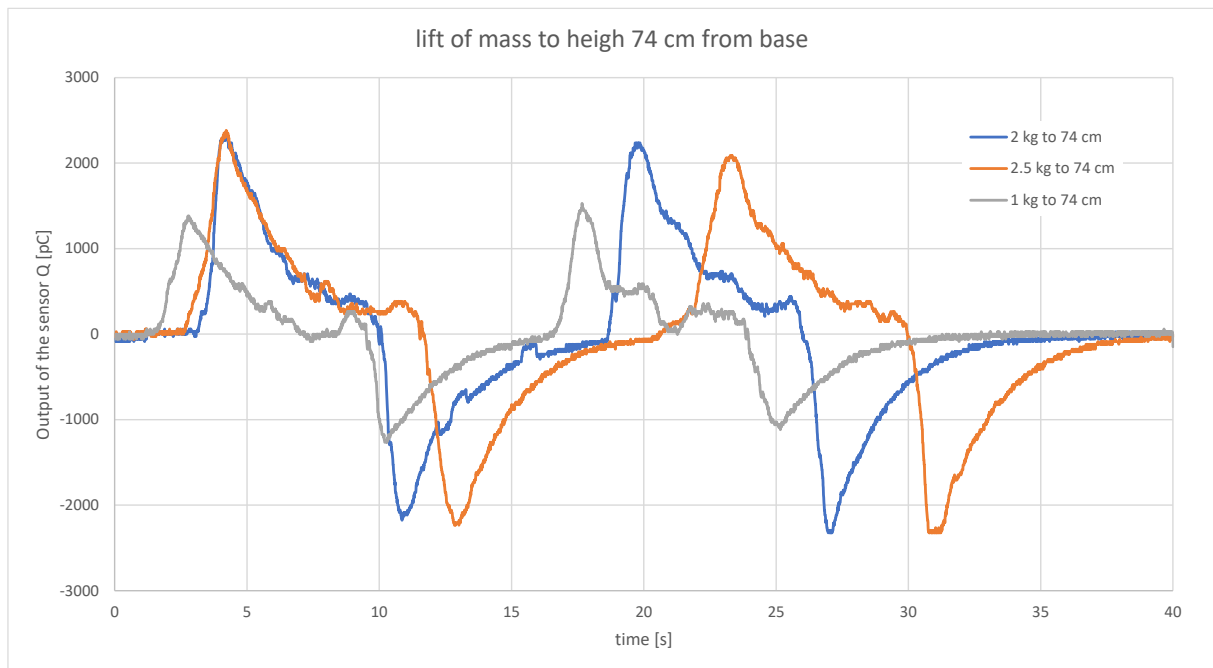


Figure 8: Output of the sensor for lift of mass measurement

3. CONCLUSION

This investigation has to provide more information and exact data for development new types of triboelectric sensors. Sensor is suitable for force measurement in frequency range up to 10 Hz, and for

displacement measurement up to 100 Hz. Partial goal for possibility of measurement displacement wasn't achieved due to this missing parameter is not possible to estimate applied work which is made. However, this work provides many inputs how achieve this information from next generation of sensors.

ACKNOWLEDGMENT

This work was supported by the Internal Grant Agency of Brno University of Technology, grant No. FEKT-S-20-6352.

The research was financially supported by the Grant Agency of Czech Republic under project No. 19-17457S.

REFERENCES

- [1] P. Zhang, Z. Zhang, and J. Cai, *Microsyst. Technol.* 27, 3507 (2021).
- [2] D. Heo, J. Chung, B. Kim, H. Yong, G. Shin, J.-W. Cho, D. Kim, and S. Lee, *Nano Energy* 72, 104719 (2020).
- [3] T. Chen, Q. Shi, K. Li, Z. Yang, H. Liu, L. Sun, J. Dziuban, and C. Lee, *Nanomaterials* 8, 613 (2018).
- [4] A. Ibrahim, A. Ramini, and S. Towfighian, *Energy Reports* 6, 2490 (2020).
- [5] H. Elahi, K. Munir, M. Eugeni, S. Atek, and P. Gaudenzi, *Energies* 13, 5528 (2020).
- [6] H. Chen, C. Xing, Y. Li, J. Wang, and Y. Xu, *Sustain. Energy Fuels* 4, 1063 (2020).
- [7] B. Ghatak, S. Banerjee, S. B. Ali, R. Bandyopadhyay, N. Das, D. Mandal, and B. Tudu, *Nano Energy* 79, 105387 (2021).
- [8] H. Askari, A. Khajepour, M. B. Khamesee, Z. Saadatnia, and Z. L. Wang, *Nano Today* 22, 10 (2018).
- [9] H. T. Baytekin, A. Z. Patashinski, M. Branicki, B. Baytekin, S. Soh, and B. A. Grzybowski, *Science* (80-.). 333, 308 (2011).
- [10] L. S. McCarty and G. M. Whitesides, *Angew. Chemie Int. Ed.* 47, 2188 (2008).
- [11] C. Xu, Y. Zi, A. C. Wang, H. Zou, Y. Dai, X. He, P. Wang, Y.-C. Wang, P. Feng, D. Li, and Z. L. Wang, *Adv. Mater.* 30, 1706790 (2018).
- [12] R. D. I. G. Dharmasena, K. D. G. I. Jayawardena, C. A. Mills, J. H. B. Deane, J. V. Anguita, R. A. Dorey, and S. R. P. Silva, *Energy Environ. Sci.* 10, 1801 (2017).
- [13] R. D. I. G. Dharmasena, K. D. G. I. Jayawardena, C. A. Mills, R. A. Dorey, and S. R. P. Silva, *Nano Energy* 48, 391 (2018).
- [14] Z. L. Wang, *ACS Nano* 7, 9533 (2013).
- [15] J. Chen and Z. L. Wang, *Joule* 1, 480 (2017).
- [16] C. Liu and A. J. Bard, *Nat. Mater.* 7, 505 (2008).
- [17] F. Galembeck, T. A. L. Burgo, L. B. S. Balestrin, R. F. Gouveia, C. A. Silva, and A. Galembeck, *RSC Adv.* 4, 64280 (2014).
- [18] Y. Zi, S. Niu, J. Wang, Z. Wen, W. Tang, and Z. L. Wang, *Nat. Commun.* 6, 8376 (2015).
- [19] J. Peng, S. D. Kang, and G. J. Snyder, *Sci. Adv.* 3, (2017).
- [20] J. Zhong, Q. Zhong, F. Fan, Y. Zhang, S. Wang, B. Hu, Z. L. Wang, and J. Zhou, *Nano Energy* 2, 491 (2013).
- [21] N. Cui, L. Gu, Y. Lei, J. Liu, Y. Qin, X. Ma, Y. Hao, and Z. L. Wang, *ACS Nano* 10, 6131 (2016).

- [22] J. Wang, Z. Wen, Y. Zi, P. Zhou, J. Lin, H. Guo, Y. Xu, and Z. L. Wang, *Adv. Funct. Mater.* 26, 1070 (2016).
- [23] S. Wang, Y. Zi, Y. S. Zhou, S. Li, F. Fan, L. Lin, and Z. L. Wang, *J. Mater. Chem. A* 4, 3728 (2016).
- [24] S. Wang, Y. Xie, S. Niu, L. Lin, C. Liu, Y. S. Zhou, and Z. L. Wang, *Adv. Mater.* 26, 6720 (2014).
- [25] J. Wang, S. Li, F. Yi, Y. Zi, J. Lin, X. Wang, Y. Xu, and Z. L. Wang, *Nat. Commun.* 7, 12744 (2016).
- [26] Y. Zi, C. Wu, W. Ding, and Z. L. Wang, *Adv. Funct. Mater.* 27, 1700049 (2017).
- [27] J. Zhu, M. Zhu, Q. Shi, F. Wen, L. Liu, B. Dong, A. Haroun, Y. Yang, P. Vachon, X. Guo, T. He, and C. Lee, *EcoMat* 2, (2020).
- [28] T. Huang, M. Lu, H. Yu, Q. Zhang, H. Wang, and M. Zhu, *Sci. Rep.* 5, 13942 (2015).
- [29] X. Wang, F. Sun, G. Yin, Y. Wang, B. Liu, and M. Dong, *Sensors* 18, 330 (2018).
- [30] J. Song, B. Yang, W. Zeng, Z. Peng, S. Lin, J. Li, and X. Tao, *Adv. Mater. Technol.* 3, 1800016 (2018).
- [31] J.-H. Zhang, Y. Li, J. Du, X. Hao, and H. Huang, *J. Mater. Chem. A* 7, 11724 (2019).
- [32] M. O. Shaikh, Y.-B. Huang, C.-C. Wang, and C.-H. Chuang, *Micromachines* 10, 438 (2019).
- [33] Y. Zheng, L. Cheng, M. Yuan, Z. Wang, L. Zhang, Y. Qin, and T. Jing, *Nanoscale* 6, 7842 (2014).
- [34] D. Li and Y. Xia, *Adv. Mater.* 16, 1151 (2004).
- [35] A. Greiner and J. H. Wendorff, *Angew. Chemie Int. Ed.* 46, 5670 (2007).
- [36] K. Castkova, J. Kastyl, D. Sobola, J. Petrus, E. Stastna, D. Riha, and P. Tofel, *Nanomaterials* 10, 1221 (2020).
- [37] D. Sobola, P. Kaspar, K. Částková, R. Dallaev, N. Papež, P. Sedlák, T. Trčka, F. Orudzhev, J. Kaštyl, A. Weiser, A. Knápek, and V. Holcman, *Polymers (Basel)* 13, 2439 (2021).
- [38] P. Černohorský, T. Pisarenko, N. Papež, D. Sobola, Ș. Țălu, K. Částková, J. Kaštyl, R. Macků, P. Škarvada, and P. Sedlák, *Materials (Basel)* 14, 6096 (2021).
- [39] P. Kaspar, D. Sobola, K. Částková, A. Knápek, D. Burda, F. Orudzhev, R. Dallaev, P. Tofel, T. Trčka, L. Grmela, and Z. Hadaš, *Polymers (Basel)* 12, 2766 (2020).

Jsme skupina E.ON, těší nás

Jsme jedním z největších energetických koncernů u nás i ve světě. Centrálu máme v Německu, ale najdete nás už v 15 zemích Evropy, včetně České republiky. Zakládáme si na tom, že naše energie můžou šetřit peníze i přírodu a čím dál víc využíváme obnovitelné zdroje.

Kdo patří do naší rodiny

E.ON Energie, a.s.

- Obchoduje s elektřinou a plynem, zajišťuje marketing a komunikaci a stará se i o výrobu energií.
- Pro zákazníky připravuje řešení na míru v oblasti fotovoltiky, tepelné techniky a elektromobility.

EG.D, a.s.

- Distributor energií, který vlastní a provozuje rozvodnou síť elektřiny zejména na jihu Čech a Moravy a rozvodnou síť plynu na jihu Čech.
- Zajišťuje připojení odběrných míst k síti a stará se o dopravu energií k zákazníkům.

E.ON Česká republika, s. r. o.

- Funguje jako podpora výše uvedeným společnostem. Zajišťuje jim služby, jako je účetnictví, právo nebo HR, a na starost má i zákaznickou péči.

Na přírodě nám záleží



E.ON Energie je jedničkou ve výkupu zelené elektřiny v České republice.



EG.D pomocí bezpečnostních prvků na sloupech vysokého napětí chrání ptáky před úrazem.



V budovách E.ONu i ve všech dobíječkách elektromobilů využíváme zelenou energii.

Nastartuj svou kariéru

#spolujsmeeon



Studentské programy

- Letní energetická akademie – 25. – 29. 7. 2022
- Letní technické brigády – od června do září
- Stipendijní program
- Diplomové/bakalářské práce



Absolventské programy

- Trainee program – od září
- Junior technik – od září

www.kariera.eon.cz

 E.ON Kariéra

 E.ON Kariéra

eg.d e.on



Numerical Modelling of Hypersonic Flow of Spacecrafts

M. Mačák¹, P. Vyroubal¹

¹Department of Electrical and Electronic Technology, Brno University of Technology, Brno 616 00, Czech Republic

E-mail: martin.macak@vut.cz, vyroubal@vut.cz

Abstract—Numerical simulations of rarefied gas flows are an important area in the design of aerospace vehicles. They can provide a suitable alternative to experiments, which can be often too complicated due to extreme conditions. Navier-Stokes equations, which describe continuum fluid flow, generally lose their applicability in low pressures. As a result, it is necessary to adjust these equations or use alternative models. This article studies the possibility of using a continuum numerical model for a simulation of a hypersonic flow of a reentry module. Based on the Knudsen number, it was shown that it is still possible to use Navier-Stokes equations either without any adjustments or with the addition of a slip flow boundary condition.

Keywords—rarefied flow, Knudsen number, Ansys Fluent, hypersonic flow, spacecraft

1. INTRODUCTION

Numerical modelling of continuum-rarefied gas flow is a research area of great interest as it can provide a convenient tool to describe and predict aerodynamic behavior of hypersonic vehicles. With rapid development of recyclable spacecrafts, the prediction of hypervelocity flow became very important. During reentry, flow around spacecraft can vary from free molecular in space up to hypersonic in the atmosphere [1, 2].

Such wide range of flows can be described by a kinetic theory governed by the Boltzmann equation [3]. However, it is known that solving the Boltzmann equation directly is very difficult and time consuming due to its complexity of the collision integral term. An alternative approach to solve the Boltzmann equation is the particle-based Direct Simulation Monte Carlo method, which tracks a large number of particles and their collisions are described in a stochastic way [4]. This method is widely used for the investigation of rarefied flows. However, as the number of molecules increases, this method starts to have unacceptable memory demands near continuum regimes, especially caused by large number of collisions [2, 4]. To estimate whether interactions on the molecular scale will affect transport of momentum and energy on the continuum scale, it is possible to calculate the ratio of the molecular mean free path to the characteristic length scale of the system. This ratio is called The Knudsen number (Kn). Different flow regimes can be identified based on this parameter. $Kn < 0.001$ describes the continuum regime, $0.001 < Kn < 0.1$ describes the slip flow regime, $0.1 < Kn < 10$ describes the transition regime and $Kn > 10$ describes the free molecular flow [5].

Well known Navier-Stokes equations are only focused on the description of a continuum flow and they show limitations in capturing nonequilibrium conditions in rarefied gas flows. There have been few attempts to increase the applicability of Navier-Stokes equations, namely implementing the effects of self-diffusion [6] and adjusting velocity boundary conditions to include the slip flow [4]. There have been attempts to provide unified models, which could be able to describe all flow regimes (Fokker-Planck [7] or Hybrid methods [8]). These models are usually very complex and cannot be easily transported into common Computational Fluid dynamics software, which makes their use somewhat problematic.

This article focuses on the applicability of common continuum solvers for the description of hypersonic flow. A simulation of a hypersonic flow around a reentry module [6] was carried out. Ansys Fluent software was used for the simulations and the performance of pressure-based and density-based solvers was compared. Additionally, the effects of slip flow were included in the study.

2. NUMERICAL MODEL

Numerical model used in this work is based on the solution of Navier Stokes equations for compressible gases. They consist of a set of nonlinear partial differential equations, which describe conservation of mass, momentum, and energy (eqs. 1-3) [9]. The simulations were carried out in Ansys Fluent software, which is a commercially available software. The software offers two numerical methods: pressure-based and a density-based solver [10].

Equation of continuity [9]:

$$\frac{\partial \rho}{\partial t} + \nabla \cdot (\rho \mathbf{v}) = 0 \quad (1)$$

Conservation of momentum [9]:

$$\frac{\partial \rho \mathbf{v}}{\partial t} + \nabla \cdot (\rho \mathbf{v} \mathbf{v}) = -\nabla p - \nabla \cdot \boldsymbol{\tau} + \mathbf{F} \quad (2)$$

Conservation of energy [9]:

$$\rho \left(\frac{\partial E_{kT}}{\partial t} + \nabla \cdot (\mathbf{v}(E_{kT} + p)) \right) - \nabla \cdot (K \nabla T) = S \quad (3)$$

Where ρ denotes density, \mathbf{v} denotes velocity vector, p denotes pressure, $\boldsymbol{\tau}$ denotes shear friction tensor, \mathbf{F} denotes a general source term vector, E_{kT} denotes internal thermodynamic temperature, K denotes thermal conductivity, T denotes thermodynamic temperature and S denotes a general energy source term.

The relation between pressure and density was described by the ideal gas law [9]:

$$\rho = \frac{p}{RT} \quad (4)$$

Where R denotes molar gas constant.

Additional parameter such as: viscosity, thermal conductivity and specific heat capacity were described by the kinetic theory of gases [11].

The Knudsen number was described in a local manner, which allows to study the rarefaction in the whole domain [5]:

$$Kn = \frac{\lambda}{\frac{\rho}{\nabla \rho}} \quad (5)$$

Where λ denotes mean free molecular path.

For the slip flow regime, when Kn is between 0.001 and 0.1, a Maxwell velocity boundary condition was used [5]:

$$\mathbf{v}_s = \frac{2 - \sigma}{\sigma} \lambda \frac{\partial \mathbf{v}}{\partial \mathbf{n}} \quad (6)$$

This equation can be also extended to include temperature effects.

Turbulence was described by a Reynolds Averaged Navier-Stokes SST $k-\omega$ model and a laminar flow model [12]. The simulations were carried out on a geometry of Apollo 6 capsule [6] shown in Fig. 1. The gas velocity was set to 1500 m/s with a turbulent intensity of 1% to represent a hypersonic flow. It was assumed that the capsule was at the altitude of approximately 25 km. The computational domain consisted of 3.3 million fluid cells with a maximum size of 50 mm. A local sizing with a maximum size of 15 mm was set to the area around the module. An inflation layer consisting of 10 cells was added to properly describe the boundary layer. For solver settings, a coupled pressure-velocity with a pseudo-transient approach was used. For spatial discretization a standard second order upwind method was applied.

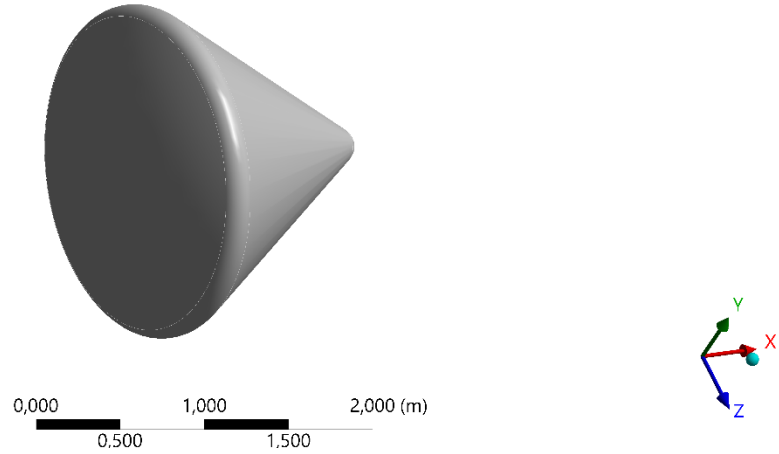


Figure 1: Geometry of Apollo 6 reentry module [6]. Gas flow was set in the direction of the x axis

3. RESULTS

After initial simulations, an estimation of local Knudsen number described by eq. 5 was carried out. The visualization of Knudsen number is shown in Fig. 2. It is possible to see that overall, Knudsen number is within the range of continuum and slip flow regimes. Increased rarefaction can be seen at the edge of the shockwave. Also edges of the module seem to be critical areas, as the Knudsen number raised to values, which represent early stages of transition flow.

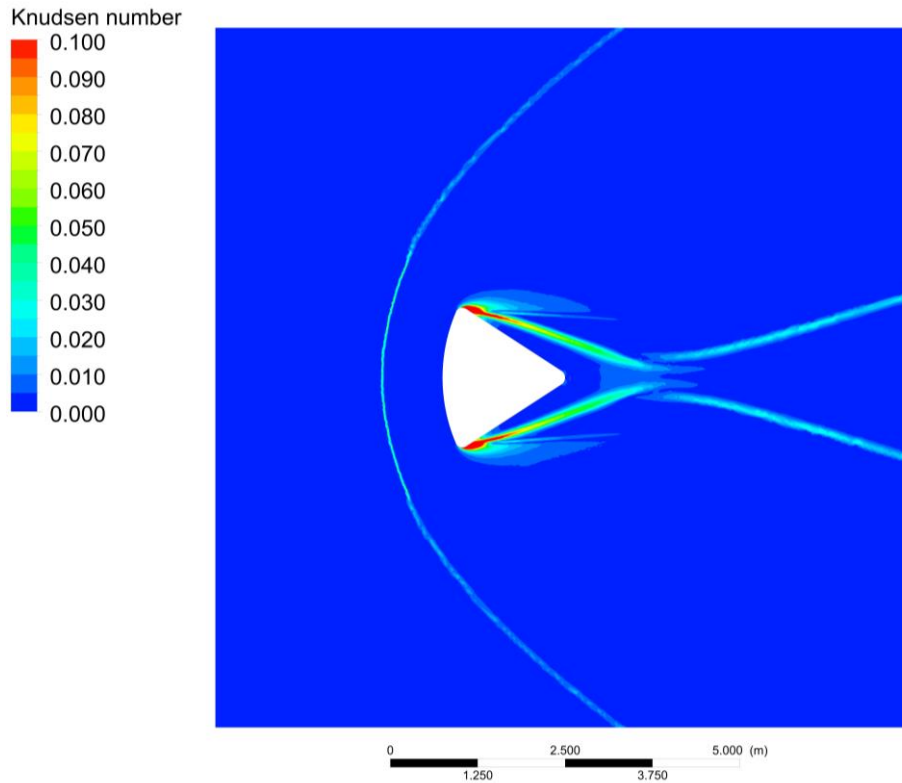


Figure 2: Visualization of a local Knudsen number.

Density and velocity distributions are shown in Fig. 3. Overall, the results obtained with the density-based solver agree with the results from the pressure-based solver. The main difference lied in the compactness of the shock wave. The density-based solver was able to describe steep gradient more accurately than the pressure-based solver. A difference was also visible in the area behind the module. Density-based solver showed a minimum density of 0.13 g/m^3 and a maximum velocity of 1725 m/s . Pressure-based solver showed a minimum density of 0.25 g/m^3 and a maximum velocity of 1530 m/s .

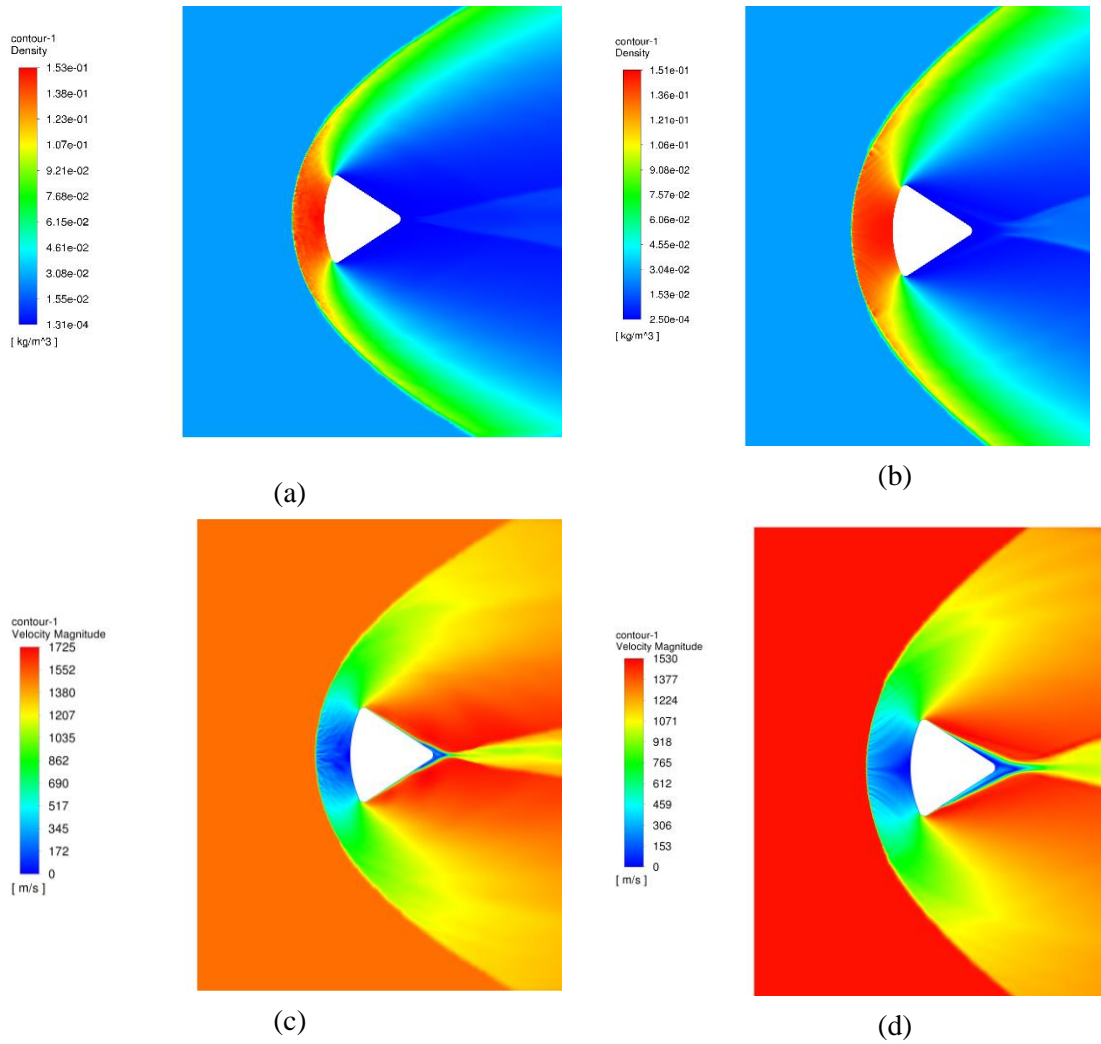


Figure 3: Density and velocity distributions at a pressure of 2500 Pa and an inflow velocity of 1500 m/s. Density distribution for density-based solver (a). Density distribution for the pressure-based solver (b). Velocity distribution for density-based solver (c). Velocity distribution for the pressure-based solver.

4. CONCLUSION

The presented results show that it is possible to use continuum solvers even for hypersonic flows. Even though Navier-Stokes equations have a limited applicability in the rarefied region, they might still produce reasonable results. The most critical point is the calculation of the Knudsen number, as its value might show that even for high-speed rarefied flow, continuum assumption can be still applied. In most cases it was only necessary to apply the slip flow condition. From comparison of presented simulations, the choice of the solver did not influence the result significantly. Surprisingly, the pressure-based solver seemed to converge much faster than the density solver, which theoretically should be able to describe high velocity compressible flows much better. A reason for this might be that pressure-based solvers are much more widely used, so they are updated more often. This information might be especially important for decreasing the simulation time for large spacecrafts. Additionally, the density-based solver does not support the slip flow boundary condition so its applicability might be slightly limited. Overall, the use of classic continuum models is advantageous due their interconnection with another physics modules in commercially available softwares. This model can be additionally extended to include more detailed slip flow boundary conditions or even the effects of the self-diffusion.

ACKNOWLEDGMENT

This work was supported by the BUT specific research program (project No. FEKT-S-20-6206).

REFERENCES

- [1] M. Fang, Z. -H. Li, Z. -H. Li, J. Liang, and Y. -H. Zhang, “DSMC modeling of rarefied ionization reactions and applications to hypervelocity spacecraft reentry flows”, *Advances in Aerodynamics*, vol. 2, no. 1, 2020, doi 10.1186/s42774-020-00030-1.
- [2] H. Xiao and K. Tang, “A Unified Framework for Modeling Continuum and Rarefied Gas Flows”, *Scientific Reports*, vol. 7, no. 1, 2017, doi 10.1038/s41598-017-13274-7.
- [3] Li Zhi-Hui, Peng Ao-Ping, Fang Fang, Li Si-Xin, and Zhang Shun-Yu, “Gas-kinetic unified algorithm for hypersonic aerothermodynamics covering various flow regimes solving Boltzmann model equation”, *Acta Physica Sinica*, vol. 64, no. 22, 2015. doi 10.7498/aps.64.224703.
- [4] D. Nabapure and R. C. Murthy K, “DSMC investigation of rarefied gas flow in a four-sided lid driven cavity: Effect of rarefaction and lid velocities”, *Journal of Computational Science*, vol. 49, 2021, doi 10.1016/j.jocs.2020.101276.
- [5] Z. Guo, J. Qin, and C. Zheng, “Generalized second-order slip boundary condition for nonequilibrium gas flows”, *Physical Review E*, vol. 89, no. 1, 2014, doi 10.1103/PhysRevE.89.013021.
- [6] G. Emanuel, “Extended Navier–Stokes equations, ultrasonic absorption and shock structure”, *Shock Waves*, vol. 25, no. 1, pp. 11-21, 2015, doi 10.1007/s00193-014-0538-z.
- [7] M. H. Gorji and P. Jenny, “An efficient particle Fokker–Planck algorithm for rarefied gas flows”, *Journal of Computational Physics*, vol. 262, pp. 325-343, 2014, doi 10.1016/j.jcp.2013.12.046.
- [8] J. M. Burt and I. D. Boyd, “A hybrid particle approach for continuum and rarefied flow simulation”, *Journal of Computational Physics*, vol. 228, no. 2, pp. 460-475, 2009, doi 10.1016/j.jcp.2008.09.022.
- [9] M. O. Bristeau, R. Glowinski, and J. Periaux, “Numerical methods for the navier-stokes equations. Applications to the simulation of compressible and incompressible viscous flows”, *Computer Physics Reports*, vol. 6, no. 1-6, pp. 73-187, 1987, doi 10.1016/0167-7977(87)90011-6.
- [10] C. Shen, F. Sun, and X. Xia, “Implementation of density-based solver for all speeds in the framework of OpenFOAM”, *Computer Physics Communications*, vol. 185, no. 10, pp. 2730-2741, 2014, doi 10.1016/j.cpc.2014.06.009.
- [11] S. G. Brush, “Development of the Kinetic Theory of Gases. V. The Equation of State”, *American Journal of Physics*, vol. 29, no. 9, pp. 593-605, 1961, doi 10.1119/1.1937858.
- [12] F. R. Menter, “Two-equation eddy-viscosity turbulence models for engineering applications”, *AIAA Journal*, vol. 32, no. 8, pp. 1598-1605, 1994, doi 10.2514/3.12149.

Means of Obtaining Mamdani Fuzzy Model of Car Driver's Dynamics

O. Mihálik and P. Fiedler

Department of Control and Instrumentation, Brno University of Technology, 61600 Brno, Czech Republic

E-mail: ondrej.mihalik1@vut.cz, fiedlerp@vutbr.cz

Abstract—The aim of the paper is creation of an easily interpretable model of human driver during a simulated elementary car driving task. This is achieved using a Hammerstein model whose non-linearity is modelled by a simple Mamdani fuzzy system. Derived closed form formulae of the model are employed to facilitate convergence of the identification algorithm and render it more accurate. The experimental results suggest that the method is suitable for modelling of lane changing manoeuvres on a motorway.

Keywords—driving simulator, Hammerstein fuzzy model, driver behaviour, non-linear dynamical system, Mamdani system

1. INTRODUCTION

Human dynamics in elementary driving tasks was extensively studied by many authors. The ground covered by them is so vast that only the leading ideas can here be touched upon. Most of these approaches rely on linear models [1], [2]. Non-linear approaches employ models such as artificial neural networks [3] or fuzzy systems [4], [6]. This paper aims at extending Jirgl's line of research [5] by generalising his linear model by adding a fuzzy non-linearity. The time series herein presented are the same as in Jirgl's paper; only the identification algorithm differs. All data were obtained using the same car driving simulator. Drivers' task was to change the driving lane on a two-lane motorway according to a visual command.

A number of modelling approaches rely on skilful adjustment of the membership functions (MFs) of a fuzzy model. This may hold for fuzzy control. Yet if we try to apply such 'manual' approach to identification, we encounter obvious disadvantages. One of them is the need for a skilled person who would conduct the identification process. The other is the involvement of human factor: the results are not deterministic and thereby practically irreproducible by other researchers. To obviate these issues, we propose obtaining a model using minimization of quadratic error between the true time series and the output of a fuzzy Hammerstein model. This paper focuses on deriving closed-form formulae of a simple Mamdani system. This enables us to employ minimization methods which make use of derivatives. Furthermore, aided by the regularity constraints, the convergence of the algorithm is rendered fast.

2. MODEL OF THE CONTROL LOOP

The control task executed by a human operator involved requests to change the driving lane at pre-defined time intervals. We propose the following Hammerstein model of the control loop:

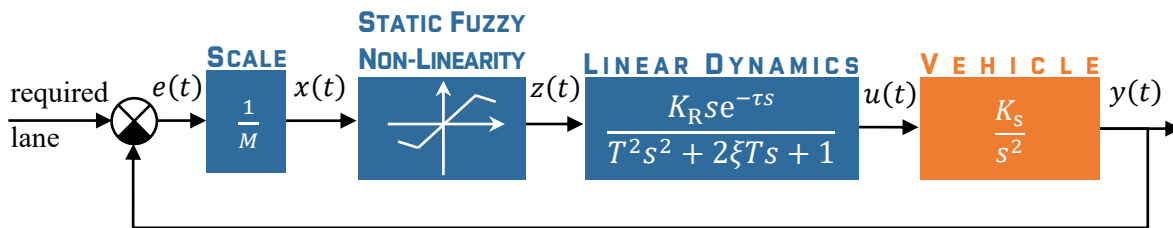


Figure 1: Block diagram of the driver (blue) and vehicle (orange)

The distance from the centre of the required lane, here denoted $e(t)$, is recorded by the simulator. Positive values of $e(t)$ correspond to those errors for which the car is displaced to the right from the centre of a lane. The driver's action $u(t)$ is also monitored. It is the angle of the steering wheel with respect

to its idle position. The quantity $x(t) = e(t)/M$ stands for the standardised input of the fuzzy system, $z(t)$ signifies the crisp output value of the fuzzy system, and $y(t)$ denotes the absolute lateral position of the car on the motorway.

The study conducted by Jirgl [5] concluded that the most suitable form of a linear model can be described by a transfer function

$$F_R(s) = \frac{K_R s}{T^2 s^2 + 2\xi T s + 1} e^{-\tau s}, \quad (1)$$

where K_R stands for the gain, T is the time constant of the system, ξ denotes the damping ratio, τ is the reaction delay of the driver, and s is the Laplace operator. The system input is the distance $z(t)$ of the vehicle from the centre of a driving lane, the output is the angle of the steering wheel $u(t)$. The situation is identical to that of **Figure 1**, except for the fuzzy non-linearity added by us. The transfer function (1) suggests that drivers, indeed, execute an ideal derivative of the error, but, due to the limited human capabilities, their output is inevitably delayed by τ and band-limited by frequency $1/T$.

3. THE FUZZY MODEL AND ITS EXPLICIT EQUATION

PI, PD, and PI-PD are perhaps the most common fuzzy controllers [7]. Judging by the form of driver's transfer function (1), a human behaves like a pure derivative controller; the P and I components are disabled. This is a blessing, for in this case the fuzzy part of the Hammerstein model has only one input. We created a set of three straightforward fuzzy rules:

IF car position IS *on the left* THEN wheel rotation IS *to the right*.

IF car position IS *centred* THEN wheel rotation IS *zero*.

IF car position IS *on the right* THEN wheel rotation IS *to the left*.

The typical shapes of MFs for an average driver are shown in the following figure.

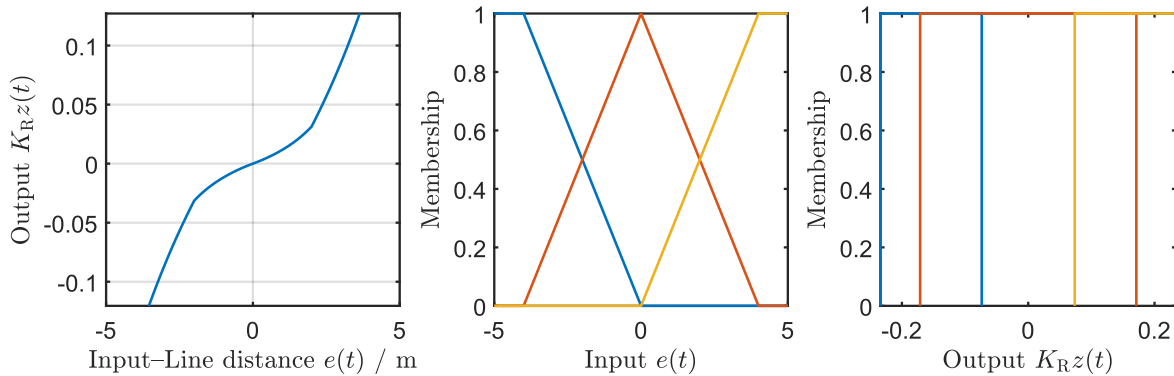


Figure 2: Input-output nonlinearity and output MFs

MATLAB supports identification of Sugeno fuzzy systems, yet we believe that Mamdani systems offer better insight into the input-output relation, mainly through graphical representation of output MFs, such as in **Figure 2**. Linguistic variables of fuzzy models offer interpretability because they are similar to human reasoning. However, employing even a simple fuzzy model would admit non-linearities of inconceivable complexity had there been no restrictions on the fuzzy MFs. This could hamper one of the main results aimed at: the interpretation of the identified model. To alleviate the issue, we propose some symmetry constraints which reduce the number of parameters of the non-linearity to two: a and b .

The input MFs were set as $L(e; -M, 0)$, $\Lambda(e; -M, 0, M)$, and $\Gamma(e; 0, M)$ functions and they are located so as to ensure that the memberships sum to one for any value of $e(t)$. Their positions are firm and do not change during the identification process.

All output MFs are Π functions. In **Figure 2** their memberships are depicted depending on $K_R z(t)$, thereby including the gain of the system in the graphical representation. The red one is centred around zero with width $2aK_R$, the remaining functions are centred around $\pm K_R$ and both have widths $2bK_R$. All above listed settings secure that no more than two rules fire at the same time. A formula describing the input-output relation relying on the *centre of gravity* defuzzification may be derived. The imposed

symmetry constraint guarantee that the input-output relation is an even function

$$z(-x) = -z(x). \quad (2)$$

Therefore, we only need to derive the formulae for $x \geq 0$. There are two possible situations, depending on the overlap of the output MFs. For non-overlapping functions (when $a + b \leq 1$) we get

$$z(x) = \begin{cases} \frac{x}{\left(1 - \frac{a}{b}\right)x - \frac{a}{b}} & \text{for } 0 \leq x \leq 1, \\ 1 & \text{for } x \geq 1, \end{cases} \quad (3)$$

where $2a$ and $2b$ are the widths of the *zero* and *to the left* or *to the right* membership functions, respectively. It is noteworthy that the nonlinearity depends but on the ratio a/b . Furthermore, the system may be reduced to linear system by selecting $a/b = 1$. This was our main justification for selecting rectangular output MFs instead of much more common triangular functions.

When the output membership functions overlap, as in **Figure 2**, then the formula is rendered more elaborate

$$z(x) = \begin{cases} \frac{1}{2} \frac{x[(1+b)^2 - a^2]}{2a + (1+b-3a)x} & \text{for } 0 \leq x \leq \frac{1}{2}, \\ \frac{1}{2} \frac{[(1-b)^2 - a^2] + x[a^2 + 4b - (1-b)^2]}{1 + a - b + (3b - a - 1)x} & \text{for } \frac{1}{2} \leq x \leq 1, \\ 1 & \text{for } x \geq 1. \end{cases} \quad (4)$$

Fortunately, these expressions need not be deciphered by the researcher, who may simply work with the graphical representations provided by **Figure 2**. We derived these expressions since they are necessary for fast and accurate identification described the next section.

4. MINIMIZATION ALGORITHMS

There are a number of approaches to identification of Takagi-Sugeno fuzzy models, such as [7] and [8]. The methods of obtaining Mamdani systems, however, seem to be scarce. Papers such as [9] and [10] discuss identification of Mamdani systems, but they rely on smooth membership functions, which might complicate the interpretation of the fuzzy reasoning.

From the mathematical point of view, fuzzy identification can be formulated as minimization of the cost functional

$$Q(\boldsymbol{\theta}) = \sum_{k=0}^{K-1} [y(kT_s) - y_m(kT_s; \boldsymbol{\theta})]^2. \quad (5)$$

Here $y(t)$ stands for the measured output of a real driver and $y_m(t; \boldsymbol{\theta})$ denotes the output of a Hammerstein fuzzy model with its parameter stacked in the vector $\boldsymbol{\theta}$. Both signals are sampled with period T_s at K time instants $t = kT_s$. The $\boldsymbol{\theta}$ includes positions of the membership functions as well as the parameters of the linear dynamics.

$$\boldsymbol{\theta} = [T \quad \xi \quad K_R \quad \tau \quad a \quad b] \quad (6)$$

The modelled output can be written as discrete convolution

$$y_m(kT_s; \boldsymbol{\theta}) = \frac{K_R}{T\sqrt{1-\xi^2}} \sum_{l=0}^{K-1} \{z(lT_s) - z[(l-1)T_s]\} e^{-\xi(k-l)T_s/T} \sin \frac{(1-\xi^2)(k-l)T_s}{T} \quad (7)$$

The optimal parameters $\boldsymbol{\theta}$ are obtained by minimization of the functional $Q(\boldsymbol{\theta})$. There are a number of minimization algorithms which differ by their running time and accuracy of the results provided. When employing a minimization algorithm, the user shall consider their suitability for the problem at hand.

Nelder-Mead, also referred to as simplex method, is undoubtedly one of the simplest search algorithms of finding the minimum of a functional. It is provided by the *fminsearch* MATLAB function. It does not make use of any derivatives. Hence it is simple to use, yet it may be inefficient owing to many evaluations of the cost functional $Q(\boldsymbol{\theta})$. We experimented with this approach. Nevertheless, the obtained results were not satisfactory, because the function would end up in different minima, depending on the

initial conditions.

Trust Region Algorithm is a more elaborate approach to minimization. The algorithm makes use of the gradient $\nabla Q(\theta)$ of the cost functional $Q(\theta)$. In our case the process of obtaining the derivatives would normally involve lengthy derivation, but, fortunately, we may use the MATLAB symbolic toolbox to differentiate formulae (3), (4) and the step response of (1) with respect to parameters (6). The total running time was halved.

5. EXAMPLES OF OBTAINED RESPONSES

Hammerstein model with Mamdani fuzzy nonlinearity provided similar accuracy as the original linear model, yet the structure admits small nonlinearities. As the input-output relation in **Figure 1** suggests, the driver has a zone with smaller gain when the error $e(t)$ is small. This can be attributed to the different widths of the output membership functions in the same figure. The reader may observe that the *zero* MF is much wider than the *to the left* or *to the right* MFs. Some of the responses to change-the-lane requirement follow.

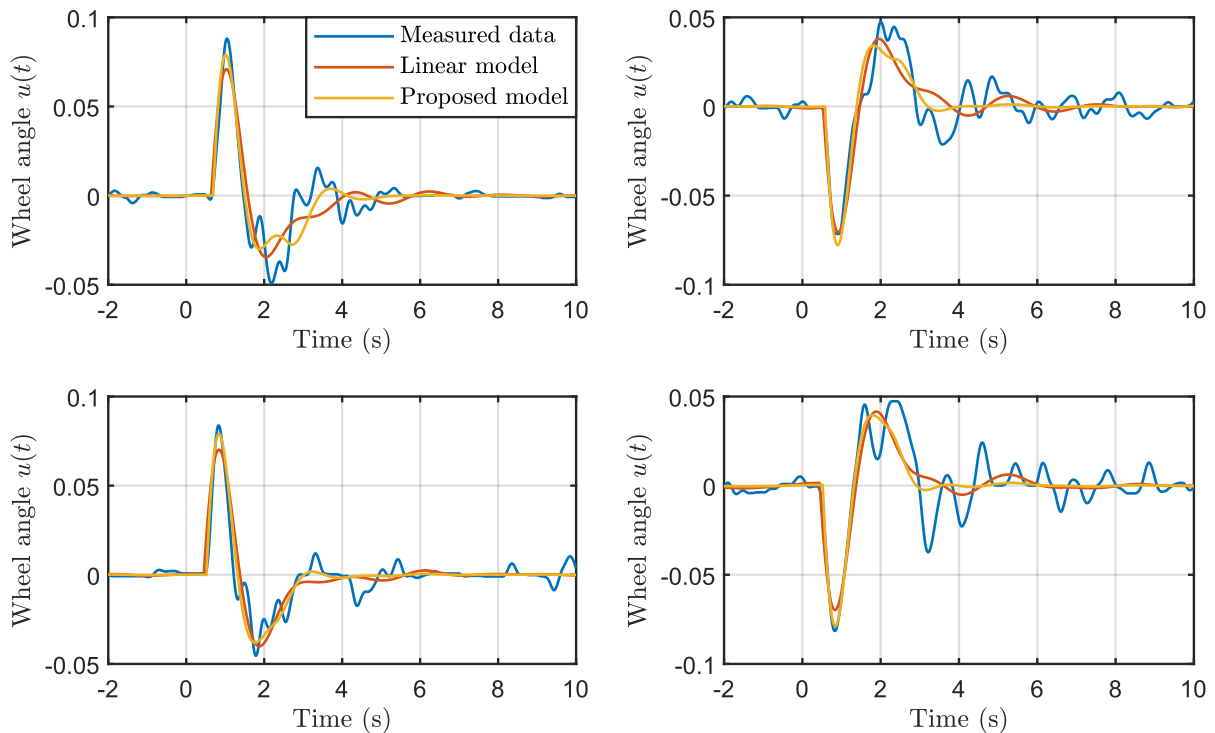


Figure 3: Comparison of the linear and proposed model responses with the measured data.

The responses to the requirement to change the driving lane were approximated by both the linear and fuzzy non-linear model. The fuzzy model, of course, never yields higher error $Q(\theta)$ than the linear model since it can be reduced to the linear model by the proper choice of its parameters a and b . This was made possible using the rectangular output MFs, as we explained in Section 3. Both models produced similar parameters of the linear dynamics. The responses from **Figure 3** are associated with the following parameters.

Table I: Parameters obtained using the linear and proposed fuzzy model

Model	T	ξ	K_R	τ	a	b	Quadratic error
Jirgl's linear model	0.289 s	0.262	0.0299	0.50 s	—	—	24.1 %
proposed fuzzy model	0.244 s	0.317	0.0335	0.57 s	1.18	0.632	21.1 %

6. CONCLUSION

The paper presented an analytical approach to identification of a simple Hammerstein system with Mamdani fuzzy non-linearity. Mathematical formulae derived by us enable straightforward evaluation

of the gradient of the loss functional. Thus obtained partial derivatives greatly facilitates convergence of the identification algorithm and render it more accurate.

Presented results confirm that the proposed model is flexible enough for description of human action exhibited during line changing manoeuvres on a motorway. Furthermore, it throws a light on human reasoning during such tasks, because it provides a means of graphical interpretation availing simple triangular and rectangular MFs. Extension of this approach may involve generalisation of the fuzzy part of the model so as to aggregate multiple inputs. This would allow application of the same mathematical tools to description of more difficult driving tasks, such as acceleration and deceleration using the pedals.

ACKNOWLEDGMENT

The completion of this paper was made possible by the grant No. FEKT-S-20-6205—“Research in Automation, Cybernetics and Artificial Intelligence within Industry 4.0” financially supported by the Internal science fund of Brno University of Technology.

REFERENCES

- [1] HESS, R. A., and A. MODJTAHEDZADEH. A control theoretic model of driver steering behavior. *IEEE Control Systems Magazine* [online]. IEEE, 1990, **10**(5), pp. 3–8 [cit. 2022-03-13]. ISSN 0272-1708. [doi 10.1109/37.60415](https://doi.org/10.1109/37.60415)
- [2] HAVLIKOVA, Marie, Sona SEDIVA, Zdenek BRADAC, and Miroslav JIRGL. A Man as the Regulator in Man-Machine Systems. *Advances in electrical and electronic engineering* [online]. VSB-Technical University of Ostrava, 2014, **12**(5), pp. 469–475 [cit. 2022-03-13]. ISSN 1336–1376. [doi 10.15598/aece.v12i5.1121](https://doi.org/10.15598/aece.v12i5.1121)
- [3] LEE, Hojin, Hyoungkyun KIM, and Seungmoon CHOI. Driving Skill Modeling Using Neural Networks for Performance-Based Haptic Assistance. *IEEE transactions on human-machine systems* [online]. IEEE, 2021, **51**(3), pp. 198–210 [cit. 2022-03-13]. ISSN 2168-2291. [doi 10.1109/THMS.2021.3061409](https://doi.org/10.1109/THMS.2021.3061409)
- [4] WANG, Weida, Tianqi QIE, Chao YANG, Wenjie LIU, Changle XIANG, and Kun HUANG. An Intelligent Lane-Changing Behavior Prediction and Decision-Making Strategy for an Autonomous Vehicle. *IEEE transactions on industrial electronics (1982)* [online]. IEEE, 2022, **69**(3), 2927–2937 [cit. 2022-03-13]. ISSN 0278-0046. [doi 10.1109/TIE.2021.3066943](https://doi.org/10.1109/TIE.2021.3066943)
- [5] JIRGL, Miroslav, Jakub ARM, and Petr FIEDLER. Developing an Unreal Engine 4-Based Vehicle Driving Simulator Applicable in Driver Behavior Analysis—A Technical Perspective. *Safety (Basel)* [online]. Basel: MDPI, 2021, **7**(2), 25 [cit. 2022-03-13]. [doi 10.3390/safety7020025](https://doi.org/10.3390/safety7020025)
- [6] GHAEMI, Sehraneh, Sohrab KHANMOHAMMADI, Mohammad Ali TINATI a Mohammad Ali BADAMCHIZADEH. A hierarchical fuzzy system for modeling driver’s behavior. *International journal of control, automation, and systems* [online]. Heidelberg: Institute of Control, Robotics and Systems and The Korean Institute of Electrical Engineers, 2012, **10**(3), 517–528 [cit. 2022-03-13]. ISSN 1598-6446. [doi 10.1007/s12555-012-0308-6](https://doi.org/10.1007/s12555-012-0308-6)
- [7] ZHANG, Huaguang, and Derong LIU. *Fuzzy modeling and fuzzy control*. Boston: Birkhauser, 2006, xiii, 416 p. ISBN 978-0-8176-4491-8.
- [8] ABONYI, J. *Fuzzy model identification for control*. Boston: Birkhäuser, 2003, 273 p. ISBN 0-8176-4238-2.
- [9] LI, Long, Zuqiang LONG, Hao YING, and Zhijun QIAO. An online gradient-based parameter identification algorithm for the neuro-fuzzy systems. *Fuzzy sets and systems* [online]. Elsevier B.V, 2022, **426**, 27–45 [cit. 2022-03-13]. ISSN 0165-0114. [doi 10.1016/j.fss.2020.11.003](https://doi.org/10.1016/j.fss.2020.11.003)
- [10] KACIMI, Mohand Akli, Ouahib GUENOUNOU, Lamine BRIKH, Fateh YAHIAOUI, and Nouh HADID. New mixed-coding PSO algorithm for a self-adaptive and automatic learning of Mamdani fuzzy rules. *Engineering applications of artificial intelligence* [online]. Elsevier, 2020, **89**, 103417 [cit. 2022-03-13]. ISSN 0952-1976. [doi 10.1016/j.engappai.2019.103417](https://doi.org/10.1016/j.engappai.2019.103417)

Metal-organic structures as additives in polyvinylidene fluoride

T. Pisarenko

Department of Physics, Faculty of Electrical Engineering and Communication, Brno University of Technology,
Technická 2848/8, 61600 Brno, the Czech Republic

E-mail: Tatiana.Pisarenko@vut.cz

Abstract—This paper describes the synthesis and characterization of the first-ever combination of polyvinylidene fluoride (PVDF) semi-crystalline polymer and iron-based metallic-organic structures (MOF). The resulting specimens were made in the form of thin fibers. It is assumed that thanks to these additives in the form of nanoparticles, the performance of PVDF nanofibers can be enhanced in the future. Both components can currently be considered as emerging materials. This is the initial successful production and presentation of results obtained by electron microscopy (SEM), Raman spectroscopy, and Fourier transform infrared spectroscopy (FTIR). These methods provided a basic overview and compared the differences in sample morphology and different phase conformations between a sample with MOF and a sample without MOF.

Keywords—MOF, PVDF, SEM, FIB, Raman spectroscopy, FTIR, characterization

1. INTRODUCTION

Nowadays, efforts to minimize fossil fuel use and the ever-increasing pursuit of energy self-sufficiency and renewable energy use have resulted in an increasing concentration of the scientific community developing new ways and options for harvesting energy with the least possible impact on the environment.

One very promising implementation seems to be the use of a semi-crystalline polymer called polyvinylidene fluoride (PVDF), which is currently in the sights of many scientists and research institutions. The growing interest in its use lies mainly in the extent to which areas it can be implemented. It is a biocompatible, highly heat-resistant material that can be applied both in the form of thin layers and in the form of nanofibers. This ferroelectric polar polymer exhibits a high piezo-, tribo-, and pyroelectric response. PVDF has several crystalline phases differing according to their phase intermolecular conformation, which is mainly influenced by the preparation method [1, 2, 3].

The so-called metallic-organic structures (MOF) can be considered as yet unexplored and suitable for combination with PVDF. As the name suggests, this is a hybrid of organic-inorganic components consisting of metals, which is the first building block and the second block are organic linkers (otherwise also called struts or organic ligands). There is a considerable amount of their organic-inorganic structural tunability depending on the application due to their properties. Ideal use is in gas storage, sensors, filters, energy storage, or biomedicine applications [4, 5].

This is the first use of a combination of PVDF and MOF Fe(BTC). Its construction and subsequent development thus lay the basis for a completely new material, which can be used for several scientific disciplines.

2. MATERIALS AND METHODS

In this work, PVDF was synthesized in combination with iron-based MOF Fe(BTC). After the successful preparation of the solution, a flexible material in the form of nanofibers as a mat was produced. Subsequently, the investigation was carried out using several characterizations and spectroscopic methods in the form of basic research. The material was compared to the same type of material but without MOF. Both types of material (PVDF and PVDF+MOF) were created under identical conditions.

2.1. Solution preparation

Firstly, 20 % polyvinylidene fluoride (Sigma Aldrich, St. Louis, USA) with molecular weight of 275.000 g/mol dissolved in dimethyl disulfide (DMDS) and acetone in a ratio of 7:3 was chosen to prepare the solution. Next, 5 % iron-based MOF nanoparticles (BTC), otherwise commercially known as Basolite F300 (Sigma Aldrich, St. Louis, USA), were mixed into the solution. The resulting solution was mixed on an electric stirrer for 24 h at 80 °C and 2000 rpm. The solution was used immediately after removal from the stirrer.

2.2. Nanofiber fabrication

The resulting sample was created in the form of a nanofiber mat. Electrostatic spinning with a 4SPIN device (Brno, Czech Republic) was used for production. The spinning took place at a temperature of 24 °C and a humidity of 23 %. The collector used was a rotating cylinder covered with aluminum foil and as an emitter one needle with a thickness of 17 GA, through which the solution flowed and which was subsequently drawn as a form of thin fibers due to the electrostatic forces between the emitter and collector. The flow through the needle was 35 μ L/min. The high voltage between the emitter and the collector was set at 50 kV, and the speed of the collector was 2000 rpm. To better understand the whole process, the fiber was wound on a roller, like a thin thread on a spool. The resulting mat, which was applied to the aluminum foil, was then cut from the cylinder.

2.3. Characterization and observation

Several methods were used to compare PVDF and PVDF+MOF samples. As already mentioned, this is basic research aimed at determining the success of producing a combination of PVDF+MOF. Thus, electrical characterization was not included because insufficient data on the ideal structure and phase conformation of the polymer has been collected so far.

Scanning electron microscopy (SEM) provided a basic idea of the material's structure. The observation was performed using a Lyra3 microscope (Tescan, Brno, Czech Republic) with an accelerating voltage of 5 kV. Particular attention was paid to the composition and typical morphology of PVDF and MOF. Their mutual fusion was verified. For further characterization, a focused ion beam (FIB) was used, thanks to which it was possible to observe a cross-section of the fibers. Prior to SEM observation, the samples were carbonized due to the accumulation of charge on their surface and the possibility of pure observation using the EM ACE600 coater (Leica, Wetzlar, Germany). The carbon layer had a thickness of 15 μ m. Half the values are sufficient in a normal situation, but for this case—observation of nanofibers, it is necessary to apply a thicker layer, as the fibers become electrically active, and when a charge is generated on their surface, they begin to twist and move. Therefore, the thin layer would not fix them sufficiently, and the resulting SEM images would not be sharp enough.

Raman spectroscopy was used to analyze and observe the occurrence of phases during production. Thanks to this, it is possible to get an idea of a specific polarization of the sample. A green laser with a power of 5 mW was used to obtain the spectrum. The integration time was 10 s, and the spectrum was accumulated 5 \times . The measurement was performed with 10 \times objective magnification. Subsequent post-processing of the resulting spectrum consisted of background subtraction and average smoothing.

Fourier transform infrared spectroscopy (FTIR) served as a complementary method to Raman spectroscopy, which thus confirmed some of the phases occurring in the produced composite. A Vertex 80v vacuum instrument (Bruker, Billerica, USA) was used to measure the absorption spectrum with a spectral range of 4000 cm^{-1} to 400 cm^{-1} . However, the resulting area of interest was focused on the range 1500 cm^{-1} to 400 cm^{-1} . Baseline correction and background subtraction were done as well.

3. RESULTS

The addition of Fe(BTC) nanoparticles resulted in an expected change in the fiber structure. Not only did the nanofibers' diameter change rapidly, but there were also swelling polymer masses in the form of beads and droplets, which were observed by SEM and cut by FIB, resulting in a different structural fingerprint and phase distribution found by Raman spectroscopy and FTIR.

3.1. Spinning and fabrication process

Due to previous experience with other additives, it was expected that problems could occur during spinning, and the resulting mat may not be firmly collected to the collector, as doped nanoparticles may affect the production process. As a reference from which all parameters were compared, the first sample without MOF was spun with already known and verified production parameters. The same setting was used for PVDF+MOF. From the course of spinning, it can be stated that the fiber mats spun smoothly and without any problems in both cases. Electrostatic spinning and production can therefore be considered successful.

3.2. Comparison of samples with and without MOF nanoparticles

After successful production, both types of samples (PVDF and PVDF+MOF) were compared. From Raman spectroscopy in Figure 1, a fingerprint of both samples can be observed, which differs considerably, especially in the proportional representation of individual bands. Upon closer examination, it is clear that the most notable difference in the ratio is achieved by the bands in the spectral region of 1524 cm^{-1} and 2975 cm^{-1} , which indicates a different representation of materials. However, the representation of the α - and β - crystalline phases in the region in the range of 740 cm^{-1} to 880 cm^{-1} is much more fascinating. The ratio of PVDF between α - and β -phase (1:2.12) is very different to PVDF+MOF α - and β -phase (1:1.27). It means that α -phase (803 cm^{-1}) increased almost twofold against β -phase (840 cm^{-1}) for doped PVDF [6].

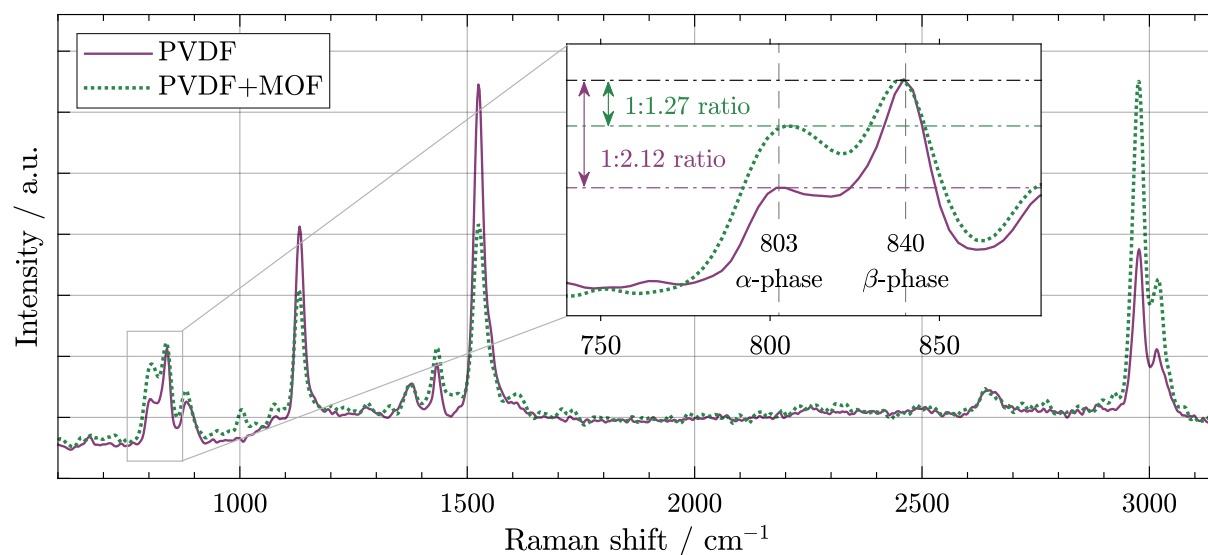


Figure 1: Raman spectroscopy with detailed area of interest— α - and β - crystalline phase region. Different ratios of characteristic bands can be seen over almost the entire spectrum width. However, the area where the α - and β -phases differ between the two selected samples PVDF and PVDF+MOF is the most attractive. The different proportions of these phases can affect the electrical behavior of the sample.

Similarly, in both Raman spectroscopy and FTIR absorption regions, Figure 2 shows characteristic areas that differ significantly from pure PVDF. Thus, in addition to the different proportions between these regions in the spectrum, specific regions of the α - and β -phases can also be seen. However, in contrast to pure PVDF, the α -phase already appears strongly in the spectrum. For pure PVDF, it was not even detected at 763 cm^{-1} , or its value was negligible [7].

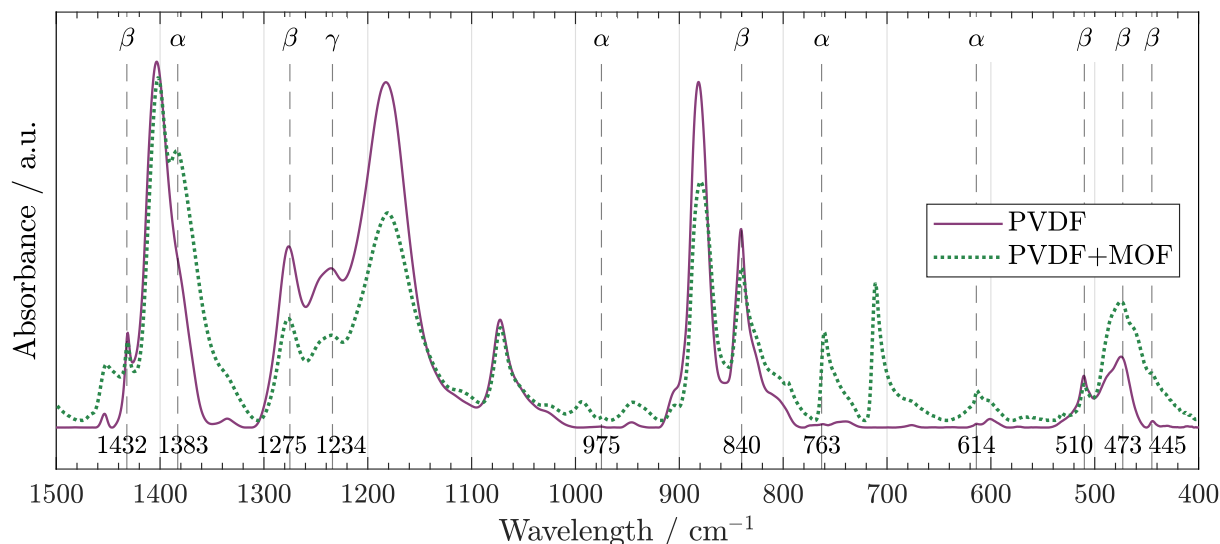


Figure 2: Comparison of two samples with and without MOF nanoparticles using Fourier transform infrared spectroscopy (FTIR). The most critical regions of the α -, β -, and γ -phases are marked. PVDF+MOF shows a strong α -phase occurrence (1383 cm^{-1} and 763 cm^{-1}) compared to pure PVDF sample.

The pure PVDF and doped PVDF+MOF fibers are very different, as shown in Figure 3. Nevertheless, it is necessary to emphasize that the production parameters were the same for both types. The first cause that has occurred due to doped MOF is the formation of balls and drops of considerably different dimensions within units up to tens of micrometers. As seen in Figure 3b, these formations have a highly porous structure and are evaluated as imperfections of the overall composite. Ordered fibers in parallel in Figure 3a can be considered made without any issues. Another parameter that changed rapidly with the addition of MOF is the thickness of the fibers, where its difference is evident in all parts of Figure 3. An irregular, wrinkled structure can be seen upon closer examination of one fiber, especially in Figure 3c. Figure 3d shows that the imperfectly smooth structure is also visible on a thinner fiber with MOF. The fiber diameter in Figure 3c is 1018 nm and in Figure 3d is 237 nm .

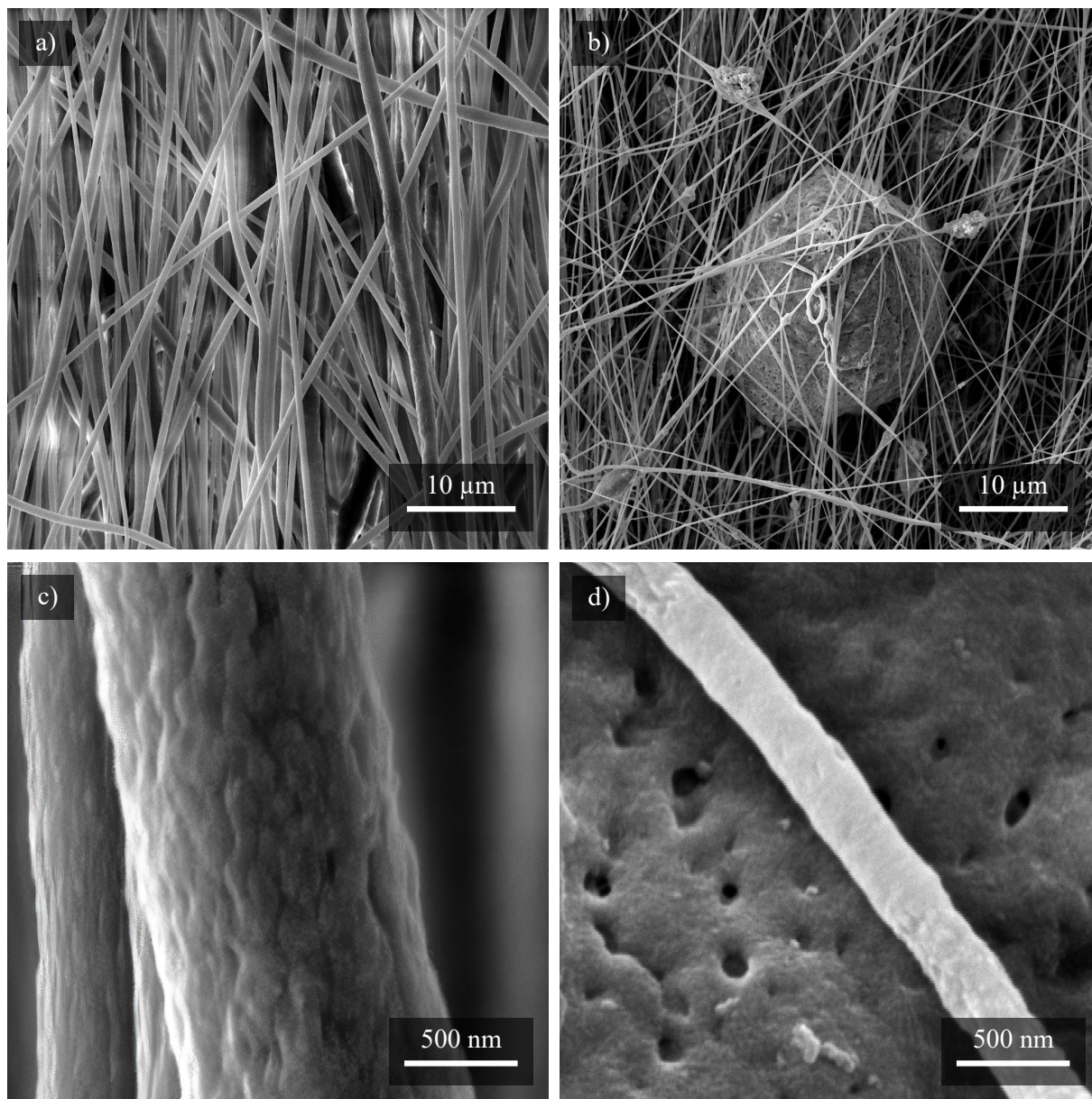


Figure 3: Samples were observed on SEM and carbonated. View of the fiber structures of **a)** pure PVDF and **b)** doped PVDF+MOF. Similarly, one fiber of **c)** pure PVDF and **d)** doped PVDF+MOF is shown in detail.

3.3. Detailed surface study of MOF doped fibers

As already mentioned, the PVDF + MOF structure created in this work is new, and many interesting and specific parts should be analyzed.

One of them is created spherical objects (shown in Figure 3b too), described in Figure 4, where FIB was also used (Figure 4b). By default, these defects are called droplets, but the almost perfect spherical structure, as seen in Figure 4, pushes it to be called as balls. A cross-section of this structure (Figure 4b) revealed that some balls are hollow and porous, especially on the surface. This phenomenon has previously been observed directly on fibers [8].

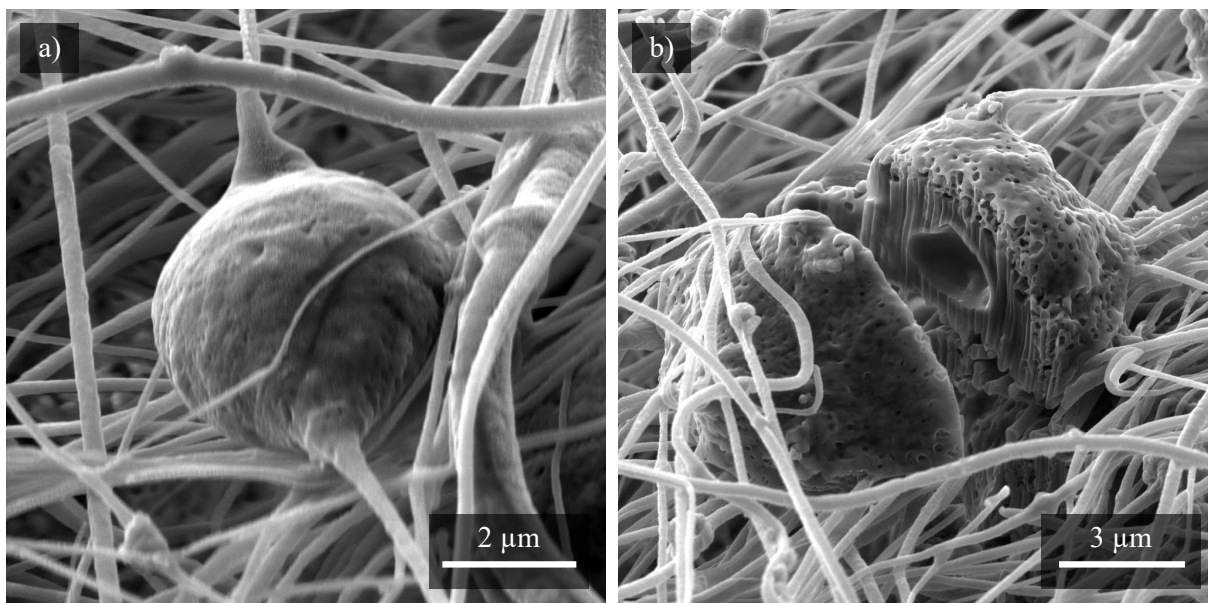


Figure 4: Formed balls after the use of MOF in the polymer. From Figure a) an almost perfect spherical structure can be seen. In Figure b) it can be seen after the FIB cross-section that this structure is in some cases hollow inside.

The last Figure 5 shows the specific formations created on each fiber. The fibers lie on a large porous structure (similar to previous Figure 4). Another change that has occurred here versus pure PVDF is that the fibers tend to split and divide, as shown in Figure 5a. These protrusions, similar to roots, try to attach to the created ball structure. It can also be confirmed that MOFs have been successfully implemented as part of SEM observations. In greater detail, their particles are visible in both Figure 5a and Figure 5b.

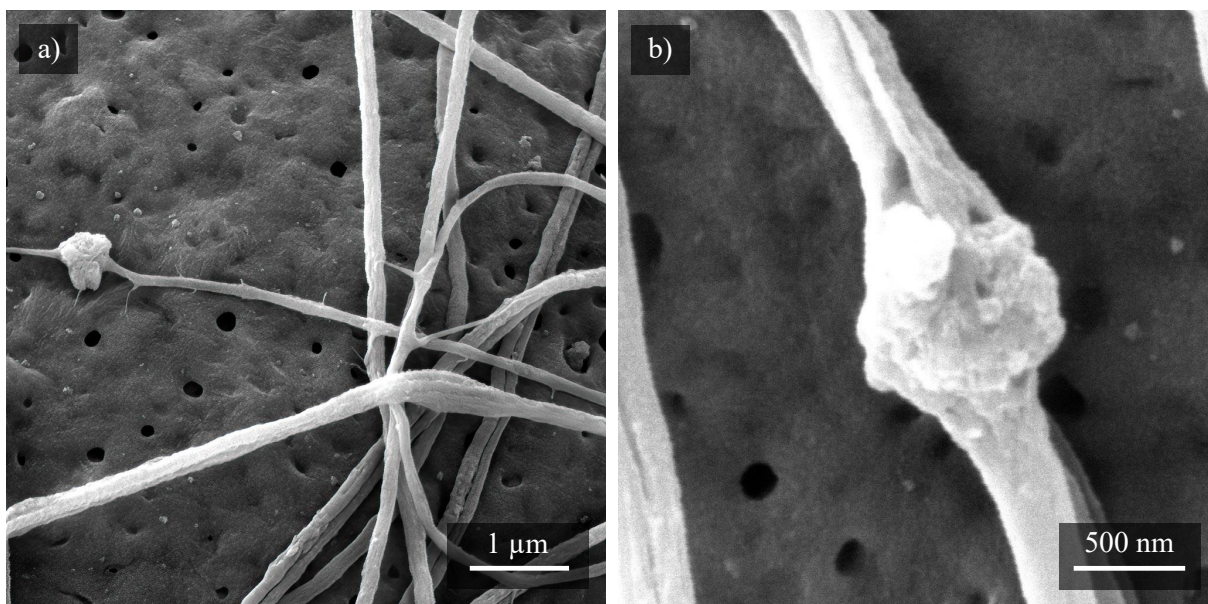


Figure 5: The MOF particles trapped in the fibers confirm both Figure a) and Figure b) in greater detail. An interesting phenomenon is the division and overgrowth of fibers into other structures, as is visualized in Figure b).

4. CONCLUSION

This article describes the production and fundamental analysis of PVDF fibers with Fe(BTC) nanoparticles. The experimental findings confirmed that MOF was successfully trapped in the fibers, but

it also caused many side effects. One of them was the creation of ball structures preventing the perfect arrangement and shape of the fibers. These spherical structures are occasionally hollow. Compared to regular pure PVDF fibers, the fibers with MOF reached very low diameters. From spectroscopic measurements, PVDF+MOF showed a significantly higher α -phase than conventional fibers. These successful observations can thus serve as a basis for the further development of iron-based PVDF nanofibers. It should also be noted that this paper does not describe the specific state of iron ion binding in the composite but its importance for increasing the piezoelectric constant. For more accurate identification and fingerprint of iron, it is appropriate to use energy dispersive spectroscopy (EDX) or attenuated total reflection infrared spectroscopy (ATR-FTIR).

ACKNOWLEDGMENT

I would like to thank my advisor, doc. Mgr. Dinara Sobola, Ph.D., for her valuable comments and guidance through this work. Research described in the paper was financially supported by the Ministry of Education, Youth and Sports of the Czech Republic under the project CEITEC 2020 (LQ1601) and by the Internal Grant Agency of Brno University of Technology, grant No. FEKT-S-20-6352, and the Grant Agency of Czech Republic under project No. 19-17457S. Part of the work was carried out with the support of CEITEC Nano Research Infrastructure supported by MEYS CR (LM2018110).

REFERENCES

- [1] C. Ribeiro, C. M. Costa, D. M. Correia, J. Nunes-Pereira, J. Oliveira, P. Martins, R. Gonçalves, V. F. Cardoso, and S. Lanceros-Méndez, “Electroactive poly(vinylidene fluoride)-based structures for advanced applications,” *Nature Protocols* 2018 13:4, vol. 13, no. 4, pp. 681–704, 3 2018. [Online]. Available: <https://www.nature.com/articles/nprot.2017.157>.
- [2] Y. Huang, G. Rui, Q. Li, E. Allahyarov, R. Li, M. Fukuto, G. J. Zhong, J. Z. Xu, Z. M. Li, P. L. Taylor, and L. Zhu, “Enhanced piezoelectricity from highly polarizable oriented amorphous fractions in biaxially oriented poly(vinylidene fluoride) with pure β crystals,” *Nature Communications* 2021 12:1, vol. 12, no. 1, pp. 1–8, 1 2021. [Online]. Available: <https://www.nature.com/articles/s41467-020-20662-7>.
- [3] P. Černohorský, T. Pisarenko, N. Papež, D. Sobola, Š. Tělu, K. Částková, J. Kaštyl, R. Macků, P. Škarvada, and P. Sedlák, “Structure Tuning and Electrical Properties of Mixed PVDF and Nylon Nanofibers,” *Materials*, vol. 14, no. 20, p. 6096, 10 2021. [Online]. Available: <https://www.mdpi.com/1996-1944/14/20/6096>.
- [4] A. E. Baumann, D. A. Burns, B. Liu, and V. S. Thoi, “Metal-organic framework functionalization and design strategies for advanced electrochemical energy storage devices,” *Communications Chemistry* 2019 2:1, vol. 2, no. 1, pp. 1–14, 7 2019. [Online]. Available: <https://www.nature.com/articles/s42004-019-0184-6>.
- [5] Z. Yan, Y. Yang, and X. Cai, “Preparation of a ferroelectric composite film metal–organic framework/PVDF,” *Journal of Polymer Research*, vol. 27, no. 12, pp. 1–8, 12 2020. [Online]. Available: <https://link.springer.com/article/10.1007/s10965-020-02349-1>.
- [6] D. Chapron, F. Rault, A. Talbourdet, G. Lemort, C. Cochrane, P. Bourson, E. Devaux, and C. Campagne, “In-situ Raman monitoring of the poly(vinylidene fluoride) crystalline structure during a melt-spinning process,” *Journal of Raman Spectroscopy*, vol. 52, no. 5, pp. 1073–1079, 5 2021. [Online]. Available: <https://onlinelibrary.wiley.com/doi/full/10.1002/jrs.6081>.
- [7] X. Cai, T. Lei, D. Sun, and L. Lin, “A critical analysis of the α , β and γ phases in poly(vinylidene fluoride) using FTIR,” *RSC Advances*, vol. 7, no. 25, pp. 15 382–15 389, 3 2017.
- [8] T. Pisarenko, N. Papež, S. Dinara, Š. Tělu, K. Částková, P. Škarvada, R. Macků, E. Ščasnovič, and J. Kaštyl, “Comprehensive characterization of PVDF nanofibers at macro- and nanolevel,” *Polymers*, vol. 14, p. 18, 2022.

Effect Of Al₂O₃ Barrier On The Field Emission Properties Of Tungsten Single-Tip Field Emitters

D. Burda^{1,2}, A. Knápek²

¹ Faculty of Electrical Engineering, Brno University of Technology, Czech Republic

² Institute of Scientific Instruments of CAS, Brno, Czech Republic

E-mail: xburda14@vut.cz

Abstract—This research aims to obtain a more in-depth understanding of the field emission properties of tungsten single-tip field emitters (STFEs) coated with a several tens of nanometer thin barrier of Al₂O₃. The introduction of an additional barrier into the metal-vacuum interface system of the emitter can be beneficial to improve its performance. The tungsten emitters were prepared using a two-step electrochemical drop-off etching technique. Thin oxide barrier coatings were prepared by using low-temperature atomic layer deposition (ALD), a chemical vapor deposition technique. Field emission was studied in an internally developed field emission microscope (FEM) working in UHV vacuum ($< 1 \cdot 10^{-7}$ Pa), and the experimental field emission data were analyzed by the so-called Murphy-Good plots. The value of the local work function of the grown oxide layer were investigated using Ultra-violet photoelectron spectroscopy (UPS).

Keywords—Cold field emission, single-tip field emitters, tungsten tip, aluminum oxide, dielectric coatings, Murphy-Good plot

1. INTRODUCTION

Motivation

The cold-field emitters which can be macroscopically described as a single-tip (STFEs) play the main role in the experiments presented in this report. STFEs can be prepared by electrochemical etching of refractory metals, which is generally a fast, few-step process not requiring costly equipment compared to the fabrication of large area field emitters (LAFEs), which is based on several time and resource consuming steps (often >10) including electron beam/UV/laser lithography. In this report, a polycrystalline tungsten wire was chosen as the main material for the fabrication of STFEs.

In electron physics, the fabrication of field emitters with enhanced emission characteristics is much sought upon. By introducing a dielectric layer into metal-vacuum interface, a new metal-dielectric-vacuum system is formed. The dielectric layer introduces new surface electron states into the electronic structure of the emitter. Altogether with the work function of the dielectric, energy gap, impurities [1], all these parameters affect the efficiency, spatial and temporal resolution of the emitted electrons.

Field Emission Theory

In the case of cold field electron emission (CFE), most electrons tunnel from electron states below Fermi level. Tunneling is assumed through the *Schottky-Nordheim* (SN) barrier. The basis of the emission analysis is built upon *Murphy-Good field electron emission theory*. The so-called extended *Murphy-Good equation* (EMG) is employed [2,3]:

$$I(V) = \{A^{\text{SN}}(\theta \exp \eta)V_R^{-\kappa}\}V^{\kappa} \exp(-\eta V_R/V) \quad (1)$$

where A^{SN} is the formal emission area assuming SN barrier tunneling, V_R is a (constant) reference measured voltage [2] needed to pull the top of the SN barrier down to Fermi level [3], $\theta(\varphi)$ and $\eta(\varphi)$ are scaling parameters, the parameter $\kappa(\eta)$ is calculated: $\kappa = 2 - \eta/6$ [2].

Applying the natural logarithm to (1):

$$\ln\{I/V^\kappa\} = \ln\{A^{\text{SN}}(\theta \exp \eta)V_R^{-\kappa}\}V^\kappa - \eta V_R/V \quad (2)$$

the equation becomes linear, $\ln\left\{\frac{I}{V^\kappa}\right\}\left(\frac{1}{V}\right)$, this form is called *theoretical Murphy-Good plot*.

2. METHODOLOGY

Electrochemical Etching

The base tungsten emitter was prepared by two-step electrochemical etching of a polycrystalline tungsten wire (GoodFellow, 99,9+%, diameter 0.3 mm). in a 3M aqueous solution of NaOH. A precise electrochemical etching station developed at ISI Brno [4] was used. The tungsten wire connected as the anode is submerged in the electrolyte, the tungsten wire is encircled by a Pt ring also submerged in electrolyte, which acts as the cathode. Due to a precise stepper motor and a programmable breaker circuit of the etching station, sharp tungsten tips with a tip radius of 100 nm and less can be obtained. To ensure that the tip surface is cleaned off hydroxide and oxide residues, the etched tips are chemically cleaned in 38% hydrofluoric acid (HF) for 20 minutes.

Atomic Layer Deposition

ALD is a high-vacuum deposition technique, in which the growth of layers is based on sequential, self-limiting surface reactions of two vapour phase precursors. ALD offers exceptional conformality, which allows the growth of a uniformly thin layer on very complex or sharp structures [5]. The nature of layer formation allows for sub-angstrom control of thickness [5] due to atom-by-atom sequential reactions of the two precursors. Thin Al_2O_3 coatings were prepared at the CEITEC Nano facility in the Ultratech-Cambridge Nanotech Fiji 200 ALD tool. The precursors used were trimethylaluminum (TMA) and water vapor, the process temperature was set at 150 °C, and the number of cycles was set at 150. Each ALD cycle consisted of steps: 1) injection of TMA, duration 0.06 s, 2) purge, duration 20 s, 3) injection of H_2O , duration 0.06 s, 4) purge, duration 20 s. The process described here results in a 15 nm thin layer of Al_2O_3 .

Field Emission Microscopy Measurement

Measurements of the emitter with and without the Al_2O_3 coating layer were all performed in the in-house developed FEM. The schematic diagram can be seen in Fig. 1. The emitters were tested in triode configuration: the emitters themselves were mounted as a cathode, a steel cylinder with the hole of 1 mm of diameter was acting as an extractor electrode, an Al-coated YAG scintillator acting as collector electrode. The emission current was measured between the Al-coating of the scintillator and the ground wire using a RBD 9103 Pico ammeter. The distance between the tip of the cathode and the scintillator was set at 40 mm. Up to +50 V bias was applied to the scintillator from the external battery supply to improve the collection of primary electrons and to suppress the generation of the secondary electrons.

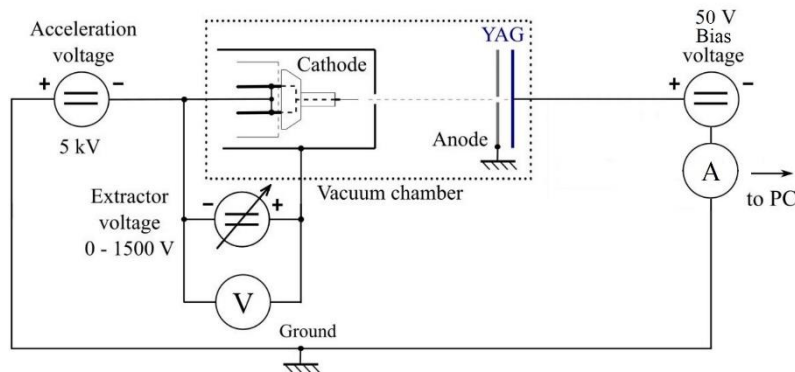


Figure 1: Diagram of the FEM in triode configuration; Al-coated Ce:YAG acts as the collector electrode.

3. RESULTS AND DISCUSSION

To protect the emitter from exploding during the measurement, the I - V characteristics shown in Figure 3 were captured in this manner: After the first ignition, the extraction voltage had been increased, so the Pico ammeter would collect a current of no more than $10\ \mu\text{A}$. This seemingly arbitrary value depends on the electron collection efficiency of the conductive Al layer sputtered on top of the scintillator, the applied bias voltage and the condition of Al layer. Based on our calculations and previous experiments, the current value of $10\ \mu\text{A}$ is regarded as “safe” for the emitters with the tip radius around $100\ \text{nm}$. The actual measurement of current and voltage started around the “safe” value and then the extraction voltage was lowered to the point there were no emission. Additionally, the coated emitter shows a very strong *switch-on effect*, i.e., the first emission does not begin at the lowest measurable current, but at a value often several orders of magnitude higher [6], in all subsequent runs the emitter behaves normally without the switch-on effect.

For the *Murphy-Good plot analysis*, the work function of the polycrystalline W tungsten emitter is $4.5\ \text{eV}$. Work function of Al_2O_3 , which was acquired experimentally by ultraviolet photoelectron spectroscopy, see Figure 2.

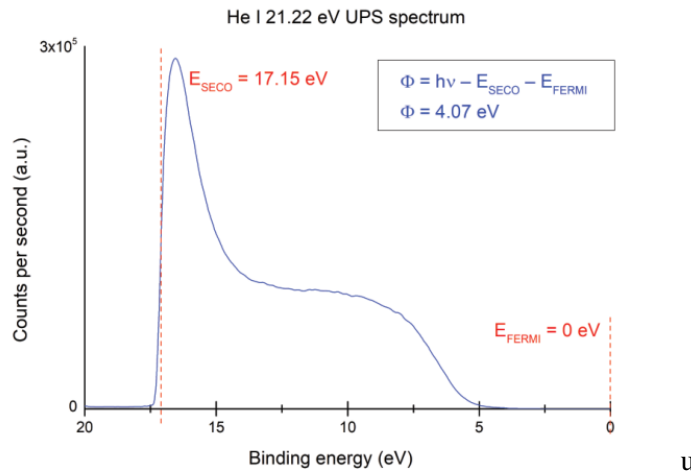


Figure 2: Determination of the local work function of Al_2O_3 thin layer. He I line $21.22\ \text{eV}$. Reproduced from [7].

Murphy-Good plots based on the collected data are shown in Figure 3. Both emitters showed nontrivial behavior, passing the orthodoxy test when the extraction voltage was set low and failing the test when the extraction voltage was set high. This is common in tungsten emitters; at high extraction voltage, slight macroscopic changes in the electrostatic field at the emitter can occur and morphology of the emitter may irreversibly change. The emission images of the Al_2O_3 coated emitters were resembled those of the multi spot emission patterns of composite emitters [6].

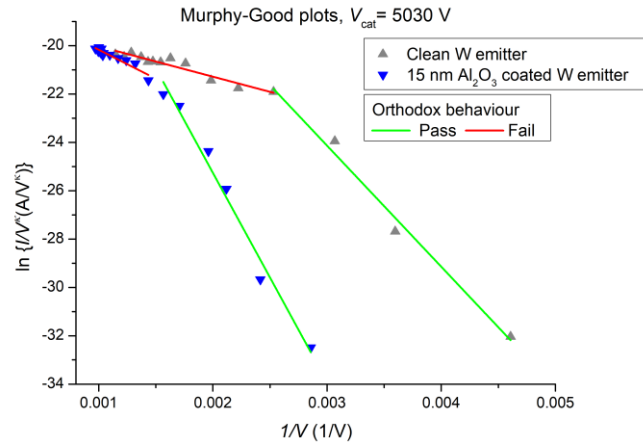


Figure 3: Murphy-Good plots of experimental I - V characteristics of measured emitter(s). Reproduced from [7].

4. SUMMARY

The research shows the possibility of fabrication of ultrathin Al_2O_3 coated tungsten emitters. Coated emitter exhibits a strong switch-on effect. Orthodox behavior can be observed when it is operated in low extraction voltage. Applying dielectric barrier coating to the emitter plays an important role in the changes of its electron emission and it is reflected in the extracted formal emission parameters. Based on experiments in similar ultra-high vacuum and extraction voltage conditions, the effect of chemical or surface geometry alterations of the emitter tip is estimated to be lower than the effect of applying Al_2O_3 coating. The atomic layer deposition technique enables fine tuning of layer thickness and high layer uniformity, features very useful for fabricating advanced field emitters with thin barrier layers. Some morphology changes were observed during the FEM measurements, which may indicate modifications of the emitter. Due to the complex nature of the interfaces in metal-dielectric-vacuum emitters, deeper understanding through simulations is anticipated soon.

ACKNOWLEDGMENT

The infrastructure was supported by RVO:68081731. The research described in this paper was partially supported by the Internal Grant Agency of Brno University of Technology, grant No. FEKT-S-20-6352. I acknowledge CzechNanoLab Research Infrastructure supported by MEYS CR (LM2018110).

REFERENCES

- [1] L. J. Brillson, “Metal-semiconductor interfaces”, *Surface Science*, vol. 299-300, pp. 909-927, 1994. doi:10.1016/0039-6028(94)90706-4
- [2] R. G. Forbes, “The Murphy–Good plot: a better method of analysing field emission data”, *Royal Society Open Science*, vol. 6, no. 12, 2019. doi:10.1098/rsos.190912
- [3] M. M. Allaham, R. G. Forbes, A. Knápek, and M. S. Mousa, “Implementation of the orthodoxy test as a validity check on experimental field emission data”, *Journal of Electrical Engineering*, vol. 71, no. 1, pp. 37-42, Feb. 2020. doi:10.2478/jee-2020-0005
- [4] A. Knápek, J. Sýkora, J. Chlumská, and D. Sobola, “Programmable set-up for electrochemical preparation of STM tips and ultra-sharp field emission cathodes”, *Microelectronic Engineering*, vol. 173, pp. 42-47, 2017. doi:10.1016/j.mee.2017.04.002
- [5] A. Warren, A. Nylund, and I. Olefjord, “Oxidation of tungsten and tungsten carbide in dry and humid atmospheres”, *International Journal of Refractory Metals and Hard Materials*, vol. 14, no. 5-6, pp. 345-353, 1996. doi:10.1016/S0263-4368(96)00027-3
- [6] M. S. Mousa and D. B. Hibbert, “Field emission of electrons from glass tips with internal conducting coats”, *Journal of Physics D: Applied Physics*, vol. 26, no. 4, pp. 697-703, Apr. 1993. doi:10.1088/0022-3727/26/4/026
- [7] D. Burda, M. Allaham, A. Knápek, D. Sobola, and M. Mousa, “Field emission properties of sharp tungsten cathodes coated with a thin resilient oxide barrier”, in *2021 34th International Vacuum Nanoelectronics Conference (IVNC)*, 2021, p. 2.

Low-Level Measurements

L. Zdražil¹, Z. Roubal²

¹Doctoral Degree Programme (1), FEEC, Brno University of Technology, Czech Republic

²Assistant Professor, FEEC, Brno University of Technology, Czech Republic

E-mail: Lukas.Zdrzil1@vutbr.cz, roubalz@vut.cz

Abstract— This paper deals with the measurement of low values of electrical voltages and currents from sources with high internal resistance. The measured values are close to the theoretical limits of achievable sensitivity, which are determined by the magnitude of the Johnson's thermal noise. Non-thermal noises are also generated in the circuit. The most significant noise after Johnson's thermal noise is flicker noise with a frequency dependence of $1/f$. Choosing an accurate operational amplifier with low input bias and noise is just as important as choosing precise passive components with low noise.

Keywords—low-level measurements, operational amplifiers, voltage noise, current noise

1. INTRODUCTION

Low-level measurements are measurements of currents in the range of nA and less, voltage measurements from sources with high internal resistance, measurements of resistances in the range of 1 G Ω and higher, and charge measurements. The measured values are close to the theoretical limits of achievable sensitivity, which are determined by the magnitude of the Johnson's thermal noise [1].

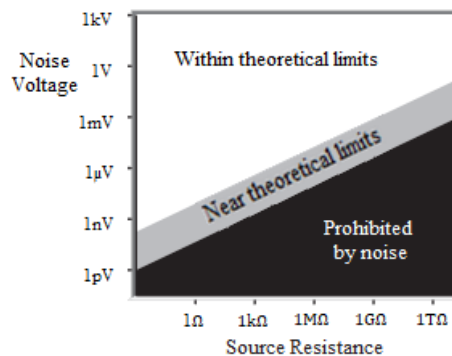


Figure 1: Theoretical limits given by Johnson's thermal noise [1]

For example, low-level measurements are used when measuring the concentration and mobility of air ions in caves [2]. These measurements are made using an aspiration condenser, which converts the charge of the ions into a very small current. The older configuration used an old INA116 instrumentation amplifier to measure the current. This paper focuses on the experimental measurements of newly manufactured precise operational amplifiers, based on which a new highly accurate and sensitive amplifier was designed [3].

2. ANALYSIS

Noise is present in all electronic circuits regardless of the types of used components and their connection. There are two types of noise in electronic circuits, distinguished by their frequency dependence. White noise is characterized by a uniform distribution in the frequency spectrum. The second type is colored noise, which is characterized by a non-uniform spectral distribution.

The most significant white noise is the Johnson's thermal noise. It occurs in conductors and semiconductors and is generated by both active and passive components. It is generated by the

movement of electrons when the temperature is above 0 K. The magnitude of the noise voltage is proportional to the square root of the magnitude of the source internal resistance, the considered noise bandwidth, and the absolute temperature in Kelvins. Current measurements are limited in a similar way to voltage measurements. The square of the noise voltage increases with the magnitude of the source resistance, while the square of the noise current decreases with the magnitude of the source resistance.

The most significant colored noise to consider when measuring current from a high internal resistance source is flicker noise. It is generated in resistors in the measuring instrument and in semiconductors. Flicker noise is particularly significant at low frequencies, as the spectral density decreases with increasing frequency according to the dependence of $1/f$. This noise is caused by defects in the crystal lattice.

Besides noise, other limitations and disturbances that have negligible effect in ordinary measurements must be considered when measuring sources with high internal resistance. For example, leakage currents, which are mainly due to the parasitic conductivity of insulators. They also form on the surface of printed circuit boards and on the surface of components due to dirt, fingerprints, and precipitated water vapor. The circuit may also generate currents due to unwanted triboelectric, piezoelectric, and electrochemical phenomena.

Instruments for low level measurements must have high-quality operational amplifiers. For low-level measurements, we usually require operational amplifiers with high gain, small input current and voltage offset and small temperature and supply drift, very small input quiescent and noise current and large input resistance. Operational amplifiers with unipolar structure with JFET type transistors and in some cases with MOSFET type transistors are usually chosen. Such operational amplifiers are called electrometer amplifiers because they are mostly used in electrometers, i.e., instruments used for low-level measurements.

3. EXPERIMENTS

Experiments in this paper mainly focus on the measurement of the spectral density of input noise voltage and input noise current of electrometric operational amplifiers. An auxiliary low-noise operational amplifier connected in series directly behind the tested operational amplifier is necessary. The power supply of the measured operational amplifier should be from a low-noise voltage source. The measurement limitation is due to the noise of the passive components and the input noise voltage and current of the auxiliary operational amplifier.

For the purpose of measuring the spectral density of the input noise voltage of an operational amplifier, the LMP7721 model from Texas Instruments was selected. It was connected as a non-inverting amplifier with grounded inputs. The differential voltage was given by input noise voltage and voltage offset. The power supply of the LMP7721 operational amplifier was unbalanced -1.5 V and 3.5 V because the input quiescent current is the lowest for this case according to the datasheet. OPA211 was selected as auxiliary low noise operational amplifier. The gain of both operational amplifiers was 40 dB and 40 dB, respectively. The board was enclosed in a shielding box. The configuration of the input noise voltage measuring system used in this paper is shown in Figure 2.

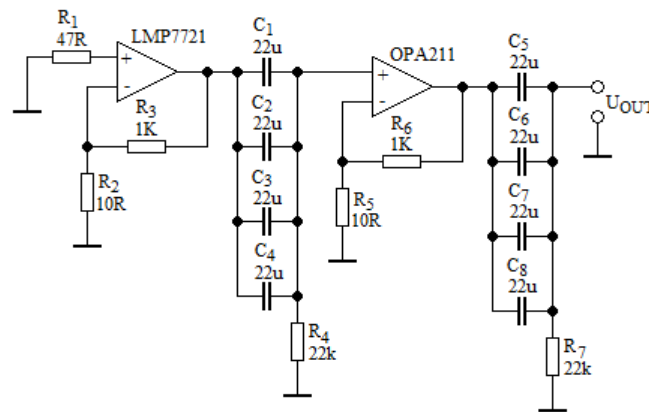


Figure 2: Configuration of measuring system for input noise voltage measurements

A low-frequency spectrum analyzer HP 35660A with a frequency range up to 100 kHz was used to measure the input noise voltage spectral density. The measurements were performed in three different frequency bands. Firstly, measurement was made without the LMP7721 operational amplifier to determine the background noise of the measurement system. Then the measurement was performed with LMP7721. One hundred measurements were averaged in each frequency band. The measured effective values at the input of the spectrum analyzer in dBV were converted to input noise voltage spectral density of the electrometric amplifier in units of $\text{nV}/\sqrt{\text{Hz}}$ using the appropriate relations. The relations and calculations are published in the literature [3]. The calculations also considered background noise, gain of both amplifiers and bandwidths of all three frequency bands.

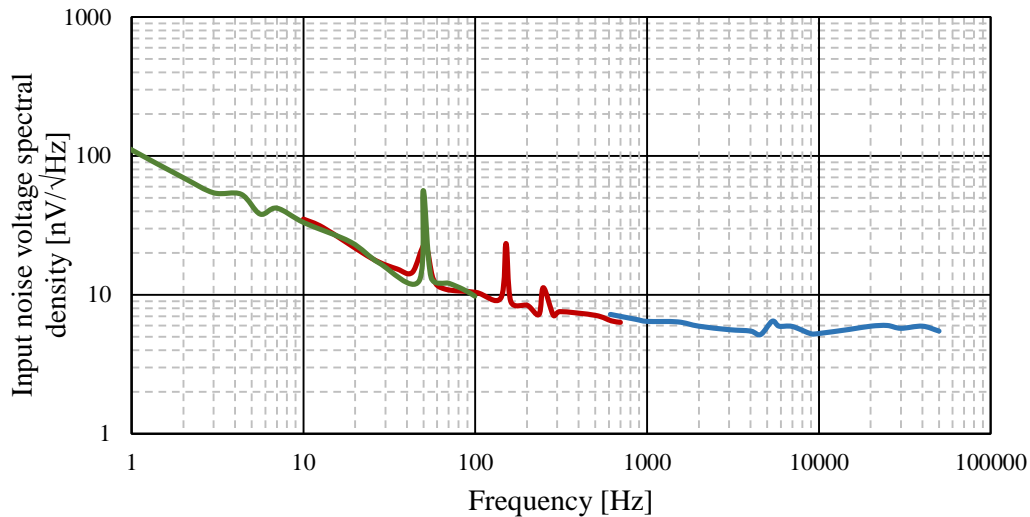


Figure 3: Measured input noise voltage spectral density of operational amplifier LMP7721

Since the system was powered from a laboratory source, the interferences at 50 Hz and 150 Hz are visible in the Figure 3. The individual frequency bands in which the measurements were made are shown in different colors. If we ignore the interferences from the grid, the measured input noise voltage spectral density of the LMP7721 operational amplifier can be compared with the graph in the datasheet. The measured spectral density is barely different from the graph presented in the datasheet. In the white noise band, the value of $6.5 \text{ nV}/\sqrt{\text{Hz}}$ was measured, the manufacturer gives the same value. In the flicker noise band, the values are very close to the values given in the datasheet.

Also, the magnitude of the input voltage offset was measured using a laboratory multimeter. The manufacturer specifies a typical input voltage offset value of $\pm 26 \mu\text{V}$ and a maximum value of $\pm 150 \mu\text{V}$. The measured value was $54 \mu\text{V}$, so the measured operational amplifier corresponds to the data given by the manufacturer.

For the experimental measurement of the input noise current spectral density, the LMC6001A operational amplifier, also from Texas Instruments, was selected. For the measurement of the input noise current of operational amplifiers with unipolar structure, whose input noise current level is very low, it is more suitable to connect the measured operational amplifier as a feedback ammeter, i.e., the current to voltage converter. There is only the input bias current of the inverting branch at the input of the operational amplifier, which is then converted to the output voltage according to the principle of the feedback ammeter. It is advisable to use guarding or a high-quality insulating material such as Teflon or ceramic to reduce the error caused by leakage currents.

A precise high-ohm feedback resistor is required for accurate measurements. Most high-ohm resistors are manufactured using thick-film technology. The disadvantage of thick film resistors is a relatively high level of flicker noise with a frequency dependence of $1/f$. For the experimental measurements, high-ohm metal oxide resistors from the company Ohmite were successfully obtained. These resistors do not produce any additional noise. The value of the used feedback resistor was $100 \text{ G}\Omega$. This circuit was also supplemented by an auxiliary amplifier OPA211 with a gain of 40 dB. The measurements were performed in a shielded chamber and the operational amplifiers were supplied from batteries. The

configuration of the input noise current measuring system used in this paper is shown in Figure 4.

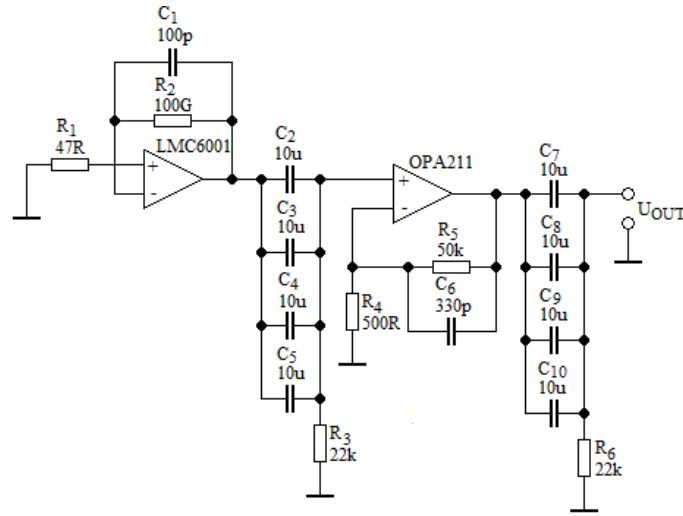


Figure 4: Configuration of measuring system for input noise current measurements

The output of the LMC6001A operational amplifier was not stable, so a 100 pF parallel capacitor was added to the feedback resistor. The resulting time constant was approximately sixty seconds, and the bandwidth was 0.016 Hz. Therefore, it was not possible to measure broadband noise. An effective input noise current of 1.8 fA was found in the band up to 0.016 Hz. This value was calculated by dividing the value of effective output voltage (18 mV) measured by the oscilloscope by total gain (gain of the measured amplifier multiplied by gain of the auxiliary amplifier), according to the output voltage calculation relation of feedback ammeter [3].

Also, the input quiescent current was measured using a laboratory multimeter controlled by a software application in the Keysight VEE environment. Figure 5 shows the time dependences of the measured output voltage and voltage offset.

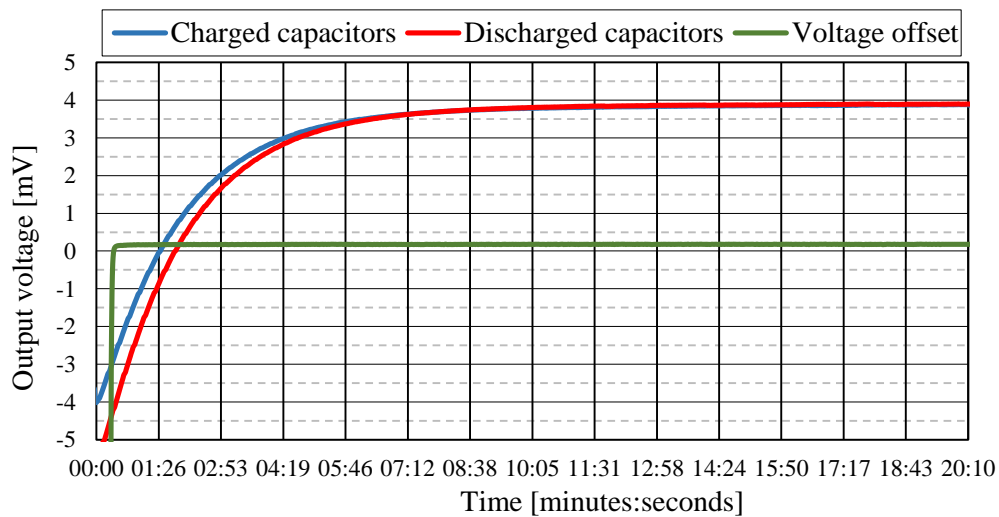


Figure 5: Time dependance of output voltage and voltage offset of operational amplifier LMC6001A

These measurements were performed without the auxiliary operational amplifier OPA211. If we divide the measured values by the size of the 100 GΩ feedback resistor, the output voltage can be converted to the input quiescent current. The measurements started when the power supply was connected. In the blue waveform, the initial value of the output voltage is higher than in the red waveform, because the

tantalum capacitors in the power supply branch of the operational amplifier have not been completely discharged. The green waveform shows the time dependence of the input voltage offset, which was measured with a 1 G Ω feedback resistor. The measured value is 0.17 mV, the manufacturer gives a maximum value of ± 10 mV. By subtracting the voltage offset from the output voltage time waveforms, the exact value of the measured input quiescent current can be determined. The two measured and then recalculated time waveforms of the input quiescent current became stable at a value of 36.9 fA after about eighteen minutes. The manufacturer specifies a typical input quiescent current value of ± 10 fA and a maximum value of ± 25 fA.

4. CONCLUSION

This paper discussed the issue of measuring low voltage and current levels close to the theoretical limits given by the noise level. To achieve such high sensitivity, it is necessary to reduce the noise voltage and current level in the measuring circuit as low as possible. The input noise voltage and the input noise current of the operational amplifiers in the first stage of the amplification cascade of the measuring instrument have a significant impact. In addition to Johnson's thermal noise, low-frequency flicker noise has a significant effect on sensitivity.

Low-level measurement is very challenging, even though the circuit design may seem simple. During the measurements, it was necessary to minimize sources of interference that would have a negligible effect in ordinary measurements. For example, leakage currents or generated currents, noise of the passive components, the effect of ambient temperature changes and humidity, grid interference and thermoelectric voltages due to the Seebeck's effect. Proper grounding is also important. A shielded chamber was utilized for measurements as well.

The spectral density of the input noise voltage of the LMP7721 operational amplifier was measured and was almost identical to the theoretical data given by the manufacturer. A value of 6.5 nV/ $\sqrt{\text{Hz}}$ was measured in the white noise band.

The broadband input noise current of the LMC6001A operational amplifier was not possible to measure because the output voltage was not stable. The bandwidth had to be significantly reduced and only the effective input noise current of 1.8 fA in the 0.016 Hz band was measured. In addition, an input quiescent current of 36.9 fA was measured.

Research in the field of low-level measurements is essential to improve the measurement setup and to improve the measurement methodology for atmospheric electricity measurements and determination of air ion concentration. Based on the experiments in this paper, a low-level amplifier for the measurement of air ion concentration was designed and constructed. The amplifier will be used for the UTEE aspiration condenser described in the article [4].

REFERENCES

- [1] *Low Level Measurements Handbook: Precision DC Currents, Voltage, and Resistance Measurements* [online]. Ohio, USA: Keithley Instruments, Inc., 2004 [cit. 2022-2-22]. Available at: <https://wiki.epfl.ch/carplat/documents/LowLevMsHandbk.pdf>.
- [2] Z. Roubal, E. Gescheidtová, K. Bartušek, Z. Szabó, M. Steinbauer, J. Überhuberová, A. Lajčíková, *Evaluating the Parameters of a Systematic Long-Term Measurement of the Concentration and Mobility of Air Ions in the Environment inside Cisarska Cave. Atmosphere* [online]. MDPI, 2021, 12(12), 1-31 [cit. 2022-03-12]. ISSN 2073-4433. Available at: <https://dspace.vutbr.cz/handle/11012/203372>.
- [3] L. Zdražil, *Návrh a optimalizace speciálního nízkourovňového zesilovače pro měření vzdušných iontů*. Available at: <https://www.vutbr.cz/studenti/zav-prace/detail/126121>. Brno University of Technology, Faculty of Electrical Engineering and Communication, Brno, 2020. Supervisor: Ing. Zdeněk Roubal, Ph.D.
- [4] Z. Roubal, K. Bartušek, Z. Szabó, P. Drexler, J. Überhuberová, *Measuring Light Air Ions in a Speleotherapeutic Cave. Measurement Science Review* [online]. Institute of Measurement Science, Slovak Academy of Sciences, 2017, 17(1), 27-36 [cit. 2022-03-08]. ISSN 1335-8871. Available at: <https://dspace.vutbr.cz/handle/11012/63824>.

Correction of gradient pulse shape distortions in radial MRI

J. Vitouš^{1,2}

¹Brno University of Technology

²Institute of Scientific Instruments, CAS

E-mail: vitous@isibrno.cz,

Abstract—This paper focuses on the optimization of gradient-pulse shapes in MRI measurement. The main topic investigated in this paper is optimization of slice-selective gradient, where imperfections may produce phase distortion in the resulting image and also signal loss in the acquired signal. A method for correction is proposed based on the Nelder-Mead algorithm followed by coordinate ascent search in the neighborhood of the found solution. The adjustment is evaluated using a simple Fast low angle shot (FLASH) sequence with radial readout. The results show a significant improvement in the Free induction decay (FID) signal magnitude, echo stability, and an improvement in the homogeneity of image phase.

Keywords—MRI, gradient, Nelder–Mead, slice, adjustment

1. INTRODUCTION

The imperfections in the Magnetic resonance (MR) gradient system are a well-known source of distortions. Therefore, pulse sequences using hardware demanding readout k-space trajectories must measure them in advance, so that they may be corrected later during reconstruction.[1][2] On the other hand, imperfections that arise during the slice selection and excitation are rarely taken care of. This is usually sufficient for common clinical sequences with cartesian k-space sampling, where the timing is not as critical and gradient slew rates are usually not as high compared to e.g. radial. On the other hand, in preclinical or experimental sequences with non-cartesian k-space sampling this might not suffice. Gradient imperfections introduce lower SNR (Signal to noise ratio), phase errors in reconstructed images and slice selection profiles imperfections.[3]

These errors arise due to four main factors. The first factor is the finite time and voltage resolution of the gradient digital to analog (DA) converters. Such errors in the slice selection gradient will cause non-ideal rephasing of the spin ensemble in the observed object (material, patient).[3][4]

The second factor is the gradient channel synchronization with respect to the radio frequency (RF) channel. Any time shift between the RF pulse and the expected slice selection gradient pulse shape will distort the excited slice profile.[4] Unfortunately, on the real systems, not only is there usually a problem with synchronization of the gradient channels with the RF channel but also a problem with synchronization of the independent gradient channels (x, y, z) between each other. This is because the physical gradient coils themselves are different for each axis, therefore each has a different inductance and a different delay. On many systems, this cannot be fully compensated.[4]

The third effect are eddy currents created by the gradient coils during switching. Today the gradient coils are shielded to minimize the effects of eddy currents.[4][5] Ideally the remaining error should be compensated by the so-called preemphasis filtering. These filters are usually digital and their purpose is to distort the input waveform so that the eddy currents effects are compensated. Neither one of those error compensation mechanisms work perfectly, therefore the effects of eddy currents will be noticeable.[5]

The fourth limitation is the gradient amplifier bandwidth, slew rate and its maximum voltage and current.[5] To switch the current in the gradient coil fast a very large voltage is needed. If not sufficient, the waveform will not be as sharp as expected, resulting in a gradient shape imperfection. The usual gradient pulse shapes used in Magnetic resonance imaging (MRI) experiments are trapezoids, with rising and falling edges limited by the maximum gradient system slew rates.[5] In addition to the slew rates limitations the bandwidth of the gradient system is not infinite as well (typically in the range of tens of kHz), therefore any sharp corners of trapezoids will be reproduced as rounded corners.[6]

When exciting slices with arbitrary (oblique) orientation these effects manifest usually even more as more physical gradient channels are used simultaneously.[5]

An improvement may be gained via additional correction of the gradient pulse shape with a measured gradient system impulse response. This method is known as correction using gradient impulse response function (GIRF).[4] This correction has been successfully used to correct the readout trajectory in ultra-short echo time sequences.[7] In this work we propose a simplified method based on gradient shape pre-correction.

2. MATERIALS AND METHODS

As the error in the slice selection rephasing is proportional to the mismatch of the area under the real gradient pulse shape curve segments, it should be sufficient to correct the areas just via simple multiplication of the gradient pulse shape segments by a constant. Since the error will be different in each spatial gradient axis, it is required to perform this adjustment for each axis, to achieve near-perfect slice selection.[5] Furthermore, non-linearity in the gradient system behavior can be expected. Therefore, it is also necessary to compensate the error for all axes at once.[5]

For testing purposes a sequence based on a FLASH (Fast low angle shot) with radial readout was selected.[5] Before the image acquisition an adjustment procedure is run, where the imaging sequence is played with the readout gradients turned off. The slice selection shape was divided into a dephasing and rephasing lobe. To achieve a near-perfect slice selection for classical symmetrical RF pulses, the area of the rephasing lobe must compensate the linear phase accumulated in the sample by the RF excitation pulse and dephasing gradient pulse shape. If we simplify the case to ideal rectangular gradient pulse shapes then the rephasing lobe (green) must have in this case the area exactly one half of the dephasing shape. That is, equal to the red area.[5] The situation in a more practical case with finite gradient slew rates can be seen in figure 1.

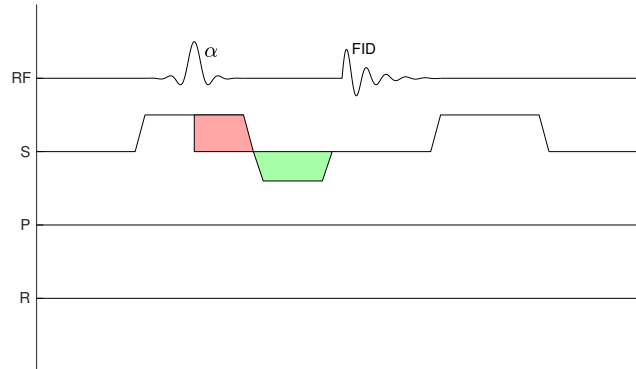


Figure 1: Schematic of the sequence used for slice selection calibration. The red and green areas must be equal. The FID is followed by a slice spoiler. α is the flip angle of the radio frequency pulse. RF represents the radio frequency channel, S represents the slice axis, R the read axis and P the phase axis.

Compensating the area of the dephasing lobe should be possible by adjusting the rephasing lobe level in each axis. To find the right level of adjustment a method is proposed based on the Nelder-Mead algorithm. The optimization problem can be stated as finding the optimal multiplicative constants (c_x, c_y, c_z) for the rephasing lobe shape in each gradient physical axis. The optimal constants should maximize the FID (Free induction decay) after the slice selection ends. This can be exploited, since minimum remaining phase dispersion in the sample translates to maximal FID. The algorithm evaluates the cost function through the so-called Digitizer fill factor, which is basically a maximum strength of the measured signal in percent of the ADC (Analog to digital converter) dynamic range. To account for any eddy currents emerging after the slice selection a delay of 100 μs is inserted between the end of slice selection and FID acquisition.

The adjustment must be performed on the system before each scan with different slice orientation,

thickness or RF pulse parameters. It was necessary to find an algorithm that would converge fast enough, so that the total scan time is not prolonged too much. Because of this a simplex method was used solved by a Nelder-Mead (NM) algorithm with constraints. The advantage of NM algorithm is small number of evaluations. To get a better solution it is followed by a coordinate ascent algorithm.

The constraints are needed, to not exceed the maximum allowed gradient amplitude. If the NM algorithm attempts to measure outside of its constraints it is penalized. The amount of penalization is equal to the sum of the function value at the current worst solution and the distance of the attempted point from the constraint. It is then possible to order the estimates from the worst to the best even when multiple points appear outside of constraints. To make the algorithm more reliable an average of two repetitions is always taken to evaluate the cost function at each measurement point.

There are two termination conditions. The first is the number of iterations, chosen to be 50 and the second is the mean distance between the simplex points, chosen to be 0.01. An important feature for optimizing mainly thicker slab excitation is automated receiver gain adjustment. Usually, the signal at the beginning of the measurement will be very low and it will gradually increase with better gradient correction. This increase may be so large, that the receiver may saturate the ADC. When the measured signal level rises above 70 % of the ADC dynamic range the receiver gain is adjusted so that the resulting signal level is below 30 %, then all the points are remeasured and the optimization may continue.

To further improve the estimate a coordinate ascent algorithm is applied to search for the best solution in the neighborhood of the solution found by the NM algorithm. This search is especially important for thin oblique slices, where the peak to be found is very narrow and usually the NM algorithm has trouble finding it. To improve the speed of the coordinate ascent algorithm and its convergence, the searched space is narrowed down after each sweep of all axes by a factor of 0.8. The algorithm terminates when the found solution is stable, i.e. the change in correction for each gradient axis is below the threshold of 0.001.

When not all physical gradient axes are used, the unused physical axes are omitted from optimization and therefore it is simplified. This makes it possible to shorten the optimization time when the slice is of for example in one of the basic orientations (axial, sagittal, coronal).

The method was implemented on a 9.4 T Bruker Biospec 94/30 USR (Bruker BioSpin MRI GmbH, Ettlingen, Germany) preclinical scanner with BGA12SHP gradient insert allowing maximum gradient field of 660 mT/m and slew rates up to 4570 T/m/s. A ball phantom filled with gel was used. The algorithm was implemented in the C programming language and directly compiled in the spectrometer control software. The results were compared to a sequence supplied by the scanner vendor from which the modified variant branches. The method is set up so that it uses the fastest possible repetition time available by the geometry of the excited slice to keep the adjustment time as short as possible. The adjustment procedure took approximately 2 minutes to complete and was tested in a standard axial orientation (using only the physical Z gradient axis for slice selection) and also in an oblique orientation at 45° angle with respect to the X and Y axis, which should be the worst-case scenario (using all gradient axes for slice selection).

The measured values after the adjustment were the FID signal magnitude after the slice selection and the maximum echo levels both with respect to the angle of radial projection of the FLASH sequence. In the image domain a phase image was observed.

3. RESULTS

The maximum echo level for axial slice orientation can be seen in figure 2(a). The results show an improvement in overall signal value while the dependency of the echo value on the projection angle is very low. A completely different situation is in figure 2(b), where the slice is angled at 45° with respect to X and Y axes. So all gradient coils are used in slice selection. The picture shows a very high fluctuations in the maximum echo levels, while the adjusted case shows far more uniform maximum echo levels with respect to the projection angle. Even greater discrepancy in results was observed in the FID signal (Table I). The signal level after the proposed adjustment increases by a factor of approximately one hundred. This signal loss in FID may be very important in spectroscopic experiments because the recovery of the signal is dependent on the readout gradients, which are not usually present in spectroscopic sequences.

The remaining fluctuations in maximum echo levels are probably caused by the imperfections of the

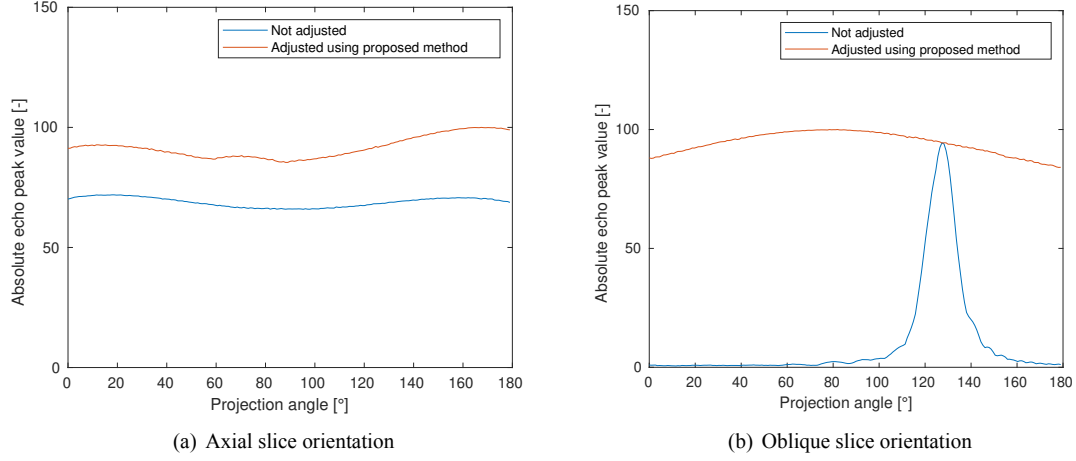


Figure 2: Maximum echo levels with respect to projection angles

readout gradients, where their resulting field orientation may not entirely be perpendicular to the field of the slice-selective gradient.

Table I: Relative average FID magnitudes

Case	Relative peak FID level [%]
Unadjusted	0.98
Adjusted	100.00

The phase images in figure 3 show a strip pattern in the unadjusted sequence. Because the echo is miscentered in the k-space a linear phase is apparent in the resulting image at an angle of approx. 45° , corresponding with the slice orientation. This phase variation is very important for compressed-sensing image reconstruction algorithms, where it might interfere with the image spatial regularization. If the phase is not at least approximately constant in the scanned volume, the image reconstruction will fail, even though the magnitude image seems to have stable brightness. This is due to the fact, that the resulting real and imaginary parts of the image have spatially varying value distribution.

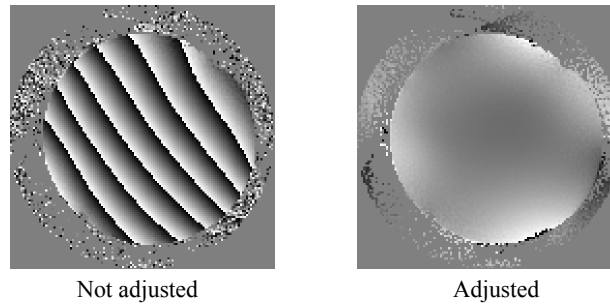


Figure 3: Phase images of an oblique oriented slice (45° read and phase directions)

4. CONCLUSION

A method for slice selection gradient for fast acquisition sequences was proposed. The correction method was tested and compared with vendor's implementation. The method resulted in increase in obtained signal for arbitrary projection angle. The difference is most notable for oblique slice orientations, where multiple gradient axes are engaged in the slice selection.

The signal magnitude rose by a factor of 100 during the FID, this result may be important in spectroscopic experiments and navigator signal estimation in cardiac imaging, where the quality i.e. SNR of the navigator is important for reliable synchronization of the acquisition.

The echo peak fluctuations were almost suppressed by the proposed method, resulting in a stable signal independent of the projection angle. This is important when not all projections are selected for reconstruction, as if only weak echoes were selected, the resulting image would lack the brightness information. This selection is performed for example in cardiac imaging to obtain an image of desired cardiac phase.

The spatial linear phase trend was entirely suppressed in the resulting phase images. The remaining phase dispersion in the image is most likely caused by the B0 magnetic field inhomogeneity and cannot be compensated using this method. An improvement is expected if traditional higher order shimming procedures are used.

ACKNOWLEDGMENT

The work was supported by the Ministry of Education, Youth and Sports of the Czech Republic (Large RI Project LM2018129 Czech-BioImaging and CZ.02.1.01/0.0/0.0/18_046/0016045) and by the Czech Science Foundation (GA22-10953S).

REFERENCES

- [1] S. Rosenzweig, H. C. M. Holme, and M. Uecker, "Simple auto-calibrated gradient delay estimation from few spokes using radial intersections (RING)," *Magnetic Resonance in Medicine*, vol. 81, pp. 1898–1906, Nov. 2018.
- [2] A. Deshmane, M. Blaimer, F. Breuer, P. Jakob, J. Duerk, N. Seiberlich, and M. Griswold, "Self-calibrated trajectory estimation and signal correction method for robust radial imaging using GRAPPA operator gridding," *Magnetic Resonance in Medicine*, vol. 75, pp. 883–896, Mar. 2015.
- [3] P. Latta, Z. Starčuk, M. Kojan, M. L. H. Gruwel, B. Tomanek, S. Trattnig, and V. Juras, "Simple compensation method for improved half-pulse excitation profile with rephasing gradient," *Magnetic Resonance in Medicine*, vol. 84, pp. 1796–1805, Mar. 2020.
- [4] S. J. Vannesjo, M. Haeberlin, L. Kasper, M. Pavan, B. J. Wilm, C. Barmet, and K. P. Pruessmann, "Gradient system characterization by impulse response measurements with a dynamic field camera," *Magnetic Resonance in Medicine*, vol. 69, pp. 583–593, Apr. 2012.
- [5] M. Bernstein, K. King, and X. Zhou, *Handbook of MRI Pulse Sequences*. Elsevier Inc., Sept. 2004. Publisher Copyright: © 2004 Elsevier Inc. All rights reserved. Copyright: Copyright 2018 Elsevier B.V., All rights reserved.
- [6] N. O. Addy, H. H. Wu, and D. G. Nishimura, "Simple method for MR gradient system characterization and k-space trajectory estimation," *Magnetic Resonance in Medicine*, vol. 68, pp. 120–129, Dec. 2011.
- [7] S. Kronthaler, J. Rahmer, P. Börnert, M. R. Makowski, B. J. Schwaiger, A. S. Gersing, and D. C. Karampinos, "Trajectory correction based on the gradient impulse response function improves high-resolution ute imaging of the musculoskeletal system," *Magnetic Resonance in Medicine*, vol. 85, no. 4, p. 2001–2015, 2020.

OBJEV SVOU PŘÍLEŽITOST VE SVĚTĚ TECHNOLOGIÍ



ŠKODA
SIMPLY CLEVER



Stáže a závěrečné práce

Studuješ a zároveň chceš získat pracovní zkušenosti? Zkus stáž ve ŠKODA AUTO. Pro talentované studenty máme připravených až 200 Kč na hodinu a s našimi odborníky můžeš konzultovat i svoji závěrečnou práci.



Trainee program

Dokončil jsi studia a přemýšlíš kam dál? Nastup do našeho Trainee programu. V průběhu jednoho roku budeš na plný úvazek pracovat v mezinárodním týmu, poznáš různá oddělení a vycestuješ na zahraniční stáž.



Doktorandský program

Aplikuj výsledky svého výzkumu v reálném prostředí, využívej nejnovější technologie a dej své disertační práci nový rozměr. Poskytneme ti flexibilní pracovní dobu a zajistíme 250 Kč na hodinu.



Volné pracovní pozice

Vyber si ze široké nabídky volných pozic, staň se součástí nejprogresivnější české firmy a tvoř s námi budoucnost automobilového průmyslu.



ŠKODA AUTO Kariéra



@WeAreSKODA



ŠKODA AUTO a.s.



ŠKODA AUTO - Career

SKODA-KARIERA.CZ

OBJEV SVOU PŘÍLEŽITOST VE SVĚTĚ TECHNOLOGIÍ



Stáže a závěrečné práce

Studuješ a zároveň chceš získat pracovní zkušenosti? Zkus stáž ve ŠKODA AUTO. Pro talentované studenty máme připravených až 200 Kč na hodinu a s našimi odborníky můžeš konzultovat i svoji závěrečnou práci.



Trainee program

Dokončil jsi studia a přemýšlíš kam dál? Nastup do našeho Trainee programu. V průběhu jednoho roku budeš na plný úvazek pracovat v mezinárodním týmu, poznáš různá oddělení a vycestuješ na zahraniční stáž.



Doktorandský program

Apikuj výsledky svého výzkumu v reálném prostředí, využij nejnovější technologie a dej své disertační práci nový rozměr. Poskytneme ti flexibilní pracovní dobu a zajistíme 250 Kč na hodinu.



Volné pracovní pozice

Vyber si ze široké nabídky volných pozic, staň se součástí nejprogresivnější české firmy a tvoř s námi budoucnost automobilového průmyslu.



MICHAL VILD
ZKOUŠKY A PROTOTYPY



ŠKODA
SIMPLY CLEVER



ŠKODA AUTO Kariéra



@WeAreSKODA



ŠKODA AUTO a.s.



ŠKODA AUTO - Career

SKODA-KARIERA.CZ

Unfolded Low-rank + Sparse Reconstruction for MRI

O. Mokry¹, J. Vitous^{1,2}

¹Brno University of Technology

²Institute of Scientific Instruments, CAS

E-mail: xmokry12@vut.cz, vitous@isibrno.cz

Abstract—We apply the methodology of deep unfolding on the problem of reconstruction of DCE-MRI data. The problem is formulated as a convex optimization problem, solvable via the primal–dual splitting algorithm. The unfolding allows for optimal hyperparameter selection for the model. We examine two approaches – with the parameters shared across the layers/iterations, and an adaptive version where the parameters can differ. The results demonstrate that the more complex model can better adapt to the data.

Keywords—DCE-MRI, proximal splitting algorithms, deep unfolding, L+S model

1. INTRODUCTION

Dynamic Contrast-Enhanced Magnetic Resonance Imaging (DCE-MRI) is a technique used in preclinical and also clinical practice, where it is usually used to assess the success of a cancer treatment. It uses a contrast agent administration and simultaneous observation using magnetic resonance. While this method is very promising, estimating the final pharmacokinetic parameters and getting high quality results is dependent on the quality of the measured data, which is very hard and time-consuming. As the goal is to obtain as good spatial and temporal resolution as possible, many techniques were proposed that exploit the so-called compressed sensing approach [1], where only a portion of the data is acquired and the full dataset is then reconstructed using some prior knowledge (see e.g. [2] for a review of different approaches). This knowledge usually relies on the fact that there exist a sparsifying transform of the data and this sparsity can be used to regularize and denoise the image.

Many methods for DCE-MRI image reconstruction have been proposed. Most approaches can be summarized as finding the solution of the general problem

$$\arg \min_{\mathbf{x} \in \mathbb{C}^N} \frac{1}{2} \|\mathbf{d} - A\mathbf{x}\|_2^2 + \lambda R(\mathbf{x}), \quad \lambda > 0, \quad (1)$$

where the complex vector $\mathbf{d} \in \mathbb{C}^M$ represents the k-space data, $\mathbf{x} \in \mathbb{C}^N$ denotes the image sequence being measured and the operator $A: \mathbb{C}^N \rightarrow \mathbb{C}^M$ represents the measurement process, where typically $M \ll N$. Note that for the sake of simplification, Eq. (1) contains all the data as vectors. The regularization term $\lambda R(\mathbf{x})$ adds a priori spatial and/or temporal information, typically using total variation [3, 4, 5] or its generalized form [6, 7]. Some methods use purely deep-learning-based using large image-to-image networks. This approach had shown great success; however, as the data get high-dimensional or with high resolution, training these networks quickly becomes infeasible [8].

In the past years a new concept emerged which combines the classical and deep-learning-based approaches – the deep unrolling/unfolding [9]. This allows for building an algorithm that respects the physical process of data acquisition (as the classical methods do), but at the same time, the regularization can be adapted to real world data instead of a hand-crafted simple model. This is done by taking a fixed number of iterations of a classical method and relaxing some parts of it into a parametrized form (e.g. using arbitrarily parametrized operator instead of a gradient step). Furthermore, the number of parameters is usually significantly lower than in classical deep networks, e.g. convolutional. This helps to learn the model even with limited datasets.

So far, many models have been presented that incorporate deep learning into standard optimization algorithms [10, 11]. However, most of the approaches start from a very simple templates such as the gradient descent algorithm applied on a task in the form (1). In contrast, we propose to unfold an algorithm for the Low-rank + Sparse (L+S) formulation, in order to learn optimal hyperparameters of this mostly very successful method [12].

In the rest of the paper, Sec. 2 provides a brief overview of the L+S model and an algorithm to solve it. Sec. 3 then proposes the unfolding approach for the algorithm, followed by the experiments in Sec. 4. Finally, Sec. 5 concludes the paper.

2. LOW-RANK + SPARSE MODEL

In the L+S approach, we model a given matrix \mathbf{M} as a sum of a low-rank matrix \mathbf{L} (with few non-zero singular values, i.e. low nuclear norm $\|\mathbf{L}\|_*$), and a sparse matrix \mathbf{S} (with few non-zero entries, which can be relaxed as low norm $\|\mathbf{S}\|_1$) [12, p. 1126]. The decomposition would be realized by solving the problem

$$\arg \min_{\mathbf{L}, \mathbf{S}} \|\mathbf{L}\|_* + \lambda \|\mathbf{S}\|_1 \quad \text{subject to} \quad \mathbf{L} + \mathbf{S} = \mathbf{M}, \quad (2)$$

where $\lambda > 0$ is a trade-off parameter between the low-rankness and sparsity of the solution.

In the context of dynamic MRI, we use the L+S model to reconstruct an image sequence that can be decomposed into slowly varying background component and a dynamic component which captures the perfusion. To develop the model, we approach the image sequence $\mathbf{x} \in \mathbb{C}^N$ as a matrix $\mathbf{X} \in \mathbb{C}^{XY \times F}$ (naturally $XYF = N$), where each column is one vectorized frame (originally of size $X \times Y$) and the number of frames is F . In such a setting, the slowly varying background $\mathbf{L} \in \mathbb{C}^{XY \times F}$ is approximately lowrank, because the rows (each representing a single pixel during time) are approximately constant. The dynamic component $\mathbf{S} \in \mathbb{C}^{XY \times F}$ is assumed to be sparse *after time differentiation*, which helps to denoise the movement. The goal is to find the components \mathbf{L}, \mathbf{S} , such that it fits the measured data \mathbf{d} , formally:

$$\hat{\mathbf{L}}, \hat{\mathbf{S}} = \arg \min_{\mathbf{L}, \mathbf{S}} \frac{1}{2} \|\mathbf{d} - \mathcal{A}(\mathbf{L} + \mathbf{S})\|_2^2 + \lambda_L \|\mathbf{L}\|_* + \lambda_S \|\mathbf{S}\|_1, \quad (3)$$

where the operator \mathcal{A} represents the acquisition process (applied on a matrix, in contrast to A of Eq. (1)). The parameters $\lambda_L, \lambda_S > 0$ control the trade-off between the data fidelity, low-rankness and sparsity of the solution $\hat{\mathbf{X}} = \hat{\mathbf{L}} + \hat{\mathbf{S}}$.

Since the objective function of (3) is non-smooth, we propose to approach it with a suitable proximal method [13]. Most of the simple algorithms are designed to minimize a sum of two functions, and the Chambolle–Pock (primal–dual) proximal algorithm (CPA) [14] can manage also a composition with a linear operator, such as T in Eq. (3). To apply the algorithm, we rearrange the problem into the following form:

$$\hat{\mathbf{L}}, \hat{\mathbf{S}} = \arg \min_{\mathbf{L}, \mathbf{S}} f \left(K \begin{bmatrix} \mathbf{L} \\ \mathbf{S} \end{bmatrix} \right) + g \left(\begin{bmatrix} \mathbf{L} \\ \mathbf{S} \end{bmatrix} \right), \quad (4)$$

where

$$f \left(\begin{bmatrix} \mathbf{u} \\ \mathbf{v} \end{bmatrix} \right) = \frac{1}{2} \|\mathbf{d} - \mathbf{u}\|_2^2 + \lambda_S \|\mathbf{v}\|_1, \quad g \left(\begin{bmatrix} \mathbf{u} \\ \mathbf{v} \end{bmatrix} \right) = \lambda_L \|\mathbf{u}\|_*, \quad K = \begin{bmatrix} \mathcal{A} & \mathcal{A} \\ 0 & T \end{bmatrix}. \quad (5)$$

A single iteration of the algorithm, given the parameters σ, τ such that $\sigma\tau \|K\|^2 < 1$, is then performed as

$$\mathbf{y}^{(k+1)} = \text{prox}_{\sigma f^*} \left(\mathbf{y}^{(k)} + \sigma K \bar{\mathbf{x}}^{(k)} \right), \quad (6a)$$

$$\mathbf{x}^{(k+1)} = \text{prox}_{\tau g} \left(\mathbf{x}^{(k)} - \tau K^* \mathbf{y}^{(k+1)} \right), \quad (6b)$$

$$\bar{\mathbf{x}}^{(k+1)} = 2\mathbf{x}^{(k+1)} - \mathbf{x}^{(k)}. \quad (6c)$$

The main variable \mathbf{x} is the concatenation of \mathbf{L} and \mathbf{S} from Eq. (4) and the dual variable \mathbf{y} belongs in the domain of the (adjoint) operator K^* . Specific forms of the involved proximal operators $\text{prox}_{\sigma f^*}$ and $\text{prox}_{\tau g}$ for the functions f, g from Eq. (5) can be derived e.g. using the properties from [13, Tab. 1] or similar literature; we leave it out now for the sake of brevity. In the context of the present paper, the important observation is that the operators include thresholding with the threshold being directly affected by the regularization parameters λ_L, λ_S .

3. UNFOLDING THE ALGORITHM

For simplicity, denote $\mathcal{I}_{\lambda_L, \lambda_S}$ a single iteration of the Chambolle–Pock algorithm (6), i.e.¹

$$\mathbf{x}^{(k+1)}, \mathbf{y}^{(k+1)} = \mathcal{I}_{\lambda_L, \lambda_S} \left(\mathbf{x}^{(k)}, \mathbf{y}^{(k)} \right). \quad (7)$$

In line with the unfolding paradigm, we propose to optimize the hyperparameters λ_L, λ_S by building and training a network of one of the forms in Alg. 1 or 2.

Algorithm 1: Tied unfolded CPA	Algorithm 2: Untied unfolded CPA
Input: Data \mathbf{d} , initialization $\bar{\mathbf{x}}^{(0)}, \mathbf{y}^{(0)}$, parameters σ, τ , number of iterations K Parameters: λ_L, λ_S Output: Prediction $\hat{\mathbf{x}} = \mathbf{x}^{(K)} = [\hat{\mathbf{L}}^\top, \hat{\mathbf{S}}^\top]^\top$ for $k = 0, 1, \dots, K - 1$ do $\mathbf{x}^{(k+1)}, \mathbf{y}^{(k+1)} = \mathcal{I}_{\lambda_L, \lambda_S} (\mathbf{x}^{(k)}, \mathbf{y}^{(k)})$ end	Input: Data \mathbf{d} , initialization $\bar{\mathbf{x}}^{(0)}, \mathbf{y}^{(0)}$, parameters σ, τ , number of iterations K Parameters: $\lambda_L^{(k)}, \lambda_S^{(k)}$ for $k = 1, \dots, K$ Output: Prediction $\hat{\mathbf{x}} = \mathbf{x}^{(K)} = [\hat{\mathbf{L}}^\top, \hat{\mathbf{S}}^\top]^\top$ for $k = 0, 1, \dots, K - 1$ do $\mathbf{x}^{(k+1)}, \mathbf{y}^{(k+1)} = \mathcal{I}_{\lambda_L^{(k)}, \lambda_S^{(k)}} (\mathbf{x}^{(k)}, \mathbf{y}^{(k)})$ end

Although our model is intentionally simple and close to the its classical template, it can be seen as a neural network with parameters as given in Alg. 1 and 2; in the tied case, these are shared across all the layers (iterations).

As in typical deep learning applications, the model can be learned using a dataset with available ground truth sequences, such as in the case of simulated data. To find the optimal parameters, we use the ADAM optimizer with base learning rate $3 \cdot 10^{-3}$ to minimize the AE loss function (sum of absolute differences). The termination criterion is set to the desired number of training epochs. The prediction (sum of the low-rank and sparse components of $\hat{\mathbf{x}}$) is compared to the ground truth and the error is backpropagated to update the parameters.

4. EXPERIMENTS AND RESULTS

The main purpose of this section is to demonstrate the differences of the tied (Alg. 1) and untied (Alg. 2) versions of the unfolded CPA. The comparison should show whether adaptive parameters promise a performance gain over the classical method with optimally pre-set regularization parameters.

For the experiment, we use a simulated dataset created using an in-house simulator that creates DCE-MRI data with given pharmacokinetic parameters and a given level of noise added to the simulated echo signals. The dataset is based on a set of perfusion maps that display a virtual rat brain with multiple ROIs with different perfusion parameters. To comply with the compressed-sensing approach, a radial readout scheme with golden-angle projection angle increments was chosen when simulating the echoes.

For the sake of training and testing, the pharmacokinetic parameters were manipulated in a random range of 0.7–1.3 multiples of the default value, and additive complex Gaussian noise with standard deviation in the range between 10^{-3} and 10^{-1} (but constant throughout the sequence) was used to perturb the data.

The hyperparameters were trained using a set of three simulated acquisitions with different levels of noise added to them. The echo signals were then grouped in 37 echoes per time frame, which, with total number of 20 000 echoes, resulting in approximately 540 time frames. In reality and with respect to the scanner configuration this would result in a frame-rate of approximately 2 fps, which should be sufficient to give good temporal resolution for further analysis.

4.1. The role of initialization

The first experiment shows the role of the initial value of λ_S in the training process. As we observe in Fig. 1, the parameter (in the tied version) does change during training only if it is initialized to a small value, but with larger initialization (exceeding the supposed optimal value) the learning process does not affect λ_S at all. This suggests that the objective function of the original problem (3) does not depend much on the sparse regularization term; at least in the case of our dataset and in the studied range of λ_S .

¹Note that the parameters λ_L, λ_S appear within the specific forms of the proximal operators.

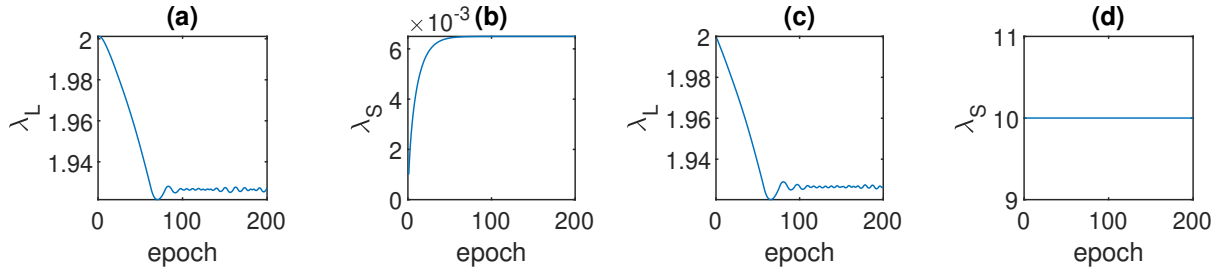


Figure 1: The role of initial value of λ_S on the training process, shown as the value of the parameters in the tied version during learning epochs: (a), (b) with initial value 10^{-6} , (c), (d) with initial value 10.

Table I: The resulting quality measures after testing

	loss after 8500 epochs	MSE	SNR per frame [dB]
tied	1202.765	$1.357 \cdot 10^{-8}$	13.522
untied	1198.046	$1.343 \cdot 10^{-8}$	13.564
non-regularized	—	$3.041 \cdot 10^{-8}$	10.073

In the case presented in Fig. 1, the value of loss function after 200 training epochs differs by less than $10^{-5} \%$. As a result, further experiments are performed with λ_S fixed to the value 0.3 in both the tied and untied version, which was empirically found as the lowest value giving best results regarding the SNR and MSE.

4.2. Comparison of the tied and untied variant

We expect that the untied version should be more adaptable to the data provided, which is demonstrated in Tab. I – the loss function is lower for the untied algorithm. Note that the difference seems minor, however, it is significant when compared to the loss function during training epochs. The difference on the testing set, measured in term of MSE and mean SNR per frame, is in favor of the untied algorithm.

Another perspective on the results is provided as Fig. 2 where we observe the learning process in the tied and untied cases, and the learned values of $\lambda_L^{(k)}$ for layers $k = 1, \dots, K = 14$. The pattern suggests that it is beneficial to keep the regularization large in the first few iterations to get a good low-rank approximation, then to re-fit to the data provided (here the parameter is low) and finally to lower the rank once more.

5. CONCLUSION

The results show that the estimation of the regularizing parameters is a difficult task and even the simple unfolded approach may sometime fail, as in the case of λ_S parameter, where the problem of vanishing gradient occurs. On the other hand, the comparison of tied and untied variant show decrease in the loss function with the more complex untied model, while giving slightly better SNR.

A bottleneck of our method is the number of layers, since the training process tends to fail for deeper architectures due to vanishing or exploding gradients. However, both the tied and untied versions are promising even for a small number of layers. It remains for the future work to test straightforward extensions of our model – either re-iterating the tied algorithm (this corresponds to running classical CPA with more iterations), or interpolating the learned parameters of the untied model. In the latter case, it is assumed to lead to better results than just re-iterating, since that would be in conflict with the observed pattern of the parameters with respect to layers (see Fig. 2(c)).

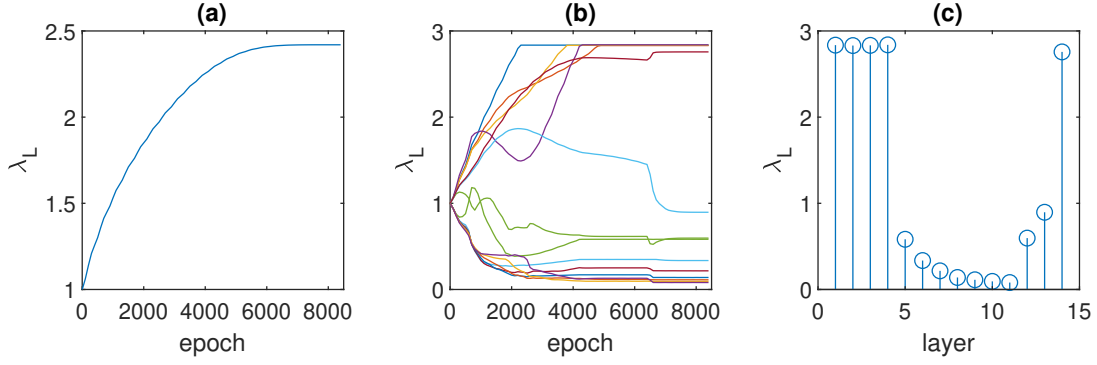


Figure 2: Comparison of the learning process in the tied (Alg. 1) and untied (Alg. 2) approach for $K = 14$ layers. Plots (a) and (b) show the evolution of λ_L and $\lambda_L^{(k)}$, $k = 1, \dots, K$ during training epochs. Plot (c) depicts the values of $\lambda_L^{(k)}$, $k = 1, \dots, K$ of the untied algorithm after 8500 epochs.

ACKNOWLEDGMENT

The work was supported by the Grant *Dynamic Magnetic Resonance Imaging via Unfolded Algorithm* (FEKT-K-22-7772) realised within the project Quality Internal Grants of BUT (KInG BUT), Reg. No. CZ.02.2.69/0.0/0.0/19_073/0016948, which is financed from the OP RDE.

REFERENCES

- [1] D. Donoho, “Compressed sensing,” *IEEE Transactions on Information Theory*, vol. 52, no. 4, 2006.
- [2] J. C. Ye, “Compressed sensing MRI: a review from signal processing perspective,” *BMC Biomedical Engineering*, vol. 1, 2019.
- [3] K. T. Block, M. Uecker, and J. Frahm, “Undersampled radial MRI with multiple coils. Iterative image reconstruction using a total variation constraint,” *Magnetic Resonance in Medicine*, vol. 57, no. 6, 2007.
- [4] H. Wang and Y. Cao, “Spatially regularized t(1) estimation from variable flip angles MRI,” *Medical physics*, vol. 39, 2012.
- [5] M. Bartoš, P. Rajmic, M. Šorel, M. Mangová, O. Keunen, and R. Jiřík, “Spatially regularized estimation of the tissue homogeneity model parameters in DCE-MRI using proximal minimization,” *Magnetic Resonance in Medicine*, vol. 82, no. 6, 2019.
- [6] F. Knoll, K. Bredies, T. Pock, and R. Stollberger, “Second order total generalized variation (TGV) for MRI,” *Magnetic Resonance in Medicine*, vol. 65, no. 2, 2011.
- [7] M. Schloegl, M. Holler, A. Schwarzl, K. Bredies, and R. Stollberger, “Infimal convolution of total generalized variation functionals for dynamic MRI,” *Magnetic Resonance in Medicine*, vol. 78, no. 1, 2017.
- [8] V. Ghodrati, J. Shao, M. Bydder, Z. Zhou, W. Yin, K.-L. Nguyen, Y. Yang, and P. Hu, “MR image reconstruction using deep learning: evaluation of network structure and loss functions,” *Quantitative Imaging in Medicine and Surgery*, vol. 9, 2019.
- [9] R. Liu, S. Cheng, L. Ma, X. Fan, and Z. Luo, “Deep proximal unrolling: Algorithmic framework, convergence analysis and applications,” *IEEE Transactions on Image Processing*, vol. 28, 2019.
- [10] D. Liang, J. Cheng, Z. Ke, and L. Ying, “Deep magnetic resonance image reconstruction: Inverse problems meet neural networks,” *IEEE Signal Processing Magazine*, vol. 37, 2020.
- [11] F. Knoll, K. Hammernik, C. Zhang, S. Moeller, T. Pock, D. K. Sodickson, and M. Akcakaya, “Deep-learning methods for parallel magnetic resonance imaging reconstruction: A survey of the current approaches, trends, and issues,” *IEEE Signal Processing Magazine*, vol. 37, 2020.
- [12] R. Otazo, E. Candes, and D. K. Sodickson, “Low-rank plus sparse matrix decomposition for accelerated dynamic MRI with separation of background and dynamic components,” *Magnetic Resonance in Medicine*, vol. 73, no. 3, 2015.
- [13] P. Combettes and J. Pesquet, “Proximal splitting methods in signal processing,” *Fixed-Point Algorithms for Inverse Problems in Science and Engineering*, vol. 49, 2011.
- [14] A. Chambolle and T. Pock, “A first-order primal-dual algorithm for convex problems with applications to imaging,” *Journal of Mathematical Imaging and Vision*, vol. 40, no. 1, 2011.

Discovering relationship between graphomotor difficulties and isochrony in childrens online handwriting

M. Gavenčíak¹, V. Zvončák¹, and J. Mekyska¹

¹Brno University of Technology, Czech Republic

E-mail: xgaven07@vutbr.cz, zvoncak@vut.cz, mekyska@vut.cz

Abstract—Approximately 30–60 % of the time children spend in school is associated with handwriting. However, up to 30% of them experience graphomotor difficulties (GD), which lead to a decrease in their academic performance. Current GD diagnostic methods are not unified and show signs of subjectivity which can lead to misdiagnosis. This paper proposes novel handwriting features based on movement isochrony that enable computerised assessment of GD with approximately 20 % error.

Keywords—Developmental dysgraphia, Graphomotor difficulties, XGBoost, Isochrony, Handwriting analysis

1. INTRODUCTION

It is estimated that school-aged children spend 31–60 % [1] of their school-time performing handwriting. It is essential that these children develop graphomotor skills (GS) to be able to write legibly even under time constraints that are put onto them in class. Handwriting proficiency is essential for a child's academic career development and its lack can negatively impact their academic performance [2].

Between 10–30 % of children experience graphomotor difficulties (GD), which are defined as problems with executing basic graphomotor elements and can manifest itself as motor-memory dysfunction, graphomotor production deficits, or motor feedback difficulties [3]. These can later lead as far as to diagnosis of developmental dysgraphia (DD) [3, 4, 5], which makes early diagnosis essential to provide children with therapeutic care [6, 7].

Currently, the process of diagnosis is performed by teams of psychologists and remedial teachers who use information such as: family anamnesis, overall school performance (behaviour, grades, etc.), intellect tests, visual-spatial ability and working memory, also taking into account the examination of handwriting process and laterality [8]. However, until now, there is no standardized tool for DD diagnosis and it is at the practitioners' discretion what tools they use.

State of the art

Thanks to the new advances in technology, digitizing tablets (digitizers) can now be used to assess handwriting proficiency, or the lack thereof, by extracting features from the sampled handwriting process, which is referred to as online handwriting. The elementary features can be classified as temporal, spatial, kinematic, and dynamic. Every examined child performs a set of exercises, which generally consists of three categories: graphomotor elements (saw, Archimedean spiral, rainbow, etc.), cognitive tasks (recall of figures from memory, complex figures), and handwriting (dictation or transcription) [9, 10].

Although the utilisation of computerized handwriting analysis during the assessment of GD is a relatively new method used in the field of specific learning disabilities, some research teams already proved its promising impact. E.g., in 2020, the team of the Brno University of Technology published a new approach to the supportive diagnosis of GD with 84 % accuracy using newly designed features based on modulation spectra, fractional-order derivatives, and tunable Q-factor wavelet transform [10]. They also investigated the possibility of using the fractional-order-derivative-based features in the computerized rating of the level of handwriting difficulties. They were able to estimate external validation scores with an error of 0.65 points (while the scale was in the range of 0–4) employing gradient boosting algorithms [11].

2. METHODOLOGY

2.1. Database

The analysis was carried out on a database of handwriting exercises performed by children in the 3rd and 4th grade of a primary school. The database consists of entries of 137 children, each carrying out two handwriting exercises; one transcription and one dictation. Among them, 10 children were diagnosed with DD. All children were assigned HPSQ-C scores, HLS scores, and BHK (Concise Evaluation Scale for Children's Handwriting) scores [12]. To obtain BHK scores, children's handwriting is evaluated on a degradation scale; the higher the score, the more impaired handwriting. Additionally, the children have been rated with subjective scores on the Likert scale by multiple remedial teachers. Some descriptive statistics could be found in Table I. Each handwriting/drawing exercise is represented as a function of time describing the position, tilt (altitude), azimuth (see Figure 2), and applied pressure of a stylus pen on a digitising tablet. The tablet/pen combination can also record the in-air pen movement approximately 1.5 cm above the surface of the tablet.

Table I: Descriptive Statistics

	Age	Grade	BHK
Mean	9.590	3.657	10.723
Median	10.000	4.000	11.000
Minimum	8.000	3.000	1.000
Maximum	11.000	4.000	18.000

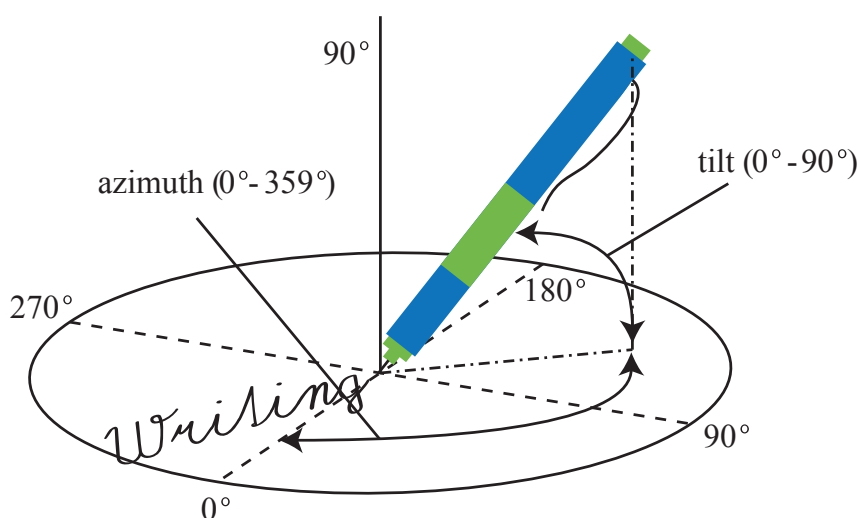


Figure 1: Schematic of the digitizing process of handwriting [13]

2.2. Feature extraction

In order to be able to objectively quantify the manifestations of DD and/or GD, certain temporal, spatial, kinematic, and dynamic features were extracted from the handwriting data. These include conventionally used features such as velocity, acceleration, jerk, pressure, writing height, and width, that were already used in previous studies [9, 10].

These baseline features were then further expanded by more complex features, based on the principle of movement isochrony – the tendency to keep the time it takes to execute a movement constant despite the length of its trajectory. This produces a linear relationship between the velocity of a movement and its length. This relationship can also be observed in handwriting [14, 15].

Assuming that the equivalent of a single movement in handwriting is a single stroke, it is then possible to plot the relationship between the stroke's velocity and length, producing a scatter plot for each child and

exercise. In total, twenty parameters aimed at quantifying the quality of the linear relationship between the two, were extracted. Namely, correlation coefficient and the convex hull algorithm were used to measure how well does the scatter plot fit to a linear regression of the points and how close together the individual points are. The slope and intercept of the linear regression were also extracted.

In addition, two different methods of stroke division were applied:

1. Contact based division – pen movement was divided into strokes based on the start and the end of contact with the tablet.
2. Velocity based division – on-surface pen movement was additionally divided into strokes if the pen reached a critically low velocity, i.e., trajectory length lower than 1/130 mm over two consecutive samples (marked as **Stop** in the result section).

While isochrony is defined using the relationship between velocity and trajectory length, the same parameters were calculated using the relationship of the movement's duration and trajectory (marked as **Velocity** or **Duration** respectively in the result section).

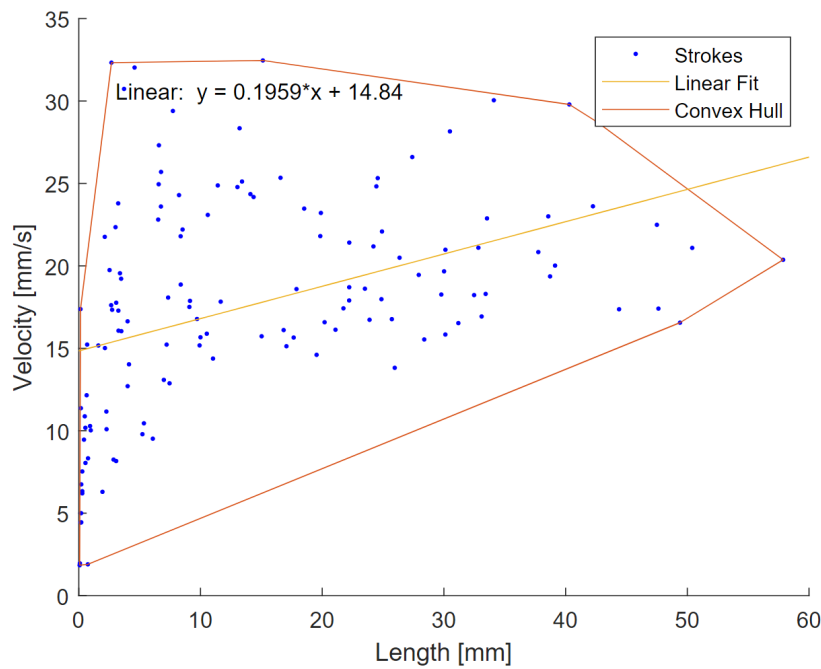


Figure 2: Illustration of parameter extraction from a velocity vs. length scatter plot.

The total number of extracted features, including the novel isochrony-based features, is 217.

2.3. Analysis

Analysis was done using the current state-of-the-art XGBoost gradient boosting algorithm with cross-validation and hyperparameter tuning. Given the relatively large feature space, compared to the number of observations, features were filtered using correlation analysis, selecting the ones showing the strongest correlation with the predicted score, and at the same time the weakest correlation with other selected features. This pre-selection yielded, in total, 46 features, including the 16 novel ones.

The confounding variables, i.e., the children's age, sex, and grade, were controlled for using linear regression. The estimator was then trained using RMSE (Root Mean Square Error) as a tuning measure. To be able to judge the estimator's performance, the metric of Estimation Error Rate (EER) is introduced and is defined as in the following equation 1:

$$EER = 100 \cdot \frac{MAE(Y_{true}, Y_{predicted})}{Y_{max} - Y_{min}}, \quad (1)$$

where Y denotes the target variable, and MAE stands for the Mean Absolute Error function.

3. RESULTS

Using the children's BHK score as the target value, and features extracted from the transcription exercise, the estimator reached an average EER of 20.29 ± 4.38 %.

Figure 3 shows the relative feature importances as modelled by the XGBoost estimator.

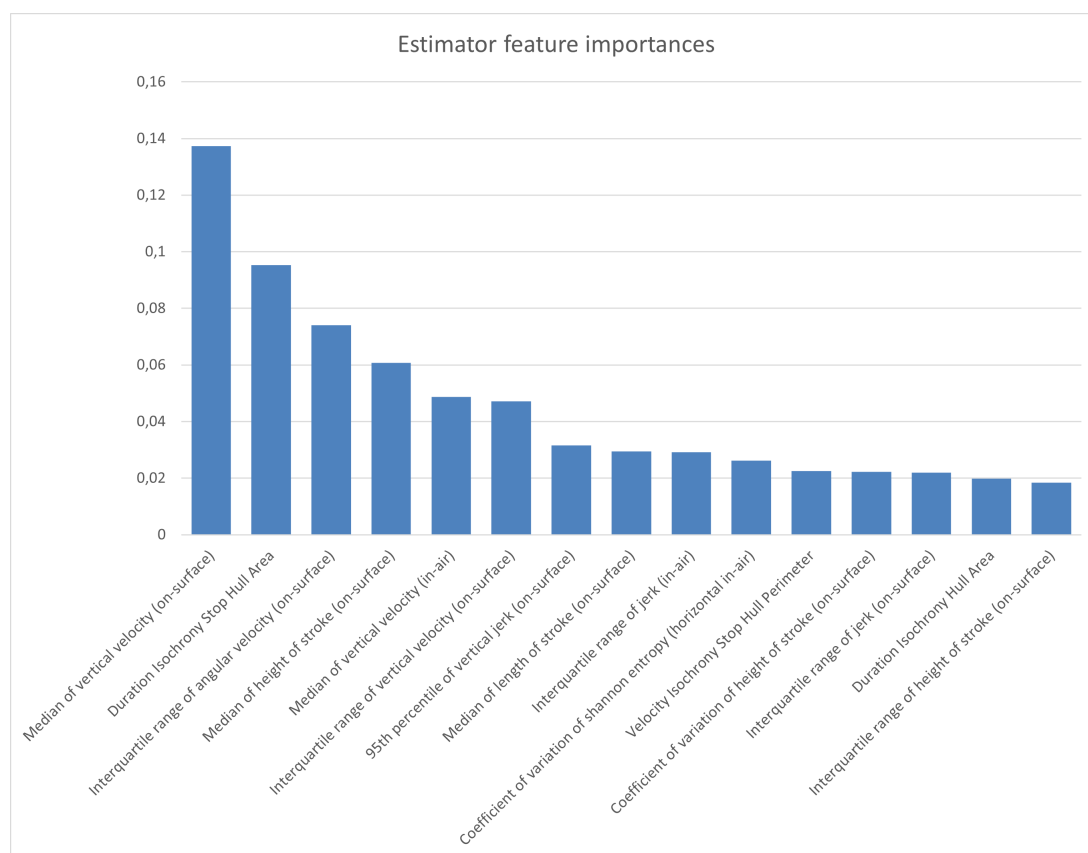


Figure 3: Top 15 features ranked by their relative feature importance. Higher value means the feature was used more often in key decisions within the decision trees.

4. DISCUSSION

While the features described as conventional in this paper can mostly be extracted from simple and repetitive exercises, the isochrony based features require more complex tasks with strokes of different lengths and shapes. This makes them more difficult to acquire as the exercises that the children complete have to contain a task that is more complex and perhaps more time consuming to complete. However, as can be seen in Figure 3, these parameters reach relatively high values of feature importance and could make automated feature-based assessment more robust.

The placement of these novel features among the most influential ones also shows that the potential feature space of handwriting parameters is not yet depleted and the exploration of more complex features (and analysis of more complex tasks) might be beneficial to further knowledge of handwriting pathology parametrization.

All the novel features that ended up being the most influential in our model were based on the convex hull algorithm, quantifying the dispersion of the scatter plot.

5. CONCLUSION

The aim of the paper was to provide an exploratory analysis on the possibility of using isochrony based handwriting features for the BHK score prediction. The inclusion of these novel features as the most influential in the XGBoost learning algorithm shows promise of their descriptive power.

ACKNOWLEDGMENT

This study was supported by a project of the Technology Agency of the Czech Republic no. TL03000287 (Software for advanced diagnosis of graphomotor disabilities).

REFERENCES

- [1] K. McHale and S. A. Cermak, "Fine motor activities in elementary school: Preliminary findings and provisional implications for children with fine motor problems," *American Journal of Occupational Therapy*, vol. 46, no. 10, pp. 898–903, Oct. 1992. [Online]. Available: <https://doi.org/10.5014/ajot.46.10.898>
- [2] B. Engel-Yeger, L. Nagauker-Yanuv, and S. Rosenblum, "Handwriting performance, self-reports, and perceived self-efficacy among children with dysgraphia," *The American Journal of Occupational Therapy*, vol. 63, no. 2, pp. 182–192, Mar. 2009. [Online]. Available: <https://doi.org/10.5014/ajot.63.2.182>
- [3] K. P. Feder and A. Majnemer, "Handwriting development, competency, and intervention," *Developmental Medicine & Child Neurology*, vol. 49, no. 4, pp. 312–317, Apr. 2007. [Online]. Available: <https://doi.org/10.1111/j.1469-8749.2007.00312.x>
- [4] J. Medwell and D. Wray, "Handwriting automaticity: the search for performance thresholds," *Language and Education*, vol. 28, no. 1, pp. 34–51, Mar. 2013. [Online]. Available: <https://doi.org/10.1080/09500782.2013.763819>
- [5] B. C. Smits-Engelsman and G. P. V. Galen, "Dysgraphia in children: Lasting psychomotor deficiency or transient developmental delay?" *Journal of Experimental Child Psychology*, vol. 67, no. 2, pp. 164–184, Nov. 1997. [Online]. Available: <https://doi.org/10.1006/jecp.1997.2400>
- [6] M. R. I. Martins, J. A. Bastos, A. T. Cecato, M. de Lourdes Souza Araujo, R. R. Magro, and V. Alaminos, "Screening for motor dysgraphia in public schools," *Jornal de Pediatria*, vol. 89, no. 1, pp. 70–74, 2013. [Online]. Available: <https://www.sciencedirect.com/science/article/pii/S0021755713000120>
- [7] C. A. Christensen, "The critical role handwriting plays in the ability to produce high-quality written text," in *The SAGE Handbook of Writing Development*. SAGE Publications Ltd, pp. 284–299. [Online]. Available: <https://doi.org/10.4135/9780857021069.n20>
- [8] B. Johnson, "Learning disabilities in children: Epidemiology, risk factors and importance of early intervention," *BMJ Medical Journal - ISSN 2348–392X*, vol. 4, no. 1, pp. 31–37, 2017.
- [9] K. Šafářová, J. Mekyska, and V. Zvončák, "Developmental dysgraphia: A new approach to diagnosis," *The International Journal of Assessment and Evaluation*, vol. 28, no. 1, pp. 143–160, 2021. [Online]. Available: <https://doi.org/10.18848/2327-7920/cgp/v28i01/143-160>
- [10] Z. Galaz, J. Mucha, V. Zvoncak, J. Mekyska, Z. Smekal, K. Safarova, A. Ondrackova, T. Urbanek, J. M. Havigerova, J. Bednarova, and M. Faundez-Zanuy, "Advanced parametrization of graphomotor difficulties in school-aged children," *IEEE Access*, vol. 8, pp. 112 883–112 897, 2020. [Online]. Available: <https://doi.org/10.1109/access.2020.3003214>
- [11] V. Zvoncak, J. Mucha, Z. Galaz, J. Mekyska, K. Safarova, M. Faundez-Zanuy, and Z. Smekal, "Fractional order derivatives evaluation in computerized assessment of handwriting difficulties in school-aged children," in *2019 11th International Congress on Ultra Modern Telecommunications and Control Systems and Workshops (ICUMT)*, 2019, pp. 1–6.
- [12] L. Hamstra-Bletz, J. DeBie, B. Den Brinker *et al.*, "Concise evaluation scale for children's handwriting," *Lisse: Swets*, vol. 1, pp. 623–662, 1987.
- [13] J. Mekyska, M. Faundez-Zanuy, Z. Mzourek, Z. Galaz, Z. Smekal, and S. Rosenblum, "Identification and rating of developmental dysgraphia by handwriting analysis," *IEEE Transactions on Human-Machine Systems*, vol. 47, no. 2, pp. 235–248, 2017. [Online]. Available: <http://ieeexplore.ieee.org/document/7530869/>
- [14] E. Pagliarini, L. Scocchia, M. Vernice, M. Zoppello, U. Balottin, S. Bouamama, M. T. Guasti, and N. Stucchi, "Children's first handwriting productions show a rhythmic structure," *Scientific Reports*, vol. 7, no. 1, Jul. 2017. [Online]. Available: <https://doi.org/10.1038/s41598-017-05105-6>
- [15] M. Gavenčiak, "Research of new online handwriting features in children with graphomotor difficulties," Master's thesis, Brno University of Technology, Faculty of Electrical Engineering and Communication, Department of Telecommunications, Brno, 2021.

Parkinson's Disease Recognition based on Sleep Metrics from Actigraphy and Sleep Diaries

M. Mikulec¹, J. Mekyska¹, and Z. Galáž¹

¹Department of Telecommunications
Faculty of Electrical Engineering and Communication
Brno University of Technology
Brno, Czech Republic

E-mail: xmikul56@vutbr.cz, mekyska@vut.cz, galaz@vut.cz

Abstract—Parkinson's disease is accompanied by sleep disorders in most cases. Therefore, patients with Parkinson's disease could be identified according to the proper sleep metrics. The study aims to train a classifier and identify proper sleep metrics, that could distinguish patients with Parkinson's disease from subjects in the control group based on data from actigraphy and sleep diaries. The study sample consisted of 23 patients with probable Parkinson's disease and 71 control subjects resulting in 654 nights of actigraphy and sleep diary data, with 26 unique features per night. XGBoost classifier was trained to distinguish the groups, scoring 80% accuracy and 52% F_1 on test data. Actigraphy-based parameters targeted at wake analysis during sleep were marked as most important. The study provided a classifier and obtained the most important parameters to identify patients with Parkinson's disease based on actigraphy and sleep diary data.

Keywords— actigraphy, machine learning, Parkinson's disease, SHAP values, sleep diary, sleep disorders, XGBoost

1. INTRODUCTION

Changes in sleep are thought to be a common process associated with aging. Secondary, it could be further compromised by medical or psychiatric diseases (e.g., dementia, depression) [1]. Idiopathic Parkinson's disease (PD) is associated with sleep disorders in 74-98% of patients [2]. Patients with mild cognitive impairment (MCI) are at risk of sleep disorders in 65% of cases [3]. The spectrum of sleep disorders is wide and includes, for example, insomnia, sleep-disordered breathing, REM behavior disorder, or restless legs syndrome [3]. Generally, there is over 60% probability that patient with dementia or mild cognitive impairment would have some sleep disorder, and therefore could be identified according to sleep parameters [3].

Although this study used data from actigraphy and sleep diary, polysomnography (PSG) is considered a gold standard measure of sleep. PSG is a really complex examination, it utilizes various sources of data, for example, electroencephalogram (EEG), electrooculogram (EOG), electrocardiogram (EKG), pulse oximetry, and pulse and respiratory effort [1, 4]. PSG is possible to distinguish phases of sleep and create a hypnogram, its results are precise and reliable, but the costs of the physical examination are significant and the examination is usually limited to one night per patient. In contrast to the fact that the metrics are measured precisely, they can be changed by an unusual laboratory environment and other unusual external influences.

Actigraphy (ACG) is a non-invasive monitoring method. An actigraph unit is a bracelet that is worn mainly on a non-dominant wrist [5]. It records the occurrence and the degree of movement of the limb, as well as the temperature, blood pressure, light intensity, etc. Compared to PSG, ACG is used in decentralized clinical studies with lower budget and it is generally targeted on home usage. ACG is eligible to collect a larger amount of data, since the unit can continuously record up to one month of data¹. On the contrary, ACG needs specialized software to identify sleep/wake intervals and due to various manufacturers and proprietary software, the results can vary significantly. It leads to initiatives to create and standardize an open access method [6, 7].

¹GENEActiv original, actigraph that was used in this study, is capable to record up to one month of continuous data depends on measurement frequency setting

Sleep diary (SD) is a widely used method for estimating sleep parameters without specialized equipment. The percentage agreement between subjective sleep diary and polysomnographic data is acceptable according to Rogers et al. ($\kappa = .87$, Sensitivity = 92.3% and Specificity = 95.6%) [8]. Low cost and straightforward usage are the main advantages of sleep diaries; however, the results depend heavily on the subject's ability to fill the diary precisely. This study was aimed at patients with a probability of PD; therefore, diary entries could produce misleading results.

Sleep parameters obtained through PS, ACG or SD might be able to distinguish subjects with sleep disorders and identify diseases such as PD. However, this field of science has many challenges and knowledge gaps. For example, Maglione et al. stated that PSG and ACG can vary dramatically in crucial parameters, and there is a significant degree of variability in precision between individual patients. It recommends ACG for the measurement of mean total sleep time (TST), sleep efficiency (SE) and wake after sleep onset (WASO) [9]. Stavitsky et al. suggest ACG as an appropriate method to measure sleep quality in PD. Furthermore, it states that SD correlates with actigraphy-derived estimates of sleep quality for patients with PD, in contrary there were no variables that were significantly related to any of the SD measures in the control group [10].

Our goal is to train a classifier that would be able to distinguish nights of patients with Parkinson's disease from control participants of the study, especially:

1. select proper algorithm for actigraphy sleep/wake recognition,
2. select and calculate sleep features,
3. train binary classifier to distinguish between patients with Parkinson's disease and control participants,
4. analyze and validate trained classifier and its selection of characteristics.

2. MATERIALS AND METHODS

2.1. Study sample

Patients were recruited with the help of St. Anne's University Hospital Brno. There were 94 subjects in total, 23 with probable Parkinson's disease (24.5%) and 71 control subjects (75.5%). The classification of the subjects was performed by neurology specialists from St. Anne's 1st Neurology clinic. Demographically, the participants were 64 ± 14 years old, there were 41 men and 53 women.

2.2. Dataset

Final dataset contains ACG and SD data for 6-7 nights from each participant, resulting in 654 nights in total with 160 entries from patients with PD and 494 entries from control subjects (CG).

Sleep/wake recognition was performed using two algorithms on actigraphy data, with first attempt to use the open access method of Hees et al. [6]. However, the metrics calculated using this method did not produce results in the final classification task and the correlation with the SD data was low. In the second final attempt, the XGBoost classifier was used based on [7]. Additionally, the training data set for sleep / wake detection was balanced using SMOTE: Synthetic Minority Over-sampling Technique [12]. The classifier scored 80% accuracy, 86% F_1 and a Mathews correlation coefficient of 0.5 on test set (40% of the Newcastle polysomnography and accelerator dataset) [13]. In validation against SD data, the algorithm reached 61% accuracy, 73.5% F_1 and a Mathews correlation coefficient of 0.05.

13 features per night were extracted for the sleep / wake classification of actigraphy data and the sleep diaries, resulting in 26 features per night in total. The features are described in Tab. I.

2.3. Data preparation

Dataset was divided into training and testing data. 60% of the data were randomly selected as training data using shuffle split, where 100 entries (25.5%) were marked as positive (probable Parkinson's disease) and 292 entries (74.5%) were marked as negative (control group). Training data were balanced using SMOTE [12]. The final training dataset consists of 584 entries with 26 features for each entry. The remaining 40% of the original dataset were kept as test data. Those data consisted of 60 positive entries (22.9%) and 202 negative (77.1%). Testing data remained imbalanced to avoid bias from SMOTE synthesis and to reflect real parameters of the dataset.

2.4. Machine learning method

Supervised machine learning method using the XGBoost tree boost classifier was used for the binary classification task of PD patients's nights and nights of control participants. Labels based on neurology specialist diagnosis were provided for supervised machine learning. Optimal hyper-parameters for

Table I: Sleep features with explanation

Feature	Explanation
Time in bed (TIB)	Time spent in bed with attempt to sleep
Sleep onset latency (SOL)	Time before sleep onset
Sleep onset latency - norm	SOL classified according to NSF norm [11]
Wake after sleep onset (WASO)	Sum of wake ups between sleep onset and sleep offset
Wake after sleep onset - norm	WASO classified according to NSF norm [11]
Wake after sleep offset (WASF)	Time between sleep offset and get up from bed
Total sleep time (TST)	Total time of sleep during night, $TST = TIB - (SOL + WASO + WASF)$
Wake bouts (WB)	Number of awakenings during night
Awakenings > 5 minutes (WB5+)	Number of awakenings longer than 5 minutes
Awakenings > 5 minutes - norm	WB5+ according to NSF norm [11]
Sleep efficiency (SE)	Ratio of TST and TIB, $SE = (TST \div TIB) \cdot 100$
Sleep efficiency - norm	SE according to NSF norm [11]
Sleep fragmentation (SF)	Ratio of WB and TST in hours, $SF = WB \div (TST \div 3600)$

the XGBoost classifier were obtained using hyper-parameters tuning method. Training validation was performed using the cross-validation method. To evaluate the ability of the models to classify PD vs. CG correctly, we employed accuracy, sensitivity, specificity, F_1 score, and the Matthews correlation coefficient (MCC), where the MCC provides a trade-off between sensitivity and specificity.

3. RESULTS

3.1. Optimal hyper-parameters

Those parameters were selected as optimal during hyper-parameters tuning phase: the number of gradient-boosted trees = 1000, boosting learning rate = 0.2, minimum loss reduction = 0.5, maximum tree depth for base learners = 8, subsample ratio of columns for each level = 0.6, subsample ratio of columns when constructing each tree = 0.4. The training process was stopped after 36 rounds to avoid overfitting.

3.2. Classification results

Results of classification during training cross-validation phase and model-trained results on test data are shown in Tab. II. The classifier has good results on both train and test data. On the contrary, MCC of 0.4 and Sensitivity of 49% underscore that the classifier can easily mistake patient with Parkinson's disease as control group patient. However, the Specificity of 89% states that the subject of the control group should not probably be mistaken for a Parkinson's disease patient.

Table II: Classification results of Parkinson's disease recognition

	Training	Test
Accuracy [%]	88	80
Sensitivity [%]	89	49
Specificity [%]	87	89
F_1 [%]	91	52
MCC	0.76	0.40

3.3. Feature importance and model interpretation

Feature importance of top 10 features is visualized in Fig. 1. The features marked (A) are obtained from actigraphy, and the features of the sleep diary are marked (D). The features extracted from the

actigraphy data that record the number and duration of awakenings between the sleep onset and offset are the most important according to the model, namely wake bouts and sleep efficiency according to the norm. Similarly, the most important SD feature is the sleep efficiency according to the norm[11].

To explain the output of the model even further, the game-theoretic approach called SHAP was used. SHAP values encode the importance that a model gives to each feature of each data point in contributing to the model's output. The results are visualized on Fig. 2. The most important features according to SHAP are also based on actigraphy, while WB remained the most important feature at all².

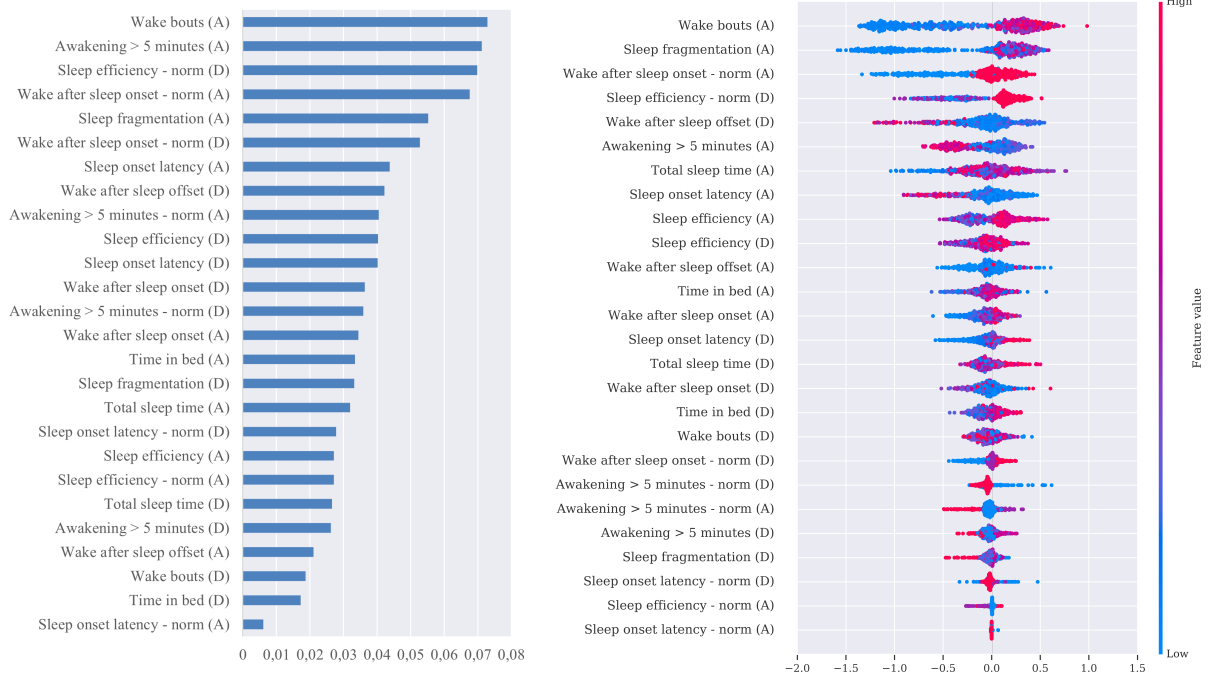


Figure 1: Feature importance (PD classification) **Figure 2:** SHAP values (features impact, PD classification)

4. DISCUSSION

Training dataset for XGBoost classifier used for the detection of sleep / wake was balanced using SMOTE. However, the results were worse than suggested using the model trained on an imbalanced dataset. Therefore, the sleep parameters calculated based on actigraphy sleep / wake recognition could be affected. The experiment should be repeated with the suggested model setting.

The study could be severely affected by the study sample and errors in its diagnosis. The diagnosis determination was made at the early stage of project NU20-04-00294 Diagnostics of Lewy body diseases in the prodromal stage based on multimodal data analysis. Due to some examinations that were incomplete and the methodology to determine the diagnosis was uncertain, the labels provided to the supervised learning algorithm could be wrong or misleading. Therefore, the experiment should be repeated after the final results of the NU20-04-00294 project.

Inaccuracies could be caused by the selection of subjects in the control group. There were patients with mild cognitive impairment diagnosis and patients with Lewy body dementia in the prodromal stage. These diseases are associated with sleep disorders in many cases, and MCI could even be an indicator of Parkinson's disease. Therefore, to make the classification much more accurate, the subjects in the control group should be healthy controls. On the contrary, the study sample perfectly matches the target group for the real-life scenario of Parkinson's disease recognition, consisting of elderly adults with sleep problems.

The model has a relatively low sensitivity. But the results are made night-by-night and not subject-by-subject. For example, RBD should not be present on all nights in a patient with probable PD. Therefore, to classify subjects, a threshold for PD-classified nights should be established. Reaching this threshold

²To replicate the results of the study and use the classifier, visit <https://github.com/BDALab/sleep-analysis-system> for source codes, or <https://nicelife.utko.feev.vutbr.cz> to see a running instance of the sleep analysis system, which contains an implemented classifier. The dataset must be requested via email due to GDPR.

will mark all nights of this patient as PD-classified. In this way, the sensitivity and overall accuracy could be dramatically increased.

5. CONCLUSION

This study proposes a new method for the detection of Parkinson's disease based on actigraphy and sleep diary data. The method achieved 80% accuracy and a Mathews correlation coefficient equal to 0.4 (49% sensitivity, 89% specificity) when compared to the diagnosis of neurological experts. Although the method has a low sensitivity for clinical use, it can detect patients with a further stage of Parkinson's disease.

ACKNOWLEDGMENT

This work was supported by grant no. NU20-04-00294 (Diagnostics of Lewy body diseases in the prodromal stage based on multimodal data analysis) of the Czech Ministry of Health and by the European Regional Development Fund no. CE1581 (Interreg niCE-life – Development of an integrated concept for the deployment of innovative technologies and services allowing independent living of frail elderly) of the European Union.

REFERENCES

- [1] K. Crowley, "Sleep and Sleep Disorders in Older Adults," *Neuropsychology Review*, vol. 21, no. 1, pp. 41–53, Mar. 2011, doi: [10.1007/s11065-010-9154-6](https://doi.org/10.1007/s11065-010-9154-6).
- [2] M. Partinen, "Sleep disorder related to Parkinson's disease," *Journal of Neurology*, vol. 244, no. 1, pp. S3–S6, Apr. 1997, doi: [10.1007/BF03160564](https://doi.org/10.1007/BF03160564).
- [3] B. Guarnieri et al., "Prevalence of Sleep Disturbances in Mild Cognitive Impairment and Dementing Disorders: A Multicenter Italian Clinical Cross-Sectional Study on 431 Patients," *Dementia and Geriatric Cognitive Disorders*, vol. 33, no. 1, pp. 50–58, 2012, doi: [10.1159/000335363](https://doi.org/10.1159/000335363).
- [4] J. V. Rundo and R. Downey, "Chapter 25 - Polysomnography," in *Handbook of Clinical Neurology*, vol. 160, K. H. Levin and P. Chauvel, Eds. Elsevier, 2019, pp. 381–392.
- [5] R. J. Cole, D. F. Kripke, W. Gruen, D. J. Mullaney, and J. C. Gillin, "Automatic sleep/wake identification from wrist activity," *Sleep*, vol. 15 5, pp. 461–9, 1992, doi: [10.1093/SLEEP/15.5.461](https://doi.org/10.1093/SLEEP/15.5.461).
- [6] V. T. van Hees et al., "A Novel, Open Access Method to Assess Sleep Duration Using a Wrist-Worn Accelerometer," *PLOS ONE*, vol. 10, no. 11, p. e0142533, Nov. 2015, doi: [10.1371/journal.pone.0142533](https://doi.org/10.1371/journal.pone.0142533).
- [7] M. Mikulec et al., "Automatic Segmentation of Actigraphy Data Utilising Gradient Boosting Algorithm," in *2021 44th International Conference on Telecommunications and Signal Processing (TSP)*, Jul. 2021, pp. 399–402. doi: [10.1109/TSP52935.2021.9522650](https://doi.org/10.1109/TSP52935.2021.9522650).
- [8] A. E. Rogers, C. C. Caruso, and M. S. Aldrich, "Reliability of sleep diaries for assessment of sleep/wake patterns," *Nursing Research*, vol. 42, no. 6, pp. 368–372, 1993, doi: [10.1097/00006199-199311000-00010](https://doi.org/10.1097/00006199-199311000-00010).
- [9] J. E. Maglione et al., "Actigraphy for the Assessment of Sleep Measures in Parkinson's Disease," *Sleep*, vol. 36, no. 8, pp. 1209–1217, Aug. 2013, doi: [10.5665/sleep.2888](https://doi.org/10.5665/sleep.2888).
- [10] K. Stavitsky, J. L. Saurman, P. McNamara, and A. Cronin-Golomb, "Sleep in Parkinson's disease: A comparison of actigraphy and subjective measures," *Parkinsonism & Related Disorders*, vol. 16, no. 4, pp. 280–283, May 2010, doi: [10.1016/j.parkreldis.2010.02.001](https://doi.org/10.1016/j.parkreldis.2010.02.001).
- [11] M. Ohayon et al., "National Sleep Foundation's sleep quality recommendations: first report," *Sleep Health*, vol. 3, no. 1, pp. 6–19, Feb. 2017, doi: [10.1016/j.sleh.2016.11.006](https://doi.org/10.1016/j.sleh.2016.11.006).
- [12] N. V. Chawla, K. W. Bowyer, L. O. Hall, and W. P. Kegelmeyer, "SMOTE: Synthetic Minority Over-sampling Technique," *Journal of Artificial Intelligence Research*, vol. 16, pp. 321–357, 2002, doi: [10.1613/jair.953](https://doi.org/10.1613/jair.953).
- [13] V. T. van Hees, S. Charman, and K. Anderson, "Newcastle polysomnography and accelerometer data," *Zenodo. org*, vol. 10, 2018, doi: [10.5281/zenodo.1160410](https://doi.org/10.5281/zenodo.1160410).
- [14] W. E. Marcílio and D. M. Eler, "From explanations to feature selection: assessing SHAP values as feature selection mechanism," in *2020 33rd SIBGRAPI Conference on Graphics, Patterns and Images (SIBGRAPI)*, Nov. 2020, pp. 340–347. doi: [10.1109/SIBGRAPI51738.2020.00053](https://doi.org/10.1109/SIBGRAPI51738.2020.00053).

Exploring the Possibilities of Automated Annotation of Classical Music with Abrupt Tempo Changes

M. Ištváněk, Š. Miklánek

Department of Telecommunications, Faculty of Electrical Engineering and Communication,
Brno University of Technology, Technická 12, 616 00 Brno, Czech Republic

E-mail: xistva02@vut.cz, xmikla12@vut.cz

Abstract—In this paper, we introduce options for automatic measure detection based on synchronization, beat detection, and downbeat detection strategy. We evaluate proposed methods on two motifs from the dataset of Leoš Janáček’s string quartet music. We use specific user-driven metrics to capture annotation efficiency simulating a scenario where a musicologist has to use the output of an automated system to create ground-truth annotations on given recordings. In the case of the first motif, synchronization outperformed other methods by detecting most of the measure positions correctly. This procedure was also the most suitable for the second motif—it achieved a low number of correct detections, but the vast majority of transferred time positions belonged within the outer tolerance window. Therefore, in most cases, only shifting operations were needed resulting in higher annotation efficiency. Results suggest that the state-of-the-art downbeat tracking is not yet efficient for expressive music.

Keywords—beat tracking, classical music, downbeat detection, DTW, music information retrieval, music performance analysis, synchronization

1. INTRODUCTION

Music Information Retrieval (MIR) is a well-established interdisciplinary area that combines technical approaches and methods with musical analysis. The MIR researchers deal with many music-driven tasks, such as automatic detection of musical features and high-level parameters, user-centric semantic retrieval, recommendation systems, or transcription of audio recordings into symbolic representations [1]. In this paper, we focus on the automatic identification or detection of measure (bar) positions in string quartet recordings, which is closely related to the challenges of Musical Performance Analysis (MPA).

Measures are musically meaningful segments with defined metric patterns. Regarding western music notation, information about their exact position in a given musical hierarchy is automatically encoded in the corresponding score (sheet music). To obtain measure positions in structurally complex music such as string quartets, one needs to have a score available. Manual labeling and annotation is a time-consuming procedure but it is a common approach to obtain ground-truth data. However, recent developments of machine learning methods may change this workflow.

One of the most established topics in MIR is beat tracking or beat detection¹. A standard beat tracking system outputs a vector of time positions that correspond to individual beats in a given music recording. In our case, we want to obtain only the first beat of each measure—such detectors do not usually distinguish the beat index within measures. Therefore, downbeat tracking systems have been developed which, together with the time position of beats², also estimate their position in a musical structure. The second option is a strategy based on the synchronization procedure. The general goal of music synchronization is to establish an alignment between musically corresponding time positions (measures in this case) of the same piece (e.g., audio-to-score or audio-to-audio alignment) [2].

In this paper, we focus on computer-generated annotations and test the state-of-the-art offline beat and downbeat tracking for measure detection on chamber music. We compare the detectors with the music synchronization technique and evaluate all methods by a user-driven metric.

¹In the context of this paper, we use the terms beat tracking and beat detection interchangeably.

²The system outputs the probability of beats and downbeats separately.

2. METHODS

2.1. Dataset

First, we introduce our dataset, which consists of two separate motifs from Janáček’s *String Quartet No. 1 “Kreutzer Sonata”*, JW 7 No. 8 and *String Quartet No. 2 “Intimate Letters”*, JW 7 No. 13, respectively. Figure 1 shows a score for the first motif. This motif contains 11 measures of the first movement. At the beginning, all strings except violoncello play *con sordino*³ and the second violin uses *finger tremolo*⁴ technique which may blur the starting point of the second bar. Furthermore, the overall dynamics is higher for the upbeat than for the downbeat. After *subito forte* (suddenly loud), the tempo changes rapidly with possible local deviations based on individual interpretation. The second motif contains 10 measures of the second movement. It is even more complex within the metric structure with many accents in the middle of measures. We selected these excerpts for their various tempo, challenging structure, and expressive nature. We gathered 17 different interpretations for each motif and carefully annotated all ground-truth measure positions. In our experiments, the first recording from both motifs by the Belcea Quartet (year of recording 2018) was selected as a reference. The remaining recordings were used for testing purposes.

The image shows a musical score for four string instruments: Violin I, Violin II, Viola, and Violoncello. The score is divided into two sections: Adagio [♩ = 63] and Con moto [♩ = 224]. The Adagio section starts with 'con sord.' and 'mf' dynamics. The Con moto section starts with 'sf' and 'p' dynamics, followed by 'dim.' markings. The Violoncello part is marked 'mf' at the beginning of the Con moto section.

Figure 1: The score for the first motif of our dataset.

2.2. Beat and downbeat detection

Beat tracking systems provide time positions of computed beats for any given music recording. In the case of neural network-based approaches, their output is usually an activation function—its value within a specified feature rate is related to the novelty function or confidence of beat occurrence. Then, peak-picking methods or probabilistic and statistical methods, such as Conditional Random Fields or Dynamic Bayesian Networks (DBN), are often used.

In this paper, we use a beat detector based on the variant of Recurrent Neural Network (RNN) [3] in combination with DBN [4] and a downbeat detector also based on RNN [5] and DBN but with different settings and functionality. We kept the default settings for the DBN with a range of possible tempo detection between 55 and 215 BPM (Beats Per Minute). This system will demonstrate the problematic part of beat tracking when applied to expressive chamber music.

The DBN estimator of downbeats outputs two vectors of data. The first one contains time positions of beats and the second their index within a measure—e.g., output vector $B = [2.5, 3]$ shows the third beat of a measure in the time of 2.5 s. Thus, we have selected only those beats that correspond to the first position of each measure creating a downbeat sequence. Ideally, the output of this modified detector should produce only the beginning of each measure and follow the ground-truth data structure. We also added the prior knowledge (2 or 3 beats per bar) about the metric structure of selected motifs into the detector.

2.3. Synchronization method

The second option to obtain time positions of measures is a synchronization procedure. This is a common approach in MPA due to its advantages. In our experiment, we use an alignment method based on

³A technique that uses a “mute pad” to soften the produced sound.

⁴The player uses fingers to alternate rapidly between two notes.

a variant of Dynamic Time Warping (DTW), called Memory-restricted Multiscale DTW (MrMsDTW) that is faster and may provide a better synchronization accuracy [6]. First, we compute chroma energy normalized statistic (CENS) features [7] of reference and target recording with a resolution of 50 features per second. MrMsDTW is applied to compute a cost-minimizing alignment between both CENS matrices and the resulting warping path is limited to be strictly monotonic by postprocessing. The ground-truth annotations are then transferred from the reference to the target recording by the resulting warping path.

This strategy has an advantage over the automated detectors—there will be always the right number of measures detected. The question is whether chroma features contain enough information for alignment to work accurately e.g. in music structures, where there is almost no new information present, but measure number increases.

2.4. User-driven metric

Each machine annotation of musical content usually ends with a certain number of mislabeled time positions. Either the desired time point may not appear in the machine annotation at all, or it is misplaced. In [8], the authors introduced the *annotation efficiency* (ae) metric, which is based on how much effort a user has to exert to manually correct detections by shifting, deleting, or inserting time positions. The insert and delete operations correspond to the counts of false negatives and false positives, respectively. The shifting should theoretically be counted twice, once as a false positive and the second time as a false negative. In practice, however, it is more sensible to count this operation separately and prioritize it over deletion and insertion, since it is the most common correction performed by the user.

The process of calculating the ae metric is as follows. First, an inner tolerance window of ± 70 ms is created around each ground truth annotation. Then, the true positives (unique detections), t^+ , are counted. Detections that match ground truth annotations are removed from further calculations and incorrect detections are marked as candidates to be shifted or removed. For each remaining annotation, an outer tolerance window of ± 1 s is then created to search for the closest detection that does not match the ground truth. If there is a detection in this window, it is marked as shift. After the analysis of unaccounted detections, the number of shifts s is calculated. The remaining annotations correspond to false negatives, f^- , with leftover detections marked for deletion and counted as false positives, f^+ . The ae metric is defined by the following equation:

$$ae = t^+ / (t^+ + s + f^+ + f^-). \quad (1)$$

3. RESULTS

First, we transferred the ground-truth annotations based on the DTW alignment method, then calculated beats and downbeats as described in section 2. Figure 2 shows the user-driven metric computation and the pipeline with all possible operations for one of the recordings. Operations are marked with different colors to increase the readability. We kept the same inner and outer tolerance window as the original beat tracking evaluation in [8].

In this case, the synchronization procedure outperforms all other methods. The final synchronized positions are not in the exact time positions, however, they mostly fit into the inner tolerance window. The value of beat confidence for the downbeat tracker was in the first motif too low—measures that have ambiguous nature were not detected at all, measures of a faster-paced segment with an abrupt change of rhythmic structure were partially omitted. On the other hand, the RNN beat tracker detected many false positives. The DBN method fills the positions between confident output beats based on their past and future occurrence—this method can work well with small deviations of tempo but fails when the rhythmic and metric structure is unpredictable and highly changing.

Table I shows the sum of all operations and annotation efficiency, recall, and precision for both motifs and each method. Synchronization outperformed other methods for the first motif with 142 correct detections and only 36 additional operations. In the second scenario, however, the beat tracking captured the highest number of correct measure positions. Although the synchronization method achieved the lowest number of all corrections and the best annotation accuracy, recall and precision remained low. Recall and precision scores may give the impression that beat and downbeat detection are more suitable tools for automatic detection of measure positions in a complex structure, but a number of deletion operations reveal that they are in fact counterproductive in this scenario. None of the proposed methods was successful considering only the second motif.

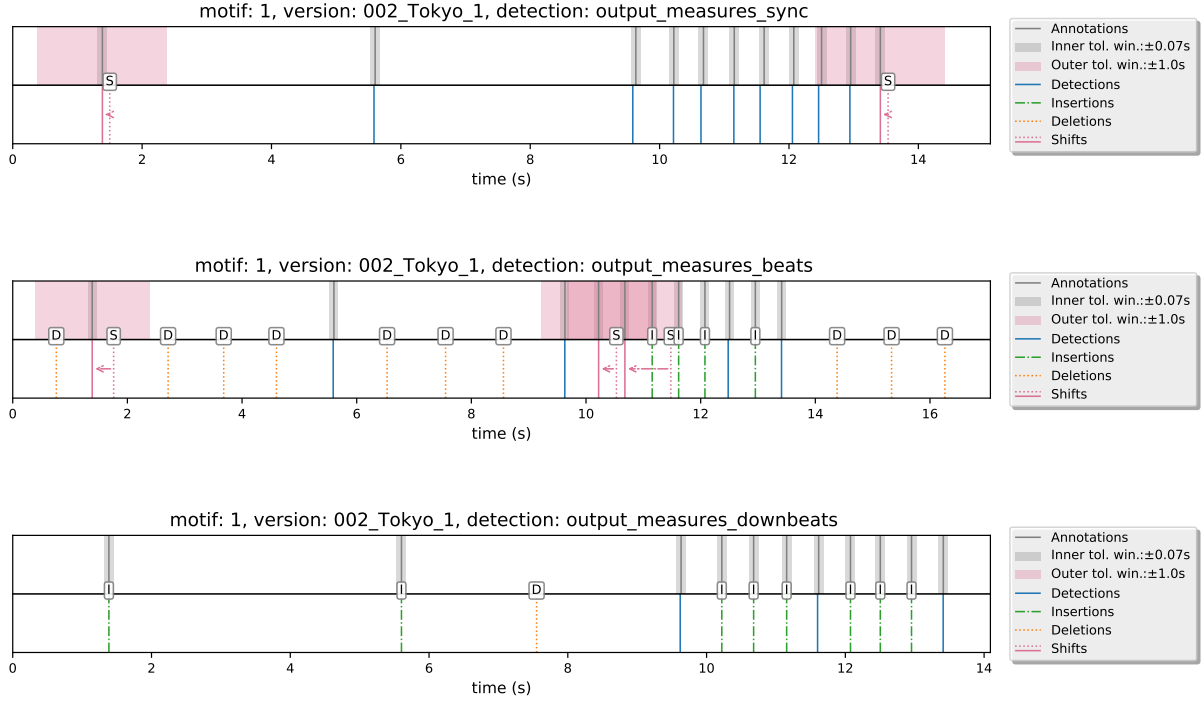


Figure 2: The user-driven metric for synchronization, beat tracking, and downbeat tracking strategy; evaluation of the Tokyo Quartet recording, first motif.

motif 1 (176 measures in total)								
method	$\sum \text{det}$	$\sum \text{ins}$	$\sum \text{del}$	$\sum \text{shf}$	$\sum \text{ops}$	ae (mean)	R (mean)	P (mean)
beat tracking	70	42	167	64	273	0.208	0.375	0.225
downbeat tracking	33	116	35	27	178	0.155	0.176	0.329
synchronization	142	2	2	32	36	0.799	0.727	0.727
motif 2 (160 measures in total)								
method	$\sum \text{det}$	$\sum \text{ins}$	$\sum \text{del}$	$\sum \text{shf}$	$\sum \text{ops}$	ae (mean)	R (mean)	P (mean)
beat tracking	67	0	516	93	609	0.101	0.356	0.087
downbeat tracking	38	61	54	61	176	0.196	0.194	0.219
synchronization	38	11	11	111	133	0.224	0.156	0.156

Table I: The number of detections, insertions, deletions, shifts, and total corrections, annotation efficiency, recall, and precision for each motif and method.

4. DISCUSSION

The synchronization procedure, even if it always detects the correct number of measures, relies only on chroma features, their resolution, and DTW accuracy. The ground-truth annotations may not be always precise—the resulting warping path can transfer reference time positions with some deviations. It depends, e.g., on the harmonic structure, occurrence of onsets, or the ADSR envelope of given instruments. If we tolerate larger deviance (such as 100 ms), almost all annotations will be transferred correctly.

The beat detector has shown an experimental role in illustrating the function of predicting the rhythmic structure and beat occurrence. In the second motif, it achieved the best recall and number of correct measure positions. However, it also detected too many false positives; that would be true even if ground-truth annotations were based on beat positions. The method of filling in beats, even in places where there is no underlying information, can work well in simpler musical structures without significant changes in rhythm and meter. Furthermore, detectors are usually trained on specific audio datasets, for which there are manual ground-truth annotations available—string quartet music is not among them.

The downbeat detector was not sensitive enough or predicted false beat indexes, although it contained prior knowledge about the musical structure (see section 2.2). Table I shows that so far, the only valid option for expressive string quartet music with many abrupt tempo changes, local tempo deviations, and weak onset and beat positions, is the synchronization strategy. Its accuracy can be improved by the choice of additional features for the alignment procedure. In this case, however, the ground-truth annotations are always needed.

5. CONCLUSION

In this contribution, we proposed and evaluated different methods of obtaining measure positions in string quartet music. We first created reference ground-truth data and then compared the synchronization method, beat tracking, and downbeat tracking based on a specific user-driven metric. This metric allows us to calculate the number of operations that one needs to make to obtain the ground-truth annotation of measure positions. We tested different strategies on two carefully selected string quartet motifs from Leoš Janáček's compositions. Both proposed segments are musically challenging, they contain many weak onset positions, ambiguous beats, and abrupt tempo and rhythm changes. Results suggest that the synchronization method is superior to all other possible options. Beat and downbeat tracking approaches are not yet efficient on very expressive pieces of classical music.

ACKNOWLEDGMENT

This work was supported by the "Identification of the Czech origin of digital music recordings using machine learning" grant, which is realized within the project Quality Internal Grants of BUT (KInG BUT), Reg. No. CZ.02.2.69 / 0.0 / 0.0 / 19_073 / 0016948 and financed from the OP RDE.

REFERENCES

- [1] M. Schedl, E. Gómez, and J. Urbano, "Music Information Retrieval: Recent Developments and Applications," *Foundations and Trends® in Inform. Retr.*, vol. 8, no. 2-3, pp. 127–261, 2014, doi: 10.1561/15000000042. [Online]. Available: <https://ieeexplore.ieee.org/document/8187204>
- [2] C. Weiß, V. Arifi-Muller, T. Prätzlich, R. Kleinertz, and M. Muller, "Analyzing Measure Annotations for Western Classical Music Recordings," in *Proc. 17th Int. Society for Music Information Retrieval Conf. (ISMIR 2016)*, 2016, pp. 517–523. [Online]. Available: <https://archives.ismir.net/ismir2016/paper/000079.pdf>
- [3] S. Böck and M. Schedl, "Enhanced Beat Tracking With Context-Aware Neural Networks," in *Proc. 14th Int. Conf. on Digital Audio Effects (DAFx-11)*, Sep. 19–23, 2011, pp. 135–139. [Online]. Available: http://www.dafx.de/paper-archive/2011/Papers/31_e.pdf
- [4] F. Krebs, S. Böck, and G. Widmer, "An Efficient State-Space Model for Joint Tempo and Meter Tracking," in *Proc. 16th Int. Society for Music Information Retrieval Conf. (ISMIR 2015)*, 2015, pp. 72–78. [Online]. Available: <https://archives.ismir.net/ismir2015/paper/000239.pdf>
- [5] F. Krebs, S. Böck, and G. Widmer, "Joint Beat and Downbeat Tracking with Recurrent Neural Networks," in *Proc. 17th Int. Society for Music Information Retrieval Conf. (ISMIR 2016)*, 2016, pp. 255–261. [Online]. Available: <https://archives.ismir.net/ismir2016/paper/000186.pdf>
- [6] T. Prätzlich, J. Driedger, and M. Müller. "Memory-Restricted Multiscale Dynamic Time Warping," in *Proc. IEEE Int. Conf. on Acoustics, Speech, and Signal Processing (ICASSP)*, 2016, pp. 569–573. [Online]. Available: https://www.audiolabs-erlangen.de/fau/professor/mueller/publications/2016_PraetzlichDriedgerMueller_MrMsDTW_ICASSP.pdf
- [7] M. Müller, F. Kurth, and M. Clausen, "Audio Matching Via Chroma-based Statistical Features," in *Proc. 6th Int. Conf. on Music Information Retrieval (ISMIR 2005)*, 2005, pp. 288–295. [Online]. Available: <https://archives.ismir.net/ismir2005/paper/000019.pdf>
- [8] A. S. Pinto, I. Domingues, and M. E. P. Davies, "Shift If You Can: Counting and Visualising Correction Operations for Beat Tracking Evaluation," in *Extended Abstracts for the Late-Breaking Demo Session of the 21st Int. Society for Music Information Retrieval Conf. (ISMIR 2020)*, 2020. [Online]. Available: https://program.ismir2020.net/lbd_421.html

On Bayer demosaicing impact on image sharpness in lens quality assessment

T. Zemčík¹, K. Horák¹

¹Brno University of Technology, Faculty of Electrical Engineering and Communications, Czech Republic

E-mail: zemcikt@vut.cz, horak@vut.cz

Abstract—In this short paper an ongoing research is introduced into the methods of simple lens quality assessment for low-cost computer vision applications. Also the paradigm of colour filter arrays (CFA), CFA images and their demosaicing are described. Further the paper introduces an experiment to compare selected demosaicing algorithms and their influences on image sharpness, and therefore on the lens quality assessment. Of the selected methods the AHD (Adaptive Homogeneity-Directed) algorithm proved the most suitable for the lens evaluation.

Keywords—Colour filter array, Bayer matrix, demosaicing, debayering, lens quality, MTF

1. INTRODUCTION

In recent years advancements in image processing and computer vision methods have made it possible for many more fields to use imaging sensors in ever increasing numbers. More and more applications are being developed that emphasise accessibility and low-cost, which at times comes with sacrifices in image quality.

In many cases cameras with interchangeable lenses are used, such as the increasingly popular Raspberry Pi camera used in conventional applications such as [1, 2], and even pushed into more specialised applications such as [3]. Lenses are typically the most expensive parts of the imaging hardware, it is thus logical that in a low-cost application usage of cheap lenses is desirable. Experience shows that some of the cheap lenses on the market come with certain defects, such as miss-alignment of the optical components, or defects to the components themselves causing aberrations. As in any machine vision application assessing the image quality is necessary for a well performing system, therefore methods have been developed to quantify the qualities of the image, such as contrast, sharpness or distortion.

As a part of an ongoing effort to find a reliable way to assess the quality of lenses, this paper aims to describe effects of various Bayer demosaicing approaches on image sharpness, and to select a suitable way to represent the colour image for measurement of image sharpness.

2. COLOUR FILTER ARRAYS AND DEMOSAICING

A colour digital image as we know it is nothing more than a simple multi-spectral image, usually consisting of three colour images (red, green and blue) that activate the three different colour light-sensitive elements (cones) in our eyes [4]. If we are to take this multi-spectral image in one-shot (rather than using a scanning method), there are several fundamental approaches.

In the first approach it is possible to decompose the image using an system of optical elements (a beam splitter) into several images, that are then passed through the desired chromatic filters, and projected onto multiple sensors (or different areas of the same sensors)- this approach was famously used in the Two-Color and Three-Color Technicolor systems [5], and is still used in specialised cameras today.

The second approach involves specialised image sensors the architecture of which allows the various colour images to be taken in one light-sensitive element. Usually the sensors involve stacked photodiode architectures, such as the X3 sensors [6]. Such sensors are however still quite rare.

The third approach uses a standard imaging sensor (most commonly a CCD or CMOS chip), that has different chromatic filters applied to the individual light-sensitive cells. This arrangement is called a CFA (Colour Filter Array), CFAs take many forms differing in how many and which filters are involved, and what their configuration is [7, 8]. This arrangement is by far the most common and de-facto the only method in use for the low-cost computer vision systems in question.

The most common CFA in low-cost cameras is the Bayer CFA, which consists of periodically repeating pattern of 2x2 arrays of one each red and blue elements, and two green elements on a diagonal [8, 9]. There exist four combinations in which this pattern can be found as illustrated by Fig. 1.



Figure 1: Four Bayer CFA element configurations, from the left: GRBG, GBRG, RGGG and BGGR

In order for an image taken by such a camera to be converted to a full colour picture, it has to go through a step known as demosaicing, in case of a Bayer CFA also known as debayering. This step converts a single grayscale image with the bayer pattern into three grayscale images each representing a single chromatic channel.

In a naive approach to demosaicing, one would first split the original image into three, copying pixels corresponding to the given component. That would yield 0.25 full R and B channels, and a 0.5 full G channel [7, 10]. The demosaicing is thus an interpolation problem. Fig. 2 shows first a section of a raw image, and selected demosaic methods applied on said section. Among the most popular demosaicing algorithms are the Variable Number of Gradients (VNG) [11], the Adaptive Homogeneity-Directed (AHD) [12] and the Aliasing Minimization and Zipper Elimination (AMaZE) [13].

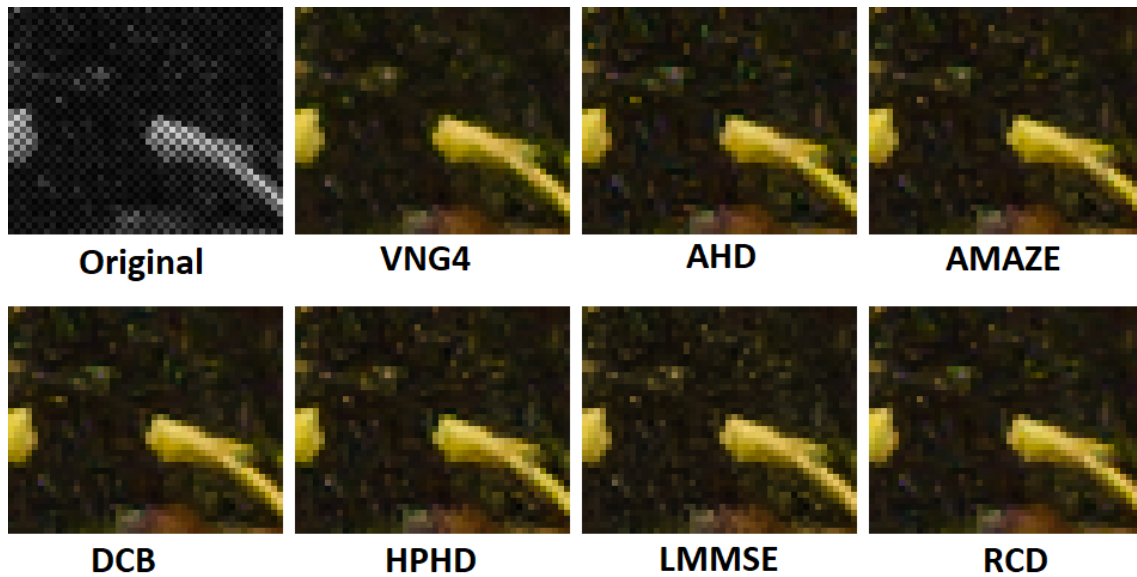


Figure 2: Examples of effects of different demosaicing algorithms on a natural image, created via RawTherapee [14]

In Fig. 2 there are apparent albeit slight differences between how the various algorithms approach the demosaicing. For instance the VNG4 algorithm introduces a stronger element of low-pass filtration, resulting in less colour artefacts at the cost of some image sharpness.

For the purposes of this paper the computational cost of the individual algorithms is disregarded as it has no bearing on the experiment, in practical deployment, however, this has crucial importance and often less optimal but better computationally performing algorithms are used. Another factor is also the implementability of the algorithms in an FPGA.

3. LENS QUALITY ASSESSMENT

For the purposes of this paper the lens quality is evaluated in terms of image sharpness. In order to be able to compare such a quality as sharpness in images, a metric is necessary. Of the several metrics available the Modular Transfer Function (MTF) was selected [15]. The measurement is based on the slanted edge method as used by the ISO 12233 standard [16, 17]. The target pattern on which the camera is tested is based on the ISO 12233 recommendations and is shown in Fig. 3 [16], all the edge detection and MTF calculations are done via the MTF Mapper Software [18]. The software first detects the edge, and identifies its direction, then pixels surrounding the edge are summed in the direction of the edge thus getting the summed edge profile with enough statistical samples.

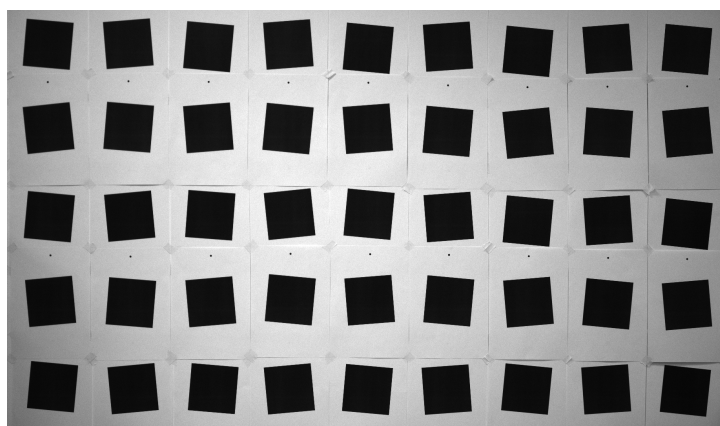


Figure 3: The sharpness test pattern

The test pattern in Fig. 3 consists of a grid of 5 by 9 printed squares each tilted 5° in alternating directions. The camera is placed so its optical axis is coincidental with the perpendicular of the centre of the pattern, and so the pattern fills the entire image.

Each edge in the pattern (four per square) generates a MTF value, and the values can then be plotted. Because the sharpness in the image is produced by the combination of all optical members in the system, it is necessary to separate the influence of the lens itself from the influences of the sensor, filters or some miss-alignment in the system. The generic C-mount lens used for this paper allows to be rotated in range of approximately 270° freely without changing the focus, thus a series of 7 images was taken every 45° . The hypothesis is that if we can observe some kind of pattern that rotates in the series, the defect can then be attributed to the lens, or alignment of the lens. Fig. 4 demonstrates such a series.

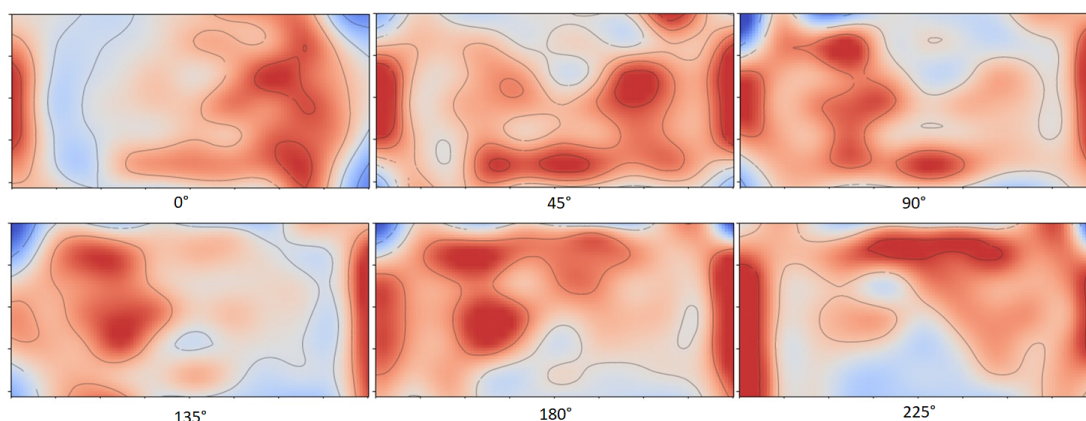


Figure 4: A series of snapshots of meridional edge MTF distribution 45° apart (only 6 out of 7 images), the heatmap represents image sharpness, the redder the sharper, the bluer the more blurred. Absolute values are irrelevant.

Fig. 4 clearly shows a rotating defect, that can thus be attributable to the lens or lens installation. It also shows that this particular lens has a very different sharpness distribution than the one usually seen in lenses (higher sharpness area around the optical axis with the sharpness decreasing towards the edges).

4. DEMOSAICING IMPACT ON MTF

In order to investigate the impact of various demosaicing approaches on the sharpness evaluation, four measurements were performed. With a new lens setup (as not to bias the observation by a known quality of the lens) images were taken and demosaiced from raw via Intel-implemented naive debayering, Accord-implemented naive debayering and Intel-implemented AHD algorithm. Fig. 5 compares the summed edge profiles.

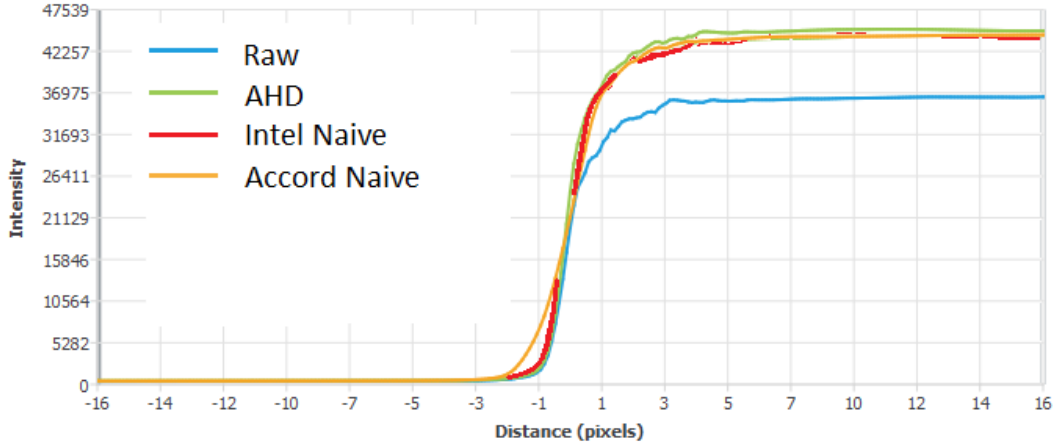


Figure 5: Summed edge profiles for: Raw (CFA image), AHD, Intel naive and Accord naive methods

As is apparent from the Fig. 5 the edge profiles for the three demosaiced images are close to each other, with the Accord naive profile being slightly softer. The Raw edge is unsurprisingly not reaching the same value, as the values of each individual pixels are very different.

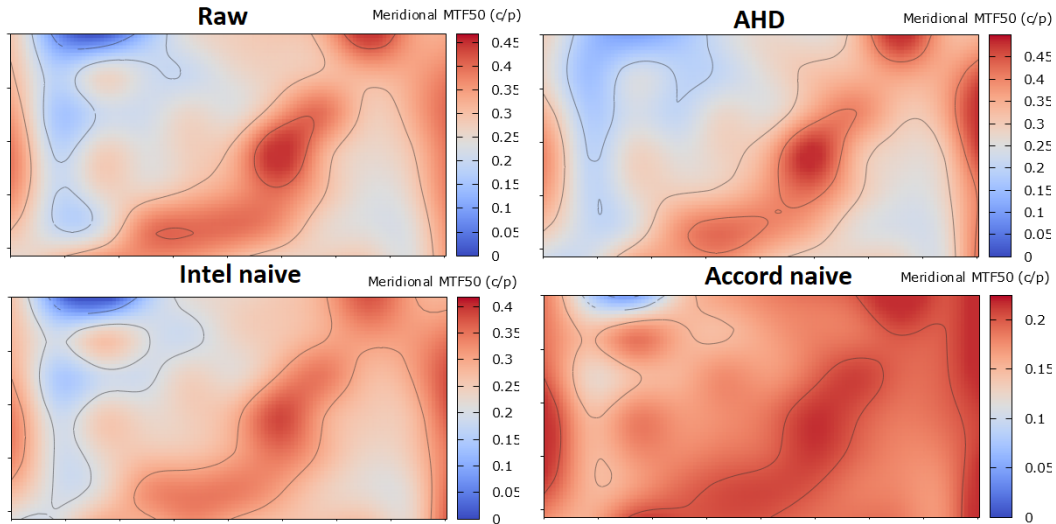


Figure 6: Meridional edge MTF50 distributions with different demosaicing algorithms, from the left: Raw (no demosaicing), AHD, Intel naive and Accord naive, the lens is in the 0° position. Larger MTF50 values mean a sharper edge.

Fig. 6 compares the same images as Fig. 5, and shows the MTF distribution. All images are obviously correspondent, so none of the algorithms changes significantly the nature of the distribution. It is also obvious that the Accord naive demosaic implementation yields substantially less sharp edges than either the raw image or the Intel naive and AHD implementations. The AHD algorithm performs altogether the best out of the selected algorithms, and is comparable to the raw image sharpness.

5. CONCLUSIONS AND FUTURE WORK

This paper has introduced a method of testing low-cost lens quality in terms of sharpness and symmetry of the lenses. It also investigated effects of some selected demosaicing algorithms on said sharpness and performed an experiment to select the best fitting of the selected demosaicing approaches. The Adaptive Homogeneity-Directed (AHD) demosaicing algorithm proved the best performer of the selected methods, and will therefore be selected for future work.

In continuation of this research the authors would like to test more algorithms than this paper shows, they would also like to investigate how various demosaicing algorithms affect the sharpness in individual chromatic components, and would like to develop a method to objectively assess the quality of wavelength compensation of the low-cost lenses (including the IR compensation). Further experiments with different slanted-edge patterns will be carried out to achieve higher spatial resolution of the MTF metric. Later we would also like to produce an automated framework for lens quality assessment.

Lastly, at the time of writing of this paper the authors have found it surprisingly difficult to convert from regular bitmap images (representing colour filter array (CFA) images) into raw image formats that would be compatible with available raw image processors for demosaicing. No available (working) file converters were found for this seemingly trivial task, the authors would therefore like to produce one in the future.

ACKNOWLEDGMENT

The completion of this paper was made possible by the grant No. FEKT-S-20-6205 - “Research in Automation, Cybernetics and Artificial Intelligence within Industry 4.0” financially supported by the Internal science fund of Brno University of Technology.

REFERENCES

- [1] T. Sorwar, S. B. Azad, S. R. Hussain, and A. I. Mahmood, “Real-time Vehicle monitoring for traffic surveillance and adaptive change detection using Raspberry Pi camera module”, in *2017 IEEE Region 10 Humanitarian Technology Conference (R10-HTC)*, 2017, pp. 481-484, doi: [10.1109/R10-HTC.2017.8289003](https://doi.org/10.1109/R10-HTC.2017.8289003).
- [2] R. Diachok, R. Dunets, and H. Klym, “System of detection and scanning bar codes from Raspberry Pi web camera”, in *2018 IEEE 9th International Conference on Dependable Systems, Services and Technologies (DESSERT)*, 2018, pp. 184-187, doi: [10.1109/DESSERT.2018.8409124](https://doi.org/10.1109/DESSERT.2018.8409124).
- [3] T. C. Wilkes, A. McGonigle, T. Pering, A. Taggart, B. White, R. Bryant, and J. Willmott, “Ultraviolet Imaging with Low Cost Smartphone Sensors: Development and Application of a Raspberry Pi-Based UV Camera”, *Sensors*, vol 16, no 10, 2016, doi: [10.3390/s16101649](https://doi.org/10.3390/s16101649).
- [4] R. C. Gonzalez and R. E. Woods, *Digital image processing*, Fourth edition. New York: Pearson, [2018].
- [5] J. A. Ball, “The Technicolor Process of Three-Color Cinematography”, *Journal of the Society of Motion Picture Engineers*, vol. 25, no. 2, pp. 127-138, 1935. doi: [10.5594/J05385](https://doi.org/10.5594/J05385).
- [6] A. Rush and P. Hubel, “X3 Sensor Characteristics”, *Journal of The Society of Photographic Science and Technology of Japan*, vol. 66, no. 1, pp. 57-60, 2003. doi: [10.11454/photogrst1964.66.57](https://doi.org/10.11454/photogrst1964.66.57).
- [7] T. Kuroda, *Essential Principles of Image Sensors*. London: CRC Press, 2006.
- [8] R. Lukac and K. N. Plataniotis, “Color Filter Arrays for Single-Sensor Imaging”, in *23rd Biennial Symposium on Communications, 2006*, 2006, pp. 352-355, doi: [10.1109/BSC.2006.1644640](https://doi.org/10.1109/BSC.2006.1644640).
- [9] Bryce E. Bayer, “Color imaging array”, U.S. Patent US3971065A, March 5, 1975.
- [10] X. Li, W. A. Pearlman, J. W. Woods, B. Gunturk, L. Zhang, and L. Lu, “Image demosaicing: a systematic survey”, p. 68221J-, doi: [10.1117/12.766768](https://doi.org/10.1117/12.766768).

- [11] E. Chang and D. Y. Pan, “Color filter array recovery using a threshold-based variable number of gradients”, in *Proceedings Volume 3650, Sensors, Cameras, and Applications for Digital Photography*; (1999), 1999, [doi:10.1117/12.342861](https://doi.org/10.1117/12.342861).
- [12] K. Hirakawa and T. W. Parks, “Adaptive homogeneity-directed demosaicing algorithm”, in *Proceedings 2003 International Conference on Image Processing* (Cat. No.03CH37429), 2003, pp. III-669-72, [doi:10.1117/12.766768](https://doi.org/10.1117/12.766768).
- [13] E Martinec, P Lee, AMAZE demosaicing algorithm. <https://rawpedia.rawtherapee.com/Demosaicing>. [As accessed 13 March 2022]
- [14] G. Horvath, *RawTherapee: Getting Started*. RawPedia Book, 2016, [RawTherapee](https://rawpedia.rawtherapee.com/).
- [15] C. S. Williams and O. A. Becklund, *Introduction to the Optical Transfer Function*, 2.nd ed. Bellingham: SPIE, 2002.
- [16] ISP 12233:2017: Photography — Electronic still picture imaging — Resolution and spatial frequency responses, 3.rd ed. Geneva: International Organization for Standardization (ISO), 2017.
- [17] K. Masaoka, T. Yamashita, Y. Nishida, and M. Sugawara, “Modified slanted-edge method and multidirectional modulation transfer function estimation”, *Optics Express*, vol. 22, no. 5, 2014, [doi:10.1364/OE.22.006040](https://doi.org/10.1364/OE.22.006040).
- [18] F. van den Bergh, “MTF Mapper: Software”, 2011, [MTF Mapper](https://rawpedia.rawtherapee.com/MTFMapper/).

VHDL-based implementation of CRYSTALS-Kyber components on FPGA

P. Jedlicka, J. Hajny

Department of Telecommunications, Faculty of Electrical Engineering and Communication,
Brno University of Technology, Technická 12, 616 00 Brno, Czech Republic

E-mail: xjedli23@vut.cz, hajny@vut.cz

Abstract—CRYSTALS-Kyber is one of the finalists of the National Institute of Standards and Technology (NIST) post-quantum cryptography competition. In this paper, we deal with effective hardware-accelerated implementations of components intended for the use in the FPGA (*Field Programmable Gate Array*) implementation of the above-mentioned lattice-based cryptography scheme. The discussed components are NTT (*Number Theoretic Transform*), inverse NTT (NTT^{-1}), CBD (*Centered Binomial Distribution*) and the Parse Algorithm (shortly Parse). The improved implementation of NTT (NTT^{-1}) requires 1189 (1568) Look-Up Tables (LUTs), 1469 (2161) Flip-Flops (FFs), 28 (50) Digital Signal Processing blocks (DSPs) and 1.5 (1.5) Block Memories (BRAMs). The latency of the design is 322 (334) clock cycles at the frequency 637 MHz which makes the presented NTT (NTT^{-1}) implementations to be currently the fastest ones. The implementations of the sampling functions (CBD and Parse) requires less than 100 LUTs and FFs with maximum latency 5 clock cycles at the frequencies over 700 Mhz. All implementations has been synthesized for the Xilinx Virtex UltraScale+ architecture.

Keywords—NTT, CBD, Parse, VHDL, FPGA, Kyber

1. INTRODUCTION

In recent years, there has been a significant progress in the field of quantum computing research. Using special algorithms, quantum computers are able to solve hard problems such as the integer factorization and the discrete logarithm much faster than conventional computers. Many of the widely used protocols with the public key that are considered to be secure are based just on the two problems mentioned above and thus they will become breakable if a quantum computer comprising a sufficient number of qubits is built. As a consequence of these facts, intensive research in the field of so-called post-quantum cryptography (PQC) has started. The PQC represents cryptosystems that are not vulnerable to quantum computer attacks. According to the currently ongoing NIST post-quantum standardization process, one of the most promising PQC cryptosystems is CRYSTALS-Kyber (shortly Kyber), a key-encapsulation mechanism (KEM) and public-key encryption algorithm.

This work presents optimized VHDL (*Very High Speed Integrated Circuit Hardware Description Language*) implementations of some crucial Kyber components such as NTT, inverse NTT and sampling functions including CBD and Parse. All implemented algorithms has been designed according to the reference implementation of Kyber in the C programming language [1].

2. RELATED WORK

Several partial or whole hardware implementations of Kyber are currently available. To the best of the author's knowledge, there is only one complete hardware implementation presented by Dang *et al.*, 2021 [2] who reached the frequency of 450 MHz on high performance devices such as Xilinx Zynq UltraScale+. Ricci *et al.* [3] present the implementation of Kyber components including NTT, inverse NTT and components based on the Keccak algorithm (SHA3-256, SHA3-512, SHAKE128, SHAKE256) using Xilinx Virtex UltraScale+ architecture. Chen *et al.* [4] present the implementation of NTT using lightweight platforms such as Xilinx Artix 7 and Xilinx Spartan 6. On the other hand, Dang *et al.*, 2020 [5] present the results of the implementation of NTT using high performance Zynq UltraScale+. Unfortunately, any of the authors mentioned above does not show the implementation results of inverse NTT. Implementation results of the sampling functions (CBD and Parse) are also not presented.

3. PRELIMINARIES

3.1. Sampling from a binomial distribution

To sample noise, Kyber uses a function CBD (Centered Binomial Distribution) described by the algorithm 1 [1]. In addition to the input byte array, there is also a parameter η at the input of the function. The double of this parameter (2η) defines the number of the input bits needed for the calculation of one coefficient of the output polynomial. Kyber uses $\eta = 2$ and $\eta = 3$.

Algorithm 1 CBD

```

1: Input: Byte array  $B = b_0, b_1, b_2, \dots, b_{64\eta-1}$ , parameter  $\eta$ 
2: Output: Polynomial  $f \in \mathcal{R}_q$ 
3:  $(\beta_0, \dots, \beta_{512\eta-1}) := \text{BytesToBits}(B)$ 
4: for  $i$  from 0 to 255 do
5:    $a := \sum_{j=0}^{\eta-1} \beta_{2i\eta+j}$ 
6:    $b := \sum_{j=0}^{\eta-1} \beta_{2i\eta+\eta+j}$ 
7:    $f_i := a - b$ 
8: return  $f_0 + f_1X + f_2X^2 + \dots + f_{255}X^{255}$ 

```

3.2. Uniform sampling

To sample elements in \mathcal{R}_q that are statistically close to a uniformly random distribution, Kyber uses a function Parse described by the algorithm 2 [1].

Algorithm 2 Parse

```

1: Input: Byte stream  $B = b_0, b_1, b_2, \dots$ 
2: Output: NTT-representation  $\hat{a} \in \mathcal{R}_q$  of  $a \in \mathcal{R}_q$ 
3:  $i := 0, j := 0$ 
4: while  $j < n$  do
5:    $d_1 := b_i + 256 \cdot (b_{i+1} \bmod 16)$ 
6:    $d_2 := b_{i+1}/16 + 16 \cdot b_{i+2}$ 
7:   if  $d_1 < q$  then
8:      $\hat{a}_j := d_1$ 
9:      $j := j + 1$ 
10:  if  $d_2 < q$  and  $j < n$  then
11:     $\hat{a}_j := d_2$ 
12:     $j := j + 1$ 
13:   $i := i + 3$ 
14: return  $\hat{a}_0 + \hat{a}_1X + \dots + \hat{a}_{n-1}X^{n-1}$ 

```

3.3. Number theoretic transform

The Number theoretic transform (NTT) is a generalization of the discrete Fourier transform, which is carried out in a finite field instead of complex numbers. Assuming a polynomial $f(x)$ with coefficients $(f_0, f_1, \dots, f_{n-1})$ and their representation in the NTT domain $(\hat{f}_0, \hat{f}_1, \dots, \hat{f}_{n-1})$, the transformations can be expressed by the following formulas [6]:

$$\hat{f}_i = \sum_{j=0}^{n-1} f_j r^{ij} \bmod(q), i = 0, 1, \dots, n-1,$$

$$f_i = \frac{1}{n} \sum_{j=0}^{n-1} \hat{f}_j r^{-ij} \bmod(q), i = 0, 1, \dots, n-1,$$

where $r = 17$ is the $2n$ -th primitive root of unity in modulo q arithmetic [1].

Kyber performs operations in the polynomial ring $\mathcal{R}_q = \mathbb{Z}[x]_q/(x^n+1)$ where n and q are two integers, i.e. $n = 256$ and $q = 3329$. Using the textbook definition for the polynomial multiplication, the achieved

time complexity is $O(n^2)$. However, the polynomial multiplication accelerated by the properties of the NTT reduces the time complexity to $O(n \log n)$. The multiplication of polynomials $f(x)$ and $g(x)$ using the NTT can be expressed by the following formula [1]:

$$f(x) \times g(x) = NTT^{-1}(NTT(f(x)) \odot NTT(g(x))),$$

where \odot is the point-wise multiplication. The NTT can be used only for the $q = 1 \bmod(2n)$ [1].

4. VHDL IMPLEMENTATION

The design has been implemented on a Virtex UltraScale+ FPGA from Xilinx in Vivado 2019.1 using the VHDL language. As the selected hardware platform and the series of the mounted FPGA suggests, the main optimization goal of the design is speed rather than area and the chosen implementation strategy corresponds to this fact. To reach as high clock frequency as possible, pipelined processing that reduces the size of combinational logic between two FFs is applied to the individual functional blocks. DSP blocks are used for almost all arithmetical operations, only incrementations or multiplications by a constant power of two are excluded. Due to the speed optimization, DSP blocks are set for the maximum latency whereas the throughput is still one output per one clock cycle. All the components follow the reference implementation [1] and their implementations are described below.

4.1. CBD

The CBD algorithm has been implemented using only Look-Up Tables and Flip-Flops. No DSP block has been utilized although there are mathematical operations. The reason of the absence of DSP blocks is a low overall number of input bits used for the calculation of one output coefficient. For $\eta = 2$, respectively $\eta = 3$, there are only 4, respectively 6, input bits. The mathematical operation based on such a small input operands can be ensured by single 6-input Look-Up Tables placed in parallel. As can be seen from the figure 1, the component uses standard AXIStream interfaces. The input data is split into η -bit fields which serves as the inputs for the parallel calculation of output coefficients. For $\eta = 2$, respectively $\eta = 3$, the input data bus has 32, respectively 24, bits and the component performs parallel computation of 8, respectively 4 output coefficients. The latency is 3 clock cycles and the throughput is one output coefficient set per one clock cycle.

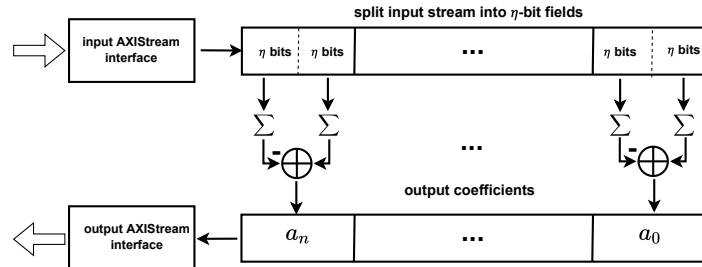


Figure 1: The block scheme of the CBD implementation

4.2. Parse

The Parse function has been implemented by applying the same methodology as in the case of the CBD algorithm including no DSP utilization and using AXIStream interfaces. The latency is 5 clock cycles and the throughput is two output coefficients set one clock cycle. The block scheme is shown in Figure 2. Invalid coefficients which do not correspond to the required range are indicated by AXIStream TKEEP signal and discarded.

4.3. NTT and Inverse NTT

The presented implementation of NTT and NTT^{-1} is based on our previous implementation described in Ricci *et. al* [3]. The NTT implementation whose block scheme is shown in Figure 3 uses 4 butterflies running in a 2x2 arrangement which leads to the computation of two iterations in parallel with 2 butterflies in each of them. Butterflies utilize Montgomery and Barrett reduction algorithm for modular reduction after multiplications. Except for input coefficients, the butterflies are supplied with the roots of unity ¹

¹ In relation to the Fast Fourier Transform also known as twiddle factors.

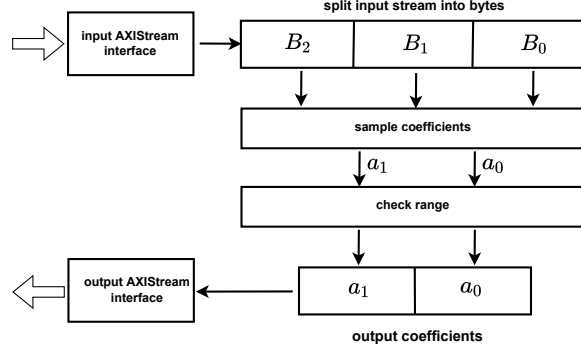


Figure 2: The block scheme of the Parse implementation

which are saved in the Read-Only memory.

The presented implementation has an improvement in added possibility for a parallel computation of two input polynomials while keeping almost the same hardware utilization. In the original version, there were delays between sets of the parallel iterations because of the latency of the butterfly structure (26 clock cycles). These delays has been eliminated by an immediate computation of the same set of parallel iterations of the second polynomial which is not dependent on the iteration results of the first polynomial. After finishing the iteration set of the second polynomial, the computation is switched back on the following iterations of the first polynomial. These feature saved approximately 80 clock cycles of the latency per each input polynomial.

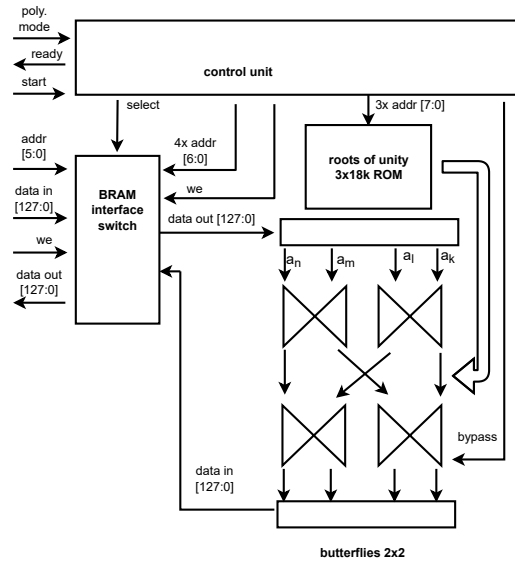


Figure 3: The block scheme of the NTT implementation

5. IMPLEMENTATION RESULTS AND COMPARISON

Table I depicts the implementation results for the presented designs and the aforementioned previous works whereas the comparison can be made only for the NTT because the other works do not mention the implementation of the NTT^{-1} and the sampling functions. The proposed HDL-based design needs on average 2 times less hardware resources and is 4 times faster than the implementation of Dang *et al.*, 2020 [5]. In comparison to the implementation of Chen *et al.* [4], our design needs on average 5 times more hardware resources but is much better optimized in terms of the clock frequency and the latency which makes our design almost 30 times faster. In comparison with our previous design (Ricci *et al.*, 2021 [3]), we have almost the same hardware utilization but, thanks to multiple polynomial calculation, we have decreased the latency by 83 clock cycles per one polynomial. Sampling functions are much less complex and thus their utilization is minimal when compared to NTT implementations.

Table I: The implementation results and the comparison with the other implementations

	LUT	FF	DSP	BRAM	LUTRAM	Frequency [MHz]	Latency [cycles]
NTT							
This work	1189	1469	28	1.5	302	637	322
Ricci <i>et al.</i> , 2021 [3]	1107	1407	28	3.5	-	637	405
Dang <i>et al.</i> , 2020 [5]	2040	3223	24	5	-	500	1271
Chen <i>et al.</i> , 2020 [4]	442	237	1	1.5	-	136	2055
Inverse NTT							
This work	1568	2161	50	1.5	368	637	334
Parse							
This work	67	94	0	0	0	702	5
CBD							
This work	56	89	0	0	0	709	3

6. CONCLUSION

To the best of the author's knowledge, we proposed in this work the fastest and most effective hardware implementations of NTT and inverse NTT which are the essential and most complex functional blocks of the lattice-based PQC schemes. The NTT and inverse NTT components are able to perform over 1,900,000 transformations per second with the clock frequency 637 MHz which is the highest reached value in comparison with the implementations of other authors whose clock frequencies are in the range between 136 MHz and 500 MHz. We also introduced highly optimized implementations of the sampling functions CBD and Parse with the clock frequency exceeding 700 MHz. These implementation results of the crucial Kyber components are great prerequisite for a highly effective and the fastest implementation of the whole cryptosystem with the clock frequency exceeding 600 MHz.

ACKNOWLEDGMENT

The presented research was financed by the Ministry of Interior under grant no. VJ02010010.

REFERENCES

- [1] R. Avanzi, J. Bos, L. Ducas, E. Kiltz, T. Lepoint, V. Lyubashevsky, J. M. Schanck, P. Schwabe, G. Seiler and D. Stehlé, "CRYSTALS-Kyber algorithm specifications and supporting documentation," *NIST PQC Round*, vol. 3, 2021.
- [2] V. B. Dang, K. Mohajerani and K. Gaj, "High-Speed Hardware Architectures and Fair FPGA Benchmarking of CRYSTALS-Kyber, NTRU, and Saber," *NIST PQC Round*, vol. 3, 2021.
- [3] S. Ricci, P. Jedlicka, P. Cibik, P. Dzurenda, L. Malina and J. Hajny, "Towards CRYSTALS-Kyber VHDL Implementation," In Proceedings of the 18th International Conference on Security and Cryptography - SECRIPT, 2021, pages 760-765.
- [4] Z. Chen, Y. Ma, T. Chen, J. Lin and J. Jing, "Towards efficient kyber on fpgas: A processor for vector of polynomials," In 25th Asia and South Pacific Design Automation Conference (ASP-DAC), 2020, pages 247-252.
- [5] V. B. Dang, F. Farahmad, M. Andrzejczak, K. Mohajerani, D. T. Nguyen and K. Gaj, "Implementation and benchmarking of round 2 candidates in the nist post-quantum cryptography standardization process using hardware and software/hardware co-design approaches," Cryptology ePrint Archive: Report 2020/795, 2020.
- [6] H. N. Nejatollahi, S. Dutt, F. Ray, I. Regazzoni, R. Banerjee, "Post-Quantum Lattice-Based Cryptography Implementations," In ACM Computing Surveys, 2019, pages 1-41.

Získej víc s IEEE



www.ieee.org

Co je to IEEE?

IEEE (Institute of Electrical and Electronics Engineers) je celosvětová nezisková organizace, která pomáhá v rozvoji technologií, inovací a excelentnosti ve prospěch lidstva. Ač vám to může znít až příliš honosně, níže najdete některé z aktivit, které tuto misi potvrzují.

Kde všude IEEE působí a kolik má členů?

IEEE vznikla v USA už v roce 1884 pod názvem AIEE. Hlavním cílem bylo spojit odborníky v elektrotechnice a sdílet nejnovější technologie ku prospěchu všech. Za jejím založením stály jména jako A.G. Bell, T.A. Edison nebo společnosti jako General Electric nebo Siemens. Značka IEEE se potom objevila až v roce 1963 po transformaci AIEE, ale to už bylo registrovaných více než 150 tisíc členů. V současnosti působí IEEE celosvětově a hlásí se k ní více než 400 tisíc členů.

Mezi hlavní aktivity IEEE patří organizování mezinárodních vědeckých konferencí, vydávání odborných publikací a mezinárodních norem (např. IEEE 802.11), podpora členů, studentské aktivity či humanitární akce.

Výhody členství v IEEE

Aktuální informace z oboru elektrotechniky

IEEE spravuje jednu z největších databází odborných publikací na světě IEEE Xplore. Tato databáze je celosvětově uznávaná a obsahuje více než 3 milióny publikací, převážně článků z konferencí a odborných časopisů.

Nástroje pro vaši kariéru

IEEE poskytuje například nástroje pro vytvoření cíleného životopisu (ResumeLab), databáze mentorů, celosvětovou databázi volných pracovních míst, atd.

Podpora odborných aktivit

IEEE vypisuje množství soutěží a grantových programů, do kterých se můžete zapojit. Váš příspěvek z EEICT můžete například přihlásit do soutěže Student Paper Contest Regionu 8. Taktéž podporuje publikační činnost a svým členům umožňuje volný přístup k licenci Overleaf PRO.

Secure Communication Between High-speed Network Gateways

P. Cívik¹, J. Hajný¹

¹Department of Telecommunications - Brno University of Technology, Czechia

E-mail: xcibik00@vutbr.cz, hajny@vut.cz

Abstract—This paper presents Field Programmable Gate Array (FPGA) powered packet-oriented solution for secure communication between high-speed network gateways which provide throughput up to 100 Gbps in each direction. To ensure data confidentiality and authenticity Advanced Encryption Standard (AES) operating in Galois-Counter Mode (GCM) with 256 bit key length is used.

Keywords—FPGA, Cryptography, Hardware acceleration, VHDL, Encryption, Decryption, AES, GCM

1. INTRODUCTION

A centralized architecture with root servers processing data from many nodes is nowadays a common trend in the field of computer networks. Servers in such architecture are responsible for coping with a huge amount of digital data and thus require offloading of data processing to hardware accelerators in order to speed-up the whole process. Confidentiality of transmitted data is also must have feature of today. Both require fast and secure solution.

This paper describes a packet-oriented solution using FPGA-based high-speed network interface card/controller (NIC) as an accelerator in the role of a network gateway. The computing power of FPGA and its high-speed interfaces ensure sufficient throughput for fast data processing. The packet-processing pipeline with AES symmetric cipher operating in GCM mode is implemented inside FPGA chip to achieve data confidentiality and authenticity at high speeds.

2. TECHNOLOGIES

Summary of main technologies used in the solution of this paper:

- **VHDL** – Very High Speed Integrated Circuits (VHSIC) Hardware Description Language is primarily used for an FPGA programming and simulation [1],
- **FPGA** – Field Programmable Gate Array is a programmable logic circuit. Configuration is specified by HDL language sources. It consists of: Input and Output Block (IOB), Configurable Logic Block (CLB) and programable horizontal and vertical interconnection [1],
- **NP4** – Netcope P4 with compiler P4₁₆/VHDL translates a P4 [2, 3] source code to a VHDL code and maps it on an FPGA platform. Compilation process is shown in the Figure 1. Netcope P4 is used in this solution to generate firmware. Its detailed description is available in [4],
- **NFB-200G2QL** – high-speed smart NIC, produced by *Netcope Technologies a.s.*, is used as a gateway. Parameters of the card are shown in the Table I [5].

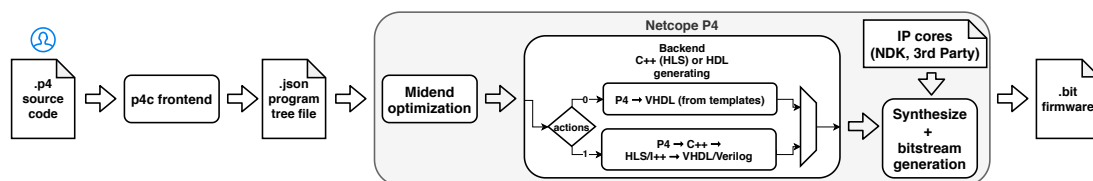


Figure 1: Compilation process

Table I: The parameters of NFB-200G2QL card [5]

Network interface	2×QSFP28
PCI Express	Gen 3 x16 + x16 (128 + 128 Gb/s)
FPGA chip	Xilinx Virtex UltraScale+ (xcvu7p-flvb2104-2-i)
On-board memory	3×72Mb QDRIIe SRAM / 3×288Mb QDRIIe SRAM

3. SOLUTION

Topology of the solution, shown in the Figure 2, consists of two NFB200G2QL boards in the role of gateway 0 (GW0) and 1 (GW1). The gateways encrypt and decrypt the whole network traffic flowing through them. Data labeled as cipher text (c) between interfaces IFC1 are encrypted, data labeled as plain text (m) are decrypted.

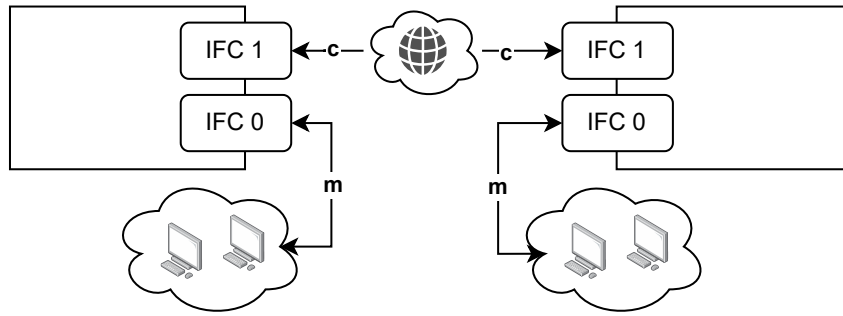


Figure 2: Gateways setup

Both cards (GW0 and GW1) are running the same firmware of logic design with high-level architecture shown in the Figure 3. The architecture consists of two atom modules, each with a separate packet-processing pipeline:

- **Atom 0** is connected to RX IFC0 (ingress port) and to TX IFC1 (egress port) - running **encryption** process,
- **Atom 1** is connected to RX IFC1 (ingress port) and to TX IFC0 (egress port) - running **decryption** process.

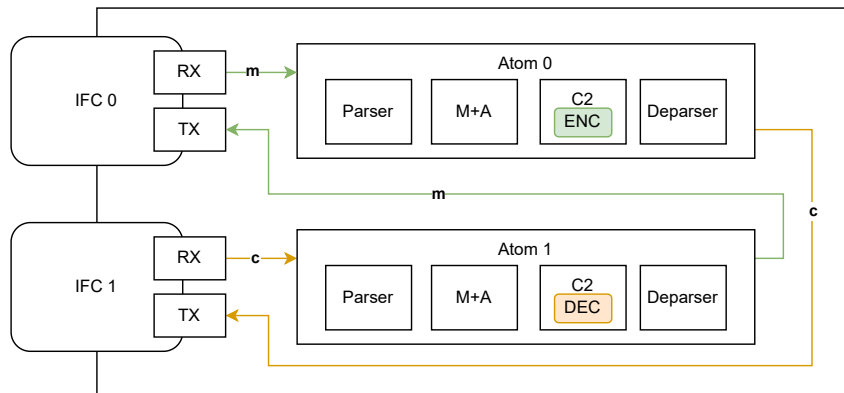


Figure 3: Firmware abstract architecture

Atom architecture consists of four main parts:

- **Parser** - parses headers and payload to separate fields (payload represents all data after last successfully parsed header). Parser behavior is defined by P4 source code.
- **Match + Action (M+A)** - implements all tables and performs various actions on packet headers and metadata values based on the P4 source code. AES keys and initial vectors (iv) are stored in these fields.
- **C2** - is a control block for cryptographic functions with access to headers, metadata and payload. The control block properly modifies the fields.
- **Deparser** - combines all fields (modified by C2) back to an outgoing packet.

The enumerated parts are also shown in the Figure 3. Tables and actions are defined by P4 source code. Their usage is configurable by rules, which are uploaded to the tables by an NP4 software tool. The rules allow us to configure different IV and/or key for various packet flows identified by specific header field values. IV and key travel from the tables as per-packet metadata through the processing pipeline.

3.1. C2 architectures

A different control block (C2) is designed for each cryptographic function. Two specific control block implementations, used also in the solution presented in this paper, are described in this section.

AES 256 GCM Encryption - encrypts a payload data of received packets and appends GCM tag after encrypted payload (shown in Figure 4). Architecture schema for encryption module is shown in the Figure 5.

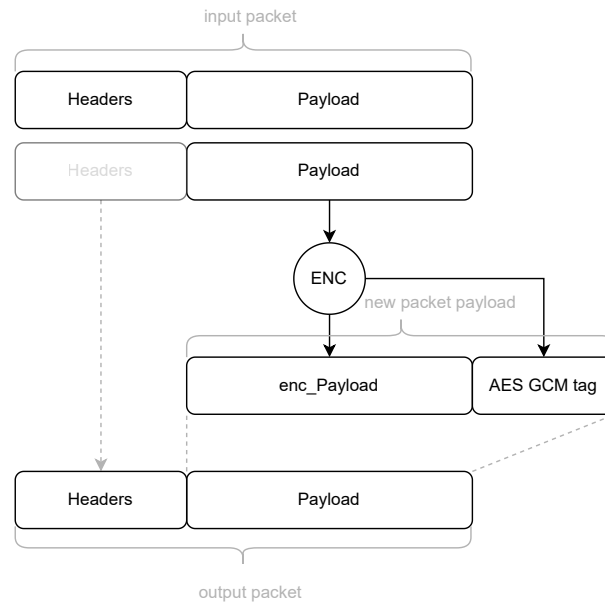


Figure 4: Packet encryption process

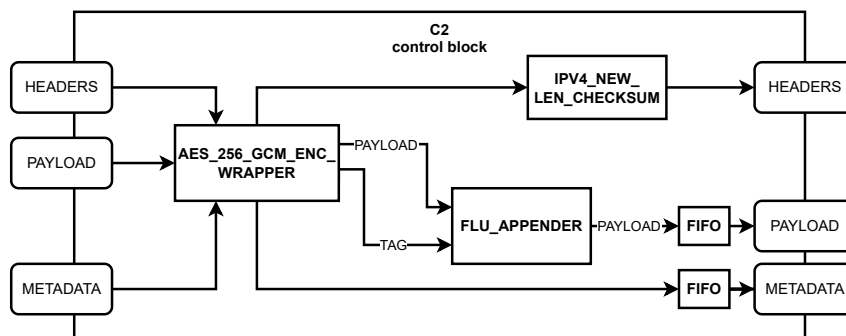


Figure 5: C2 control block architecture for AES 256 GCM Encryption

AES 256 GCM Decryption - decrypts a payload data of received packets, removes GCM tag from the payload and checks its correctness. If the tag is incorrect, the TTL (Time To Live) field in IP (Internet Protocol) header of outgoing packet is set to 0 (shown in Figure 6). Architecture schema for decryption module is shown in the Figure 7.

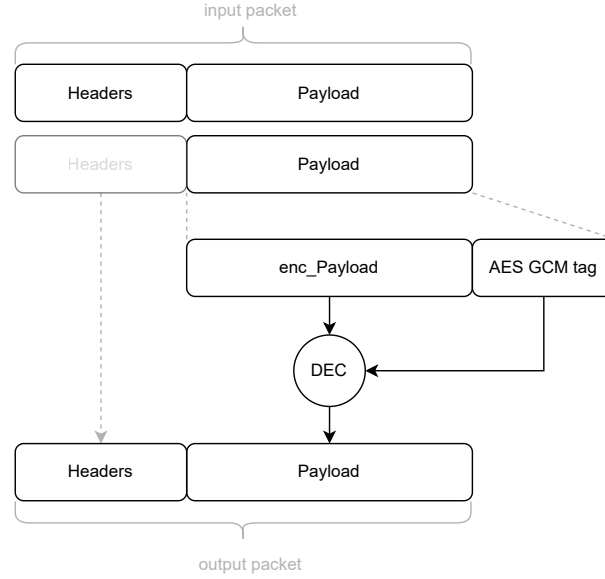


Figure 6: Packet decryption process

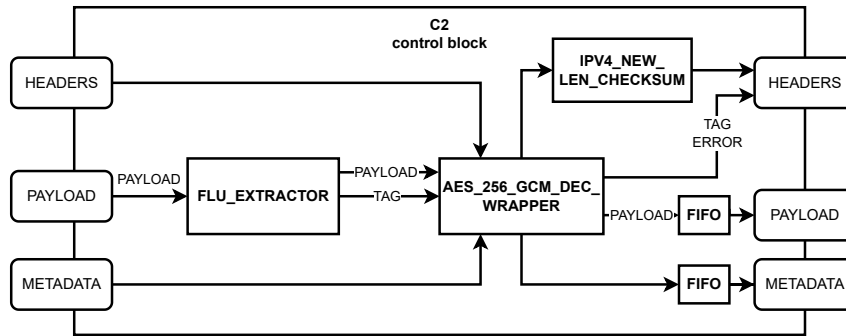


Figure 7: C2 control block architecture for AES 256 GCM Decryption

3.2. AES 256 GCM

The operations of encryption and decryption are provided by components of AES symmetric cipher with 256-bit key-length operating in GCM mode and processing 128-bit data blocks. The advantage of GCM mode is that it provides both features - encryption/decryption and authentication. The AES_256_GCM module uses four main components: Encryption, Decryption, Expansion and GCM [4].

4. CURRENT AND FUTURE WORK

Currently, we are working on the optimization of encryption and decryption components to achieve better throughput.

The first step is an overall parallelization of packet processing achievable by application of several parallel AES pipelines on a per-packet basis. Figure 8 shows an abstract scheme for parallelization of encryption process. The second step is to optimize processing of the internal AES module in order to achieve maximum throughput at minimum latency, e.g. focus on optimization of Galois Multiplication component. Current throughput state, shown in the Table II, presents our current two versions, original one and first parallelized and optimized one.

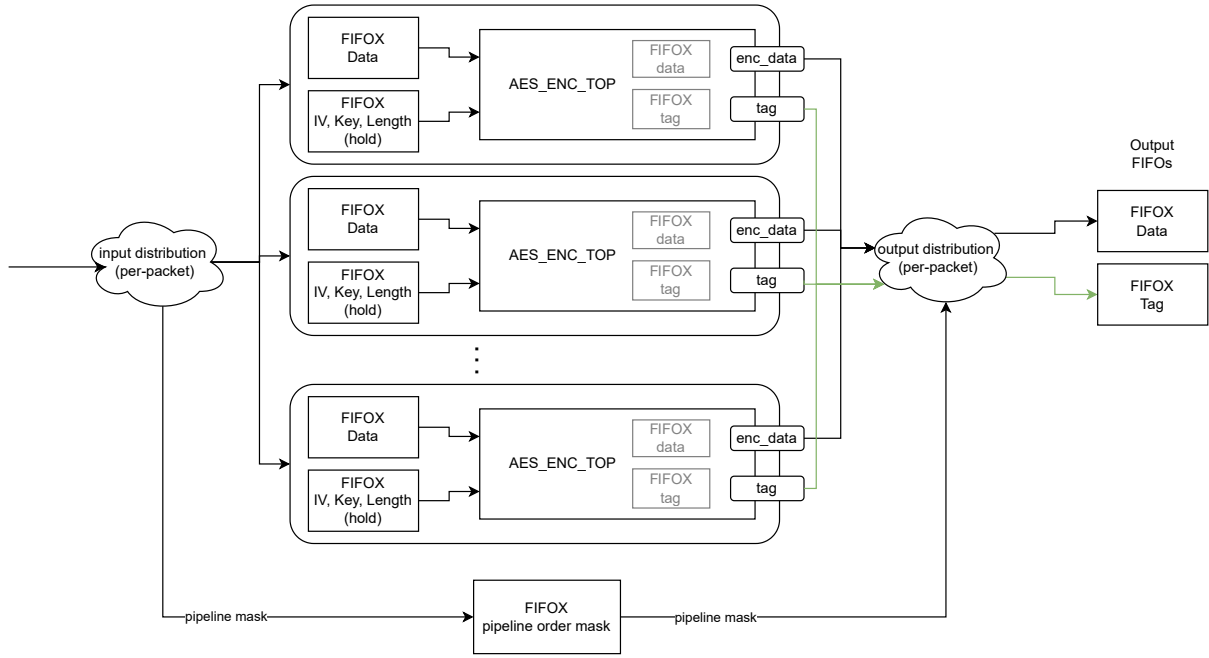


Figure 8: Abstract architecture of parallel AES top component

Table II: Current encryption core throughput for 1024 B packets

Type	Rate [Gbps]
Original	0.18
Parallelization & optimization v1.0	5.84

5. CONCLUSION

This paper describes solution based on a smart NIC with FPGA chip as a hardware accelerator and a gateway for secure high-speed packet-oriented communication. Symmetric cipher of AES 256 GCM and other packet-processing components were implemented in VHDL. Three-level verification was created for each component. NP4 compiler was extended to generate a firmware with different per-atom function depending on a data flow direction. A practical minimum viable product (MVP) was successfully demonstrated in a real environment. In future work, we expect a throughput increase achieved by further optimization and parallelization of the encryption and decryption components.

ACKNOWLEDGMENT

This work is supported by the Ministry of the Interior of the Czech Republic, program IMPAKT1, under grant VJ01010008, project Network Cybersecurity in the Post-Quantum Era.

REFERENCES

- [1] PINKER, Jiří a Martin POUPA. *Číslicové systémy a jazyk VHDL*. Praha: BEN - technická literatura, 2006. ISBN 80-7300-198-5.
- [2] BOSSHART, P.; DALY, D.; GIBB, G.; aj.: *P4: Programming Protocol-Independent Packet Processors*. *ACM SIGCOMM Computer Communication Review*, year 3, Num. 44, 2014: s. 87–95, ISSN 0146-4833
- [3] *P4 16 Language Specification*. Version 1.2.0-rc. The P4 Language Consortium, 2019. Available from: <https://p4.org/p4-spec/docs/P4-16-v1.2.0.pdf>
- [4] MALINA, Lukáš, David SMÉKAL, Sara RICCI, Peter CÍBIK and Jakub HRABOVSKÝ. *Hardware-Accelerated Cryptography for Software-Defined Networks with P4*. SECITC, 2020.
- [5] Netcope products: *Netcope FPGA boards (NFB)* [online]. [cit. 2019-11-11]. Available from: <https://www.netcope.com/en/products/fpga-boards>

Readiness of Anonymous Credentials for Real Environment Deployment

Raúl Casanova-Marqués^{1,2} and Petr Dzurenda¹

¹Department of Telecommunications, Brno University of Technology, Brno, Czech Republic

²Institute of New Imaging Technologies, Universitat Jaume I, Castellón, Spain

E-mail: casanova@vut.cz, dzurenda@vut.cz

Abstract— Attribute-based Credentials (ABCs) are a promising technology for protecting users' privacy and digital identity. We can use ABCs in a multitude of contexts. For instance, we can prove the validity of transportation tickets, demonstrate the legal age, prove the health status, or certify access rights in the company environment. All of this, we can do without disclosing complete personal identity. Nevertheless, ABCs generally require computational power that some wearable devices cannot cope with. In this paper, we present our implementation of a privacy-enhancing authentication system based on ABCs technology. The system is suitable for deployment in real-world scenarios and uses a wide range of differently powerful user devices (e.g., smart cards, smartphones, and wearables). Based on our implementation results, we also discuss the implementations aspects of ABCs, their readiness, and usability in real-world applications.

Keywords— PEAS, Privacy-Enhancing, Authentication, Identity, Cryptography, Deployment, Constrained Devices, MULTOS, Java Card, Android, Wearables.

1. INTRODUCTION

Digital privacy has become one of the hottest topics recently. Daily, users use different services that can jeopardize their privacy, reveal and compromise their identity. These services include personal tickets for public transportation, access to university or work institutions using personal cards, access to online cloud services, and many others. Service providers may profile and track their users because of the usage of unique personal information during user authentication. They can learn users' interests and movements. Due to the current increase in electronic authentications, user privacy become even more important topic. Therefore, it is necessary to develop systems that allow not only to authenticate, but also to protect the identity and privacy of users.

Anonymous Attribute-based Credentials (ABC) systems are introduced as a technology capable of preserving privacy and protecting the identity of users in insecure scenarios. These schemes permit anonymous authentication of users without disclosing their personal data such as their name, age, or nationality. In addition, they provide unlinkability or untraceability of authentication transactions. This technology would enable the use of public transportation by only demonstrating a valid ticket, accessing a corporate environment, or proving the health status without revealing the user identity. However, ABCs schemes have some drawbacks to consider. Due to the computational complexity that these protocols require, wearable and other restricted devices are not powerful enough to provide feasible runtimes for implementation in real-world environments. Furthermore, user revocation also stands as a challenge for attribute-based credential systems, see [1] for more details. The authors of [2] designed and implemented an attribute-based authentication system for standard smart cards. Although this scheme did not provide for user revocation, the results on MULTOS-based smart cards were superb. Recently, the authors presented an extended version of their implementation [3]. This extension includes revocation mechanisms from [1] also with promising results.

In this paper, we present a real environment implementation of our Privacy-Enhancing Authentication System (PEAS) which is based on the cryptographic core presented in [3]. Our implementation supports all sets of privacy-preserving features (i.e., anonymity, unlinkability, and untraceability) and involves several personal devices with different computational power. The paper concludes with a discussion on our PEAS implementation results, implementations aspects, and overall readiness of the ABCs technology for real-world applications.

2. PRIVACY-ENHANCING AUTHENTICATION SYSTEM

In this section, we introduce our PEAS system, its architecture, building blocks, and mechanisms for privacy-preserving authentication that does not disclose the entire user identity to a verifier. In fact, users reveal only a bit of information about their identity throughout the verification procedure (e.g., name, citizenship, affiliation). PEAS authentication sessions are anonymous, unlinkable, and untraceable. As a result, the authentication scheme ensures users' privacy, and therefore, prevents profiling and tracking of users. However, the revocation and identification of malicious users, who committed a misconduct, remain possible by involving a third trusted party called Revocation Authority.

The cryptographic core of PEAS is built on Revocable Keyed-Verification Anonymous Credentials (RKVAC) proposed in [3]. The core is optimized and extended for deployment in real applications. In addition, it is also practical to run on restricted platforms such as smart cards, smartphones, and smartwatches. The developed system is user-focus, which implies that users are the true owners of their personal data, and hence, have control over what information to share with whom and when. The PEAS implementation consists of software applications for all involved system entities, i.e., Issuer of attributes, Revocation Authority, Verifier of attributes, and User devices holding the personal attributes. The architecture is depicted on Figure 1.

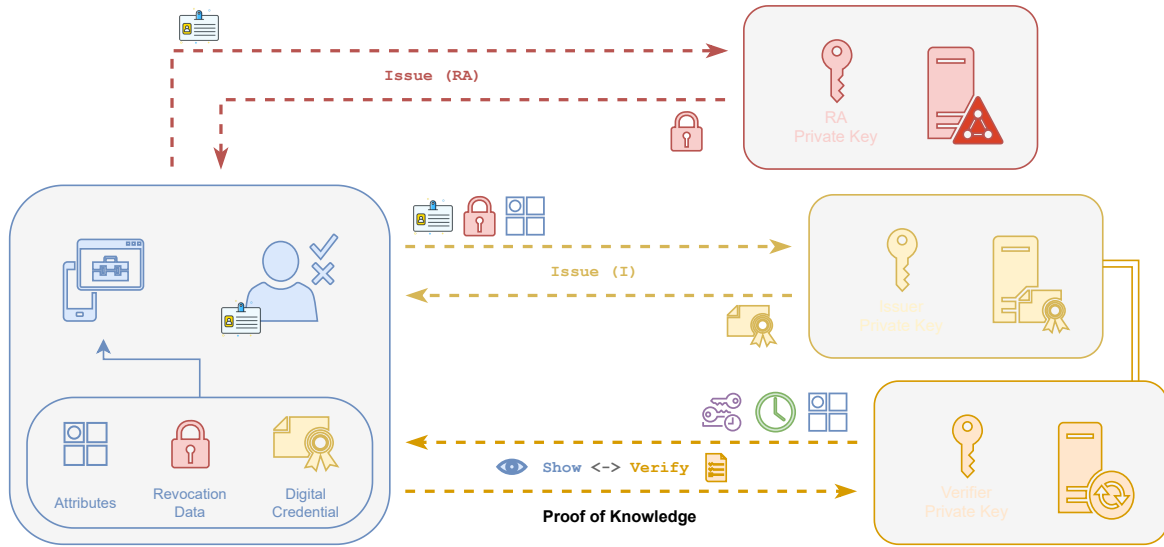


Figure 1: Architecture of the PEAS system.

2.1. Implementation Details

PEAS is extremely modular in its implementation. The front-end components are built as web-based or mobile applications and may be expanded independently with additional features. The PEAS core consists of standalone applications which comprise all basic and cryptographic operations, and allow system entities to communicate with each other. Communication is conducted using channels such as Transmission Control Protocol over Internet Protocol (TCP/IP), Personal Computer / Smart Card (PC/SC) including Near-Field Communication (NFC), and Bluetooth. All PEAS fundamental pieces may be readily upgraded and layered. Additionally, we used docker for straightforward deployment.

The PEAS core is developed in the C programming language and relies on several third-party libraries. Namely, we used `pcsc-lite` and `ccid` libraries for PC/SC connections; `libjson` and `libwebsockets` for web server connections; `zlib`, `gmp`, `openssl`, and `mcl` for cryptographic support, as well as our `libpeas` library for RKVAC operations. Moreover, the core allows the entities that constitute the system to carry out the following operations: 1) Issuer holds Issuer's Private key for creating digital credentials (i.e., signing user's attributes), 2) Revocation Authority holds RA Private key for creating revocation attributes for users, 3) Verifier shares Issuer's Private key with Issuer and verifies users' anonymous credentials, 4) User holds and proves possession of his/her attributes to Verifier within presented anonymous credentials.

2.2. PEAS web servers

The front-end uses the PEAS core to operate. The web layer allows controlling intuitively the core operations through a web interface, and log all the activities that are being conducted. We employed JavaScript, Node.js, HTML, CSS and Vue web technologies, including the third-party library, Vuetify (2.4.5), for setting up the GUI components.

The web-based PEAS implementation proffers the following protocols/communication interfaces among the fundamental components: a) Rest API: allowing communication between the Graphical User Interface (GUI) and the web server when the GUI initiates the communication. b) Web Socket: permitting communication between the GUI and the web server in real-time, or when the web server initiates the communication. c) Stdio: enabling web servers to pass instructions into console apps.

2.3. PEAS user devices

To further the vision on the scope of PEAS in real use cases, we developed the user applications for Android-based smartphones and smartwatches, and MULTOS and Java Card smart cards. They are fully compatible with each other, and can communicate with the other entities in the system. The applications conduct all cryptographic steps necessary for attribute ownership verification, and work with up to nine personal attributes that can be issued repeatedly. The tenth attribute is reserved for the revocation attribute issued by the Revocation Authority, allowing us to revoke user credentials from the system.

The Android applications match the current trend of people utilizing their phones/smartwatches as personal items, and allow users to avoid using smart cards. On the other hand, smart cards provide a secure hardware module for storing and processing sensitive data such as cryptographic keys. They are used in applications with both tamper-resistance and tamper-evidence requirements.

Smartphone and smartwatch applications are developed in the Java 14.0.1 programming language, and employ low-level functions written in C to speed up the PEAS cryptographic core. To do so, we used the Android Native Development Kit (NDK). In addition to the standard Android and Java libraries, we used the com.herumi.mcl third-party library for cryptographic operations. Both applications can use NFC and Bluetooth technologies to communicate with other entities in the system. Moreover, personal access to the program can be protected by a 4-digit Personal Identification Number (PIN) or the user's fingerprint. For security considerations, attribute issuance can be disabled.

3. EXPERIMENTAL RESULTS

We utilized personal devices to interact with PEAS system via PC/SC and Bluetooth communication interfaces. In particular, we used MULTOS contact smart card using T=0 protocol, Java Card contactless smart card using T=1 protocol. Both smartphone and smartwatch support NFC and Bluetooth.

The hardware and software specifications of benchmarked user devices are as follows: MULTOS ML4 (MCU: SC23Z018, OS: MULTOS 4.2, RAM: 2.0 KB), Java Card J3H145 (MCU: P60D144, OS: JCOP 3 v3.0.4, RAM: 2.558 KB), Galaxy S21 5G (SM-G991B/DS; CPU: Exynos 2100, OS: Android 12, RAM: 8 GB), Galaxy Watch4 Classic (4WPN; CPU: Exynos W920, OS: Wear OS 3.2, RAM 1.5 GB), and Galaxy Watch Active2 (2D8E; CPU: Exynos 9110, OS: Tizen 5.5.0.2, RAM 1.5 GB).

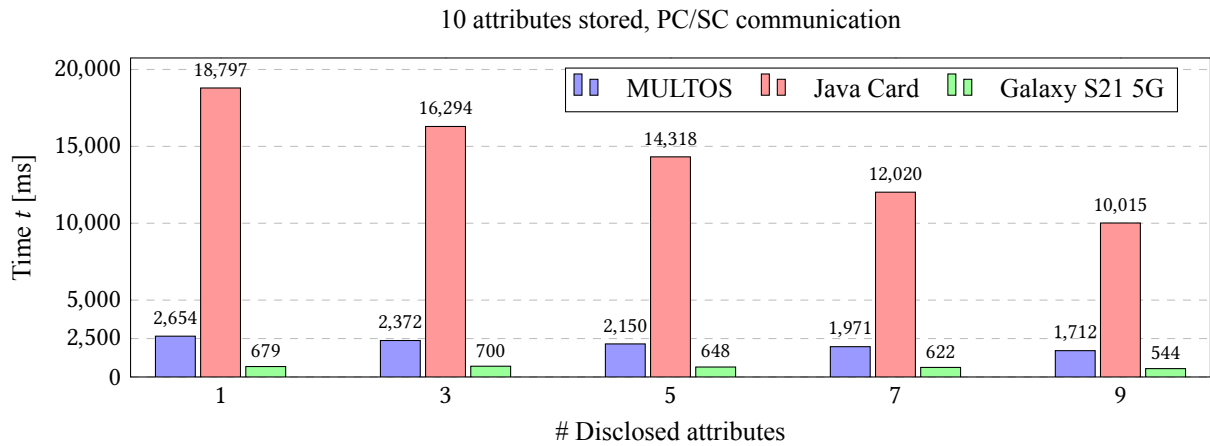


Figure 2: Speed comparison of PEAS execution (user part) on PC/SC-enabled devices.

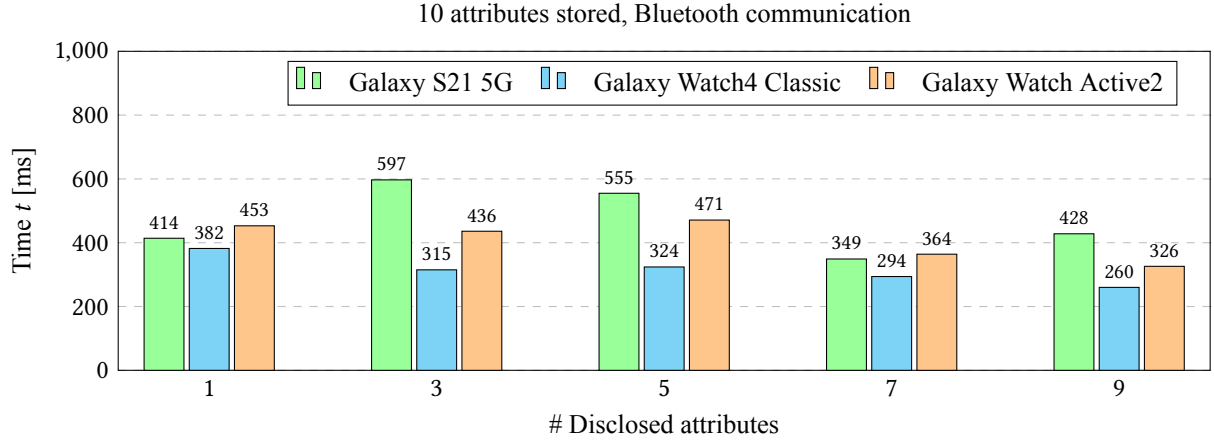


Figure 3: Speed comparison of PEAS execution (user part) on Bluetooth-enabled devices.

The Figure 2 shows results for devices using PC/SC for transmitting data. The Figure 3 comprises the results of those devices which use Bluetooth. The benchmarks reflect the computation time plus the communication overhead. We measured and expressed the benchmarks in milliseconds. Furthermore, we used a standard personal computer to run the Issuer, Verifier and Revocation Authority entities, while the user entity was represented by smart cards, smartphones, and smartwatches. As can be seen in Figure 2, the performance of smart cards is not the fastest. The Java Card results are impractical for deployment in real environments, so they are shown only for comparison. Moreover, in the case of the smartphone, it can be observed in Figure 3 that using Bluetooth as communication technology, the transmission overhead is considerably reduced, achieving faster results. Smartwatches can also be deemed viable due to their computing time.

4. READINESS AND IMPLEMENTATION ISSUES

Our PEAS system uses the ABCs scheme introduced in [2]. This scheme shows significantly better performance results than other ABCs state-of-the-art solutions such as U-Prove or Idemix. Although the performance results yield promising results, the computational power required by the scheme would hinder the implementation of ordinary smart cards. On the one hand, MULTOS-based cards can offer an optimistic solution if we consider a smaller number of personal attributes stored in the credentials (e.g., less than 5). However, the main drawback is to find manufacturers who provide all the indispensable cryptographic operations. MULTOS-based cards include support for operations on elliptic curves only on demand. On the other hand, Java Card technology-based smart cards are absolutely impracticable due to the absence of elementary cryptographic operations. The Java Card cryptographic Application Programming Interface (API) supports execution of some standard protocols on the coprocessor, but not access to modular arithmetic operations and elliptic curve operations. The software implementation of these operations adds significant overhead and unduly slows down execution, hampering the development of attribute-based authentication schemes.

During the PEAS implementation, we identified several flaws that may be used to attack the system, compromise the user's privacy, and lead to either a partial or entire loss of privacy and anonymity. These vulnerabilities are located in the transmission phase of the nonce, the epoch, and the list of attributes to be disclosed, and they are feasible because the user does not verify the origin of the data, see Figure 4.

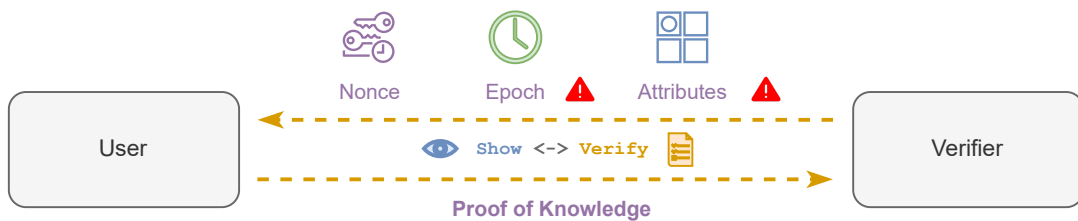


Figure 4: Security flaws during the Show and Verify algorithms.

System developers should consider the following aspects during the deployment of ABCs:

- *Unauthorized APDU commands* — Anyone can send personalization, issue revocation information, or issue attributes.

Solution: We devised a life cycle for the protocol's execution. It is not possible to personalize the smart card or the Android application again once it has been personalized. It also applies to the issuance of revocation information and attributes. However, it is possible to issue the attributes multiple times in the Android application by explicitly enabling it in the application settings.

- *Malicious epoch* — Either a verifier or an external attacker can send a malicious epoch (e.g., short or too large, repeating the old ones, etc.) and corrupt the proper functioning of the protocol.

Solution: The epoch must be digitally signed by the verifier so that the user may be sure it came from a genuine entity in the system.

- *Identity disclosing risk* — A dishonest participant might start the conversation by requesting the entire set of attributes, resulting in a total loss of privacy and anonymity.

Solution: Verifiers must have a certificate signed by a trusted authority whose legitimacy can be proven by users. The certificate must include the attributes that the verifier can request to disclose.

Before adopting the ABCs system, aforementioned security issues should be addressed. Furthermore, it should be noted that it will increase the complexity of the system and slow down its execution. Even if we consider ABCs without our security extensions suggested above, the usage of smart cards remains impractical. On the other hand, smartphones and smartwatches are a practical and realistic choice. In fact, they follow current user interest, since they are faster and more user-friendly. The device display can provide an interface to users, allowing them to know and decide which attributes will be disclosed.

5. CONCLUSION

In this paper, we developed and implemented the PEAS system in everyday devices. The system is based on an attribute-based credentials protocol with the capability to revoke users. PEAS was tested on smart cards, smartphones, and smartwatches. Performance on smart cards leaves much to be desired due to lack of vendor, cryptographic operations support, and limited resources. On the other hand, performance on smartphone and smartwatch devices is promising. We identified some weakness that should be considered during the deployment of ABCs to the real-world applications. The issues stem mostly from a lack of data authenticity in communication. Nonetheless, as the results show, current ABCs are practical and eligible for deployment in real-world contexts, particularly when we consider wearables and smartphones as user devices. These devices are fast and can execute the scheme smoothly, even when the protocol's complexity is raised owing to our security needs.

ACKNOWLEDGMENT

The authors gratefully acknowledge funding from European Union's Horizon 2020 Research and Innovation programme under the Marie Skłodowska Curie grant agreement No. 813278 (A-WEAR: A network for dynamic wearable applications with privacy constraints, <http://www.a-wear.eu/>), and from DOPRAVA 2020+ programme under the Technology Agency of the Czech Republic grant agreement No. CK03000040 (Protection of data flows in shared means of transport).

REFERENCES

- [1] J. Camenisch, M. Drijvers, and J. Hajny, "Scalable Revocation Scheme for Anonymous Credentials Based on n-times Unlinkable Proofs", in *Proceedings of the 2016 ACM on Workshop on Privacy in the Electronic Society*, 2016, pp. 123-133.
- [2] J. Camenisch, M. Drijvers, P. Dzurenda, and J. Hajny, "Fast Keyed-Verification Anonymous Credentials on Standard Smart Cards", in *ICT Systems Security and Privacy Protection*, Cham: Springer International Publishing, 2019, pp. 286-298.
- [3] J. Hajny, P. Dzurenda, R. Casanova-Marqués, and L. Malina, "Privacy ABCs: Now Ready for Your Wallets!", in *2021 IEEE International Conference on Pervasive Computing and Communications Workshops and other Affiliated Events (PerCom Workshops)*, 2021, pp. 686-691.

Experimental Platform for Sensor Fusion Positioning Methods Evaluation

R. Juran¹

¹Brno University of Technology, Faculty of Electrical Engineering and Communication,
Department of Telecommunications, Technická 12, 61600 Brno, Czech Republic

E-mail: radovan.juran@vut.cz

Abstract—Position and context awareness is becoming greater in importance as one of the key enablers of the Industry 4.0 concept, with impact on analysis and optimizing production processes, their direct control, increasing and ensuring the safety of personnel and technology, as well as enabling traceability of products. There are many approaches to achieve a real-time location system (RTLS) capable of providing positioning data, yet each approach usually has its limits given by the physical principles of technology which it is primarily based on; mostly a wireless signal transmission where the performance boundaries lay in non-line-of-sight (nLoS) scenarios. Current literature already presents various approaches capable of dealing with these shortcomings and presents various combinations of sensors based on different phenomena, the drawbacks of which are mutually compensated, known as sensor fusion. This work presents practical design of a compact platform, which utilizes Ultra-WideBand (UWB) as one of the predominant wireless technologies for wireless positioning with IEEE 802.15.4z compliant radio integrated circuits in cooperation with a 9-axis absolute orientation sensor, expandable with add-on boards.

Keywords—UWB, IMU, sensor fusion, SR040, SR150, positioning, localisation

1. INTRODUCTION

The spectrum of the Industry 4.0 concept is really broad, as are the benefits and new possibilities of flexible manufacturing that the implementation of digital technologies can bring to manufacturing. The digitization focuses on automation and optimization of production as a whole: it benefits from machine to machine communication (M2M), collects data, helps to better plan, manage and predict production. Thus, application of digital technologies can significantly increase the production and competitiveness of manufacturing companies. Position awareness is an integral part of the Industry 4.0 concept of Industrial Internet of Things (IIoT) usually referred to as Real Time Location System (RTLS) or Indoor Positioning System (IPS). Such scalable localization systems for industrial applications reduce asset search time, speed up manufacturing and logistics processes, and optimize material flow with dynamic real-time location data for each product or a part of the production [1].

The use of any GPS-like system is problematic inside buildings, because the signal is usually weak to penetrate the walls, hence it is necessary to design and manage a special local infrastructure for an indoor location system. There are many approaches to do so, utilizing technologies based on various physical principles, both passive and active wireless radio technologies, such as RFID, Wi-Fi, Bluetooth or Ultra-Wide Band (UWB), or motion sensors, such as accelerometers, gyroscopes and magnetometers. Each of these technologies have fundamental pros and cons, stemming from the nature of the physical principles on which they are based. To overcome these shortcomings, descriptions of the principle called *sensor fusion* appears in the literature, with already promising results published. It involves various data filters, algorithms for the data fusion, including machine learning classification, and many other aspects opened for research and practical industrial applications.

As for the wireless part, the UWB impulse radio is now in the spotlight as very promising, accurate and robust technology for precise localisation and positioning with centimeter accuracy, becoming one of the key enablers of industrial RTLS systems. With new chips available in the market and their integration to mobile devices by major players such as Apple or Samsung followed by others, wearables, and other consumer electronics, or automotive key fobs, there is a significant stimulation of innovation and integration of UWB radio. Estimated number of sold UWB chips is expected to further grow at least by 2025, as presented with reference to [2] in publicly available documents [3], which in terms of numbers means over 1 billion annual UWB technology-enabled device shipments [1], opening new opportunities along with new challenges to cope with.

2. UTILIZATION OF UWB AND SENSOR FUSION IN REAL TIME LOCATION SYSTEMS

The ultra-wideband (UWB) technology operates in a spectrum of 3.1–10.6 GHz [1]. This technology is not entirely new, but it is experiencing a renaissance these days thanks to new possibilities of using the radio spectrum, sanctioned by the FCC (US) and ETSI (EU) especially considering transmission power levels and spectrum usage. Thanks to its simplicity, robustness and time granularity given by transmission of short impulses in a wide band (channels of 500 MHz) and thus ability to obtain an accurate Time-of-Flight (ToF) between the transmitter and receiver, it is able to calculate nearly instantly mutual relative position of the two devices withing ranges exceeding higher tens of meters. This is incomparable to systems relying for example on received signal strength indication (RSSI), which can be easily attenuated by real world environment, where multi-path and interference occurs.



Figure 1: The History of UWB, image inspired by [1]

Based on results available in literature, using the inertial measurement units (IMU) in combination with the UWB to optimize positioning accuracy appears to be potentially advantageous in general, because each of these technologies is based on a different physical principle, which provides unique desired properties, but on the other hand creates certain limitations, deviations and errors.

The potentially positive effects of the combination and integration of the IMU with the UWB are especially valuable in the case of non-line-of-sight (nLoS) scenarios, where barriers between the transmitter and receiver in the environment lead to degradation or complete loss of the UWB radio signal. On the other hand, the published literature describes the sole use of only IMU sensors for localization rather than problematic, as these sensors generally suffer from instability of their own bias, noise and cumulative position drift error after a certain period of operation. With accumulation it becomes a systematic error and thus the accuracy of the results decreases [4, 5, 6, 7].

It would have been worth a complex, comprehensive research review of its own to describe the variety of the sensor fusion methods already implemented or opened to discussion, which is out of the scope of this work, with and will be the goal closer to achieve only after the evaluation of the device presented in this work. Therefore, this part shall present a paradigm, based on fact that literature offers already a lot of methods of sensor fusion. With a suitable combination of accelerometer, gyroscope and magnetometer, all angles to the horizontal starting position can be determined and mutual drift can be compensated, or the mean square error can be further reduced using more reference sensors [7, 8]. There are also algorithms and methods of signal filtering that can contribute to further suppression of the mentioned inaccuracies, such as the Kalman filter and its varieties [4, 5].

Table I shows comparison of several works from recent time period, which usually refer to to Quorvo (formerly Decawave) DWM1000 chip as the base for UWB communication, compliant with the standard IEEE 802.15.4-2011. There is not yet any larger research or evaluation hardware capable of the latest IEEE 802.15.4z, presented as the mainstay of this work by the NXP SR040 (and SR150 respectively), either as UWB tag alone or in sensor-fusion context. This encourages the development of an own, open platform, capable of meeting the latest standards and trends as a basis for comparative experiments.

Table I: Comparison of sensor fusion methods, means of their evaluation and error correction towards pure UWB

Reference	Year	Method
[4]	2020	Radio chip DWM1000 and IMU chip MPU9250, Kalman filter
[5]	2020	Radio chip DWM1000 and Pixhawk platform, Kalman filter
[6]	2020	Pure IMU, integration of accelerometer and gyro data, moving average
[7]	2021	simulation
[8]	2019	simulation, DWM1000 on Pozyx platform (IEEE 802.15.4-2011), PX4 Flow sensor

However, there are also two major throwbacks of sensor fusion tag technology mass production, where cost plays significant role. Firstly, the introduction of algorithmic methods generally increases the overall performance requirements and secondly, more accurate data samples require a higher sample rate, which in both cases increases the overall power requirements, which is a critical parameter for a battery-powered device with long battery life expectation. This even further increases with the number of sensors used together with the dimensions of the final device design and its final price. Yet, this might remain an application-dependent question.

As an example, let us discuss a publicly available data-set accompanied by article reference [8], which can be used for describing the data fusion in terms of principles of algorithms and their results. The authors present a simulator, which they designed based on their own measurement campaign in a known environment from a set of real sensors utilizing physics simulator tool called Gazebo and machine learning methods to describe the model of environment based on collected data samples, in which authors simulate tracking of a forklift model. Algorithm used in this case utilizes Kalman filter, a method widely used to address tracking problems, in this case iterated extended Kalman filter (IEKF). The IEKF is then applied by the authors to the pure UWB x, y coordinates data, then UWB plus IMU and finally UWB, IMU and PX4 optical flow sensor. Their results show mean absolute error with 95% confidence interval. For using solely UWB in their strongly nLoS scenarios the average error exceeded 1 m with large variance, but adding IMU reduces the error considerably to tenths of a meter. On top of that, introducing optical flow sensor gets the error below 0.2 m. Considering LoS situation, the results of each approach are closely bounded around expected (true) trajectory.

Authors of [8] claim, that UWB location accuracy is strongly LoS dependent, and thus justify the sensor fusion method as a clear way to increase the overall localization accuracy of a RTLS system. Yet, if the authors admit, that when there is a strong LoS for UWB, it is capable enough on its own, thus opening question of the system cost – on the one hand, mass production of such tracking tags can increase the cost of acquiring them, but at the same time it can save the cost of covering larger spaces with a sufficient number of UWB anchors to ensure sufficient LoS; on the other hand, if the target environment of the deployed RTLS system contains previously known obstacles, or the location of the anchors is sufficient for normal operation of this system, then the remaining sensors would remain practically unused, thus being redundant both in cost and occupied space.

3. DESIGN OF RTLS TAG PLATFORM FOR SENSOR FUSION EVALUATION

The design is based on the evaluation kit by MobileKnowledge [9] and is intended to become its modular extension, as well as being able to get integrated into any other existing RTLS ecosystems. The core is QN9090 MCU by NXP, which incorporates low-power MCU based upon Arm Cortex-M4 CPU, equipped by Bluetooth Low-Energy (BLE 5.0), and NFC capabilities. Via the SPI bus, the SR040 UWB radio integrated circuit is connected to the MCU, intended to be used as a tag (transmitter) with its counterpart SR150 as an anchor (receiver). The I2C bus is mainly used to communicate with the BNO055 9-axis sensor, which is highly integrated inertial measurement unit consisting of an accelerometer, a magnetometer and a gyroscope. On top of that, being based on the capabilities of the tags in the kit, NXP EdgeLock secure element SE050 is also part of this platform, utilizing the I2C bus. As the proposed device is not a customer-oriented product, but is intended to provide a data acquisition platform for research and evaluation, the space constraints play no role here and thus all the buses and leftover GPIO pins are accessible, with the idea of prototyping in mind. Also, as the time advances, USB-C enters consumer electronics as well as the designer labs, hence USB type C connector will be incorporated for powering and communication.

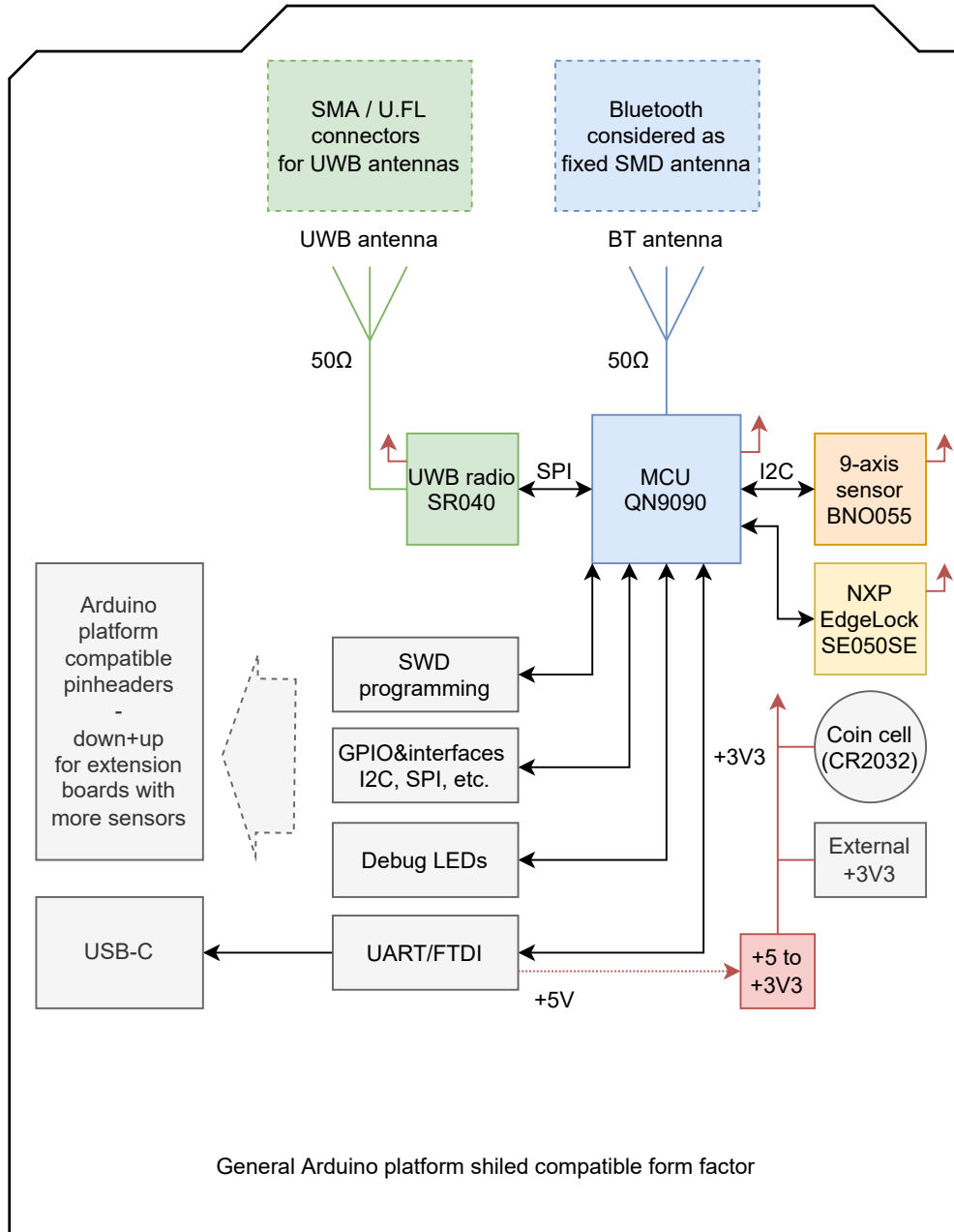


Figure 2: Block scheme of the proposed evaluation platform on an Arduino-compatible shield

At the beginning of the project, there was an idea to utilize a planar antenna directly on the board, as there are this kind of solutions available for free on-line (e.g. Quorvo). This solution would however require pretests and evaluation, especially with intention of use higher frequencies (e.g. 8 GHz of UWB Channel 9). Thus, being a prototyping board, a SMA / U.FL antenna connector was chosen to consider to be used to further open abilities of the platform to also assess various antenna designs in practical scenarios. All the signal paths shall be calculated to 50 Ω to meet impedance matching.

Embracing the portability and universality, the board keeps Arduino-compatible shield pin-header layout, as this platform is used by authors of the corresponding kit for their anchor board, and other manufacturers kits such as most of the NXP dev kits, STM Nucleo boards etc., so it can work either standalone or become an extension itself, based solely on the developer's preferences of intended MCU and other functionalities to be used. This opens versatility for data collection across many common embedded development platforms, as well as utilizing other already available Arduino-compatible shields with other various sensors, with the possibility to incorporate them into the sensor fusion system.

4. CONCLUSION

In this paper, the concept of sensor fusion approach to RTLS and IPS systems is described. This idea shall address the performance boundaries of purely wireless-radio based systems, which lay in nLoS scenarios, affected by distortion, multi-path or signal loss. These methods published in literature seem promising in terms of position accuracy improvements and overall error reduction, which represents a generally accepted paradigm, that sensor fusion is worth its attention.

On the other hand, available results of algorithmic methods are usually scattered among various types of hardware used for data acquisition. This is the key motivation for developing of a testing platform for evaluation, whose center of gravity is the UWB, as one of the predominant RTLS technologies, together with IMU sensors and extended modularity which benefits from versatility of Arduino-platform shield pinout. Another key contribution besides ability to change the antenna for any off-the-shelf or custom type is that the proposed platform can itself get integrated into an ecosystem of most available evaluation and development kits, making it a more versatile platform for wider variety of applications.

This all-in-one platform shall open way for comparative evaluation and validation studies of sensor fusion methods, which is a natural follow-up step for the future work. Attention will also be focused on verification and possible optimization of the proposed design in another iterations.

ACKNOWLEDGMENT

This work was supported by the Technology Agency of Czech Republic project No. FW03010424.

REFERENCES

- [1] A. Zignani and S. Tomsett, "Ultra-wideband (uwb) for the iot – a fine ranging revolution?" 2021. [Online]. Available: <https://www.nxp.com/webapp/Download?colCode=UWBWP>
- [2] T. S. R. (TSR), "2020 ultra wideband market analysis," 2020. [Online]. Available: <https://www.t-s-r.co.jp/en/report/3445/>
- [3] "Comments of the ultra wide band (uwb) alliance before the federal communications commission: Further notice of proposed rulemaking mid-band spectrum between 3.7 and 24 ghz," 6 2020. [Online]. Available: <https://ecfsapi.fcc.gov/file/106301642100595/UWBA%20Comments%20FCC%206GHz%20FNPRM%20June%2029%202020%20final.pdf>
- [4] H. Zhang, Z. Zhang, N. Gao, Y. Xiao, Z. Meng, and Z. Li, "Cost-effective wearable indoor localization and motion analysis via the integration of uwb and imu," *Sensors*, vol. 20, p. 344, 1 2020.
- [5] W. You, F. Li, L. Liao, and M. Huang, "Data fusion of uwb and imu based on unscented kalman filter for indoor localization of quadrotor uav," *IEEE Access*, vol. 8, pp. 64 971–64 981, 2020.
- [6] S. S. Bangera, T. D. Shiyana, G. K. Srinidhi, Y. R. Vasani, and M. S. Rao, "Mems-based imu for pose estimation," pp. 1–14, 2020.
- [7] B. V. Krishnaveni, K. S. Reddy, and P. R. Reddy, "Indoor tracking by adding imu and uwb using unscented kalman filter," *Wireless Personal Communications*, 11 2021.
- [8] V. Barral, P. Suárez-Casal, C. J. Escudero, and J. A. García-Naya, "Multi-sensor accurate forklift location and tracking simulation in industrial indoor environments," *Electronics (Switzerland)*, vol. 8, 10 2019.
- [9] MobileKnowledge, "Mobile knowledge uwb kit." [Online]. Available: <https://www.themobileknowledge.com/product/mk-uwb-kit-sr150-sr040/>

Comparison of machine learning models in outdoor temperature sensing by commercial microwave link

Ondřej Pospíšil¹, Petr Musil¹ and Radek Fujdiak¹

¹Brno University of Technology, FEEC, Department of Telecommunications, Brno, Czech Republic

E-mail: xpospi89@vut.cz, xmusal56@vutbr.cz, fujdiak@vut.cz

Abstract—The main objective of this work is to focus on outdoor temperature prediction using machine learning based on parameters from commercial microwave links. This information can be used to refine the weather information at a given link location. Three machine learning models (random forest, linear regression, and lasso) are used for prediction using a combination of two datasets (ERA5 weather dataset and CML monitoring database dataset). The results were evaluated based on two evaluation metrics (R^2 and mean absolute error (MAE)). In this work, the ERA5 outdoor temperature was found to be correlated with the temperature of the microwave link unit, and results were obtained with an accuracy of 0.87144 based on the MAE metric. Thus, the results can fairly well predict actual outdoor temperatures in the microwave link area based on the microwave link unit temperature.

Keywords— microwave link, machine learning, random forest, linear regression, lasso

1. INTRODUCTION

Possibilities of weather observation based on opportunistic approach by using commercial microwave links (CML) operated within cellular networks have been a subject of research for many years [1]. Numerous studies were already published where they mainly targeted the estimation of rainfall derived from attenuation of a microwave signal within the CML [2, 3]. The studies have shown that commercial microwave links could provide vast possibilities of very accurate weather observations and also predictions even within very short time periods (e.g. tens of seconds).

Beside measuring rainfall, researchers in study [4] also focused on sensing the temperature through a network of devices, where temperature sensors are built-in and monitored for different reasons - usually for monitoring whether the inner temperature of the device is within its safe operational range. Study [5] collects data from smartphones from 8 different cities to determine the temperature in different periods of the year. Some microwave units of microwave links also provide a possibility of monitoring the inner temperature of the outdoor unit (ODU) placed usually on the roof of buildings where they are directly affected by the actual weather at the given location. In this article we use temperature data obtained from CML via SNMP (Simple network management protocol).

Obtained values of inner temperature of ODU is being affected by two groups of factors:

- **factors increasing temperature:** sunbeams falling directly on the surface of ODU, heat produced by the electronics of the ODU, actual modulation scheme and transmission power of the whole microwave link.
- **factors decreasing temperature:** air flow and wind of temperature lower than the ODU temperature, precipitation (rain and snowfall).

Factors influencing the device temperature tend to affect the microwave unit in a different way throughout the year. Warmer months of the year have predominant effect of temperature increase caused by high intensity of sun radiation that warms up the chassis of the unit. Strong storms with high rain intensity also might cause immediate drop of the device temperature due to the cooling effect of raindrops which spray over the microwave unit chassis. On the other hand in colder months the intensity of sun radiation is significantly lower than in the summer period of the year. Cold wind and precipitation lead to further decrease of the device temperature. The difference of temperature characteristics in a typical summer and winter week can be seen in Figure 1.

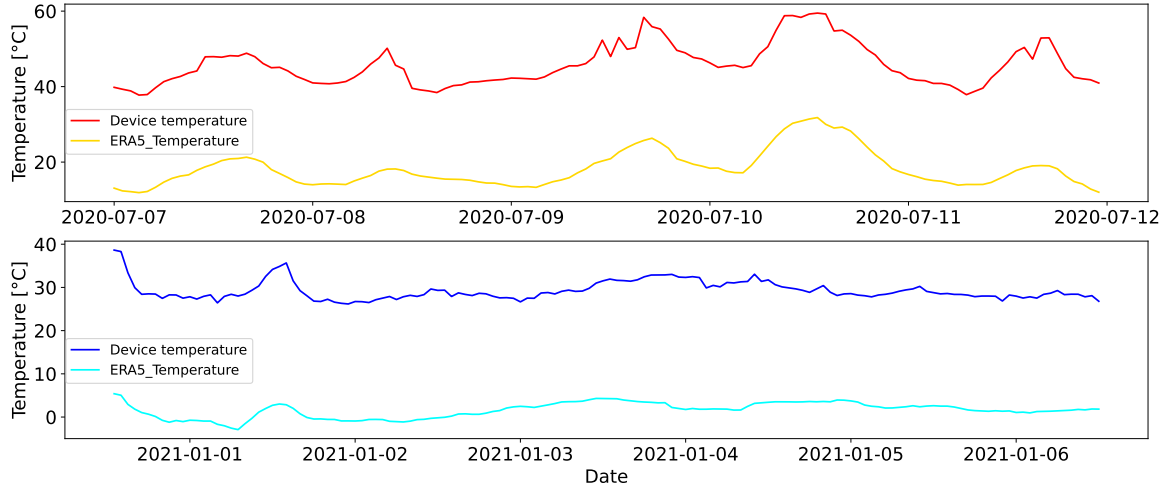


Figure 1: ERA5 temperature and device temperature in July and in January.

If all factors that influence the temperature of ODU were considered, we could estimate the actual outside temperature with a very high accuracy. Microwave links operators usually run networks consisting of large numbers of microwave units which could form a distributed network of sensors which could provide additional data for weather observation and monitoring that could improve accuracy of predictions. If temperature readings from precise certified weather stations were taken as reference, network of microwave link units with their coordinates would form a map that could provide a detailed overview about detailed temperature changes with high accuracy. Temperature trends of this microwave unit network could be also used as an estimate of cloudiness, sun radiation, wind, etc., due to its increase/decrease in the temperature of ODU. In this article we utilize methods of machine learning to produce accurate estimates of the outdoor temperature.

2. METHODS

The analysis consists of exploring the possibilities of predicting weather patterns based on information from microwave links. A large amount of data is generated and stored from these microwave links and can be used to refine information about weather conditions at the locations where they are deployed. Based on these data, we attempted to predict values from the ERA5 weather model. We focused on prediction using regression. For this we used machine learning methods namely Random forest, Linear regression and Lasso. The algorithms were chosen because of the nature of the data in the dataset, which are based on time series. We have also chosen the three given methods because of their frequent use with good results in works dealing with weather forecasting.

2.1. Dataset

For purposes of this work we were using two separate datasets:

- **ERA5 weather dataset** is being covered by the project of the European Centre for Medium-Range Weather Forecasts (ECMWF) which provides hourly estimates of a large number of meteorological and climatological variables. The data cover the whole Earth surface on a 30 km grid in the various heights up to 80 km. They are obtained via the reanalysis process, which combines the observations data (e.g. measurements from satellites, weather stations, radars (where available) but also aircrafts, radiosondes, ships, etc.) with past short-range weather forecasts. The method used at ECMWF for the combination of these atmospheric data is called four-dimensional variational data assimilation (4D-Var). The temperature parameter is the temperature of the air at 2 meters above the surface of land, sea or in-land waters. It is calculated by interpolating between the lowest model level and the Earth's surface, taking account of the atmospheric conditions.
- **CML monitoring database dataset** consist of monitored parameters of each microwave link which is being performed by the commercial microwave link operator. Collection and analysis of such data helps to determine early degradation of microwave link parameters such as signal degradation, radio interference, length of outages, etc. Such data could be also used in weather observation and analysis as a secondary use-case. Every microwave link is being interrogated every 30 seconds via

SNMP and all the information is being stored in the server database. Such values are being stored for 3 months, data older than 3 months are being downsampled and averaged to 5 minutes.

The dataset was created from the values from one microwave link. We have different datasets for 79 individual microwave links. We performed tests on 5 links in parallel and we obtained values that showed small variation. A description of our results is demonstrated using data from a single microwave link. Thus, the dataset used for the regression has a total of 17 parameters. The parameters can be divided into three categories, namely the parameters from the microwave link, the parameters from the ERA5 model (information about the weather in the microwave link area) and the time parameters:

- **Parameters from the microwave links:** Signal, signal to noise ratio, modulation scheme and device temperature.
- **Parameters from ERA5:** Temperature, horizontal wind speed in m/s, vertical wind speed in m/s, cloud cover in the range 0-1 (0 = clear, 1 = completely cloudy), hourly precipitation in m, hourly snowfall in m.
- **Time parameters:** Unixtime, year, month, day, day of the week, day of the year, time.

The dataset contains information on individual microwave links and weather values from ERA5 in hourly intervals. The dimension of the dataset is 14317 rows and 17 columns (14317,17). The data was collected from the period 26.06.2020 - 14.02.2022. For training and testing, the dataset was divided into two sets with a ratio of 80% training data to 20% testing data. In order to achieve the objectives of the work, all the parameters from the microwave link were extracted. Based on these parameters, the ERA5 temperature (the actual temperature from the ERA5 model at a given location) was first predicted.

In Table I, the first three rows of the dataset can be seen. It contains the following parameters. The first two parameters are the index number (not counted as a separate column, it is only informative) and unixtime. Then there are six values from the ERA5 weather model. ERA5_Temp (outdoor temperature), ERA5_W_u (wind speed in horizontal vector), ERA5_W_v (wind speed in vertical vector both values in meters per second), ERA5_Clouds (cloud value), ERA5_Prec (precipitation value) and ERA5_S (snowfall value). There are also 4 parameters from the microwave link, namely signal (signal strength), quality (signal quality), Mod (modulation) and temp (device temperature). The time values are Year, M (month), D (day), dW (day of the week), dY (day of the year) and T (time).

Table I: Sample of the first lines of the dataset.

	Unixtime	ERA5_Temp	ERA5_W_u	ERA5_W_v	ERA5_Clouds	ERA5_Prec	ERA5_S	signal	quality	Mod	temp	Year	M	D	dW	dY	T
0	1593158400	20.164209	-2.927006	0.287172	0.966443	0.000158	0.0	-48.913	27.74	5.0	50.242	2020	6	26	4	178	8
1	1593162000	21.133203	-2.709867	-0.281766	0.973783	0.000092	0.0	-48.797	27.74	5.0	49.048	2020	6	26	4	178	9
2	1593165600	20.563867	-3.737828	0.562858	0.553122	0.000126	0.0	-48.080	28.38	5.0	46.196	2020	6	26	4	178	10

2.2. Approach

As part of the regression problem, we addressed the temperature prediction (ERA5 model) in the microwave link area based on the microwave link parameters. Here, the most important parameter for this prediction was the temperature of the microwave link device itself. For this prediction, we dropped all other information from the ERA5 model from the dataset so that it would not affect the prediction. Subsequently, we used the three machine learning models namely Random forest, Linear regression and Lasso. For training, testing and evaluation of the individual machine learning models we used the best known machine learning library scikit-learn. We validated the evaluation and procedure on five different independent microwave link datasets.

2.3. Evaluation metrics

We used two popular metrics for evaluating regression models, namely R squared (R^2) and Mean Absolute Error (MAE). R^2 or the coefficient of determination, means how much of the variance of the depending variable can be explained with the variance of the independent variable. Simplified R^2 compares models predictions to the mean of the targets. The values can range from negative infinity (meaning very bad results) to the positive value of 1 (the best possible result). The MAE is calculated as the average of the sum of the absolute differences between the predicted values and the actual values. That is, how far on average the model predictions are from the actual values.

3. RESULTS

3.1. Regression results

In this section, we present experimental results of the regression models used for temperature prediction (ERA5_Temperature). The results of each model can be seen in Table II. These models are namely Random forest, Linear regression and Lasso.

Table II: Results of regression models for forecasting.

Regression	Train		Test	
	R^2	MAE	R^2	MAE
Random forest	0.99708	0.32080	0.97960	0.87144
Linear regression	0.94773	1.51182	0.94401	1.55142
Lasso	0.93874	1.62440	0.93385	1.67967

From the results in the table, it can be seen that the most appropriate model for this problem is the random forest regressor. Its R^2 value for the test data is 0.97960 and the MAE value is 0.87144, that is, the predicted data differ on average by 0.87144. The prediction could be refined with more data. The other two models already achieve worse values and are quite inaccurate. The Lasso model predicts the worst values when the predicted values differ from the actual values on average by 1.6796.

Next, we plotted the prediction results of each model into individual graphs which can be seen in Figure 2. Due to the large number of samples, we plotted only the first 100 rows in the graphs for clarity. So on the x-axis is the row index and on the y-axis is the ERA5 Temperature. The actual temperature is marked as the blue square and the predicted temperature as the red circle.

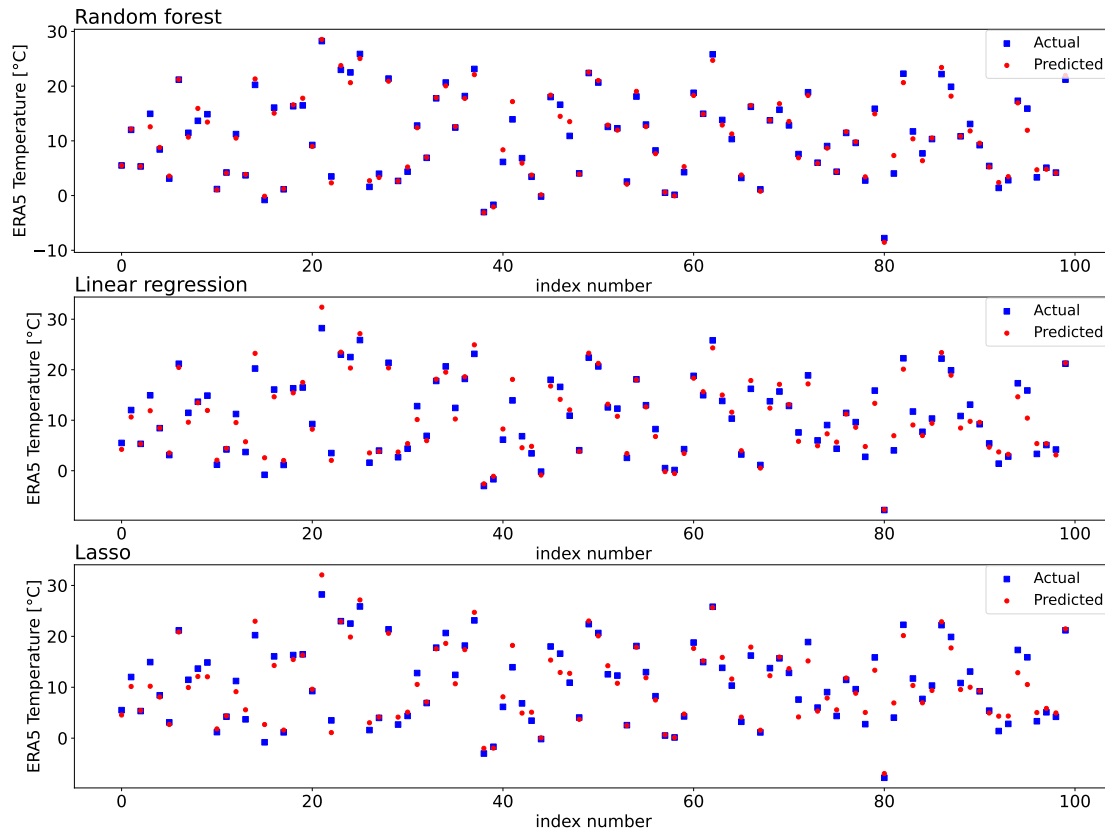


Figure 2: Actual and predicted values of the regression models.

According to the results it can be seen that the most accurate is the Random forest model, where the overlap of values is quite frequent, but there is a lot of deviation. On the other two models we can see already larger individual deviations of the prediction.

4. DISCUSSION

The main idea of the work was to investigate the possibilities of outdoor temperature prediction based on the values from commercially used microwave links, from which parameters such as signal strength, signal quality, modulation and device temperature can be obtained. As expected, the results show that the greatest influence on the prediction of the outdoor temperature for the models is the device's temperature. Thanks to this value, the outdoor temperature within a given microwave link can be predicted quite well after training. This information can be useful for adding information to weather models that may lack more precise data from a given area, and thus make this weather data more accurate. Of the three models chosen, the random forest had the best results. The reason may be that, in general, random forests provide better results and perform well on large data sets as they are able to handle missing data well by creating estimates for the missing data.

The limitations of our solution are mainly in testing fewer models and not using deep learning models. Furthermore, the hyperparameters of each model could also be better tuned in the future. The plan is to use other machine learning models, especially deep learning, which could make our results more accurate.

5. CONCLUSION

In this paper, we compared several machine learning methods for predicting ERA5 Temperature within our own dataset from a single microwave link. We validated the individual model values on four additional microwave link datasets, and the average difference for the MAE evaluation metric across the test results was as follows for each model: random forest – 0.03834, linear regression – 0.1283, and Lasso – 0.1562. From the point of view of the results, the random forest regressor seems to be the most appropriate model. Its accuracy was 0.97960 based on the evaluation metric R^2 and 0.87144 based on the MAE metric. With more weather values from the ERA5 weather model, we want to further explore the possibility of detecting other parameters such as cloud cover, precipitation, wind and snow. As mentioned in the text, the prediction of rainfall was not very successful for these models. Therefore, we would approach this problem by multiclass classification, where we would add several classes to the rain values based on the amount of rainfall. We would then use these values to predict how high the precipitation is based on the defined classes. In this way, other parameters (snowfall, wind, cloud cover, etc.) could also be approached. It would also be useful to compare deep learning methods with these results.

ACKNOWLEDGMENT

The described research is part of the grant project registered under no.TK02030013 and funded by the Technology Agency of the Czech Republic. This project was also supported by the company CBL Communication by light s.r.o. which provided datasets for this work. Authors would like to thank especially Mr. David Smékal for his willing cooperation.

REFERENCES

- [1] H. Leijnse, R. Uijlenhoet, and J. N. M. Stricker, "Hydrometeorological application of a microwave link: 2. Precipitation", *Water resources research*, vol. 47, no. 4, 2007. doi [10.1029/2006WR004989](https://doi.org/10.1029/2006WR004989).
- [2] C. Chwala and H. Kunstmann, "Commercial microwave link networks for rainfall observation: Assessment of the current status and future challenges", *WIREs Water*, vol. 6, no. 2, 2019, doi: [10.1002/wat2.1337](https://doi.org/10.1002/wat2.1337).
- [3] M. Fencl, M. Dohnal, P. Valtr, M. Grabner, and V. Bares, "Atmospheric observations with E-band microwave links - challenges and opportunities", *Atmospheric measurement techniques*, vol. 13, no. 12, pp. 6559-6578, 2020. doi [10.5194/amt-13-6559-2020](https://doi.org/10.5194/amt-13-6559-2020).
- [4] D. Vos, A. M. Ste, M. J. Zander, A. Overeem, H. Leijnse, B. G. Heusinkveld, G. J. Steeneveld, and R. Uijlenhoet, "Hydrometeorological monitoring using opportunistic sensing networks in the Amsterdam metropolitan area", *Bulletin of the American Meteorological Society*, vol. 101, no. 2, pp. E167-E185, 2020. doi [10.1175/BAMS-D-19-0091.1](https://doi.org/10.1175/BAMS-D-19-0091.1).
- [5] A. Overeem, J. C. R. Robinson, H. Leijnse, G. J. Steeneveld, B. K. P. Horn, and R. Uijlenhoet, "Crowdsourcing urban air temperatures from smartphone battery temperatures", *Geophysical research letters*, vol. 40, no. 15, pp. 4081-4085, 2013. doi [10.1002/grl.50786](https://doi.org/10.1002/grl.50786).

Beam Deflection Analysis of the Turbulent Matrix Model

A. Kovalova and L. Hudcova

Brno University of Technology, Czech Republic

E-mail: xkoval13@vut.cz, hudcova@vut.cz

Abstract—This paper is focused on the analysis of optical beam deflection by propagation through a matrix model of a turbulent cascade. The technique of turbulent cell modeling with a matrix description of the used optical elements is explained. There are introduced two turbulent models. In the first model, the influence of the position and dimensions of the turbulent cells on the beam deflection is observed. In the second model, the matrix turbulent medium between the transmitter and receiver is matrix-defined due to the data from the analysis of the deflection parameters.

Keywords—Atmospheric turbulence, matrix optics, cascade of turbulent cells, turbulent model, ABCD matrix

1. INTRODUCTION

The atmosphere is considered a non-stationary and inhomogeneous medium in which the occurrence of turbulence is a common phenomenon [1]. Nevertheless, the volume of atmospheric turbulence in the horizontal direction can be considered homogeneous and stationary [2]. Atmospheric turbulence, generated by a temperature differential between the Earth's surface and the atmosphere, causes distortion effects on optical communication waves. Temperature variations and wind-speed fluctuations create unstable air masses, causing them eventually to break up into turbulent cells of many different scale sizes [1]. Depending on the size of the turbulent cells, various phenomena occur [3], such as scintillation, beam wander, incident angle fluctuations, etc.

The model described in this paper operates with large turbulent cells whose diameter is larger than the width of the optical beam, which causes the beam to wander [1]. Because of the different refractive indices of the turbulent cells, the laser beam passing through the turbulent cell is deflected from the original direction [4]. This turbulent matrix model assumes a stationary atmosphere and can be used for horizontal communication channel modeling. Then, it would be possible to simulate a communication channel and predict the propagation of the optical beam. The simulation would provide data to direct the optical beam before communication initiates.

2. TURBULENT MATRIX MODEL

The turbulent model is based on geometric optics. Each turbulent cell is approximated by a thick lens [5]. There exists a beam tracking technique that describes thick lenses via ABCD matrices or also called ray transfer matrices [6]. Calculation of deflection parameters takes form [7]

$$\begin{pmatrix} x_{OUT} \\ \theta_{OUT} \end{pmatrix} = \begin{pmatrix} A & B \\ C & D \end{pmatrix} \begin{pmatrix} x_{IN} \\ \theta_{IN} \end{pmatrix}, \quad (1)$$

where the deflection of the beam on the output plane x_{OUT} and the angle of deflection of the beam from the optical axis θ_{OUT} create the vector. The mathematical technique connects the outgoing beam vector with the incoming beam vector.

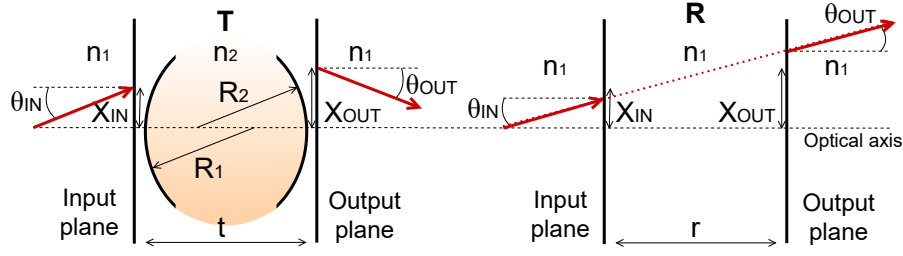


Figure 1: Model of turbulent cell and inter-turbulent space [5]

The beneficial feature of this model is that it includes not only information about changes in the refractive index, which characterizes the turbulent atmosphere, but also the dimensions of the turbulent cell as is shown in the Figure 1. The ABCD matrix defined for the thick lens takes the form [6]

$$T = \begin{pmatrix} A & B \\ C & D \end{pmatrix} = \begin{pmatrix} 1 & 0 \\ \frac{n_2 - n_1}{R_2 n_1} & \frac{n_2}{n_1} \end{pmatrix} \begin{pmatrix} 1 & t \\ 0 & 1 \end{pmatrix} \begin{pmatrix} 1 & 0 \\ \frac{n_1 - n_2}{R_1 n_2} & \frac{n_1}{n_2} \end{pmatrix}, \quad (2)$$

where n_1 is refractive index outside of turbulent cell, n_2 is refractive index of the turbulent cell itself, R_1 presents radius of curvature of the first surface, R_2 presents radius of curvature of the second surface and t is the center thickness of lens [5, 6]. Each inter-turbulent space is defined by its ABCD matrix [5]

$$R = \begin{pmatrix} A & B \\ C & D \end{pmatrix} = \begin{pmatrix} 1 & -r \\ 0 & 1 \end{pmatrix}, \quad (3)$$

where r denotes the width of the area with constant refractive index. The matrix is derived using a trigonometric function and paraxial approximation. The presence of paraxial rays is a condition for using this technique [6] for which the following applies

$$\tan(\theta) \approx \theta, \quad (4)$$

where θ represents the angle formed by the optical beam with the auxiliary axis parallel to the optical axis of the system [5]. More detailed description of the derivation and calculation can be found in [5].

3. ANALYSIS OF TURBULENT MODEL

This section is focused on modeling of turbulent cascade and the laser beam deflection analysis. According to the previous description, two models are created using mentioned optical elements. The first model has defined turbulent cells parameters and the second model has no defined turbulent medium. Both models have predetermined beam input deflections so that the beam deflection meets the paraxial condition.

3.1. Calculation of the Deflection at the Receiver

In this simulation, the nature of turbulence (position of five turbulent cells in a cascade), the dimensions, and state variables of individual cells are known. Each turbulent cell is defined by an immediate refractive index value that is temperature, pressure, and spectral dependent, as indicated by the relation [1]

$$n(\lambda) = 1 + 77.6 \cdot 10^{-6} (1 + 7.52 \cdot 10^{-3} \cdot \lambda^{-2}) \frac{P}{T}, \quad (5)$$

where P is air pressure and T is the thermodynamic temperature at a given location. The spectral dependence is related to the specific wavelength laser with which the communication link is implemented. The refractive indices found in Table I are calculated according to the mentioned relation (5), assuming a constant value of air pressure $P = 102850$ Pa and laser wavelength $\lambda = 632.8 \mu\text{m}$. The values of the refractive index vary due to different thermodynamic temperatures.

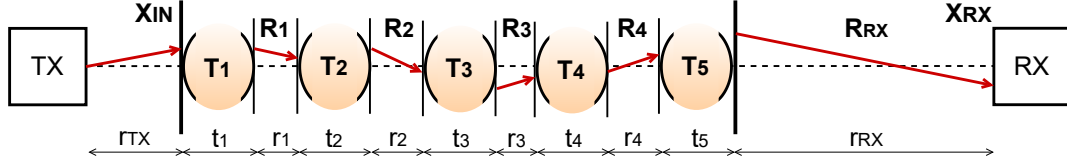


Figure 2: Cascade model of the turbulent medium in the communication link

Figure 2 shows the layout of the transmitter/receiver and the turbulent area. Each turbulent cell is defined by its ray transfer matrix denoted as T_1 – T_5 and each inter-turbulent space is defined by matrix denoted as R_1 – R_4 [5] and R_{RX} is matrix defining the area between the turbulence and the receiver of length r_{RX} .

In addition to the quantities characterizing turbulent cells, inter-turbulent distances are also predetermined. All of these dimensions are uniformly distributed random numbers generated according to the ranges listed in the Table I and Table II.

Table I: Parameters defining turbulent cells, where R denotes the radii of curvature of the cells ($R = R_1 = R_2$), t denotes their central thickness, both of them are randomly generated in given ranges, and T is the thermodynamic temperature determining the value of the refractive index n .

Cell order	1.	2.	3.	4.	5.
R [cm]	2–6	5–10	2–6	1–5	2–6
t [cm]	2–4	3–6	2–6	1–3	2–6
T [(K)]	295.15	296.15	295.15	294.15	297.15
n [-]	1.027549	1.027456	1.027549	1.027643	1.027363

Table II: Transmitter/receiver distances r_{TX}/r_{RX} to turbulent cascade and inter-turbulent distances r_{14} .

r_{TX} [m]	r_1 [cm]	r_2 [cm]	r_3 [cm]	r_4 [cm]	r_{RX} [m]
0.5–1	1–2	5–10	5–15	2–8	1–2

The input deflection angle θ_{IN} of the beam is equal to 0.05° . Using the known distance r_{TX} and the tangent function, the deflection on the input plane of the first turbulent cell x_{IN} is obtained. By creating a turbulent model and setting the deflection of the input beam, the individual vectors are obtained using the matrix technique

$$\begin{pmatrix} x_2 \\ \theta_2 \end{pmatrix} = T_1 \begin{pmatrix} x_{IN} \\ \theta_{IN} \end{pmatrix}, \quad \begin{pmatrix} x_3 \\ \theta_3 \end{pmatrix} = R_1 \begin{pmatrix} x_2 \\ \theta_2 \end{pmatrix}, \quad \dots \quad (6)$$

where x_2 denotes the beam deflection at the output plane of the first turbulent cell and θ_2 is the angle of beam deflection outgoing from the first turbulent cell. x_3 is the deflection at the input of the second turbulent cell with the incoming beam angle θ_3 , etc.

Due to the presence of paraxial rays, the calculation of the deflection vector can be simplified. The detected deflection vector is calculated by multiplying the matrices in the form [5]:

$$X_{RX} = R_{RX} \cdot T_5 \cdot R_4 \cdot T_4 \cdot R_3 \cdot T_3 \cdot R_2 \cdot T_2 \cdot R_1 \cdot T_1 \cdot X_{IN}. \quad (7)$$

This mathematical apparatus leads to the output data shown in Figure 3. The graph 3 a) shows the dependence, which demonstrates the influence of the receiver distance r_{RX} on the detected deflection. The greater the distance is, the more significant the beam deflection is. The negative values on the y-axis indicate the beam deflections below the optical axis. The graph 3 b) shows the change in the values of individual elements of the ABCD matrix for a randomly generated turbulent cascade.

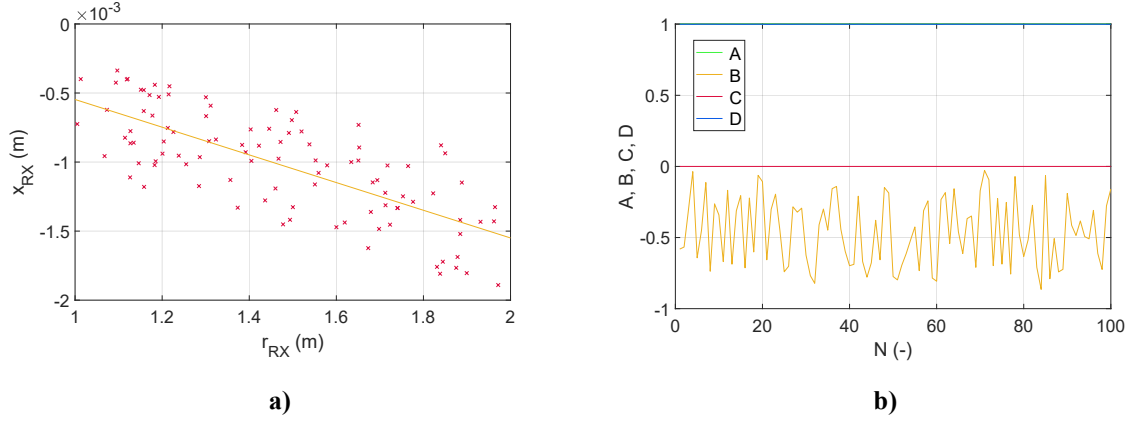


Figure 3: Simulation outputs: a) detected output deflections after passing through a turbulent cascade and its dependence on the receiver distance, b) ABCD parameters of the whole turbulent cascade

3.2. Calculation of ABCD Matrix Using Input and Detected Deflections

In this simulation, the turbulent area is unknown. The input parameters for this model are the initial deflections of the transmitted beam and the deflections detected on the receiver. The aim is to obtain an ABCD matrix describing the entire turbulence. The input deflection angle θ_{IN} of the beam is equal to 0.05° , and the input deflection increases linearly with increasing transmitter distance r_{TX} in the range of $0.1 - 10$ m.

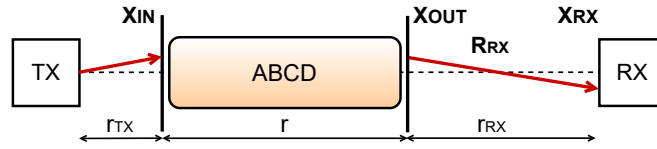


Figure 4: Cascade model of turbulent medium

First to be determined are the beam deflections parameters in the output plane of the turbulent cascade x_{OUT} , θ_{OUT} forming the vector denoted X_{OUT} . The implementation of matrix (3) results in an expression

$$\begin{pmatrix} x_{OUT} \\ \theta_{OUT} \end{pmatrix} = \begin{pmatrix} 1 & -r_{RX} \\ 0 & 1 \end{pmatrix} \begin{pmatrix} x_{RX} \\ \theta_{RX} \end{pmatrix}, \quad (8)$$

which can be symbolically rewritten according to Figure 4 in the form:

$$X_{OUT} = R_{RX} \cdot X_{RX}. \quad (9)$$

The ABCD matrix of whole turbulent cascade is calculated from the equation:

$$\begin{pmatrix} x_{OUT} \\ \theta_{OUT} \end{pmatrix} = \begin{pmatrix} A & B \\ C & D \end{pmatrix} \begin{pmatrix} x_{IN} \\ \theta_{IN} \end{pmatrix}. \quad (10)$$

By rewriting the matrix form of the calculation, a system of two equations with four unknowns (A, B, C, D) is obtained. The values A and D of the matrix defining the entire turbulence were close to the one in the previous model. For this reason, it is assumed to simplify that the A and D are equal to one. The solution of the system are these equations for the all parts of the turbulence matrix

$$A = 1, \quad B = \frac{x_{OUT} - x_{IN}}{\theta_{IN}}, \quad C = \frac{\theta_{OUT} - \theta_{IN}}{x_{IN}}, \quad D = 1. \quad (11)$$

Figure 5 a) shows the input data, which are input and detected deflections and in Figure 5 b), the values B and C of the ABCD matrix are calculated for the given input data. The most significant change is visible for the value of B because in the numerator there are relatively higher values of deflections compared to

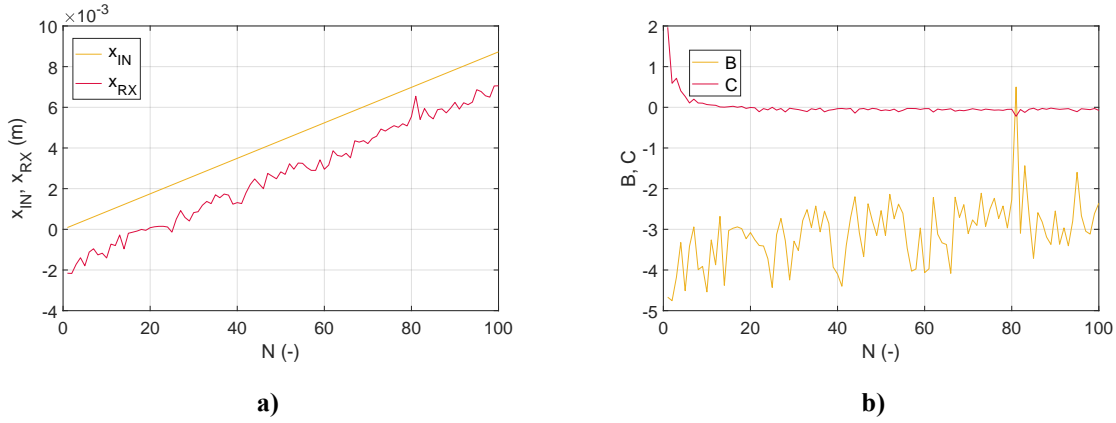


Figure 5: Simulation outputs: a) beam input and detected output deflections after passing through a turbulent cascade, b) parameters B and C from the ABCD matrix and their change for N realizations of the beam transition by turbulent cascade

the value of C. Parameter C has low values of the angles in the numerator and, on the other hand, a high value of the deflection in the denominator, which leads to its low value.

4. CONCLUSION

Simulations for two models were performed in which the turbulence was described by matrix optics using ABCD optical elements definition. In the first model, turbulence is modeled using given dimensions, distances, and changes in refractive indices. The use of matrix multiplication leads to results indicating the movement of the beam on the detector as a function of the receiver distance. For the second model, the input data are the deflections parameters of the incoming beam to the turbulent area and the detected deflections on the receiver. The turbulent area is unknown, only the positions of turbulence to the transmitter and receiver are known. The output is the reverse modeling of turbulence from the obtained deflection data. In the future, it is possible to create turbulence models using measured meteorological data and measured deflections of the test beams and thus determine the effective direction of optical beam transmission.

ACKNOWLEDGMENT

This publication is based upon work from COST Action CA19111 - European Network on Future Generation Optical Wireless Communication Technologies (NEWFOCUS), supported by COST (European Cooperation in Science and Technology).

The research was supported also by the project FEKT-S-20-6361.

REFERENCES

- [1] L. C. Andrews and R. L. Philips, *Laser beam propagation through random media*. Bellingham: SPIE Press, 1998.
- [2] L. Hudcova and O. Wilfert, "Prediction of atmospheric turbulence on the basis of weather conditions," 2017 Conference on Microwave Techniques (COMITE), 2017, pp. 1–5.
- [3] M. Hulea, X. Tang and S. Rajbhandari, "A review on effects of the atmospheric turbulence on laser beam propagation – An analytic approach," 2016 10th International Symposium on Communication Systems, Networks and Digital Signal Processing (CSNDSP), 2016, pp. 1–6.
- [4] C. Lamprecht, P. Bekhrad, H. Ivanov and E. Leitgeb, "Modelling the Refractive Index Structure Parameter: A ResNet Approach," 2020 International Conference on Broadband Communications for Next Generation Networks and Multimedia Applications (CoBCom), 2020, pp. 1–4.
- [5] A. Kovalova and L. Hudcova, "Matrix Model of the Turbulent Cells Cascade," *Radioengineering*, unpublished manuscript.
- [6] A. Gerrard and J. M. Burch, *Introduction to matrix methods in optics*. New York: Dover, 1994.
- [7] H. Kogelnik and T. LI, "Laser beams and resonators," *Proceedings of the IEEE*, vol. 54, no. 10, pp.1312–1329, 1966.



STUDENT EEICT



BRNO UNIVERSITY OF TECHNOLOGY
FACULTY OF ELECTRICAL ENGINEERING AND COMMUNICATION
TECHNICKÁ 3058/10, 616 00 BRNO, CZECH REPUBLIC



BRNO FACULTY OF ELECTRICAL
UNIVERSITY ENGINEERING
OF TECHNOLOGY AND COMMUNICATION

www.eeict.cz



www.fekt.vut.cz

